Springer Series in Solid-State Sciences 197

Masafumi Udagawa
Ludovic Jaubert *Editors*

Spin Ice

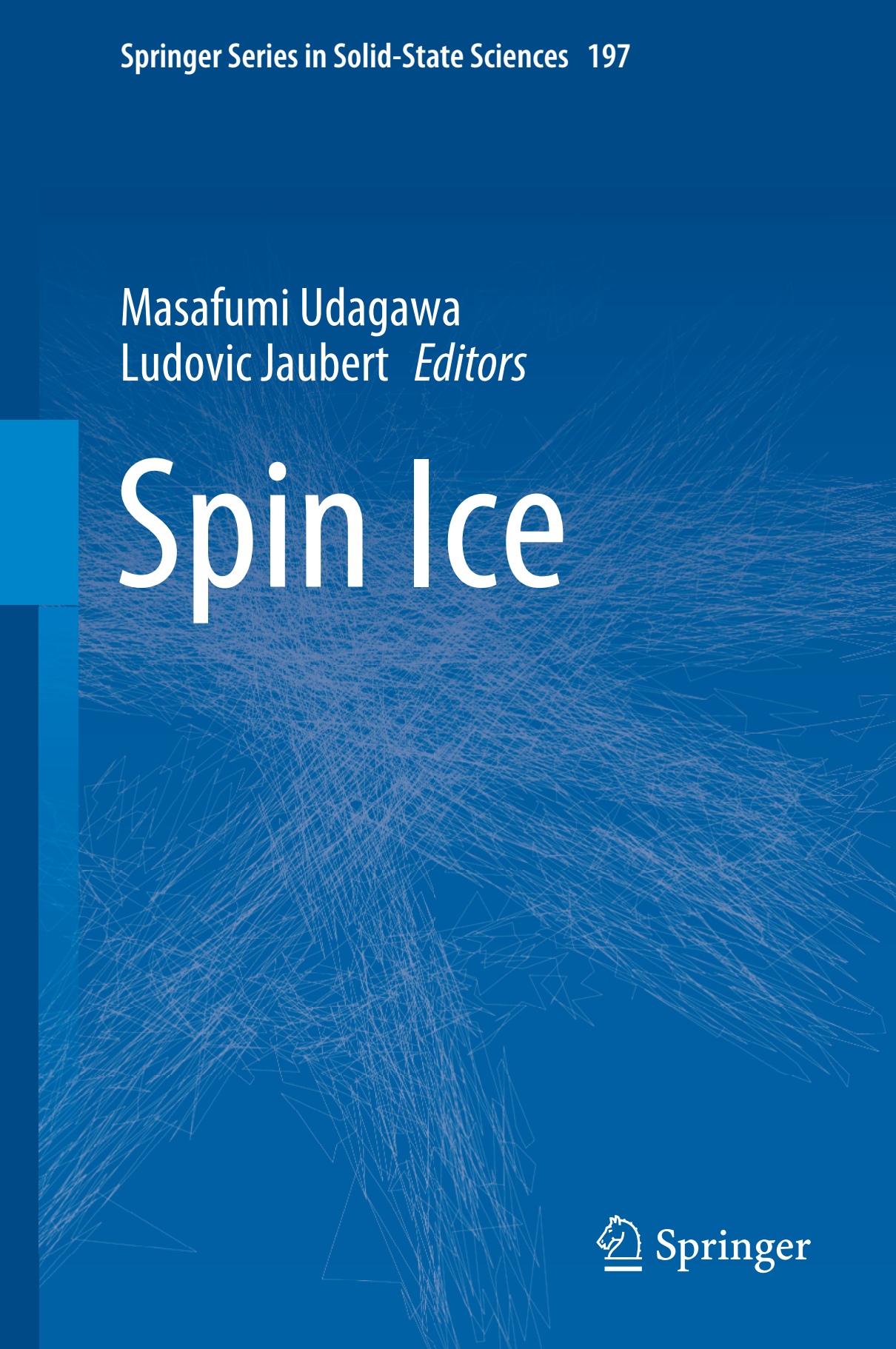

Springer

Springer Series in Solid-State Sciences

Volume 197

The Springer Series in Solid-State Sciences features fundamental scientific books prepared by leading and up-and-coming researchers in the field. They strive to communicate, in a systematic and comprehensive way, the basic principles as well as new developments in theoretical and experimental solid-state science.

We welcome submissions for monographs or edited volumes from scholars across this broad domain. Topics of current interest include, but are not limited to:

- Semiconductors and superconductors
- Quantum phenomena
- Spin physics
- Topological insulators
- Multiferroics
- Nano-optics and nanophotonics
- Correlated electron systems and strongly correlated materials
- Vibrational and electronic properties of solids
- Spectroscopy and magnetic resonance

More information about this series at http://www.springer.com/series/682

Masafumi Udagawa · Ludovic Jaubert
Editors

Spin Ice

Springer

Editors
Masafumi Udagawa
Department of Physics
Gakushuin University
Tokyo, Japan

Ludovic Jaubert
Laboratoire Ondes et Matière d'Aquitaine
Université de Bordeaux, CNRS
Bordeaux, France

ISSN 0171-1873 ISSN 2197-4179 (electronic)
Springer Series in Solid-State Sciences
ISBN 978-3-030-70858-0 ISBN 978-3-030-70860-3 (eBook)
https://doi.org/10.1007/978-3-030-70860-3

This Springer imprint is published by the registered company Springer Nature Switzerland AG
The registered company address is: Gewerbestrasse 11, 6330 Cham, Switzerland

Preface

Most of us discovered magnetism during our childhood, intrigued by this invisible force between the red and blue parts of a coloured bar magnet. This attraction—in every sense of the term—resonates with explorers of distant worlds and their compass, with the fridge magnets of our daily life, tokens of summer memories and even with the powers of superheroes. The mysterious charm of magnets has often piqued our curiosity and must have attracted many kids into science, including maybe some of you, esteemed readers. How many of us have wondered how to separate the red and blue parts of a magnet, keeping the north and south poles in different hands? In this book, we will endeavour to show how our child dream can be realised in a crystal known as "spin ice".

The term spin ice was introduced by Mark Harris, Steve Bramwell and collaborators in 1997. First applied to the rare-earth oxide, $Ho_2Ti_2O_7$, this term quickly covered a broad range of compounds, $Dy_2Ti_2O_7$, $Ho_2Sn_2O_7$, more recently $CdEr_2Se_4$... with magnetic ions lying on the so-called pyrochlore lattice. While magnets traditionally order when cooled down, resulting in a vanishing entropy, spin-ice compounds turned out to remain disordered down to unexpectedly low temperatures. The reason for this magnetic disorder is the presence of a macroscopically degenerate ground state with a finite residual entropy. And the key point of the discovery is that this degenerate manifold is analogue to the one predicted by Linus Pauling for water ice back in 1935! The spin moments of the magnetic system respect the same local (ice) rule than the position of protons in water ice. This analogy gave its name to spin ice and initiated decades of research between chemists, experimentalists and theorists to understand this fascinating system.

To begin with, this degenerate ground state challenges our intuition. As condensed matter physicists, we often see the world through the prism of Landau-Ginzburg-Wilson (LGW) theory. However, LGW theory relies on the existence of an order parameter, and thus of a broken symmetry, which is absent in spin ice. A new approach is thence necessary. Climbing on the shoulders of another giant of the twentieth century—Philip Warren Anderson—the solution is to apply the principle that "More is different". The local constraint imposed by the ice rule on spins translates into a coarse-grained zero-divergence constraint on the

magnetisation field. In other words, the spin-ice ground state is described by a fluctuating Coulomb gauge field, i.e. respecting the equations of a magnetic field. This gauge field is populated by a disordered assembly of magnetic lines which are the new, extended, degrees of freedom of the system. When these magnetic lines cross the lattice, they carry a winding number allowing for the definition of topological sectors. By definition here, the winding number is proportional to the magnetisation. Spin ice thus offers a unique opportunity to manipulate topological sectors, inducing topological phase transitions, with external probes such as a magnetic field.

But the magic of spin ice is that this emergent gauge field differs in one crucial aspect from the standard description of electromagnetism. Excitations out of the ground state are point-like topological defects, always created and annihilated by pairs, that break the local zero divergence. As such these quasi-particles are sources and sinks of the magnetic field in the crystal and behave precisely like positive and negative magnetic charges! The long-range Coulomb potential between them is simply a rewriting of the magnetic dipolar interaction between spins. Besides, thanks to the remarkable geometry of the pyrochlore lattice these magnetic charges are deconfined; two magnetic monopoles created by one single spin flip. This is the definition of fractionalisation, a common phenomenon in one dimension, but a remarkable feature in our three-dimensional world.

In a nutshell, the north and south poles of a (tiny) magnet can be separated in a spin-ice crystal, making our child dream come true!

Since these magnetic charges are mobile, they rearrange the magnetic lines along their wake and are responsible for non-trivial dynamics both at and out-of equilibrium. On many aspects, the wake left by two monopoles moving away from each other is a classical analogue of the Dirac strings hypothesised by Paul Dirac in 1931. When quantum fluctuations are included, quantum dynamics of the effective magnetic field induces an emergent electric field. The analogy to electromagnetism is then fully established—enriched with magnetic charges—and emergent photon excitations become possible at very low energy.

Research on spin ice has been a remarkable example of joint evolution between experiment and theory, with exciting experimental results leading to a constant improvement of the model and motivating new directions, and with theoretical ideas directly tested in the lab. For example, the zero-temperature residual entropy was measured via calorimetry early on. DC– and AC–SQUID magnetometers were also readily available to measure the susceptibility and magnetic relaxation. In particular, magnetic relaxation offered one of the early experimental signatures of magnetic monopoles in spin ice. Spin ice also owes part of its fame to the impressive work of chemists who managed to grow single crystals long of several centimetres. This achievement was instrumental in many ways. Because of the single-ion anisotropy, it allowed for a systematic analysis using an external magnetic field applied along different orientations. These orientations were as many viewpoints helping to build a global picture of spin-ice physics. By using a [111] field as an effective chemical potential for monopoles, a liquid-gas phase diagram with a critical end point was observed. This confirmed the interacting, but

nonetheless deconfined, nature of the magnetic charges. Additionally, big single crystals made neutron scattering, and in particular inelastic and polarised neutron scattering, accessible in the full three-dimensional Fourier space. Neutron scattering quickly became the microscopic probe of excellence for spin ice. Correlations of the Coulomb gauge field appear as a characteristic singularity called "pinch points", while the overall scattering pattern, reminiscent of a hexagonal snow flake, nowadays serves as an icon of spin-ice physics. Chemical pressure—i.e. substituting a non-magnetic ion by another one—also became a powerful tool to tune the Hamiltonian while approximately keeping the nature of the magnetic ions intact.

Where does spin ice stand in the Physics family picture? One of our goal in this book is to show that what makes spin ice truly unique is not its specificity but rather its generality. A special model or material sometimes provides crucial insights into the mechanisms underlying our world. The Ising model gives us an essential perception about phase transitions and critical phenomena. Spin ice is one of these gift systems which unveil key aspects of physics. The passage from the microscopic spin system to the emergent gauge field and topological sectors, as well as the presence of magnetic monopoles, is well understood. Spin ice has become a textbook example for concepts beyond the Landau-Ginzburg-Wilson paradigm that are at the heart of modern-day condensed matter physics: topology, emergent phenomena, fractionalisation... Most importantly, spin ice embodies these concepts in real materials.

The generality of spin ice makes contact with diverse areas of physics. Its macroscopic degeneracy is just one step away from the notion of quantum superposition and the possibility of long-range entanglement. The quest for quantum spin-ice materials, in the broad sense, is an active field of research and the diversity of directions to consider makes it a very promising path for exotic physics. With the emergence of magnetic charges, spin ice also offers a new platform for the study of electrolytes, or more precisely "magnetolytes", enriched by the plethora of experimental probes available to magnetic systems. Playing with chemical pressure and temperature, different regimes are available from weakly to strongly correlated. In parallel, the extended degrees of freedom populating the ground-state manifold share fundamental properties with polymers, cosmic strings and even Stochastic Loewner Evolutions (SLE) in mathematics.

Moving away from standard spin ice, the coupling to itinerant electrons opens the door to a new field. Itinerant spin ice is one of the cradles of the phenomenon called topological Hall effect. The inherent non-coplanar magnetic configurations lead to a finite spin-scalar chirality, which gives non-trivial transport properties with an anomalous velocity of the propagating electrons. Another ambitious direction is the engineering of spin ice via nanotechnology. Many aspects of spin ice can be reproduced by using an artificial network of permalloy nano-islands, or colloids. Artificial spin ice has become a field of research on its own, with its own challenges and a rich versatility of models that are often limited only by the imagination of the physicist.

How to use this book? After the introductory chapters I and II, the book is divided into two main parts: "canonical spin ice" (Chaps. 3–8) and "beyond spin ice" (Chaps. 9–16). It is recommended to read the book linearly. However, since the chapters are to a good extent independent, it is also possible to jump directly to the chapter of interest, where references to the necessary notions in the book are referenced. For a given topic, theory chapters are generally followed by their experimental counterpart.

The introductory chapters provide a general background to understand the crystal structure, its relation to the physical model and the chemistry of spin ice. Chapter 1 addresses the microscopic basis of spin ice, where the canonical spin Hamiltonian is derived from the underlying electronic model. Chapter 2 treats the material basis of spin ice, introducing the synthesis of pyrochlore materials.

The first part provides a detailed presentation of classical spin ice. Chapter 3 introduces the concept of magnetic monopoles after describing the ground-state Coulomb phase. It covers the concepts of residual entropy, emergent electromagnetism and fractionalisation. Chapter 4 gives the collection of experimental results on the dynamics of spin ice. Chapter 5 addresses the effect of a magnetic field along different orientations, with a special focus on the liquid-gas-type phase diagram. Chapter 6 details the topological structure of the ground-state manifold and its analogy to loop models. Chapter 7 models spin ice as an assembly of monopoles, and accounts for the unusual equilibrium/non-equilibrium properties of spin ice. Chapter 8 focuses on the experimental verification of the Coulomb phase and monopole description of spin ice.

The second part explores new areas beyond canonical spin ice, including quantum coherence, itinerant electrons and artificial lattices. Chapter 9 gives the theoretical introduction to quantum spin ice, based on the gauge-mean-field theory. Chapter 10 presents the evidence, especially numerical, for the realisation of quantum spin ice in microscopic theoretical models. Chapter 11 details the analytical technique indispensable to spin ice and quantum spin ice. Chapter 12 summarises the experimental status for the realisation of quantum spin ice, in the broad sense, in pyrochlore oxides. Chapter 13 addresses the basics of itinerant spin ice and its application to a material. Chapter 14 gives an experimental summary of itinerant spin ice. Chapter 15 gives the theoretical description of artificial spin ice. The final chapter, Chap. 16, summarises the experimental status of the field of artificial spin ice.

Tokyo, Japan — Masafumi Udagawa
Bordeaux, France — Ludovic Jaubert

Contents

Contributors

Leon Balents Kavli Institute of Theoretical Physics, University of California, Santa Barbara, USA

Owen Benton Max Planck Institute for the Physics of Complex Systems, Dresden, Germany

Steven T. Bramwell Department of Physics and Astronomy and London Centre for Nanotechnology, University College London, London, UK

C. Castelnovo TCM group, Cavendish Laboratory, University of Cambridge, Cambridge, UK

Gia-Wei Chern Department of Physics, University of Virginia, Charlottesville, USA

T. Fennell Laboratory for Neutron Scattering and Imaging, Paul Scherrer Institute, Villigen, Switzerland

M. J. P. Gingras Department of Physics and Astronomy, University of Waterloo, Waterloo, Ontario, Canada;
Quantum Materials Program, Canadian Institute for Advanced Research, MaRS Centre, Toronto, ON, Canada

Zenji Hiroi Institute for Solid State Physics, University of Tokyo, Chiba, Japan

P. C. W. Holdsworth Université de Lyon, ENS de Lyon, Université Claude Bernard, CNRS, Lyon, France

L. D. C. Jaubert CNRS, LOMA, University of Bordeaux, Bordeaux, France

Christopher H. Marrows School of Physics & Astronomy, University of Leeds, Leeds, UK

K. Matsuhira Kyushu Institute of Technology, Kitakyushu, Japan

P. A. McClarty Max Planck Institute for the Physics of Complex Systems, Dresden, Germany

Roderich Moessner Max Planck Institute for the Physics of Complex Systems, Dresden, Germany

S. Nakatsuji Institute for Solid State Physics, University of Tokyo, Chiba, Japan

D. Prabhakaran Department of Physics, Clarendon Laboratory, University of Oxford, Oxford OX1 3PU, UK

J. G. Rau Department of Physics, University of Windsor, Windsor, Ontario, Canada

Kate A. Ross Colorado State University, Fort Collins, CO, USA

Toshiro Sakakibara Institute for Solid State Physics, University of Tokyo, Chiba, Japan

Lucile Savary Université de Lyon, ENS de Lyon, Université Claude Bernard, CNRS, Laboratoire de Physique, Lyon, France

Nic Shannon Okinawa Institute of Science and Technology Graduate University, Okinawa, Japan

Masafumi Udagawa Department of Physics, Gakushuin University, Tokyo, Japan

Chapter 1
Spin Ice: Microscopic Physics

M. J. P. Gingras, P. A. McClarty, and J. G. Rau

Abstract This chapter describes the microscopic physics of the rare-earth pyrochlore oxides, focussing on the lattice structure, the strong spin-orbit coupling, the crystal electric field and the large magnetic moment. We explain each of these in turn and how they are connected before examining the types of interaction that may arise in rare-earth pyrochlores. Taking all these ingredients together, we arrive at a relatively straightforward effective model that is known to capture, in quantitative detail, the thermodynamics of the classical spin ice materials.

1.1 Introduction

The remarkable collective magnetic behaviour of spin ice materials at low temperature rests on the confluence of various microscopic properties. Starting from the atomic physics of the lanthanides and through a rapid tour of aspects of 20th century magnetism, we explain how spin ice physics originates. At the end of this chapter, if we have done our job well, the reader should appreciate how spin ice physics arises in rare-earth magnets and why the existence of spin ices is a robust consequence of a few fundamental microscopic ingredients: the crystal structure, quantum mechanics and spin-orbit coupling.

M. J. P. Gingras (✉)
Department of Physics and Astronomy, University of Waterloo, Waterloo, Ontario, Canada

Quantum Materials Program, Canadian Institute for Advanced Research, MaRS Centre, West Tower 661 University Ave., Suite 505, Toronto, ON M5G 1M1, Canada
e-mail: gingras@uwaterloo.ca

P. A. McClarty
Max Planck Institute for the Physics of Complex Systems, Dresden, Germany

J. G. Rau
Department of Physics, University of Windsor, 401 Sunset Avenue, Windsor, Ontario N9B 3P4, Canada

M. Udagawa and L. Jaubert (eds.), *Spin Ice*, Springer Series in Solid-State Sciences 197,
https://doi.org/10.1007/978-3-030-70860-3_1

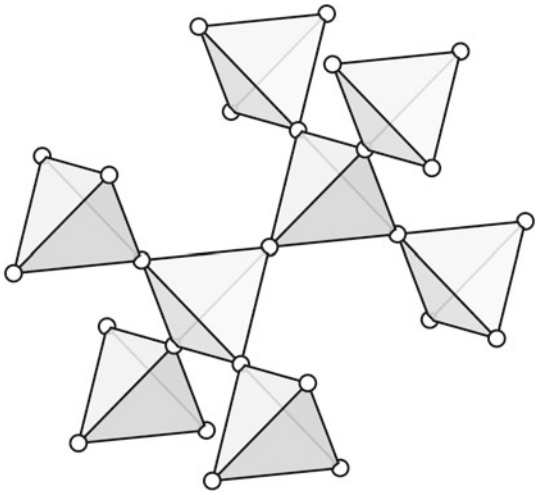

Fig. 1.1 Illustration of a projection of a part of the pyrochlore lattice

Spin ice physics arises in materials with magnetic ions residing on sites of the pyrochlore lattice of corner-sharing tetrahedra depicted in Fig. 1.1. It is useful to view the pyrochlore lattice as a face-centered cubic (FCC) Bravais lattice with a tetrahedral basis. The pyrochlore lattice is one of a handful of regular three-dimensional lattices of corner-sharing triangular or tetrahedral units. Examples of three-dimensional corner-sharing triangular lattices include the garnet lattice which is the lattice occupied by magnetic Gd^{3+} ions in $Gd_3Ga_5O_{12}$ [1–3] and the hyperkagomé lattice occupied by magnetic Ir^{4+} in $Na_4Ir_3O_8$ [4]. The pyrochlore structure itself is known to arise in various spinels with composition AB_2O_4 [5] where the magnetic B ions live on the pyrochlore sites and in the pyrochlore form of FeF_3 where the magnetic Fe^{3+} ions occupy a regular pyrochlore lattice [6]. The family of compounds with this lattice structure that have attracted the most interest over the past twenty-five years or so are the "227" materials [7], $A_2B_2O_7$, where both the A and B ions live on the respective sites of two distinct but interpenetrating pyrochlore lattices. This chapter focuses on the latter class of materials. Even among examples of this class, there are cases with magnetic ions on the A sites alone (e.g. $Tb_2Ti_2O_7$ [8]), only the B sites (e.g. $Y_2Mo_2O_7$ [9]) and both sites (e.g. $Tb_2Mo_2O_7$ [10]). The known spin ice materials are A site 227 materials, which originally counted $Ho_2Ti_2O_7$ [11] and $Dy_2Ti_2O_7$ [12], but now also comprise $Ho_2Sn_2O_7$ [13, 14], $Dy_2Sn_2O_7$ [13, 15], $Ho_2Ge_2O_7$ [16] and $Dy_2Ge_2O_7$ [16]. Spin ice behaviour has also been reported in the $CdEr_2Se_4$ spinel, where Er^{3+} is the magnetic ion [17].

Before discussing the physical realization of spin ice physics in real materials, we introduce what is perhaps the simplest pyrochlore spin ice model [18, 19]. We consider magnetic moments on the sites of the pyrochlore lattice with a strong Ising anisotropy. On each site i, we denote the angular moment as $\mathbf{J}_i$. Due to the anisotropy, this is an Ising variable and may be written as $\mathbf{J}_i = \mathsf{J}\sigma_i\hat{\mathbf{z}}_i$, where J is the magnitude of the angular momentum, $\sigma_i = \pm 1$ and $\hat{\mathbf{z}}_i$ is the moment orientation relative to the

lab frame and which is along the local cubic [111] direction. Now, suppose there is a Heisenberg exchange coupling between nearest-neighbour moments of the form

$$H = -\mathcal{J}_{\rm ex} \sum_{\langle ij \rangle} \mathbf{J}_i \cdot \mathbf{J}_j = -\mathcal{J}_{\rm ex}\, \mathsf{J}^2 \sum_{\langle ij \rangle} (\sigma_i \sigma_j)\, \hat{\mathbf{z}}_i \cdot \hat{\mathbf{z}}_j. \tag{1.1}$$

Here we are using a convention where $\mathcal{J}_{\rm ex} > 0$ represents ferromagnetic coupling between the $\mathbf{J}_i$ while $\mathcal{J}_{\rm ex} < 0$ is antiferromagnetic. Since these moments are constrained by the strong anisotropy to point along the local cubic [111] directions, we have $\hat{\mathbf{z}}_i \cdot \hat{\mathbf{z}}_j = -1/3$ for nearest neighbours. Thus, in the local frame, the model with original ferromagnetic $\mathcal{J}_{\rm ex} > 0$ becomes an effective antiferromagnetic Ising model on the pyrochlore lattice with coupling $\mathcal{J}_{\rm ex}\mathsf{J}^2/3$ [18, 19]. We may write the Hamiltonian in the form

$$H = \mathcal{J}_{\rm ex} \frac{\mathsf{J}^2}{3} \sum_{\langle ij \rangle} \sigma_i \sigma_j = \mathcal{J}_{\rm ex} \frac{\mathsf{J}^2}{3} \frac{1}{2} \sum_{\boxtimes} \left[\left(\sum_{i \in \boxtimes} \sigma_i \right)^2 - 4 \right],$$

where the sum $\sum_{\boxtimes}$ runs over all tetrahedra formed by the nearest-neighbour bonds. It is clear that the ground state has all $\sum_{i \in \boxtimes} \sigma_i = 0$; in other words, two spins are $+1$ and two spins are -1 on each tetrahedron. This local constraint is called the "ice rule".[1] However, so far, there is nothing special about this constraint: it arises in any antiferromagnet with an even number of spins in a fully connected cluster out of which the lattice may be built. The remarkable feature of this model lies in the number of ways the local constraint may be satisfied. On a bipartite lattice, say a cubic lattice for which the elementary unit is a single cube, the lattice can be tiled in only two distinct ways. On the pyrochlore lattice, the number of ground states scales exponentially in the volume of the system [22]. One way of seeing this is as follows: we draw a curve through each vertex of the A tetrahedra with one spin pointing into the tetrahedron. In the ice state, each tetrahedron has two such vertices so such a curve must either extend across the system or close up on itself. Conversely, each ice state can be viewed as a tangle of loops such that a loop passes through every tetrahedron exactly once. The set of ice states corresponds to the complete set of such loop coverings on the lattice. Evidently, as the number of sites increases arithmetically, the number of such configurations increases exponentially. A rough way of counting the number of such states, due to Pauling who first performed the analogous calculation for water ice [23], is to reweight the total number of spin configurations 2^N by the number of ice states per tetrahedron, which is 6 out of 16 states. We find $2^N (6/16)^{N/2}$ states where $N/2$ is the number of tetrahedra for a system with N spins. This gives the famous

[1] Specifically, this is the second Bernal-Fowler ice rule which specifies that in common hexagonal water ice, two protons must be "near" and two protons must be "far" from each oxygen O^{2-} ion [20, 21]. The first Bernal-Fowler ice rule, which is not relevant to spin ice, states that there must be one and only one proton on each O^{2-}–O^{2-} bond.

Pauling entropy [23] of $(Nk_B/2)\ln(3/2)$ which is an excellent approximation to the exact entropy for this model.[2]

In summary, the pyrochlore lattice Ising model of (1.1) has an extensive ground state degeneracy composed of all states satisfying the so-called ice rule. This is quite different from most magnetic systems, Ising or not, which typically have a subextensive ground state entropy. The remarkable consequences of the enormous density of magnetic states and their unusual correlations will occupy much of the rest of this volume. However, in the remainder of this chapter, we shall see how a variant of (1.1) arises in real magnetic pyrochlore oxide materials. The outline of the chapter is as follows. In the next section, we discuss the principal energy scales in rare-earth magnets and the nature of the atomic moments. In Sect. 1.3, we describe the crystal field and its consequences, and finally, in Sect. 1.4, we indicate how effective magnetic couplings between the rare-earth ions arise from the microscopic physics.

1.2 Rare-Earth Magnetism

As discussed in the Introduction, known examples of spin ice physics occur in rare-earth pyrochlore oxides [7]. In these materials, the magnetism originates from the rare-earth (lanthanide) ions due to the presence of unpaired $4f$ electrons, with the low energy physics deriving from a hierarchy of energy scales. The spin-orbit coupling is a dominant magnetic energy scale - on the order of 1 eV and hence comparable to other atomic energy scales. Also, the $4f$ orbitals are well-localized so that the Hund's coupling in these systems is large. Below this scale, at around 0.01 – 0.1 eV, there is a crystal field and, finally, couplings between the moments are on the scale of 0.01 – 0.1 meV. This large separation of energy scales is central to the manifestation of spin ice physics.

From the strong spin-orbit coupling, it follows that the atomic magnetic energy levels are, to an excellent approximation, eigenstates of the total angular momentum $\mathbf{J} \equiv \mathbf{L} + \mathbf{S}$. Since the Hund's coupling is large, Hund's rules work well in this class of magnets so the moment of the "would be free" rare-earth ions may be determined straightforwardly from the electronic configuration. The rare-earths tend to form tri-valent ions in the solid state, though Ce and Pr often adopt a tetravalent (4+) valence state and Eu and Yb can be divalent (2+). To take the example of Ho^{3+} with configuration $[Xe]4f^{10}$, Hund's rules imply that $\mathsf{L} = 6$, $\mathsf{S} = 2$ and $\mathsf{J} = 8$. For Dy^{3+}, we have $[Xe]4f^9$ and so $\mathsf{L} = 5, \mathsf{S} = 5/2$ and $\mathsf{J} = 15/2$.[3] The combination of f electron physics, with the associated strong spin-orbit coupling, can evidently cause

[2] Within the Pauling approximation, the entropy for water ice and spin ice are the same. The small corrections to Pauling's value for water ice [24] and spin ice [25] have been computed. These corrections are not exactly the same for the two systems since water ice is hexagonal while spin ice is cubic.

[3] Both Ho^{3+} and Dy^{3+} have more than a half-filled $4f$ shell and thus $\mathsf{J} = \mathsf{L} + \mathsf{S}$ is maximized as opposed to being minimized ($\mathsf{J} = \mathsf{L} - \mathsf{S}$) for a less than half-filled shell [26].

the intrinsic magnetic moment to be large [26]. We shall return to this important point later in the chapter.

Following the arguments above, an effective model for the magnetism in the rare-earth pyrochlore oxides begins with well-defined moments of total angular momentum J. Such a model takes the following schematic form

$$H = H_{\mathrm{CF}} + H_{\mathrm{Int}} + H_{\mathrm{ME}} + H_{\mathrm{Z}}, \tag{1.2}$$

where H_{CF} is the single-ion crystal field which is discussed in the next section. H_{Int} contains the interactions between the rare-earth ions and $H_{\mathrm{Z}} = -\mathrm{g}_{\mathrm{L}}\mu_{\mathrm{B}} \sum_i \mathbf{J}_i \cdot \mathbf{B}$ is the Zeeman coupling of the moments to an external magnetic field $\mathbf{B}$ where g_{L} is the Landé g-factor and μ_{B} is the Bohr magneton. The spin-orbit coupling allows lattice and magnetic degrees of freedom to hybridize. The magneto-elastic coupling, H_{ME}, includes terms coupling the single-ion moment to the lattice as well as a coupling between the magnetic exchange and the structural degrees of freedom. Such couplings have been shown to be significant in spin ice materials through ultrasound measurements in a magnetic field [27], but they do not appear to have a direct bearing on the static properties of these materials at temperatures below $O(10^1)$K. In the next section, we focus on H_{CF}, which is the largest of these pieces.

1.3 Single-Ion Physics

After spin-orbit coupling, Hund's coupling and the Coulomb interaction, the next most important energy scale in rare-earth magnets is the crystal field. This is the electrostatic interaction between the electronic charge density at the magnetic ion and its local anisotropic environment. Owing to the spin-orbit coupling, this splitting of electrostatic origin lifts the $2\mathrm{J}+1$-fold degeneracy of the atomic levels, in a way that is partly constrained by the symmetry of the crystal at the magnetic sites [28–31], thus generating magnetic anisotropy.

The fact that lattice symmetry plays an important role in determining the crystal-field physics [28–31] gives us an opportunity to discuss the crystal structure of the $A_2B_2\mathrm{O}_7$ pyrochlores, with A^{3+} a lanthanide rare-earth ion, in some more detail [7]. In spin ice materials, the lattice symmetries are characterized by the space group $\mathrm{Fd}\bar{3}\mathrm{m}$. The pyrochlore sites belong to the 16d Wyckoff sites for this space group, the titanium sites occupy the 16c sites which, as mentioned in the Introduction, also form a pyrochlore lattice. The oxygen ions occupy the 48f and 8b sites. These site symmetries allow for a single free parameter, x, which controls the position of the oxygen at the low symmetry 48f site. For $\mathrm{Ho_2Ti_2O_7}$, $x \sim 0.3285$ while $x \sim 0.3275$ for $\mathrm{Dy_2Ti_2O_7}$ [7]. For $x = 3/8$, the oxygen ions neighbouring each rare-earth magnetic ion would form a perfect cube. For $x \neq 3/8$, this cube becomes distorted along the local crystallographic cubic [111] direction, forming a ditrigonal scalenohedron, so that each magnetic ion has a local $D_{3\mathrm{d}}$ point group symmetry which includes a three-

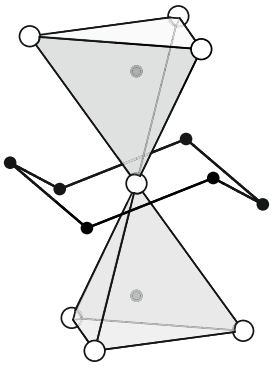

Fig. 1.2 Illustration of the positions of the oxygen ions neighbouring each rare-earth ion (white circle). The oxygen cage is a cube that has been elongated along the crystallographic [111] direction. The central white ion linking the two tetrahedra is a rare-earth ion. The six black oxygen ions that surround it occupy the 48f positions on a puckered hexagon while the two gray oxygen ions at the center of the two tetrahedra occupy the 8b positions

fold rotation about the appropriate [111] direction [7]. The oxygen cage around each rare-earth ion is illustrated in Fig. 1.2.

We now present a streamlined discussion of the theory of the crystal field interaction. For further details we refer to [28–31]. Consider a single magnetic rare-earth ion centered at the origin. The electrostatic potential V at the rare-earth ion due to the neighbouring ions is given schematically by

$$H_{\mathrm{CF}} = \sum_{i=1}^{8} V(\mathbf{r} - \mathbf{R}_i) + \cdots , \tag{1.3}$$

where the ellipsis denotes ions beyond the neighbouring shell of the nearest eight oxygen ions and

$$V(\mathbf{r} - \mathbf{R}_i) = \frac{eQ}{4\pi\epsilon_0} \int d^3\mathbf{r} \frac{\rho(\mathbf{r})}{|\mathbf{r} - \mathbf{R}_i|}, \tag{1.4}$$

with $\rho(\mathbf{r})$ the $4f$ electron density at $\mathbf{r}$ and Q is the effective (screened) charged of the surrounding O^{2-} ions. This Hamiltonian must be invariant under the elements of the local rare-earth site symmetry group $D_{3\mathrm{d}}$. The Wigner-Eckart theorem tells us that the matrix elements of the crystal-field Hamiltonian can be computed from a Hamiltonian written in terms of effective operators which are polynomial in the total angular momenta components J^α. Also, the crystal-field matrix elements involve atomic $4f$ wavefunctions with orbital angular momentum $\mathsf{L} = 3$. Since there is a pair of such wavefunctions in the matrix element, the rules of addition of angular momenta imply that the effective crystal-field Hamiltonian should contain operators that are products of at most six J^α. A further constraint is that operators with odd total angular momentum cannot arise due to time-reversal symmetry. The local $D_{3\mathrm{d}}$

point group symmetry imposes a further considerable restriction on the form of the Hamiltonian so that, in the end, the crystal-field Hamiltonian takes the form

$$H_{\mathrm{CF}} = B_2^0 \hat{O}_2^0 + B_4^0 \hat{O}_4^0 + B_4^3 \hat{O}_4^3 + B_6^0 \hat{O}_6^0 + B_6^3 \hat{O}_6^3 + B_6^6 \hat{O}_6^6, \tag{1.5}$$

where $\hat{O}_l^m$ are the so-called Stevens operators which transform like spherical harmonics Y_l^m under rotations [32]. The Stevens operators can be written in terms of products of angular momentum operators. For example, $\hat{O}_2^0 \equiv 3\mathsf{J}_z^2 - \mathsf{J}(\mathsf{J}+1)$ and $\hat{O}_6^6 \equiv (1/2)(\mathsf{J}_+^6 + \mathsf{J}_-^6)$. In summary, the effect of the crystal field on the $2\mathsf{J}+1$ magnetic levels is strongly constrained by the general considerations given above leaving at most six free B_l^m parameters. We discuss below the experimental determination of these parameters and hence the single-ion crystal-field level wavefunctions.

First, we describe the qualitative features of the crystal-field splitting produced by (1.5). One should draw a distinction between half-odd integer (Kramers) or integer (non-Kramers) total angular momentum, or equivalently having, respectively, an odd or even number of electrons in the $4f$ shell. In the former case, time reversal symmetry ensures that the degeneracy of the levels split by the crystal-field potential is an even number. In the latter case, there is no such constraint and any degeneracy is protected solely by the crystal symmetries. The overall scale of the crystal-field splitting is about 0.1 eV (10^3 K) in the rare earths with typical inter-level splittings of order 10^1 to 10^2 Kelvin [7].

One important consequence of the crystal-field splitting is the generation of a magnetic anisotropy at the single-ion level. Owing to the $D_{3\mathrm{d}}$ site symmetry, this anisotropy has one distinguished axis which is along the local $\hat{\mathbf{z}}_i$ ([111]) direction for each magnetic sublattice. We consider those cases where the crystal-field ground state is a doublet which is relevant to the spin ices [33]. If the doublet states are denoted $|+\rangle$ and $|-\rangle$, the magnetic anisotropy is determined by the matrix elements of $\mathbf{J} = (\mathsf{J}^x, \mathsf{J}^y, \mathsf{J}^z)$ computed from these states where the components are naturally taken to refer to a frame with $\hat{\mathbf{z}}$ axis along this local [111] direction.

More explicitly, the magnetic dipole moment μ is given by $\boldsymbol{\mu} = \mathrm{g_L}\mu_{\mathrm{B}}\mathbf{J}$ where, again, $\mathrm{g_L}$ is the Landé g-factor. Defining pseudo-spin operators for the doublet as $\boldsymbol{S} = \frac{1}{2}\sum_{\alpha\beta=\pm} |\alpha\rangle \langle\beta| \boldsymbol{\sigma}_{\alpha\beta}$, where $\boldsymbol{\sigma} = \sigma^x\hat{\mathbf{x}} + \sigma^y\hat{\mathbf{y}} + \sigma^z\hat{\mathbf{z}}$ with σ^μ the μ component Pauli matrix, and where we define the g-tensor as $\boldsymbol{\mu} \equiv \mu_{\mathrm{B}}\mathrm{g}\cdot\mathbf{S}$. In this local basis, the g-tensor is diagonal and can be parameterized as $\mathrm{g} = (\mathrm{g}_\perp, \mathrm{g}_\perp, \mathrm{g}_\parallel)$. For non-Kramers ions, the time reversal properties of the states ensure that one can choose a basis such that the matrix elements of J^x and J^y vanish leaving only $\langle +|\,\mathsf{J}^z\,|+\rangle = -\langle -|\,\mathsf{J}^z\,|-\rangle$. Such a moment is Ising-like with $\mathrm{g}_\perp = 0$, with this anisotropy being protected when the scale of coupling between the moments is much smaller than the gap to the first excited crystal-field level. This is the case for the $Ho_2(Ti,Sn,Ge)_2O_7$ classical spin ices, but not for $Tb_2(Ti,Sn,Ge)_2O_7$ [7]. In Kramers ions, the local crystal symmetry determines the crystal-field wavefunctions but not their ordering in energy. In general,

both $g_\perp$ and $g_\parallel$ are nonzero. Strong *single-ion* Ising magnetism then corresponds to the limit $g_\perp/g_\parallel \to 0$. This is the case for the $Dy_2(Ti,Sn,Ge)_2O_7$ classical spin ices.[4]

Because crystal-field doublets in non-Kramers ions are protected only by the crystal symmetry, time reversal invariant perturbations such as lattice distortions may break the degeneracy. In $Ho_2Ti_2O_7$ spin ice, no splitting of the ground state crystal-field doublet has been detected and it is clear that the energy scale of interactions between the moments is much greater than any such splitting. The reason for the lack of a Jahn-Teller distortion is that the ground state doublets are predominantly $|\mathsf{J} = 8, \mathsf{M} = \pm 8\rangle$ angular momentum states, which are not directly mixed by the magneto-elastic coupling [33], so splitting would involve mixing with excited crystal-field states [34]. In that case, the doublet is protected by the large crystal-field gap $\Delta \sim 280$ K. We note, however, that a large gap is not a necessary condition for the preservation of a magnetic doublet in non-Kramers magnets: the single-ion doublet is seemingly not split in the non-Kramers pyrochlores $Tb_2Ti_2O_7$ [35] and $Pr_2Zr_2O_7$ [36], which have a gap, Δ, much smaller than $Ho_2Ti_2O_7$. In these materials, any splitting appears significantly smaller than the scale of the magnetic interactions.

Kramers crystal-field doublets are protected by time reversal symmetry — like the atomic angular momentum J, they transform non-trivially under time-reversal. However, though it superficially resembles a spin-1/2, this doublet need not transform like one under lattice symmetries. For example, in Dy^{3+} in $Dy_2Ti_2O_7$ spin ice, most of the weight of the ground state single-ion wavefunction is concentrated at large M from which it follows that transverse matrix elements of the angular momentum are small and the free ion has an Ising response to a magnetic field. Yet, the three components of the pseudo-spin do not transform in the same way. In particular, one of the transverse components transforms like a component of an octupole under lattice symmetries while the other two components transform like a dipole [37]. The transformation properties of the single-ion doublet in $Ho_2Ti_2O_7$ and $Dy_2Ti_2O_7$ constrain the form of the transverse part of magnetic exchange interactions between the pseudo-spins in different ways [33]. While these interactions are known to be

[4] As we are ultimately interested in the collective magnetic properties of these rare-earth pyrochlore materials, it is useful here to comment on some aspects of time-reversal symmetry of the crystal-field states for the rare-earth ions. For even electron systems, the action of the time reversal operator Θ is $\Theta^2 = 1$ in contrast to the case of odd electron systems for which $\Theta^2 = -1$. In general, for the amplitude corresponding to total angular momentum and its projection onto the $\hat{\mathbf{z}}$ axis $|\mathsf{J}, \mathsf{M}\rangle$, time reversal acts like $\Theta c^{\mathsf{J}}_{\mathsf{M}} |\mathsf{J}, \mathsf{M}\rangle = (-)^{\mathsf{J}+\mathsf{M}} (c^{\mathsf{J}}_{\mathsf{M}})^\star |\mathsf{J}, -\mathsf{M}\rangle$. Here, $c^{\mathsf{J}}_{\mathsf{M}}$ are expansion coefficients in the spectral decomposition of the crystal field doublet in terms of $|\mathsf{J}, \mathsf{M}\rangle$. For a non-Kramers doublet, $\Theta|\pm\rangle = |\mp\rangle$. The crystal-field Hamiltonian can be chosen to have real matrix elements in the basis of J, M and likewise for the eigenstates. Now, consider matrix elements of transverse components of the angular momentum between the two states of the crystal-field ground doublet.

$$\langle +| \mathsf{J}^+ |-\rangle = \langle +| \Theta^\dagger \Theta \mathsf{J}^+ \Theta^\dagger \Theta |-\rangle = -\langle -| \mathsf{J}^- |+\rangle . \tag{1.6}$$

Furthermore, $\langle +|\mathsf{J}^+|-\rangle = \langle -|\mathsf{J}^-|+\rangle^\star$. It follows that the matrix element vanishes. No such constraint holds for matrix elements between identical states of the doublet. However, we may show that

$$\langle +| \mathsf{J}^\alpha |+\rangle = \langle +| \Theta^\dagger \Theta \mathsf{J}^\alpha \Theta^\dagger \Theta |+\rangle = -\langle -| \mathsf{J}^\alpha |-\rangle . \tag{1.7}$$

The doublet corresponds to an Ising degree of freedom if these matrix elements are nonvanishing.

small [33], their small nonzero values may have implications for low temperature dynamics of these two materials [38–41].

So far, we have discussed the properties of the crystal-field ground state in terms of matrix elements of the angular momentum **J**. It is also worth mentioning that operators polynomial in **J** of higher degree $d \leq 2\mathsf{J}$ will, in general, have nonvanishing matrix elements between the states of the doublet. In other words, the doublet has a series of multipole moments. We have focussed on the dipolar component for the purposes of introducing the essential background to spin ice physics. However, we return in the next section to the multipole components when we discuss the interactions between the magnetic ions defined by $H_{\rm Int}$.

The crystal-field parameters B_l^m are commonly fitted using various spectroscopic data. Crystal-field excitations in the rare-earth pyrochlore can be sharply resolved using, for example, inelastic neutron scattering, electron spin resonance (ESR) and Raman scattering. Several studies have been devoted to refining the crystal-field parameters in spin ice materials $Dy_2Ti_2O_7$ and $Ho_2Ti_2O_7$ [42–48]. The data consists, in each case, of transition energies and intensities. Since these can be computed straightforwardly from (1.5), the data can be used to obtain the B_l^m parameters. In such an analysis, at least for $Ho_2Ti_2O_7$ and $Dy_2Ti_2O_7$, one need not worry about couplings between the moments because these lie at a much lower energy scale than the crystal-field splitting. The situation for $Tb_2Ti_2O_7$ is more complicated [49–51]. To our knowledge, the earliest such study of the crystal field in a spin ice material ($Ho_2Ti_2O_7$) was based on a fit to inelastic neutron data described in [42]. The crystal-field level scheme obtained from that work consists of a ground state doublet with a moment of about 10 $\mu_{\rm B}$ followed by another state at about 20 meV. The ground state wavefunction arising from the fit is predominantly $|\mathsf{J} = 8, \mathsf{M} = \pm 8\rangle$. These results on $Ho_2Ti_2O_7$ have been corroborated by other studies [46, 47]. The overall spectrum spans an energy of about 80 meV which is typical in these materials. For $Dy_2Ti_2O_7$, susceptibility measurements allow a determination of the moment in the crystal-field ground state of about 10 $\mu_{\rm B}$ [43] and a Raman scattering study [45] suggests a crystal-field gap of about 35 meV. In order to be compatible with the measured moment, the ground state doublet of $Dy_2Ti_2O_7$ must have its weight concentrated in the $|\mathsf{J} = 15/2, \mathsf{M} = \pm 15/2\rangle$ states [33].

1.4 Microscopic Interactions in Insulating Rare Earth Magnets with Application to the Spin Ices

With the single-ion properties well-established, we now can move on to describing the interactions between the rare-earth ions. These will be most conveniently formulated within the **J**-manifolds, a level of description lying part way between the bare atomic rare-earth $4f$ electrons and the crystal-field ground state doublets. There are many different microscopic mechanisms that contribute to such interactions, including magneto- and electrostatic interactions, super-exchange, direct exchange and

more [33]. Of these, the magnetostatic and super-exchange interactions are believed to be most important in the canonical spin ices $Dy_2Ti_2O_7$ and $Ho_2Ti_2O_7$.

We first tackle the direct magnetostatic interaction. This magnetic dipole-dipole interaction (MDD) is not only one of the simplest but, due to the large moment $\mu = g_L J \mu_B \sim 10\,\mu_B$ of the free Dy^{3+} and Ho^{3+} ions, it is also the largest interaction present both in $Ho_2Ti_2O_7$ and $Dy_2Ti_2O_7$. It can be written

$$H_{\rm MDD} = \frac{\mu_0}{4\pi} \sum_{i<j} \left[\frac{\boldsymbol{\mu}_i \cdot \boldsymbol{\mu}_j}{|\mathbf{r}_{ij}|^3} - \frac{3\left(\boldsymbol{\mu}_i \cdot \hat{\mathbf{r}}_{ij}\right)\left(\boldsymbol{\mu}_j \cdot \hat{\mathbf{r}}_{ij}\right)}{|\mathbf{r}_{ij}|^3} \right], \tag{1.8}$$

where $\mathbf{r}_{ij} = \mathbf{r}_i - \mathbf{r}_j$ is the vector from site i to site j and $\hat{\mathbf{r}}_{ij} \equiv \mathbf{r}_{ij}/|\mathbf{r}_{ij}|$. The strength of this interaction is known exactly without adjustable parameters, fixed by electromagnetic constants and the single-ion magnetic moment $\boldsymbol{\mu}_i = g_L \mu_B \mathbf{J}_i$. Projecting into the ground doublet maps $P\mathbf{J}_i P = \frac{1}{2} g_\parallel \sigma_i^z \hat{\mathbf{z}}_i$ and gives the dipolar Ising model [52, 53]

$$H_{\rm MDD} = D r_{\rm nn}^3 \sum_{i<j} \left[\frac{\hat{\mathbf{z}}_i \cdot \hat{\mathbf{z}}_j}{|\mathbf{r}_{ij}|^3} - \frac{3\left(\hat{\mathbf{z}}_i \cdot \hat{\mathbf{r}}_{ij}\right)\left(\hat{\mathbf{z}}_j \cdot \hat{\mathbf{r}}_{ij}\right)}{|\mathbf{r}_{ij}|^3} \right] \sigma_i^z \sigma_j^z, \tag{1.9}$$

where $D = \frac{1}{4} g_\parallel^2 \mu_B^2 \mu_0/(4\pi r_{\rm nn}^3)$ and $r_{\rm nn}$ is the nearest-neighbour distance. This dipolar coupling has often been presented through the value taken for nearest-neighbour sites, $D_{\rm nn} \equiv 5D/3 \sim 2.35$ K for both $Dy_2Ti_2O_7$ [52, 53] and $Ho_2Ti_2O_7$ [58].

The derivation of the super-exchange interaction is significantly more involved, though we will see that, in the end, its consequences are rather simple. Fundamentally, super-exchange arises through virtual processes that transfer charge between the rare-earth ions. As the separation of the rare-earth ions is large compared to their size, this charge hopping is expected to be mediated through the surrounding ligands. Even proceeding through these ligands, these processes decay rapidly with distance and thus can be considered to be limited to nearest neighbours to a good approximation. The simplest setting in which to discuss super-exchange is perhaps the single-orbital Hubbard model [29],

$$-t \sum_{\langle ij \rangle} \left(c_{i\sigma}^\dagger c_{j\sigma} + \text{h.c.} \right) + U \sum_i n_{i\uparrow} n_{i\downarrow}, \tag{1.10}$$

where $c_{i\sigma}^\dagger$ creates an electron at site $\mathbf{r}_i$ with spin $\sigma = \uparrow, \downarrow$ and t is the hopping amplitude between nearest-neighbour sites. Super-exchange manifests itself in the localized limit where $U \gg t$. Including the virtual charge transfer processes at 2nd order in degenerate perturbation theory yields an effective antiferromagnetic spin-spin interaction

$$\frac{2t^2}{U} \sum_{\langle ij \rangle} \sum_{\sigma\sigma'} \left(P_1 c_{i\sigma}^\dagger c_{i\sigma'} P_1 \right) \left(P_1 c_{j\sigma'}^\dagger c_{j\sigma} P_1 \right) = \frac{4t^2}{U} \sum_{\langle ij \rangle} \boldsymbol{S}_i \cdot \boldsymbol{S}_j, \tag{1.11}$$

where P_1 projects into singly occupied states, those which minimize the Hubbard interaction U. In this simple case, the form of the exchange interaction is completely dictated by spin rotation symmetry and the fact that for $S = 1/2$ the spin operators $\boldsymbol{S}_i$ form a complete basis at each site. This basic picture in fact carries over to the multi-orbital case where the orbital angular momentum is quenched and the moment is spin only. In this more general setting, though the spin moment can have $S > 1/2$, the interactions remain predominantly Heisenberg-like, as in (1.11), at lowest order in the virtual charge transfer processes. Terms that go beyond this, such as a biquadratic coupling $\sim \left(\boldsymbol{S}_i \cdot \boldsymbol{S}_j\right)^2$, only appear through higher order virtual charge transfer processes [29]. This general fact can be understood by noting the two electron hops in the 2nd order process can transfer at most $1/2 + 1/2 = 1$ units of (spin) angular momentum. If the on-site interactions preserve the total spin, then this implies that only interactions between vector (rank-1) operators such as $\boldsymbol{S}_i$ will be generated at leading order.

After this short detour we are ready to confront the large **J** moments relevant for $Dy_2Ti_2O_7$ and $Ho_2Ti_2O_7$. Due to the large spin-orbit coupling, these moments are decidedly not spin only and have large contributions coming from both the orbital and spin moments of the electrons. Following the argument above, we see that without the quenched orbital moment the virtual processes will depend strongly on the orbital content of the hoppings. The analogue to (1.10) is given by

$$-\sum_{\langle ij\rangle}\sum_{mm'}\sum_{\sigma}\left(t_{ij}^{mm'}f_{im\sigma}^{\dagger}f_{jm'\sigma}+\text{h.c.}\right)+\sum_{i}H_{\text{ion}}(i), \tag{1.12}$$

where $f_{im\sigma}^{\dagger}$ creates an f electron at $\mathbf{r}_i$ with orbital quantum number $m = 0, \pm1, \pm2, \pm3$ with spin $\sigma = \uparrow, \downarrow$. The single-ion Coulomb repulsion, spin-orbit coupling and crystal field are encapsulated in the last term, $H_{\text{ion}}(i)$. The hopping interactions $t_{ij}^{mm'}$ can be generated by a variety of processes. For example, they can arise via the intermediate oxygen ligands, where they would be of order $\sim t_{pf}^2/\Delta_{pf}$, where t_{pf} is a measure of the f-p rare earth-oxygen atomic wavefunction overlap, and Δ_{pf} is the energy cost to create a hole on the oxygen site. Though important quantitatively, we will not need to get into the details of the structure of these hoppings to understand their implications for spin-ice physics.

As carrying out the relevant 2nd order perturbation theory with the full single-ion interactions is quite complicated, for illustrative purposes we shall make the drastic "charging-approximation" that nonetheless preserves all of the essential features of the full result [33]. This approximation assumes that the energy to add or remove an electron, $E(f^{n\pm1}) - E(f^n) \sim U$, where $n = 9$ for Dy^{3+} and $n = 10$ for Ho^{3+}, dominates over the smaller splittings within each f^n manifold. These smaller splittings arise due to interactions such as Hund's or spin-orbit coupling that depend on more than simply the overall charge. As these are still much larger than the hoppings, the interactions can then be projected into the final **J**-manifold as determined by Hund's rules. The smaller crystal-field terms will be treated at leading order in perturbation theory along with the hoppings t. The derivation of the effective Hamiltonian then

closely follows the textbook derivation of (1.11) and yields $H_{\text{eff}} = H_{\text{SE}} + \sum_i H_{\text{CF}}(i)$ in which we have re-introduced the crystal-field interaction in $H_{\text{CF}}(i)$ as it appeared in (1.5) and

$$H_{\text{SE}} = \sum_{\langle ij \rangle} \sum_{m_\alpha, m'_\alpha} \sum_{\sigma_\alpha} \frac{2t_{ij}^{m_1 m'_1} t_{ij}^{m_2 m'_2}}{U} \left(P_{\mathsf{J}} f^\dagger_{im_1\sigma_1} f_{im_2\sigma_2} P_{\mathsf{J}} \right) \left(P_{\mathsf{J}} f^\dagger_{jm'_2\sigma_2} f_{jm'_1\sigma_1} P_{\mathsf{J}} \right), \tag{1.13}$$

where P_{J} projects into the $\mathsf{J} = 15/2$ states for Dy^{3+} and the $\mathsf{J} = 8$ states for Ho^{3+}. The structural similarity to the simple Heisenberg model shown in (1.11) is apparent. The combinations $\sim P_{\mathsf{J}} f^\dagger_{im\sigma} f_{im'\sigma'} P_{\mathsf{J}}$ are local to each site and thus can be expressed via functions of the moment operators $\mathbf{J}_i$. As discussed in the previous section these $\mathbf{J}$-manifolds carry much more than just a magnetic dipole moment, supporting a wide array of higher multipole moments. These multipole operators can be defined using the same Stevens operators $\hat{O}_k^q(\mathbf{J}_i)$ that appear in the crystal-field potential with k being the rank of the multipole which runs from 0 to $2\mathsf{J}$. The operators appearing in the super-exchange interaction can thus be written in terms of these multipoles as

$$P_{\mathsf{J}} f^\dagger_{im\sigma} f_{im'\sigma'} P_{\mathsf{J}} = \sum_{kq} A_{kq}^{mm'\sigma\sigma'} \hat{O}_k^q(\mathbf{J}_i). \tag{1.14}$$

Applying this to each part of (1.13), the super-exchange interactions can thus be schematically written as

$$H_{\text{SE}} = \sum_{\langle ij \rangle} \sum_{kk'} \sum_{qq'} M_{ij}^{kk'qq'} \hat{O}_k^q(\mathbf{J}_i) \hat{O}_k^{q'}(\mathbf{J}_j), \tag{1.15}$$

where the $M_{ij}^{kk'qq'}$ elements encode a very large number of possible interactions constants built from the $t_{ij}^{mm'}$ hoppings, the Coulomb repulsion U and the $A_{kq}^{mm'\sigma\sigma'}$ constants.

Admittedly, the full complexity of the multipolar interactions described by (1.15) is daunting. This is further compounded by the fact that this is in some sense the simplest treatment of these interactions; forgoing the simplifying approximations we exploited will further increase the complexity. Even projecting into the ground doublet offers little help without further information on the structure of these interactions. This stands in stark contrast to the essentially parameter-free magnetic dipole-dipole interaction we encountered earlier in (1.9). Thankfully, all is not lost: building on the observation we used to constrain the spin-only case, we can prune these interactions to a much more manageable level. Consider then the operators $f^\dagger_{im\sigma} f_{im'\sigma'}$ and the constraints on how the spin and orbital angular momentum can be transferred. We see that this operator can transfer at most $1/2 + 1/2 = 1$ units of spin angular momentum, and at most $3 + 3 = 6$ units of orbital angular momentum. Thus this operator can carry at most $6 + 1 = 7$ units of total angular momentum, or equivalently *can only be composed of multipole operators of rank-7 or smaller*. This result

holds true even if we lift some of the approximations made to arrive at (1.13), such as the charging-approximation [33], strongly constraining the multipolar interactions in (1.15). Note that even though the rank of the multipoles is constrained, the allowed multipolar interactions strongly deviate from the purely Heisenberg or rank-1 interactions one might naïvely expect. Indeed, the Heisenberg interaction we used in (1.1) was simply a convenient fiction; the true interactions in the **J**-manifold are highly anisotropic and involve many multipolar couplings [33].

With these facts in hand, we are now ready to project into the ground doublets of Dy^{3+} and Ho^{3+}. Consider a multipole operator $\hat{O}_k^q(\mathbf{J}_i)$ with rank $k \leq 7$. Since the crystal-field doublet is almost perfectly of the form $|\pm\rangle \approx |\mathsf{J}, \mathsf{M} = \pm\mathsf{J}\rangle$ for these two ions, only operators with $q = 0$ have diagonal matrix elements and only operators with $q = \pm 2\mathsf{J}$ have off-diagonal matrix elements. Since for both Dy^{3+} and Ho^{3+} one has $2\mathsf{J} > 7$, the off-diagonal matrix elements of the super-exchange vanish for all multipoles that are coupled via super-exchange. Explicitly, we therefore have for these two ions

$$\langle \mathsf{J}, \pm\mathsf{J}| \hat{O}_k^q(\mathbf{J}_i) |\mathsf{J}, \pm\mathsf{J}\rangle = \begin{cases} \pm\lambda_k \delta_{q0}, & k \text{ odd} \\ \text{const.}, & k \text{ even} \end{cases}, \qquad \langle \mathsf{J}, \pm\mathsf{J}| \hat{O}_k^q(\mathbf{J}_i) |\mathsf{J}, \mp\mathsf{J}\rangle = 0\,. \tag{1.16}$$

We thus see that all of the multipoles $\hat{O}_k^q(\mathbf{J}_i)$ originating from super-exchange project into the Ising variable σ_i^z or an irrelevant constant. The super-exchange interactions, when projected into the ground state doublets, are thus reduced to

$$PH_{\mathrm{SE}}P = P \sum_{\langle ij \rangle} \sum_{kk'} \sum_{qq'} M_{ij}^{kk'qq'} \hat{O}_k^q(\mathbf{J}_i) \hat{O}_{k'}^{q'}(\mathbf{J}_j) P = J_{\mathrm{nn}} \sum_{\langle ij \rangle} \sigma_i^z \sigma_j^z + \text{const.} \tag{1.17}$$

The entire set of couplings $M_{ij}^{kk'qq'}$ has been encapsulated via the λ_k parameters into a single parameter J_{nn}, a nearest-neighbour Ising interaction.

The final set of interactions between the ground doublets of Dy^{3+} and Ho^{3+} thus include the magnetic dipole-dipole interactions and super-exchange contribution to the nearest-neighbour term. This is the dipolar spin ice model (DSI) [52, 53]

$$H_{\mathrm{DSI}} = J_{\mathrm{nn}} \sum_{\langle ij \rangle} \sigma_i^z \sigma_j^z + \frac{3 D_{\mathrm{nn}} r_{\mathrm{nn}}^3}{5} \sum_{i<j} \left[\frac{\hat{\mathbf{z}}_i \cdot \hat{\mathbf{z}}_j}{|\mathbf{r}_{ij}|^3} - \frac{3\left(\hat{\mathbf{z}}_i \cdot \hat{\mathbf{r}}_{ij}\right)\left(\hat{\mathbf{z}}_j \cdot \hat{\mathbf{r}}_{ij}\right)}{|\mathbf{r}_{ij}|^3} \right] \sigma_i^z \sigma_j^z. \tag{1.18}$$

This model has one free parameter (J_{nn}) that can be determined by comparison with experimental data. Fitting to the observed properties of $Dy_2Ti_2O_7$ and $Ho_2Ti_2O_7$, one finds this nearest-neighbour part to be significant, with $J_{\mathrm{nn}} \approx -1.1$ K for $Dy_2Ti_2O_7$ [53–57] and $J_{\mathrm{nn}} \approx -0.52$ K in $Ho_2Ti_2O_7$ [58]. A naive super-exchange calculation also argues for a negative J_{nn} [33].

One key feature of this model is that it is purely classical, without any transverse effective exchange between the two states of the ground doublets. It is most important to realize this is not simply a consequence of the large J; such a semi-classical argument only holds when the rank of the multipolar interactions are much smaller than J.

Nor is it a consequence of the Ising nature of the single-ion ground crystal-field doublet alone ($g_\perp \approx 0$). In our discussion we instead saw that this was a consequence of the microscopic structure of the super-exchange interactions and the spectral $|\mathsf{J}, \mathsf{M}\rangle$ decomposition of the $|\pm\rangle$ doublet states. Specifically, the key ingredients were (a) the rank-7 limit to the super-exchange interactions and (b) the strongly predominant $|\mathsf{J}, \mathsf{M} = \pm\mathsf{J}\rangle$ composition of the ground doublets. A third implicit assumption was, (c) due to the large crystal-field energy scale ~ 300 K, we could project into ground doublets and ignore further perturbation corrections from the excited states. Each of these ingredients are approximate and a more complete treatment of the couplings would introduce quantum effects into the dipolar spin ice model [59]. Such departures from the Ising model are expected to be small enough [33] that most existing measurements of the spin ice materials may be described to an excellent approximation by $H_{\rm DSI}$, perhaps supplemented with further neighbour exchange couplings [54–57]. However, the precise magnitude of any small quantum interactions and their importance in describing $Dy_2Ti_2O_7$ and $Ho_2Ti_2O_7$ are still matters of active research [33].

The dipolar spin ice model of (1.18) looks quite different from the simplified effective model for spin ice, (1.1), discussed at the beginning of this chapter. In particular, (1.1) has only nearest-neighbour interactions. If (i) $D_{\rm nn}$ were much smaller than $J_{\rm nn}$ and if (ii) $J_{\rm nn}$ were positive, then (1.18) would approximate (1.1) up to the broken degeneracy of the ice states brought about by the long-range interaction [60–62]. However the reality is more subtle; neither (i) nor (ii) is true, instead $D_{\rm nn} \sim 2.35$ K, that is $D_{\rm nn} > |J_{\rm nn}|$, and $J_{\rm nn} < 0$. First of all, the effective nearest-neighbour interaction is $J_{\rm eff} \equiv J_{\rm nn} + D_{\rm nn}$ which is positive as required for spin ice physics to arise at low energies in accordance with (1.1) and the discussion following it. In other words, spin ice physics arises in $Dy_2Ti_2O_7$ and $Ho_2Ti_2O_7$ *only because* the dipolar coupling is large. This need not be the case for systems such as $Pr_2(Sn,Zr)_2O_7$ [36, 63] where the magnetic dipole moment is small *and* it appears that $J_{\rm nn} > 0$.[5] One may refer to such a system as an exchange-coupled spin ice, as opposed to the $(Dy,Ho)_2(Ti,Sn,Ge)_2O_7$ dipolar spin ice systems. But should one not worry that the further neighbour part of the dipolar interaction might kill off the degeneracy of the spin ice states [60–62]? This issue will be addressed in greater detail later in this volume (e.g. see Chap. 3 by Moessner). For now, we simply remark that the degeneracy-breaking caused by the dipolar interaction is anomalously weak because the long-ranged part of the interaction is "self-screened" [60, 62]. This, in turn, is a consequence of the matching of the magnetic correlations among the ice states

[5] One also expects to find effective exchange terms coupling the transverse components of the pseudo-spin $S = 1/2$ describing the ground doublet in these compounds [63, 64] as well as in $Tb_2Ti_2O_7$ [51] and in $Yb_2Ti_2O_7$ [65, 66]. These introduce quantum fluctuations within the degenerate spin ice manifold and may give rise to a *quantum spin ice* state [67]. Three mechanisms generating effective transverse exchange and quantum dynamics have been discussed in the literature: (i) virtual crystal field fluctuations [51] (e.g. in $Tb_2Ti_2O_7$), (ii) sufficiently high-rank multipolar interactions in non-Kramers systems [63, 64] (e.g. in $Pr_2(Sn,Zr)_2O_7$) and (iii) multipolar, including dipolar, interactions in Kramers systems [65, 66, 68, 69] (e.g. in $Yb_2Ti_2O_7$ and $Er_2Ti_2O_7$) This will be discussed in further detail in subsequent chapters (e.g. see Chap. 9 by Savary and Balents, Chap. 10 by Shannon and Chap. 12 by Ross).

and the correlations induced by the dipolar interaction [62]. The net result is that the dipolar spin ice model, and the nearest-neighbour spin ice model lead to quite similar physics [70]. One quantitative difference is the diffuse neutron scattering pattern of the two systems in the spin ice regime [21, 55, 58], with scattering features in the case of the dipolar spin ice model signaling the eventual development of long-range order if thermal equilibrium can be maintained down to sufficiently low temperature. In the spin ice regime, the presence of the long-range dipolar interaction has two principal consequences. One is the presence of singular correlations arising purely from the dipolar interaction [71] which is singular at reciprocal lattice points — so-called "pinch points" [72] — and not due to the formation of the ice-rules at low-temperature in the spin ice regime [73]. The second is the presence of an energetic $1/r$ magnetic Coulomb potential between quasiparticle excitations in spin ice — the fractionalized magnetic monopoles [70, 74].

In summary, in this Chapter we have discussed how the strong separation of energy scales that exists between the various single-ion and ion-ion interaction terms in Dy- and Ho-based insulating rare-earth oxides ultimately leads to the classical Ising *dipolar spin ice* (DSI) model [52, 53]. We argued that quantum corrections arising as effective exchange couplings between the transverse components of the pseudospins describing the low-energy crystal field doublet are minimal. Other compounds in the $A_2B_2O_7$ family with different rare-earth ions, such as Pr, Gd, Tb, Er and Yb, would not necessarily be described by such a classical Ising model. Most of the remainder of this volume will discuss in more detail how spin ice physics manifests in real materials, and how the DSI model captures many of the key aspects of their physics. Additional chapters will address materials where the quantum corrections are non-negligible and the exciting potential realizations of *quantum spin ice* [51, 63, 64, 66, 67].

References

1. P. Schiffer, A.P. Ramirez, D.A. Huse, A.J. Valentino, Phys. Rev. Lett. **73**, 2500 (1994). https://doi.org/10.1103/PhysRevLett.73.2500
2. P. Schiffer, A.P. Ramirez, D.A. Huse, P.L. Gammel, U. Yaron, D.J. Bishop, A.J. Valentino, Phys. Rev. Lett. **74**, 2379 (1995). https://doi.org/10.1103/PhysRevLett.74.2379
3. J.A. Quilliam, S. Meng, H.A. Craig, L.R. Corruccini, G. Balakrishnan, O. A. Petrenko, A. Gomez, S.W. Kycia, M.J.P. Gingras, J.B. Kycia, Phys. Rev. B **87**, 174421 (2013). https://doi.org/10.1103/PhysRevB.87.174421
4. Y. Okamoto, M. Nohara, H. Aruga-Katori, H. Takagi, Phys. Rev. Lett. **99**, 137207 (2007). https://doi.org/10.1103/PhysRevLett.99.137207
5. S.-H. Lee, C. Broholm, W. Ratcliff, G. Gasparovic, Q. Huang, T.H. Kim, S.-W. Cheong, Nature **418**, 856 (2002). https://doi.org/10.1038/nature00964
6. A. Sadeghi, M. Alaei, F. Shahbazi, M.J.P. Gingras, Phys. Rev. B **91**, 140407 (2015). https://doi.org/10.1103/PhysRevB.91.140407
7. J.S. Gardner, M.J.P. Gingras, J.E. Greedan, Rev. Mod. Phys. **82**, 53 (2010). https://doi.org/10.1103/RevModPhys.82.53

8. J.S. Gardner, S.R. Dunsiger, B.D. Gaulin, M.J.P. Gingras, J.E. Greedan, R.F. Kiefl, M.D. Lumsden, W.A. MacFarlane, N.P. Raju, J.E. Sonier, I. Swainson, Z. Tun, Phys. Rev. Lett. **82**, 1012 (1999). https://doi.org/10.1103/PhysRevLett.82.1012
9. M.J.P. Gingras, C.V. Stager, N.P. Raju, B.D. Gaulin, J.E. Greedan, Phys. Rev. Lett. **78**, 947 (1997). https://doi.org/10.1103/PhysRevLett.78.947
10. B.D. Gaulin, J.N. Reimers, T.E. Mason, J.E. Greedan, Z. Tun, Phys. Rev. Lett. **69**, 3244 (1992). https://doi.org/10.1103/PhysRevLett.69.3244
11. M.J. Harris, S.T. Bramwell, D.F. McMorrow, T. Zeiske, K.W. Godfrey, Phys. Rev. Lett. **79**, 2554 (1997). https://doi.org/10.1103/PhysRevLett.79.2554
12. A.P. Ramirez, A. Hayashi, R.J. Cava, R. Siddharthan, B. S.Shastry, Nature **399**, 333 (1999). https://doi.org/10.1038/20619
13. K. Matsuhira, Y. Hinatsu, K. Tenya, H. Amitsuka, T. Sakakibara, J. Phys. Soc. Jpn. **71**, 1576 (2002). https://doi.org/10.1143/JPSJ.71.1576
14. H. Kadowaki, Y. Ishii, K. Matsuhira, Y. Hinatsu, Phys. Rev. B **65**, 144421 (2002). https://doi.org/10.1103/PhysRevB.65.144421
15. K. Matsuhira, M.Wakeshima, Y. Hinatsu, C. Sekine, C. Paulsen,T. Sakakibara, S. Takagi, J. Phys.: Conf. Ser. **320**, 012050 (2011). https://doi.org/10.1088/1742-6596/320/1/012050
16. H.D. Zhou, J.G. Cheng, A.M. Hallas, C.R. Wiebe, G. Li, L. Balicas, J.S. Zhou, J.B. Goodenough, J.S. Gardner, E.S. Choi, Phys. Rev. Lett. **108**, 207206 (2012). https://doi.org/10.1103/PhysRevLett.108.207206
17. J. Lago, I Živković, B.Z. Malkin, J. Rodriguez Fernandez, P. Ghigna, P. Dalmas de Réotier, A Yaouanc, T. Rojo, Phys. Rev. Lett. **104**, 247203 (2010). https://doi.org/10.1103/PhysRevLett.104.247203
18. S.T. Bramwell, M.J. Harris, J. Phys.: Condens. Matter **10**, L215 (1998). https://doi.org/10.1088/0953-8984/10/14/002
19. R. Moessner, Phys. Rev. B **57**, 5587 (1998). https://doi.org/10.1103/PhysRevB.57.R5587
20. J.D. Bernal, R.H. Fowler, J. Chem. Phys. **1**, 515 (1933). https://doi.org/10.1063/1.1749327
21. S.T. Bramwell, M.J.P. Gingras, Science **294**, 1495 (2001). https://doi.org/10.1126/science.1064761
22. P.W. Anderson, Phys. Rev. **102**, 1008 (1956). https://doi.org/10.1103/PhysRev.102.1008
23. L. Pauling, J. Am. Chem. Soc. **57**, 2680 (1935). https://doi.org/10.1021/ja01315a102
24. J.F. Nagle, J. Math Phys. **7**, 1484 (1966). https://doi.org/10.1063/1.1705058
25. R.R.P. Singh, J. Oitmaa, Phys. Rev. B **85**, 144414 (2012). https://doi.org/10.1103/PhysRevB.85.144414
26. N.W. Ashcroft, N.D. Mermin, *Solid State Physics* (Harcourt, 1976)
27. S. Erfanifam, S. Zherlitsyn, S. Yasin, Y. Skourski, J. Wosnitza, A.A. Zvyagin, P. McClarty, R. Moessner, G. Balakrishnan, O.A. Petrenko, Phys. Rev. B **90**, 064409 (2014). https://doi.org/10.1103/PhysRevB.90.064409
28. A. Abragam, B. Bleaney, *Electron Paramagnetic Resonance of Transition Ions* (Dover, 1986)
29. P. Fazekas, *Lecture Notes on Electron Correlation and Magnetism* (World Scientific, 1999)
30. M.T. Hutchings, in *Solid State Physics*, vol. 16, ed. by F. Seitz, D. Turnbull (Academic, New York, 1964), p. 227
31. K.R. Lea, M.J.M. Leask, W.P. Wolf, J. Phys. Chem. Solids **23**, 1381 (1962). https://doi.org/10.1016/0022-3697(62)90192-0
32. P.-A. Lindgard, J. Phys. C **8**, 3401 (1975). https://doi.org/10.1016/0304-8853(85)90225-2
33. J.G. Rau, M.J.P. Gingras, Phys. Rev. B **92**, 144417 (2015). https://doi.org/10.1103/PhysRevB.92.144417
34. L.G. Mamsurova, K.S. Pigal'skii, K.K. Pukhov, N.G. Trusevich, L.G. Shcherbakova, Sov. Phys. JETP **67**, 550 (1988). http://www.jetp.ac.ru/cgi-bin/e/index/e/67/3/p550?a=list
35. B.D. Gaulin, J.S. Gardner, P.A. McClarty, M.J.P. Gingras, Phys. Rev. B **84**, 140402(R) (2011). https://doi.org/10.1103/PhysRevB.84.140402
36. K. Kimura, S. Nakatsuji, J-J. Wen, C. Broholm, M. B. Stone, E. Nishibori, H. Sawa, Nature Comm. **4**, 1934 (2013). https://doi.org/10.1038/ncomms2914

37. Y-P. Huang, G. Chen, M. Hermele, Phys. Rev. Lett. **112**, 167203 (2014). https://doi.org/10.1103/PhysRevLett.112.167203
38. K. Matsuhira, Y. Hinatsu,T. Sakakibara, J. Phys.: Condens. Matter **13**, L737 (2001). https://doi.org/10.1088/0953-8984/13/31/101
39. J. Snyder, J.S. Slusky, R.J. Cava, P. Schiffer, Nature **413**, 48 (2001). https://doi.org/10.1038/35092516
40. J.A. Quilliam, L.R. Yaraskavitch, H.A. Dabkowska, B.D. Gaulin, J.B. Kycia, Phys. Rev. B **83**, 094424 (2011). https://doi.org/10.1103/PhysRevB.83.094424
41. H.M. Revell, L.R. Yaraskavitch, J.D. Mason, K.A. Ross, H.M.L. Noad, H.A. Dabkowska, B.D. Gaulin, P. Henelius, J.B. Kycia, Nat. Phys. **9**, 34 (2013). https://doi.org/10.1038/nphys2466
42. S. Rosenkranz, A.P. Ramirez, A. Hayashi, R.J. Cava, R. Siddharthan, B.S. Shastry, J. Appl. Phys. **84**, 5914 (2000). https://doi.org/10.1063/1.1323535
43. Y.M. Jana, A. Sengupta, D. Ghosh, J. Mag. Mag. Materials **248**, 7 (2002). https://doi.org/10.1016/S0304-8853(01)00983-0
44. B. Z. Malkin, A. R. Zakirov, M. N. Popova, S. A. Klimin, E. P. Chukalina, E. Antic-Fidancev, P. Goldner, P. Aschehoug, G. Dhalenne, Phys. Rev. B **70**, 075112 (2004) https://doi.org/10.1103/PhysRevB.70.075112
45. T.T.A. Lummen, I.P. Handayani, M.C. Donker, D. Fausti, G. Dhalenne, P. Berthet, A. Revcolevschi, P.H. M. van Loosdrecht, Phys. Rev. B **77**, 214310 (2008). https://doi.org/10.1103/PhysRevB.77.214310
46. B.Z. Malkin, T.T.A. Lummen, P.H.M. van Loosdrecht, G. Dhalenne, A.R. Zakirov, J. Phys.:Condens. Matter **22**, 276003 (2010). https://doi.org/10.1088/0953-8984/22/27/276003
47. A. Bertin, Y. Chapuis, P. Dalmas de Réotier, A. Yaouanc, J. Phys.:Condens. Matter **24**, 256003 (2012). https://doi.org/10.1088/0953-8984/24/25/256003
48. M. Ruminy, E. Pomjakushina, K. Iida, K. Kamazawa, D.T. Adroja, U. Stuhr, T. Fennell, Phys. Rev. B **94**, 024430 (2016). https://doi.org/10.1103/PhysRevB.94.024430
49. J.S. Gardner, B.D. Gaulin, A.J. Berlinsky, P. Waldron, S.R. Dunsiger, N.P. Raju, J.E. Greedan, Phys. Rev. B **64**, 224416 (2001). https://doi.org/10.1103/PhysRevB.64.224416
50. Y.-J. Kao, M. Enjalran, A. Del Maestro, H.R. Molavian, M.J.P. Gingras, Phys. Rev. B **68**, 172407 (2003). https://doi.org/10.1103/PhysRevB.68.172407
51. H.R. Molavian, M.J.P. Gingras, B. Canals, Phys. Rev. Lett. **98**, 157204 (2007). https://doi.org/10.1103/PhysRevLett.98.157204
52. R. Siddharthan, B.S. Shastry, A.P. Ramirez, A. Hayashi, R.J. Cava, S. Rosenkranz, Phys. Rev. Lett. **83**, 1854 (1999). https://doi.org/10.1103/PhysRevLett.83.1854
53. B.C. den Hertog, M.J.P. Gingras, Phys. Rev. Lett. **84**, 3430 (2000). https://doi.org/10.1103/PhysRevLett.84.3430
54. Y. Tabata, H. Kadowaki, K. Matsuhira, Z. Hiroi, N. Aso, E. Ressouche, B. Fåk, Phys. Rev. Lett. **97**, 257205 (2006). https://doi.org/10.1103/PhysRevLett.97.257205
55. T. Yavorskii, T. Fennell, M.J.P. Gingras, S.T. Bramwell, Phys. Rev. Lett. **101**, 037204 (2008). https://doi.org/10.1103/PhysRevLett.101.037204
56. J.P.C. Ruff, R.G. Melko, M.J.P. Gingras, Phys. Rev. Lett. **95**, 097202 (2005). https://doi.org/10.1103/PhysRevLett.95.097202
57. P. Henelius, T. Lin, M. Enjalran, Z. Hao, J. G. Rau, J. Altosaar, F. Flicker, T. Yavors'kii, M.J.P. Gingras, Phys. Rev. B **93**, 024402 (2016). https://doi.org/10.1103/PhysRevB.93.024402
58. S.T. Bramwell, M.J. Harris, B.C. den Hertog, M.J.P. Gingras, JS. Gardner, D.F. McMorrow, A.R. Wildes, A.L. Cornelius, J.D.M. Champion, R.G. Melko, T. Fennell, Phys. Rev. Lett. **87**, 047205 (2001). https://doi.org/10.1103/PhysRevLett.87.047205
59. P.A. McClarty, O. Sikora, R. Moessner, K. Penc, F. Pollmann, N. Shannon, Phys. Rev. B **92**, 094418 (2015). https://doi.org/10.1103/PhysRevB.92.094418
60. M.J.P. Gingras, B.C. den Hertog, Can. J. Phys. **79**, 1339 (2001). https://doi.org/10.1139/p01-099
61. R.G. Melko, B.C. den Hertog, M.J.P. Gingras, Phys. Rev. Lett. **87**, 067203 (2001). https://doi.org/10.1103/PhysRevLett.87.067203

62. S. V. Isakov, R. Moessner, S. L. Sondhi, Phys. Rev. Lett. **95**, 217201 (2005). https://doi.org/10.1103/PhysRevLett.95.217201
63. S. Onoda, Y. Tanaka, Phys. Rev. B **83**, 094411 (2011). https://doi.org/10.1103/PhysRevB.83.094411
64. S. Lee, S. Onoda, L. Balents, Phys. Rev. B **86**, 104412 (2012). https://doi.org/10.1103/PhysRevB.86.104412
65. K.A. Ross, L. Savary, B.D. Gaulin, L. Balents, Phys. Rev. X **1**, 021002 (2011). https://doi.org/10.1103/PhysRevX.1.021002
66. L. Savary, L. Balents, Phys. Rev. Lett. **108**, 037202 (2012). https://doi.org/10.1103/PhysRevLett.108.037202
67. M.J.P. Gingras, P.A. McClarty, Rep. Prog. Phys. **77**, 056501 (2014). https://doi.org/10.1088/0034-4885/77/5/056501
68. S. Onoda, J. Phys.: Conf. Ser. **320**, 012065 (2011). https://doi.org/10.1088/1742-6596/320/1/012065
69. J.G. Rau, S. Petit, M.J.P. Gingras, Phys. Rev. B **93**, 184408 (2016). https://doi.org/10.1103/PhysRevB.93.184408
70. L.D.C. Jaubert, P.C.W. Holdsworth, J. Phys.: Condens. Matter **23**, 164222 (2011). https://doi.org/10.1088/0953-8984/23/16/164222
71. A. Sen, R. Moessner, S.L. Sondhi, Phys. Rev. Lett. **110**, 107202 (2013). https://doi.org/10.1103/PhysRevLett.110.107202
72. R. Youngblood, J.D. Axe, B.M. McCoy, Phys. Rev. B **21**, 5212 (1980). https://doi.org/10.1103/PhysRevB.21.5212
73. C.L. Henley, Annu. Rev. Condens. Matter Phys. **1**, 179 (2010). https://doi.org/10.1146/annurev-conmatphys-070909-104138
74. C. Castelnovo, R. Moessner, S.L. Sondhi, Nature **451**, 42 (2008). https://doi.org/10.1038/nature06433

Chapter 2
Crystal Growth of Pyrochlore Compounds

D. Prabhakaran

Abstract I will review some of the crystals in the pyrochlore family, which have been grown by flux growth, optical floating-zone and other techniques. The presence of defects in the crystals, such as: stuffing or sight mixing, mixed rare earth valency states, disorder and oxygen non-stoichiometry can have a strong effect on the structural and magnetic properties of the crystal. I will discuss some of the crystal defects using a few examples.

2.1 Introduction

Geometrically frustrated magnetic materials are fascinating due to their interesting behaviours such as: spin-liquid, spin-glass and spin-ice. The general formula for pyrochlore compound is $A_2B_2O_6O'$, which comes from the mineral $NaCaNb_2O_6F$ [1]. The space group of this structure is F*d3m* (No. 227) with eight molecules per unit cell ($z = 8$). Here the atoms (A, B) which have a valency of either (2^+, 5^+) or (3^+, 4^+) respectively, are called α-pyrochlore compounds. AOs_2O_6 type compounds are called β pyrochlores [2] which crystallise in the non-centrosymmetric F43m space group (Fig. 2.1). The most studied A sites are: Bi, Tl, lanthanides, In or Sc, parallelly the B sites are: 3d, 4d or 5d elements. Either one, or both sub-lattices can be magnetic or non magnetic for example: in the case of $Dy_2Ti_2O_7$, Dy is magnetic, and in the case of $Y_2Ir_2O_7$, Ir is magnetic. The majority of these oxides are insulators however, a few classes of materials exhibit different properties such as: colossal magnetoresistance evident in the $Tl_2Mn_2O_7$ [3]; metal-insulator transition in $Nd_2Ir_2O_7$ [4]; ferromagnetism in $Lu_2V_2O_7$ [5]; anti-ferromagnetism and superconductivity in $Cd_2Re_2O_7$ [6]. Depending on the ionic radius ratio (r_{A+}/r_{B+}), the stable phase can be prepared in atmospheric conditions (ratio between 1.46 to 1.8).

D. Prabhakaran (✉)
Department of Physics, Clarendon Laboratory, University of Oxford, Oxford OX1 3PU, UK
e-mail: d.prabhakaran@physics.ox.ac.uk

M. Udagawa and L. Jaubert (eds.), *Spin Ice*, Springer Series in Solid-State Sciences 197,
https://doi.org/10.1007/978-3-030-70860-3_2

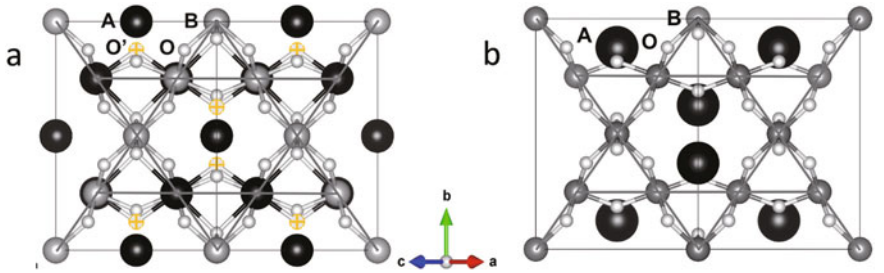

Fig. 2.1 Crystal structure of $A_2B_2O_6O'$, **a** α-pyrochlore and **b** β-pyrochlore along [110] direction

However, a few classes of materials need a high pressure synthesis route in order to stabilise its oxidation state and pyrochlore structure of the B site atom (Mn, Ge, Pb). Subramanian et al. [7] reviewed the structural and physical properties of a whole range of oxide pyrochlore compounds in detail; Gardner et al. [8] discussed some of the recent works on the magnetic pyrochlore compounds and, more details about the single-ion theory of these materials have been discussed in Chap. 1.

In the $A_2B_2O_6O'$ pyrochlore structure, the A site occupies the 16d location (1/2, 1/2, 1/2) with 8 coordination (6O + 2O′) and the B site occupies the 16c location (0,0,0) with 6 coordination (6O) forming two distinct interpenetrations of the three-dimensional network of the corner-sharing tetrahedra. Both O (x, 1/8, 1/8) and O′ (3/8, 3/8, 3/8) occupy the 48f and 8b sites, respectively. Here, x is the adjustable position parameter for the O atom which can be measured from X-ray or neutron structural analysis, with its possible values being between $x = 0.3125$ (perfect octahedron of O atoms surrounding the B atoms) and $x = 0.375$ (perfect cube of O atoms surrounding the A atoms), but the normal range would be 0.320–0.345.

Pyrochlore structural defects or disorders can occur due to the removal of the oxygen atom from the weaker O′ site compared to that of O site [7, 9]. Moreover, in the defective fluoride structure, the B-O-B bond angle will be around 110° whereas in the stoichiometric pyrochlore structure it will be between 120° and 140°. The defectiveness increases [10] with large size B atoms like Zr and Hf, with the increase of rare earth atomic number A atoms (Dy-Lu).

A wide range of growth techniques such as flux, optical floating-zone, Czochralski, chemical vapour transport, Bridgman and high pressure were employed to grow pyrochlore single crystals and some of them are listed in Table 2.1. Recently pulsed laser deposition technique has been used to prepare epitaxial pyrochlore films on a $Y_2Ti_2O_7$ substrate to study the strain effect on the magnetic property of the film [11]. Among these, flux and optical floating-zone techniques have been most widely used to prepare the majority of the pyrochlore family of materials, discussed further in this chapter.

Table 2.1 Some of the pyrochlore crystals grown by different techniques

Method	Material	Reference	Method	Material	Reference
Flux	$RE_2Ti_2O_7$	[23]	Floating-zone	$RE_2Ti_2O_7$	[13, 16], [36]–[39], [44]
	$RbCoCrF_6$	[33, 34]		$RE_2Zr_2O_7$	[51]
	$Y_2Pt_2O_7$	[26]		$RE_2Mo_2O_7$	[45, 46]
	$Pr_2Ir_2O_7$	[29]		$RE_2V_2O_7$	[53]
	$Tb_2Sn_2O_7$	[27]		$NaCaCo_2F_7$	[40]
	$RE_2Sn_2O_7$	[27, 28]		$Pr_2Hf_2O_7$	[52]
	$Pb_{1.86}Mg_{0.24}Nb_{1.76}O_{6.5}$	[24]			
	$Pb_2Sc_{0.5}Ta_{1.5}O_{6.5}$	[25]			
	$Bi_2Ru_2O_7$	[30]			
	$RbCoCrGF_6$	[33, 34]			
Czochralski	$RE_2Ti_2O_7$	[55, 56]	Chemical Vapour Transport	$Cd_2Re_2O_7$	[6]
	$CsMnFeF_6$	[66]	(CVT)	$Cd_2Os_2O_7$	[64]
				$Pr_2Te_2O_7$	[65]

2.2 Experimental

2.2.1 Material Synthesis

Most of the pyrochlore compounds such as titanates, stannates, zirconates, vanadates, molybdates and iridates were prepared using the solid state reaction technique or ceramic technology route. Rare earth oxide chemicals are very fine powders, so they tend to absorb moisture or have a mixed valency state. Hence, it is important to heat-treat the powder at around 1100 °C for 12h in air before weighing the chemicals. Knop et al. [12] prepared a wide range of pyrochlore titanates and germanates and reported the mixed valency state of Tb using thermal analysis. Polycrystalline samples were prepared by mixing A site rare earth oxides (RE_2O_3), and B site transition metal oxides (TiO_2, SnO_2, ZrO_2, VO_2, MoO_2 or IrO_2) according to their stoichiometric molar ratio and sintering at different high temperatures (1000–1450 °C) in air, or in a controlled atmosphere, for example, $RE_2Mo_2O_7$ under a flow of Argon while $Nd_2Ir_2O_7$ under vacuum for several hours or days with intermediate grindings to obtain the single phase compounds [4, 5, 12–17]. Other polycrystalline pyrochlores such as magnate, lead and germanate are prepared using high pressure (>2GPa) synthesis in order to stabilise the cubic phase, Pb^{4+} and Mn^{4+} ionic states respectively [3, 18].

2.2.2 *Flux Growth Technique*

The flux growth technique is a high temperature solution growth process, wherein the flux melts at high temperatures and acts as solvent. It is used to crystallise a wide range of materials which possess some of the following properties: incongruent melting (decomposes before melting), high melting point, high vapour pressure, and phase transition below the melting point. In a normal flux growth, first the constituents of the target compound are dissolved at a high temperature in a flux, commonly an oxide, molten salt, halide or metal, packed inside a platinum or refractory crucible or evacuated quartz tube [19–21]. Referring to the relevant chemical phase diagram is very important for selecting the flux ratios and growth temperature. A narrow region of pyrochlore phase is shown in the Y_2O_3-TiO_2 chemical phase diagram [22] in Fig. 2.2a. Stoichiometric amounts of the starting chemicals and suitable flux are mixed and packed into a platinum crucible and covered with a tight lid to prevent the evaporation loss and loaded into a high temperature furnace. The growth temperature varies between 750 °C and 1250 °C depending on the material, a controlled atmosphere (Ar, N_2), air or a vacuum have been used and the melt will be slowly cooled down below the melting point of the flux at a rate of 1–5 °C/h and finally cool down to room temperature at 50 °C/h. Spontaneous nucleation will occur mostly at the bottom or the walls of the crucible due to supersaturation, which will produce many crystals of different sizes where the temperature gradient is high [19, 20]. After the growth, the flux will be removed by using warm dilute acetic and nitric acid solutions, and

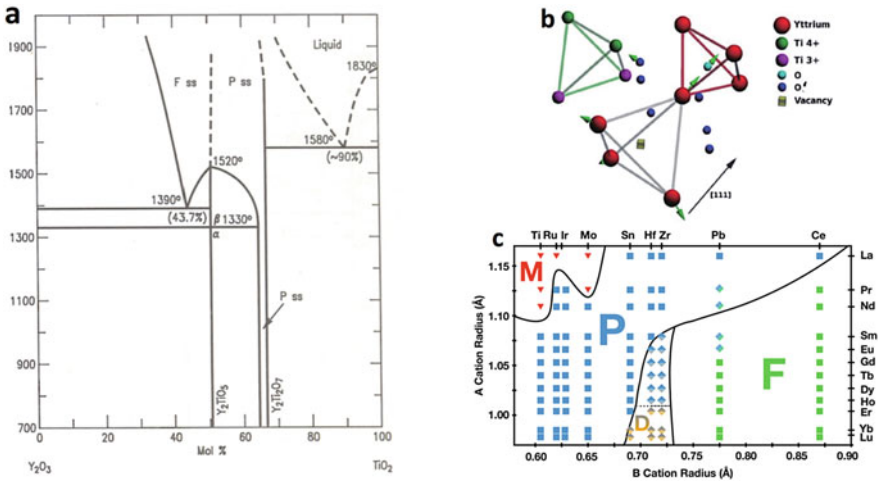

Fig. 2.2 **a** Y_2O_3-TiO_2 chemical phase diagram Figure no. 6024 reproduced from [22] with permission from the American Ceramic Society **b** diagram of O′ vacancies and the associated distortion of the surrounding lattice with displacement from [9] with permission from Nature Materials **c** Formation of different stable $A_2B_2O_7$ phases by varying the A and B cations; M-Monoclinic P-cubic pyrochlore, D-disordered and F-fluorite

octahedral shaped millimetre size crystals can be separated. In this technique there are certain disadvantages: (i) the crystal size will be small; (ii) flux inclusion may be present in the grown crystal. Most of the earlier pyrochlore crystals were grown using Pb based flux compounds but now, due to health risks and environmental pollution, there are severe restrictions for using the Pb based compounds in some laboratories.

The first pyrochlore $RE_2Ti_2O_7$ octahedral crystal, of size 3mm was grown by using PbF_2 flux at 1230 °C for a week in a closed platinum crucible by Garton and Wanklyn [23]. The combination of PbF_2 and PbO_2 did not produce any crystals. However, oxygen deficient cubic $Pb_{1.86}Mg_{0.24}Nb_{1.76}O_{6.5}$ single crystals have been grown using PbO flux. Here, Mg occupies the B site and the oxygen position parameter $x = 0.3175$ lies within the pyrochlore range but without any ordering of the Mg ions [24]. Recent neutron scattering experiments suggest that by removing the oxygen O′ atom (8b) the unit cell value increases due to the Coulomb repulsion between the O′ vacancies and the A octahedral (Fig. 2.2b) [9]. The oxygen deficiency creates a defect in the system and in order to compensate for the charge, a fraction of either A or B atom valency has to decrease from 3^+ to 2^+ or 4^+ to 3^+, respectively. Combinations of $PbO:PbF_2:B_2O_3$ fluxes have been used by Petrova et al. [25] to grow $Pb_2Sc_{0.5}Ta_{1.5}O_{6.5}$ single crystals. By varying the A and B cations, several different stable $A_2B_2O_7$ polycrystalline phases has been synthesised; M-monoclinic, P-cubic, D-disordered and F-fluorite as shown in Fig. 2.2c.

Metallic greenish $RE_2Pt_2O_7$ crystals were grown by Ostorero and Makram [26] using PbO-PbO_2 mixed flux in a tightly covered platinum crucible under 12 bar oxygen pressure and the melt was cooled from 1290 °C down to 940 °C following which it was quenched in order to avoid the $Pb_2Pt_2O_7$ crystallisation. Recently small size $RE_2Sn_2O_7$ single crystals have been grown using $Na_2B_4O_7$-NaF flux through spontaneous nucleation [27, 28]. Both the solute ($RE_2Sn_2O_7$) ratio and slow cooling rate (2 °C/day) are very important for inclusion free growth. In order to improve the size, Guo et al. [27] introduced a $Tb_2Ti_2O_7$ seed crystal (top seeded solution growth) with a 20% solute percentage and yielded a 4mm size crystal. Since stanates have an incongerant melting point, it can't be grown using the melt technique. Moreover Tin oxide has a huge vapour pessure which limits the floating zone growth.

The as grown $Tb_2Sn_2O_7$ crystal is dark in colour because Tb^{3+} losses an electron and becomes Tb^{4+} in a oxygen environment, especially in the cubic phase, however by annealing the same crystal under vacuum it becomes a transparent yellow in colour as shown in Figs. 2.3a, b. However, the colour of the $Dy_2Sn_2O_7$ crystal did not change after the heat treatment (Fig. 2.3c).

Rare earth iridates have different properties such as: insulator, ($Y_2Ir_2O_7$); metal-to-insulator, ($Nd_2Ir_2O_7$) and metallic ($Bi_2Ir_2O_7$, $Bi_2Ru_2O_7$). The crystals were grown using rare earth chlorides, KF and Bi_2O_3 flux [29, 30], respectively. Mugavero et al. [31] reviewed the crystal growth of rare earth oxides containing complex platinum group metal oxide compounds using several hydroxide fluxes. Since IrO_2 has a high vapour pressure at high temperatures, it is almost impossible to grow the crystal using the optical floating-zone technique. Small size iridate crystals can be grown using flux or high pressure techniques and they are stable in air. Millican et al. [29] grew octahedral shaped $RE_2Ir_2O_7$ single crystals (Fig. 2.3d) using 1:200

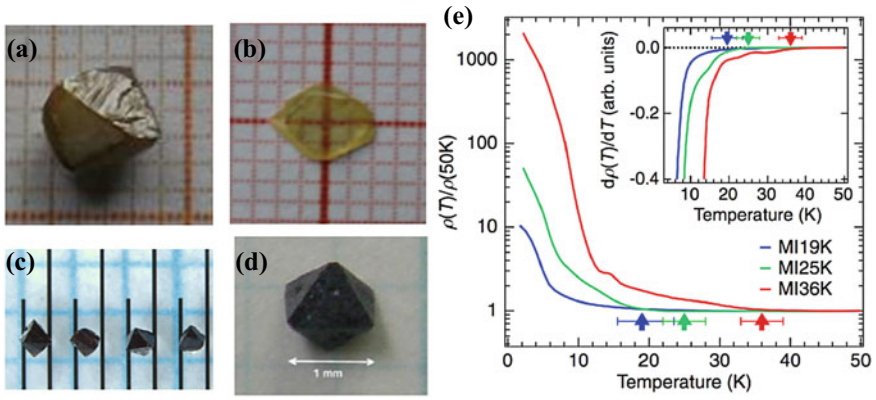

Fig. 2.3 **a** As grown $Tb_2Sn_2O_7$ crystal and **b** annealed under vacuum from [27] **c** as grown $Dy_2Sn_2O_7$ flux crystal from [28] **d** flux grown octahedral shaped $Pr_2Ir_2O_7$ crystal from [29]. **e** Temperature dependence of the resistivity of three different $Nd_2Ir_2O_7$ crystals from [32]. Reprinted figures from [27–29] with permission from Elsevier and from [32] with permission from the American Physical Society

KF flux ratio molten at 1100 °C and slowly cooled down to 850 °C at 2–3 °C/h rate and fast cooled to room temperature. After cleaning the flux, several crystals were harvested and had their electrical and magnetic properties checked individually. Because, even a slight variation in the Ir/Nd ratio (1% or 2%) of the single crystal will shift the metal-insulator (MI) transition temperature from 35K to 19K as shown in Fig. 2.3e [32].

$AM^{2+}M^{3+}F_6$ (A=K, Rb, Cs; M^{2+}=Fe, Co, Ni, Zn; M^{3+}=Al, V, Cr, Fe), pyrochlore fluoride compounds have been grown using different flux compounds like, KCl, NaCl, PbF_2 or RbCl [33, 34]. Some of those growths were not successful due to the presence of oxygen in the melt. The majority of these compounds are cubic with F*d3m* space group and antiferromagnetic nature without any long range magnetic order.

2.2.3 Optical Floating-Zone Technique

For the optical floating-zone growth, first polycrystalline starting materials are prepared by using solid state reaction technique as described in Sect. 2.2.1. The single phase powder is then compressed in the form of cylindrical rods (6–12 mm diameter and up to 12 cm length) and sintered at 1250–1450 °C for 12 h in air or a controlled atmosphere. Single crystals were grown under different atmospheres (air, O_2, Ar, Ar+O_2, Ar+H_2, or CO+CO_2) at a rate of 1–10 mm/h with both feed and seed rod counter rotated at 10–30 rpm however, a slower growth rate would help to minimize the defects in the crystal [13, 14, 16, 35–40]. As grown crystals are annealed under

different conditions in order to remove the defects and are discussed in the following section.

The first floating-zone technique was developed to grow silicon and ferrite crystals using a carbon-arc or xenon-arc as a source and it was later replaced by the halogen lamp as a heating source [41, 42]. In this technique, the optical light is focused to a narrow region in order to melt the tip of a polycrystalline rod and also a single crystal seed; then either the beam or polycrystalline and seed rods are simultaneously moved upwards, allowing for a slow re-crystallization of the sample in a single crystal form. In the last fifteen years, this technique has rapidly expanded both in research laboratories and industry to prepare large size and high quality single crystals. The grown crystals are chemically very pure because the melt does not involve any contact with the crucible during growth which reduces the cross contamination in the crystal. There are a few commercial optical zone furnaces available now: single mirror (Russian design-ScIDre, Dresden), double mirror (Cannon-Japan, Cyperstar-France and Quantum Design-USA) and four mirror (CSI-Japan) as shown in Fig. 2.4a. In all these furnaces, either halogen or xenon lamps are used as a heating source, which will go to very high temperatures; ~ 2000 °C in the case of halogen, and ~2800 °C in the case of xenon, and can also apply high pressure up to 300 bar. This technique has some disadvantages; (i) high vapour pressure materials can't be grown because it will reduce the light passing through the glass tube; (ii) steep temperature gradients (~50–100 °C/mm) may induce some thermal cracks in the growing crystal. Currently, compact high power lasers have been developed as a source that can go up to 2800 °C with a very narrow beam size. This will be advantageous when growing highly volatile materials and can allow the use of solvents to grow incongruently melting materials like $BiFeO_3$ [43].

The first rare earth titanate single crystal was grown using optical floating-zone technique to study its piezoelectric property by Kimura et al. [36]. Pyrochlore titanates $RE_2Ti_2O_7$ (RE = Sm-Lu) melt congruently at around 1850°C and many groups have successfully grown several centimetre cubic size high quality crystals suitable for neutron scattering experiments using this technique [13, 14, 37–39]. Li et al. [44] grew a whole range of rare earth titanates by optimizing the growth conditions individually and studied their structure and physical parameters. Site mixing and oxygen deficiency are the common issues in these family of materials which are discussed in greater detail in Sect. 2.2.6.

Pyrochlore molybdate $RE_2Mo_2O_7$ compounds exhibit ferromagnetism due to the double-exchange mechanism between neighbouring Mo spins. A few groups have grown different rare earth Mo compounds under argon atmosphere using the floating-zone technique [45, 46]. However, due to the volatility of MoO_2, it is very difficult to grow a large crystal. As grown crystals are oxygen deficient, which leads them to assume a metallic state. So, after the growth the crystal has to be annealed under oxygen atmosphere in order to improve the oxygen stoichiometry. Among the rare earth molybdates, both Sm and Nd are metallic, others from Gd to Lu are ferromagnetic insulators and their lattice constant decreases with an increase in rare earth atomic number. Under high pressure or by substituting divalent Ca to the Gd site, $Gd_{2-x}Ca_xMo_2O_7$ become metallic [47].

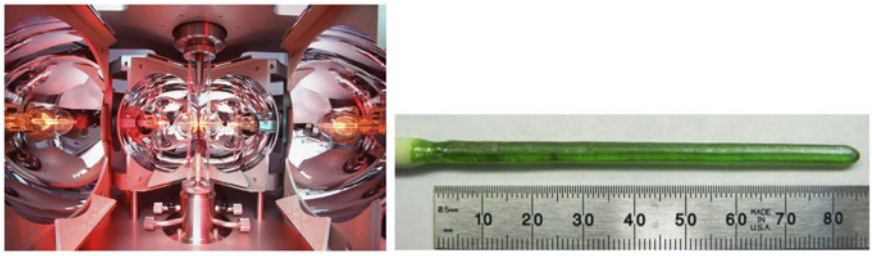

Fig. 2.4 (Left) Photograph of a four mirror Optical-floating zone furnace. (Right) As-grown $Pr_2Zr_2O_7$ crystal. Reprinted figure from [50] with permission from Elsevier

For the first time, a bismuth based pyrochlore $Bi_{1.89}Fe_{1.16}Nb_{0.95}O_{6.95}$ single crystal was grown by Miiller et al. [48], a slight site mixing of Fe atom on both A and B sites are necessary in order to stabilise the cubic phase and a strong short-range disorder appears due to the displacement of Bi^{3+} and O′ from their ideal position. In the case of $Tb_2Nb_2O_7$, both Tb and tetravalent Nb^{4+} ($4d^1$ s = 1/2) are magnetic, but the compound exhibits spin-glass behaviour due to the nearest-neighbour interaction and Jana et al. [49] prepared the sample using Tb_4O_7, NbO_2 and Nb chemicals under Ar atmosphere in an image furnace. Recently, the fluorine based pyrochlore $NaCaCo_2F_7$ was grown using the optical floating-zone technique. Here the A site elements, both Na and Ca are disordered, whereas the B site Co is fully ordered [40].

Some of the rare earth zirconates $RE_2Zr_2O_7$ (RE = La-Gd) will crystalize in cubic pyrochlore structures and their melting temperatures are well above 2400 °C, so xenon lamps are necessary to achieve this very high temperature. In particular, $Pr_2Zr_2O_7$ has attracted much attention due to its quantum spin-liquid property at low temperature. Matsuhira et al. [14] successfully grew dark green colour crystals under oxygen flow atmosphere by taking out excess Pr in the starting material in order to compensate for the evaporation loss and have grown a stoichiometric (Pr/Zr = 1.0) crystal. To study the effect of Pr/Zr ratio in the crystal, Koohpayeh et, al.[50] prepared different Pr compositions ($Pr_{2+x}Zr_{2-x}O_{7-x/2}$, $-0.02 \leq x \leq 0.02$) and crystals were grown with different rotation and pulling rates under 1 bar static high pure argon atmosphere. They used an argon atmosphere both for sintering and growth which has helped to reduce the Pr evaporation and also prevent the formation of Pr^{4+} inclusions and has resulted in light green colour crystal as shown in Fig. 2.4b. Recently several lanthanide zirconates and hafnates single crystals have been grown using different growth conditions by Ciomaga Hatnean et al. [51, 52].

$Ho_2V_2O_7$ and $Lu_2V_2O_7$ are ferromagnetic Mott insulators and the spontaneous magnetization appears below T_c = 70K. These pyrochlore vanadates are grown by the floating-zone technique using an argon atmosphere at a very slow growth rate of 0.6-1mm/h; Onose et al. [53] experimentally observed the thermal Hall effect caused by spin excitation in the $Lu_2V_2O_7$.

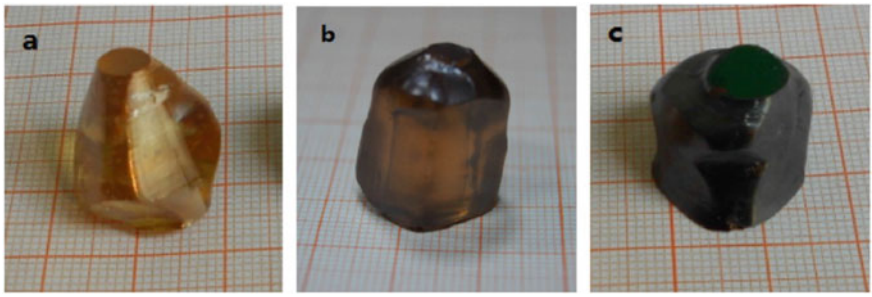

Fig. 2.5 $Gd_2Ti_2O_7$ crystal grown **a** along [111] direction under 0.8 bar N_2 pressure **b** along [100] direction under 0.6 bar N_2 pressure, **c** along [111] direction under 0.6 bar 98% N_2 + 2% O_2 crystal pictures. Reprinted figure from [56] with permission from Elsevier

2.2.4 Czochralski Technique

Czochralski growth is a pulling technique from the melt using a single crystal seed [54] and it has been recently used to grow $Dy_2Ti_2O_7$ crystal along [111] direction with a pulling rate of 1.5 mm/h in an iridium crucible using a radio frequency (RF) induction heating source. In order to reduce the colour centres, the grown crystal was annealed at 700 °C for 48h in air [55]. GuO et al. [56] grew the $Gd_2Ti_2O_7$ crystals under different atmospheres at a rate of 1–1.5 mm/h using both [111] and [100] seed crystals respectively. The pure nitrogen atmosphere grown crystal was light brown in colour (Fig. 2.5a, b) whereas 2% oxygen mixed gas grown crystal was dark brown colour as shown in Fig. 2.5c. Though the excess oxygen has changed the colour of the crystal, no change has been observed either in the powder x-ray or XPS spectra of all three crystals.

2.2.5 Characterisation

Both polycrystalline powders as well as grown crystals were carefully checked with powder x-ray diffraction to confirm the chemical phase purity and identify the crystal structure. Thermogravimetry analysis (TGA) is also used to analyse the high temperature reaction, oxidation, reduction and oxygen content estimation of the material. Scanning electron microscopy (SEM) is used to study the surface morphology of the grown crystals. Electron micro probe analysis (EMPA) and x-ray photo emission spectroscopy (XPS) techniques are employed to analyse the chemical composition and check the homogeneity across the length of the crystal. Single crystal x-ray diffraction has been used to study the crystal structure even with small crystals of the order of 10–50 micrometres. To identify the crystallographic orientations of a bulk crystal, the x-ray Laue technique has been used. Small size crystals were cut along

different crystallographic orientations and used to study their magnetic, transport and thermal properties.

2.2.6 Defects in the Crystal

The as grown crystal colour will vary with respect to the growth atmospheres, rotation and cooling rates, however the dark colour will change into a light colour after the post annealing heat treatment. This problem is common for all growth techniques including, flux, optical floating-zone and Czochralski. The darker colour could be due to the defects present in the crystal which will act as colour centres, either due to mixed valency states of the A or B atom or oxygen deficiency or a slight disorder may appear because of the high temperature gradient during the cooling process of the crystal after the growth. It can be removed by annealing the crystal at 1000–1300 °C for 12–72 h under the flow of different gas (O_2, Ar, CO/CO_2) or vacuum.

Many laboratories have successfully prepared the single phase stoichiometric $RE_2Ti_2O_7$ powder compounds by using the solid state reaction or sol-gel techniques without any trace of impurity or disorder. However, it has been a real challenge to prepare a well ordered single crystal that is vital for many of the crucial experiments such as neutron scattering, muon and heat capacity measurements. Li et al. [44] have applied a 4 bar oxygen pressure during the growth of $Dy_2Ti_2O_7$ and the grown crystal colour was dark brown and after the oxygen annealing treatment at 900 °C it became a light colour. Contradictory to this report, Kang et al. [55], have grown the same crystal under Ar atmosphere by Czochralski pulling method and it was annealed in air at 700 °C for 48 h to remove the defects but the colour remained a dark brown. The same piece of crystal was annealed again under the flow of ammonia with the same temperature and it was found that the colour changed from brown to yellow. The optical absorption loss in the wavelength range 380–580 nm of the oxygen annealed crystal was twice as high as the ammonia annealed crystal and hence the oxygen deficient crystal would be desirable for magneto-optical device fabrication. So, the colour issue is not just an oxygen deficiency problem but also due to the disorder in the system. To demonstrate this concept we initially grew a crystal under argon and oxygen mixed gas flow and after the termination of the growth, the lamp power was reduced down to around 1200 °C and the atmosphere was removed and the crystal was annealed under vacuum for 12 h. As shown in Fig. 2.6a, the annealed top part of the crystal became a light yellow (indicated by a vertical arrow) due to the reduction in the disorder/colour centres. Similarly, the bottom part of the crystal (Fig. 2.6b) was also annealed separately under vacuum and the colour changed from dark brown to light yellow colour as shown in Fig. 2.6c. Most of the optical furnaces effective hot zone range is around 2 cm and hence the sintering is effective in that part of the crystal. Magnetization versus applied field data of the as grown $Dy_2Ti_2O_7$ dark brown crystal grown under argon flow and the same crystal annealed under oxygen flow (light brown colour) measured along the [100] direction at 1.8 K is shown in

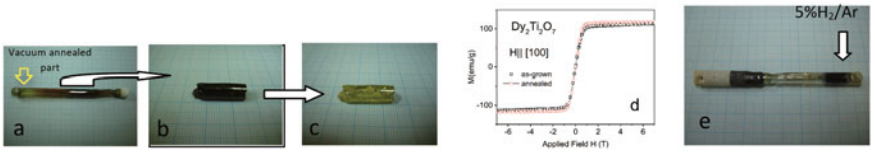

Fig. 2.6 $Dy_2Ti_2O_7$ crystal **a** grown under Ar/O_2 and annealed under vacuum (vertical arrow), **b** as-grown brown colour crystal and **c** the same crystal annealed under vacuum, **d** magnetisation versus applied field of the as grown and oxygen annealed crystal measured at 1.8 K and **e** $Y_2Ti_2O_7$ grown under O_2 (transparent part), $5\%H_2/Ar$ (indicated by an arrow)

Fig. 2.6d. A slight increase in the saturation magnetic moment was observed on the oxygen annealed crystal.

On the other hand, the $Y_2Ti_2O_7$ growth started with an oxygen atmosphere and in the later part of the growth its atmosphere was switched to $5\%H_2/Ar$ mixed gas. Due to the reduced atmosphere in the later part of the growth, the colour changed from transparent to dark blue (as pointed out by an arrow in Fig. 2.6e), due to the presence of Ti^{3+}. However, it became colourless after oxygen treatment.

To study the stability of the pyrochlore structure on the $Dy_2Ti_2O_7$ system, we have grown single crystals of Sc^{3+}substituted to the Ti^{4+} site and the corresponding oxygen cation will also be reduced in order to compensate for the charge. The crystals were zone melted twice; they were grown at a faster speed of 15 mm/h (premelting) and then the same crystal was grown again at a slower rate of 1-3mm/h under static 2 bar oxygen atmosphere. All the Sc substituted as grown crystals colour were yellow as shown in Fig. 2.7a, b ($x = 0.5$ and $x = 1$) and annealing had no effect. The pyrochlore structure remains cubic for values of upto $x = 0.67$ and when $x = 1$ it becomes a disordered fluorite structure. The powder x-ray pattern of different x values are shown in Fig. 2.7c and the pyrochlore characteristic peaks (111) and (331) are present for up to $x = 0.67$ but for the $x = 1$ sample both these peaks vanish and Fig. 2.7d shows the complete disappearance of the (331) peak.

Among the rare earth titanates, $Yb_2Ti_2O_7$ is of special interest due to their quantum spin liquid property. Some experiments suggest that it has a long range ferromagnetic order at around 200 mK range [17], while other experiments did not show any long range order [57]. This controversial report could be due to a very slight variation in the chemical composition (as much as 1–2% stuffing (A to B site mixing)) or defects present in the single crystal, but it was not realised earlier including the oxygen deficiency [58]. These defects are more prone to be in single crystals compared to powders. Heat capacity measurement on the powder sample shows a sharp peak around 260mK as a first order phase transition (Fig. 2.8a) whereas, the single crystal peak was several times smaller in amplitude and the transition temperature moved down to below 200mK and in some crystals shows no peaks at all as shown in Fig. 2.8b [17]. Recently, Arpino et al. [59] reported the highest heat capacity value for a stochiometric single crystal, the likes of which have only been attributed to powder data thus far and even 1–2% doping has shown to broaden the peak and decrease the transition temperature as shown in Fig. 2.8c. Both stoichiometric and defect free

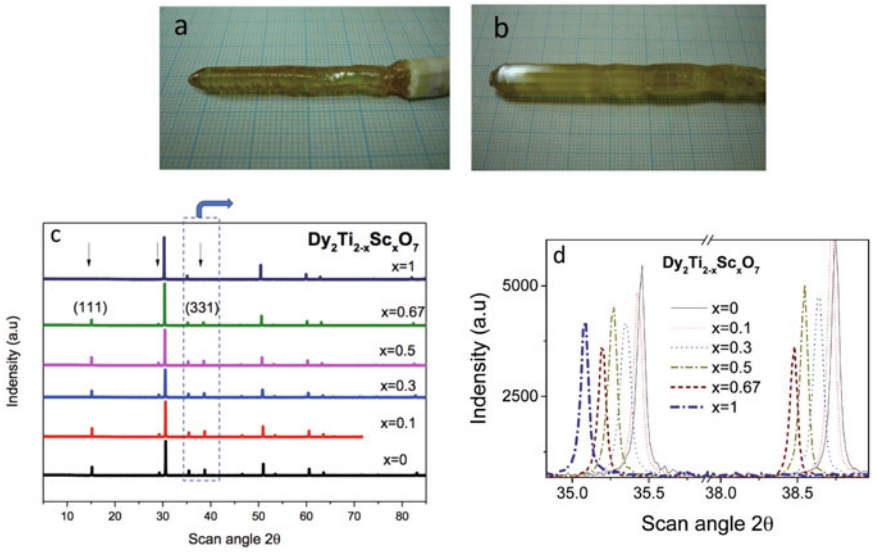

Fig. 2.7 As grown crystals **a** $Dy_2Ti_{1.5}Sc_{0.5}O_{6.75}$ **b** $Dy_2TiScO_{6.5}$ **c** crystal powder x-ray pattern of $Dy_2Sc_xTi_{2-x}O_{7-x/2}$ **d** expanded part (331) of the x-ray spectrum (**c**)

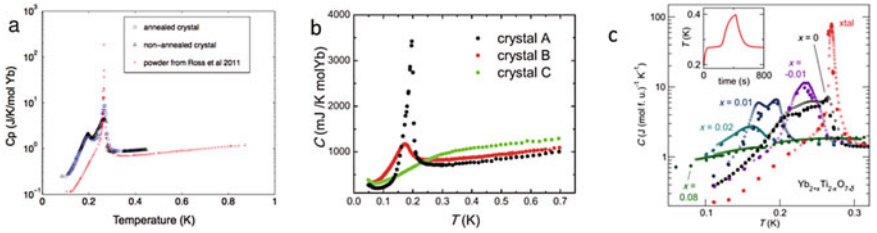

Fig. 2.8 Heat capacity as a function of temperature of $Yb_2Ti_2O_7$ **a** powder and single crystals from [58] **b** three different single crystals from [17] and **c** stochiometric single crystal and sintered rods of $Yb_{2+x}Ti_{2-x}O_{7-\delta}$ from [59]. Reprinted figures from [58, 59] with permission from the American Physical Society and from [17] with permission from Nature Communications

crystals are necessary for the strong peak in the heat capacity measurement. Another clear experimental evidence for the long range order was carried out by Chang et al. [17] using polarized neutron scattering experiments on a slowly grown crystal which showed a clear depolarization below 210 mK.

During crystal growth, stabilising the $Yb_2Ti_2O_7$ molten zone for a long time under an oxygen atmosphere is very difficult. To overcome this problem, we grew a large size crystal as shown in Fig. 2.9a under an argon atmosphere at 1.5mm/h which produced a black coloured crystal. Though Yb^{3+} is more stable than Yb^{2+}, a fraction of Yb^{2+} could be present in the as grown sample. This defect along with the oxygen deficiency can be removed by annealing the crystal at 1200 °C under oxygen flow for 48 h. This will transform the as-grown black crystal into an almost transparent

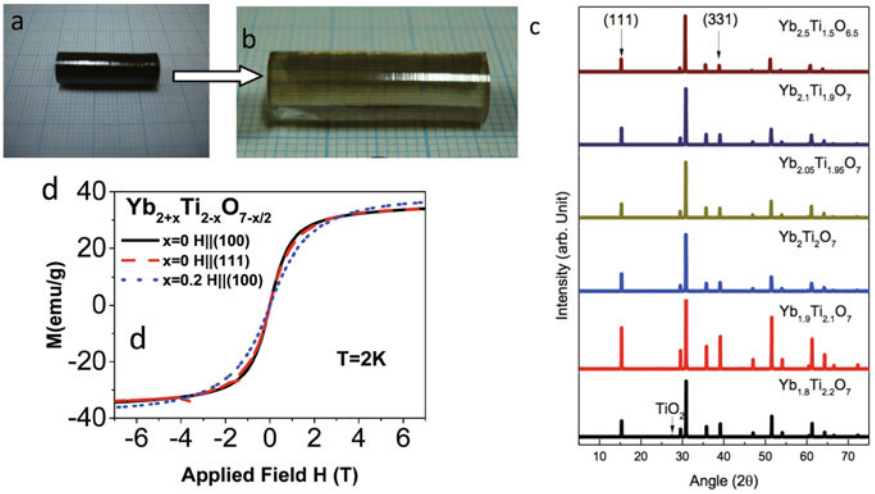

Fig. 2.9 **a** As-grown $Yb_2Ti_2O_7$ crystal grown under Ar atmosphere **b** same crystal after annealed under oxygen atmosphere. **c** Crystal powder x-ray pattern of $Yb_{2+x}Ti_{2-x}O_{7-x/2}$ **d** Magnetisation versus applied field curve for $x = 0$ and 0.2 crystals measured at 2K

colour as shown in Fig. 2.9b and as evident in the heat capacity data [60] at around 200 mK it shows a sharp peak similar to Chang et al. [17]. Li et al. [44] have grown $Yb_2Ti_2O_7$ crystal under 1 bar oxygen pressure at a growth rate of 3 mm/h, but the colour of the crystal was brown and did not show any heat capacity peak around 200mK.

Stuffing has been studied on the polycrystalline $Ho_{2\pm x}Ti_{2-x}O_{7-x/2}$ system by Lau et al. [61] and found that the magnetic Ho atom will randomly occupy the non-magnetic Ti atom and for $x = 0.67$, and it becomes a fluorite crystal structure. It also changes the magnetic interactions from ferromagnetic to antiferromagnetic due to the changes in the dipole interaction. However, recent high resolution synchrotron studies on the $Ho_2Ti_2O_7$ system suggest that a slight stuffing could be present in most of the melt grown rare earth titanates [62]. To explore the stuffing effect on the $Yb_{2\pm x}Ti_{2-x}O_{7-x/2}$ (x = –0.2, –0.1, 0, 0.05, 0.1, 0.2 , 0.3 and 0.5) system, single crystals were successfully grown for $x \geq 0$, but the $x = -0.1$ and –0.2 growth was not successful due to the presence of TiO_2 second phase in the melt. Yb^{3+} substitution to the Ti^{4+} site removed O′ atom to compensate for the charge in the Ti tetrahedra, and hence the four neighbouring Yb^{3+} ions move away from the vacancy (Fig. 2.2b) which increases the cell parameter value from 10.04Å to 10.159Å [62]. The crystal powder XRD pattern of $Yb_{2\pm x}Ti_{2-x}O_{7-x/2}$ is shown in Fig. 2.9c, all the Yb stuffed samples were cubic pyrochlore phase up to $x = 0.5$ which shows the (111) and (331) a characteristic sign of ordered pyrochlore phase as explained by Klef et al. [10]. Magnetic hysteresis versus applied field for the $x = 0$ and $x = 0.2$ crystal measured along [100] direction at 2 K (Fig. 2.9d) shows a slight variation.

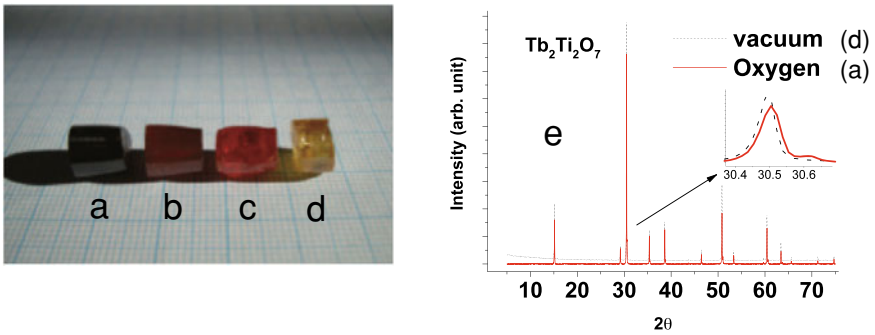

Fig. 2.10 $Tb_2Ti_2O_7$ crystal **a** as grown **b** annealed under vacuum **c** annealed under CO/CO_2 **d** grown under argon atmosphere **e** crystal powder x-ray pattern of oxygen and vacuum annealed sample

Terbium has two valency state 3^+ and 4^+. Although 3^+ is more stable, in high temperature oxygen environment, a small percentage will convert into Tb^{4+}. Most of the $Tb_2Ti_2O_7$ crystal have been grown under oxygen or argon atmosphere and they are black or light yellow in colour due to the presence of Tb^{4+} inclusions or oxygen vacancies. The as-grown black colour crystal (Fig. 2.10a) was annealed under a vacuum at around 1200 °C for 12 h and it became a brown colour as shown in Fig. 2.10b. Another black crystal was annealed under CO/CO_2 (1:9) flow at 1200 °C for 45h and the colour has changed to bright red as shown in Fig. 2.10c. Whereas, re-growing a previously grown crystal under argon flow conditions causes a colour change from brown to light yellow (Fig. 2.10d). A similar colour change was also reported on the $Tb_2Sn_2O_7$ solution grown crystal as shown in Fig. 2.3b [27]. The black crystal powder was annealed under oxygen flow at 1200 °C and the powder x-ray data showed additional peaks due to the presence of Tb^{4+}, but the vacuum annealed crystal powder pattern was very sharp without any additional peaks as shown in Fig. 2.10e. Recently a large thermal Hall response has been reported on an argon annealed transparent single crystal [63].

2.3 Conclusions

I have explained the most common crystal growth techniques that are used for pyrochlore crystal growth. The thermodynamics of the material determines the growth technique that is used. Electrical and magnetic properties are very sensitive to any site mixing and oxygen deficiency in the crystals. Defect free crystals are very important in understanding the structural and physical properties of the material. In order to improve the quality of the crystal, more characterisation studies are needed to truly understand the growth behaviours and mechanisms; subsequently this new understanding will shed light on ideas to improve quality. Further exploration of high pressure synthesis and the chemical vapour transport growth techniques could lead to the discovery of new materials.

Acknowledgements I would like to thank Prof. Andrew Boothroyd for his support throughout the project. A part of the work was done by Ms. Sichen Wang during her MPhys project work. I would also like to thank Dr. Sean Giblin for his discussion. I greatly acknowledge EPSRC EP/H033939/1 for the financial support.

References

1. H.R. von Gaertner, Neues Jb. Mineralog., Geol. Palaontol., Beilage-Bd. Abt. A **61**, 1 (1930)
2. G. Schuck, S.M. Kazakov, K. Rogacki, N.D. Zhigadlo, J. Karpinski, Phys. Rev. B **73**, 144506 (2006). https://doi.org/10.1103/PhysRevB.73.144506
3. M.A. Subramanian, B.H. Toby, A.P. Ramirez, W.J. Marshall, A.W. Sleight, G.H. Kwei, Science **273**, 81 (1996). https://doi.org/10.1126/science.273.5271.81
4. K. Matsuhira, M. Wakeshima, Y. Hinatsu, S. Takagi, J. Phys. Soc. Jpn. **80**, 094701 (2011). https://doi.org/10.1143/JPSJ.80.094701
5. H. Ichikawa, L. Kano, M. Saitoh, S. Miyahara, N. Furukawa, J. Akimitsu, T. Yokoo, T. Matsumura, M. Takeda, K. Hirota, J. Phys. Soc. Jpn. **74**, 1020 (2005). https://doi.org/10.1143/JPSJ.74.1020
6. R. Jin, J. He, S. McCall, C.S. Alexander, F. Drymiotis, D. Mandrus, Phys. Rev. B **64**, 180503 (2001). https://doi.org/10.1103/PhysRevB.64.180503
7. M.A. Subramanian, G. Aravamudan, G.V. Subba Rao, Prog. Solid St. Chem. **15**, 55 (1983). https://doi.org/10.1016/0079-6786(83)90001-8
8. J.S. Gardner, M.J.P. Gingras, J.E. Greedan, Rev. Mod. Phys. **82**, 53 (2010). https://doi.org/10.1103/RevModPhys.82.53
9. G. Sala, M.J. Gutmann, D. Prabhakaran, D. Pomaranski, C. Mitchelitis, J.B. Kycia, D.G. Porter, C. Castelnovo, J.P. Goff, Nat. Mater. **13**, 488 (2014). https://doi.org/10.1038/nmat3924
10. W.E. Klef, G. Weitz, J. Inorg, Nucl. Chem. **31**, 2367 (1969). https://doi.org/10.1016/0022-1902(69)80566-X
11. L. Bovo, X. Moya, D. Prabhakaran, Y-Ah Soh, A.T. Boothroyd, N.D. Mathur, G. Aeppli and S.T. Bramwell, Nat. Commun. **5**, 3439 (2014). https://doi.org/10.1038/ncomms4439
12. O. Knop, F. Brisse, L. Castelliz, Can. J. Chem. **47**, 971 (1968). https://doi.org/10.1139/v69-155
13. J.S. Gardner, B.D. Gaulin, D.M. Paul, J. Cryst. Growth **191**, 740 (1998). https://doi.org/10.1016/S0022-0248(98)00382-0
14. K. Matsuhira, C. Sekine, C. Paulsen, M. Wakeshima, Y. Hinatsu, T. Kitazawa, Y. Kiuchi, Z. Hiroi, S. Takagi, J. Phys.: Conf. Ser. **145**, 012031 (2009). https://doi.org/10.1088/1742-6596/145/1/012031
15. R.S. Roth, J. Research NBS **56**, 2643 (1956). https://doi.org/10.6028/JRES.056.003
16. H. Fukazawa, R.G. Melko, R. Higashinaka, Y. Maeno and M.J.P. Gingras, Phys. Rev. B **65**, 054410 (2002). https://doi.org/10.1103/PhysRevB.65.054410
17. L.J. Chang, S. Onoda, Y. Su, Y.J. Kao, K.D. Tsuei, Y. Yasui, K. Kakurai, M.R. Lees, Nat. Commun. **3**, 1989 (2012). https://doi.org/10.1038/ncomms1989
18. H.D. Zhou, S.T. Bramwell, J.G. Cheng, C.R. Wiebe, G. Li, L. Balicas, J.A. Bloxsom, H.J. Silverstein, J.S. Zhou, J.B. Goodenough, J.S. Gardner, Nat. Commun. **2**, 478 (2011). https://doi.org/10.1038/ncomms1483
19. B.M. Wanklyn, in, *Crystal Growth*, Vol.1, ed. by B.R. Pamplin (Pergamon Press, Oxford, 1974), pp. 93–262
20. D. Elwell, H.J. Scheel, *Crystal Growth from High-Temperature Solutions* (Academic Press, London, 1975)
21. P.C. Canfield, Z. Fisk, Philos. Mag. **65**, 1117 (1992). https://doi.org/10.1080/13642819208215073

22. E.M. Levin, Carl R. Robbins, H.F. McMurdie, 1964, Ed., Phase diagrams for Ceramists (The American Ceramic Society, Inc)
23. G. Garton, B.M. Wanklyn, J. Mater. Sci. **3**, 395 (1968). https://doi.org/10.1007/BF00550983
24. N. Wakiya, A. Saiki, N. Ishizawa, K. Shinozaki, N. Mizutani, Mater. Res. Bull. **28**, 137 (1993). https://doi.org/10.1016/0025-5408(93)90082-O
25. D. Petrova, S. Dobreva, M. Veleva, J. Macicek, M. Gospodinov, Mater. Res. Bull. **32**, 1543 (1997). https://doi.org/10.1016/S0025-5408(97)00136-0
26. J. Ostorero, H. Makram, J. Cryst. Growth **24–25**, 677 (1974). https://doi.org/10.1016/0022-0248(74)90404-7
27. F.Y. Guo, Q.P. Wan, Y. Hou, L.Z. Zhang, H. Fu, J.Z. Chen, J. Cryst. Growth **397**, 19 (2014). https://doi.org/10.1016/j.jcrysgro.2014.04.002
28. D. Prabhakaran, S. Wang and A. T. Boothroyd J. Cryst. Growth **468**, 335 (2017) http://doi.org/10.1016/j.jcrysgro.2016.10.069
29. J.N. Millican, R.T. Macaluso, S. Nakatsuji, Y. Machida, Y. Maeno, J.Y. Chan, Mater. Res. Bull. **42**, 928 (2007). https://doi.org/10.1016/j.materresbull.2006.08.011
30. B. Rehak, K. Horcic, M. Frumar, L. Koudelka, J. Cryst. Growth **68**, 647 (1984). https://doi.org/10.1016/0022-0248(84)90472-X
31. J. Mugavero III Samuel, R. William, Gemmill, P. Irina, Roof and Loye Hans-Conrad zur, J. Solid State Chem. **182**, 1950 (2009). https://doi.org/10.1016/j.jssc.2009.05.006
32. M. Nakayama, Takeshi Kondo, Z. Tian, J.J. Ishikawa, M. Halim, C. Bareille, W. Malaeb, K. Kuroda, T. Tomita, S. Ideta, K. Tanaka, M. Matsunami, S. Kimura, N. Inami, K. Ono, H. Kumigashira, L. Balents, S. Nakatsuji, S. Shin, Phys. Rev. Lett. **117**, 056403 (2016). https://doi.org/10.1103/PhysRevLett.117.056403
33. J. Nouet, C. Jacoboni, G. Ferey, J.Y. Gerard, R.D. Pape, J. Cryst. Growth **8**, 94 (1971). https://doi.org/10.1016/0022-0248(71)90028-5
34. B.M. Wanklyn, F.R. Wondre, B.J. Garrard, J. Cermak, W. Davison, J. Mater. Sci. **16**, 2303 (1981). https://doi.org/10.1007/BF00542395
35. T. Ito, T. Ushiyama, Y. Yanagisawa, R. Kumai, Y. Tomioka, Cryst. Growth Des. **11**, 5139 (2011). https://doi.org/10.1021/cg201068m
36. M. Kimura, S. Nanamatsu, K. Doi, S. Matsushita, M. Takahashi, Jpn. J. Appl. Phys. **11**, 904 (1972). https://doi.org/10.1143/JJAP.11.904
37. G. Balakrishnan, O.A. Petrenko, M.R. Lees, D. McK Paul, J. Phys.: Condens. Matter **10**, L723 (1998). https://doi.org/10.1088/0953-8984/10/44/002
38. H.A. Dabkowska, A.B. Dabkowski, *Handbook of Crystal Growth* (Springer, Berlin, 2010), p. 367
39. D. Prabhakaran, A.T. Boothroyd, J. Cryst. Growth. **318**, 1053 (2011). https://doi.org/10.1016/j.jcrysgro.2010.11.049
40. W. Krizan, R.J. Cava, Phys. Rev. B **89**, 214401 (2014). https://doi.org/10.1103/PhysRevB.89.214401
41. R.P. Poplawsky, J.E. Thomas JR., Rev. Sci. Instr. **31**, 1303 (1960). https://doi.org/10.1063/1.1716879
42. T. Akashi, K. Matumi, T. Okada, T. Mizutani, IEEE Trans. Magn. **5**, 285 (1969). https://doi.org/10.1063/1.88415
43. T. Ito, T. Ushiyama, Y. Yanagisawa, Y. Tomioka, I. Shindo, A. Yanase, J. Cryst. Growth **363**, 264 (2013). https://doi.org/10.1016/j.jcrysgro.2012.10.059
44. Q.J. Li, L.M. Xu, C. Fan, F.B. Zhang, Y.Y. Lv, B. Ni, Z.Y. Zhao, X.F. Sun, J. Cryst. Growth **377**, 96 (2013). https://doi.org/10.1016/j.jcrysgro.2013.04.048
45. Y. Taguchi, Y. Tokura, Phys. Rev. B **60**, 10280 (1999). https://doi.org/10.1103/PhysRevB.60.10280
46. S. Singh, R. Suryanarayanan, R.S. Martin, G. Dhalenne, A. Revcolevschi, J. Cryst. Growth **308**, 237 (2007). https://doi.org/10.1016/j.jcrysgro.2007.07.057
47. N. Hanasaki, M. Kinuhara, I. Kezsmarki, S. Iguchi, S. Miyasaka, N. Takeshita, C. Terakura, H. Takagi, Y. Tokura, Phys. Rev. Lett. **96**, 116403 (2006). https://doi.org/10.1103/PhysRevLett.96.116403

48. W. Miiller, L. Causeret, C.D. Ling, J. Phys.: Condens. Matter **22**, 486004 (2010). https://doi.org/10.1088/0953-8984/22/48/486004
49. Y.M. Jana, O. Sakai, R. Higashinaka, H. Fukazawa, Y. Maeno, P. Dasgupta, D. Ghosh, Phys. Rev. B **68**, 174413 (2003). https://doi.org/10.1103/PhysRevB.68.174413
50. S.M. Koohpayeh, J.-J. Wen, B.A. Trump, C.L. Broholm, T.M. McQueen, J. Cryst. Growth **402**, 291 (2014). https://doi.org/10.1016/j.jcrysgro.2014.06.037
51. M. Ciomaga Hatnean, M.R. Lees, G. Balakrishnan, J. Cryst. Growth **418**, 1 (2015). https://doi.org/10.1016/j.jcrysgro.2015.01.037
52. M.C. Hatnean, R. Sibille, M.R. Lees, M. Kenzelmann, V. Ban, V. Pomjakushin, G. Balakrishnan, J. Phys.: Condens. Matter **29**, 075902 (2017). https://doi.org/10.1088/1361-648X/29/7/075902
53. Y. Onose, T. Ideue, H. Katsura, Y. Shiomi, N. Nagaosa, Y. Tokura, Science **329**, 297 (2010). https://doi.org/10.1126/science.1188260
54. J. Brain Mullin, *Bulk Crystal Growth: Basic Techniques and Growth Mechanisms and Dynamics*, ed. by P. Rudolph, Elsevier, Oxford, UK (2015). https://doi.org/10.1016/C2013-0-09791-5
55. J. Kang, Z. Fang, X. Chen, W. Liu, F. Guo, S. Wu, Y. Zhang, J. Chen, J. Alloys Compd. **599**, 170 (2014). https://doi.org/10.1016/j.jallcom.2014.02.081
56. F.Y. Guo, W.H. Zhang, M. Ruan, J.B. Kang, J.Z. Chen, J. Cryst. Growth **402**, 94 (2014). https://doi.org/10.1016/j.jcrysgro.2014.05.011
57. A. Yaouanc, P.D. de Reotier, C. Marin, V. Glazkov, Phys. Rev. B **84**, 172408 (2011). https://doi.org/10.1103/PhysRevB.84.172408
58. K.A. Ross, Th Proffen, H.A. Dabkowska, J.A. Quilliam, L.R. Yaraskavitch, J.B. Kycia, B.D. Gaulin, Phys. Rev. B **86**, 174424 (2012). https://doi.org/10.1103/PhysRevB.86.174424
59. K.E. Arpino, B.A. Trump, A.O. Scheie, T.M. McQueen, S.M. Koohpayeh, Phys. Rev. B **95**, 094407 (2017). https://doi.org/10.1103/PhysRevB.95.094407
60. J.D. Thompson, P.A. McClarty, D. Prabhakaran, I. Cabrera, T. Guidi, R. Coldea, Phys. Rev. Lett. **119**, 057203 (2017). http://doi.org/10.1103/PhysRevLett.119.057203
61. G.C. Lau, B.D. Muegge, T.M. McQueen, E.L. Duncan, R.J. Cava, J. Solid State Chem. **179**, 3126 (2006). https://doi.org/10.1016/j.jssc.2006.06.007
62. K. Baroudi, B.D. Gaulin, S.H. Lapidus, J. Gaudet, R.J. Cava, Phys. Rev. B **92**, 024110 (2015). https://doi.org/10.1103/PhysRevB.92.024110
63. M. Hirschberger, J.W. Krizan, R.J. Cava, N.P. Ong, Science **348**, 106 (2015). https://doi.org/10.1126/science.1257340
64. A.W. Sleight, J.L. Gillson, J.F. Weiher, W. Bindloss, Solid State Commun. **14**, 357 (1974). https://doi.org/10.1016/0038-1098(74)90917-X
65. F.A. Weber, T. Schleid, Z. Anorg, Allg. Chem. **626**, 1285 (2000). https://doi.org/10.1002/(SICI)1521-3749(200006)626:6<1285::AID-ZAAC1285>3.0.CO;2-B
66. A.P. Ayala, C.W.A. Paschoal, I. Guedes, W. Paraguassu, P.T.C. Freire, J. Mendes Filho, R.L. Moreira, J.Y. Gesland, Phys. Rev. B **66**, 214105 (2002). https://doi.org/10.1103/PhysRevB.66.214105

Chapter 3
Spin Ice As a Coulomb Liquid: From Emergent Gauge Fields to Magnetic Monopoles

Roderich Moessner

Abstract This chapter provides an introduction to the Coulomb phase of spin ice. After reviewing conventional notions of order and disorder, as well as the emergence of quasiparticles, we show how spin ice is special in that it exhibits an *emergent gauge field* with fractionalised excitations in the form of magnetic monopoles. This is a property of a topological magnetic phase, a Coulomb phase of the corresponding emergent gauge theory, which even harbours irrational magnetic charge and observable 'Dirac strings'. We provide a broad overview of unusual and novel phenomena arising in spin ice, including the notion of residual entropy, the possibility of generating dimensional reduction to kagome ice via application of a magnetic field, the role of disorder, magnetoelectric phenomena, and various unusual phase transitions.

3.1 Order and Disorder in Magnetism

In order to appreciate what is fundamentally new about the spin ice state, let us first briefly summarise the notions of order and disorder in condensed matter physics. Indeed, these notions have in large part been developed and studied in the context of magnetism.

The simplest model which allows such a demonstration is provided by a model which is, literally, the Ising model of magnetism. Its basic degrees of freedom are Ising variables $\sigma_i^z = \pm 1$. Their locations, i, are most simply chosen to reside on a lattice Λ, e.g. a simple (hyper)cubic lattice in d dimensions hosting N sites.

The Ising degrees of freedom can interact. For an ordering transition in $d \geq 2$, it is sufficient to allow for an interaction between pairs of nearest neighbours on the lattice, denoted by $\langle ij \rangle$, which allocates an energy $+J$ if the spins are aligned, and $-J$ if they are antialigned:

R. Moessner (✉)
Max Planck Institute for the Physics of Complex Systems, Dresden, Germany
e-mail: moessner@pks.mpg.de

M. Udagawa and L. Jaubert (eds.), *Spin Ice*, Springer Series in Solid-State Sciences 197,
https://doi.org/10.1007/978-3-030-70860-3_3

$$H_{\rm Ising} = J \sum_{\langle ij \rangle} \sigma_i^z \sigma_j^z \ . \tag{3.1}$$

Here, the exchange constant J is negative for ferromagnetic, and positive for antiferromagnetic, interactions which favour a pair of spins to be (anti)aligned. The partition function of the Ising model at inverse temperature $\beta = 1/T$ is then given in terms of the Ising Hamiltonian $H_{\rm Ising}$ as

$$Z_{\rm Ising} = {\rm Tr}_{\{\sigma_i\}} \exp(-\beta H_{\rm Ising}) \ . \tag{3.2}$$

Here, the ${\rm Tr}_{\{\sigma_i\}}$ amounts to a sum over all possible spin configurations.

3.1.1 Symmetry Breaking

Let us for concreteness first consider the ferromagnet, for which in the limit of low temperature, $\beta \to \infty$, energy minimization is enforced, which means that each spin is to be aligned with all of its neighbours. There are two ways of achieving this, either for all spins to point up, or for all spins to point down. In fact, these two states have exactly the same energy, as they are related by the global spin inversion symmetry of the Ising model, $\sigma_i^z \to -\sigma_i^z \ \forall i$.

The process by which either one or the other of these two states is chosen is known as symmetry breaking; for an in-depth account of this remarkable phenomenon, we refer to appropriate textbooks such as [1]. In brief, symmetry breaking can be diagnosed by the local order parameter m, given by the expectation value of the total spin $\sigma_{\rm tot}^z = \sum_k \sigma_k^z$

$$m_{\rm Ising} = \frac{1}{N} \lim_{h \to 0} \lim_{N \to \infty} {\rm Tr}_{\{\sigma_i\}} \sigma_{\rm tot}^z \exp(-\beta H_{\rm Ising} - \beta h \sigma_{\rm tot}^z)/Z, \tag{3.3}$$

where the infinitesimal symmetry-breaking field h needs to vanish after the thermodynamic limit $N \to \infty$ is taken.

By contrast, in the limit of high temperature, $\beta \to 0$, all configurations have the same weight in the partition function, and $m_{\rm Ising}$ vanishes. This disordered state is just a simple paramagnet, distinguished sharply by the absence of symmetry breaking, in contrast to the ordered ferromagnet.

A local order parameter arising as a consequence of the breaking of a global symmetry are the basic ingredients for our understanding of conventional ordered phases. These themes can be embellished considerably. Most importantly, different systems are distinguished by the symmetry of the Hamiltonian, which can be much larger than just simple Ising inversion. In the much-studied case of a classical Heisenberg model, the degrees of freedom can be taken to be classical three-component unit vectors $\mathbf{S_i}$, interacting via

$$H_{\text{H'berg}} = J \sum_{\langle ij \rangle} \mathbf{S_i} \cdot \mathbf{S_j} \,. \tag{3.4}$$

Here, a ferromagnet will therefore reduce the continuous symmetry group of the Hamiltonian, when a direction of the magnetisation is chosen.

3.1.2 Emergence of New Degrees of Freedom

Such phase transitions go along with the emergence of new natural degrees of freedom. For example, in an ordered Ising ferromagnet at low temperatures, it is more efficient to specify where the domain walls between oppositely oriented ordered domains lie, as these are much sparser on account of their suppressed weight due to their energetic cost, rather than the spins themselves. For the Heisenberg case, the breaking of the continuous spin-rotation symmetry in turn leads to the appearance of spin waves, which correspond to continuous twists in real space of the spin direction. In the limit of the twist being slow, the energetic cost for introducing a spin wave vanishes–this is a general feature of so-called Goldstone modes accompanying the breaking of a continuous symmetry.

3.1.3 Landau–Ginzburg–Wilson Theory

As the distinction between a symmetry being either intact or broken is a sharp one (going along with non-analyticities in behaviour of observables such as the magnetisation defined above), this implies that there must be a well-defined transition point separating ordered and disordered phases. The final ingredient in our present understanding is that of universality—namely that apparently rather different microscopic Hamiltonians give rise to transitions identical in many respects provided that the symmetry breaking involved is the same.

For instance, if the model we had considered had been an antiferromagnet rather than a ferromagnet on a hypercubic lattice, the breaking of the Ising symmetry would proceed in exactly the same way, en route to reaching the doubly degenerate ground state of the antiferromagnet. This degeneracy follows from the fact that the hypercubic lattice is bipartite: this means that the lattice can be separated into two sublattices so that each site only has neighbours on the opposite sublattice. This can be seen directly by assigning to each site at coordinate $(x_1, \ldots, x_d)$ a parity $(-1)^{\sum_{i=1}^{d} x_i}$, so that even parity sites adjacent only to odd parity sites and vice versa. It is thus possible to define precisely two states where each spin is antialigned with all its neighbours, namely those with spins pointing up on one sublattice, and down on the other, or vice versa.

Piecing together this understanding of order, disorder and phase transitions is a grand achievement, and befitting it, the community has settled on a grand name for it, namely that of the Landau–Ginzburg–Wilson paradigm.

3.2 Magnetism Beyond the Landau–Ginzburg–Wilson Paradigm

The main attraction of spin ice is that it is different from both conventional disordered magnets and from conventional ordered magnets. Whether or not such unconventional systems—which are not covered by the classification of phases outlined above—do at all exist was first asked by Wegner in his original work on lattice gauge theories [2], and formulated concretely and pursued with perseverance by Anderson starting in the 1970s [3, 4]. While Anderson himself had already identified some aspects of the special behaviour of magnets on the pyrochlore lattice in the 1950s [5], it nonetheless took almost another half century until the special role of spin ice was fully appreciated. The remainder of this chapter, and indeed most of this book, is devoted to an exposition of these unusual features. With the quantum chemical origins presented in Chap. 1, we take simple model Hamiltonians abstracted from these as the starting point of our presentation.

3.3 The Minimal Model for the Coulomb Liquid: Nearest-Neighbour Spin Ice

Many of the special features of spin ice can already be gleaned by analysing a simple Ising model on the pyrochlore lattice composed of N spins (Fig. 3.1):

$$H_{\text{Ising}} = J \sum_{\langle ij \rangle} \sigma_i^z \sigma_j^z = \frac{J}{2} \sum_{\alpha} \tau_\alpha^2 \ + \text{cst.} \tag{3.5}$$

Here τ_α is the sum of the Ising spins residing on one of the $N/2$ tetrahedra labelled by α:

$$\tau_\alpha = \sum_{i \in \alpha} \sigma_i^z \ . \tag{3.6}$$

The physics of a ferromagnetic $J < 0$ is pretty much the same as for an Ising ferromagnet on a cubic lattice: a high-temperature paramagnet gives way to a ferromagnet in a standard Ising transition. The global ground state of this Hamiltonian is doubly degenerate, with all spins pointing up, or all spins pointing down.

Things change quite dramatically for the antiferromagnet, $J > 0$: instead of having two degenerate ground states, as described above for the hypercubic lattice, we find there are many more such states–each state in which every tetrahedron has

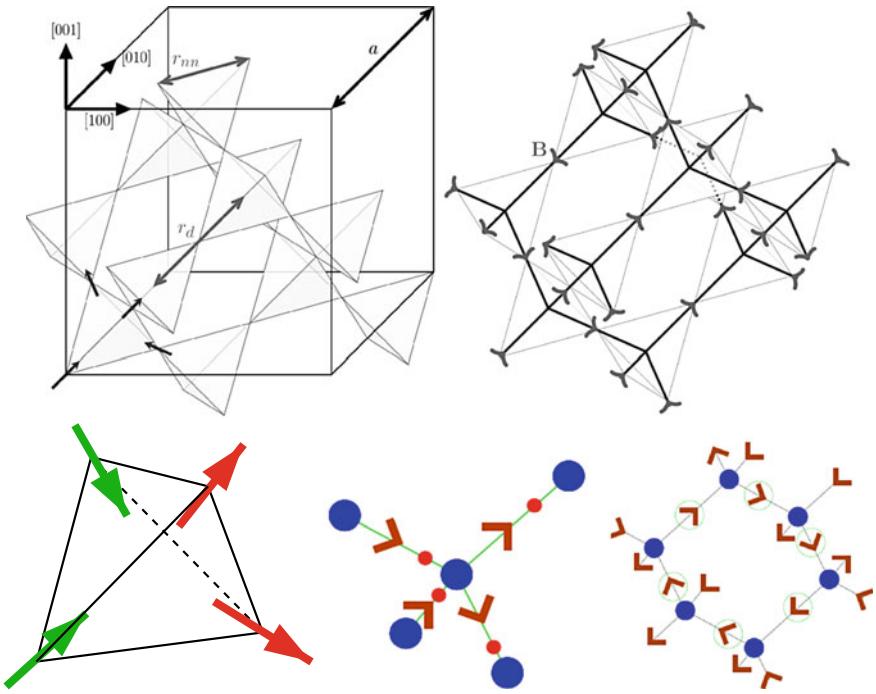

Fig. 3.1 Top left: the pyrochlore lattice of spin ice, embedded in a cube showing the principal directions. This lattice consists of tetrahedra sharing corners. Top right: The centrepoints of the tetrahedra of the pyrochlore lattice (thin lines) define a diamond lattice (thick lines). The spins, site variables on the former, become link variables (arrows) on the bonds of the latter. Bottom left: the ground state condition, (3.7), stipulates that two spins point 'up' (into the tetrahedron), and two point 'down' (out of the tetrahedron). Bottom centre: represented as link variables on the diamond lattice, the spins can be thought of as a lattice flux **B** (brown arrows). This lattice flux exhibits an emergent conservation law: states obeying the ground state condition have $\nabla \cdot \mathbf{B} = 0$ for each tetrahedron, i.e. the total amount of flux coming into the tetrahedron equals the total flux going out. This is known as the ice rule from a similarity to the local physics of hydrogen and oxygen ions in solid water: the four-fold coordinated O^{2-} ions (blue circles) are hydrogen bonded, with the H^+ ions (i.e. protons) (red circles) located not symmetrically on the bond. Each O^{2-} ion has two protons close, and two further away. By pointing the brown arrows towards the protons, the ice rules for spin ice emerge from those for water ice. Bottom right: a set of spins (encircled in green) arranged head-to-tail on a loop may be inverted to produce another ground state configuration. Such a loop has zero net magnetisation

$$\tau_\alpha = 0 \tag{3.7}$$

is a ground state. This can already be seen for a single tetrahedron, where there are two ferromagnetic ground states as per usual, but six antiferromagnetic ones: to obtain $\tau = 0$, one needs to choose two of the four spins to point up: there are $\binom{4}{2} = 6$ different such choices, and hence six ground states out of the $2^4 = 16$ spin configurations of a single tetrahedron. We note on the side that these six states

are all symmetry-equivalent: a tetrahedron has six symmetry-equivalent bonds, and choosing a ground state amounts to choosing which of these six bonds has two spins pointing up at its ends.

This argument does not tell us how many states fulfill (3.7). It turns out that the number of ground states scales exponentially with the number of tetrahedra in the system. Since the number of symmetries does not, this means that most ground states are not symmetry-related—this is a situation characteristic of systems known as 'highly frustrated'. The scaling of the number of ground states with N has been computed exactly in $d = 2$ by Lieb using the Bethe ansatz, and estimated approximately in $d = 3$:

$$\mathcal{N}_{2d} = \left(\frac{4}{3}\right)^{\frac{3N}{4}} \tag{3.8}$$

$$\mathcal{N}_{3d} = \left(\frac{3}{2}\right)^{\frac{N}{2}} . \tag{3.9}$$

$\mathcal{N}_{3d}$ was obtained by Pauling using the following simple estimate: a system with N spins has 2^N configurations; with each of $N/2$ tetrahedra permitting only a fraction of $6/16$ of configurations, so that $\mathcal{N}_{3d} = 2^N(6/16)^{N/2}$. This estimate is independent of dimensionality, and it obviously does not agree exactly with the value for $d = 2$. In $d = 3$, the best theoretical estimate was provided by Nagle to be $\frac{1}{N}\log \mathcal{N}_{3d} = 0.20501(5)$ [6], while a Monte Carlo simulation obtained $\frac{1}{N}\log \mathcal{N}_{3d} = 0.2051(1)$ [7].

This number can in fact be measured directly, as an exponentially large number of states W goes along with a nonvanishing entropy, according to the formula $S = k \log W$ immortalised on Boltzmann's tombstone bearing the equation involving his constant k [8]. By measuring the specific heat, C, in a spin ice material, between a high temperature T_p and a low temperature in the spin ice regime T_i, one can use the formula for the change in entropy, $\Delta S = \int_{T_i}^{T_p} \frac{C}{T} dT$. At high temperature, the paramagnet has entropy log 2 per spin, as in a perfect paramagnet, each spin has two possible states it can be in with equal probability. Such an entropy measurement was carried out on a series of rare earth titanates by Blöte [9], and later in a direct search for the Pauling entropy by Ramirez [10]. This latter data, shown in Fig. 3.2, provided decisive support for the identification of the rare earth magnet $Dy_2Ti_2O_7$ as a spin ice material.

Fundamentally unlike the cases of the hypercubic magnets discussed above, we here need to investigate the statistical mechanics of an exponentially large number of ground states. It turns out that this exponential degeneracy underpins the special behaviour of the spin ice compounds, and is therefore key to the new physics observed there.

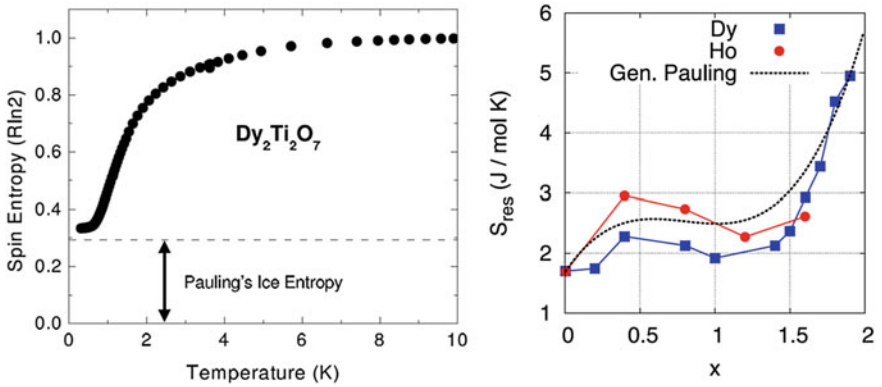

Fig. 3.2 Left: the entropy of spin ice DTO as a function of temperature. Upon cooling, a residual entropy well-approximated by Pauling's estimate $\mathscr{S}_p = \frac{1}{N} \log \mathscr{N}_{3d} = \frac{1}{2} \log \frac{3}{2}$ remains, adapted from [10] with permission from Nature. Right: low-temperature values of the entropy for diluted spin ice $Dy_{2-x}Y_xTi_2O_7$ and $Ho_{2-x}Y_xTi_2O_7$, compared with theoretical results from a simple Pauling approximation which treats all tetrahedra as independent, adapted from [76] with permission from the American Physical Society

3.3.1 Coarse-Graining and Emergent Gauge Field

The above considerations in themselves do not tell us what the long-distance correlations present in the ensemble of spin ice configurations are. In fact, from known solutions of two-dimensional Ising models with exponentially large degeneracies, it is well-known that there can be exponentially decaying correlations, such as in the kagome Ising magnet [11]; or algebraically decaying correlations, such as in the triangular Ising antiferromagnet [12]; or even long-ranged correlations, such as on the fully frustrated model whose ground states map onto the dimer model on the square-octagon lattice. The ordering therefore appears to be a question of 'detail', and the challenge is to identify the different universal behaviours—i.e., the set of generic outcomes obtained when considering different lattice models.

For conventionally ordered systems, a successful way of approaching this question is presented by the renormalisation group, which can be pictorially encoded by block-spin transformations. For example, on a square lattice Ising magnet, grouping spins into 3×3 blocks, one can introduce a majority rule: a new coarse-grained spin is assigned to point in the direction of the majority of the 9 spins in the block. Appropriately iterating this procedure, one finds as a function of coupling strength one of three scale-free fixed points: either a perfect paramagnet with vanishing correlations, a perfectly ordered ferromagnet, or a critical point separating these two.

Here, we address how to do the coarse-graining for spin ice. One 'boring' outcome is that—as turns out to be the case in the example of the kagome Ising antiferromagnet [11]—all there is to do is to notice that the ground state is continuously connected

to the perfect paramagnet. Thus, the old block-spin prescription leads to the conventional result.

However, the situation in spin ice has some additional structure: it turns out that here (as in the abovementioned example of the triangular lattice Ising antiferromagnet), one can define an emergent conservation law, which is most easily visualised by transforming the spin system on the pyrochlore lattice into a model of link variables on the diamond lattice. This proceeds as follows, see Fig. 3.1.

This diamond lattice is formed by the midpoints of the tetrahedra of the pyrochlore lattice; the pyrochlore sites in turn are located at the midpoints of the diamond lattice bonds ('links'). (The pyrochlore lattice is hence known as the medial lattice of the diamond lattice.)

The link variables are next defined as follows. Given the diamond lattice is bipartite, one can orient each link to point from one of its sublattices (labelled A) to the other (labelled B); and the link variable is defined to point from sublattice A to B if the Ising variable on the pyrochlore site corresponding to the link is +1; and if it is −1, the link variable points from sublattice B to A.

It now follows that for a system obeying the ice rule, each diamond lattice site has two link variables pointing towards it, and two away. Thus, defining each link to carry a unit of flux, **B**, the direction of which is given by the link variable, it follows that this flux has vanishing (lattice) divergence.

Such a vanishing divergence implies a conservation law, just as the conservation of charge leads to Kirchhoff's current law stating that the total amount of current flowing into a node of a network of resistors must equal the current flowing out. In spin ice, however, the conservation law is not of such fundamental origin, but rather, it is *emergent*: it only appears when the ground state condition of the Ising Hamiltonian, (3.7), is enforced.

How to coarse-grain such a conservation law is a priori not obvious. In a block-spin transformation, for instance, having no net flux into a group of 9 nodes is much less constraining than demanding no net flux for each node individually. The resolution in the case of spin ice is to define a field which is in itself divergence-free, and to effect the coarse-graining on this. How to do this is in itself not difficult—we already know from the context of Maxwell's equations that

$$\nabla \cdot \mathbf{B} = 0 \Longrightarrow \mathbf{B} = \nabla \times \mathbf{A} \tag{3.10}$$

This in turn defines the emergent gauge field **A**. So far, all we have done is to redefine variables from Ising spins to an emergent gauge field, and we have not resolved any of the issues regarding the long-distance correlations. However, we are in a much better position to guess now—as we know that broken symmetries and conservation laws are what determines long-distance correlations even in conventional systems. *Assuming*, somewhat optimistically, that spin ice is something novel which makes do without breaking any symmetries, the question then is: what is the simplest ansatz for the behaviour of the action in terms of the emergent gauge field **A** under coarse-graining.

Let us try a form which is analytic and of the lowest allowed power, as one might intuit based on an analogy to Maxwell's magnetostatics, namely

$$S = \frac{\mathscr{K}}{2} \int d^d r (\nabla \times \mathbf{A})^2 = \frac{\mathscr{K}}{2} \int d^d r \, \mathbf{B}^2 \,, \tag{3.11}$$

where for spin ice, the integral is over $d = 3$-dimensional real space. $\mathscr{K}$ is a stiffness constant taking the place of the permittivity/permeability of space.

Such an ansatz can be physically motivated, again see Fig. 3.1. If one can identify a set of spins arranged head-to-tail on a closed loop, it is possible to invert all of these simultaneously to obtain another state obeying the ice rules. Since such a loop has zero total magnetisation, one sees that upon coarse-graining on a lengthscale given by the size of the loop, two configurations contribute to the partition function, the original one, and that with the spins on the loop flipped. (In passing, we note that the statistical properties of such loops are of great interest in their own right, see [13]). In terms of the coarse-grained field, there should thence be a weighting in favour of a vanishing field, which is just what is achieved by the form of (3.11).

This, being a quadratic action, can now be solved analytically. A helpful insight is that the conservation law in (3.10) in Fourier space reads $\mathbf{q} \cdot \mathbf{B} = 0$: the 'longitudinal' part of $\mathbf{B}$ must vanish. This can be written in form of a longitudinal projector, $\mathbb{P}_L$, which has eigenvalues 1 for the longitudinal components, and 0 for those transverse to it, so that we need to demand $\mathbb{P}_L \mathbf{B} = (\hat{\mathbf{q}} \cdot \mathbf{B})\hat{\mathbf{q}} = 0$, where the hat denotes that $\hat{\mathbf{q}}$ is a unit vector to ensure that $\mathbb{P}_L^2 = \mathbb{P}_L$. Its complement is the transverse projector $\mathbb{P}_T = \mathbb{I} - \mathbb{P}_L$. Equation 3.11, can thus be written as

$$S = \frac{\mathscr{K}}{2} \int d^d r \left[\frac{1}{\lambda} (P_L \mathbf{B})^2 + (P_T \mathbf{B})^2 \right] , \tag{3.12}$$

with $\lambda \to 0$ in order to enforce the transverseness condition on $\mathbf{B}$. The (matrix) inverse of this expression is now readily found, using the fact that the projectors square to themselves, and that $\mathbb{P}_T \mathbb{P}_L = 0$.

One thus finds that the spin correlations of the field $\mathbf{B}$ have a simple form dictated by the transverse projector $\mathbb{P}_T$:

$$\langle B_i(\mathbf{q}) B_j(\mathbf{q}) \rangle \sim \frac{1}{\mathscr{K}} \left\{ \delta_{ij} - \frac{q_i q_j}{q^2} \right\} . \tag{3.13}$$

Transformed back into real space, this implies that the correlations decay algebraically, like $(3\cos^2\theta - 1)/r^3$, the dipolar form familiar from Maxwell magnetostatics.

All the mappings that we have done along the way only introduce some staggering, as well as geometric, factors relating spins to the field $\mathbf{A}$—for details, see [14, 15]—but the resulting correlations remain of this algebraic r^{-3} form. Also, the magnitude of $\mathscr{K}$ is not determined by the above considerations, and it therefore needs to be

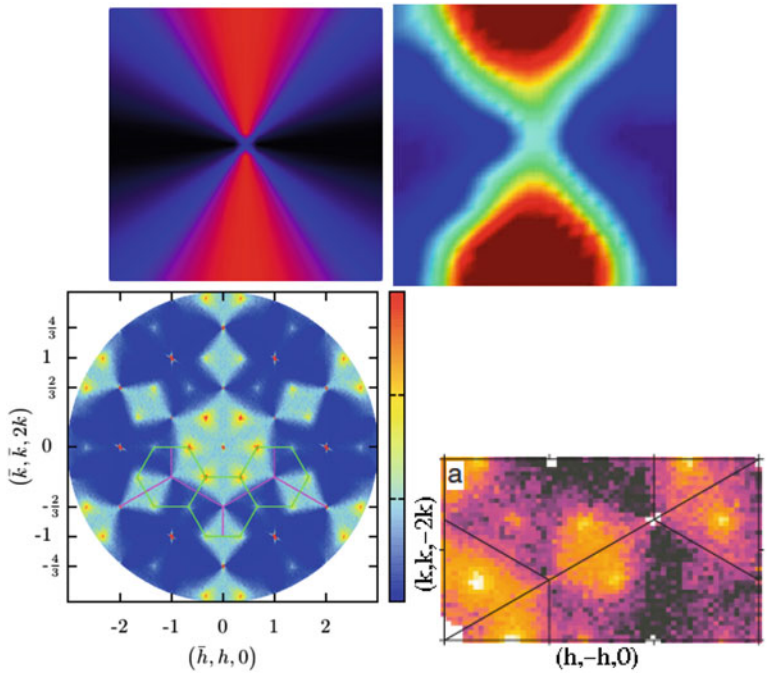

Fig. 3.3 Correlations of spin ice in reciprocal space. Dark (bright) areas denote low (high) correlations. Top left: schematic form of predicted pinch-point in the spin structure factor of spin ice, following from the ansatz (3.11). Numerical simulations exhibit this form in detail [14]. Top right: Pinchpoints are also visible in neutron scattering experiment [16, 17], but with some smearing due to defects resulting from thermal or disorder effects, as well as finite instrument resolution. Reprinted from [16] with permission from Science. Bottom left: numerical simulations of the spin correlations in kagome ice, i.e. spin ice with a field applied in the [111] direction, see Sect. 3.6. Besides the pinch points, visible are: (i) Bragg peaks (e.g. at [–220]) due to a net ordered moment and (ii) logarithmic peaks (e.g. at the corners of the Brioullin zones marked in green) indicating dimensional reduction to an effectively two-dimensional emergent gauge field. Reprinted from [18] with permission from the American Physical Society. Bottom right: logarithmic peaks as seen in experiment [19], reprinted from [19] with permission from the Journal of the Physical Society of Japan

obtained separately. In practise, determining it in an approximation based on a large number of spin components has turned out to work well [14].

Neutron scattering experiments measure spin correlations in reciprocal space, and the form of (3.13) immediately suggests an unusual and characteristic fingerprint: the correlators are neither smooth (as in a paramgnet with only short-range correlations), nor divergent like in a Bragg peak diverging with system size. Rather, the correlators are non-analytic, but only in that they are non-differentiable: there exist so-called pinch-points where lines of low and high scattering intensity cross, as illustrated in Fig. 3.3. The pinch-points are the manifestation of the new state of magnetic matter, the spin ice state.

3.3.2 *Fractionalisation with Strings Attached*

New states of matter go along with new excitations—be it the transverse phonons which appear when a gas crystallises, or the magnons when Heisenberg magnets enter a ferromagnetic state. In this respect, spin ice does not disappoint—there emerge a set of fractionalised excitations quite unlike what is known from conventional magnetic systems. To see how these come about, consider the cartoon of spin ice in Fig. 3.4, which focuses on the divergence-free nature of the spin arrangements by denoting each link variable as an arrow pointing between tetrahedra, with the tetrahedra themselves no longer shown. Spin ice corresponds to a soup of such arrows, all pointing head-to-tail.

Flipping one spin, and hence reversing such an arrow, breaks ice rule in the two tetrahedra it belongs to. This, however, turns out not to be an elementary excitation—flipping a string of further spins separates the two defect tetrahedra, without incurring any further cost in energy. These two defect tetrahedra can therefore move independently, and separate arbitrarily far. They are fractionalised, deconfined excitations: fractionalised because a single spin flip generates two such excitations; and deconfined because the energy cost of separating them infinitely far remains finite.

Even though the two defects can move independently, they can only be introduced pairwise, in the same way that there is electron-positron creation only in charge-neutral pairs, even though these two particles can then move around independently. In the same sense, the defects in spin ice also carry a charge: if one labels the endpoints with $+$ and $-$ depending on whether the tetrahedron has an excess of link variables pointing in or out, a spin flip corresponds to charge-neutral pair creation.

Each defect is a source/sink of flux $\mathbf{B}$, depending on its sign. The flux between the two defects, as they are separated, is carried by the flipped string of spins. Thus, for any surface enclosing a volume of spin ice, one can count the difference between the number of strings pointing in and out, and thereby determine the net emergent gauge charge inside; this is the appropriate form of Gauss' law for the emergent gauge field. As one finds a conserved charge taking on integer values just like in Maxwell electromagnetism, one identifies the spin ice state as the deconfined Coulomb phase of a U(1) gauge theory. Spin ice is the first three-dimensional spin model known to exhibit such an emergent gauge structure.

3.4 Dipolar Spin Ice and Projective Equivalence

We have so far used a simple Ising model with antiferromagnetic nearest-neighbour interactions in order to discuss the basic features of the statistical mechanics of spin ice. The microscopic Hamiltonian, however, turns out to be considerably more complex than H_{Ising} (3.1). Indeed, it was pointed out in a seminal work by Siddharthan et al. [20] that in spin ice, dipolar interactions are stronger than superexchange ones, so that the Hamiltonian to be considered, now known as the dipolar spin ice model, looks much more complex:

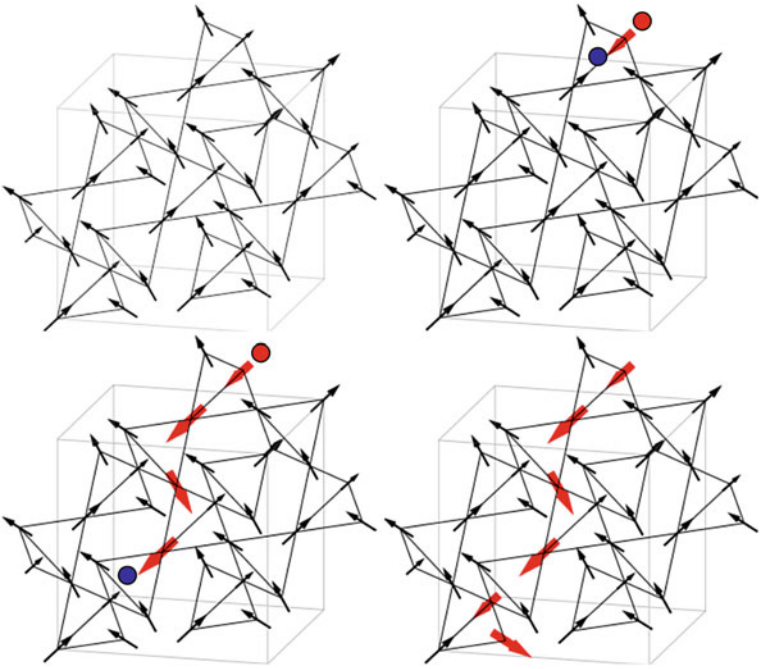

Fig. 3.4 Flipping a spin in a spin ice ground state configuration (top left) generates two defect tetrahedra, which host oppositely charged defects (top right). These can be separated by flipping further spins arranged head-to-tail along a string (bottom left). Once the string connects the top and the bottom boundary (bottom right), another ground state configuration is obtained, whose magnetisation differs from the original one. In this plot, the starting state is fully polarised along the [100] direction, as would be selected by a strong applied field in that direction. When the field strength is lowered, such strings play an important role in the Kastelyn transition: in the absence of magnetic monopoles, the fully polarised state has no local degrees of freedom, so that the lowest-energy excitations are such infinitely long strings, which are completely suppressed above the critical field. The resulting transition looks like a first-order transition on the high-field side, while it is continuous on the low-field side, see Sect. 3.6.1

$$H_{\rm dip} = -J \sum_{\langle i,j \rangle} \mathbf{S}_i \cdot \mathbf{S}_i + D r_{\rm nn}^3 \sum_{i>j} \frac{\mathbf{S}_i \cdot \mathbf{S}_i}{|\mathbf{R}_{ij}|^3} - \frac{3(\mathbf{S}_i \cdot \mathbf{R}_{ij})(\mathbf{S}_j \cdot \mathbf{R}_{ij})}{|\mathbf{R}_{ij}|^5}. \tag{3.14}$$

The insights going into the derivation of this Hamiltonian are described in the opening chapter of this book, Chap. 1.

This naturally leads to the question how on earth a Hamiltonian as complex as $H_{\rm dip}$ can manage to mimick the behaviour of the much simpler $H_{\rm Ising}$: the Pauling entropy was measured for a material described by the former, but derived theoretically for the latter!

Self-screening of the dipolar interactions and projective equivalence
The appearance of the Pauling entropy even in dipolar spin ice is well-established numerically by Monte Carlo simulation [21]. An important hint of how this happens is provided by a mean-field theory analysis of den Hertog and Gingras [22]. They considered the Fourier transform of the dipolar interaction Hamiltonian, which can be evaluated numerically. The spectrum of H_{dip} has four bands, as there are four effectively scalar degrees of freedom in the unit cell containing four spins. Crucially, the band lowest in energy is almost entirely flat. This is a signature of frustration and the resulting degeneracy: any two configurations which can be constructed out of this band alone will be effectively degenerate.

In fact, the entire mode spectrum of H_{dip} looks very similar indeed to that of H_{Ising}—the main difference being the appearance of a gap in the spectrum of H_{dip} between the two nearly flat and the two dispersive bands (with a feature at the zone centre reflecting in turn a topological property of the band touching point involving eigenmodes of the Hamiltonian wrapping around the periodic boundaries of the torus used for the Fourier transformation, see [23]). It therefore seems that the dipolar interaction manages to screen itself, mimicking the nearest-neighbour interaction as a result.

This picture turned out to be largely correct—it was found that not only the flatness of the lowest band, but also the concomitant eigenfunctions are almost identical between H_{dip} and H_{Ising} [24]. In other words, the operation of projecting the spins onto the ground states of either H_{dip} or H_{Ising} are essentially identical. This feature, which is mathematically somewhat intricate, was termed projective equivalence.

Quite generally, this suggests a way of deforming Hamiltonians (spin or even hopping problems[1]) to yield high degeneracies: after finding its eigensystem, keep the eigenvectors of the lowest band as they are, but replace its non-trivial dispersion by a flat one. This can be Fourier-transformed back to obtain a new, more degenerate Hamiltonian in real space, which will differ from the original one by longer-range terms decaying exponentially if the original spectrum above the flat band was gapped, and only algebraically otherwise. For spin systems, where the hard spin constraint is not implemented in such mean-field theories, this works best if there exists already for the original Hamiltonian a large low-energy sector of spin configurations made up of eigenvectors of the lowest band exclusively.

3.5 Magnetic Monopoles

In order to derive the existence of the fractionalised excitations mentioned above, we never had to refer to the magnetic moment of the spins underlying the dipolar spin ice Hamiltonian in Sect. 3.4. However, adding the magnetic moment gives additional

[1] As an aside, we note that projective equivalence has effectively also been used in the study of fractional Chern insulators [25–27] to obtain dispersionless bands with nonzero Chern number in which interacting electrons at appropriate filling then exhibit a fractional quantum Hall effect.

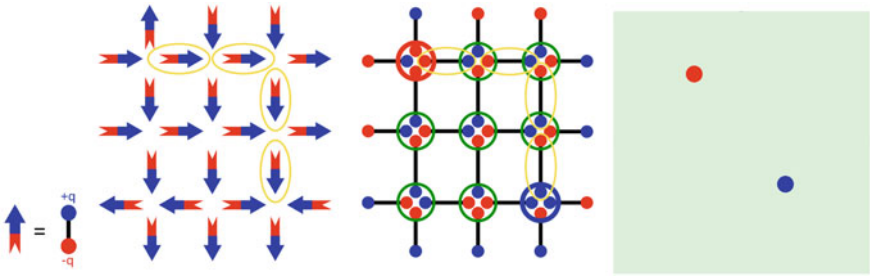

Fig. 3.5 Left: a magnetic dipole of strength μ can be replaced by a pair of magnetic charges separated by a distance r_d. Flipping a 'Dirac string' of spins (encirceld in yellow) starting from a spin ice ground state configuration leaves behind two sites with equal and opposite nonzero net magnetic charges (encircled red and blue), while the other sites are charge neutral (encircled in green). Upon coarse-graining, the neutral sites are replaced by an effective medium mediating entropic interactions between the charged sites, which also experience a net magnetic Coulomb interaction between their charges of size $\pm 2\mu/r_d$

meaning to the charges at either end. The easiest way to see this pictorially is to replace the dipole moment by two equal and opposite *magnetic* charges, $\pm\mu/r_d$, where r_d is the lattice constant of the diamond lattice (see Fig. 3.4). This dumbbell of charges then by construction has the magnetic dipole moment μ of a spin in the spin ice material. Note that, with this choice of variables, the ice rule (and hence the divergence-free nature of the diamond lattice nodes) amounts to the demand that each diamond lattice site be charge-neutral: each in-pointing link variable contributes a pair of charges opposite in sign to those corresponding to the out-pointing link variables.

Reversing string of spins as in Sect. 3.3.2 thus yields pair of opposite charges of size $\pm 2\mu/r_d$ at the ends of the string, as illustrated in Fig. 3.4 This is a remarkable result—spin ice manages to fractionalise magnetic dipoles into independently mobile magnetic charges. This is one of the reasons these fractionalised particles were christened magnetic monopoles [28].

Indeed, to make a connection to standard magnetostatics, it is instructive to do an elementary computation to show how these fractionalised particles come to exhibit magnetic Coulomb interactions. This proceeds by writing down the potential set up by a string of dipoles, which amounts to a continuum approximation, where the flipped string of spins is assigned a dipole moment density of $2\mu/r_d$. Using the fact that the potential of a dipole is just the $\nabla \frac{1}{|r-r'|}$, the expression for the potential at site r is given by a line integral along the string Λ parametrised by r':

$$V(r) = \frac{2|\boldsymbol{\mu}|}{r_d} \int_{\Lambda} d\mathbf{r}' \cdot \nabla \frac{1}{|r - r'|} = q_m \left(\frac{1}{|r - r_a|} - \frac{1}{|r - r_b|} \right). \tag{3.15}$$

Here the equality simply follows from the fundamental theorem of calculus, that the line integral of the gradient of a function is given by the function evaluated at the

endpoints of the line, denoted by $r_{a,b}$. This in particular shows why the details of the shape and length of the flipped strings are immaterial for the magnetostatic potential set up by the monopoles at its ends.

The natural description of the Coulomb phase of spin ice is therefore in terms of an emergent gauge field, **A**, and pointlike excitations gauge-charged under it, the magnetic monopoles. As usual, having identified the natural variables, some known results can be summarised and understood more succinctly, and new phenomena can be more crisply identified and described. To these we turn next.

3.5.1 Self-Screening and Residual Ordering Tendency

The first mystery that is immediately explained is the projective equivalence noted above, which manifested itself in the Pauling entropy being measured for *dipolar* spin ice. As the ground states are locally charge neutral by force of the ice rules (associated already with the nearest-neighbour Hamiltonian) alone, the long-range nature of the interactions no longer plays a role. This is the self-screening mechanism.

Of course, the dumbbell model is only an approximation. However, it suggests to do a multipole expansion not for the spins, but for the tetrahedra, with a vanishing monopole moment being enforced by the ice rules. It then becomes apparent that this is an unstable procedure—the tetrahedral multipoles compete with, say, further neighbour or more complex spin interactions which may be both present and unknown. As is often the case for frustrated magnets, many instabilities compete. However, the multipole expansion makes a clear prediction of the ordering tendency. To this day, no ordering in the canonical spin ice compounds $\{Ho,Dy\}_2Ti_2O_7$ has been experimentally established, even though a possible precursor of ordering at very long timescales has been seen in [29], and Chap. 4.

3.5.2 Irrational Charge and Emergent Versus Intrinsic Gauge Charges

The fractionalised particles carry a magnetic charge derived above, $q_m = 2\mu/r_d$. This charge is in general irrational, since the magnetic moment μ can be tuned continuously, e.g. by applying hydrostatic pressure to the sample [30]. Indeed, there is a priori no reason why the charge in question should not be irrational, as already noticed in the seminal "unit model" of Nagle for water ice [31], where an irrational electric charge arose quite naturally. Indeed, irrational charge already exists in chemistry, where its topological origin was perhaps not noted as the concepts were not crisply available at the time of its discovery; and because irrational charge is not uncommonly used when describing chemical bonding. However, the important point here is that the deconfined fractional charge is not just redistributed in a given molecule, or

between two sublattices of a chemically bonded lattice system. Rather the irrational charges can move independently (in the form of ionic or Bjerrum defects) through the system.

The monopole charge defined in Sect. 3.3.2, independently of the magnetic moment of the monopole, however, does not change alongside this continuously variable magnetic charge. The defect tetrahedra are therefore doubly gauge charged: with the intrinsic magnetic charge attached to the magnetic dipole moment on one hand; and the emergent gauge charge attached to the flux **B** defined in Sect. 3.3.2 on the other. The former is not constitutive to the emergent Coulomb phase, as it derives from the preexisting Maxwell gauge theory; in particular, if the basic degrees of freedom had been electric dipoles, the resulting fractionalised particles would carry an irrational electric charge, as is actually the case in water ice [31]. Rather, it is the emergent gauge charge which is fundamentally associated with the spin ice phase. The reason this duplication of charges was overlooked for a long time is that the mathematical structures are identical—their contributions to the overall Coulomb interaction between defect tetrahedra are simply additive, albeit with a different temperature dependence. This is an accident, which can be removed in an interesting way explained in Sect. 3.6.2.

3.5.3 'Dirac Strings'

The alert reader may now feel uncomfortable—surely, it is not possible to have continuously variable magnetic charge; after all, Dirac introduced magnetic monopoles because their existence led to the mutual quantisation of electric and magnetic charges [32]. His line of argument runs as follows. If a magnetic monopole exists, and one wants to keep the divergence-free nature of the magnetic field, the magnetic flux emanating from the monopole must be supplied in an unobservable way. The trick to achieve this was provided by the Dirac string: an infinitely thin (and hence invisible) tube through which the flux is transported to the monopole. However, quantum mechanics can detect magnetic fluxes without seeing the tube, as it will lead to an Aharonov Bohm effect for electron interference experiments with paths passing either side of the Dirac string. In order to pick up only trivial relative phases between such paths, Dirac was led to posit that the corresponding Aharonov-Bohm phase must be a multiple of 2π, and that therefore, the product of magnetic and electric charge needs to be quantised.

The way spin ice avoids coming in conflict with this line of argument is that its 'Dirac strings' are observable. These are just the flipped strings of link variables used in establishing fractionalisation in the first place, Sect. 3.3.2, and they are observable! The physics of Dirac strings in itself is a rich and interesting subject. They present an unusual type of extended degree of freedom, which exhibits intriguing statistical properties. These are striking enough that a separate chapter of this book, written by one of its editors, is devoted to them (see Chap. 6).

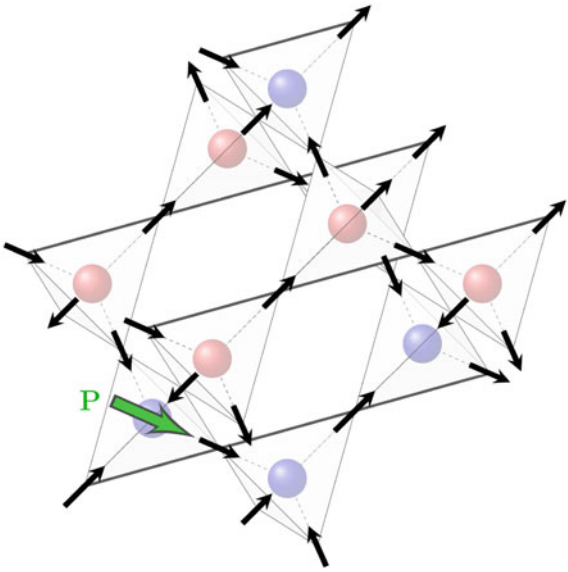

Fig. 3.6 The electric dipole moment associated with a magnetic monopole due to magnetostriction is shown in the tetrahedron on the bottom left. The indicated magnetic monopole crystal can arise when the energy cost of monopole creation is surmounted by the gain from their interaction, e.g. due to their electric dipole moments

3.5.4 Magnetolyte Physics and Magnetricity

Given magnetic monopoles interact via a Coulomb interaction suggests that their collective physics should be that of a Coulomb liquid. The fact that the interaction is magnetic rather than electric does not greatly matter here—the equations do not care about the provenance of prefactors in a 'magnetolyte' as opposed to an electrolyte usually described by Coulomb liquid physics.

Such an analogy was in fact already invoked when explaining hitherto puzzling experiments about spin ice in a field [7, 28, 33], described in Sect. 3.6. It has since been greatly extended to study thermodynamics and dynamics of spin ice, with ideas ranging from Debye screening [34–36] all the way to an analysis of the nonlinear nonequilibrium response of spin ice in terms of the venerable Wien effect discovered in electrolytes in the 1930s [37–39]. These items are also covered in Chaps. 7 and 8.

3.5.5 Electric Properties of Magnetic Monopoles

It is a priori not natural for a magnetic monopole in spin ice also to carry electric charge, as magnetic and electric dipole moments have different transformation properties under time reversal: while the direction of the magnetic moment changes (as can be seen by representing it as an angular momentum, which is odd under time reversal), the electric dipole moment remains unchanged.

Restricting to the case of electrically neutral magnetic dipoles as underlying degrees of freedom, it is more natural for the magnetic monopole in turn to exhibit

an electric dipole moment. This follows already from a toy model of spin ice incorporating spin-lattice coupling leading to magnetostriction [40]. Assuming for concreteness that satisfied bonds shorten, while frustrated bonds lengthen, this leads to a distortion of the crystal lattice around a magnetic monopole. Of course, it is not necessarily the pyrochlore lattice of magnetic ions which needs to be deformed. Electric polarisation can also be a consequence of the displacement of the intervening oxygen anions following the Goodenough-Kanamori-Anderson rules [40], or of the spin-current model of multiferroics because of the non-colinearity of neighbouring spins [41–44]. At any rate, based on symmetry arguments illustrated in Fig. 3.6, electric dipoles are only allowed on singly-charged magnetic monopoles. Since the electric field is protected by time-reversal invariance, it is independent of the magnetic charge. Its direction does, however, depend on the spin configuration and has been shown to be parallel to the minority spin—the one pointing "in" for a 3 out –1 in state, and vice-versa. Where to observe these electric degrees-of-freedom? Since monopoles are a necessary ingredient, the liquid-gas transition in a field—see the next section and Chap. 5—is one natural place to look at: there, the density of monopoles jumps, from being small to nearly saturated at low temperatures.

Beyond influencing the electric properties of the material, the cooperative consequences of the presence of electric interactions are also worth noting. The magnetic Coulomb potential in spin ice is relatively weak, especially compared to the energy scale characteristic of elementary electric charges separated by the same distance. Hence, the electric dipolar interaction between monopoles might be able to stabilise novel long-range ordered structures of magnetic charges, paving the way for an emergent "magnetic crystallography".

To analyse such phenomena, it is necessary to consider the strength of symmetry-allowed effective magneto-electric coupling in detail. This will depend on the chemistry of the material. $Tb_2Ti_2O_7$ is in this context a promising candidate, with noticeably strong spin-phonon coupling [45–49], spins described by an Ising-like doublet [50, 51] and a possible Coulomb phase at low temperatures [52, 53]. Monte Carlo simulations have shown that electric dipoles carried by monopoles order the spin-ice model into a double-layer structure of magnetic charges (see Fig. 3.6) [54]. This order bears a macroscopic magnetic moment along the [110] direction and is thus stabilised by a [110] external magnetic field. The fact that such order has been observed in $Tb_2Ti_2O_7$ under a strong [110] field [55, 56] indicates the possibility for the importance of electric dipole moments carried by magnetic monopoles [54]. More generally, this exotic property of spin ice indicates the need for the exploration of structured 'internal' degrees-of-freedom buried inside quasi-particle excitations in correlated magnets.

3.6 The Coulomb Phase in a Magnetic Field

The experimentally relevant feature of the topological magnetism of spin ice lies in the fact that there exists a regime of finite width in which a description in terms of

an emergent gauge field is simple and efficient. There exists always a nonvanishing density of thermally activated defects; beyond the lengthscale set by their density, the behaviour of spin ice crosses over to that of a normal paramagnet—it is only in the limit of $T \to 0$ that a mathematically well-defined Coulomb phase emerges. In practise, as the temperature is lowered, the crossover into the spin ice Coulomb regime takes place as the Boltzmann factor for exciting a monopole becomes considerably less than 1. This roughly happens when cooling below the peak in the specific heat known as the Schottky anomaly.

The Coulomb regime is then stable to further perturbations provided their strength is lower than the thermal fluctuations at a given energy. In the limit of $T \to 0$, an arbitrarily weak perturbation—such as some further-neighbour interactions—will lead to an ordering transition. This situation is shared with many other frustrated magnets, where a generic spin liquid regime exists in a temperature window defined by the strength of perturbations to an idealised model Hamiltonian on one hand, and the energy scale of that model Hamiltonian on the other.

Among all possible perturbations, some are perhaps more interesting than others. We reserve particular attention to an applied magnetic field for a number of reasons. Firstly, it is straightforwardly available in laboratories. Secondly, in the case of spin ice, it couples directly to a topological quantity: a magnetic field drives the monopoles across the system [57], thereby winding up Dirac strings until the sample is fully magnetised.

A crucial property of the Ising spins in spin ice is that their moments point in different directions according to which of the four sublattices of the pyrochlore lattice they reside on. These local easy axes are defined by the line joining the centres of the tetrahedra that share the spin in question; these are just the four bond directions of the diamond lattice, Fig. 3.1, which correspond to the four different sites of a tetrahedron, or the dashed lines in Fig. 3.7.

This fact endows the applied field with a particular versatility, as its orientation with respect to the quartet of local easy axes can induce qualitatively remarkably varied behaviour. This is the subject of this section, which will cover an unusual topological transition in three dimensions known as Kasteleyn transition to a uniformly inert state via a mechanism involving one-dimensional extended strings; a two-dimensional kagome ice regime, where the emergent gauge field undergoes dimensional reduction; as well as to a set of orthogonal chains only half of which are fully pinned. This interesting physics will be discussed in detail in the following chapters (see Chaps. 5 and 6). Here, we consider only the first two items on this list, and in particular focus our discussion less on the rich and varied phenomenology of the resulting magnetisation processes, and more on their explanation in terms of the physics of emergent gauge fields and its manipulation.

3.6.1 Kasteleyn Transition

Applying a field in the crystallographic [001] direction (Fig. 3.1) is particularly simple: in this case, the Zeeman energy is the same for spins on all four sublattices with different easy axes. Secondly, there exists a fully polarised state which both minimises the Zeeman energy and satisfies both the ground state condition $\tau_\alpha = 0$.

This fully polarised state is non-degenerate—flipping any spin costs Zeeman energy. Therefore, there will be at least two regimes, one for weak fields where the entropy of the spin ice manifold dominates; and another at high fields, where the Zeeman energy dominates.

In Ising magnets, there need not be a phase transition between these two regimes, as the external field acts as a symmetry-breaking perturbation, so that a continuous crossover to the unique fully polarised state is possible. Indeed, this is what happens at any finite strength of the magnetic-interaction energy scale.

However, if the ground state condition $\tau_\alpha = 0$ is strictly enforced, a new and highly unusual phase transition does appear [58]. It results from a special feature of the fully polarised state, namely that it is dynamically very inert: since spin flips can only appear in strings of spins arranged head-to-tail, for a fully polarised state, these strings have to span the entire system (Fig. 3.4).

The Zeeman cost involved thence grows with the linear system size L, as flipping each spin incurs a Zeeman energy penalty of E_Z. However, this cost can be counterbalanced by the entropics of such strings, as their path is not predetermined: at each step, there is a choice through which of the two in-pointing spins of a tetrahedron to exit, amounting to an entropic contribution to the free energy of $T \log 2$ per flipped spin. The free energy of a single string is thus

$$F_s = -L(T \ln 2 - E_Z) \,, \tag{3.16}$$

where $E_Z = 2h/\sqrt{3}$ is the Zeeman energy cost of anti-aligning a spin with the field of strength h. When $F_s > 0$ at low T, the corresponding Boltzmann factor, $\exp(-F_s/T) \sim \exp[L(\ln 2 - E_Z/T)]$ is exponentially small in L, and hence strings are completely suppressed—the fully polarised state permits no fluctuations.

By contrast, when $F_s < 0$, strings will be present. Details of how they appear depend on their effective interactions. In the absence of further perturbations, there is an entropic repulsion between the strings—when two strings pass through the same tetrahedron, there is no choice to be made which spins to flip. The density of strings therefore increases continuously from zero. The corresponding transition is known as a Kasteleyn transition, and it is unusual in that on one side, it looks like an ordinary second-order phase transition; while on the other, the complete suppression of fluctuations lends air of an extreme first-order transition.

The entropic repulsion of the strings can be counteracted by an energetic attraction, which may e.g. be achieved via spin-phonon coupling by straining the crystal [59] or by further neighbour couplings [60]. When the strings are effectively attractive, the Kasteleyn transition is replaced by a first-order jump in the magnetisation. Right

in between those two, there is a possibility of an 'infinite-order' transition, in which an extensive number of levels are exactly degenerate at the transition [59].

These features are all manifestations of the unusual string-like nature of the excitations in spin ice. Theories to account for those therefore invoke extended degrees of freedom. A particularly elegant description is to identify the strings in d dimensions with world lines of bosons in $d-1$ dimensions [58, 61]. Thence, the Kasteleyn transition becomes the transition of the dilute Bose gas, which is the same as the commensurate-incommensurate transition [62].

In an actual experiment, the ice rule will not be perfectly enforced, due to the finite energy cost of magnetic monopoles, the presence of which allows strings to terminate. A detailed scaling analysis of the resulting critical behaviour has been carried out in [63].

3.6.2 Kagome Ice

An additional convenient feature of the magnetic field in spin ice is provided by its interplay with the non-collinear easy axes of the four sublattices. By choosing a field direction which has unequal projection on these axes, one can selectively distinguish between the axes, and therefore use a uniform field in the laboratory to emulate a staggered field as far as the sublattices are concerned [64].

A field in the crystallographic [111] direction has a projection onto one easy axis three times the size of that onto the three others. This one sublattice will therefore be pinned first. The spins on this sublattice form triangular lattices stacked along the field direction, to which they are perpendicular (Fig. 3.7).

These triangular lattices alternate with kagome lattices hosting the spins of the other three sublattices. Each triangle of this kagome lattice needs to have one spin antialigned with the field in order to satisfy the condition $\tau_\alpha = 0$. Denoting this spin by a dimer connecting the midpoints of the two triangles it belongs to yields a mapping of spin ice ground states onto dimer coverings of stacked honeycomb lattices (Fig. 3.7) [5, 7, 33, 65].

The statistical mechanics of the corresponding dimer models is well-understood. In particular, the residual entropy of this state, known as kagome ice, is still extensive, and indeed exactly known to be $\mathscr{S}_{kagome} = 0.0808 k_{\mathrm{B}}/\mathrm{spin}$ [66].

Dimensional reduction of gauge field

What's particularly intriguing about this state, however, is the fact that the emergent gauge field is now restricted to inhabit the two dimensions of the kagome/honeycomb lattice only: it has undergone dimensional reduction! Gauge fields in two dimensions have only one component, and are known as height fields. They no longer come with a local gauge invariance, a fact which is reflected in a richer operator content of the coarse-grained field theories. These additional operators in turn go along with new features in the structure factor directly diagnosing the dimensional reduction. This is nicely revealed in changes in the spin correlations, depicted from numerical

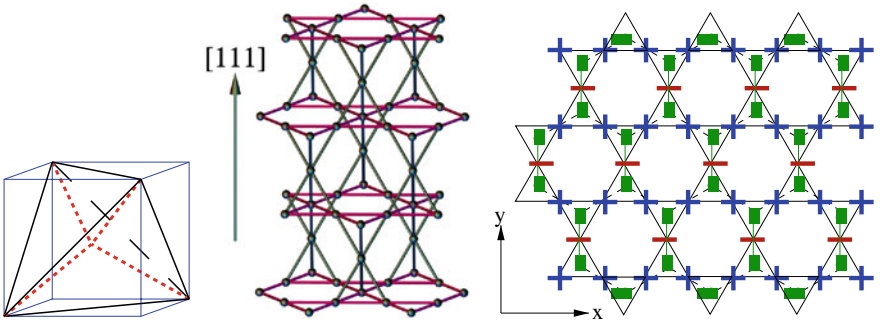

Fig. 3.7 Left: a tetrahedron inscribed in a unit cell, showing the local easy axes (dashed lines) in the [111] directions along which the magnetic moments are constrained to point. Middle: a slab of the pyrochlore lattice cut perpendicular to the [111] axis, reprinted from [33]. Layers of kagome lattices (purple) alternate with triangular layers. All spins on the latter are polarised swiftly as their projection onto a field in the [111] direction is large. The kagome layers then host kagome ice, a two-dimensional version of spin ice with an emergent two-dimensional gauge field and concomitant logarithmic Coulomb interactions. Right: In kagome ice, two out of three spins of each triangle point along the field; the third one can be denoted by a dimer joining the centres of the triangles it belongs to, so that the ground states of kagome ice map onto hardcore dimer coverings of the honeycomb lattice formed by the centres of the triangles. Reprinted from [65] with permission from the American Physical Society

simulations [67] in Fig. 3.3. These show a pair of new features. The first is related to the appearance of a finite net moment induced by the field [18], which shows up as Bragg peaks at the centres of the Brioullin zone of the structural unit cell. The second is due to the presence of these additional operators. These reflect algebraically decaying correlations with a tripled unit cell, and they grow logarithmically with system size [65].

Other consequences involve a change in the effective interaction of monopoles in this regime. With the emergent U(1) gauge field restricted to two dimensions, the corresponding entropic Coulomb interaction no longer decays inversely with separation between a pair of charges as it does in $d = 3$. Instead, the distance dependence is logarithmic, as behooves a Coulomb interaction in $d = 2$—this is just the interaction which features in Kosterlitz' RG treatment of the Coulomb gas. At the same time, the intrinsic magnetostatic Coulomb interaction continues to have the conventional $d = 3$ behaviour.

As in the case of the [001] field, there is a weak-field regime in which the $d = 3$ spin ice behaviour persists. From the kagome ice regime, this is reached via string defects involving flipping spins in successive triangular layers. Unlike in the [001] case, the strings can flip any number of spins in the kagome layers, so that their entropy is sufficiently large to ensure a non-vanishing string density regardless of the ratio of Zeeman to magnetic energy, so that there is a simple crossover between the spin- and kagome-ice regimes. It is only upon tilting the field away from the [111] direction so that the string meandering in the kagome plane also incurs a Zeeman energy cost that a Kasteleyn transition arises [65].

Tuning the Plasma Parameter: Liquid-Gas Transition

In the case of kagome ice, there is a separate transition to a high-field saturated state, on account of the competition between Zeeman and magnetic energies: for sufficiently strong fields, the spins antialigned with the field will flip to gain the former at the expense of the latter [33]. In the language of the dimer model, these correspond to monomers—triangles not hosting a spin antialigned with the field. Indeed, fractionalisation in $d = 2$ follows immediately in this picture: by removing a dimer, two monomers on its endpoints are left behind, which can then be separated subject to an entropic Coulomb attraction. These monomers are of course just the monopoles restricted to two dimensions, and it is in this context that their presence was first noted in spin ice [65].

This mapping to a monomer-dimer model leads to a profound prediction: there is a theorem by Heilmann and Lieb which says that no phase transition can appear in such a model away from vanishing monomer density, the only option being continuous crossovers. This prediction applies to the nearest-neighbour model for kagome ice in a field.

This prediction, in turn, is at variance with experimental facts: spin ice in a [111] magnetic field exhibits a well-developed first-order phase transition with a critical endpoint, as was noted well before the existence and properties of magnetic monopoles were properly understood [33, 68]. The origin of the apparent violation of the Heilmann-Lieb theorem lies in the omission of the magnetic (intrinsic) Coulomb interactions, which retain in their three-dimensional form even in the kagome ice regime as the field lines of the intrinsic magnetic field are not restricted to the kagome planes. Like this, the monopoles are magnetostatically coupled in $d = 3$ to monopoles in other kagome planes [28].

Since the creation cost of the monopoles can be lowered by applying a field—all the way to a negative value in the saturated state—this brings forth another important feature of field control of spin ice: it allows a tuning of the plasma parameter Γ, the ratio of a typical Coulomb energy to temperature

$$\Gamma = \frac{\mu_0 q_m^2}{4\pi \langle r \rangle T} , \tag{3.17}$$

where $\langle r \rangle \sim \rho^{-1/3} \approx \exp[\Delta/3T]$ is the field-dependent typical monopole separation, set by their density ρ, which in turn follows from an (appropriately renormalised) monopole creation cost Δ. In zero field, Γ therefore vanishes at low T on account of the exponentially small monopole density, as well as at inevitably high T as $\langle r \rangle \geq r_d$. It turns out that the maximum in between is not sufficient to exhibit collective physics beyond screening of the Coulomb interaction. However, in a field, the lowering of $\langle r \rangle$ is sufficient to push the Coulomb system in a more strongly interacting regime, where there does exist a first-order cooperative phase transition into a high-density regime for the monopoles.

In fact, the phase diagram of spin ice is identical to that of a Coulomb liquid, which has been studied extensively due to the intrinsic interest of the critical endpoint of

the line of first-order phase transitions separating the two regimes mentioned above. Spin ice, in fact, has provided an interesting model system for studying the critical properties of this endpoint in much detail (see Chap. 7).

3.7 Disorder in a Coulomb Phase—Diluted Spin Ice

In materials science, there are plenty of sources of disorder. So, it is not surprising that in spin ice, disorder takes on many forms. Disorder can as a matter of principle not be avoided, and unfortunately, it is not always clear what kinds of disorder are present; and how to quantify low levels of disorder. As different types of disorder have different impact on the properties of the system—often in themselves not easy to understand—this makes analysing experimental data quite tricky. A beautiful case in point is the study of the effects of small amounts of oxygen non-stoichiometry on the slow dynamics of the DTO spin ices [69].

Indeed, in the context of frustrated magnets, the effect of disorder, and its possible role in promoting the appearance of glassy behaviour, is a subject dating back to the very beginning. The highly frustrated magnetic material SCGO [70], which kicked off much of the interest in frustrated magnets around the year 1990, does exhibit not an ordering but a freezing transition terminating the cooperative paramagnetic phase at the lowest temperatures [71]. Detailed studies of the local properties of SCGO have since been undertaken [72], and concomitant theoretical work has demonstrated that while adding disorder to a topological magnet gives rise to a very interesting phenomenology, the assumptions about either nature or level of disorder present in SCGO were likely erring on the optimistic side. For an overview of this fascinating subject, we refer the reader to a publication by Canals and Cepas [73], who list compounds and settings in which disorder and glassiness have been investigated.

A different take on the situation is to move away from the limit of small and unknown disorder, towards a setting in which disorder is introduced intentionally. By investigating how various physical quantities scale with the level of disorder, it can then become possible to develop a more detailed theory of the effects of disorder. In this vein, experimental studies have been undertaken of changing the ratios of the constituent atoms in a material. This can lead, for instance, to an occupancy of normally non-magnetic sites with magnetic ions ('stuffing') [74–76]. Conversely, one can replace some magnetic ions with non-magnetic ones ('dilution') [77–79]. The latter is relatively straightforwardly achieved for rare earth magnets, whose chemical behaviour is not sensitively linked to the magnetic properties, so that quantities like ionic radii change little when replacing, say, Dy^{3+} ions and their huge magnetic moments with non-magnetic Y^{3+} ions.

A particular motivation for considering dilution with non-magnetic ions lies in the fact that this facilitates access to the gauge-charged sector of the emergent gauge theory. Following such a strategy is promising in all kinds of topological condensed matter systems. The reason is that, basically, one can think of the dilution as leading to a hole in the system. For example, in two dimensions, a hole is a topological

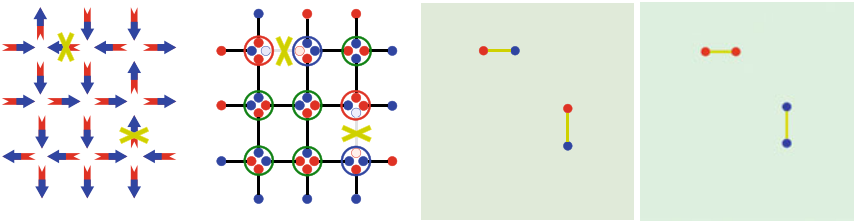

Fig. 3.8 Genesis of ghost spins and their effective interactions. Removing a spin leaves behind a pair of tetrahedra with nonzero net charge. Deleting those tetrahedra which are satisfied (as in Fig. 3.5) leaves behind dipole moments opposite to those which have been removed. These interact like ordinary dipole moments, but with an additional entropic contribution due to their emergent gauge charge. Flipping a string of spins between the two ghost dipoles in turn generates a pair of ghost monopoles (right panel), a gauge-charged excitation of the missing spins without a counterpart in conventional spin glasses. Reprinted figure from [82] with permission from the American Physical Society

object in the sense that paths around it are non-contractible—a hole turns a disk into an annulus. One can then have a flux going through the hole. Of course, a hole generated by a single non-magnetic site in the lattice is still microscopic in size, so that the flux can interact strongly with the remaining lattice degrees of freedom, but nonetheless it is a natural location to nucleate or bind excitations such as a monopole.

3.7.1 Thermodynamics of Diluted Spin Ice

Already the thermodynamics within the Coulomb phase of diluted spin ice, at least in the nearest-neighbour model H_{Ising}, holds a surprise: the zero-point entropy changes non-monotonically with the amount of dilution. This follows from the fact that the level of underconstraint for tetrahedra with m spins missing is non-monotonic with m. For tetrahedra, $m = 0$, a fraction of $f_4 = 6/16 = 0.375$ of configurations are ground states; for triangles, $m = 1$, $f_3 = 6/8 = 0.75 > f_4$, while for a dimer, $f_2 = 1/2 = 0.5$ and a single spin of course has $f_1 = 2/2 = 1$. Using the Pauling mean-field estimate, the zero-point entropy thence changes non-monotonically as the prevalent value of m decreases upon dilution, as displayed in Fig. 3.2.

Indeed, this is not at all the end of the story. A detailed numerical analysis for H_{dip}, in agreement with a set of experiments [80, 81], found that, as the temperature is lowered further and further, the 'zero-point entropy' is gradually released, indicating residual interactions beyond those captured by H_{Ising}. This follows naturally from the monopole picture: in dipolar spin ice, configurations with different monopole locations need not be degenerate, unlike in the case of H_{Ising}. As diluted tetrahedra with odd m contain monopoles in the ground state, these will therefore interact, and lift the degeneracy automatically, in an instance of the visibility of the intrinsic gauge charge carried by 'excitations' nucleated at disorder sites.

These findings raise the question: is there a simple effective Hamiltonian which allows us to describe the physics of diluted spin ice? To determine such a Hamiltonian, one needs to identify both the effective low-energy degrees of freedom and the interactions between them.

3.7.2 Ghost Spins

The nature of the low-energy degrees of freedom is both surprising and simple: these are dipoles *at the location of the missing spins* [82]. This is easy to see pictorially, Fig. 3.8: at low temperature, the ice rules enforce charge neutrality of each tetrahedron. However, for tetrahedra with one missing spin, it is not possible to have charge neutrality, as the number of charges is odd. As a missing spin creates a pair of neighbouring defective tetrahedra, their lowest-energy configuration is to be oppositely charged–they therefore have a dipole moment equal in size to that of the missing spin.

Replacing the missing spin would cancel the moment of the ghost spin to yield an allowed spin ice state. Therefore, the dipole moment of the ghost spins is opposite to that of the missing spin. This is analogous to the properties of a missing electron in a filled band in a solid—what is left behind is a hole with a charge of the same size of the electron, but an opposite sign.

From this analogy, the effective interaction between the ghost spins can be immediately read off—the sign change is immaterial for an interation between a pair of ghost spins, so that we obtain a standard dipolar Hamiltonian for the ghost spins as effective low-energy description of the diluted system. In fact, the dipolar interaction strength is enhanced as the couplings of the intrinsic magnetic moments of the ghost spins is supplemented by that due to the emergent gauge field, which takes on the same dipolar form, to give an effective interaction constant [82]

$$D_{\text{eff}} = D + \frac{3T}{\sqrt{2}\pi} \tag{3.18}$$

3.7.3 Topological Spin Glass

The resultant effective Hamiltonian presents a huge simplification over the microscopic ones in terms of the original spins. Instead of treating a dense system of spins, the degrees of freedom are the much sparser ghost spins. The low-temperature properties of such a disordered dipolar system are themselves not well-known, in large part due to the difficulty of simulating disordered long-range interacting systems, and the notorious difficulty in identifying spin glass transitions.

However, it does turn out to be possible to demonstrate that the ghost spin Hamiltonian does undergo a standard spin glass transition [82]. One particular feature of

this transition is that its critical coupling is proportional to the level of dilution, $T_x \sim x$. This follows directly from the fact that dipolar interactions scale as $1/r^3$. As the density is given by the inverse cube of a typical separation scale of the impurities, $x \sim 1/\rho^3$, one finds that typical terms appearing in the Hamiltonian scale as $1/r_{\text{typ}}^3 \sim 1/\rho^3 \sim x$. Simulations indicate that it is the typical terms in the Hamiltonian which set the scale of the phase transition, and hence $T_x \sim x$.

3.7.4 Ghost Monopoles, Hydrogenic and Continuum States

Thanks to their origin in a topological phase, the ghost spins turn out to have some additional structure beyond that of a simple missing dipole. Most immediately, they can be 'ionised' by emitting a monopole into the bulk, which creates a 'ghost monopole' at the impurity (see Fig. 3.8) [83]. This can be achieved by flipping a string of spins terminating in one of the tetrahedra which share the ghost spin.

This is an instance of the possibility mentioned above of an impurity nucleating a gauge-charged object. While the ghost spins map onto a conventional dipolar spin glass, with only a renormalised transition temperature due to the entropic contribution to their mutual interactions, they also betray their origin as collective degrees of freedom in a topological spin liquid by exhibiting behaviour—such as their capacity to be ionised—entirely absent from a conventional dipolar spin glass.

While monopoles are present neither in the spin glass nor in the undiluted ground state of spin ice, their creation energy is nonetheless lowered for the spin glass compared to that of a bulk monopole. This is a consequence of the fact that no energy has to be invested in violating the ground-state condition on the two defect tetrahedra. In the limit of low temperatures, these cheaper ghost monopoles will therefore dominate in number over the bulk monopoles. The crossover appears when $\exp(-\Delta/T) \sim x \exp(-\Delta_g/T)$, where Δ and Δ_g are the respective bulk and ghost monopole excitation energies.

The monopole emitted in the ionisation process can disappear into the bulk (where it may recombine with a ghost monopole at another impurity site), but given its charge is equal and opposite to that of the ghost monopole, it might also be bound to the impurity site. This is analogous to the situation of a donor impurity in a semiconductor, which may either give up its electron completely, or have it form a hydrogenic bound state centered on the impurity.

Either of these states can be used to further probe the nature of the spin ice state. Purely classically, the energies of a stationary monopole bound to an impurity monopole are discrete, reflecting the discreteness of the Coulomb interaction energy sampled at discrete locations. In particular, the discrete energy spectrum is due to the presence of the intrinsic magnetic charge of the monopoles—in the pure nearest-neighbour model, the energy of a monopole is independent of its distance from the ionised impurity.

Quantum mechanically, there are bound states where the monopole is not stationary. When the binding energy of the monopole is weak, and the bound state large,

this in principle maps onto the standard problem of a hydrogenic state [83]; however, details depend on whether the spin background is endowed with an autonomous quantum dynamics, or whether spins only flip as a result of the monopole itself hopping past them.

Moving beyond bound states, the monopoles in the presence of quantum dynamics acquire a dispersion. The bandwith of the dispersion is given by the size of the hopping matrix element, i.e. the spin flip terms in the Hamiltonian. It is important to note that this bandwidth of the single-monopole manifold of states is considerably larger than, say, the quantum mechanical splitting of the spin ice manifold itself, as—in the absence of ring-exchange terms in the microscopic Hamiltonian—the effective dynamics of the latter proceeds via virtual excited states comprising monopole excitations; the corresponding matrix elements are therefore suppressed. It will be interesting to follow experimental progress along these lines, with a couple promising studies already undertaken in recent times [84, 85].

3.8 What About Water Ice?

With all these developments concerning spin ice, it is natural to ask whether any insights can be fed back into our understanding of water ice. Of course, plenty of work has been devoted to research on water ice; for readers interested in an introduction to the physics of water ice, a suitable starting point is the book by Petrenko and Whitworth [86]. Indeed, water ice has been around for an awfully long time, presumably many of our cave-dwelling ancestors have had occasion to ponder its peculiar properties. In the age of modern science, Linus Pauling formulated the ice rules early on [87], and their role for the genesis of pinchpoints [88] were noted in the course of time.

Nonetheless, spin ice has provided a distinct and often complementary perspective, both from the point of view of questions asked, and as regards the methods employed. We illustrate this with a simple piece of work on the proton correlations in water ice. Common water ice, the phase known as hexagonal ice I_h, itself is somewhat more complex than spin ice, in the sense that its lattice structure is not as simple as that of cubic ice I_c corresponding to spin ice. In the latter, the oxygen atoms reside on a diamond lattice, while in the former, they form a wurtzite structure with a unit cell of eight atoms.

The correlations are therefore not straigthforward to determine, and while much modelling has been undertaken to describe them, a simple analytic understanding has been missing. It turns out that one method which has been used successfully for spin ice can plug this gap. We apply a self-consistent Gaussian approximation introduced to Heisenberg frustrated magnets in [89], which has been employed extensively for the study of spin ice[14]. With this method, we consider the correlations in reciprocal space—where the pinchpoints were identified in spin ice.

Figure 3.9 shows these correlations in a direct comparison of theory [90] and experiment [91]. The attraction of the self-consistent Gaussian approximation is that

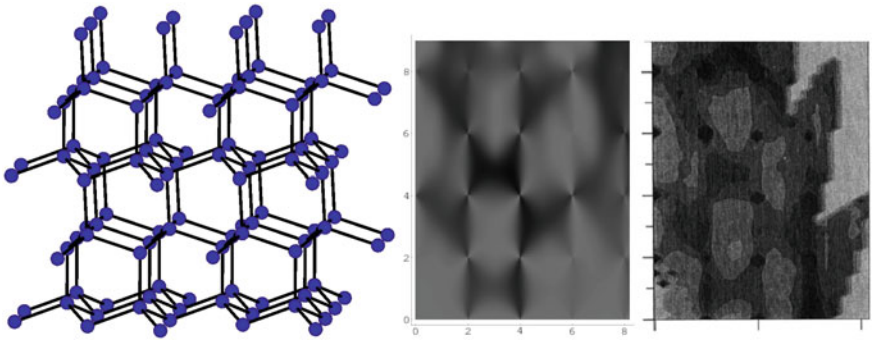

Fig. 3.9 Left: wurtzite structure formed by the oxygen ions in hexagonal water ice I_h. Middle (theory) and right (experiment): diffuse neutron scattering structure factor for hexagonal water ice I_h in one plane of reciprocal space. Reprinted figures (middle and left panels) from [90] with permission from the American Physical Society and (right panel) from [91] with permission from Taylor & Francis Ltd

it has no free parameters, and is analytically tractable, providing a mathematical expression in closed form. This, however, also implies that it will not be able to fully model the experimental results, as it does not include information on any aspects such as disorder or the detailed proton-proton interaction. As the figure shows, it nonetheless provides a simple starting point for understanding which elements of the experimental results are directly due to the ice rules, and which require more detailed study. In particular, many gross features of high and low intensities, along with location and orientation of the pinch points, follow directly from this analytical study.

3.9 Summary and Outlook

Spin ice is a remarkable material in that it realises a fractionalised magnetic phase in three dimensions, the first material to achieve such a feat. Given the properties of this Coulomb liquid can be rather easily understood, this makes spin ice into a poster child of topological condensed matter physics. It is perhaps one of the best settings in which to learn about the phenomenology of fractionalised and topological phases, and to provide an introduction to the physical and mathematical concepts for their description. This we have attempted to do in providing the complete line of arguments leading from a microscopic Hamiltonian via coarse-graining to an effective low-energy description involving the emergent gauge field and its excitations, the magnetic monopoles, whose properties naturally lead us to understand even the collective physics of spin ice at low temperature.

The salient point we have encountered centre on the emergent gauge field and the excitations charged under it. This is the new physics beyond Landau–Ginzburg–

Wilson, many aspect of which are only now being studied, and which a good portion of this book is about.

The Coulomb phase physics presented so far knows many extensions. First of all, it is not restricted to Ising spins, but instead appears as well for continuous spin models, in particular the Heisenberg pyrochlore antiferromagnet [14, 92]. The Heisenberg version of the ice rules states that the total spin of each tetrahedron needs to vanish. Unlike the Ising case, however, infinitesimal displacements of spins out of such ground states are possible, so that there are excitations at arbitrarily small energies, and also, there is thence no concept of a fixed charge of a magnetic monopole. By appropriately generalising ideas from magnetolyte physics incorporating these ideas [93], much of the framework presented here can, however, be carried over.

More ambitiously, the nature of the constraint can also be modified, in order to obtain a broader range of projectors, and concomitant more complex forms of emergent gauge structures. For the example of Heisenberg spins with only nearest-neighbour interactions, a broader range of behaviour can thus be accessed provided one allows for a generalised set of anisotropic interactions, which even includes pinch lines (rather than pinch points) in the dynamical structure factor for one particular choice of parameters [94].

In addition, the Coulomb phase physics generalises under the addition of quantum fluctuations, as already noted in early works on the subject [15, 95]. Here, one finds electric charges on top of the magnetic ones discussed above. We mention to the reader the caveat that the nomenclature is sometimes reversed, a choice somewhat more natural for the nearest-neighbour model where the intrinsic magnetic Coulomb charge is absent; however, since there is a duality between magnetic and electric degrees of freedom in $3 + 1$ dimensions, this is purely a matter of convention.

Spin ice is not the only place in physics where magnetic monopoles have been invoked. In condensed matter physics alone, several sightings have been proposed or reported. In a family of micromagnetic systems collectively termed artificial spin ice, monopole crystals have been posited, and much of the physics of kagome ice is realised there in two-dimensional micromagnetic arrays; for a review, see [96]. Monopoles in reciprocal space have also become prominent, e.g. in the context of Weyl semimetals [97] but there the notions of deconfinement, and of intrinsic magnetic charge, are absent entirely. In the study of Skyrmion lattice physics in systems such as MnSi [98], the concept of a monopole appears when considering the dynamics of the (dis)appearance of Skyrmions in non-equilibrium settings [99]. Finally, near the surface of a topological insulator, an electric charge induces an image which carries both (intrinsic) magnetic and electric charges. In the effective theory of such a system, this is due to the presence of a term coupling the electric and magnetic fields, of the form $\mathbf{E} \cdot \mathbf{B}$, which leads to a contribution to the constitutive equations allowing a divergence-free $\mathbf{B}$ field to go along with a source of magnetic field $\mathbf{H}$. In this setting, such an image monopole is not a freely mobile quasiparticle, but rather, it is attached to the external electric charge.

In high-energy physics, the search for a 'proper' elementary monopole continues. Its major difference to the magnetic monopoles in spin ice is that it is supposed to come with a Dirac string that is unobservable. At present, its main disadvantage is

that it has never been observed. However, given the fact that magnetic monoples have been invoked over almost a century and in various guises and complexities, surely it can only be a matter of time until the progress promised by the advances in experimental high-energy physics lead to a discovery of a magnetic monopole as an elementary particle.

Acknowledgements I am very grateful to my numerous collaborators in the work discussed here. It is almost impossible to single out any individuals here, but it was with Claudio Castelnovo, Sergei Isakov and Shivaji Sondhi that much of the conceptual framework presented here was developed. I am also grateful to the editors of this volume, Ludovic Jaubert and Masafumi Udagawa, for much encouragement, support and patience. I also thank the former, along with Peter Holdsworth, for help with the figures, and Maximilian Schulz for comments on the manuscript.

References

1. P.M. Chaikin, T.C. Lubensky, J. Stat. Phys. **83**, 1263 (1996). https://doi.org/10.1007/BF02179565
2. F. Wegner, J. Math. Phys. **12**, 2259 (1971). https://doi.org/10.1063/1.1665530
3. P.W. Anderson, Science **177**, 393 (1972). https://doi.org/10.1126/science.177.4047.393
4. P.W. Anderson, Mater. Res. Bull. **8**, 153–160 (1973). https://doi.org/10.1016/0025-5408(73)90167-0
5. P.W. Anderson, Phys. Rev. **102**, 1008–1013 (1956). https://doi.org/10.1103/PhysRev.102.1008
6. J.F. Nagle, J. Math. Phys. **7**, 1484 (1966). https://doi.org/10.1063/1.1705058
7. S.V. Isakov, K.S. Raman, R. Moessner, S.L. Sondhi, Phy. Rev. B **70**, 104418 (2004). https://doi.org/10.1103/PhysRevB.70.104418
8. https://en.wikipedia.org/wiki/Boltzmann's_entropy_formula
9. H.W.J. Blote, R.F. Wielinga, W.J. Huiskamp, Physica **43**, 549 (1969). https://doi.org/10.1016/0031-8914(69)90187-6
10. A.P. Ramirez, A. Hayashi, R.J. Cava, R. Siddharthan, B.S. Shastry, Nature **399**, 333–335 (1999). https://doi.org/10.1038/20619
11. M.B. Geilikman, Zh. Eksp. Teor. Fiz. **66**, 1166 (1974); or Sov. Phys. J. Exp. Theor. Phys. **39**, 570 (1974). http://www.jetp.ac.ru/cgi-bin/e/index/e/39/3/p570?a=list
12. J. Stephenson, J. Math. Phys. **11**, 420 (1970). https://doi.org/10.1063/1.1665155
13. L.D.C. Jaubert, M. Haque, R. Moessner, Phys. Rev. Lett. **107**, 177202 (2011). https://doi.org/10.1103/PhysRevLett.107.177202
14. S.V. Isakov, K. Gregor, R. Moessner, S.L. Sondhi, Phys. Rev. Lett. **93**, 167204 (2004). https://doi.org/10.1103/PhysRevLett.93.167204
15. M. Hermele, M.P.A. Fisher, L. Balents, Phys. Rev. B **69**, 064404 (2004). https://doi.org/10.1103/PhysRevB.69.064404
16. D.J.P. Morris, D.A. Tennant, S.A. Grigera, B. Klemke, C. Castelnovo, R. Moessner, C. Czternasty, M. Meissner, K.C. Rule, J.-U. Hoffmann, K. Kiefer, S. Gerischer, D. Slobinsky, R.S. Perry, Science **326**, 411 (2009). https://doi.org/10.1126/science.1178868
17. T. Fennell, P.P. Deen, A.R. Wildes, K. Schmalzl, D. Prabhakaran, A.T. Boothroyd, R.J. Aldus, D.F. McMorrow, S.T. Bramwell, Science **326**, 415 (2009). https://doi.org/10.1126/science.1177582
18. M. Brooks-Bartlett, S.T. Banks, L.D.C. Jaubert, A. Harman-Clarke, P.C.W. Holdsworth, Phys. Rev. X **4**, 011007 (2014). https://doi.org/10.1103/PhysRevX.4.011007
19. H. Kadowaki, N. Doi, Y. Aoki, Y. Tabata, T.J. Sato, J.W. Lynn, K. Matsuhira, Z. Hiroi, J. Phys. Soc. Jpn. **78**, 103706 (2009). https://doi.org/10.1143/JPSJ.78.103706

20. R. Siddharthan, B.S. Shastry, A.P. Ramirez, A. Hayashi, R.J. Cava, S. Rosenkranz, Phys. Rev. Lett. **83**, 1854 (1999). https://doi.org/10.1103/PhysRevLett.83.1854
21. B.C. den Hertog, M.J.P. Gingras, Phys. Rev. Lett. **84**, 3430 (2000). https://doi.org/10.1103/PhysRevLett.84.3430
22. M.J.P. Gingras, B.C. den Hertog, Can. J. Phys. **79**, 1339 (2001). https://doi.org/10.1139/p01-099
23. D.L. Bergman, C. Wu, L. Balents, Phys. Rev. B **78**, 125104 (2008). https://doi.org/10.1103/PhysRevB.78.125104
24. S.V. Isakov, R. Moessner, S.L. Sondhi, Phys. Rev. Lett. **95**, 217201 (2005). https://doi.org/10.1103/PhysRevLett.95.217201
25. T. Neupert, L. Santos, C. Chamon, C. Mudry, Phys. Rev. Lett. **106**, 236804 (2011). https://doi.org/10.1103/PhysRevLett.106.236804
26. E. Tang, J.-W. Mei, X.-G. Wen, Phys. Rev. Lett. **106**, 236802 (2011). https://doi.org/10.1103/PhysRevLett.106.236802
27. K. Sun, Z. Gu, H. Katsura, S. Das Sarma, Phys. Rev. Lett. **106**, 236803 (2011). https://doi.org/10.1103/PhysRevLett.106.236803
28. C. Castelnovo, R. Moessner, S.L. Sondhi, Nature **451**, 42 (2008). https://doi.org/10.1038/nature06433
29. D. Pomaranski, L.R. Yaraskavitch, S. Meng, K.A. Ross, H.M.L. Noad, H.A. Dabkowska, B.D. Gaulin, J.B. Kycia, Nat. Phys. **9**, 353 (2013). https://doi.org/10.1038/NPHYS2591
30. R. Moessner, S.L. Sondhi, Phys. Rev. Lett. **105**, 166401 (2010). https://doi.org/10.1103/PhysRevLett.105.166401
31. J.F. Nagle, Chem. Phys. **43**, 317 (1979). https://doi.org/10.1016/0301-0104(79)85200-3
32. P.A.M. Dirac, Proc. R. Soc. Lond. A **133**, 60–72 (1931). https://doi.org/10.1098/rspa.1931.0130
33. K. Matsuhira, Z. Hiroi, T. Tayama, S. Takagi, T. Sakakibara, J. Phys.: Condens. Matter **14**, L559–L565 (2002). https://doi.org/10.1088/0953-8984/14/29/101
34. L.D.C. Jaubert, P.C.W. Holdsworth, Nat. Phys. **5**, 258 (2009). https://doi.org/10.1038/NPHYS1227
35. C. Castelnovo, R. Moessner, S.L. Sondhi, Phys. Rev. B **84**, 144435 (2011). https://doi.org/10.1103/PhysRevB.84.144435
36. S.T. Bramwell, J. Phys.: Condens. Matter **23**, 112201 (2011). https://doi.org/10.1088/0953-8984/23/11/112201
37. L. Onsager, J. Chem. Phys. **2**, 599–615 (1934). https://doi.org/10.1063/1.1749541
38. S.T. Bramwell, S.R. Giblin, S. Calder, R. Aldus, D. Prabhakaran, T. Fennell, Nature **461**, 956 (2009). https://doi.org/10.1038/nature08500
39. V. Kaiser, S.T. Bramwell, P.C.W. Holdsworth, R. Moessner, Phys. Rev. Lett. **115**, 037201 (2015). https://doi.org/10.1103/PhysRevLett.115.037201
40. D.I. Khomskii, Nat. Commun. **3**, 904 (2012). https://doi.org/10.1038/ncomms1904
41. H. Katsura, N. Nagaosa, A.V. Balatsky, Phys. Rev. Lett. **95**, 057205 (2005). https://doi.org/10.1103/PhysRevLett.95.057205
42. I.A. Sergienko, E. Dagotto, Phys. Rev. B **73**, 094434 (2006). https://doi.org/10.1103/PhysRevB.73.094434
43. M. Mostovoy, Phys. Rev. Lett. **96**, 067601 (2006). https://doi.org/10.1103/PhysRevLett.96.067601
44. A. Sarkar, S. Mukhopadhyay, Phys. Rev. B **90**, 165129 (2014). https://doi.org/10.1103/PhysRevB.90.165129
45. I.V. Aleksandrov, B.V. Lidsky, L.G. Mamsurova, M.G. Neigauz, K.S. Pigal'skii, K.K. Pukhov, N.G. Trusevich, L.G. Shcherbakova, J. Exp. Theor. Phys. **62**, 1287 (1985). https://www.jetp.ac.ru/cgi-bin/e/index/e/62/6/p1287?a=list
46. L.G. Mamsurova, K.S. Pigal'skii, K.K. Pukhov, J. Exp. Theor. Phys. Lett. **43**, 755 (1986). https://www.jetpletters.ac.ru/ps/1413/article_21511.shtml
47. J.P.C. Ruff, Z. Islam, J.P. Clancy, K.A. Ross, H. Nojiri, Y.H. Matsuda, H.A. Dabkowska, A.D. Dabkowski, B.D. Gaulin, Phys. Rev. Lett. **105**, 077203 (2010). https://doi.org/10.1103/PhysRevLett.105.077203

48. T. Fennell, M. Kenzelmann, B. Roessli, H. Mutka, J. Ollivier, M. Ruminy, U. Stuhr, O. Zaharko, L. Bovo, A. Cervellino, M.K. Haas, R.J. Cava, Phys. Rev. Lett. **112**, 017203 (2014). https://doi.org/10.1103/PhysRevLett.112.017203
49. P. Bonville, A. Gukasov, I. Mirebeau, S. Petit, Phys. Rev. B **89**, 085115 (2014). https://doi.org/10.1103/PhysRevB
50. M.J.P. Gingras, B.C. den Hertog, M. Faucher, J.S. Gardner, S.R. Dunsiger, L.J. Chang, B.D. Gaulin, N.P. Raju, J.E. Greedan, Phys. Rev. B **62**, 6496 (2000). https://doi.org/10.1103/PhysRevB.89.085115
51. H. Cao, A. Gukasov, I. Mirebeau, P. Bonville, C. Decorse, G. Dhalenne, Phys. Rev. Lett. **103**, 056402 (2009). https://doi.org/10.1103/PhysRevLett.103.056402
52. T. Fennell, M. Kenzelmann, B. Roessli, M.K. Haas, R.J. Cava, Phys. Rev. Lett. **109**, 017201 (2012). https://doi.org/10.1103/PhysRevLett.109.017201
53. S. Petit, P. Bonville, J. Robert, C. Decorse, I. Mirebeau, Phys. Rev. B **86**, 174403 (2012). https://doi.org/10.1103/PhysRevB.86.174403
54. L.D.C. Jaubert, R. Moessner, Phys. Rev. B **91**, 214422 (2015). https://doi.org/10.1103/PhysRevB.91.214422
55. J.P.C. Ruff, B.D. Gaulin, K.C. Rule, J.S. Gardner, Phys. Rev. B **82**, 100401 (2010). https://doi.org/10.1103/PhysRevB.82.100401
56. A.P. Sazonov, A. Gukasov, I. Mirebeau, P. Bonville, Phys. Rev. B **85**, 214420 (2012). https://doi.org/10.1103/PhysRevB.85.214420
57. I.A. Ryzhkin, J. Exp. Theor. Phys. **101**, 481–486 (2005). https://doi.org/10.1134/1.2103216
58. L.D.C. Jaubert, J.T. Chalker, P.C.W. Holdsworth, R. Moessner, Phys. Rev. Lett. **100**, 067207 (2008). https://doi.org/10.1103/PhysRevLett.100.067207
59. L.D.C. Jaubert, J.T. Chalker, P.C.W. Holdsworth, R. Moessner, Phys. Rev. Lett. **105**, 087201 (2010). https://doi.org/10.1103/PhysRevLett.105.087201
60. Y.-Z. Chou, Y.-J. Kao, Phys. Rev. B **82**, 132403 (2010). https://doi.org/10.1103/PhysRevB.82.132403
61. S. Powell, J.T. Chalker, Phys. Rev. B **78**, 024422 (2008). https://doi.org/10.1103/PhysRevB.78.024422
62. C.S.O. Yokoi, J.F. Nagle, S.R. Salinas, J. Stat. Phys. **44**, 729 (1986). https://doi.org/10.1007/BF01011905
63. S. Powell, Phys. Rev. B **87**, 064414 (2013). https://doi.org/10.1103/PhysRevB.87.064414
64. R. Moessner, Phys. Rev. B **57**, R5587 (1998). https://doi.org/10.1103/PhysRevB.57.R5587
65. R. Moessner, S.L. Sondhi, Phys. Rev. B **68**, 064411 (2003). https://doi.org/10.1103/PhysRevB.68.064411
66. M. Udagawa, M. Ogata, Z. Hiroi, J. Phys. Soc. Jpn. **71**, 2365–2368 (2002). https://doi.org/10.1143/JPSJ.71.2365
67. A. Harman-Clarke, Ph.D. thesis, University College London and Ecole Normale Supérieure de Lyon (2011)
68. T. Sakakibara, T. Tayama, Z. Hiroi, K. Matsuhira, S. Takagi, Phys. Rev. Lett. **90**, 207205 (2003). https://doi.org/10.1103/PhysRevLett.90.207205
69. G. Sala, M.J. Gutmann, D. Prabhakaran, D. Pomaranski, C. Mitchelitis, J.B. Kycia, D.G. Porter, C. Castelnovo, J.P. Goff, Nat. Mater. **13**, 488–493 (2014). https://doi.org/10.1038/NMAT3924
70. X. Obradors, A. Labarta, A. Isalgué, J. Tejada, Solid State Comm. **65**, 189 (1988). https://doi.org/10.1016/0038-1098(88)90885-X
71. A.P. Ramirez, Annu. Rev. Mater. Sci. **24**, 453 (1994). https://doi.org/10.1146/annurev.ms.24.080194.002321
72. L. Limot, P. Mendels, G. Collin, C. Mondelli, B. Ouladdiaf, H. Mutka, N. Blanchard, M. Mekata, Phys. Rev. B **65**, 144447 (2002). https://doi.org/10.1103/PhysRevB.65.144447
73. O. Cépas, B. Canals, Phys. Rev. B **86**, 024434 (2012). https://doi.org/10.1103/PhysRevB.86.024434
74. G.C. Lau, R.S. Freitas, B.G. Ueland, B.D. Muegge, E.L. Duncan, P. Schiffer, R.J. Cava, Nat. Phys. **2**, 249 (2006). https://doi.org/10.1038/nphys270

75. H.D. Zhou, C.R. Wiebe, Y.J. Jo, L. Balicas, Y. Qiu, J.R.D. Copley, G. Ehlers, P. Fouquet, J.S. Gardner, J. Phys.: Condens. Matter **19**, 342201 (2007). https://doi.org/10.1088/0953-8984/19/34/342201
76. X. Ke, R.S. Freitas, B.G. Ueland, G.C. Lau, M.L. Dahlberg, R.J. Cava, R. Moessner, P. Schiffer, Phys. Rev. Lett. **99**, 137203 (2007). https://doi.org/10.1103/PhysRevLett.99.137203
77. J. Snyder, J.S. Slusky, R.J. Cava, P. Schiffer, Phys. Rev. B **66**, 064432 (2002). https://doi.org/10.1103/PhysRevB.66.064432
78. M. Kajnaková, M. Orendác, A. Orendácová, A. Vlcek, T. Fennell, S.T. Bramwell, J. Magn. Magn. Mater. **272–276**, e989–991 (2004). https://doi.org/10.1016/j.jmmm.2003.12.702
79. G. Ehlers, J.S. Gardner, C.H. Booth, M. Daniel, K.C. Kam, A.K. Cheetham, D. Antonio, H.E. Brooks, A.L. Cornelius, S.T. Bramwell, J. Lago, W. Häussler, N. Rosov, Phys. Rev. B **73**, 174429 (2006). https://doi.org/10.1103/PhysRevB.73.174429
80. T. Lin, X. Ke, M. Thesberg, P. Schiffer, R.G. Melko, M.J.P. Gingras, Phys. Rev. B **90**, 214433 (2014). https://doi.org/10.1103/PhysRevB.90.214433
81. S. Scharffe, O. Breunig, V. Cho, P. Laschitzky, M. Valldor, J.F. Welter, T. Lorenz, Phys. Rev. B **92**, 180405(R) (2015). https://doi.org/10.1103/PhysRevB.92.180405
82. A. Sen, R. Moessner, Phys. Rev. Lett. **114**, 247207 (2015). https://doi.org/10.1103/PhysRevLett.114.247207
83. O. Petrova, R. Moessner, S.L. Sondhi, Phys. Rev. B **92**, 100401(R) (2015). https://doi.org/10.1103/PhysRevB.92.100401
84. K. Kimura, S. Nakatsuji, J.-J. Wen, C. Broholm, M.B. Stone, E. Nishibori, H. Sawa, Nat. Commun. **4**, 1934 (2013). https://doi.org/10.1038/ncomms2914
85. L. Pan, N.J. Laurita, K.A. Ross, B.D. Gaulin, N.P. Armitage, Nat. Phys. **12**, 361 (2015). https://doi.org/10.1038/nphys3608
86. V.F. Petrenko, R.W. Whitworth, *Physics of Ice* (Oxford University Press, Oxford, 1999). ISBN 9780198518945
87. L. Pauling, J. Am. Chem. Soc. **57**, 2680 (1935). https://doi.org/10.1021/ja01315a102
88. R. Youngblood, J.D. Axe, B.M. McCoy, Phys. Rev. B **21**, 5212 (1980). https://doi.org/10.1103/PhysRevB.21.5212
89. D.A. Garanin, Benjamin Canals. Phys. Rev. B **59**, 443 (1999). https://doi.org/10.1103/PhysRevB.59.443
90. S.V. Isakov, R. Moessner, S.L. Sondhi, D.A. Tennant, Phys. Rev. B **91**, 245152 (2015). https://doi.org/10.1103/PhysRevB.91.245152
91. J.C. Li, V.M. Nield, D.K. Ross, R.W. Whitworth, C.C. Wilson, D.A. Keen, Philos. Mag. B **69**, 1173 (1994). https://doi.org/10.1080/01418639408240187
92. R. Moessner, J.T. Chalker, Phys. Rev. B **58**, 12049 (1998). https://doi.org/10.1103/PhysRevB.58.12049
93. A. Sen, R. Moessner, S.L. Sondhi, Phys. Rev. Lett. **110**, 107202 (2013). https://doi.org/10.1103/PhysRevLett.110.107202
94. O. Benton, L.D.C. Jaubert, H. Yan, N. Shannon, Nat. Commun. **7**, 11572 (2016). https://doi.org/10.1038/ncomms11572
95. R. Moessner, S.L. Sondhi, Phys. Rev. B **68**, 184512 (2003). https://doi.org/10.1103/PhysRevB.68.184512
96. C. Nisoli, R. Moessner, P. Schiffer, Rev. Mod. Phys. **85**, 1473 (2013). https://doi.org/10.1103/RevModPhys.85.1473
97. X. Wan, A. Turner, A. Vishwanath, S.Y. Savrasov, Phys. Rev. B **83**, 205101 (2011). https://doi.org/10.1103/PhysRevB.83.205101
98. U.K. Rößler, A.N. Bogdanov, C. Pfleiderer, Nature **442**, 797–801 (2006). https://doi.org/10.1038/nature05056
99. P. Milde, D. Köhler, J. Seidel, L.M. Eng, A. Bauer, A. Chacon, J. Kindervater, S. Mühlbauer, C. Pfleiderer, S. Buhrandt, C. Schütte, A. Rosch, Science **340**, 1076 (2013). https://doi.org/10.1126/science.1234657

Chapter 4
Dynamics

K. Matsuhira

Abstract The dynamics of typical spin ice compound $Dy_2Ti_2O_7$ investigated by mainly AC susceptibility and DC magnetization are represented. In addition, considering the results of μSR and neutron scattering measurements, the common features in spin dynamics are discussed in comparison with the other spin in ice compounds. The spin dynamics of spin ice show a quite unique behavior. The temperature dependence of relaxation time $\tau(T)$ can be roughly described by three regimes. (I) Above 10 K, the temperature dependence of the relaxation time $\tau(T)$ is effectively explained on the basis of the Arrhenius law with an energy barrier E_B = 200–300 K. (II) In the temperature range of 2–10 K, $\tau(T)$ is almost constant. (III) Below 2 K, $\tau(T)$ increases again, and reaches ∼1 s at ∼0.7 K. Spin ice state is formed. The dynamics above 10 K is due to single ion process and mixing with excited states; E_B corresponds to the energy of the excited CEF levels which results in the Ising-like anisotropy. At low temperature below 10 K, the dynamics comes from the creation or annihilation of magnetic monopoles, and their diffusion. In the narrow temperature range ∼0.5–1 K, the thermal activated dynamics is observed; the energy barrier of ∼9 K is obtained for $Dy_2Ti_2O_7$. The results indicate that a description taking into account the long range Coulomb interaction between the monopoles is needed to explain the dynamics below 1 K. Below 0.5 K, $\tau(T)$ show a clear deviation from the thermal activated dynamics toward temperature independent relaxation. Furthermore, recent topics on the very slow spin dynamics at very low temperature are also represented.

K. Matsuhira (✉)
Kyushu Institute of Technology, Kitakyushu, Japan
e-mail: Matuhira@elcs.kyutech.ac.jp

M. Udagawa and L. Jaubert (eds.), *Spin Ice*, Springer Series in Solid-State Sciences 197,
https://doi.org/10.1007/978-3-030-70860-3_4

4.1 Spin Dynamics of Spin Ice Compounds to Spin Ice State

Spin ice compounds do not show a long ranged ordering (LRO) at least down to 80 mK [1]. It is important to investigate "How spin ice state is formed on cooling". Various measurements such as AC magnetization, NMR, μSR, neutron scattering are known to investigate the spin dynamics. Among them, the easiest method is AC magnetic susceptibility. In the AC magnetic susceptibility, the response of magnetization is observed when AC magnetic field with the field frequency f is applied to the sample. For AC magnetic field $H = H_0\exp(i\omega t)$, where ω is the angular frequency ($\omega = 2\pi f$), the induced AC magnetization with some delay is described by $M = M^*(\omega)\exp(i\omega t)$ where only the response from the same field frequency is considered for simplicity. Then, the AC magnetic susceptibility $\chi_{\mathrm{AC}} = (M/H)$ is described by

$$\chi_{\mathrm{AC}} = \chi' - i\chi'' \tag{4.1}$$

where χ' is the real part and χ'' is the imaginary part. In the case of $\omega = 0$, χ_{AC} is equal to DC magnetic susceptibility χ_0; then, $\chi'' = 0$. As the AC field frequency of 1–10 kHz is commonly used, the dynamics in the range of time scale from 1 s to 10^{-4} s can be measured; using SQUID magnetometer, very slow dynamics up to 100 s can be investigated as it is possible to measure the AC magnetic susceptibility down to 1 mHz.

Next, let's introduce the analysis method of AC magnetic susceptibility data using empirical form. Now we consider that spin obeys the relaxation process with single relaxation time τ; the response function is $\Phi(t) = \exp(-t/\tau)$. This is called "Debye formula" [2]. Then, χ_{AC} of Debye formula is described by the following equation

$$\frac{\chi_{\mathrm{AC}}(\omega, T)}{\chi_0} = \frac{1}{1 + i\omega\tau(T)} \tag{4.2}$$

Then, the real and imaginary parts are derived as follows:

$$\frac{\chi_{\mathrm{AC}}(\omega, T)}{\chi_0} = \frac{1}{1 + (\omega\tau)^2} - i\frac{\omega\tau}{1 + (\omega\tau)^2} \tag{4.3}$$

$$\frac{\chi'}{\chi_0} = \frac{1}{1 + (\omega\tau)^2} \tag{4.4}$$

$$\frac{\chi''}{\chi_0} = \frac{\omega\tau}{1 + (\omega\tau)^2} \tag{4.5}$$

Figure 4.1 shows the real and imaginary parts of Debye formula (black curves). The real part χ' has a constant value of χ_0 when $\omega\tau$ goes to zero. When $\omega\tau \gg 1$, χ' is nearly zero; if the relaxation time of spin is much larger than the time scale in the AC field frequency $1/(2\pi f)$, the spin can not response during the time

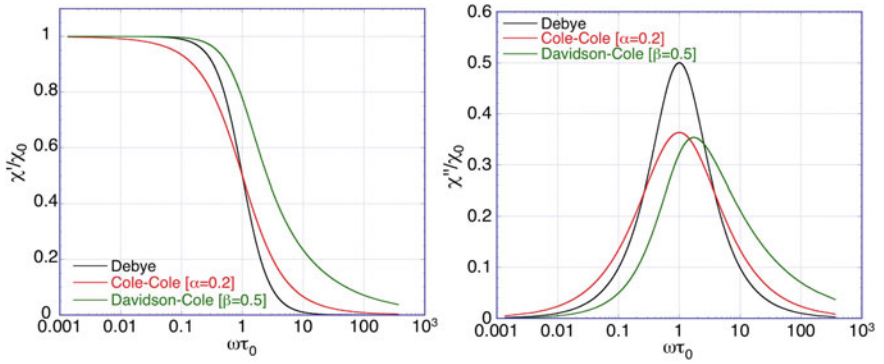

Fig. 4.1 Real (left) and imaginary (right) parts of Debye, Cole-Cole [$\alpha = 0.2$], and Davidson-Cole [$\beta = 0.5$] formulas

scale. The imaginary part χ'' is a symmetric function in logarithmic scale with a maximum at $\omega = 2\pi f = 1/\tau$. Therefore, from the maximum frequency f_{m} derived in the frequency scan of χ'', the magnetic relaxation time $\tau = 1/(2\pi f_{\mathrm{m}})$ is obtained.

In general system, it is often observed than the relaxation time is not single. Instead, the relaxation time has a wide distribution. The relaxation can be interpreted as the summation of Debye formula with many different τ. Defining a distribution function of the relaxation time $F(\tau/\tau_0)$ in the interval $d\ln(\tau/\tau_0)$, the expression becomes

$$\frac{\chi_{\mathrm{AC}}(\omega, T)}{\chi_0} = \int_{-\infty}^{\infty} \frac{F(\tau/\tau_0)}{1 + i\omega\tau} d\ln(\tau/\tau_0). \tag{4.6}$$

Acctually, it is well known that the experimental result is described by some empirical formulas. In this typical case, Cole-Cole formula is well known as follows:

$$\frac{\chi_{\mathrm{AC}}(\omega, T)}{\chi_0} = \frac{1}{1 + [i\omega\tau_0(T)]^{1-\alpha}} \tag{4.7}$$

$$\frac{\chi'}{\chi_0} = \frac{1 + (\omega\tau_0)^{1-\alpha}\sin\frac{\alpha\pi}{2}}{1 + 2(\omega\tau_0)^{1-\alpha}\sin\frac{\alpha\pi}{2} + (\omega\tau_0)^{2(1-\alpha)}} = \frac{1}{2}\left(1 - \frac{\sinh x}{\cosh x + \sin\frac{\alpha\pi}{2}}\right) \tag{4.8}$$

$$\frac{\chi''}{\chi_0} = \frac{(\omega\tau_0)^{1-\alpha}\cos\frac{\alpha\pi}{2}}{1 + 2(\omega\tau_0)^{1-\alpha}\sin\frac{\alpha\pi}{2} + (\omega\tau_0)^{2(1-\alpha)}} = \frac{1}{2}\frac{\cos\frac{\alpha\pi}{2}}{\cosh x + \sin\frac{\alpha\pi}{2}} \tag{4.9}$$

where $x \equiv (1-\alpha)\ln(\omega\tau_0)$ [3]. The parameter α that has a value between 0 and 1 describes a measure of distribution; when $\alpha = 0$, this formula reduces to Debye formula with a single relaxation time. As is shown in Fig. 4.1, although the imaginary part χ'' is a symmetric function in logarithmic scale with a maximum at $\omega = 2\pi f = 1/\tau_0$, in comparison with Debye formula, the maximum value is smaller and the

width is wider. Cole-Cole formula is characterized by the existence of the long-tail to short and long τ_0 in the distribution. It is known that the magnetic relaxation in spin glass system is well described by Cole-Cole formula [4].

For the other empirical formula, Davidson-Cole formula is also known as follows;

$$\frac{\chi_{\mathrm{AC}}(\omega, T)}{\chi_0} = \frac{1}{(1 + i\omega\tau_c)^{\beta}} \tag{4.10}$$

$$\frac{\chi'}{\chi_0} = (\cos\phi)^{\beta}\cos\beta\phi \tag{4.11}$$

$$\frac{\chi''}{\chi_0} = (\cos\phi)^{\beta}\sin\beta\phi \tag{4.12}$$

where $\omega\tau_c = \tan\phi$ and τ_c is cutoff of the distribution in relaxation time [5]. The parameter β that has a value between 0 and 1 describes a measure of distribution. When $\beta = 1$, this formula reduces to Debye formula with a single relaxation time. τ_c is the maximum value in the distribution of relaxation time. As is shown in Fig. 4.1, the imaginary part χ'' is an asymmetric function in logarithmic scale. The maximum value is smaller and the shape of χ'' is lifted up at high ω side (or short τ_0). Davidson-Cole formula is characterized by the maximum cutoff time τ_c and the long-tail to short τ_0 exist in the distribution of relaxation time. The dielectric relaxation in glycerine is described by Davidson-Cole formula [5]. As is shown later, the magnetic relaxation in spin ice is characterized by Davidson-Cole formula.

Figure 4.1 shows the real and imaginary parts of Cole-Cole [$\alpha = 0.2$] (red curve) and Davidson-Cole [$\beta = 0.5$] (green curve) formulas, respectively. The imaginary part χ'' in Cole-Cole formula is a symmetric function in logarithmic scale with a maximum at $\omega = 2\pi f = 1/\tau_0$. On the other hand, the imaginary part χ'' in Davidson-Cole formula is an asymmetric function in logarithmic scale; it does not show a maximum at $\omega = 2\pi f = 1/\tau_0$. Consequently, from the shape of $\chi''(f)$, we can easily estimate the appropriate fitting formula. When the shape of $\chi''(f)$ is close to the Debye formula, it is useful to estimate the typical relaxation time τ_{t} using $\tau_{\mathrm{t}} = 1/(2\pi f_m)$.

In addition, as another way to investigate the type of dynamics, $\chi'' - \chi'$ plot (so-called "Cole-Cole plot") is well known. Figure 4.2 shows the $\chi'' - \chi'$ plot of Debye, Cole-Cole [$\alpha = 0.2$], and Davidson-Cole [$\beta = 0.5$] formulas. In this plot, Debye formula shows a semicircle. Cole-Cole formula shows a circular arc. In the case of Davidson-Cole formula, the slope against χ'/χ_0 has a characteristic feature. At $\chi'/\chi_0 = 1$ (in the low frequency limit or DC time scale), the angle of $\pi/2$ is the same as Debye formula. This is responsible for the existence of maximum cutoff time τ_c. At $\chi'/\chi_0 = 0$ (in the high frequency limit or short τ_0 limit), the curve intersect at a smaller angle, which is similar to Cole-Cole formula. This is responsible for the existence of short long-tail of distribution in relaxation time. This way is also useful to know the dynamics.

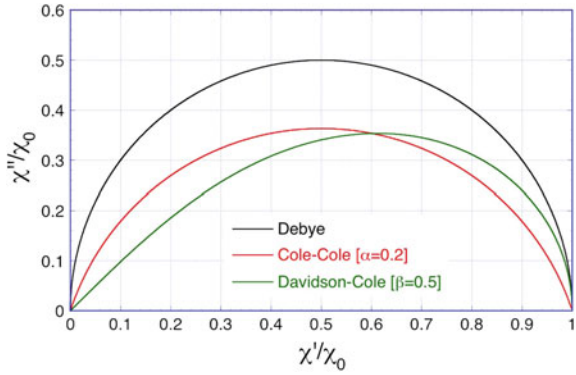

Fig. 4.2 $\chi'' - \chi'$ plot of Debye, Cole-Cole [$\alpha = 0.2$], and Davidson-Cole [$\beta = 0.5$] formulas. In the high frequency limit, χ'/χ_0 goes to 0. In the low frequency limit (or DC time scale) χ'/χ_0 goes to 1

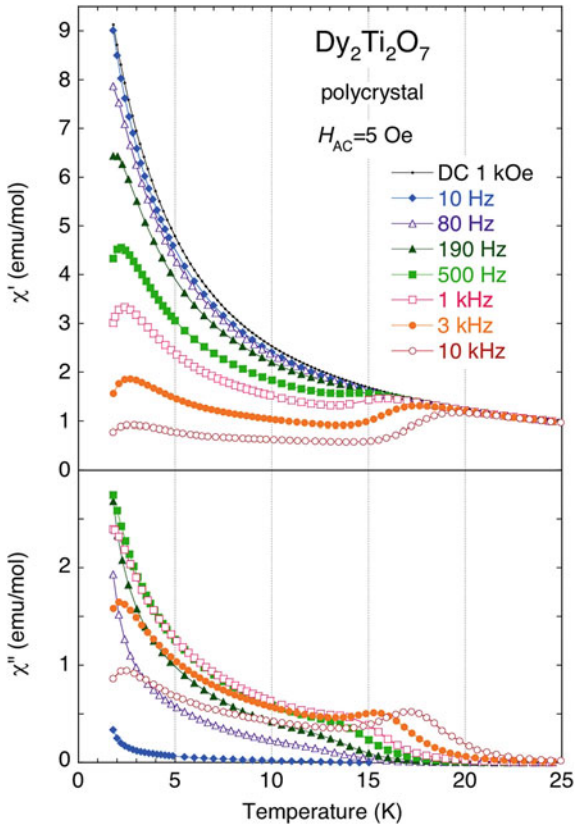

Fig. 4.3 AC magnetic susceptibility of $Dy_2Ti_2O_7$ above 1.8 K, reprinted from [6] with permission from the Institute of Physics

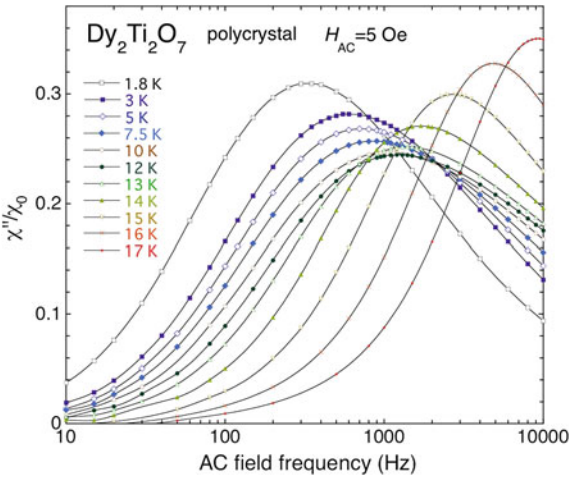

Fig. 4.4 $\chi''(f)$ of $Dy_2Ti_2O_7$ at various temperature ($T \geq 1.8$ K), which is normalized by DC magnetic susceptibility χ_0, reprinted from [6] with permission from the Institute of Physics

Let's move on to the AC magnetic susceptibility χ_{AC} of spin ice. Figure 4.3 shows the χ_{AC} of typical spin ice compound $Dy_2Ti_2O_7$ above 1.8 K [6]; the same data is also reported in [7]. On cooling, χ' at 10 Hz monotonically increases at least down to 1.8 K. χ'' at 10 Hz begins to increase below 10 K and indicates an upturn below 2 K. As the AC field frequency increases, the increase of χ' is suppressed and χ'' begins to increase. At 10 kHz, both χ' and χ'' show the anomalies at 18 K and 2 K. On the other hand, DC magnetic susceptibility has no anomaly. Therefore, this anomaly observed in χ_{AC} does not come from a static origin but characteristic dynamics of spin ice.

In order to see the temperature dependence of relaxation time, $\chi''(f)$ at various temperature, which is normalized by DC magnetic susceptibility χ_0, are shown in Fig. 4.4 [6]. $\chi''(f)$ shows a single broad peak. On cooling, the peak position, which is defined by the maximum frequency f_m, shifts to lower frequency side. The shape of $\chi''(f)$ at 1.8 K is a nearly symmetric function of $\log f$. The curves show a small shoulder on their high frequency sides. The characteristic is in agreement with Davidson-Cole formula. The shape becomes broader with increasing temperature up to 10 K; the peak height becomes smaller. Furthermore, above 10 K, the shape becomes shaper as temperature increases. The results mean that the distribution of becomes wider down to 10 K and sharper below 10 K on cooling. Next, $\chi'' - \chi'$ plot at various temperature are in Fig. 4.5 [6]. The deviation from semi-circle indicates the distribution of τ. The curves above 14 K are well fitted by Davidson-Cole formula. As the parameter β decreases on cooling, the distribution certainly becomes wider down to 10 K. Below 14 K, although the good fitting is not obtained using a simple empirical model, the curves has a characteristic Davidson-Cole shape (maximum cutoff time and short long-tail in distribution of τ). This is a first observation of the magnetic relaxation characterized by Davidson-Cole formula.

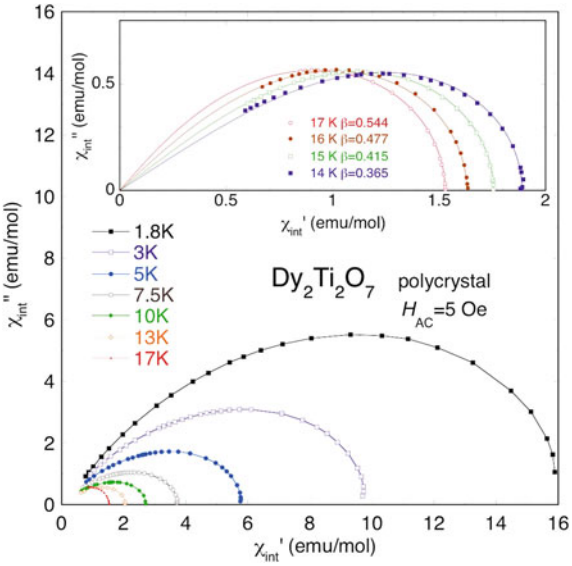

Fig. 4.5 $\chi'' - \chi'$ plot of $Dy_2Ti_2O_7$ at various temperature ($T \geq 1.8$ K). Data is made by the correction of demagnetization effect. Inset shows the fitting by Davidson-Cole formula, reprinted from [6] with permission from the Institute of Physics

Next, the temperature dependence of relaxation time $\tau(T)$ is shown in Fig. 4.6. It should be noted that the *typical* relaxation time is estimated using $\tau = 1/(2\pi f_m)$, which is derived in Fig. 4.4, as the relaxation time has a distribution. In addition, the typical relaxation time is estimated in a similar manner ($\tau = 1/(2\pi f_m)$) using the maximum position (T_m^H) in $d(T\chi')/dT$ in order to get the relaxation time in the higher temperature range (above 14 K). We can confirm that the similar value can be estimated. Above 15 K, $\tau(T)$ obeys the Arrhenius law $\tau(T) = \tau_0 \exp(E_B/T)$ with E_B = 220 K; τ_0 is estimated to be 5×10^{-11} s. On cooling, τ becomes long and reaches to 0.1 ms at 13 K. Below 13 K, $\tau(T)$ is flattened in the temperature range of 3–10 K. Below 3 K, $\tau(T)$ becomes faster again. As is discussed in the next section, the dynamics below 3 K is a consequence of the formation of spin ice state.

The spin dynamics in $Dy_2Ti_2O_7$ above 2 K is microscopically investigated by muon spin relaxation (μSR) [5]; μSR measurement probes the dynamics of local fields in the sample [8]. As the spin dynamics of $Dy_2Ti_2O_7$ becomes slow on cooling, in μSR measurement, it is observed that the depolarization of the muon beam becomes faster with decreasing temperature. The data above 70 K are well fitted to a power exponential function $P_z(t) = a_0 \exp(-\lambda t)^\beta + b_k$ where a_0 is the total relaxing asymmetry, λ is muon depolarization rate and b_k is a background term. The exponent β change from 1 at 300 K to 0.60 at 70 K. The temperature dependence of λ shows thermal activated type with the activation energy of 210 K. This value is consistent with that derived by AC magnetic susceptibility. Below 60 K, the depolarization is well fitted by the phenomenological function $P_z(t) = (a_0/3)[(1 - C)\exp(-\lambda_{dyn} t) + C] + b_k$ where C accounts for non-relaxing fraction on cooling and $\lambda_{dyn} = 2\nu/3$ is the dynamical muon spin depolarization rate for the damping of the 1/3-tail. The $\tau(T)$ for $Dy_2Ti_2O_7$ probed by μSR measurements

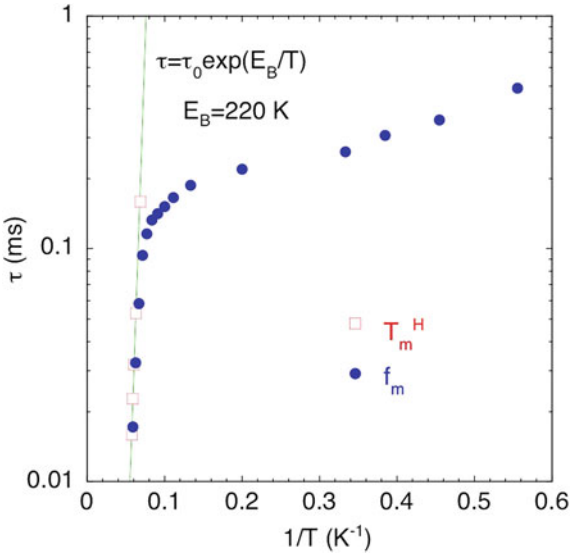

Fig. 4.6 Temperature dependence of relaxation time $\tau(T)$ of $Dy_2Ti_2O_7$ ($T \geq 1.8$ K), reprinted from [6] with permission from the Institute of Physics

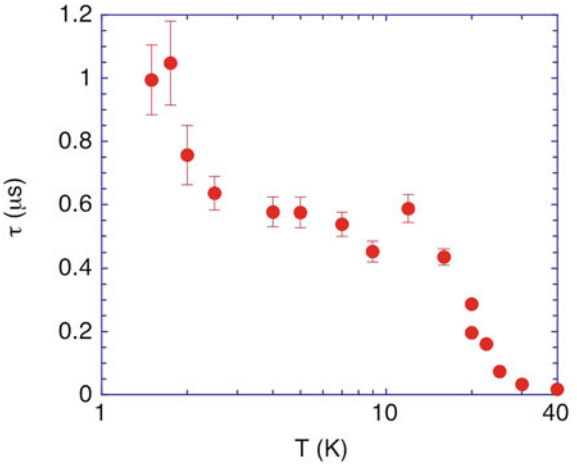

Fig. 4.7 Thermal evolution of the derived relaxation time for $Dy_2Ti_2O_7$ probed by μSR measurements, reproduced from [8] with permission from © IOP Publishing—All rights reserved

is shown in Fig. 4.7. This relaxation time is obtained by $\tau = 1/\nu$. The flattening of $\tau(T)$ in the range of 3–10 K is also observed. The upturn of $\tau(T)$ below 3 K is related to the formation of spin ice states. However, we can notice that there are a large difference ($\sim 10^3$) of τ between the AC magnetic susceptibility ($\sim$ms) and μSR measurements ($\sim\mu$s). The time window in these measurements is different. Although the same temperature dependence of $\tau(T)$ is observed, it is suggested that a different relaxation process is sensed in these experiments.

The characteristic $\tau(T)$ observed in $Dy_2Ti_2O_7$ is also observed even in another typical spin ice compound $Ho_2Ti_2O_7$; these are common feature in spin ice. The $\tau(T)$

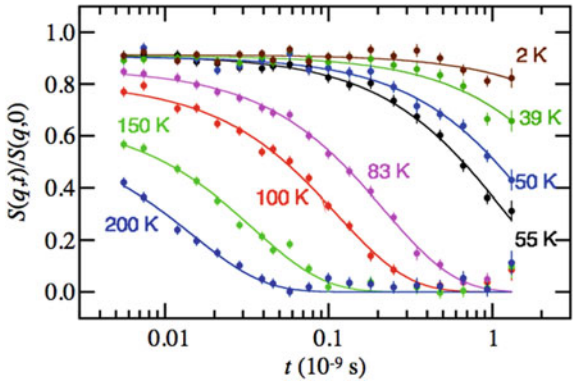

Fig. 4.8 Normalized relaxation function $S(q,t)/S(q,0)$ measured for a polycrystalline sample of $Ho_2Ti_2O_7$ by using NSE technique, reproduced from [9] with permission from © IOP Publishing—All rights reserved

of $Ho_2Ti_2O_7$ up to high temperature range is investigated by using neutron spin echo (NSE) technique [9]. NSE technique directly establishes the dynamic correlation function $S(\mathbf{Q}, t)$. The quantity of $S(\mathbf{Q}, t)/S(\mathbf{Q}, 0)$ represents the relaxation of Fourier components of the magnetization. The dynamic range of NSE is $\tau \sim 10^{-14} - 10^{-7}$s. Figure 4.8 shows the $S(q,t)/S(q,0)$ for a polycrystalline sample of $Ho_2Ti_2O_7$; in all over the temperature range, the observed relaxation can be well fitted by a simple exponential function $F(\mathbf{Q}, t) = (1 - B)\exp[-\Gamma t]$. The $\Gamma(T)$ is fitted to an Arrhenius law $\Gamma(T) = 2\Gamma_h \exp[-E_B/T]$ with the activation energy E_B = 29312 K and attempt frequency $\Gamma_h = 1.1 \pm 0.2 \times 10^{11}$ Hz. The observed activation energy (290 K) of $Ho_2Ti_2O_7$ is in agreement with that (210–220 K) of $Dy_2Ti_2O_7$. These energy value are close to the splitting energy of first excited crystalline electric field (CEF) levels from the ground state doublet. Furthermore, the observed $S(\mathbf{Q}, t)$ are Q-independent. Therefore, the dynamics of spin ice compounds at high temperature, which obey Arrhenius law with E_B = 200–300 K, are caused by a strong Ising spin character due to the single-ion CEF states.

Next, let's discuss the time scale τ_0 in the flattening of $\tau(T)$; this is another feature in dynamics of spin ice. The value of τ_0 in $Dy_2Ti_2O_7$ is much larger than in $Ho_2Ti_2O_7$; τ_0 in $Ho_2Ti_2O_7$ is too small to observe using χ_{AC} measurements. The τ_0 in $Ho_2Ti_2O_7$ is derived by very high resolution inelastic neutron scattering measurements [10]. Figure 4.9 shows the $\tau(T)$ of $Ho_2Ti_2O_7$. In the backscattering energy scan measurements, a temperature dependence of energy width is observed at peak of magnetic diffuse scattering. From the value of full width at half maximum (FWHM) of the scattering, the relaxation time (lifetime) is derived [10]. Above 40 K, the observed $\tau(T)$ is fitted by Arrhenius law activation energy E_B = 123 K; this is in qualitative agreement with the result of NSE. The flattening of $\tau(T)$ is clearly observed in the temperature range of 3-30 K. We should note the large difference ($\sim 10^4$) of time scale between $Dy_2Ti_2O_7$ ($\sim$0.2 ms) and $Ho_2Ti_2O_7$ ($\sim$10 ns) in the region flattening of $\tau(T)$. It is considered that this difference in time scale may be due to the fact that Dy^{3+} is a Kramers ion while Ho^{3+} is not.

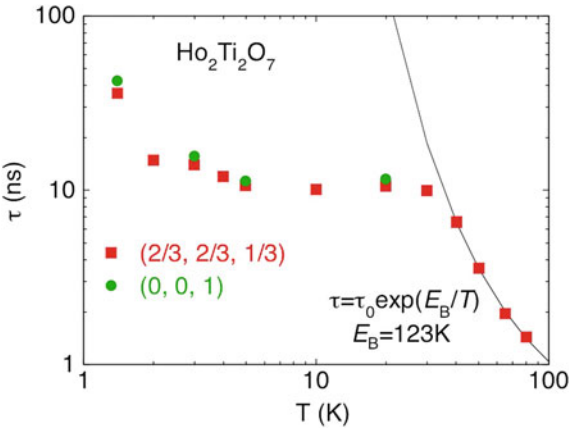

Fig. 4.9 Temperature dependence of the relaxation time of $Ho_2Ti_2O_7$ obtained by backscattering measurements in very high-resolution neutron inelastic scattering experiment, adapted from [10] with permission from the American Physical Society

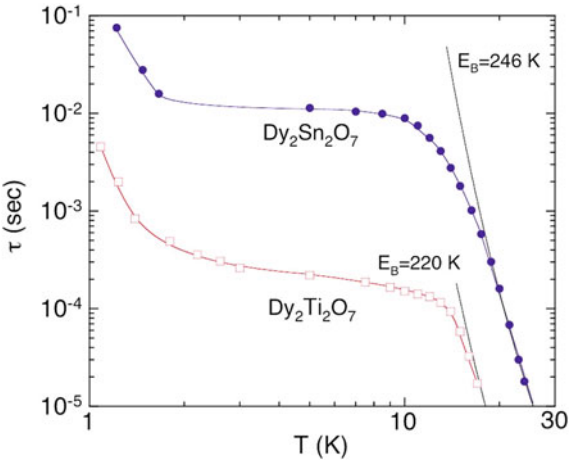

Fig. 4.10 Temperature dependence of τ of $Dy_2Sn_2O_7$, reprinted from [11]

Next, Fig. 4.10 shows the temperature dependence of τ of another Dy spin ice compound $Dy_2Sn_2O_7$ [11]. The $\tau(T)$ data is derived from the maximum frequency f_m in $\chi''(f)$ using $\tau = 1/(2\pi f_m)$; the observed $\chi''(f)$ is close to Davidson-Cole formula. The lattice parameter of $Dy_2Sn_2O_7$ (10.399 Å) is larger than that of $Dy_2Ti_2O_7$ (10.124 Å) [12]. Therefore, the main nearest neighbor dipolar interaction of $Dy_2Sn_2O_7$ becomes 10% smaller. The feature of $\tau(T)$ in $Dy_2Sn_2O_7$ is similar to that in $Dy_2Ti_2O_7$. The $\tau(T)$ above 20 K obeys Arrhenius law with E_B = 246 K. The derived E_B is comparable with $Dy_2Ti_2O_7$. However, the value of τ of $Dy_2Sn_2O_7$ is 10-100 times larger in the region of flattening. It should be noted that the dynamics of $Dy_2Sn_2O_7$ is much slower than those of $Dy_2Ti_2O_7$.

4.2 Spin Dynamics of Typical Spin Ice Compound $Dy_2Ti_2O_7$ at Low Temperature

The pyrochlore oxide $Dy_2Ti_2O_7$ is considered to be a typical example of spin ice compound. As is discussed in the previous section, after the flattening of $\tau(T)$ in the temperature range of 3–10 K, $\tau(T)$ increases again below 2 K. Recent theoretical studies reveal that the excitations from the ground state can be described by the creation of magnetic monopoles [13]. Violating the ice rules by making a spin flip on the ground state configuration leads to a pair of point-like defects. Therefore, at low temperature below 10 K, the dynamics comes from the creation or annihilation of magnetic monopoles, and their diffusion. According to the "magnetic monopole picture", as the monopole density is high in the region of flatten $\tau(T)$, it is interpreted that there are few double defects [14].

Figure 4.11 shows $\tau(T)$ of polycrystalline $Dy_2Ti_2O_7$ down to 0.82 K which is obtained by data of $\chi''(f)$ [14, 15]. The observed $\tau(T)$ in the restricted temperature range between 2.5 and 5 K is well fitted by an Arrhenius law $\tau(T) = \tau_0 \exp(E_p/T) = \tau_0 \exp(2J_{eff}/T)$ where J_{eff}= 1.1 K. Below 2 K, $\tau(T)$ becomes slower than the expected Arrhenius law with E_p = 2.2 K; $\tau(T)$ in the temperature range between 0.82 and 2 K can be fitted by an Arrhenius law with $E_p = 6J_{eff}$. The analysis result of diffusive motion of magnetic monopoles by classical Monte Calro (MC) simulation well reproduces the experimental result at least down to 0.82 K.

On cooling, the spin dynamics below 2 K becomes very slow. The temperature dependence of DC magnetization of single crystal $Dy_2Ti_2O_7$ measured under field-cooled (FC) and zero-field-cooled (ZFC) conditions is shown in Fig. 4.12. DC magnetization curves clearly show a thermal hysteresis below 0.65 K. This means that the $\tau(T)$ reaches the typical time scale of DC magnetization (1-10 s). The similar difference between ZFC and FC DC magnetization is observed in the other spin ice compounds [15, 16]. From the viewpoints of AC magnetic susceptibility, $\chi'(T)$ rapidly goes to zero, which is similar to the ZFC curve of DC magnetization,

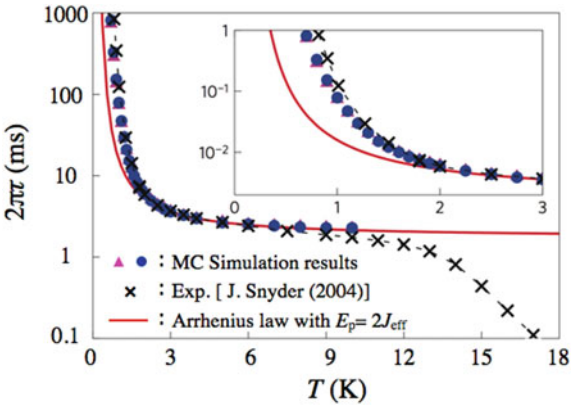

Fig. 4.11 The experimental and MC simulation results of relaxation time for $Dy_2Ti_2O_7$ down to 0.82 K [14, 15]. Red curve shows the Arrhenius law with $E_p = 2J_{eff}$. Reprinted figure from [14] with permission from Nature Physics

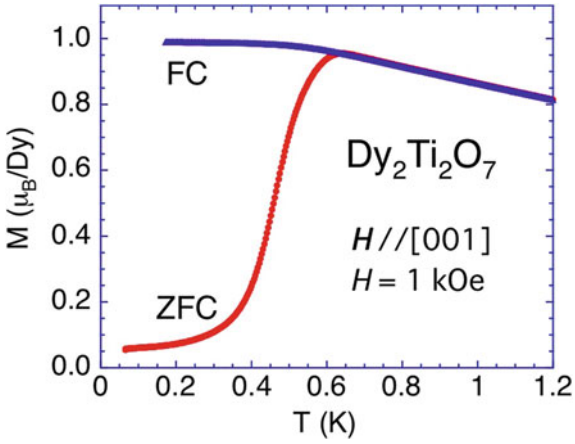

Fig. 4.12 The temperature dependence of DC magnetization of single crystal $Dy_2Ti_2O_7$ measured under FC and ZFC conditions; the measurement is performed by a capacitive Faraday force magnetometer [17, 18]

and then $\chi''(T)$ shows a broad peak as $\tau(T)$ is much larger than the time scale in the AC field frequency $1/(2\pi f)$; the spin can not response during the time scale [6, 7, 11, 16].

The $\chi''(f)$ of single crystal $Dy_2Ti_2O_7$ in the temperature range from 0.5 to 1.9 K is shown in Fig. 4.13 [19]. The AC field is applied along [111] direction. The data are in qualitative agreement with a previous study done on a polycrystalline samples between 0.8 and 1.8 K [15]. The shape of $\chi''(f)$ curve is very close to a Lorentzian symmetric function. The maximum frequency in $\chi''(f)$ shifts to lower frequency on cooling. However, $\chi''(f)$ show a small but clearly discernible shoulder on their high frequency sides, indicating the existence of a second relaxation time. As is shown in Fig. 4.13, $\tau(T)$ below 0.50 K goes beyond the time window in the present AC magnetic susceptibility measurement. In order to evaluate $\tau(T)$ below 0.50 K, the relaxation of the magnetization $M(T)$ is measured by using the protocol as follows; (i) a weak DC magnetic field of 10 or 5 Oe is applied. (ii) the sample is warmed up to 0.90 K for a wait period of 30 s. (iii) the heater power was cut, and the sample was subsequently rapidly cooled down, dropping below 0.4 K in less than 10 s and settling down to below 0.1 K after 600 s. (iv) the heater power was restored and regulated and stabilized at the target temperature for an additional 600 s. (v) Finally the applied field is cut (in a time $t \leq 0.1$ s). Figure 4.14 shows the relaxation of the magnetization $M(t)$. The relaxation time becomes very slow on cooling. At 0.08 K, $M(t)$ decreases by only 0.35% after 10^5 s ~16.7 h! The very slow relaxation still occurs at 0.08 K. The LRO, which is expected in the numerical calculation [20, 21], is prevented by the very slow dynamics in the range of time scale in our daily life.

To account for the whole set of measurements ($\chi''(f)$ between 0.50 and 1.9 K and $M(t)$ below 0.60 K), the data is well fitted by 2-τ Debye model as follows:

$$\chi''(f) = \chi_L \frac{2\pi f \tau_L}{1 + (2\pi f \tau_L)^2} + \chi_S \frac{2\pi f \tau_S}{1 + (2\pi f \tau_S)^2}, \tag{4.13}$$

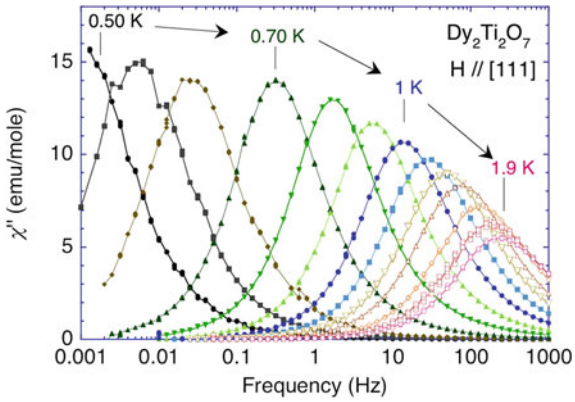

Fig. 4.13 $\chi''(f)$ of single crystal $Dy_2Ti_2O_7$ at 0.50, 0.55, 0.60, 0.70, 0.80, 0.90, 1.0, 1.1, 1.2, 1.3, 1.5, 1.7 and 1.9 K, reprinted from [19] with permission from the Journal of the Physical Society of Japan

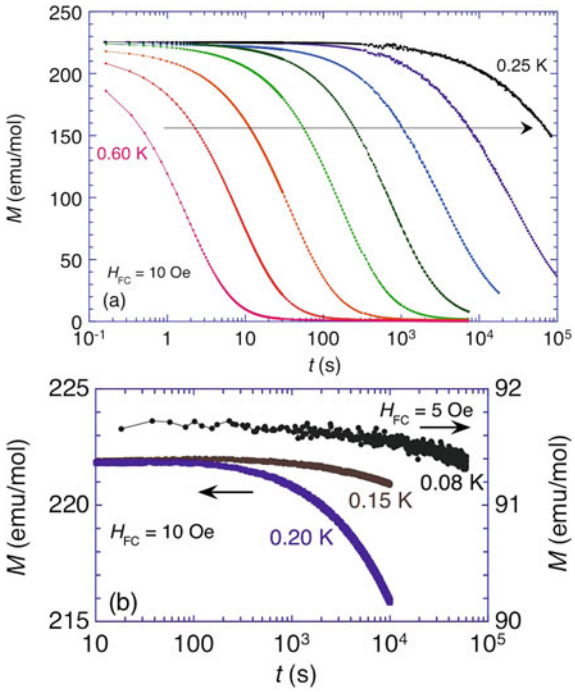

Fig. 4.14 Relaxation of magnetization of single crystal $Dy_2Ti_2O_7$ due to field quench after FC at **a** 0.60, 0.55, 0.50, 0.45, 0.40, 0.35, 0.30, 0.25 K and **b** 0.20, 0.15, and 0.08 K, reprinted from [19] with permission from the Journal of the Physical Society of Japan

$$M(t) = M_{\mathrm{L}}\exp\left(-\frac{t}{\tau_{\mathrm{L}}}\right) + M_{\mathrm{S}}\exp\left(-\frac{t}{\tau_{\mathrm{S}}}\right) + M_0, \tag{4.14}$$

where χ_{L}, χ_{S}, M_{S}, M_{L}, and M_0 are fitting parameters, and τ_{L} and τ_{S} are the short and long relaxation times [19]. The fits are rather good over a large frequency or time range although they are not perfect and small differences can be seen at higher frequency and at very short or very long times. However, the fitting results show

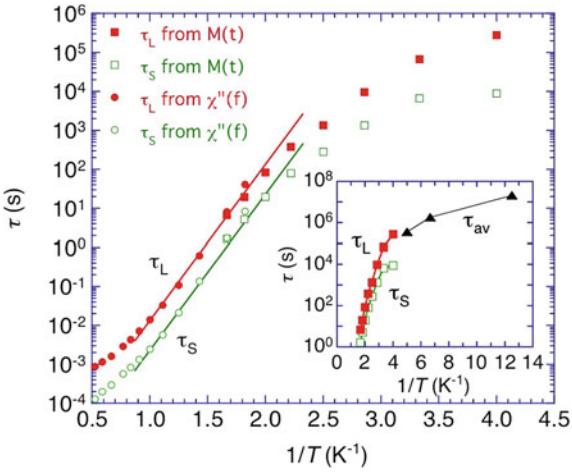

Fig. 4.15 Temperature dependence of relaxation time (τ_L, τ_S and τ_{AV}) of single crystal $Dy_2Ti_2O_7$. Solid line show the Arrhenius law with $E_p = 9.2$ K, reprinted from [19] with permission from the Journal of the Physical Society of Japan

that the bulk of the relaxation can be reasonably described by two relaxation times. Below 0.25 K, the average relaxation time τ_{AV} is estimated using a simple exponential relaxation because the relaxation of the magnetization is so slow that the data cannot be fitted within the 2-τ model.

Figure 4.15 shows the temperature dependence of relaxation time (τ_L, τ_S and τ_{AV}) of single crystal $Dy_2Ti_2O_7$. Assuming the Arrhenius law in the temperature range 0.5–1 K, the energy barrier E_p of 9.2 K (8–9 J_{eff}) is obtained. This Arrhenius fit describes only a narrow temperature range. A description taking into account the long range Coulomb interaction between the monopoles is needed to explain the dynamics below 1 K. Below 0.5 K, $\tau(T)$ show a clear deviation from the thermal activated dynamics toward temperature independent relaxation. Assuming the Arrhenius law for τ_{AV} below 0.2 K, a value of $E_P \sim 0.5$ K is derived. This value is smaller than a single defect value $2J_{eff}(\sim 2.2K)$ expected in the low temperature limit. Therefore, it is very hard to understand the dynamics at least below 0.2 K by the Arrhenius law. As the possible origin quantum dynamics (QD) effect between two spins is considered. This effect results from the anisotropic super-exchange coupling between neighboring Kramers doublets [22]. The QD come from the spin-flip exchange interaction may suppress the increasing of $\tau(T)$ in the low temperature limit. Although this effect is expected to be smaller in the $Dy_2Ti_2O_7$ because of the large spin and the strong anisotropy, a quantum mechanical treatment of the spins will be necessary to clarifying the spin dynamics of spin ice at very low temperature.

The similar field-quench measurements by applying a small magnetic field of 5 mOe are performed up to 1.1 K; $M(t)$ is obtained from 0.475 K up to 1.1 K [23]. Analyzing the data using Monte Carlo simulations of magnetic monopole gas governed by Metoropolis dynamics, the important points on dynamics are revealed. The observed decay is not simple exponential function ($\exp(-t/\tau)$), but rather a stretched exponential function ($\exp[-(t/\tau)^{\beta}]$) with $\beta \sim 0.7$–0.8; the data is qualitatively consistent with the results shown in Fig. 4.14a. This stretched exponential

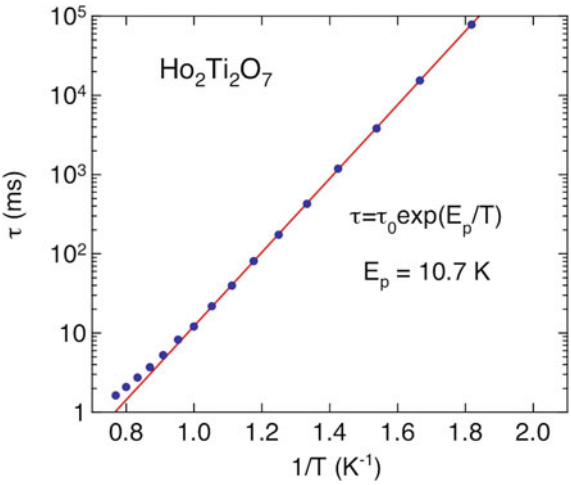

Fig. 4.16 Temperature dependence of $\tau(T)$ of single crystal $Ho_2Ti_2O_7$ which is derived by AC magnetic susceptibility, reprinted from [25] with permission from the American Physical Society. $\tau(T)$ is obtained by using $\tau = 1/(2\pi f_m)$. Solid line shows the Arrhenius law with E_p = 10.7 K

decay is reproduced by the calculation under open boundary condition instead of periodic boundary condition. This is caused by a surface effect. Next, the observed stretched exponential decay is followed by a very slow long-tail relaxation. In the pyrochlore oxides, site exchange often occurs [24]. From the results of calculation on the magnetic monopoles in the vicinity of the extra spins, this long-tail behavior is caused by a very small percentage (0.30%) of extra (stuffed) spins. Even in the clean sample used in these measurements, a very low level of stuffed spins are expected. This means the magnetic monopoles in the vicinity of the stuffed spins has a long life time; the monopole density becomes higher.

Finally, let's compare the low temperature dynamics of another typical spin ice $Ho_2Ti_2O_7$ with that of $Dy_2Ti_2O_7$. Similar shape of χ_{AC} data in spin ice $Ho_2Ti_2O_7$ is obtained in the temperature range of 0.5–1.3 K [25]. Although the similar asymmetric feature of $\chi''(f)$ is observed, as is shown in Fig. 4.13, the careful analysis reveals that the spectra can not be perfectly fitted using simple empirical forms (Cole-Cole, Davidson-Cole, etc.) described in the previous section. Figure 4.16 indicates the temperature dependence of $\tau(T)$ of single crystal $Ho_2Ti_2O_7$ which is derived by assuming $\tau = 1/(2\pi f_m)$ where f_m is maximum frequency in $\chi''(f)$. The obtained τ ($\sim$1.2 ms) at 1.2 K is similar to that of $Dy_2Ti_2O_7$. On cooling, the obtained τ reaches to the time scale of DC magnetization measurement ($\sim$1 s) at $\sim$0.7 K; this is slightly higher than 0.65 K for $Dy_2Ti_2O_7$. Therefore, the spin dynamics of $Ho_2Ti_2O_7$ becomes slower below 1 K. Assuming the Arrhenius law in the temperature range 0.5–1 K, the energy barrier E_p of 10.7 K $\sim 6J_{eff}$ (J_{eff} = 1.83 K for $Ho_2Ti_2O_7$) is obtained; the value of E_p is the similar value to 9.2 K for $Dy_2Ti_2O_7$. However, in comparison with the E_p scaled by J_{eff}, the value of $6J_{eff}$ for $Ho_2Ti_2O_7$ is smaller than $8–9J_{eff}$ for $Dy_2Ti_2O_7$. It is speculated that this difference of E_p is caused by the interaction between magnetic monopoles. This is one of the future problems in spin dynamics of spin ice.

Finally, let's remark the important points of dynamics of spin ice. First, the dynamics of spin ice has a characteristic slow dynamics which is quite different from disordered systems such as spin glass. Under thermal equilibrium state, the density of magnetic monopoles becomes very low at low temperature. Next, the magnetization measurements can not detect the dynamics between the states with $M = 0$. In order to detect such dynamics, the microscopic probe such as nuclear quadrupole resonance and μSR is useful to detect a fluctuation of local field. The future progress is expected.

4.3 Topics on Slow Dynamics of $Dy_2Ti_2O_7$ at Very Low Temperature

Let's present recent two topics on slow spin dynamics of typical spin ice compound $Dy_2Ti_2O_7$. One is the controlled creation of non-equilibrium population of magnetic monopoles using the "magnetothermal avalanche quench" technique [26]. Another is the specific heat behavior in thermally equilibrium state carefully measured during a very long time thermal relaxation [28]. These topics are related to very slow dynamics of spin ice below 0.5 K as is described in the previous section.

The relaxation time to thermal equilibrium state becomes very long at low temperature; the relaxation time reaches $10^7 s \sim 10$ days at 100 mK. Furthermore, the density of magnetic monopoles becomes very small at low temperature. However, in order to study the dynamics of magnetic monopoles at low temperature, it is necessary and desirable to create more magnetic monopoles. Recently, a method to create more magnetic monopoles in the non-equilibrium state has been developed using the "magnetothermal avalanche quench (AQ)" technique. Furthermore, the AQ technique can also control the monopole. Figure 4.17 shows the procedure to produce magnetic monopoles in the non-equilibrium state using AQ technique for $Dy_2Ti_2O_7$. The sample is connected to a cold thermal bath (mixing chamber in a ^{3}He-^{4}He dilution refrigerator) by the Cu sample holder; the temperature of mixing chamber $T_{\rm mix}$ is normally 75 mK. Figure 4.17a shows the time dependence of $T_{\rm mix}$ compared with that of the applied field $H(t)$ and the measured sample magnetization $M(t)$. Applying a magnetic field, the magnetic work on the sample is abruptly converted into internal heat, which causes a sudden increase in temperature inside the sample ($T_{\rm int}$); $T_{\rm int}$ is raised to approximately 900 mK in this . While $T_{\rm mix}$ remains below 200 mK. Figure 4.17b–g shows the behavior of the sample in this procedure (Fig. 4.17a). Before the procedure, the sample at 75 mK is first magnetized to $-2.5\mu_{\rm B}$/Dy in a magnetic field of -0.2 T (Fig. 4.17b). At time $t = 0$, the magnetic field is rapidly reversed from -0.2 to $+0.2$ T at a rate of 0.55 T/s. The magnetization follows with some delay. The magnetic Zeeman energy released from the spins rapidly heats the interior of the sample to $T_{\rm int} \sim 900$ mK, and the heat then leaks out of the sample to the mixing chamber as seen as a spike in $T_{\rm mix}$ (Fig. 4.17c). As $T_{\rm mix}$ remains below 200 mK, the sample is cooled very quickly at the cooling rate $\sim$0.07 K/s at 500 mK

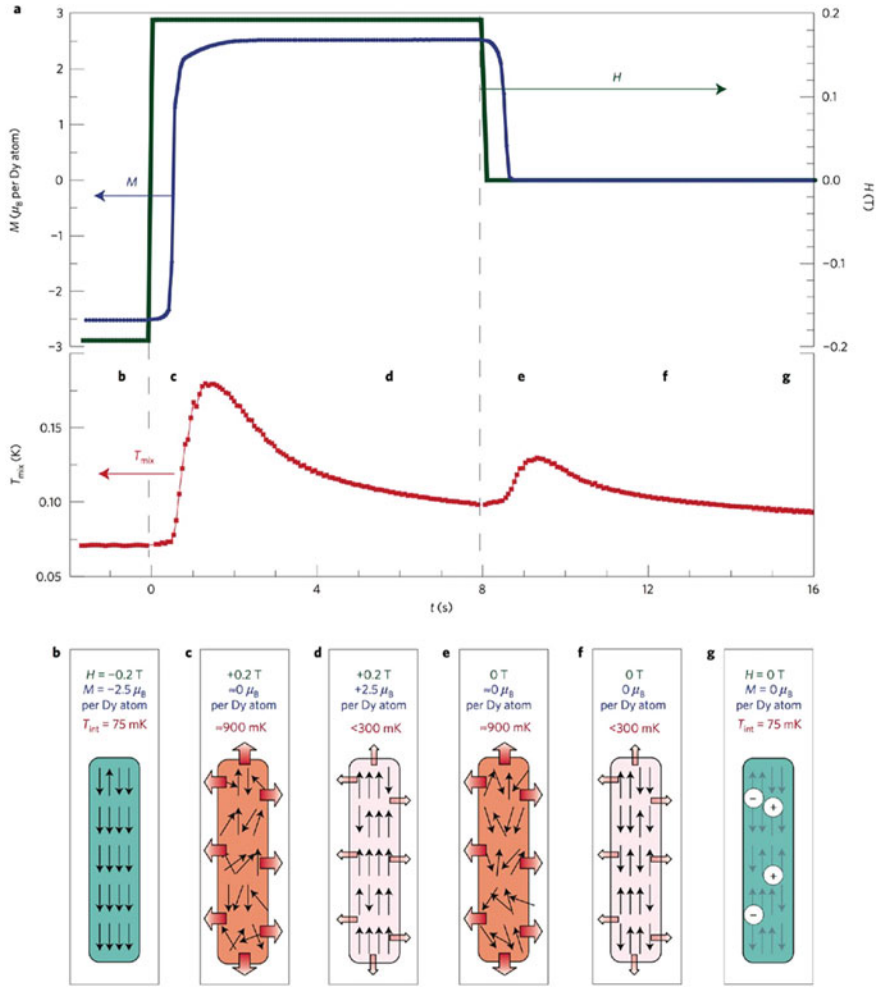

Fig. 4.17 The procedure to produce magnetic monopoles in the non-equilibrium state using AQ technique for $Dy_2Ti_2O_7$, reprinted from [26] with permission from Nature Physics. Through the application of magnetic fields H, the internal sample temperature $T_{\rm int}$ is raised to approximately 900 mK and then rapidly quenched, while the temperature of the cold cryostat mixing chamber $T_{\rm mix}$, which is thermally linked to the Cu sample holder, remains below 200 mK. **a** The time dependence of $T_{\rm mix}$ compared with that of the applied field $H(t)$ and the measured sample magnetization $M(t)$. **b**–**g** The Illustrations showing the behavior of the sample in this procedure. The detail is described in the text

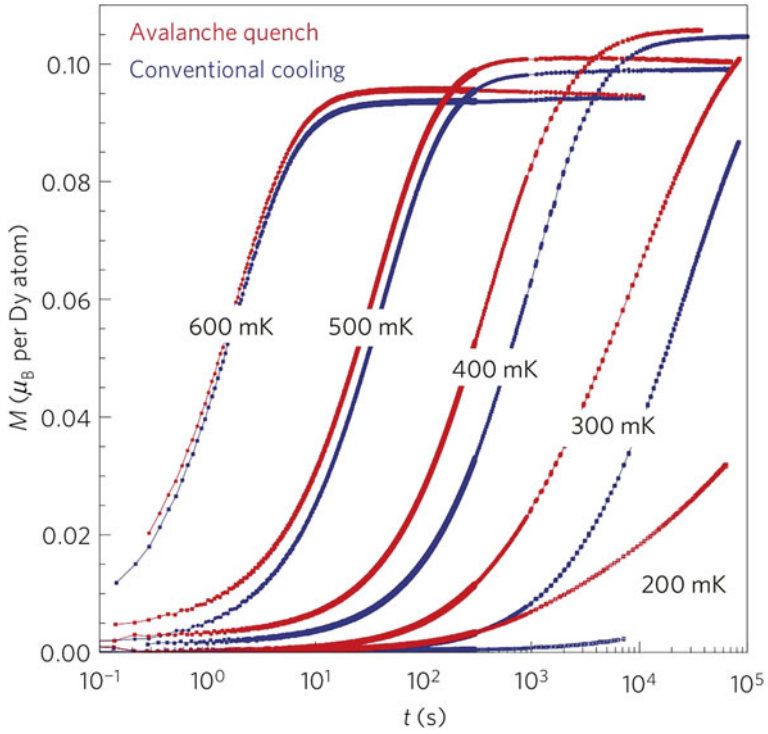

Fig. 4.18 Relaxation of magnetization $M(t)$ of $Dy_2Ti_2O_7$ at fixed temperatures from 600 to 200 mK when a magnetic field of 5 mT is applied at $t = 0$ after conventional zero field cooling (blue) or AQ technique (red), reprinted from [26] with permission from Nature Physics

(Fig. 4.17d). At $t = 8$ s, the magnetic field is then removed, and the sample avalanches again with less energy. T_{int} approaches 900 mK again (Fig. 4.17e). The heat is again swiftly evacuated to the mixing chamber and $M(t)$ approaches zero (Fig. 4.17f). The result of the fast magnetothermal quench leads to non-equilibrium states with a very large density of monopoles (defects) (Fig. 4.17g).

Figure 4.18 shows the relaxation of magnetization $M(t)$ when a magnetic field of 5 mT is applied at $t = 0$ after conventional zero field cooling (blue) or AQ technique (red) [26]. Clearly the relaxation curves of AQ technique response faster than the conventional ZFC. The difference between the two protocols becomes more obvious below 300 mK. According to the model discussed in [27], $\mathbf{J} = \partial \mathbf{M}(t)/\partial t$ means the magnetic monopole current density. Therefore, AQ technique allows to flow a larger magnetic monopole current in non-equilibrium state. It is expected that this AQ technique develops the study of magnetic monopole current in spin ice.

Next another topics is the specific heat behavior in thermally equilibrium state carefully measured during a very long time thermal relaxation. As the relaxation time becomes very long at low temperature, it takes very long time to get thermal

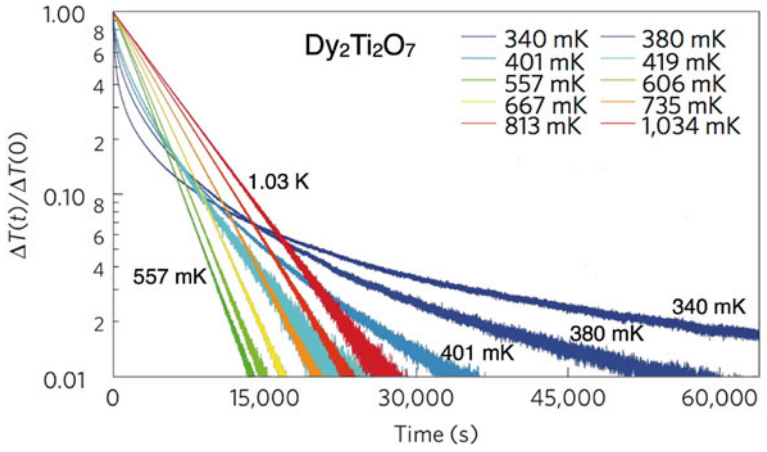

Fig. 4.19 Normalized thermal relaxation $\Delta T(t)/\Delta T(t=0)$ at various temperature for single crystal $Dy_2Ti_2O_7$, reprinted from [28] with permission from Nature Physics

equilibrium state; the relaxation time of $Dy_2Ti_2O_7$ is beyond 100 s below ∼500 mK. The time scale of specific heat measurement is of the order of 10-100 s in a relaxation method of recent commercial system and a standard quasi-adiabatic heat pulse method; the time scale in first report on residual entropy of $Dy_2Ti_2O_7$ is 15 s [29]. Therefore, in order to get the specific heat of thermal equilibrium state below 0.5 K, it is necessary to carefully measure the relaxation for a longer time. Figure 4.19 shows the thermal relaxation at various temperature where the time dependence of temperature $\Delta T(t)$ is normalized by the value at $t = 0$ s [28]. In general, the relaxation becomes faster as the specific heat of sample is smaller. Viewing the $\Delta T(t)$ curves in the initial 10^3 s, the relaxation becomes faster on cooling; the integral of $\Delta T(t)$ which is proportional to specific heat $C(T)$ decreases with decreasing temperature. However, extending the time scale beyond 10^4 s, the relaxation becomes slower on cooling below 419 mK. The obtained relaxation time is in qualitative agreement with that in the magnetization measurements;as shown in Fig. 4.15, the deviation from the Arrhenius law for $\tau(T)$ is also observed below 0.5 K. This means that $C(T)$ increases with decreasing temperature below ∼0.5 K. Therefore, this results reveals that the total specific heat below ∼0.5 K is underestimated in previous measurements [29]. The specific heat for single crystal $Dy_2Ti_2O_7$ obtained in thermally equilibrium state is shown in Fig. 4.20 [28]. The result above 0.6 K is consistent with the previous results. Below 0.6 K, the difference appears and below 0.5 K, C/T turn to increase on cooling. The residual entropy reported in previous measurements is partially released. Furthermore, in the numerical calculation on dipolar spin ice model, a first order transition to a LRO with $\mathbf{Q}$=(0,0,2π/a) is found at $T_c \sim 0.18$ K. The result suggests the existence of LRO at lower temperature. The essential question "What is the true ground state of spin ice compound $Dy_2Ti_2O_7$?" is still open [21]. Further study for this essential problem is desirable.

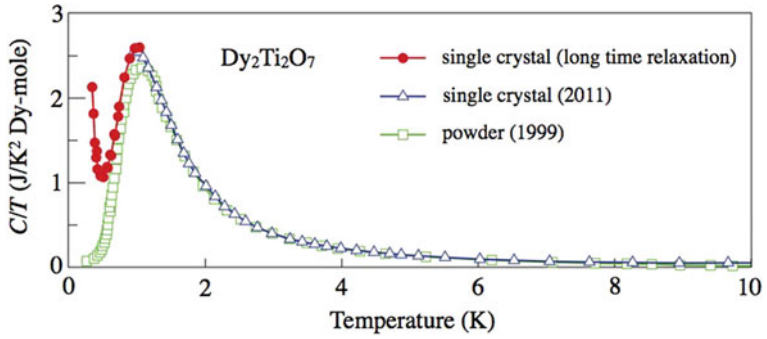

Fig. 4.20 The specific heat for single crystal $Dy_2Ti_2O_7$ obtained in thermally equilibrium state down to 0.34 K, reprinted from [28] with permission from Nature Physics

References

1. S.T. Bramwell, M.J.P. Gingras, Science **294**, 1495 (2001). https://doi.org/10.1126/science.1064761
2. P. Debye, *The collected papers of Peter J. W. Debye*, (Interscience Pub., New York, 1954)
3. K.S. Cole, R.H. Cole, J. Chem. Phys. **9**, 341 (1941). https://doi.org/10.1063/1.1750906
4. C. Dekker, A.F. Arts, H.W. de Wijn, A.J. van Duyneveldt, J. Mydosh, Phys. Rev. B **40**, 11243 (1989). https://doi.org/10.1103/PhysRevB.40.11243
5. D.W. Davidson, R.H. Cole, J. Chem. Phys. **18**, 1417 (1950). https://doi.org/10.1063/1.1747496; J. Chem. Phys. **19**, 1484 (1951). https://doi.org/10.1063/1.1748105
6. K. Matsuhira, Y. Hinatsu, T. Sakakibara, J. Phys. Condens. Matter **13**, L737 (2001). https://doi.org/10.1088/0953-8984/13/31/101
7. J. Snyder, J.S. Slusky, R.J. Cava, P. Schiffer, Nature (London) **413**, 48 (2001). https://doi.org/10.1038/35092516
8. J. Lago, S.J. Blundell, C. Baines, J. Phys.: Condens. Matter **19**, 326210 (2007). https://doi.org/10.1088/0953-8984/19/32/326210
9. G. Ehlers, A.L. Cornelius, M. Orendac, M. Kjnakova, T. Fennell, S.T. Bramwell, J.S. Gardner, J. Phys.: Condens. Matter **15**, L9 (2003). https://doi.org/10.1088/0953-8984/15/2/102
10. J.P. Clancy, J.P.C. Ruff, S.R. Dunsiger, Y. Zhao, H.A. Dabkowska, J.S. Gardner, Y. Qiu, J.R.D. Copley, T. Jenkins, B.D. Gaulin, Phys. Rev. B **79**, 014408 (2009). https://doi.org/10.1103/PhysRevB.79.014408
11. K. Matsuhira, M. Wakeshima, Y. Hinatsu, C. Sekine, C. Paulsen, T. Sakakibara, S. Takagi, J. Phys.: Conf. Ser. **320**, 012050 (2011). https://doi.org/10.1088/1742-6596/320/1/012050
12. M.A. Subramanian, G. Aravamudan, G.V. Subba Rao, Prog. Solid State Chem. **15**, 55 (1983). https://doi.org/10.1016/0079-6786(83)90001-8
13. C. Castelnovo, R. Moessner, S.L. Sondhi, Nature (London) **451**, 42 (2008). https://doi.org/10.1038/nature06433
14. L.D.C. Jaubert, P.C.W. Holdsworth, Nat. Phys. **5**, 258 (2009). https://doi.org/10.1038/NPHYS1227; J. Phys.: Condens. Matter **23**, 164222 (2011). https://doi.org/10.1088/0953-8984/23/16/164222
15. J. Snyder, B.G. Ueland, J.S. Slusky, H. Karunadasa, R.J. Cava, P. Schiffer, Phys. Rev. B **69**, 064414 (2004). https://doi.org/10.1103/PhysRevB.69.064414
16. K. Matsuhira, Y. Hinatsu, K. Tenya, T. Sakakibara, J. Phys.: Condens. Matter **12**, L649 (2000). https://doi.org/10.1088/0953-8984/12/40/103

17. T. Sakakibara, H. Mitamura, T. Tayama, H. Amitsuka, Jpn. J. Appl. Phys. **33**, 5067 (1994). https://doi.org/10.1143/JJAP.33.5067
18. T. Sakakibara, private communications
19. K. Matsuhira, C. Paulsen, E. Lhotel, C. Sekine, Z. Hiroi, S. Takagi, J. Phys. Soc. Jpn. **80**, 123711 (2011). https://doi.org/10.1143/JPSJ.80.123711
20. R.G. Melko, B.C. den Hertog, M.J.P. Gingras, Phys. Rev. Lett. **87**, 067203 (2001). https://doi.org/10.1103/PhysRevLett.87.067203
21. P.A. McClarty, O. Sikora, R. Moessner, K. Penc, F. Pollmann, N. Shannon, Phys. Rev. B **92**, 094418 (2015). https://doi.org/10.1103/PhysRevB.92.094418
22. S. Onoda, Y. Tanaka, Phys. Rev. Lett. **105**, 047201 (2010). https://doi.org/10.1103/PhysRevLett.105.047201; Phys. Rev. B **83**, 094411 (2011). https://doi.org/10.1103/PhysRevB.83.094411
23. H.M. Revell, L.R. Yaraskavitch, J.D. Mason, K.A. Ross, H.M.L. Noad, H.A. Dabkowska, P. Henelius, J.B. Kycia, Nat. Phys. **9**, 34 (2013). https://doi.org/10.1038/nphys2466
24. K.A. Loss, Th Proffen, H.A. Dabkowska, J.A. Quilliam, L.R. Yaraskavitch, J.B. Kycia, B.D. Gaulin, Phys. Rev. B **86**, 174424 (2012). https://doi.org/10.1103/PhysRevB.86.174424
25. J.A. Quilliam, L.R. Yaraskavitch, H.A. Dabkowska, B.D. Gaulin, J.B. Kycia, Phys. Rev. B **83**, 094424 (2011). https://doi.org/10.1103/PhysRevB.83.094424
26. C. Paulsen, M.J. Jackson, E. Lhotel, B. Canals, D. Prabhakaran, K. Matsuhira, S.R. Giblin, S.T. Bramwell, Nat. Phys. **10**, 135 (2014). https://doi.org/10.1038/nphys2847
27. I.A. Ryzhkin, J. Exp. Theor. Phys. **101**, 481 (2005). https://doi.org/10.1134/1.2103216
28. D. Pomaranski, L.R. Yaraskavitch, S. Meng, K.A. Ross, H.M.L. Noad, H.A. Dabkowska, B.D. Gaulin, J.B. Kycia, Nat. Phys. **9**, 353 (2013). https://doi.org/10.1038/NPHYS2591
29. A.P. Ramirez, A. Hayashi, R.J. Cava, R. Siddharthan, B.S. Shastry, Nature **399**, 333 (1999). https://doi.org/10.1038/20619

Chapter 5
Magnetic Field as an External Probe of Spin Ice Anisotropy

Toshiro Sakakibara and Zenji Hiroi

Abstract A variety of interesting aspects of the spin ice physics are revealed in the characteristic responses to magnetic fields of varied magnitudes and directions. The residual entropy of the spin ice state at $H = 0$ is removed when magnetic field is applied along the [100] or [110] direction, while, upon increasing H along [111], it is transformed first into the kagomé ice state with a reduced degeneracy and then to a nondegenerate state via a first-order, liquid-gas type transition by breaking the ice rule. Effects of inclining magnetic field away from [111] and [112] are investigated by magnetization measurements and compared with a theoretical prediction. A Kasteleyn transition predicted for the former case is not observed in actual compounds probably due to the slow spin dynamics, while a ferromagnetic transition of sublattice spins are found for magnetic fields between [111] and [112].

5.1 A System Composed of Isolated Tetrahedra

To discuss the magnetic field effect on a spin ice, it would be instructive to start with a system composed of isolated tetrahedra. Whereas this simple system remains paramagnetic down to $T = 0$, it helps understand the basic features of the magnetic anisotropy that the spin-ice system would exhibit.

A classical Ising Hamiltonian of a single tetrahedron can be written as

$$\mathscr{H} = J \sum_{\langle i,j \rangle} \sigma_i^{z_i} \sigma_j^{z_j} - \mathbf{H} \sum_{i=1}^{4} \boldsymbol{\sigma}_i, \tag{5.1}$$

T. Sakakibara (✉) · Z. Hiroi
Institute for Solid State Physics, University of Tokyo, Chiba, Japan
e-mail: sakaki@issp.u-tokyo.ac.jp

M. Udagawa and L. Jaubert (eds.), *Spin Ice*, Springer Series in Solid-State Sciences 197,
https://doi.org/10.1007/978-3-030-70860-3_5

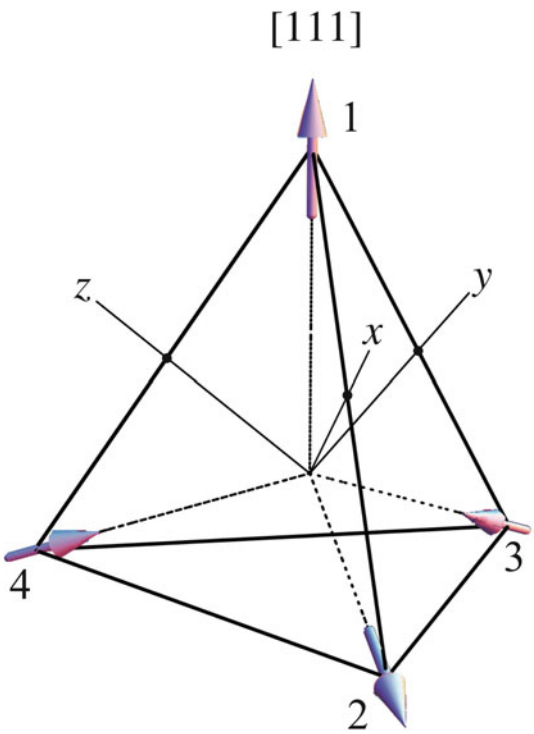

Fig. 5.1 One of the 2-in 2-out spin configurations, the ψ_x state, in which the total moment is parallel to the x direction; x, y and z axes are defined parallel to [100], [010] and [001], respectively. The ψ_y (ψ_z) state is obtained by flipping spin 3 (4) outward and the other two spins in the basal triangle inward with keeping spin 1 outward

where the first summation is over the 6 pairs, H is a magnetic field, and $\boldsymbol{\sigma}_i$ ($= \boldsymbol{z}_i \sigma_i^{z_i}$, $\sigma_i^{z_i} = \pm 1$) denotes the spin on the ith site having its own Ising axis $\boldsymbol{z}_i$ along the local $\langle 111 \rangle$ direction. The $2^4 = 16$ spin configurations split into three levels at $H = 0$: a sixfold state $\sum_i \sigma_i^{z_i} = 0$ with two spins pointing inward and two spins pointing outward (2-in 2-out), an eightfold state $\sum_i \sigma_i^{z_i} = \pm 2$ with three (one) spins in and one (three) spin(s) out (3-in 1-out/1-in 3-out), and a doubly degenerate state $\sum_i \sigma_i^{z_i} = \pm 4$ with all spins in or all spins out (all-in all-out). When $J > 0$, the 2-in 2-out (all-in all-out) state has the lowest (highest) energy. Each of these 16 configurations can be labeled by the direction of the total moment

$$\boldsymbol{m} = \sum_{i=1}^{4} \boldsymbol{\sigma}_i . \tag{5.2}$$

One can easily find that $\boldsymbol{m}$ of the 2-in 2-out state is parallel to one of the $\langle 100 \rangle$ directions ($m = 4/\sqrt{3}$). We can thus represent the sixfold 2-in 2-out state as $\{\psi_x, \psi_y, \psi_z, \psi_{-x}, \psi_{-y}, \psi_{-z}\}$, whose definitions are self evident. Figure 5.1 shows the ψ_x state as an example. Likewise, the eightfold 3-in 1-out/1-in 3-out state has its $\boldsymbol{m}$ parallel to one of the $\langle 111 \rangle$ directions ($m = 2$), and can be represented as

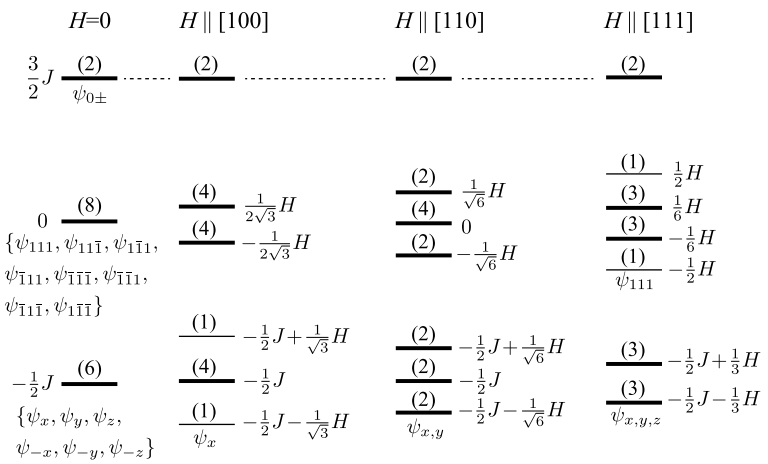

Fig. 5.2 Zeeman splitting of the energy levels described by Hamiltonian (5.1) for the three principal directions. The energy per spin of each level represented by a horizontal stroke is shown on the left or right, and the degeneracy is given in the parenthesis above. Configurations ψ_α of some relevant states are also given. Note that ψ_x and $\psi_{x,y}$ are always the ground states for $H \parallel [100]$ and [110], respectively, while ψ_{111} takes the place of $\psi_{x,y,z}$ at large fields for $H \parallel [111]$

$\{\psi_{111}, \psi_{\bar{1}\bar{1}1}, \psi_{1\bar{1}\bar{1}}, \dots\}$. The twofold all-in all-out state has $\boldsymbol{m} = 0$ and we write this state as $\psi_{0\pm}$.

5.1.1 Zeeman Effect and Magnetization

When a magnetic field is switched on, each of the 2-in 2-out states exhibits a Zeeman shift depending on the field direction. When H is applied along [100], ψ_x becomes the lowest energy state, leaving no degeneracy. For $H \parallel [110]$, the ground state is doubly degenerate $\{\psi_x, \psi_y\}$. When a not too strong H is applied along [111], a triply degenerate state $\{\psi_x, \psi_y, \psi_z\}$ remains in the ground state. The full level schemes for the Zeeman splitting of the 16 states are shown in Fig. 5.2 for the three principal field directions.

Field and temperature dependences of the magnetization M can be given by

$$M = T \frac{\partial}{\partial H} \ln \left(\sum_\alpha e^{-E_\alpha / T} \right), \tag{5.3}$$

where the summation is over all the 16 configurations, and E_α denotes their energy. Figure 5.3a shows the calculated results of the magnetic moment per spin for the three directions at $T/J = 1.6$. Substantial anisotropy develops in high fields, and the moment saturates to the values $1/\sqrt{3}$, $1/2$ and $1/\sqrt{6}$ for the [100], [111] and [110]

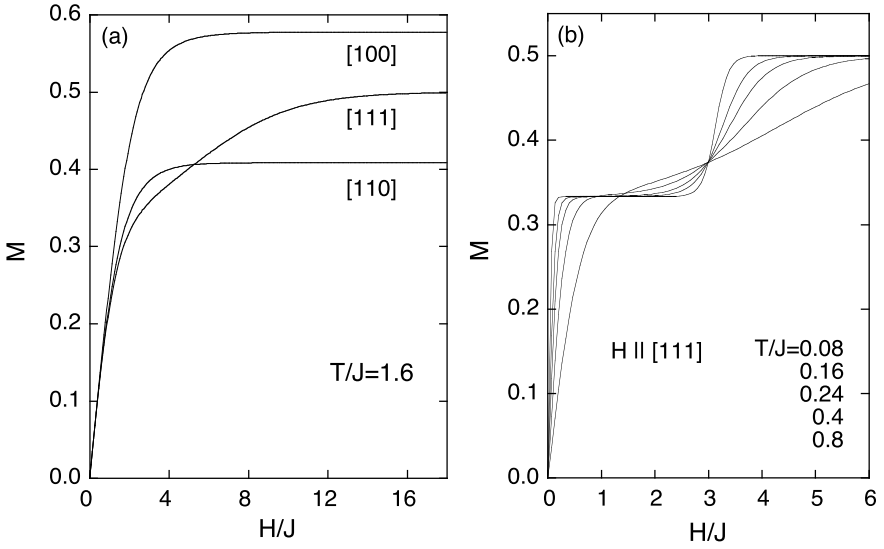

Fig. 5.3 Calculated magnetizations per spin for an isolated tetrahedron. The three principal field directions are compared at $T/J = 1.6$ in (**a**) and the temperature dependences are shown for $H \parallel [111]$ in (**b**)

directions, respectively. Note that the magnetization is isotropic in a low-field limit, because of global tetrahedral symmetry of the system in zero field. Moreover, to be focused in the next paragraph is the slower saturation for the [111] direction than the other two directions.

5.1.2 Spin-Flip Crossover in H Near the [111] Direction

For $H \parallel [111]$, the Zeeman shift of the ψ_{111} excited state is larger than that of the ground state $\{\psi_x, \psi_y, \psi_z\}$ (Fig. 5.2). Hence, a level crossing from a triply degenerate 2-in 2-out state to a non-degenerate 3-in 1-out state occurs at

$$H_c = 3J. \tag{5.4}$$

Figure 5.3b shows the evolution of calculated magnetization curves for $H \parallel [111]$ upon cooling. Since a small magnetic field lifts the degeneracy of the 2-in 2-out state and stabilizes the triply degenerate $\psi_{x,y,z}$ state, a magnetization plateau at 1/3 of the full moment appears at low magnetic fields. Then, a sudden rise in magnetization is observed at $H = H_c$. The differential susceptibility dM/dH at H_c is proportional to T^{-1} and diverges at $T = 0$, so that the rise becomes a jump at $T = 0$. This magnetization jump is caused by flipping one spin in the 2-in 2-out state. For instance,

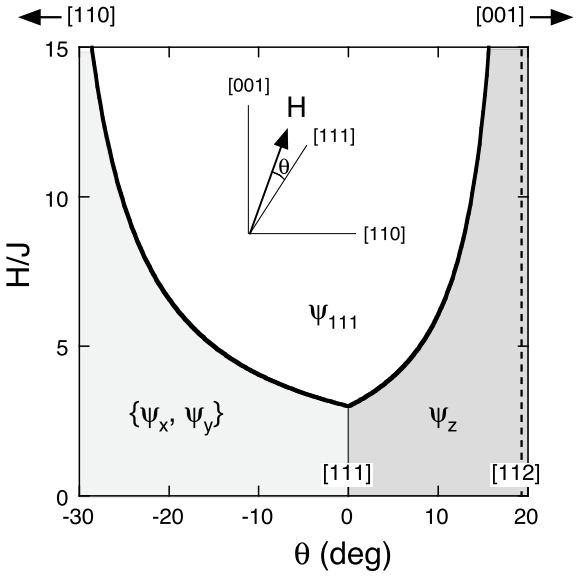

Fig. 5.4 Ground state configurations for an isolated tetrahedron. Spin-flip crossovers occur from ψ_z and $\{\psi_x, \psi_y\}$ to ψ_{111} for $\theta > 0$ to [112] and < 0 to [110], respectively, as shown by the thick lines. Inset: definition of the angle θ

spin 2 of the ψ_x state (Fig. 5.1) has a component antiparallel to H and undergoes a flip at $H = H_c$. Note that this spin flip is not a phase transition but a crossover, because the system under consideration is composed of independent tetrahedra.

When H is tilted from [111] in the $(1\bar{1}0)$ plane, threefold symmetry is broken and the ground-state degeneracy is (partially) lifted. We define the angle θ between H and the [111] direction as shown in Fig. 5.4. For $\theta > 0$ (< 0), the ground state becomes the non-degenerate ψ_z (doubly degenerate $\{\psi_x, \psi_y\}$) state. The spin-flip crossover still occurs in a finite angular range. Expressing the magnetic field as

$$\mathbf{H} = H(\mathbf{e}_{111}\cos\theta + \mathbf{e}_{\bar{1}\bar{1}2}\sin\theta), \tag{5.5}$$

where $\mathbf{e}_{111}$ and $\mathbf{e}_{\bar{1}\bar{1}2}$ denote unit vectors along [111] and $[\bar{1}\bar{1}2]$, respectively, the crossover field can be obtained as

$$\begin{aligned} H_c &= \frac{3J}{\cos\theta - 2\sqrt{2}\sin\theta}, \quad (\theta > 0) \\ H_c &= \frac{3J}{\cos\theta + \sqrt{2}\sin\theta}, \quad (\theta < 0). \end{aligned} \tag{5.6}$$

Angular variation of H_c is shown in Fig. 5.4 by a thick solid line. H_c diverges at $H \parallel [112]$ ($\theta \approx 19.5°$) and $H \parallel [110]$ ($\theta \approx -35.3°$).

5.2 Spin Ice in Magnetic Fields

5.2.1 Magnetization Anisotropy: Overview

In the spin-ice compounds $Dy_2Ti_2O_7$ (DTO) and $Ho_2Ti_2O_7$ (HTO), magnetic ions form a pyrochlore lattice: a network of corner-linked tetrahedra. A minimal model describing the spin ice compounds assumes the nearest-neighbor interaction

$$\mathscr{H} = J_{\rm eff} \sum_{\langle i,j \rangle} \sigma_i^{z_i} \sigma_j^{z_j} - \mu \mathbf{H} \sum_i \boldsymbol{\sigma}_i, \tag{5.7}$$

where the first summation is now over all the nearest-neighbor pairs, and μ is a parameter defining the magnitude of the magnetic moment of the rare-earth ions (μ = 10 and 10.6 μ_B/ion for DTO [1] and HTO [2], respectively). $J_{\rm eff}$ is an effective nearest-neighbor interaction consisting of an antiferromagnetic exchange and a ferromagnetic dipolar interaction, and is estimated to be ferromagnetic in total: $J_{\rm eff} \simeq 1.1$ [3] and $\simeq 1.8$ K [4] for DTO and HTO, respectively. Within this model, the ground state at $H = 0$ is a macroscopically degenerate 2-in 2-out state, in which all the six configurations $\{\psi_x, \psi_y, \psi_z, \psi_{-x}, \psi_{-y}, \psi_{-z}\}$ are randomly distributed over the system under the constraint of the ice rule. Note that each magnetic ion is shared by two tetrahedra, and hence the energy of the 2-in 2-out ground state becomes $-J_{\rm eff}$ per spin, a factor of two different from that for the isolated tetrahedron model discussed in the previous section. Accordingly, the spin-flip critical field in a [111] magnetic field at $T = 0$ is given by

$$H_c = 6J_{\rm eff}/\mu \tag{5.8}$$

which yields $H_c \simeq 0.98$ and $\simeq 1.52$ T for DTO and HTO, respectively.

With these in mind, one can compare the magnetization of a spin ice with that of the isolated tetrahedron model. Figure 5.5 shows the magnetization of (a) DTO [1] and (b) HTO [2] measured at 1.8 and 1.6 K, respectively, for H along the three principal directions [100], [110] and [111]. It is observed that the simple model (Fig. 5.3a) can reproduce the observed magnetization anisotropy reasonably well: whereas the magnetization is isotropic at low fields, a strong anisotropy develops with increasing H, and the saturation moment, in particular for DTO, is in good agreement with the predicted anisotropy ratio

$$M_{100} : M_{111} : M_{110} = \frac{1}{\sqrt{3}} : \frac{1}{2} : \frac{1}{\sqrt{6}}. \tag{5.9}$$

A magnetization plateau and a subsequent jump have been expected to occur for $H \parallel [111]$ (Fig. 5.3b). However, they are not well resolved in these data in Fig. 5.5 obtained at relatively high temperatures $T \gtrsim J_{\rm eff}$.

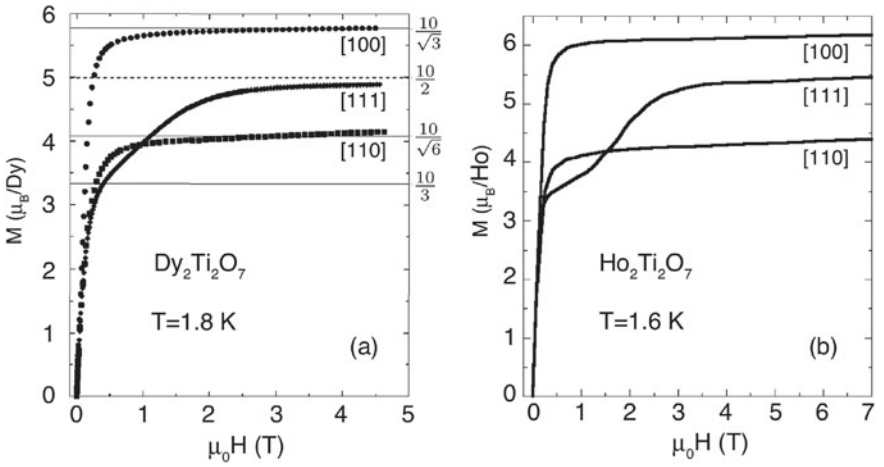

Fig. 5.5 Magnetizations of **a** $Dy_2Ti_2O_7$ ($T = 1.8$ K) [1] and **b** $Ho_2Ti_2O_7$ ($T = 1.6$ K) [2] in magnetic fields parallel to [100], [110] and [111]. Reprinted figures from [1, 2] with permission from the American Physical Society

It has been predicted by numerical calculations that a long-range part of the dipolar interaction completely lifts the ground-state degeneracy at $H = 0$ and selects a unique ordered state ("$\mathbf{q} = (0, 0, 2\pi/a)$" phase) [5]. In reality, however, the long-range ordering is inhibited by the extremely slow dynamics of the system at low temperatures, and the system remains in a spin-ice state. Therefore, the nearest-neighbor spin-ice (NNSI) model (5.7) is practically useful in describing the spin ice anisotropy. Later in this section, nevertheless, we will see that the long-range part of the dipolar interaction does play an essential role in the magnetization along and near the [111] direction. In what follows, we discuss the response of the spin ice to a magnetic field in more detail.

5.2.2 *Response to a Magnetic Field: H ∥ [100]*

For this field direction, the ground state of a unit tetrahedron is ψ_x. We can fill all the tetrahedra in the pyrochlore lattice with the ψ_x configuration under the ice rule, and this uniform state ("$\mathbf{q} = 0$" state) obviously becomes the ground state. Figure 5.6a shows the spin arrangement in a [100] field. The pyrochlore lattice can be viewed as an ABC stacking of triangular and kagomé planes along a $\langle 111 \rangle$ direction; a single kagomé plane and two adjacent triangular planes projected on a (111) plane are shown in Fig. 5.6 for simplicity.

Figure 5.7 shows the $M(H)$ curves of DTO in a [100] magnetic field, measured at $T = 0.08$, 0.57 and 0.87 K. For $T \lesssim 0.6$ K, the $M(H)$ curve in a low field region exhibits a large hysteresis due to a slow relaxation associated with a spin rearrange-

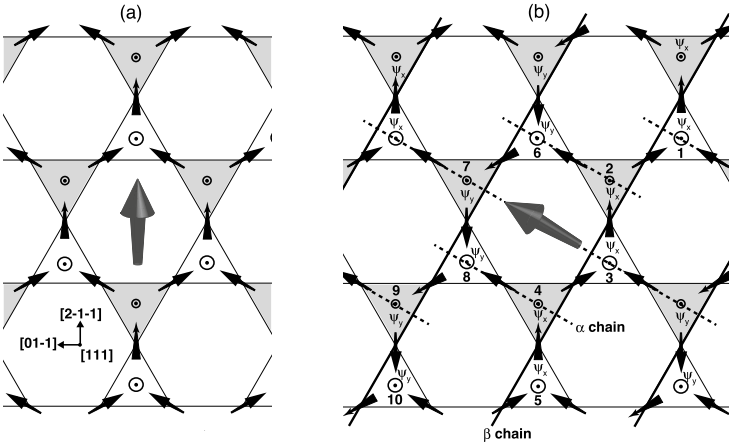

Fig. 5.6 Possible spin arrangements for $H \parallel [100]$ (**a**) and [110] (**b**). A slab of the pyrochlore lattice viewed along the [111] direction is depicted, which consists of a single kagomé plane and two adjacent triangular planes above and below. White (shaded) triangles indicate tetrahedra facing out of (into) the paper. The large arrows represent the field directions projected on the (111) plane. Note that all the spins on the triangular planes (dots) are all directed along [111] (out of the paper), so that it is enough to consider only spins in the kagomé planes. Solid arrows with a large (small) arrow head represent spins having a positive (negative) [111] component in the kagomé plane. Shown in (**a**) for $H \parallel [100]$ is the $\mathbf{q} = 0$ state in a [100] magnetic field, in which all the tetrahedra are in the ψ_x configuration. One example of the stable states for $H \parallel [110]$ is given in (**b**). Thick solid (dashed) lines indicate β (α) chains running perpendicular (parallel) to H

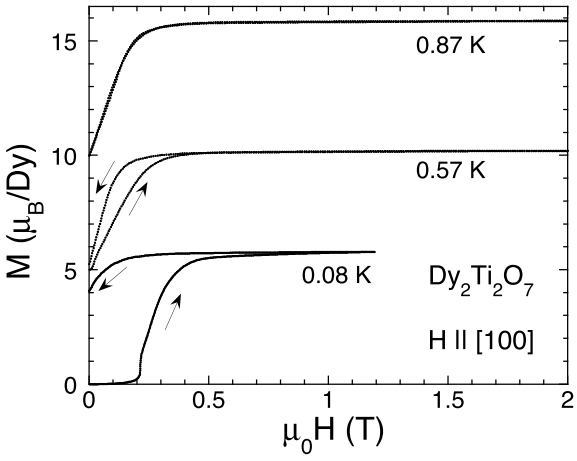

Fig. 5.7 Magnetization of $Dy_2Ti_2O_7$ for $H \parallel [100]$, measured at $T = 0.08$, 0.57 and 0.87 K. Each plot is vertically shifted by 5 μ_B/Dy for clarity. Clear hystereses between field-increasing and decreasing (marked by arrows) curves are observed at 0.57 and 0.08 K

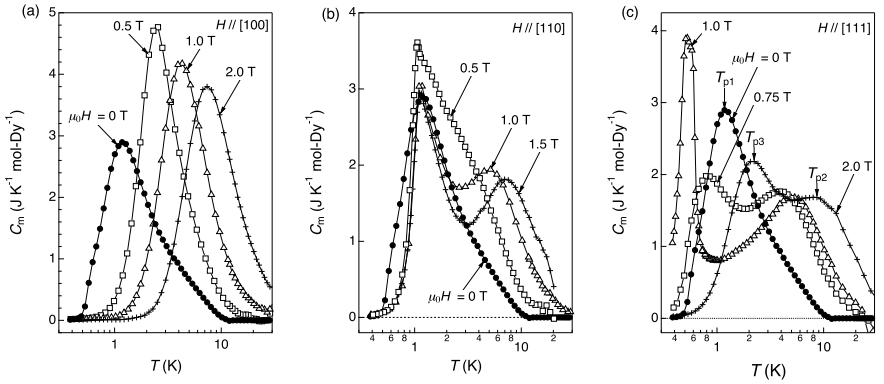

Fig. 5.8 Evolutions of magnetic heat capacity C_{m} of DTO measured with increasing magnetic fields along the three directions: **a** [100], **b** [110], and **c** [111] [7, 8]. A lattice contribution of αT^3 with $\alpha = 4.85 \times 10^{-4}$ J K^{-4} mol-Dy^{-1} has been subtracted from the raw data. Reprinted figures from [7, 8] with permission from the Journal of the Physical Society of Japan

ment from the fully-disordered spin ice to the $\mathbf{q} = 0$ state. Above ∼0.5 T, the $\mathbf{q} = 0$ state is attained and the $M(H)$ is fully saturated, and nothing happens at higher fields.

Magnetic heat capacity C_{m} of DTO shows a broad peak at around 1 K in zero field (Fig. 5.8), indicating the spin ice freezing; the residual entropy S_{r} estimated is 1.66 J K^{-1} mol-Dy^{-1}, which is in good agreement with the Pauling entropy of 1.68 J K^{-1} mol-Dy^{-1} [6]. When a magnetic field of 0.5 T is applied along the [100] direction, the peak shifts to a higher temperature and is significantly enhanced (Fig. 5.8a), suggesting a loss in S_{r}. In fact, as shown in Fig. 5.9, S_{r} becomes almost zero near $H = 0.5$ T [7]. On further increasing field, the peak just moves to higher temperatures. Thus, both M and C_{m} indicate that the $\mathbf{q} = 0$ state has been thoroughly selected at $H > 0.5$ T.

5.2.3 *Response to a Magnetic Field: H ∥ [110]*

For $H \parallel [110]$, the doubly degenerate $\{\psi_x, \psi_y\}$ state of a unit tetrahedron does not give rise to macroscopic degeneracy in the pyrochlore lattice, because either of the two states can be arranged in a consistent way to form a unique long-range order. Otherwise, the two states can be mixed in the pyrochlore lattice to give a not macroscopic but certain degeneracy. An example of the spin arrangements in a [110] magnetic field is shown in Fig. 5.6b. In this field configuration, it is convenient to view the pyrochlore lattice as composed of mutually orthogonal linear chains [9]: "α chains" running parallel to H, and "β chains" perpendicular to H [8]. Note that spins on the α chains are forced to align by H, while those on the β chains should be independent of H. Assume that tetrahedron 1 is in the ψ_x state. Then, those tetrahedra (2∼5) having spins on the same β chain all take the ψ_x state to satisfy the ice rule. Accord-

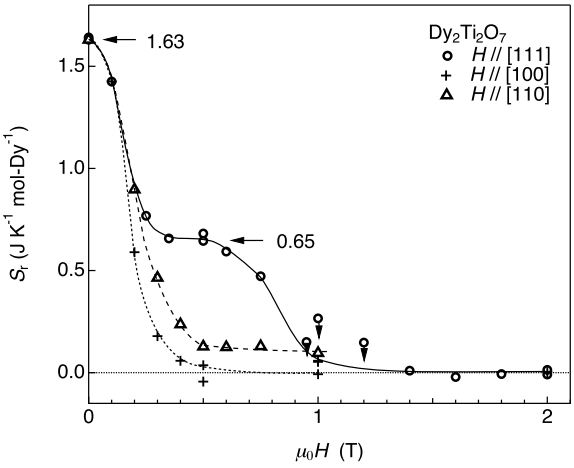

Fig. 5.9 Field dependences of the residual entropy S_r in the three field directions [7, 8]. The dotted, broken and solid lines are guides to the eyes for $H \parallel [100]$, [110] and [111], respectively. A background coming from an experimental error in determining magnetic entropy particularly at high temperatures has been subtracted from the raw data [7]. The S_r data for $H \parallel [111]$ near 1 T overestimates actual values because of proximity to the liquid-gas transition, and must be close to zero

ingly, spins on this β chain ferromagnetically align in the $[1\bar{1}0]$ direction. Within the NNSI model, the configuration of tetrahedra 6∼10 sharing the adjacent β chains has two possibilities: ψ_x or ψ_y. Figure 5.6b shows the latter case, in which the β chain belonging to tetrahedra 6∼10 has a ferromagnetic component along the $[\bar{1}10]$ direction. Note that all the α chains are ferromagnetically aligned parallel to H, while the β chains always have two possibilities. Degeneracy thus remains with respect to the direction of the ferromagnetic component of the β chains, whose entropy is, however, not macroscopically large.

According to the numerical calculations [10], the long-range dipole interaction stabilizes the ordered structure shown in Fig. 5.6b, in which the ferromagnetic β chains are antiferromagnetically coupled to each other ("$\mathbf{q} = X$" order). This long-range ordered state, however, is again dynamically inhibited from being accessed experimentally, and the system remains in a partially-ordered state [9].

Figure 5.8b shows an evolution of the heat capacity of DTO with increasing magnetic field along the [110] direction, which is quite different from that at $H \parallel [100]$. At $H = 0.5$ T, where the S_r has been removed almost completely (Fig. 5.9), the peak in C_m remains at nearly the same temperature as for $H = 0$ with a shoulder appearing at a higher temperature. With further increasing field, the first peak still remains at the same temperature and the second peak moves to higher temperatures. The first peak is assigned to a spin freezing on the β chain, which is independent of field, while the second Schottky-type peak is from the spin freezing on the α chain. Interestingly,

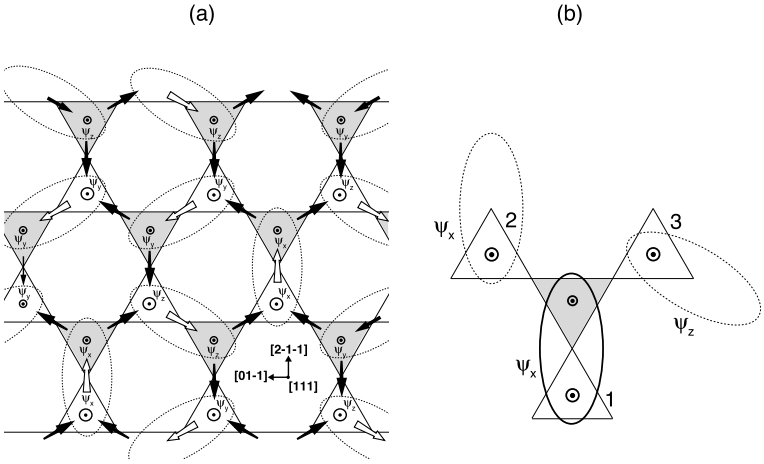

Fig. 5.10 **a** An example of the kagomé ice states in a [111] magnetic field. White arrows indicate spins having a component antiparallel to H. If the minority spin on each triangle is replaced by a dimer (as shown by solid oval), the spin configuration can be mapped to dimer configuration, which covers the entire lattice without overlap. **b** Example of local dimer arrangements on the kagomé plane. The shaded triangle at the center forms a dimer with one of the three white triangles 1–3, and a ψ_x dimer state with the triangle 1 is shown as an example (solid oval). In this situation, the triangles 2 (3) cannot take a ψ_z (ψ_y) dimer state. Thus, we expect 3×2^2 ways for this cluster

however, C_{m} of the β chain cannot be reproduced within the ferromagnetic Ising spin chain model taking into account long-range dipole interactions [8].

5.2.4 Response to a Magnetic Field: H ∥ [111]

5.2.4.1 Kagomé Ice State

When a weak field is applied along [111], the triply degenerate state $\{\psi_x, \psi_y, \psi_z\}$ of a unit tetrahedron results in macroscopic degeneracy in the kagomé planes of the pyrochlore lattice ("kagomé ice" state), as first revealed by a heat capacity experiment [11][1]. Figure 5.10a shows an example of the spin arrangements of the kagomé ice (KI) state. In this field region, all the spins on the triangular lattices (dots) are forced to align along [111] by the magnetic field, while the 2-in 2-out rule is still satisfied by all the tetrahedra. This leads to a modified ice rule on the kagomé lattices; 2-in 1-out (1-in 2-out) configuration is satisfied on white (shaded) triangles in the kagomé plane. The modified ice rule leads to a macroscopic residual entropy, which indeed has been observed by heat capacity measurements in a [111] field [7, 11, 13].

[1] Wills and coworkers [12] theoretically found a similar macroscopic degeneracy on the pure kagomé lattice and called it "kagomé spin ice".

C_m of DTO at $H \parallel [111]$ behaves very differently from those at other field directions, as shown in Fig. 5.8c. The single peak at $H = 0$ splits into two peaks with increasing H, typically shown for $H = 0.75$ T in the figure. The one at a low temperature corresponds to a spin freezing on the kagomé net, while the other at a high temperature is ascribed to a spin freezing on the triangular site. Then, the former peak turns into a sharp and intense peak at around 0.5 K in a narrow field range around 1 T, which is related to the liquid-gas transition between the KI state and the 3-in 1-out/1-in 3-out state as discussed next. With further increasing field, the sharp peak becomes again broad and shifts to higher temperatures. The variation of S_r exhibits a "plateau" at 0.65 J K^{-1} mol-Dy^{-1} at $H \sim 0.5$ T (Fig. 5.9), which corresponds to the residual entropy of the KI state [7].

Under the constraint of the modified ice rule, it can be easily shown that each configuration $\{\psi_x, \psi_y, \psi_z\}$ always appears as a dimer (Fig. 5.10a). The residual entropy of the KI state can thus be estimated by counting the number of ways of the dimer covering, applying Pauling's method [7]. Assume that the number of the tetrahedra facing out of the paper (white triangles in Fig. 5.10a) is N. Since each triangle can take any of the three dimer states $\{\psi_x, \psi_y, \psi_z\}$, the number of ways for whole system is 3^N if we completely ignore correlations among white triangles. Not all of these states are, however, allowed because of correlations in dimer occupations. Figure 5.10b shows a local arrangement of dimers on a kagomé plane. The shaded triangle at the center forms a dimer with one of the three white triangles 1–3, and a dimer with the triangle 1 (ψ_x dimer) is shown as an example. In this situation, triangles 2 and 3 can take only two dimer states each because of a ψ_x dimer on the triangle 1. Thus, we approximately have 3×2^2 ways out of 3^3 states for this cluster. Therefore, the total entropy is calculated by

$$S_r \simeq k_B \ln \left(3^N \left(\frac{3 \times 2^2}{3^3} \right)^N \right) = N k_B \ln \left(\frac{4}{3} \right), \tag{5.10}$$

which amounts to 0.598 J K^{-1} mol-Dy^{-1}. The estimated S_r of the KI state is in good agreement with the experimentally observed value of 0.65 J K^{-1} mol-Dy^{-1} as shown in Fig. 5.9 [7]. The exact S_r of the KI state has been determined to be 0.671 J K^{-1} mol-Dy^{-1} by rigorously treating the dimer covering problem [14].

5.2.4.2 Magnetization Plateau and A Liquid-Gas Transition

In the KI state, the magnetization exhibits a plateau with 1/3 of the full moment as expected from the isolated tetrahedron model shown in Fig. 5.3b. Figure 5.11 shows the $M(H)$ curves of DTO for $H \parallel [111]$ obtained at low temperatures [15]. A clear plateau with the moment value $3.2 - 3.3\ \mu_B$/Dy develops on cooling below 1 K. The large hysteresis seen in the low-field region below 0.3 T at $T = 0.35$ K is due to the slow relaxation of the magnetization associated with a spin rearrangement from the zero-field spin-ice to the KI state, like the case for $H \parallel [100]$ (Fig. 5.7).

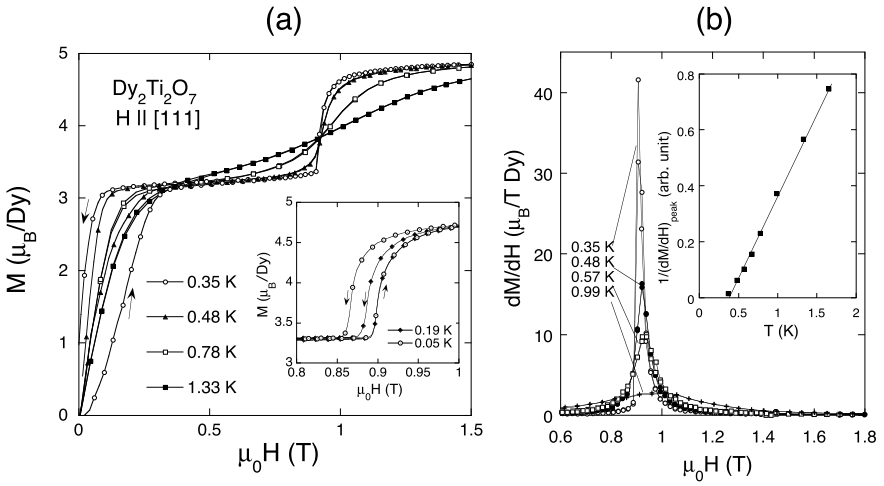

Fig. 5.11 Magnetizations and the differential susceptibility of DTO for magnetic fields parallel to the [111] direction [15]. **a** Magnetizations obtained at several temperatures above 0.35 K are shown in the main panel, and those at $T = 0.19$ and 0.05 K near the spin-flip field are shown in the inset. **b** Temperature evolution of dM/dH near H_c is shown in the main panel, and the temperature variation of the inverse of the dM/dH at H_c is shown in the inset. Reprinted figures from [15] with permission from the American Physical Society

Near $H = 0.9$ T, a clear magnetization jump can be seen in the $M(H)$ in Fig. 5.11. This is the ice-rule breaking spin flip into the 3-in 1-out/1-in 3-out state in which a ψ_{111} configuration is uniformly aligned. Spins responsible for this spin-flip process are those having antiparallel components to the field, indicated by white arrows in Fig. 5.10a; each of these spins undergoes a flip at H_c at which the Zeeman energy overcomes its interaction energy. Directions of all the other spins remain unchanged across the magnetization jump. Within the NNSI model (5.7), H_c at $T = 0$ is given by (5.8). Making use of the H_c value of $\simeq 0.9$ T from Fig. 5.11a, we obtain $J_{\rm eff} \simeq 1.01$ K, which can be compared with the value $J_{\rm eff} \simeq 1.11$ K estimated from the analysis of the zero-field specific heat [3]. Note that there is no appreciable hysteresis in the magnetization jump at H_c even at a low temperature of 0.35 K, in contrast to the large hysteresis at low fields. This difference in hysteresis may be related to the dynamics of spin flip. The first jump at low fields involves a ring-exchange process composed of more than three spin flipping from one 2-in 2-out to another 2-in 2-out configuration, whereas the second jump at 0.9 T is governed by a single-spin flipping process from a 2-in 2-out to 3-in 1-out/1-in 3-out configuration; the latter must be much faster than the former. A tiny hysteresis is eventually observed at 0.86–0.9 T below $T = 0.19$ K as shown in the inset of Fig. 5.11a, which is probably due to a phase transition mentioned below.

We have to remember that the spin flip in the NNSI model does not cause a phase transition. This is because spins undergoing the flip at H_c are not interacting with each other, so that no cooperative phenomenon is expected; the spin flip predicted by

this model is essentially the same as that of the isolated tetrahedron model discussed in Sect. 5.1. Interestingly enough, this is not the case in real spin-ice systems. Let us focus on the temperature evolution of the sharpness of the magnetization jump in DTO. As shown in Fig. 5.11b, the differential susceptibility dM/dH makes a local maximum at H_c. The peak height in dM/dH is therefore a good measure of the sharpness of the magnetization jump. The inset to Fig. 5.11b shows the temperature variation of the inverse of the peak height, $(dM/dH)^{-1}_{\rm peak}$. On cooling below 1.5 K, $(dM/dH)^{-1}_{\rm peak}$ almost linearly decreases and tends to vanish at $T_{\rm cr} \simeq 0.4$ K [15]. This clearly evidences the existence of a phase transition, contrary to the expectation of the NNSI model. In addition, below $T_{\rm cr}$, a small but clear hysteresis appears in $M(H)$ as shown in the inset of Fig. 5.11a, indicating that the spin flip at H_c becomes a first-order transition at lower temperatures. This first-order transition is of a liquid-gas type, terminating at the critical endpoint $T_{\rm cr}$, and must be driven by a long-range part of the dipolar interaction as discussed in Chaps. 1 and 3.

The residual entropy S_r of the KI state is discontinuously released upon the first-order phase transition into the non-degenerate 3-in 1-out/1-in 3-out state. Indeed, S_r estimated by the heat capacity measurements vanishes above H_c as shown in Fig. 5.9 [7]. At a temperature above $T_{\rm cr}$, however, the magnetic field variation of the entropy $S(H)$ is predicted to exhibit a giant peak at H_c [16]. This is because the 2-in 2-out configurations $\{\psi_x, \psi_y, \psi_z\}$ degenerate with a ψ_{111} configuration of the 3-in 1-out/1-in 3-out state at $H = H_c$. Analysis based on the Bethe approximation indicates that the entropy peak amounts to 2.44 J K^{-1} mol-Dy^{-1} [16]. This giant peak in $S(H)$ has been observed by a magnetocaloric effect (MCE) experiment on DTO [17]. The MCE measurements make use of the thermodynamic relation

$$\left(\frac{\partial S}{\partial H}\right)_T = -\frac{C}{T}\left(\frac{\partial T}{\partial H}\right)_S . \tag{5.11}$$

The quantity $(\partial T/\partial H)_S$ on the right side can be obtained quasicontinuously by measuring a change of the sample temperature when H is slightly increased in a semiadiabatic condition. Integration of (5.11) by H in the range $\mu_0 H \geq 0.4$ T gives the entropy change $\Delta S = S(H) - S(0.4\ \text{T})$ as shown in Fig. 5.12 [17] for temperatures 0.35, 0.4 and 0.5 K. At these temperatures, $S(0.4\ \text{T})$ should be nearly equal to the S_r of the KI state. The entropy peak at $T = 0.5$ K is therefore estimated to be 1.67 J K^{-1} mol-Dy^{-1}. Presence of the entropy peak of similar magnitude has also been reported by the heat capacity measurements [7].

The plot for $T = 350$ mK in Fig. 5.12 shows that the entropy peak is strongly suppressed and ΔS abruptly decreases at H_c. This behavior is due to the occurrence of the first-order transition. Interestingly, the entropy release can still be seen at 1.4 T, well beyond the critical field of 0.9 T. The slow approach to the fully polarized state is also evidenced by the magnetization data for $T = 50$ mK in Fig. 5.11; whereas the onset of the magnetization jump at ~ 0.9 T is very sharp, $M(H)$ does not reach full saturation immediately above H_c and a gradual increase can still be seen at 1 T. The true origin of this asymmetric behavior of the first-order transition is not

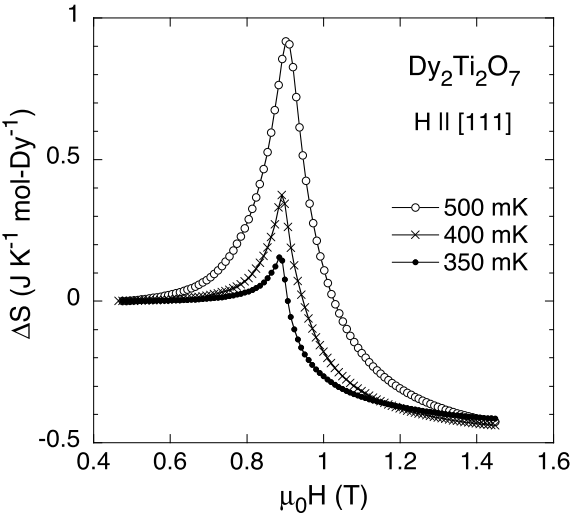

Fig. 5.12 Entropy change ΔS in DTO by application of H along the [111] direction. The data were obtained from magnetocaloric effect measurements, reprinted from [17] with permission from the Journal of the Physical Society of Japan

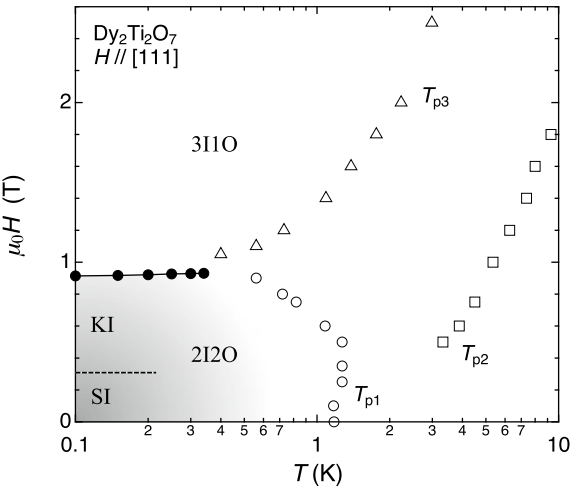

Fig. 5.13 Phase diagram of DTO for H parallel to the [111] direction, obtained by the heat capacity [7] and the magnetization [15] measurements. Solid line indicates the first-order liquid-gas transition line. KI and SI denote the regions of the kagomé ice and the spin ice, respectively. 2I2O and 3I1O represent the 2-in 1-out and 3-in 1-out/1-in 3-out states, respectively. T_{p1}, T_{p2} and T_{p3} indicate the temperatures of peaks observed in the heat capacity

clear at present. In this regard, the measurements of the field dependences of the heat capacity [18] and the ac susceptibility [19] of DTO suggest the existence of an intermediate state between the KI and fully polarized states in magnetic fields close to the [111] direction. Further studies will be needed to clarify these points.

Figure 5.13 summarizes the phase diagram of DTO for H parallel to the [111] direction, obtained by the heat capacity [7] and the magnetization [15] measurements. The solid line indicates the first-order liquid-gas transition line determined from the $M(H)$ measurements, which terminates at $T_{cr} \simeq 0.4$ K and $H_c \simeq 0.9$ T. Interestingly, the transition line seems to reach the field axis with a finite slope [15]. This indicates that there is a change in entropy even at $T \to 0$. This outstanding feature distinguishes

the transition from others. Open symbols in the phase diagram show the temperatures T_{p1}, T_{p2} and T_{p3} at which peaks are observed in the temperature variation of the heat capacity. T_{p1} is a crossover temperature to the spin ice state, whereas T_{p2} and T_{p3} correspond to freezings of single spins having different Zeeman energies; T_{p2} is the freezing temperature of apical spins in the triangular planes which have the Ising axis parallel to H, whereas T_{p3} is ascribed to freezing of spins on the kagomé plane into the 3-in 1-out/1-in 3-out state [7].

5.2.5 *Effect of Tilting H from [111]*

5.2.5.1 Kasteleyn Transition

When a weak magnetic field is slightly tilted away from [111], the threefold symmetry is broken and the three configurations ψ_x, ψ_y and ψ_z in the KI state become nonequivalent. Consider that H acquires an increased component along the [001] direction. Apparently, the ground state of the NNSI model (5.7) for any small tilting angle of H becomes the $\mathbf{q} = 0$ state with the ψ_z configuration, whose spin structure is given by a clockwise rotation of the lattice in Fig. 5.6a by 120°. One might therefore wonder how fragile the KI state is against a tiny misalignment of H from [111]. At a finite temperature, however, a gain in entropy should compete with a loss in energy, and maintains a disordered state in a finite range of the field orientation near [111]. The disordered state is terminated by a phase transition called "Kasteleyn transition" [20, 21].

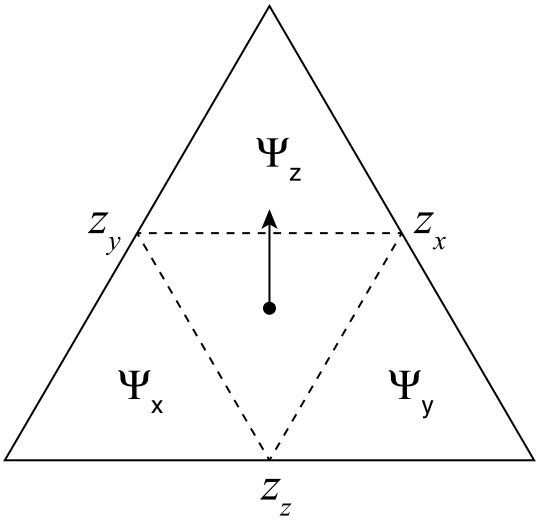

Fig. 5.14 Schematic phase diagram for the Kasteleyn transition at a finite temperature, indicating four phases. Ψ_x, Ψ_y and Ψ_z are the $\mathbf{q} = 0$ ordered phases with ψ_x, ψ_y and ψ_z configurations, respectively. The triangle region at the center is a disordered state. The arrow indicates a trajectory when H is tilted from [111] towards [001] direction ($\theta > 0$)

Figure 5.14 shows the schematic phase diagram for the Kasteleyn transition [20], where $\Psi_\alpha(\alpha = x, y, z)$ denotes the $\mathbf{q} = 0$ ordered phase of the ψ_α configuration, and the triangle region at the center is a disordered phase including the KI state. z_α represents the statistical weight defined by the Zeeman energy of the configuration ψ_α as

$$z_\alpha = \exp[\mu \mathbf{m}_\alpha \mathbf{H}/(k_\mathrm{B}T)], \tag{5.12}$$

where $\mathbf{m}_\alpha$ is a magnetic moment per tetrahedron given by (5.2) and is now parallel to x, y or z direction. In this triangular phase diagram, the distance of a point to the axis z_α is proportional to z_α. It has been shown that a phase transition to the ordered state Ψ_α occurs when the criterion

$$z_\alpha = z_{\alpha'} + z_{\alpha''}. \tag{5.13}$$

is satisfied [20, 21]. This gives the phase boundaries shown by the dashed lines in Fig. 5.14.

Assume that the magnetic field is expressed by (5.5) (Fig. 5.4). Increasing the angle θ then results in an enhancement of z_z keeping $z_x = z_y$ as indicated by an arrow in Fig. 5.14, and induces a phase transition into the Ψ_z state at $z_z = z_x + z_y$. The critical angle θ_c for the transition is then given by

$$k_\mathrm{B}T = (2\sqrt{2}/\ln 2)\mu H \sin\theta_c. \tag{5.14}$$

The Kasteleyn transition exhibits quite unusual properties. As θ increases towards the critical value θ_c from the disordered side, the entropy vanishes as

$$S \propto (\theta_c - \theta)^{1/2}. \tag{5.15}$$

The expectation value of m_z, the z component of the magnetization, approaches its saturation value $m_z^{\mathrm{sat}} = 4/\sqrt{3}$ as

$$m_z^{\mathrm{sat}} - \langle m_z \rangle \propto (\theta_c - \theta)^{1/2}. \tag{5.16}$$

In the ordered state Ψ_z, therefore, $S = 0$ and $\langle m_z \rangle$ is fully saturated; there are no thermal fluctuations.

Experimental detection of the Kasteleyn transition, in particular by thermodynamic measurements, has not been successful so far, probably because of slow dynamics of the system. Possible evidence for the Kasteleyn transition has been reported in a neutron scattering experiment on HTO in a tilted magnetic field [22].

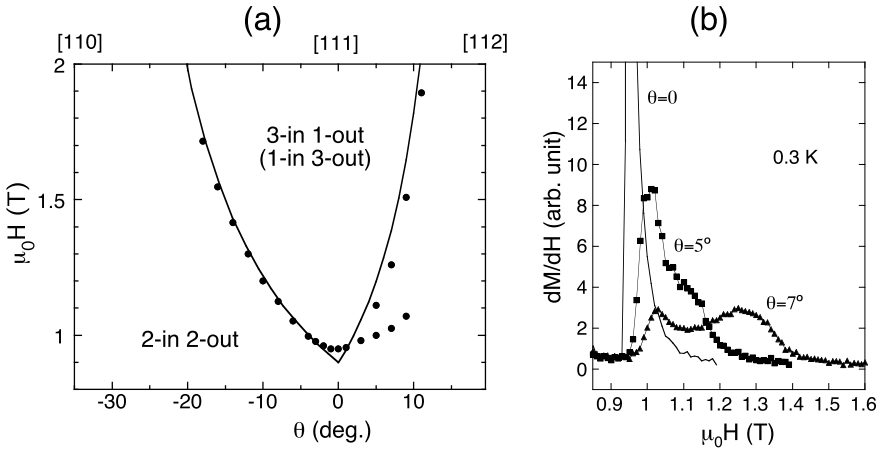

Fig. 5.15 **a** Angular variation of the spin-flip transition in DTO, obtained by magnetization measurements at $T = 0.3$ K [23]. Symbols are the experimental data points for H_c and solid lines represent the angular variation of the model (5.17) with $J_{\rm eff} = 1.01$ K. **b** dM/dH data for $\theta = 0, 5$ and 7 degrees [23]. A two-peak structure is observed in dM/dH for $\theta = 5$ and 7 degrees, resulting in the two branches of $H_c(\theta)$ in the angular interval of $5 \leq \theta \leq 10$ degrees in (**a**). Adapted figures from [23] with permission from the Institute of Physics

5.2.5.2 Angular Variation of H_c

When H is rotated in the $(1\bar{1}0)$ plane away from [111], the angular variation of the spin flip critical field H_c of the NNSI model for $T = 0$ should vary as expected by the isolated tetrahedron model (5.6) (Fig. 5.4) by replacing J with $2J_{\rm eff}$

$$H_c = \frac{6J_{\rm eff}}{\cos\theta - 2\sqrt{2}\sin\theta}, \quad (\theta > 0)$$
$$H_c = \frac{6J_{\rm eff}}{\cos\theta + \sqrt{2}\sin\theta}, \quad (\theta < 0). \tag{5.17}$$

Here, the ground state is a Ψ_z state for $\theta > 0$ and a mixture of $\{\psi_x, \psi_y\}$ configurations for $\theta < 0$ [2]. Figure 5.15a shows the angular variation of H_c of DTO at $T = 0.3$ K determined from the magnetization measurements [23]. Overall, the NNSI model explains the observed $H_c(\theta)$ remarkably well.

However, it is evident that a positive departure from the simple model exists near $\theta = 0$. This discrepancy is ascribed to the entropy-releasing liquid-gas transition that cannot be derived from the NNSI model. The positive departure of the experimental H_c is partly due to a finite-temperature effect of the first-order transition. According to the thermodynamic Clausius-Clapeyron relation

[2] At a finite temperature, the $H_c(\theta)$ diagram for the NNSI model might become complicated at a finite θ due to a coexistence of ψ_z and $\{\psi_x, \psi_y\}$ configurations. Note that ψ_z and $\{\psi_x, \psi_y\}$ configurations have locally different H_c for $\theta \neq 0$ in the NNSI model.

$$\frac{dH_c}{dT} = -\frac{\Delta S}{\Delta M}, \tag{5.18}$$

where ΔX denotes the magnitude of a discontinuity in a quantity X across a first-order phase transition, the critical field H_c of an entropy-releasing first-order transition ($\Delta S < 0$) should increase with temperature ($dH_c/dT > 0$). For DTO, $\mu_0 dH_c/dT$ for the [111] direction is estimated to be 0.08 T/K from the experimental values of $\Delta M \approx 1\ \mu_B$/Dy and $\Delta S \approx -0.5$ J K^{-1} mol-Dy^{-1} [15]. This effect increases H_c by 0.024 T at $T = 0.3$ K. As H is tilted towards [110] direction ($\theta < 0$) at a finite temperature, the residual entropy of the initial 2-in 2-out state continuously decreases because of a continuous reduction of the statistical weight z_z (Fig. 5.14), and hence $|\Delta S|$ becomes progressively small, resulting in a disappearance of the thermal shift of H_c on decreasing θ towards [110].

Another interesting feature of $H_c(\theta)$ can be seen in the region $5 \leq \theta \leq 10$ degrees. As shown in Fig. 5.15b, the dM/dH data in this angle range has a two-peak structure. Accordingly, the peak positions in dM/dH fall on two distinct branches in the H_c vs. θ plot in Fig. 5.15a [23]. The data points of the upper branch closely follow the angular dependence of (5.17), and can be ascribed to a spin-flip from the $\mathbf{q} = 0$ ordered state (Ψ_z state). As we discuss in the next subsection, this spin flip is associated with a ferromagnetic ordering on an fcc sublattice, and becomes a first order transition at low temperatures. Those of the lower branch, on the other hand, connects with the liquid-gas transition at $\theta = 0$ and exhibit much weaker angular variation, fading away with increasing θ. It appears that the disordered KI state is coexisting with the Ψ_z state in a finite range of θ. Note that such a bifurcation of $H_c(\theta)$ is not observed for $\theta < 0$ [23].

The bifurcation of the spin-flip critical field for $\theta > 0$ suggests a discontinuous change in the ground-state configuration as a function of θ, and might be related to the Kasteleyn transition predicted in this angular region at a finite H (Fig. 5.14). The observed behavior of the magnetization, however, appears to be at odds with the discussion in the preceding subsection, according to which a continuous phase transition from the KI state to the Ψ_z state should occur. Experimentally, no clear phase boundary has been observed so far. A sharp phase transition might be hindered by slow dynamics of spins. We note that a similar two-peak structure has also been reported in the field dependences of the heat capacity [18] and the ac susceptibility [19] of DTO in magnetic fields close to the [111] direction.

5.2.5.3 Ferromagnetic Order on an fcc Sublattice

The spin-flip transition of the spin ice for H near the [112] direction ($\theta > 10$ degrees region in Fig. 5.15a) is expected to take place from the fully-ordered Ψ_z state into the 3-in 1-out/1-in 3-out state of a ψ_{111} configuration, accompanying no change in the entropy. It has been demonstrated that this transition also becomes of first order at low temperatures [24–26].

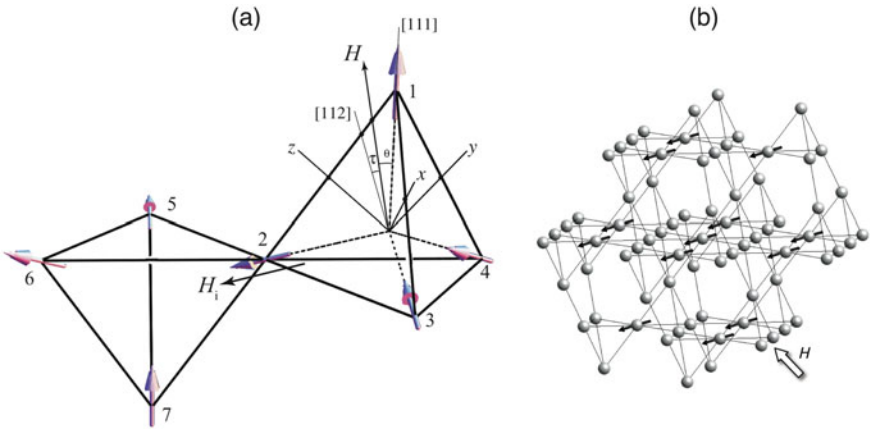

Fig. 5.16 Spin configuration in a magnetic field tilted away from [111] towards [112] direction. Shown in (**a**) is the local ψ_z configuration. The angle τ ($0 < \tau < 19.5°$) is measured between H and the [112] direction. Spin 2 has a component antiparallel to H and undergoes a flip at $H_c(\theta)$. Other spins 1, 3-7 are strongly pinned by H and exert an internal field H_i along the $[\bar{1}\bar{1}1]$ direction on spin 2. In the pyrochlore lattice, spin 2's form an fcc sublattice and are ferromagnetically aligned at low temperatures as shown by solid arrows in (**b**)

Figure 5.16 shows the local ψ_z configuration of a spin ice in a magnetic field tilted away from [111] towards the [112] direction. Whereas spins 1, 3-7 on $(\bar{1}\bar{1}1)$ kagomé planes are pinned by H, spin 2 has a component antiparallel to H and undergoes a flip at high fields. Note that spin 2's are third neighbors in the pyrochlore lattice, comprising an fcc sublattice, and are forced to uniformly align under the ice rule, *i.e.*, by an internal field H_i from the neighboring spins on the kagomé planes.

Consider that a strong field is applied along the [112] direction in Fig. 5.16. Spin 2 is then perpendicular to H and remains inert. As H is tilted back towards the [111] direction, a field component antiparallel to H_i appears, given by $H \sin \tau$ where τ is the angle between H and the [112] direction. At a certain critical angle τ_c, a condition

$$H \sin \tau_c + H_i = 0 \tag{5.19}$$

is satisfied and the internal field on spin 2 is just compensated. This is what happens on the $H_c(\theta)$ line at $\theta > 0$ in Fig. 5.15a. A question is whether spin 2 becomes free (paramagnetic) on the $H_c(\theta > 0)$ line. The answer is no, if the long-range dipolar interaction is taken into account. Indeed, the dipolar interaction produces a ferromagnetic coupling among spin 2's [24]. Thus, spin 2's are ferromagnetically ordered on the $H_c(\theta > 0)$ line at $T = 0$. The spin flip transition at $H_c(\theta > 0)$ is then identical to a moment inversion of an Ising ferromagnet, which is of first order below a critical temperature T_c. For DTO, T_c has been obtained to be 0.28 K and 0.26 K by ac susceptibility [25] and dc magnetization [26] measurements, respectively.

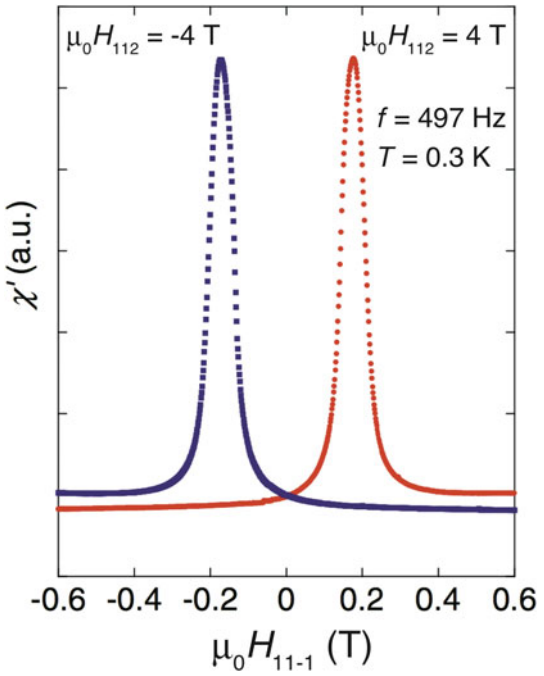

Fig. 5.17 Dependence of the real part of the ac susceptibility χ' on the field strength along the $[11\bar{1}]$ direction, measured under another strong magnetic field $\mu_0 H_{112} = \pm 4$ T applied along the [112] direction, reprinted from [25] with permission from the American Physical Society

Figure 5.17 shows the result of the ac susceptibility ($\chi_{\rm ac}$) measurements performed using a vector magnet [25]. In this experiment, a strong magnetic field H_{112} of 4 T was applied along the [112] direction to pin the spins on the kagomé planes. A small field $H_{11\bar{1}}$ was then swept along the $[11\bar{1}]$ direction, perpendicular to H_{112}, and $\chi_{\rm ac}$ was measured with an ac field applied parallel to $H_{11\bar{1}}$. $\chi_{\rm ac}$ thus directly probes the longitudinal susceptibility of the fcc sublattice moment. A giant peak is observed in $\chi_{\rm ac}$ at $H_{11\bar{1}}$ near 0.2 T, indicating that the compensation (5.19) occurs at this field. Switching H_{112} to -4 T reverses all the spins, and hence $H_{\rm i}$ changes its sign. Accordingly, the compensation field moves to $H_{11\bar{1}} \sim -0.2$ T as shown in Fig. 5.17. With a careful correction for the misalignment of H_{112}, the correct compensation field is estimated to be $H_{11\bar{1}} = 0.25 \pm 0.01$ T [25]. This corresponds to $J_{\rm eff} = 0.84$ K.

Figure 5.18a shows the angular variation of the dc magnetization M_H of DTO with H near the [112] direction, measured by rotating a magnetic field $\mathbf{H}$ in the $(1\bar{1}0)$ plane at various temperatures [26]. Here M_H is defined as $M_H = \mathbf{MH}/H$, a component of the total magnetization parallel to H. The total magnetization can be written as $\mathbf{M} = \mathbf{M}_{\rm K} + \mathbf{M}_{\rm F}$, where $\mathbf{M}_{\rm K}$ and $\mathbf{M}_{\rm F}$ denote the magnetic moment of the spins on the $(\bar{1}\bar{1}1)$ kagomé planes and that of the fcc sublattice, respectively. Note that $\mathbf{M}_{\rm F}$ is parallel to $[\bar{1}\bar{1}1]$, and $\mathbf{M}_{\rm K}$ is almost field independent at low temperatures because

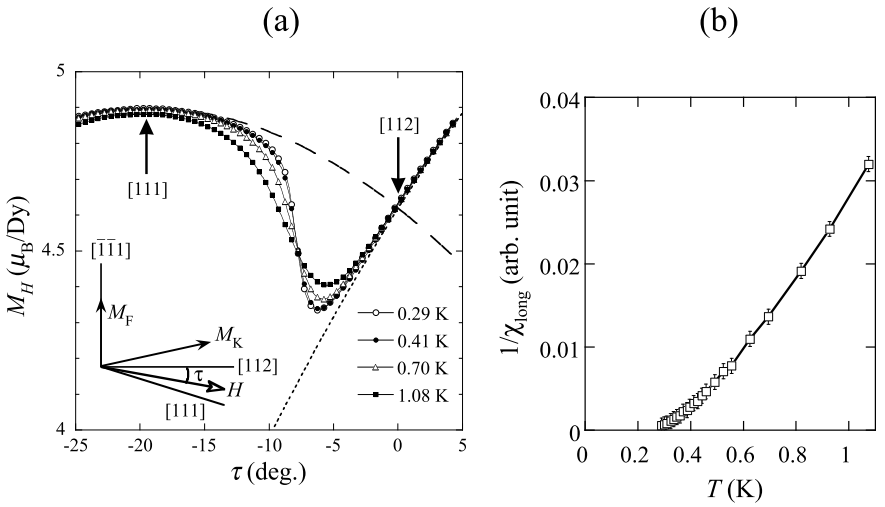

Fig. 5.18 **a** Angular variation of the magnetization of DTO measured in a magnetic field of 2 T rotated in the $(1\bar{1}0)$ plane, reprinted from [26] with permission from the Institute of Physics. Dashed (dotted) line indicates the angular dependence of the magnetization of 3-in 1-out/1-in 3-out (2-in 2-out Ψ_z) state. **b** Temperature variation of the inverse longitudinal susceptibility $\chi_{\rm long}^{-1} = [dM/d(H\sin\tau)]^{-1}$ of the fcc sublattice magnetization, adapted from [26] with permission from the Institute of Physics

spins on the kagomé planes are strongly pinned by **H**. One can then extract $M_{\rm F}$ from the experimental data in Fig. 5.18a, as a function of the longitudinal magnetic field $H\sin\tau$. Figure 5.18(b) shows the temperature variation of the reciprocal of the longitudinal susceptibility $\chi_{\rm long}^{-1}$ for $M_{\rm F}$. It can be seen that $\chi_{\rm long}^{-1}$ diverges near 0.26 K [26], evidencing a ferromagnetic transition in the fcc sublattice. The observed critical temperature $T_{\rm c} \simeq 0.26$ K indicates the presence of a small antiferromagnetic third nearest-neighbor interaction $J_3 \simeq -0.03$ K, in addition to the ferromagnetic dipolar interaction [24].

5.2.5.4 Summary

In this article, we discussed the response of the classical spin ice compound $Dy_2Ti_2O_7$ (DTO) to magnetic fields of various orientations. The macroscopic entropy of the 2-in 2-out spin ice state at $H = 0$ is removed by a magnetic field in an anisotropic manner, whose overall behavior can be understood by a simple nearest-neighbor spin-ice model. In a not-too-strong [111] magnetic field, for instance, the spin-ice state transforms into a kagomé ice state with a partially reduced entropy.

When the magnetic field is further increased along the [111] direction, an ice-rule-breaking first-order transition is observed at low temperatures from the kagomé ice state into a fully-polarized 3-in 1-out/1-in 3-out state. This first-order transition,

which is of liquid-gas type, cannot result from the simple nearest-neighbor spin-ice model, and provides evidence for a crucial role of the long-range dipolar interaction. This first-order transition was later understood in terms of a condensation of interacting magnetic monopoles that emerge from the dipolar spin-ice model. The observed first-order transition in DTO is however quite asymmetric near the critical field, and the magnetization exhibits a slow approach to full saturation. This behavior is not well understood yet and thus call for further investigations.

When the magnetic field is tilted from the [111] to the [112] direction, the kagomé ice state is predicted to undergo a continuous phase transition, called Kasteleyn transition, into the $\mathbf{q} = 0$ ordered state. In this $\mathbf{q} = 0$ state, the ice-rule breaking spin flip becomes a first-order transition that is explained by an inversion of the spins ferromagnetically-aligned on an fcc sublattice. In reality, however, some inhomogeneity occurs between the kagomé ice and the $\mathbf{q} = 0$ states in DTO, and no thermodynamic evidence for the sharp Kasteleyn transition is obtained. Future work is needed to understand the phase transitions in a magnetic field slightly tilted off the [111] direction.

References

1. H. Fukazawa, R.G. Melko, R. Higashinaka, Y. Maeno, M.J.P. Gingras, Phys. Rev. B **65**, 054410 (2002). https://doi.org/10.1103/PhysRevB.65.054410
2. O.A. Petrenko, M.R. Lees, G. Balakrishnan, Phys. Rev. B **68**, 012406 (2003). https://doi.org/10.1103/PhysRevB.68.012406
3. B.C. den Hertog, M.J.P. Gingras, Phys. Rev. Lett. **84**, 3430 (2000). https://doi.org/10.1103/PhysRevLett.84.3430
4. S.T. Bramwell, M.J. Harris, B.C. den Hertog, M.J.P. Gingras, J.S. Gardner, D.F. McMorrow, A.R. Wildes, A.L. Cornelius, J.D.M. Champion, R.G. Melko, T. Fennell, Phys. Rev. Lett. **87**, 047205 (2001). https://doi.org/10.1103/PhysRevLett.87.047205
5. R.G. Melko, B.C. den Hertog, M.J.P. Gingras, Phys. Rev. Lett. **87**, 067203 (2001). https://doi.org/10.1103/PhysRevLett.87.067203
6. A.P. Ramirez, A. Hayashi, R.J. Cava, R. Siddharthan, B.S. Shastry, Nature **399**, 333 (1999). https://doi.org/10.1038/20619
7. Z. Hiroi, K. Matsuhira, S. Takagi, T. Tayama, T. Sakakibara, J. Phys. Soc. Jpn. **72**, 411 (2003). https://doi.org/10.1143/JPSJ.72.411
8. Z. Hiroi, K. Matsuhira, M. Ogata, J. Phys. Soc. Jpn. **72**, 3045 (2003). https://doi.org/10.1143/JPSJ.72.3045
9. T. Fennell, O.A. Petrenko, G. Balakrishnan, S.T. Bramwell, J.D.M. Champion, B. Fåk, M.J. Harris, D.McK. Paul, Appl. Phys. A **74**, S889 (2002). https://doi.org/10.1007/s003390201638
10. R.G. Melko, M.J.P. Gingras, J. Phys.: Condens. Matter **16**, R1277 (2004). https://doi.org/10.1088/0953-8984/16/43/R02
11. K. Matsuhira, Z. Hiroi, T. Tayama, S. Takagi, T. Sakakibara, J. Phys.: Condens. Matter **14**, L559 (2002). https://doi.org/10.1088/0953-8984/14/29/101
12. A. S. Wills, R. Ballou, C. Lacroix, Phys. Rev. B **66**, 144407 (2002). https://doi.org/10.1103/PhysRevB.66.144407
13. R. Higashinaka, H. Fukazawa, Y. Maeno, Phys. Rev. B **68**, 014415 (2003). https://doi.org/10.1103/PhysRevB.68.014415
14. M. Udagawa, M. Ogata, Z. Hiroi, J. Phys. Soc. Jpn. **71**, 2365 (2002) https://doi.org/10.1143/JPSJ.71.2365

15. T. Sakakibara, T. Tayama, Z. Hiroi, K. Matsuhira, S. Takagi, Phys. Rev. Lett. **90**, 207205 (2003) https://doi.org/10.1103/PhysRevLett.90.207205
16. S.V. Isakov, K.S. Raman, R. Moessner, S.L. Sondhi, Phys. Rev. B **70** 104418 (2004) https://doi.org/10.1103/PhysRevB.70.104418
17. H. Aoki, T. Sakakibara, K. Matsuhira, Z. Hiroi, J. Phys. Soc. Jpn. **73**, 2851 (2004) https://doi.org/10.1143/JPSJ.73.2851
18. R. Higashinaka, H. Fukazawa, K. Deguchi, Y. Maeno, J. Phys. Soc. Jpn. **73**, 2845 (2004) https://doi.org/10.1143/JPSJ.73.2845
19. S.A. Grigera, R.A. Borzi, D.G. Slobinsky, A.S. Gibbs, R. Higashinaka, Y. Maeno, T.S. Grigera, Pap. Phys. **7**, 070009 (2015) https://doi.org/10.4279/PIP.070009
20. P.W. Kasteleyn, J. Math. Phys. **4**, 287 (1963) https://doi.org/10.1063/1.1703953
21. R. Moessner, S.L. Sondhi, Phys. Rev. B **68**, 064411 (2003) https://doi.org/10.1103/PhysRevB.68.064411
22. T. Fennell, S.T. Bramwell, D.F. McMorrow, P. Manuel, A.R. Wildes, Nat. Phys. **3**, 566 (2007) https://doi.org/10.1038/nphys632
23. H. Sato, K. Matsuhira, T. Sakakibara, T. Tayama, Z. Hiroi, S. Takagi, J. Phys.:Condens. Matter **19**, 145272 (2007) https://doi.org/10.1088/0953-8984/19/14/145272
24. J.P.C. Ruff, R.G. Melko, M.J.P. Gingras, Phys. Rev. Lett. **95**, 097202 (2005) https://doi.org/10.1103/PhysRevLett.95.097202
25. R. Higashinaka, Y. Maeno, Phys. Rev. Lett. **95**, 237208 (2005) https://doi.org/10.1103/PhysRevLett.95.237208
26. H. Sato, K. Matsuhira, T. Tayama, Z. Hiroi, S. Takagi, T. Sakakibara, J. Phys.: Condens. Matter **18**, L297 (2006) https://doi.org/10.1088/0953-8984/18/22/L04

Chapter 6
Topology of the Vacuum

L. D. C. Jaubert

Abstract Before being known for the emergence of monopoles, spin ice draw the attention of the community for its extensively degenerate ground state. We have seen in previous chapters how a Coulomb gauge field emerges from the coarse-graining of this ground state. It is the goal of this chapter to connect this field-theory picture with its topological nature. In this context, spin ice is a three-dimensional vertex model, divided into topological sectors. Topological sectors are connected between each other via string updates. These strings may become the intrinsic excitations of exotic phase transitions when the degeneracy of the Coulomb phase is lifted, and can be mapped onto world lines for bosons in the corresponding quantum problem in (2+1) dimensions. As an alternative point of view, we will also discuss how the spin-ice ground state is equivalent to a fully packed loop model, whose statistics is reminiscent of critical percolation and Brownian motion in two and three dimensions respectively.

6.1 The Vacuum is Not Empty

6.1.1 A 6-Vertex Model

We know from the previous chapters that spin ice is modelled by Ising spins on the pyrochlore lattice, made of corner-sharing tetrahedra. It means there are $2^4 = 16$ possible configurations per tetrahedron, as illustrated in Fig. 6.1. Ferromagnetic nearest-neighbour coupling favours the six "2 in - 2 out" states forming the extensive ground-state ensemble of spin ice [1, 2].

L. D. C. Jaubert (✉)
CNRS, LOMA, University of Bordeaux, Bordeaux, France
e-mail: ludovic.jaubert@u-bordeaux.fr

M. Udagawa and L. Jaubert (eds.), *Spin Ice*, Springer Series in Solid-State Sciences 197,
https://doi.org/10.1007/978-3-030-70860-3_6

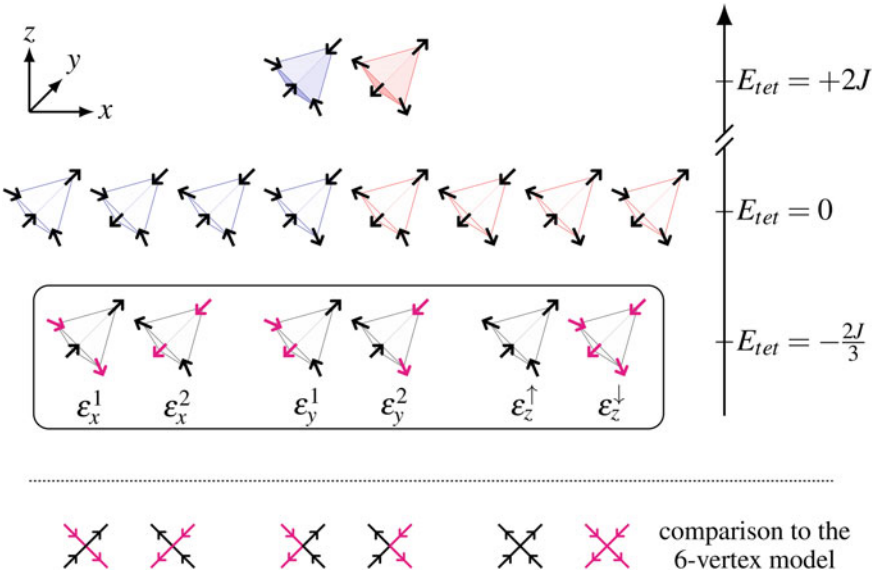

Fig. 6.1 Top: the 16 spin-ice configurations with six vacuum ground states (grey), eight first excited states with charge ± 1 (light blue/red) and two highly excited states with charge ± 2 (blue/red). The blue/red colours correspond to the positive/negative sign of magnetic charges. This chapter will mostly focus on the six "2 in - 2 out" states (grey), paired by time-reversal symmetry $\{\varepsilon_x, \varepsilon_y, \varepsilon_z\}$. The latter pair is split into up and down in anticipation of Sect. 6.3. The magenta spins correspond to the strings as defined in Fig. 6.2. The vertical axis on the right is the energy per tetrahedron due to the nearest-neighbour ferromagnetic coupling J. The cubic axes are given in the top left corner. **Bottom: the two-dimensional 6-vertex model.**

Each 2 in - 2 out state can be seen as a vertex, sitting at the centre of the tetrahedron, with two arrows pointing inwards and two arrows pointing outwards. The spin-ice ground state is thus the three-dimensional (3D) version of the venerable 6-vertex model. Historically, the 6-vertex model was motivated by the work of Slater on the ferroelectric KH_2PO_4 [3]. It was later brought into two dimensions (2D) where analytical methods are possible beyond mean field. It has been solved exactly in 2D in a series of paper by Lieb [4, 5] and Sutherland [6, 7]. For an overview of the problem, we refer to Baxter's famous textbook [8].

Moving back from two to three dimensions has qualitative consequences. For example, the six vertices are paired by time-reversal symmetry (Fig. 6.1). In 3D, each vertex carries a finite magnetisation along the x, y or z cubic axis. However, in absence of a third dimension, one of the pair of the 2D 6-vertex model becomes antiferromagnetic, and thus inequivalent to the other two (see the central pair at the bottom of Fig. 6.1). As explained in Chaps. 15 and 16, this difference has important consequences for two-dimensional realisations of spin ice, in artificial lattices [9, 10]. There, long-range dipolar interactions lift the 2 in - 2 out degeneracy in favour of these two antiferromagnetic vertices. Extensive degeneracy is recovered by an offset

in height between the vertical and horizontal lines of nano-islands [10, 11] or by using intervening nano-disks as interaction modifiers [12]. In 3D, the degeneracy of the Coulomb phase is only weakly lifted by magnetic dipolar interactions, thanks to projective equivalence (see Chap. 3 and [13]). This is why in this chapter, long-range interactions will be mostly ignored.

Some of the fundamental differences between the statistical properties of the Coulomb phase in two and three dimensions will be discussed in details in Sect. 6.2. But before that, a few definitions are necessary. In particular, what do we mean by *topology* in spin ice?

6.1.2 Stochastic Worm Dynamics

What kind of dynamics is allowed in the Coulomb phase? A single spin flip is forbidden as it would break the local ice rule . But a closed chain of spins pointing alternatively "in - out - in - out ..." can be flipped without creating any excitations. This move is called a *worm*. The smallest worm on the pyrochlore lattice is illustrated by the orange dashed hexagon in Fig. 6.2. The left/right panels of the figure are interchangeable by flipping the six spins of the worm, at no energy cost.

The name "worm" comes from the eponymous algorithm using this dynamics to decorrelate ice models in Monte Carlo simulations [14]. The worm algorithm has been introduced in the context of spin ice in [15, 16]. In practice, a worm is initiated

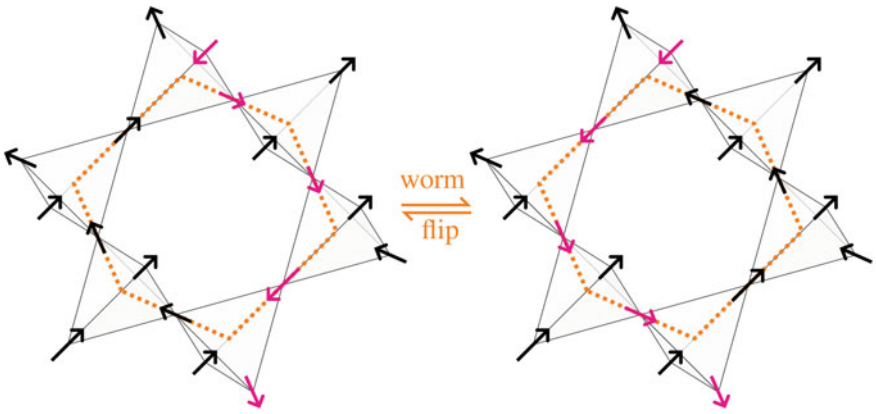

Fig. 6.2 Worms and strings are made of a chain of spins pointing alternatively "in - out - in - out ..." such that flipping them does not break the ice rules. The dashed orange hexagon is an example of the smallest worm on the pyrochlore lattice. The line of magenta spins represents a portion of a string, made of spins pointing down, and going through the entire system from top to bottom. The hexagonal worm flip corresponds to a fluctuation of the string. While the number of strings in a configuration defines its topological sector, non-winding worms allow for fluctuations within a given topological sector

by choosing a spin at random on the lattice, which necessarily points inside a given tetrahedron. The worm then propagates by exiting this tetrahedron through one of the two outward spins with probability p. Again, this second spin necessarily points inside a second tetrahedron. The process is then repeated until, eventually, the worm closes on itself. If it closes on the initial spin, then it is called a long worm. If it closes on an intermediate spin, with the dangling part being erased from the worm, then it is called a short worm. A worm is thus inherently stochastic; at each step, it has to choose between two possibilities in order to move from one tetrahedron to the next. For the nearest-neighbour spin-ice model, in absence of any perturbations, the probability p is equal to $1/2$ and is the same for all steps. In presence of a perturbation, the six vertices are not equivalent anymore, and p will take a different value depending on the local spin environment [14, 17, 18]. This way, the Monte-Carlo condition of detailed balance can be imposed at each step. The algorithm is thus (mostly) rejection free, and is called a *directed* worm algorithm. In the ordered phases of topological phase transitions (see Sect. 6.3), detailed balance often requires the additional possibility of backtracking, i.e. to be able to go back to the tetrahedron visited at the previous step. This backtracking is an algorithmic consequence of the absence of string excitations, in the thermodynamic limit, below the critical point of certain transitions.

In the literature, the worm algorithm is also commonly referred to as a loop algorithm. In this chapter, we will be careful not to mix the two terms—worms and loops—because the notion of loops will be reserved to a different kind of degrees of freedom, presented in Sect. 6.2. The concept of directed worm algorithms is also used in Quantum Monte Carlo, allowing for efficient simulations across parameter space (see e.g. [19] and Chap. 10).

Beyond their numerical aspects, worms can be seen as a vector field of the magnetisation. Because they are always closed in the ground state of spin ice, they respect the condition of zero-divergence, supporting the emergence of a Coulomb gauge field theory (see Chap. 3 and [20]).

To make connection with topology, one needs to make a distinction between winding and non-winding worms. These terms are properly defined for a system with periodic boundary conditions (Fig. 6.3a, b). A non-winding worm is a one-dimensional object that can be continuously deformed into something vanishingly small in all dimensions. The hexagon of Fig. 6.2 is a simple example, but more complicated, non-winding worms are possible. A non-winding worm may pass through a boundary of the system, as long as it "comes back". In other words, if we copy enough images of the system via the periodic boundary conditions, a non-winding worm will always eventually close on itself and has a finite size. A winding worm on the other hand shall never close and will extend to infinity. This is where the topology makes an apparition, since we have the possibility to define objects that are preserved under continuous deformations. However, worms are stochastic. They can be studied as emergent one-dimensional degrees of freedom, but the arbitrariness of their construction makes it difficult to use them as a property of a given spin configuration. To solve this problem, we will need to introduce a more deterministic variant of the worms: the strings.

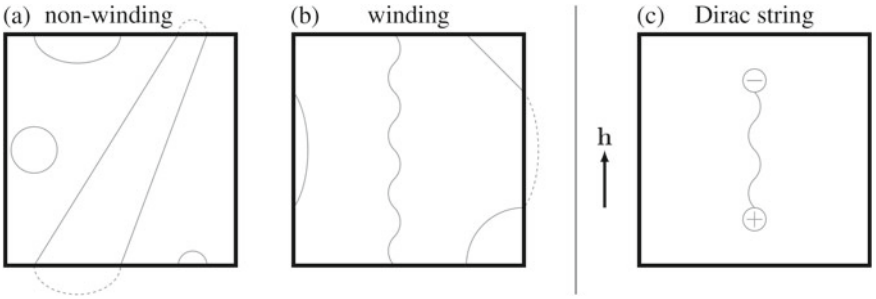

Fig. 6.3 (a) Winding and (b) non-winding one-dimensional degrees of freedom. Two examples are given per box (thin solid lines), with the images due to periodic boundary conditions represented by dashed lines out of the boxes. The definition of "(non-)winding" is valid for worms and loops. (c) In a strong [001] magnetic field **h**, all spins point up. In this set up, a **Dirac string** is a portion of a regular string ending on two topological charges. The two charges are confined because the Zeeman energy cost of the Dirac string is proportional to its length

6.1.3 Topological Sectors Made of Fluctuating Strings

The best way to understand the topological sectors in spin ice is probably by starting with a fully magnetised state. Let's say that all spins point up, along the [001] axis, i.e. all vertices correspond to $\varepsilon_z^{\uparrow}$ in Fig. 6.1. If we define m_z as the magnetic order parameter along the [001] axis, then we have a saturated configuration with $m_z = +1$. Starting from this configuration, it is easy to see that the only move respecting the ice rule is a worm crossing the entire system from top to bottom. The winding lines of Fig. 6.3b are schematic examples of this kind of non-local move, which we shall call a *string*. Within our convention, a string is made of spins pointing down. The fact that the string scales linearly with the system size makes the fully magnetised state a topological sector by itself, corresponding to a vacuum of strings.

Topological sectors in spin ice are defined by their winding number, w_z, i.e. the number of strings they contain along the z direction. It is important to understand that a string is a deterministic object. For any given spin configuration, it is possible to determine a unique ensemble of strings by colouring all the vertices of the system as done for the 2 in - 2 out states of Fig. 6.1; the downward magenta spins form the strings. The only arbitrary choice would be for the $\varepsilon_z^{\downarrow}$ vertex where two strings are crossing. This distinction is usually irrelevant but if necessary, it can easily be imposed by choosing a convention. A string always goes "straight" from top to bottom, moving from a (001) layer to the next one just below. Of course, as long as time-reversal symmetry is respected, it is equivalent to consider strings made of upward spins and the saturated configuration with $m_z = -1$ as a vacuum. But once this choice is fixed, there is a one-to-one mapping between spin and string configurations.

To put this definition in practice, let us consider a system made of $L_x \times L_y \times L_z$ cubic unit cells (see Fig. 6.6b for the definition of a cubic unit cell). The total number

of sites is $N = 16L_xL_yL_z$ and a string is made of $4L_z$ spins, i.e. exactly the number of layers of spins in the [001] direction. To go from one saturated state to its time-reversal symmetric, one needs to flip $4L_xL_y$ strings. The relation between the winding number and magnetisation is

$$m_z = 1 - \frac{w_z}{2L_xL_y} \tag{6.1}$$

Since (6.1) is valid in all three directions, the above equation can be written in vector form

$$\mathbf{m} = \begin{pmatrix} 1 \\ 1 \\ 1 \end{pmatrix} - \frac{1}{2L^2}\mathbf{w} \,. \tag{6.2}$$

Topological sectors and magnetisation are thus equivalent concepts in the Coulomb phase of spin ice. From (6.2) transpires the fact that the winding numbers $\{w_x, w_y, w_z\}$ are not independent from each other. For example if $w_z = 0$, then $w_y = w_z = 2L_xL_y$ since $|\mathbf{m}| \leqslant 1$. An interesting property of the topological sectors is that a cut along a (001) layer directly indicates w_z, by counting how many spins are pointing down in the layer. Equation (6.1) then immediately gives m_z. Taking advantage of the topology of the spin-ice ground state, it is thus possible to calculate the magnetisation, $\mathbf{m}$, of a given spin configuration by measuring a quantity of size $\mathcal{O}\left(N^{2/3}\right)$, instead of the usual $\mathcal{O}(N)$.

Since non-winding worms do not carry any magnetisation, they cannot change the topological sector. On the other hand their dynamics correspond to the fluctuation of strings, as illustrated in Fig. 6.2 for an hexagonal worm. From a dynamical point of view, in absence of winding worms, the system can be considered as topologically ordered, since it cannot evolve between different topological sectors. There is thus topological ergodicity breaking [21], making contact with the glassiness of classical topological systems that has been observed even in absence of structural disorder [22, 23]. We won't go into the details here since two chapters of this book (4 and 7) are dedicated to the dynamics of spin-ice materials. But we shall conclude this section by mentioning the mediating source of dynamics in real materials, namely the topological charges.

6.1.4 Topological Charges Out of the Vacuum

Excitations out of the spin-ice ground state are point-like topological defects (Fig. 6.1). Worms can terminate on these charges, which serve as sources or sinks of the vector field carried by the worms. The topological nature of these defects comes from the fact that the vector field emerging from them cannot be removed by continuous deformations. As a consequence, the Gauss' law confers a gauge charge

to these defects, that can only take a discrete set of values: ± 1 and ± 2. Neutrality of the system imposes in spin ice that the charges are created and annihilated by pairs. To move around in the system, the defects must modify the surrounding vector field, thus imposing constraints on the spin configurations. This has consequences on the entropy of the configuration, inducing an entropic Coulomb potential between the topological defects [24, 25].

In presence of magnetic dipolar interactions, an effective magnetic charge is attached to the topological defects [26]. The magnetic charge is not quantised though; hydrostatic or chemical pressure can modify its numerical value [27]. Since the magnetic charges derives from the three-dimensional dipolar interaction between spins, the resulting magnetic Coulomb potential is always three dimensional, even in planar artificial spin ice. On the other hand, the entropic Coulomb potential between the gauge charges depends on the dimension of the lattice: logarithmic in 2D and $1/r$ in 3D. Remarkably, in presence of a weak non-magnetic dilution of the lattice, impurity sites can be seen as "ghost spins" [28] on top of an unperturbed 2 in - 2 out configuration. These ghost spins interact with the rest of the system via dipolar interactions of energetic (magnetic) and entropic origins (see Chap. 3).

From a practical point of view, the topological charges mediate the dynamics of the system in spin-ice materials [29]. The creation, propagation and annihilation of a pair of charges is indeed equivalent to the dynamics of a worm. It has further been shown in Monte Carlo simulations that a very diluted, but finite, density of charges was enough to equilibrate the system down to very low temperatures, even in absence of a dedicated worm algorithm [30].

To conclude, let us consider a given spin configuration with a unique pair of topological charges. Since the construction of worms is stochastic, it is always possible to define several "in - out - in - out ..." paths to connect the two charges. However, if there is an external perturbation fixing a preferred (cubic) axis—say a magnetic field $\mathbf{h}$ along the [001] direction—then the portion of string connecting these two charges can be defined in a unique way, as illustrated in Fig. 6.3c. This portion of string is the minimum distance between the two defects, and represents the confinement of these topological excitations due to the magnetic field [26, 31]; to separate a pair of charges cost an energy proportional to its length. This portion of string is a classical analogue of a Dirac string [26] and has been observed in Fourier space via neutron scattering measurements [32].

6.2 Loop Statistics of the Coulomb Phase

In the next section, we will study how topological sectors can be manipulated via external perturbations, inducing unconventional phase transitions. But before that, let us describe the intrinsic properties of the 2 in - 2 out ensemble of states by considering another type of one-dimensional degrees of freedom that has not been mentioned so far: the loops.

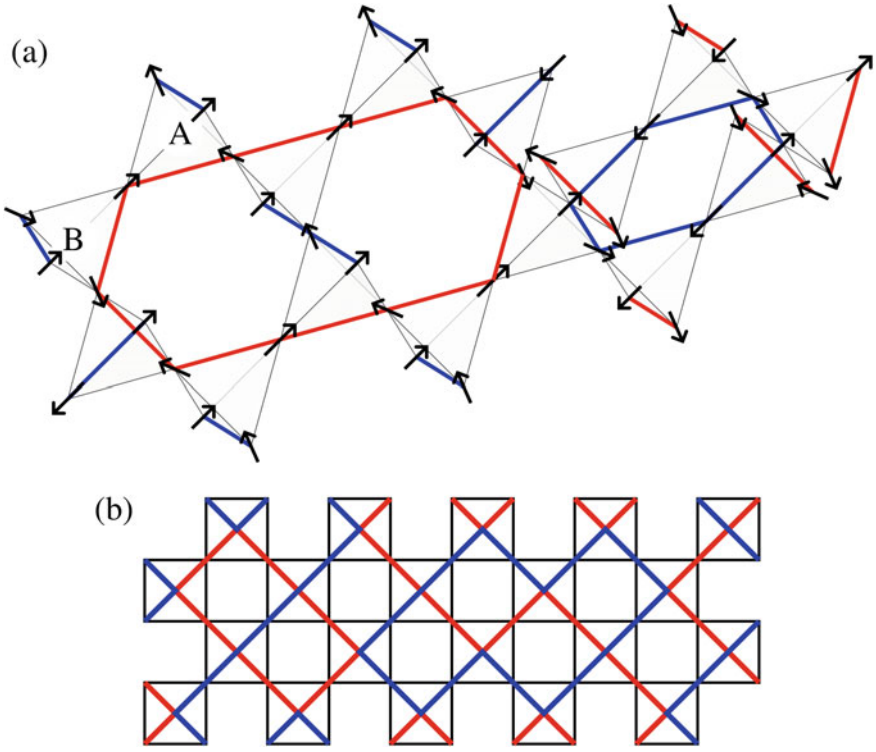

Fig. 6.4 Loops: (a) The centres of tetrahedra form a bipartite (diamond) lattice made of A and B tetrahedra sublattices. Connecting together all the spins pointing inside a A tetrahedron form extended one-dimensional degrees of freedom, coloured in red here. In absence of topological defects, these 1D structures necessarily close on themselves, forming *loops*. The red loops occupy half of the lattice, the other half supporting blue loops made of outward spins. Once the colouring choice is fixed, there is a one-to-one mapping between the corresponding spin- and loop-configurations. (b) The same mapping is valid in two dimensions on the checkerboard lattice

As opposed to worms and strings, loops do not follow an "in - out - in - out ..." structure. They are defined by connecting on one hand all the inwards spins together (the red loops of Fig. 6.4a) and on the other hand all the outwards spins (the blue loops of Fig. 6.4a). This definition of in/out spins is necessarily done with respect to a given tetrahedron sublattice (A or B). Once this arbitrary choice of sublattice is fixed—which is irrelevant to the physics—there is a bijective mapping between the red/blue loop configuration and the underlying spin configuration. The same definition can be applied to the checkerboard lattice (Fig. 6.4b)

The definition of loops is thus deterministic, as opposed to the stochastic construction of worms. The statistics of loops offers an alternative description of the spin-ice ground state, away from the more traditional Coulomb gauge field theory.

In the rest of this section, let us consider a system with periodic boundary conditions and $N = 4L^2$ sites in 2D and $16L^3$ sites in 3D. Most of the numerical results

presented in this section come from [33]. The Coulomb phase is often described as "critical", because of its algebraic spin-spin correlation. In the language of loops, this criticality takes the form of power-law distributions $\mathscr{P}(\ell)$ of the loop length ℓ [33] (Fig. 6.5a, c). To understand this behaviour, let us start with the two-dimensional case.

6.2.1 Loops in Two Dimensions

On the 2D checkerboard lattice, the Coulomb phase maps onto a two-flavour fully packed loop model (FPL^2) on the square lattice [34] (Fig. 6.4b). The two flavours are the red and blue loops, and the full compactness is due to every vertex of the square lattice being occupied by a loop. If $\mathscr{C}_b$ and $\mathscr{C}_r$ are respectively the total number of blue and red loops in a given configuration, the FPL^2 is characterised by two fugacities n_b and n_r giving a weight, $(n_b^{\mathscr{C}_b}\, n_r^{\mathscr{C}_r})$, to this configuration in the partition function. In the present case applied to the Coulomb phase, all configurations are equivalent, independently of the number of loops $\mathscr{C}_b$ and $\mathscr{C}_r$. It means that $n_{\text{blue}} = n_{\text{red}} = n = 1$. At this special point, it is also possible to consider the system as a fully packed loop model with one flavour of loop (FPL) and fugacity $n = 1$ [35]. For $n \leqslant 2$, the FPL is critical [34] with a scaling invariance of $\mathscr{P}_{2D}(\ell)$, as observed in Fig. 6.5a. Powerful analytical methods are available for scaling-invariant problems in 2D, such as the Coulomb gas approach. This method offers an exact calculation of the exponent $\tau = 2 + 1/7$ of the power law, $\mathscr{P}_{2D}(\ell) \sim \ell^{-\tau}$ [34–36], consistent with Monte Carlo simulations, $\tau = 2.14 \pm 0.01$, (Fig. 6.5a). More precisely, the loop-length distribution of non-winding loops follows

$$\mathscr{P}_{2D}(\ell) = A\,\frac{L^2}{\ell^\tau} \;\Leftrightarrow\; \mathscr{P}_{2D}(\ell)\; L^{D_f} = A\,\left(\frac{L^{D_f}}{\ell}\right)^{\tau}\,, \tag{6.3}$$

where A is a constant of order $\mathscr{O}(1)$ and $D_f = 2/(\tau - 1) = 7/4$ is the fractal dimension of the loops D_f [37, 38]. The value of $7/4$ is consistent with the scaling of the radius of gyration for non-winding loops (see the solid black line in Fig. 6.5b). In simulations, the radius of gyration is measured as,

$$R \equiv \left\langle \sqrt{\frac{1}{\ell}\sum_{i=1}^{\ell}(\mathbf{r}_i - \bar{\mathbf{r}})^2} \right\rangle \;\propto\; \ell^{1/D_f}\,, \tag{6.4}$$

where $\langle ... \rangle$ is the statistical average, $\mathbf{r}_i$ is the position of site i inside a loop of length ℓ, and

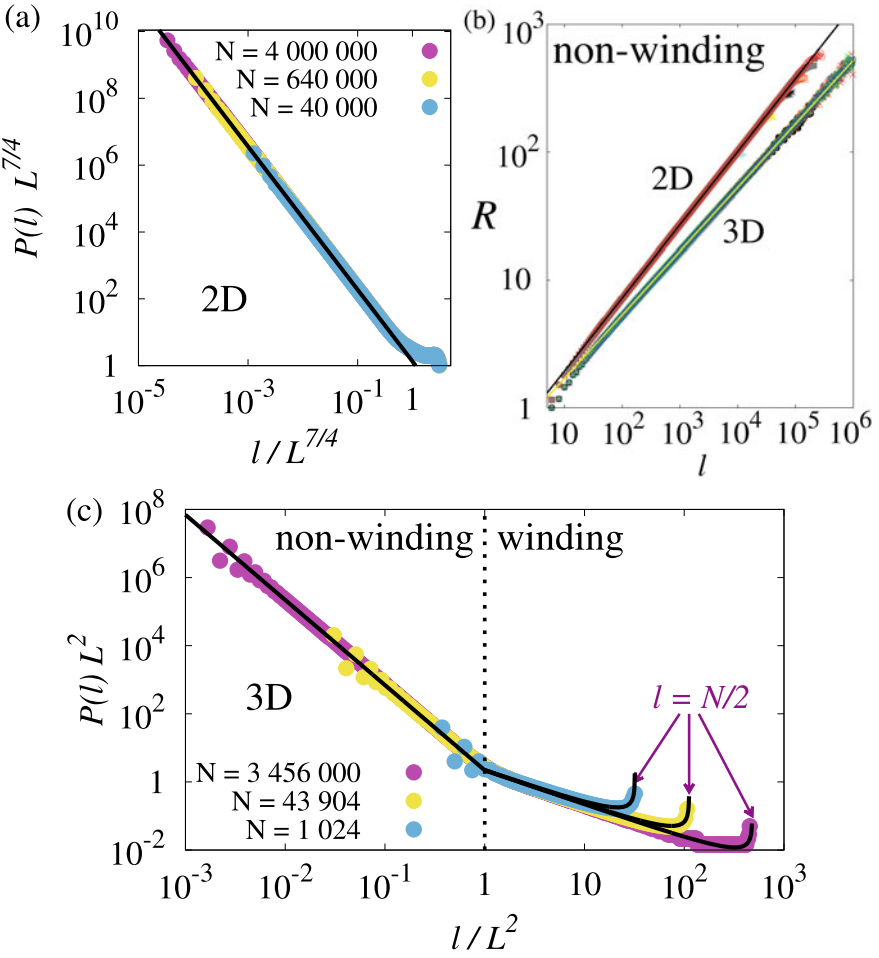

Fig. 6.5 Loop statistics: (b) The fractal dimension of the non-winding loops, $D_f = 7/4$ in 2D and $D_f = 2$ in 3D, is given by the scaling of the radius of gyration R (6.4). Up to $\ell \lesssim L^{D_f}$, the loop-length distribution, $\mathscr{P}(\ell)$, follows a scaling behaviour for non-winding loops: (a) $\ell^{-(2+1/7)}$ on checkerboard and (**c**) $\ell \lesssim L^2$ on pyrochlore. Above $\ell \gtrsim L^{D_f}$, the distribution is dominated by winding loops. It gives rise to a small deviation in 2D (**a**), but develops into an entire different scaling law in 3D (**c**); $\mathscr{P}_{3D}(\ell) \sim \ell^{-1}$, followed by a divergence at $\ell = N/2$. Panels (**a**, **c**) have been adapted from [33] with permission of the American Physical Society.

$$\bar{\mathbf{r}} \equiv \frac{1}{\ell} \sum_{i=1}^{\ell} \mathbf{r}_i \ , \tag{6.5}$$

is the geometrical centre of the loop.

A global picture starts to emerge. Since $\mathscr{P}_{2D}$ scales like L^2 for a given loop length ℓ (6.3), we have an extensive number of loops whose length distribution scales like

a power law. While power laws are usually characterised by an absence of length scale, the fact that $\tau > 2$ means that the average loop length does not diverge [36]. On the contrary, it quickly converges to a non-trivial value, $\langle \ell \rangle_{2D} \approx 24.7$. As for the fractal dimension, one could have naively expected a similarity with self-avoiding walks (SAW), $D_f^{\mathrm{SAW}} = 4/3$, since loops never intersect themselves, nor cross another loop of the same colour. The value $D_f = 7/4$ is nevertheless the one of the hull of clusters at critical percolation [37]. To rationalise this, one needs to realise that for any configuration in the Coulomb phase, the ensemble of bonds in the system is precisely divided into two halves: red and blue. This corresponds to the critical value of bond percolation on the square lattice. Of course, the FPL^2 model is more complexed than percolation. However, it has been argued that neither short-range nor sufficiently rapidly decaying algebraic correlations influence the exponents of critical percolation [39]. Based on this argument, the $1/r^2$ correlations of the Coulomb phase are marginal, with an anisotropy making them vanish in some directions [20, 40]. This might tip the influence of correlations towards irrelevance (up to possibly small logarithmic corrections) and explain why we find the same fractal dimension as for critical percolation.

The analogy to percolation raises an interesting parallel. For a square system at criticality, the number of percolating domains is of order $\mathcal{O}(1)$. Here, the analogues of percolating domains would be winding loops, crossing the system from one side to the other. Their number is indeed, on average, 1.86 ± 0.01 per configuration, independently of the system size $L \gg 1$ [33]. Winding loops are responsible for the deviation at $\ell \sim L^{7/4}$ away from the power law in the loop-length distribution (Fig. 6.5a). However, the distribution of winding loops continues to scale like $\ell / L^{7/4}$. It means that the fraction of the system occupied by winding loops vanishes like $L^{7/4}/L^2 = L^{-1/4}$ in the thermodynamic limit. This scenario is fundamentally different in three dimensions.

6.2.2 Loops in Three Dimensions

While the two-dimensional distribution is clearly dominated by the universal behaviour of non-winding loops for $n = 1$, the 3D loop-length distribution is divided into three distinctive parts (Fig. 6.5c) [33, 41]:

$$\ell \lesssim \lambda \approx 20 \Rightarrow \mathscr{P}_{3D}(\ell) \text{ is non-universal, due to the lattice mesh,} \tag{6.6}$$

$$\lambda \ll \ell \lesssim L^2 \Rightarrow \mathscr{P}_{3D}(\ell) = B \, \frac{L^3}{\ell^{5/2}} \, , \tag{6.7}$$

$$L^2 \lesssim \ell \lesssim L^3 \Rightarrow \mathscr{P}_{3D}(\ell) = B' \, \frac{1}{\ell \sqrt{1 - \dfrac{\ell}{N/2}}} \, . \tag{6.8}$$

The first part is fairly small, $\ell \lesssim \lambda \approx 20$. Here, $\mathscr{P}_{3D}(\ell)$ oscillates around the scaling law of (6.7). This oscillation is non-universal, and is due to the fact that the pyrochlore lattice favours loops of length $\ell \in \{6, 10, 14, ...\}$ over loops of length $\ell \in \{8, 12, 16, ...\}$. Since the system is fully packed, this difference of behaviour may be rationalised from the point of view of their excluded volume. The former kind of loops are (mostly) planar, as illustrated for $\ell = 6$ and 10 in Fig. 6.4a, while the latter kind necessarily has to bend. For example, loops $\ell = 10$ can be crossed by a loop of a different color, which is impossible for $\ell = 8$. From this point of view, the excluded volume of the latter is larger than for the former, which might be the reason for this oscillation. As ℓ increases, it becomes statistically less and less likely for loops to remain flat; most of the loops occupy a finite volume and the oscillations disappear. The non-universal behaviour is also visible for the scaling of the radius of gyration which deviates from the power law for small ℓ (Fig. 6.5b). Being a feature of the pyrochlore lattice, other 3D Coulomb phases are not expected to show the same behaviour. $\mathscr{P}_{3D}(\ell)$ should probably be labeled $\mathscr{P}_{\text{pyro}}(\ell)$ when referring to the oscillations for $\ell \lesssim \lambda \approx 20$.

Influence of the microscopic details of the lattice also exist in 2D. They are unnoticeable at the naked eye in Fig. 6.5a, but a small deviation from the power law is visible in the radius of gyration for small ℓ (Fig. 6.5b).

The second part of the loop-length distribution corresponds to the scaling of non-winding loops (6.7). In 3D, their radius of gyration gives a fractal dimension $D_f = 2$ (Fig. 6.5b), i.e. the same as for a Brownian motion (BM) even though loops are self avoiding. Remarkably, the passage from $D_f = 7/4$ in 2D to $D_f = 2$ in 3D is the same as for polymer solutions at the θ point [42]. Arguments from polymer physics justify that in a dense solution in 3D, the presence of other polymers may counteract the self-avoidance, giving rise to BM universality. The apparition of Brownian physics provides a continuum framework for the scaling of (6.7) [43]. In 3D, the probability for a BM to go from $\mathbf{r}_0$ to $\mathbf{r}$ after ℓ steps is

$$p(\mathbf{r}_0, \mathbf{r}; \ell) = \frac{1}{(2\pi\ell)^{3/2}} \exp\left[-\frac{(\mathbf{r}-\mathbf{r}_0)^2}{2\ell}\right]. \tag{6.9}$$

The probability to close the loop, i.e. $\mathbf{r} = \mathbf{r}_0$, is $(2\pi\ell)^{-3/2}$. Summing over all possible starting positions, $(\times N)$, and accounting for the arbitrary starting position along the loop of size ℓ, $(\times 1/\ell)$, the loop-length distribution of non-winding loops is

$$P_{3D}^{\text{nw}}(\ell) \approx \frac{N}{\ell}\frac{1}{(2\pi\ell)^{3/2}} \sim \frac{L^3}{\ell^{5/2}} \tag{6.10}$$

However, a loop of length $\ell \sim L^2$ has a radius of gyration, $R \sim \ell^{1/D_f} \sim L$. In a system with periodic boundary conditions, it means loops of length $\ell \gtrsim L^2$ start to see themselves on the other side of the system, forming winding loops. Let us consider a BM starting at site $\mathbf{r}_0$ and closing in a mirror image of the system at distance $\mathbf{r}_0 + \mathbf{n}L$ where $\mathbf{n} = (n_x, n_y, n_z) \in \mathbb{Z}^3$ are the Cartesian coordinates of the

mirror image in units of the linear system size L. The distance travelled by the BM is $\sqrt{n_x^2+n_y^2+n_z^2}\,L$. Using (6.9), the probability for the BM to close at $\mathbf{r}_0$ in the original system (non-winding) or in a mirror image (winding) is

$$\sum_{n_x,n_y,n_z=-\infty}^{\infty} \frac{\exp\left[-\frac{(n_x^2+n_y^2+n_z^2)\,L^2}{2\ell}\right]}{(2\pi\,\ell)^{3/2}} = \left(\sum_{n=-\infty}^{\infty} \frac{e^{-\frac{n^2\,L^2}{2\ell}}}{\sqrt{2\pi\,\ell}}\right)^3 \approx \frac{1}{L^3}\,. \tag{6.11}$$

Again, summing over all starting positions, modulo the arbitrariness within a loop, $(\times N/\ell)$, the loop-length distribution of (mostly) winding loops is $P_{3D}^{\rm w}(\ell) \sim 1/\ell$, which is the leading term of (6.8). The physics of Brownian motion thus accurately explains the two scaling laws of Fig. 6.5c and their crossover at $\ell \sim L^2$. Colloquially speaking, the loops of our model "want" to be of fractal dimension 2. On one hand, there is not enough space in 2D, which is why the fraction of winding loops disappear and the fractal dimension is smaller, $D_f = 7/4$. On the other hand, the extra dimension in 3D allows for the distribution of winding loops to spread. This behaviour is closely related to Pólya's theorem stating that a $D-$dimensional random walk is recurrent for $D \in \{1, 2\}$ and transient for $D \geqslant 3$.

However, the $1/\ell$ scaling of the distribution does not account for the divergence at $\ell = N/2$ in Fig. 6.5c. This divergence is due to a vanishingly small number of winding loops occupying a finite fraction of the system: respectively 41%, 30% and 12% on average for the first, second and third longest loops in the system [33]. The non-mean-field correction to the winding-loop statistics is particularly non trivial and has been solved exactly in a *tour de force* by Adam Nahum et al. [41]. Using a combination of the O(n) σ model and replica methods, they have shown that this correction follows a Poisson-Dirichlet distribution proportional to $(1 - \ell/(f\,N))^{n/2-1}$, with n being the fugacity of undirected loops and f a non-universal constant of the model. In our model, one finds $f \approx 1/2$ because loops are limited to 50% of the system, due to their bi-colour. The divergence of the distribution is thus a consequence of the fugacity of the loops, $n = 1 < 2$.

With a logarithmic number, $\log L$, of winding loops occupying 93.7% of the system, and an extensive number, L^3, of non-winding loops confined in its complement, the average loop length $\langle\ell\rangle_{3D} = 227.5 \pm 0.5$ is an order of magnitude larger than in 2D, but remains remarkably finite. To give an order of magnitude, even for a system of $N \sim 8\,000\,000$ sites, the number of winding loops is around 7. Because of these gigantic loops occupying a finite fraction of the system, there is a finite probability for two spins to sit on the same loop, in presence of periodic boundary conditions [33]. This finite probability is responsible for partial antiferromagnetic long-range order in valence-bond states on bipartite lattices [44, 45].

To conclude, let us mention the role of these loops played in the dynamics of systems beyond classical spin ice. We have seen in the first part of this chapter that worms and strings are the natural paths for the propagation of topological charges. In

the charge ice [46, 47] and quantum spin ice [48] models, loops also play the role of an effective rail for the hopping of confined pairs of spinons. This dynamic has been dubbed a "leapfrog" move [48], and is non-ergodic since confined along a given loop. When spin ice, with collinear Ising spins, is coupled to itinerant electrons via a large Hund coupling, these loops also serve as natural paths for itinerant electrons [49–51]. As a feedback to the localised magnetism, the electron hopping induces a non-trivial fugacity to the loops. For systems with open boundaries, the winding loops break up into several filaments terminating on the surfaces, inducing conductivity.

6.3 Topological Phase Transitions

Up to now, we have considered that all configurations in the Coulomb phase are equivalent. It is now time to perturb the ground state of spin ice in order to lift its extensive degeneracy, and see what kind of phase transition takes place. In this section we will continue to consider that the nearest-neighbour coupling is much bigger than any other energy scale, i.e. all tetrahedra are 2 in - 2 out, even at finite temperature. This will have two immediate consequences. Firstly, transitions will often be topological in nature, naturally described in terms of topological-sector excitations. Secondly, the ice rule implies that the disordered phase at high temperature, above any eventual transitions, is not a standard paramagnet but a classical spin liquid with algebraic correlations. As studied in a family of classical and quantum dimer models [52–61], algebraic correlations in the disordered phase do not fit within the traditional Landau-Ginzburg-Wilson theory of phase transitions. It is this aspect we are going to explore in the context of spin ice, where our textbook intuition about critical phenomena loses its footing, and continuous/discontinuous transitions are not necessarily what they seem.

6.3.1 Repulsion Between Strings: The Kasteleyn Transition

Let us start with the influence of a magnetic field, **h**, in the [001] direction, favouring the fully saturated configuration with only $\varepsilon_z^{\uparrow}$ tetrahedra everywhere (Fig. 6.1).

$$\text{Tetrahedron energies in a [001] field:} \quad \varepsilon_z^{\uparrow} < \varepsilon_x = \varepsilon_y < \varepsilon_z^{\downarrow} \tag{6.12}$$

Since all symmetries of the Hamiltonian are broken by **h**, no critical points are *a priori* expected at finite temperature. This is where the topology of the Coulomb phase comes into play, inducing the so-called Kasteleyn transition [62]. This transition in spin ice has first been studied in 2D: on the checkerboard lattice as an idealised planar version of pyrochlore [63], and in a realistic experimental setting as a perturbation of the kagome-ice phase [64, 65], when the magnetic field is tilted away from the [111] direction [66, 67] (see Chap. 5 for a detailed discussion). Here we will focus on its

full three-dimensional version in a [001] field [17], whose fluctuations are directly related to the topological sectors defined in Sect. 6.1.3.

First of all, why is there a transition? Since the configuration with saturated magnetisation is a topological sector by itself, any relaxation out of this ground state requires a string excitation. The Zeeman energy per spin is $\pm h/\sqrt{3}$. For a system made of L_z cubic unit cells along the [001] direction and 4 layers of spins per cubic unit cells, the Zeeman energy cost of the string is $\delta U = 8L_z h/\sqrt{3}$. As illustrated by the magenta spins in Fig. 6.2, strings can fluctuate. To be more precise, a string alone in the system has two possibilities to propagate from one layer to the next; e.g. tetrahedra ε_x^1 and ε_y^1 have the same entry site (top layer) and two different possibilities to exit (bottom layer). This confers an entropic gain, $\delta S = 4L_z \ln 2$, to the string. The difference of free energy is [17]

$$\delta F = \delta U - T\delta S = 4L_z \left(\frac{2h}{\sqrt{3}} - T \ln 2 \right) \begin{cases} < 0 \text{ when } T > T_K \\ > 0 \text{ when } T < T_K \end{cases} \tag{6.13}$$

$$\text{with} \quad T_K = \frac{2h}{\sqrt{3} \ln 2} \, . \tag{6.14}$$

In the thermodynamic limit, $L_z \to +\infty$, string excitations are suppressed for $T < T_K$ ($\delta F \to +\infty$) and the system remains completely frozen with saturated magnetisation. For $T > T_K$, string excitations are possible ($\delta F \to -\infty$) and the system relaxes. When two strings meet in a given tetrahedron, the energy cost is the same but the entropic gain disappears; there is only one possible state, namely $\varepsilon_z^{\downarrow}$. Strings are entropically repulsive and an incremental value of the temperature is necessary to visit topological sectors of decreasing magnetisation. The magnetisation, m_z, is thus continuous at the transition.

Despite the apparent simplicity of the above argument, the value of the Kasteleyn transition temperature T_K is correct and has been confirmed numerically [17]. Because the upper critical dimension d_c of the Kasteleyn transition is $d_c = 3$ [68], thermodynamic quantities can be calculated via Husimi-tree calculations, up to logarithmic corrections, giving for the magnetisation

$$T < T_K : m_z = 1 \, , \tag{6.15}$$

$$T > T_K : m_z = \frac{\sinh(2\beta h)}{2 - \cosh(2\beta h)} \, , \tag{6.16}$$

as plotted in Fig. 6.6a. For $t \equiv (T - T_K)/T_K \to 0^+$, the magnetisation scales to first order $\mathcal{O}(t)$ as $m_z = 1 - \left(\frac{8}{3} \ln 2\right) t$. It means one can define the critical exponent $\beta = 1$ for $T > T_K$ and β'=0 for $T < T_K$, with no critical fluctuations at low temperatures. This asymmetry of criticality is the reason why the Kasteleyn transition is sometimes referred to as a $3/2-$order transition [69]; somewhere in between a first- and second-order transition

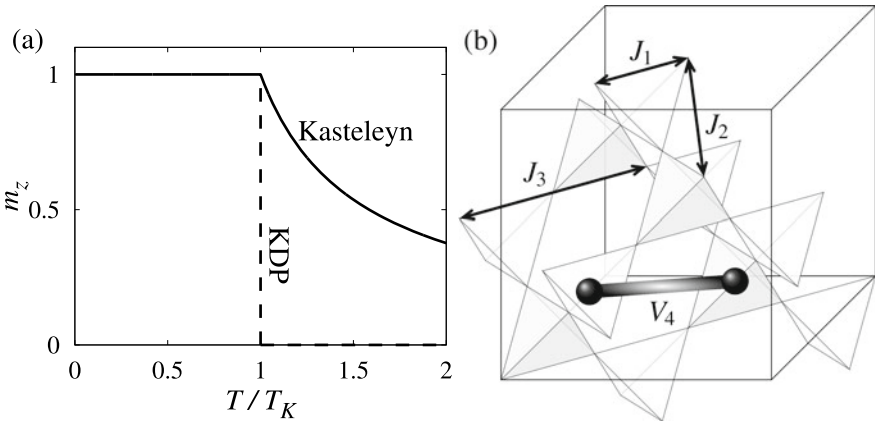

Fig. 6.6 (a) **Kasteleyn and KDP transitions**, where the magnetisation, m_z, is saturated below the transition, without any fluctuations. At T_K, m_z displays either a kink in a [001] magnetic field (Kasteleyn), or a discontinuous jump under uniaxial [001] pressure (KDP). In both cases, the high-temperature phase is adiabatically connected to the Coulomb phase with dipolar spin-spin correlations. (b) **A cubic unit cell of the pyrochlore lattice** is made of 16 sites (see the corners of the four dark tetrahedra). For each site, there are 6 first, 12 second and 6 third nearest neighbours. J_1, J_2 (resp. J_3) couple spins on different (resp. same) sublattices. While the third nearest-neighbour coupling across hexagons is not considered here (6.18) [70], the term V_4 of (6.20) couples the four-site magnetisation of tetrahedra sitting opposite from each other across hexagons [71]

As an elegant and complementary approach, strings can be treated as world lines for hard-core bosons, moving in the two-dimensional xy plane, with the $z-$direction taken as imaginary time [17, 72]. In the thermodynamic limit, the classical 3D Kasteleyn transition at finite temperature maps onto a zero-temperature 2D Bose-Einstein condensation. Since strings cannot terminate in the bulk—they cross the system from top to bottom—the number of bosons is conserved. The reduced temperature t plays the role of a chemical potential for bosons μ. The low-temperature, fully saturated, configuration corresponds to a vacuum of bosons for $\mu < \mu_0$, with condensation at $\mu = \mu_0$. In the Bose-Einstein condensate (BEC) for ($t > 0 \Leftrightarrow \mu > \mu_0$), there is a Goldstone mode resulting from the broken phase-rotation symmetry [72]. Interestingly, this off-diagonal long-range order of the BEC can be interpreted as deconfinement in the high-temperature Coulomb phase, responsible for the dipolar correlations betweens spins. However, as $\mu \to \mu_0^+$, the speed of sound in the condensate vanishes like $\sqrt{\mu - \mu_0}$ [72]. In the spin language, it means that the dipolar correlations evolve into a strongly anisotropic regime between the $z-$direction and the x, y plane. The two-point correlation function between a reference spin $\mathbf{S}_0$ and a spin $\mathbf{S}_i$ at position (x, y, z) becomes

$$C(r, z) = \langle S_0 \cdot S_i \rangle - \langle S_0 \rangle \langle S_i \rangle \propto \frac{1}{z} \exp\left(-\frac{r^2}{\rho\, z}\right) , \tag{6.17}$$

where $r = \sqrt{x^2 + y^2}$ and ρ is a microscopic length scale. This form reflects the dilution of strings at T_K^+. Once the contribution of the saturated magnetic background is subtracted, what remains is the string auto-correlation, characteristic of a 2D random walk propagating in time z.

The present analogy with world lines of bosons is remarkable on several fronts. First of all, (6.17) has been beautifully used in neutron scattering experiments as a signature of classical analogues of Dirac strings in the $Ho_2Ti_2O_7$ spin-ice materials [32] (see Chap. 8).

Also, as we discussed at the beginning of this section, the Kasteleyn transition is not a priori expected to obey the traditional Landau-Ginzburg-Wilson (LGW) theory of phase transitions. However, the BEC fits within this theory. The trick was to reverse the roles: the low-temperature ordered phase is now a vacuum, while the troublesome algebraic spin-spin correlations of the high-temperature Coulomb phase emerge from the off-diagonal long-range order of the BEC [72]. However, the quantum mapping in (2+1) dimension should not be considered as a general method to transform a non-LGW problem into "LGW friendly". For example, when applied to a specific classical dimer model on the cubic lattice, the quantum mapping gives rise to a non-LGW transition between a bosonic superfluid and a Mott insulator at fractional filling [59, 61].

The BEC mapping also provides a framework for the inclusion of topological charges. In the BEC analogy, these defects are generated by source terms for the boson operator. As a consequence, the phase-rotation symmetry is intrinsically broken and the Kasteleyn transition disappears [72]. Alternatively, in terms of renormalisation-group theory, the Kasteleyn transition is a confinement/deconfinement critical point. The loss of the transition in presence of topological charges means that the charge fugacity, $z = \exp[-\Delta E_c/T]$ where ΔE_c is the energy cost for a charge, is a relevant perturbation [73]. If $\Delta E_c/T_K$ is large but finite, the Kasteleyn transition becomes a sharp crossover, and the kink of the magnetisation at T_K is smoothed out [17, 74], comparing qualitatively well with experimental measurements on $Ho_2Ti_2O_7$ [75, 76] and $Dy_2Ti_2O_7$ [17, 77]. A careful scaling analysis shows that the logarithmic corrections are quickly washed out in presence of topological defects [74].

To conclude, one should mention that in presence of dipolar interactions, the fully saturated configuration enters in competition with the antiferromagnetic ground state of the dipolar spin ice model. This competition stabilises half-magnetisation plateau at intermediate values of the magnetic field [78–80].

6.3.2 Non-Repulsive Strings : KDP and 1st Order Transitions

An external magnetic field is not the only way to stabilise a fully saturated magnetic configuration. Here we will explore two other mechanisms, which do not break time reversal symmetry: further nearest-neighbour couplings [70] and uniaxial pressure [18].

In rare-earth pyrochlores, further neighbour exchange is usually considered negligible because of the short-range nature of the $4f$ orbitals. Precise analysis of neutron scattering measurements have nonetheless suggested that a weak ferromagnetic second-neighbour coupling is present in $Dy_2Ti_2O_7$ [81–83]. Also, in Tb-based pyrochlores, quantum fluctuations due to the presence of a low-lying singlet in the single-ion crystal field can be renormalised as effective classical J_2 and J_3 couplings [70, 84]. Here we will consider an interaction between second $\langle\langle ...\rangle\rangle$ and third $\langle\langle\langle ...\rangle\rangle\rangle$ nearest neighbours (Fig. 6.6b)

$$\mathscr{H}' = J_2 \sum_{\langle\langle i,j\rangle\rangle} \mathbf{S}_i \cdot \mathbf{S}_j + J_3 \sum_{\langle\langle\langle i,j\rangle\rangle\rangle} \mathbf{S}_i \cdot \mathbf{S}_j \tag{6.18}$$

where $\mathbf{S}_i$ are Ising spins parallel to their local easy axes. Within the 2 in - 2 out ensemble of configurations, J_2 and J_3 have the same effect, up to a prefactor [85]. Hence, all discussions can be made based on the J_3 interaction only. In particular, ferromagnetic couplings, $J_3 < 0$, lift the spin-ice ground-state degeneracy in favour of one of the six fully saturated configurations [70, 83, 86].

As for uniaxial pressure along the [001] direction, the resulting distortion lifts the 2 in - 2 out degeneracy at the level of each tetrahedron: (ε_z) versus $(\varepsilon_x, \varepsilon_y)$. The anisotropic shape of $4f$ orbitals makes it difficult to predict which one is expected to be the lowest in energy [87], but an analysis [18] of one of the rare experiments of a spin-ice material under uniaxial pressure [88] indicates that for $Dy_2Ti_2O_7$, such uniaxial pressure favours ε_z:

$$\text{Tetrahedron energies under [001] uniaxial pressure: } \varepsilon_z < \varepsilon_x = \varepsilon_y \tag{6.19}$$

with the energy difference $\Delta = \varepsilon_x - \varepsilon_z > 0$. Equation (6.19) corresponds to a special case of the 6-vertex model, namely the ferroelectric KDP transition [3, 5, 89]. The acronym KDP stands for potassium dihydrogen phosphate KH_2PO_4, one of the most venerable example of a ferroelectric material. Please note that [001] uniaxial strain tend to occur naturally in thin films grown in the [110] or [001] directions because of the lattice mismatch between the film and the substrate [90].

At low temperature, the same reasoning as for the Kasteleyn transition applies. The ground states correspond to different topological sectors, each of them made of a unique configuration. Any excitation respecting the ice rule requires a string update with an energy cost, δU, and an entropy gain, δS, diverging with system size. For the uniaxial distortion, $\delta U = 4L_z\Delta$ and $\delta S = 4L_z \ln 2$, giving a transition temperature at $T_{\text{KDP}} = \Delta / \ln 2$ (same calculations as in (6.14)). For the further-neighbour perturbation, the argument is more evolved since the J_3 term couples spins within the string. The propagation of the string is biased by this interaction and the entropy gain is not simply $\ln 2$ per layer. Nonetheless, the string fluctuates at finite temperature (the J_2, J_3 terms are finite) and the entropy gain of a single string scales with the system size L_z (the J_2, J_3 couplings are short range). Monte Carlo simulations have confirmed a first-order transition at finite temperature [70].

And here is the main difference with the Kasteleyn case: the transitions are discontinuous. This is because the uniaxial strain and further-neighbour coupling respect time-reversal symmetry. The high-temperature, disordered, phase is necessarily non magnetic, with $m_z = 0$. With a single phase transition separating the low- and high-temperature phases, the magnetisation must be discontinuous (Fig. 6.6a). By following a similar argument, Nagle has shown exactly the discontinuity of the KDP transition in any dimensions [91].

What does it mean in terms of strings? Once a first string has appeared in the sample at the transition temperature, a ferromagnetic J_3 interaction makes it easier to create a second string in its vicinity, making the strings attractive. In other words, once the system has reached the transition temperature with enough entropy to stabilise the first string, there is already enough thermal fluctuations in the system to create a second, third ... string. It is an avalanche effect, and the transition is first order.

For KDP, the transition is more subtle. The order parameter is discontinuous, but the transition is not first order. It is a multi-critical point of infinite order [18, 89, 92] with a flat free energy. From Landau theory, critical points of infinite order can be of two types [92]: infinitely smooth (e.g. the Berezinky-Kosterlitz-Thouless transition) or infinitely sharp, as is the case here. The criticality of the transition has been confirmed numerically by the extinction of the surface tension between domains. Its main consequence is that every topological sector becomes equivalent at the transition [18]. In the framework of the quantum counterpart model in (2+1) dimensions, this equivalence of topological sectors corresponds to an enhancement of symmetry from the U(1) Coulomb phase to the SU(2) KDP critical point. Interestingly, the two-point correlation function as $T \to T^+_{\rm KDP}$ is described by the same formula as in (6.17) for the Kasteleyn transition. This is because at the KDP critical point, the strings "do not see each other" and the auto-correlation of the string with itself dominates. Between Kasteleyn and KDP, the magnetic background surrounding each string is of course different, but is subtracted by the term, $(-\langle S_0\rangle\langle S_i\rangle)$, in (6.17), giving in the end the same correlation.

As mentioned earlier, the discontinuity of the transition is a consequence of the time-reversal symmetry of the Hamiltonian. However, this discontinuity is imposed only if there is a single phase transition. In presence of two (or more) transitions, an intermediate phase may connect the low-temperature saturated order with the high-temperature, non-magnetic, disordered phase. Stephen Powell has shown that such scenario was indeed possible [71] by perturbing the KDP transition via the following interaction

$$V_4 \sum_{[t,t']} \Theta(\mathsf{S}_t, \mathsf{S}_{t'}) \ , \tag{6.20}$$

where $\mathsf{S}_t = \sum_{i\in t} \mathbf{S}_i$ is the total magnetic moment of tetrahedron t and

$$\Theta(\mathsf{S}, \mathsf{S}') = \begin{cases} 1 & \text{if } \mathsf{S} = \mathsf{S}' = \pm 4/\sqrt{3}\ \mathbf{e}_z \\ 0 & \text{otherwise} \end{cases} \ ,$$

with $\mathbf{e}_z$ the unit vector along the $z-$direction. The sum of (6.20) runs over all pairs of tetrahedra sitting opposite to each other in hexagons, as illustrated in Fig. 6.6b. This new term adds a second energy scale to the problem, allowing for two separate ordering processes. For positive V_4, it hinders the onset of magnetisation imposed by the uniaxial distortion. This opens a finite region in temperature where the magnetisation is continuously increasing from zero at T_{c1} to saturation at T_{c2}. This intermediate region, $T_{c2} < T < T_{c1}$, is at the same time ferromagnetically ordered with $|m_z| > 0$, and a Coulomb phase whose topological excitations are deconfined and interact via an entropic Coulomb potential [71]. Such phase has been dubbed a Coulomb ferromagnet (CFM) in the context of the quantum spin ice Hamiltonian [93, 94], as will be discussed in Chaps. 9 and 12. The transition at T_{c1} is of the 3D Ising universality class with spontaneous $\mathbb{Z}_2$ symmetry breaking. Because of the dipolar correlations between spins, this transition might be at its upper critical dimension. At T_{c2} on the other hand, there is no symmetry breaking. We have a Kasteleyn transition between a long-range order with saturated magnetisation and a Coulomb phase with finite magnetisation.

6.4 Conclusion

In this chapter, we have reviewed how the emergence of extended degrees of freedom are related to the topological properties of spin ice. The 2 in - 2 out ground-state ensemble can be decomposed into topological sectors, separated from each other by extended strings of spins spanning the system. These strings carry a finite magnetisation and the winding vector associated to a topological sector is directly related to the magnetisation of the system (6.2). Fluctuations within a topological sector are done via non-winding worms, i.e. closed fluxes of spins carrying zero magnetisation. The spin-ice ground state is a vacuum for topological excitations. Each excitation carries a charge which can only take a discrete set of values, $\{\pm 1, \pm 2\}$, and is created and annihilated in pair of opposite sign. A charge alone cannot vanish by any continuous transformation of the system. From a more general point of view [95], the ground state of spin ice is topological in the sense that it is a disordered phase with non-trivial global properties—supporting a Coulomb gauge field—but without being described by a local order parameter.

In addition to worms and strings, which represent fluxes of magnetisation, another kind of one-dimensional degree of freedom can be defined: the loops. In this language, the Coulomb phase is a bi-colour fully packed loop model, FPL^2. Once the colour choice has been fixed, there is a bijective mapping between loop- and spin-configurations. The fractal dimension of loops is $D_f = 7/4$ in 2D (related to critical percolation) and $D_f = 2$ in 3D (related to Brownian motion), in analogy with the physics of polymer solutions at the θ point. The loop statistics in 2D and 3D are respectively dominated by non-winding and winding loops. Some of the winding loops in 3D occupy a finite fraction of the system, and their statistics follow a non-trivial Poisson-Dirichlet distribution.

The extensive degeneracy of the 2 in - 2 out ground state can be lifted by external perturbations. The resulting transitions are topological in nature, characterised by the effective interaction between string excitations:

- Kasteleyn transition in a [001] field ⇒ repulsion between strings
- KDP transition in a [001] uniaxial distortion ⇒ non-interacting strings
- 1st-order transition with 2nd and 3rd neighbour coupling ⇒ attraction between strings

Strings represents the world lines for bosons in the corresponding quantum problems in (2+1) dimensions, and their auto-correlation dominates the two-point correlation of the system as $T \to T_K^+$.

In the future, nano-lithography should be a useful experimental framework for the study of these phenomena in 2D, thanks to the recent realisation of the Coulomb phase in artificial square ice [11, 12]. As an intermediate step between two and three dimensions, the confinement of these topological sectors in a slab geometry opens the path for new properties in thin films of spin-ice materials [90, 96–100]. And of course, the realisation of a quantum spin ice would offer a coherent quantum dynamics for worms (see Chaps. 9, 10 and 12).

While the present chapter has focused on the 2 in - 2 out Coulomb phase of classical spin ice, we should conclude this chapter by mentioning a few other types of Coulomb phases. For example, as mentioned in Sect. 6.3.1, the kagome ice can be stabilised in the magnetisation plateau of spin ice in a [111] field, giving rise to a 2D Kasteleyn transition when the field is canted away from the [111] direction (see Chaps. 3 and 5). The kagome-ice phase is also expected at very low temperature in thermalised artificial lattices (see Chaps. 15 and 16). A different 3D Coulomb phase also appears in the dimer model on the diamond lattice [101–103], which has been discussed in the context of the magnetisation plateau observed in $HgCr_2O_4$ and $CdCr_2O_4$ [104–106].

This Coulomb phase on the diamond lattice corresponds to the emergent gauge field co-existing with the antiferromagnetic order in fragmented spin liquids [107]. Indeed, when a high density of single charges is imposed, an exotic phase is stabilised [30, 107]: half of the degree of freedom are long-range ordered, while the other half corresponds to a disordered Coulomb gauge field. This co-existence has been observed experimentally in $Nd_2Zr_2O_7$ [108], $Dy_3Mg_2Sb_3O_{14}$ [109], $Ho_2Ir_2O_7$ [110]... The topological properties of these systems remain for the time being poorly understood [25].

Acknowledgements I am especially grateful to Peter Holdsworth, Roderich Moessner and John Chalker, with whom many of the ideas discussed in this chapter have been developed. I also acknowledge insightful discussions with Claudio Castelnovo, Adam Nahum and Stephen Powell on these topics. I would like to thank the people in the Theory of Quantum Matter Unit in Okinawa where this book was initiated, and my colleagues at the "Laboratoire d'Ondes et Matière d'Aquitaine" in Bordeaux where it was concluded.

References

1. M.J. Harris, S.T. Bramwell, D.F. McMorrow, T. Zeiske, K.W. Godfrey, Phys. Rev. Lett. **79**, 2554 (1997). https://doi.org/10.1103/PhysRevLett.79.2554
2. A.P. Ramirez, A. Hayashi, R.J. Cava, R. Siddharthan, B.S. Shastry, Nature **399**, 333 (1999). https://doi.org/10.1038/20619
3. J.C. Slater, J. Chem. Phys. **9**, 16 (1941). https://doi.org/10.1063/1.1750821
4. E.H. Lieb, Phys. Rev. **162**, 162 (1967). https://doi.org/10.1103/PhysRev.162.162; Phys. Rev. Lett., **18**, 1046 (1967). https://doi.org/10.1103/PhysRevLett.18.1046; Phys. Rev. Lett., **18**, 692 (1967). https://doi.org/10.1103/PhysRevLett.18.692
5. E.H. Lieb, Phys. Rev. Lett. **19**, 108 (1967). https://doi.org/10.1103/PhysRevLett.19.108
6. B. Sutherland, C.N. Yang, C.P. Yang, Phys. Rev. Lett. **19**, 588 (1967). https://doi.org/10.1103/PhysRevLett.19.588
7. B. Sutherland, Phys. Rev. Lett. **19**, 103 (1967). https://doi.org/10.1103/PhysRevLett.19.103
8. R.J. Baxter, *Exactly Solved Models in Statistical Mechanics* (Dover Publications, Mineola, New-York, 2007). ISBN 10: 0486462714
9. R.F. Wang et al., Nature **439**, 303 (2006). https://doi.org/10.1038/nature04447
10. G. Moller, R. Moessner, Phys. Rev. Lett. **96**, 237202 (2006). https://doi.org/10.1103/PhysRevLett.96.237202
11. Y. Perrin, B. Canals, N. Rougemaille, Nature **540**, 410 (2016). https://doi.org/10.1038/nature20155
12. Erik Östman et al., Nat. Phys. **14**, 375 (2018). https://doi.org/10.1038/s41567-017-0027-2
13. S.V. Isakov, R. Moessner, S.L. Sondhi, Phys. Rev. Lett. **95**, 217201 (2005). https://doi.org/10.1103/PhysRevLett.95.217201
14. G.T. Barkema, M.E.J. Newman, Phys. Rev. E **57**, 1155 (1998). https://doi.org/10.1103/PhysRevE.57.1155
15. R.G. Melko, B.C. den Hertog, M.J.P. Gingras, Phys. Rev. Lett. **87**, 067203 (2001). https://doi.org/10.1103/PhysRevLett.87.067203
16. R.G. Melko, M.J.P. Gingras, J. Phys.: Condens. Matter **16**, R1277 (2004). https://doi.org/10.1088/0953-8984/16/43/R02
17. L.D.C. Jaubert, J.T. Chalker, P.C.W. Holdsworth, R. Moessner, Phys. Rev. Lett. **100**, 067207 (2008). https://doi.org/10.1103/PhysRevLett.100.067207
18. L.D.C. Jaubert, J.T. Chalker, P.C.W. Holdsworth, R. Moessner, Phys. Rev. Lett. **105**, 087201 (2010). https://doi.org/10.1103/PhysRevLett.105.087201
19. O.F. Syljuasen, A.W. Sandvik, Phys. Rev. E **66**, 046701 (2002). https://doi.org/10.1103/PhysRevE.66.046701
20. C.L. Henley, Annu. Rev. Condens. Matter Phys. **1**, 179 (2010). https://doi.org/10.1146/annurev-conmatphys-070909-104138
21. C. Castelnovo, C. Chamon, Phys. Rev. B **76**, 174416 (2007). https://doi.org/10.1103/PhysRevB.76.174416
22. O. Cépas, B. Canals, Phys. Rev. B **86**, 024434 (2012). https://doi.org/10.1103/PhysRevB.86.024434
23. O. Cépas, Phys. Rev. B **90**, 064404 (2014). https://doi.org/10.1103/PhysRevB.90.064404
24. C. Castelnovo, R. Moessner, S.L. Sondhi, Phys. Rev. B **84**, 144435 (2011). https://doi.org/10.1103/PhysRevB.84.144435
25. L.D.C. Jaubert, Spin **5**, 1540005 (2015). https://doi.org/10.1142/S2010324715400056
26. C. Castelnovo, R. Moessner, S.L. Sondhi, Nature **451**, 42 (2008). https://doi.org/10.1038/nature06433
27. C. Castelnovo, R. Moessner, S.L. Sondhi, Annu. Rev. Condens. Matter Phys. **3**, 35 (2012). https://doi.org/10.1146/annurev-conmatphys-020911-125058
28. A. Sen, R. Moessner, Phys. Rev. Lett. **114**, 247207 (2015). https://doi.org/10.1103/PhysRevLett.114.247207
29. L.D.C. Jaubert, P.C.W. Holdsworth, Nat. Phys. **5**, 258 (2009). https://doi.org/10.1038/NPHYS1227

30. R.A. Borzi, D. Slobinsky, S.A. Grigera, Phys. Rev. Lett. **111**, 147204 (2013). https://doi.org/10.1103/PhysRevLett.111.147204
31. I.A. Ryzhkin, J. Exp. Theor. Phys. **101**, 481 (2005). https://doi.org/10.1134/1.2103216
32. D.J.P. Morris et al., Science **326**, 411 (2009). https://doi.org/10.1126/science.1178868
33. L.D.C. Jaubert, M. Haque, R. Moessner, Phys. Rev. Lett. **107**, 177202 (2011). https://doi.org/10.1103/PhysRevLett.107.177202
34. J.L. Jacobsen, J. Kondev, Nucl. Phys. B **532**, 635 (1998). https://doi.org/10.1016/S0550-3213(98)00571-9
35. J. Kondev, Phys. Rev. Lett. **78**, 4320 (1997). https://doi.org/10.1103/PhysRevLett.78.4320
36. J.L. Jacobsen, J. Vannimenus, J. Phys. A: Math. Gen. **32**, 5455 (1999). https://doi.org/10.1088/0305-4470/32/29/306
37. H. Saleur, B. Duplantier, Phys. Rev. Lett. **58**, 2325 (1987). https://doi.org/10.1103/PhysRevLett.58.2325
38. J. Kondev, C.L. Henley, Phys. Rev. Lett. **74**, 4580 (1995). https://doi.org/10.1103/PhysRevLett.74.4580
39. A. Weinrib, B.I. Halperin, Phys. Rev. B **27**, 413 (1983). https://doi.org/10.1103/PhysRevB.27.413
40. S.V. Isakov, K. Gregor, R. Moessner, S.L. Sondhi, Phys. Rev. Lett. **93**, 167204 (2004). https://doi.org/10.1103/PhysRevLett.93.167204
41. A. Nahum, J.T. Chalker, P. Serna, M. Ortuño, A.M. Somoza, Phys. Rev. Lett. **111**, 100601 (2013). https://doi.org/10.1103/PhysRevLett.111.100601
42. B. Duplantier, H. Saleur, Phys. Rev. Lett. **59**, 539 (1987). https://doi.org/10.1103/PhysRevLett.59.539
43. D. Austin, E.J. Copeland, R.J. Rivers, Phys. Rev. D **49**, 4089 (1994). https://doi.org/10.1103/PhysRevD.49.4089
44. K.S.D. Beach, Anders W. Sandvik, Nucl. Phys. B **750**, 142 (2006). https://doi.org/10.1016/j.nuclphysb.2006.05.032
45. A. Fabricio Albuquerque, F. Alet, R. Moessner, Phys. Rev. Lett. **109**, 147204 (2012). https://doi.org/10.1103/PhysRevLett.109.147204
46. P. Fulde, K. Penc, N. Shannon, Ann. Phys. **11**, 892 (2002). https://doi.org/10.1002/1521-3889(200212)11:12<892::AID-ANDP892>3.0.CO;2-J
47. P.A. McClarty, A. O'Brien, F. Pollmann, Phys. Rev. B **89**, 195123 (2014). https://doi.org/10.1103/PhysRevB.89.195123
48. S. Kourtis, C. Castelnovo, Phys. Rev. B **94**, 104401 (2016). https://doi.org/10.1103/PhysRevB.94.104401
49. H. Ishizuka, M. Udagawa, Y. Motome, Phys. Rev. B **83**, 125101 (2011). https://doi.org/10.1103/PhysRevB.83.125101
50. L.D.C. Jaubert, S. Piatecki, M. Haque, R. Moessner, Phys. Rev. B **85**, 054425 (2012). https://doi.org/10.1103/PhysRevB.85.054425
51. J.W.F. Venderbos, M. Daghofer, J. van den Brink, S. Kumar, Phys. Rev. Lett. **109**, 166405 (2012). https://doi.org/10.1103/PhysRevLett.109.166405
52. D.A. Huse, W. Krauth, R. Moessner, S.L. Sondhi, Phys. Rev. Lett. **91**, 167004 (2003). https://doi.org/10.1103/PhysRevLett.91.167004
53. T. Senthil, A. Vishwanath, L. Balents, S. Sachdev, M.P.A. Fisher, Science **303**, 1490 (2004). https://doi.org/10.1126/science.1091806
54. O.I. Motrunich, A. Vishwanath, Phys. Rev. B **70**, 075104 (2004). https://doi.org/10.1103/PhysRevB.70.075104
55. F. Alet et al., Phys. Rev. Lett. **94**, 235702 (2005). https://doi.org/10.1103/PhysRevLett.94.235702
56. F. Alet, G. Misguich, V. Pasquier, R. Moessner, J.L. Jacobsen, Phys. Rev. Lett. **97**, 030403 (2006). https://doi.org/10.1103/PhysRevLett.97.030403
57. G. Misguich, V. Pasquier, F. Alet, Phys. Rev. B **78**, 100402 (2008). https://doi.org/10.1103/PhysRevB.78.100402

58. D. Charrier, F. Alet, P. Pujol, Phys. Rev. Lett. **101**, 167205 (2008). https://doi.org/10.1103/PhysRevLett.101.167205
59. S. Powell, J.T. Chalker, Phys. Rev. Lett. **101**, 155702 (2008). https://doi.org/10.1103/PhysRevLett.101.155702
60. G. Chen, J. Gukelberger, S. Trebst, F. Alet, L. Balents, Phys. Rev. B **80**, 045112 (2009). https://doi.org/10.1103/PhysRevB.80.045112
61. S. Powell, J.T. Chalker, Phys. Rev. B **80**, 134413 (2009). https://doi.org/10.1103/PhysRevB.80.134413
62. P.W. Kasteleyn, J. Math. Phys. **4**, 287 (1963). https://doi.org/10.1063/1.1703953
63. G.I. Watson, J. Stat. Phys. **94**, 1045 (1999). https://doi.org/10.1023/A:1004547503489
64. K. Matsuhira, Z. Hiroi, T. Tayama, S. Takagi, T. Sakakibara, J. Phys.: Condens. Matter **14**, L559 (2002). https://doi.org/10.1088/0953-8984/14/29/101
65. M. Udagawa, M. Ogata, Z. Hiroi, J. Phys. Soc. Jpn. **71**, 2365 (2002). https://doi.org/10.1143/JPSJ.71.2365
66. R. Moessner, S.L. Sondhi, Phys. Rev. B **68**, 064411 (2003). https://doi.org/10.1103/PhysRevB.68.064411
67. T. Fennell, S.T. Bramwell, D.F. McMorrow, P. Manuel, A.R. Wildes, Nat. Phys. **3**, 566 (2007). https://doi.org/10.1038/nphys632
68. S.M. Bhattacharjee, Europhys. Lett. **15**, 815 (1991). https://doi.org/10.1209/0295-5075/15/8/002
69. J.F. Nagle, Proc. Natl. Acad. Sci. U. S. A. **70**, 3443 (1973). https://doi.org/10.1073/pnas.70.12.3443
70. Y.-Z. Chou, Y.-J. Kao, Phys. Rev. B **82**, 132403 (2010). https://doi.org/10.1103/PhysRevB.82.132403
71. S. Powell, Phys. Rev. B **91**, 094431 (2015). https://doi.org/10.1103/PhysRevB.91.094431
72. S. Powell, J.T. Chalker, Phys. Rev. B **78**, 024422 (2008). https://doi.org/10.1103/PhysRevB.78.024422
73. S. Powell, Phys. Rev. Lett. **109**, 065701 (2012). https://doi.org/10.1103/PhysRevLett.109.065701
74. S. Powell, Phys. Rev. B **87**, 064414 (2013). https://doi.org/10.1103/PhysRevB.87.064414
75. T. Fennell et al., Phys. Rev. B **72**, 224411 (2005). https://doi.org/10.1103/PhysRevB.72.224411
76. L.D.C. Jaubert, J.T. Chalker, P.C.W. Holdsworth, R. Moessner, J. Phys.: Conf. Ser. **145**, 012024 (2009). https://doi.org/10.1088/1742-6596/145/1/012024
77. H. Fukazawa, R.G. Melko, R. Higashinaka, Y. Maeno, M.J.P. Gingras, Phys. Rev. B **65**, 054410 (2002). https://doi.org/10.1103/PhysRevB.65.054410
78. S.-C. Lin, Y.-J. Kao, Phys. Rev. B **88**, 220402 (2013). https://doi.org/10.1103/PhysRevB.88.220402
79. M.L. Baez, R.A. Borzi, J. Phys.: Condens. Matter **29**, 055806 (2017). https://doi.org/10.1088/1361-648X/aa4e6a
80. S. Powell, J. Phys. A: Math. Theor. **50**, 124001 (2017). https://doi.org/10.1088/1751-8121/aa5bc6
81. J.P.C. Ruff, R.G. Melko, M.J.P. Gingras, Phys. Rev. Lett. **95**, 097202 (2005). https://doi.org/10.1103/PhysRevLett.95.097202
82. T. Yavors'kii, T. Fennell, M.J.P. Gingras, S.T. Bramwell, Phys. Rev. Lett. **101**, 037204 (2008). https://doi.org/10.1103/PhysRevLett.101.037204
83. P. Henelius et al., Phys. Rev. B **93**, 024402 (2016). https://doi.org/10.1103/PhysRevB.93.024402
84. H.R. Molavian, M.J.P. Gingras, B. Canals, Phys. Rev. Lett. **98**, 157204 (2007). https://doi.org/10.1103/PhysRevLett.98.157204
85. G.-W. Chern, R. Moessner, O. Tchernyshyov, Phys. Rev. B **78**, 144418 (2008). https://doi.org/10.1103/PhysRevB.78.144418
86. P.A. McClarty et al., Phys. Rev. B **92**, 144418 (2015). https://doi.org/10.1103/PhysRevB.92.144418

87. J.G. Rau, M.J.P. Gingras, Phys. Rev. B **92**, 144417 (2015). https://doi.org/10.1103/PhysRevB.97.144417
88. M. Mito et al., J. Magn. Magn. Mater. **310**, E432 (2007). https://doi.org/10.1016/j.jmmm.2006.10.441
89. H. Takahashi, Proc. Phys. Math. Soc. Japan **23**, 548 (1941). https://doi.org/10.11429/ppmsj1919.23.0_548
90. L. Bovo et al., Nat. Commun. **5**, 3439 (2014). https://doi.org/10.1038/ncomms4439
91. J.F. Nagle, Commun. Math. Phys. **13**, 62 (1969). https://doi.org/10.1007/BF01645270
92. L. Benguigui, Phys. Rev. B **16**, 1266 (1977). https://doi.org/10.1103/PhysRevB.16.1266
93. K.A. Ross, L. Savary, B.D. Gaulin, L. Balents, Phys. Rev. X **1**, 021002 (2011). https://doi.org/PhysRevX.1.021002
94. L. Savary, L. Balents, Phys. Rev. Lett. **108**, 037202 (2012). https://doi.org/10.1103/PhysRevLett.108.037202
95. Claudio Castelnovo, in *Topological Aspects of Condensed Matter Physics*, ed. by C. Chamon, M.O. Goerbig, R. Moessner, L.F. Cugliandolo. Lecture Notes of the Les Houches Summer School: Volume 103, (Oxford University Press, 2017). https://doi.org/10.1093/acprof:oso/9780198785781.003.0012
96. D.P. Leusink et al., Appl. Phys. Lett. Mater. **2**, 032101 (2014). https://doi.org/10.1063/1.4867222
97. K. Kukli et al., Thin Solid Films **565**, 261 (2014). https://doi.org/10.1016/j.tsf.2014.06.028
98. L. Bovo, C.M. Rouleau, D. Prabhakaran, S.T. Bramwell, Nanotechnology **28**, 055708 (2017). https://doi.org/10.1088/1361-6528/aa5112
99. L.D.C. Jaubert, T. Lin, T.S. Opel, P.C.W. Holdsworth, M.J.P. Gingras, Phys. Rev. Lett. **118**, 207206 (2017). https://doi.org/10.1103/PhysRevLett.118.207206
100. E. Lantagne-Hurtubise, J.G. Rau, M.J.P. Gingras, Phys. Rev. X **8**, 021053 (2018). https://doi.org/10.1103/PhysRevX.8.021053
101. D.L. Bergman, G.A. Fiete, L. Balents, Phys. Rev. B **73**, 134402 (2006). https://doi.org/10.1103/PhysRevB.73.134402
102. O. Sikora, F. Pollmann, N. Shannon, K. Penc, P. Fulde, Phys. Rev. Lett. **103**, 247001 (2009). https://doi.org/10.1103/PhysRevLett.103.247001
103. O. Sikora, N. Shannon, F. Pollmann, K. Penc, P. Fulde, Phys. Rev. B **84**, 115129 (2011). https://doi.org/10.1103/PhysRevB.84.115129
104. K. Penc, N. Shannon, H. Shiba, Phys. Rev. Lett. **93**, 197203 (2004). https://doi.org/10.1103/PhysRevLett.93.197203
105. H. Ueda, H.A. Katori, H. Mitamura, T. Goto, H. Takagi, Phys. Rev. Lett. **94**, 047202 (2005). https://doi.org/10.1103/PhysRevLett.94.047202
106. D.L. Bergman, R. Shindou, G.A. Fiete, L. Balents, Phys. Rev. Lett. **96**, 097207 (2006). https://doi.org/10.1103/PhysRevLett.96.097207
107. M.E. Brooks-Bartlett, S.T. Banks, L.D.C. Jaubert, A. Harman-Clarke, P.C.W. Holdsworth, Phys. Rev. X **4**, 011007 (2014). https://doi.org/10.1103/PhysRevX.4.011007
108. S. Petit et al., Nat. Phys. **12**, 746 (2016). https://doi.org/10.1038/nphys3710
109. J.A.M. Paddison et al., Nat. Commun. **7**, 13842 (2016). https://doi.org/10.1038/ncomms13842
110. E. Lefrançois et al., Nat. Commun. **8**, 209 (2017). https://doi.org/10.1038/s41467-017-00277-1

Chapter 7
Modelling of Classical Spin Ice: Coulomb Gas Description of Thermodynamic and Dynamic Properties

C. Castelnovo and P. C. W. Holdsworth

Abstract The Coulomb gas description of spin ice has revolutionized our understanding of these systems. Built on the remarkable self screening of the dipolar spin ice model, the emergence of magnetic monopole quasi-particles has allowed a depth of analytic and conceptual progress that is far beyond the spin description. After defining the magnetic Coulomb gas, or magnetolyte, we bench mark it against dipolar spin ice, before presenting a Debye-Hückel theory modified to take into account the underlying constraints of the spin degrees of freedom. The calculated specific heat compares favourably with simulation and experiment, with quantitative agreement at high and at low temperature. Moving to dynamical properties, we show how the temperature dependence of experimentally observed relaxation time scales is captured by monopole dynamics. We show that the magnetolyte exhibits non-Ohmic contributions to the monopole conductivity, the AC Wien effect, and we propose detailed protocols for its observation in experiments. Thermal and field quenches take the magnetolyte far from equilibrium, exposing a cornucopia of phenomena characteristic of reaction diffusion processes, dimer absorption and kinetically constrained models.

7.1 Introduction

The last ten years have seen frustrated pyrochlore magnets at the centre of a vast research effort, leading to the discovery of phenomena outside the conventional paradigms for magnetic materials, both in classical and quantum regimes. The start-

C. Castelnovo (✉)
TCM group, Cavendish Laboratory, University of Cambridge, Cambridge, UK
e-mail: cc726@cam.ac.uk

P. C. W. Holdsworth
Université de Lyon, ENS de Lyon, Université Claude Bernard, CNRS, Laboratoire de Physique, F-69342 Lyon, France

M. Udagawa and L. Jaubert (eds.), *Spin Ice*, Springer Series in Solid-State Sciences 197,
https://doi.org/10.1007/978-3-030-70860-3_7

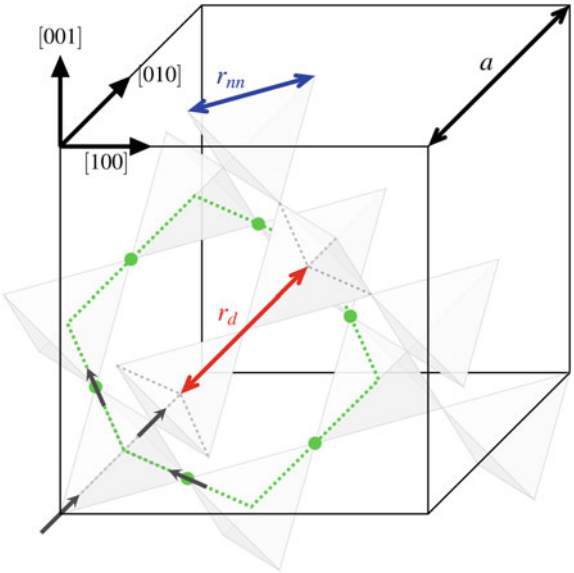

Fig. 7.1 Pyrochlore lattice: The spins are located at the corners of every tetrahedron and are constrained to point along their local [111] axis represented by the dashed lines. There are two types of tetrahedra that we shall call the *down* tetrahedra (bottom left with the four spins) and the *up* tetrahedra. Each *down* tetrahedron is connected to four *up* ones, and vice-versa. The cube represents a unit cell with 8 tetrahedra (4 of each kind) and 16 spins, and defines the [100] (x), [010] (y) and [001] (z) axes. We introduce the length of the unit cell $a \simeq 10$ Å as well as the distance between nearest neighbour spins $r_{\rm nn} = \frac{\sqrt{2}}{4}\, a \simeq 3.5$ Å and between the centres of two connected tetrahedra $r_d = \frac{\sqrt{3}}{4}\, a \simeq 4.3$ Å. The smallest close loop encompasses 6 spins (see green dotted loop)

ing point of this revolution is the representation of the constraints on the local spin configurations that characterize the extensive low energy manifolds of these materials as effective gauge fields [1]. The emergence of this gauge physics endows the low temperature regime with topological properties, leading to Coulomb phase correlations [2], magnetic monopole excitations [3–6], phase transitions lying outside the established Landau-Ginzburg-Wilson framework [7–9], and model quantum electrodynamics [10, 11] emanating from new classes of quantum spin liquids [12].

Spin ice systems [13, 14] such as $Dy_2Ti_2O_7$ and $Ho_2Ti_2O_7$ are a cornerstone example of this emergence. They can be described by a corner sharing network of tetrahedra forming a pyrochlore lattice of localized magnetic moments, as shown in Fig. 7.1. The pairwise interaction is made up of both exchange and dipolar terms and the physics of spin ice has been shown to be well represented by the dipolar spin ice (DSI) Hamiltonian [15],

$$\mathscr{H} \;=\; Jm^2 \sum_{\langle i,j\rangle} \mathbf{S}_i \cdot \mathbf{S}_j \;+\; Dm^2 \sum_{i>j} \left[\frac{\mathbf{S}_i \cdot \mathbf{S}_j}{\left|\mathbf{r}_{ij}\right|^3} - \frac{3\left(\mathbf{S}_i \cdot \mathbf{r}_{ij}\right)\left(\mathbf{S}_j \cdot \mathbf{r}_{ij}\right)}{\left|\mathbf{r}_{ij}\right|^5} \right], \quad (7.1)$$

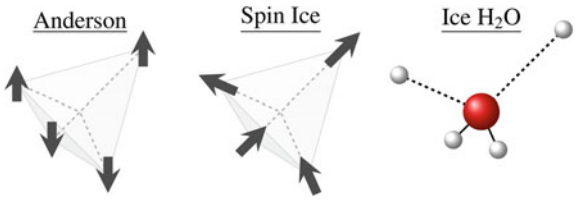

Fig. 7.2 Lowest energy state for a single tetrahedron: The pseudo spins σ_i correspond to Anderson's model for antiferromagnetic spinels [18]. The spins map directly to proton positions in water ice: the white spheres are the hydrogen atoms and the red one is the oxygen. A spin pointing *into* (resp. *out of*) a tetrahedron corresponds to a *down* (resp. *up*) spin in the Anderson model and a short covalent bond (resp. long H-bond) in water ice

where the rare earth ions carry a moment of the order of 10 Bohr magnetons, $m = 10\,\mu_B$, $\mathbf{S}_i$ is a spin of unit length, $\langle i, j\rangle$ indicates a sum over nearest neighbour pairs and $\mathbf{r}_{ij}$ is the vector joining spin sites i and j. Subsequent, more refined versions of the DSI also include second and third neighbour exchange couplings [16, 17]. The coupling constants are on the 1 K energy scale; for example for $Dy_2Ti_2O_7$, $|J|m^2 \simeq 3.72$ K and $Dm^2 \simeq 1.41$ K (assuming the distances $\mathbf{r}_{ij}$ are measured in units of the pyrochlore lattice constant $r_{\rm nn}$) [15]. These energy scales are 100 times smaller than the crystal field terms that confine the spins along the axis joining the centres of two adjacent tetrahedra, forming a local set of body centered cubic axes:

$$\begin{aligned} \mathbf{S}_1 &= \frac{\sigma_1}{\sqrt{3}}[-1,-1,1], \qquad \mathbf{S}_2 = \frac{\sigma_2}{\sqrt{3}}[1,1,1], \\ \mathbf{S}_3 &= \frac{\sigma_3}{\sqrt{3}}[1,-1,-1], \qquad \mathbf{S}_4 = \frac{\sigma_4}{\sqrt{3}}[-1,1,-1], \end{aligned} \tag{7.2}$$

where $\sigma_i = \pm 1$ is an Ising pseudo-spin with the chosen convention that $\sigma_i = 1$ corresponds to a moment pointing out of a *down* tetrahedron and into an *up* tetrahedron (see Fig. 7.1). As a result, at energies smaller than ~ 1 K, the moments behave as Ising spins along their local axis.

The lowest energy states of a single tetrahedron are the six configurations with two spins pointing inwards and two outwards—the Bernal Fowler 2in-2out ice rule, from which spin ice gets its name [13], as shown in Fig. 7.2. Indeed, restricting the Hamiltonian to nearest neighbor interactions (nearest neighbour spin ice—NNSI) leads to a macroscopically degenerate ground state manifold of so called Pauling states which maps directly onto the set of disordered proton configurations in the cubic phase of water ice. The "Pauling entropy", S_P [19] associated with these states is well approximated by a random phase type argument: take a sample of $2N_0$ spins decorating N_0 tetrahedra; for each tetrahedron, 6 out of the 16 configurations satisfy the ice rules, so that roughly a fraction $\left(\frac{6}{16}\right)^{N_0}$ of the total phase space, $W_0 = 2^{2N_0}$, satisfies the ice rules: $S_P \approx k_B N_0 \ln\left(\frac{3}{2}\right)$.

The nearest neighbor approximation already gives a good description of spin ice materials, as the high symmetry of the pyrochlore lattice gives the Hamiltonian a

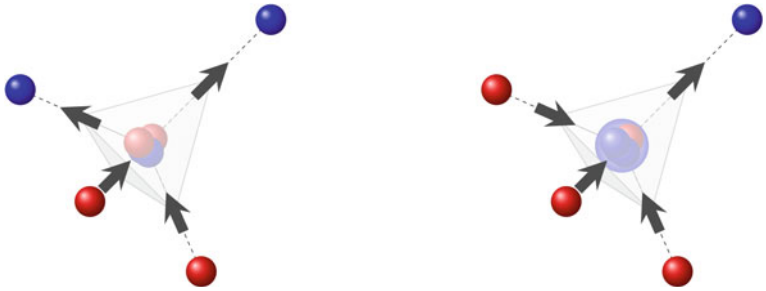

Fig. 7.3 Dumbbell model: Each magnetic dipole is seen as two charges sitting on the vertices of the diamond lattice (dashed lines). 2in-2out is the vacuum (left panel) whereas 3in-1out is a positive charge (right panel)

remarkable property: the long range part of the dipole interactions are almost perfectly screened [15, 20]. As a consequence, the Pauling states are quasi-degenerate even for the full dipolar Hamiltonian. This highly degenerate low energy sector of states constrained to the 2in-2out ice rules leads to spin liquid behavior with an emergent gauge symmetry—the Coulomb phase with characteristic dipolar spin correlations and pinch point scattering patterns [21]. The degeneracy is ultimately lifted by terms of quadrupolar order, generated by the cubic symmetry [20], leading to a small band width for the Pauling states. Model DSI therefore undergoes a conventional ordering transition at low temperature, on the scale of the quadrupolar coupling strength ($\ll J, D$) [16, 17, 22].

The screening of the long range interactions can be understood by making a further simplification to the Hamiltonian, (7.1), extending the point dipoles into infinitesimally thin magnetic needles lying along the axes linking the centres of adjoining tetrahedra of the pyrochlore lattice [3, 23] (see Fig. 7.1). The needles touch at the diamond lattice sites so that, by construction, the 2in-2out Pauling states are degenerate in this model and the small low energy bandwidth is absorbed by the transformation. The richness of spin ice is in this smallness: the DSI is, to an excellent approximation, a vertex model which is at the heart of its emergent properties. This is to be compared with its two dimensional equivalent—square ice. Here, the symmetry is much lower with the result that the bandwidth of Pauling states for point dipoles is large and replacing them with needles is a poor approximation [23]. Charge superposition at the vertices generates a diverging energy scale. However, this is a constant for each vertex and can be successfully absorbed into a self energy term [3]. The needles can hence be thought of as dumbbells of charge from which monopoles can be constructed: the ensemble of degenerate ground states form a vacuum in which monopoles can be excited by reversing the orientation of a needle, breaking the ice rules on a pair of neighbouring sites, as shown in Fig. 7.3. The needle flip changes the magnetic moment by $\Delta M = \pm 2m$ along the local body centered cubic axis and transports magnetic charge over a distance r_d, so that the elementary charge of a moving quasiparticle is $\pm Q$, with $Q = 2m/r_d$.

Within the dumbbell approximation, the Hamiltonian can be written as:

$$\mathscr{H} - \mathscr{H}_0 = \frac{1}{2}\sum_{\alpha\neq\beta}\frac{\mu_0 Q_\alpha Q_\beta}{4\pi r_{\alpha\beta}} + \frac{1}{2}v_0\sum_\alpha Q_\alpha^2, \tag{7.3}$$

where Q_α is the total magnetic charge on diamond lattice site α and $r_{\alpha\beta}$ the distance separating diamond sites α and β, μ_0 is the magnetic permeability and v_0 is an on-site term whose value is calculated from estimating spin flip energies in the dipolar model (see SI of [3]). $\mathscr{H}_0$ is the ground state energy of (7.1), written in the dumbbell approximation; namely, $\mathscr{H}_0 = -(N_0/2)v_0Q^2$. Hence magnetic monopoles [3] emerge as quasi-particle excitations from the ground state configurations of the dumbbell model of spin ice.

The ice rules and their consequent violation impose that $Q_\alpha = 0, \pm Q, \pm 2Q$ only. The single charges correspond to 3in-1out (3out-1in) vertices and the double charges to 4in and 4out. The diagonal term provides the chemical potentials for both monopoles (μ) and double monopoles (μ_2):

$$\left\langle \frac{1}{2}v_0\sum_\alpha Q_\alpha^2 \right\rangle = -\mu N - \mu_2 N_2, \tag{7.4}$$

where $\mu = -v_0Q^2/2$, $\mu_2 = 4\mu = -2v_0Q^2$, and where the (thermally averaged) number of single and double monopoles are N and N_2 respectively. The chemical potential fixes the energy scale, $2\Delta = -2\mu$ (> 0) required to introduce a neutral pair of monopoles and separate them to infinite distance [24]. In this representation the internal energy can thus be written as $U = U_C - \mu N - \mu_2 N_2$, where

$$U_C = \left\langle \frac{1}{2}\sum_{\alpha\neq\beta}\frac{\mu_0 Q_\alpha Q_\beta}{4\pi r_{\alpha\beta}} \right\rangle \tag{7.5}$$

is the thermally averaged Coulomb energy. Namely, spin ice can be described as a grand canonical lattice Coulomb gas! At low temperature, double monopoles can be neglected, leaving a simple monopole fluid.

In the rest of this article we refer to the monopole fluid generated by the dumbbell model Hamiltonian as a "magnetolyte", in analogy with a lattice electrolyte, or lattice Coulomb gas (Coulomb liquid). The two differ by the constraints imposed by the spin (dumbbell) configurations. Notably, while the electrolyte vacuum has zero entropy, the magnetolyte vacuum is made up of the 2in-2out spin configurations and has a finite (Pauling) entropy, S_P. The moments satisfy the local divergence free condition, mapping onto an emergent gauge field and making up a network of 'Dirac strings' along which monopoles can move, in analogy with real Dirac monopoles. Monopole creation, destruction and motion involves spin flips. Hence, a monopole displacement leaves a string of overturned dipoles that re-arrange the network, as shown in Fig. 7.4, influencing both the static and the dynamic properties. The mag-

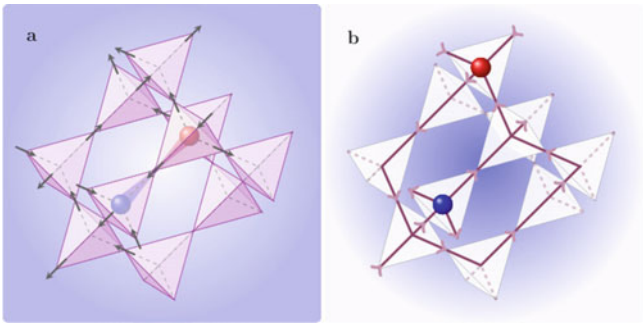

Fig. 7.4 Emergence of monopoles: **a** The magnetic ions (Ho^{3+} or Dy^{3+}) lie on the sites of the pyrochlore lattice and are constrained to the bonds of the diamond lattice (dashed lines). Local topological excitations 3in-1out or 3out-1in correspond to magnetic monopoles with positive (blue sphere) or negative (red sphere) charges respectively. **b** The diamond lattice provides the skeleton for the network of Dirac strings with the position of the monopoles restricted to the vertices. The orientation of the Dirac strings shows the direction of the local field lines in **H**. Adapted figure from [5] with permission from Nature Physics

netolyte can be restricted to single charged monopoles by setting $\mu_2 = -\infty$, which limits the tetrahedra to 14 vertex configurations—6 empty, 4 north poles (3in-1out) and 4 south poles (3out-1in), or extended to include double monopoles and all 16 vertices.

7.2 Emergent Electrolyte Physics in Spin Ice

In the previous section we have presented a simplified model for spin ice that can be understood as a spin liquid "vacuum" with an emergent gauge symmetry inherited from the 2in-2out local constraints that minimise the energy. The vacuum hosts classical fractionalised excitations that take the form of free magnetic charges in three dimensions, or emergent magnetic monopoles.

In this section we address the question of how quantitatively the magnetolyte picture reproduces the physics of either the DSI model, from which it is derived, or spin ice materials. We find that it works remarkably well, providing an understanding that goes far beyond that given by state of the art techniques for localized spin systems. Notice that the magnetolyte description trades complex many body spin correlations that become progressively stronger at low temperatures for a vacuum with point charge excitations that become exponentially less dense and hence easier to model and simulate.

A qualitative phase diagram for spin ice is shown in Fig. 7.5. The low temperature region begins at around 2 K for both Holmium and Dysprosium Titanate. This corresponds to the experimental observation of the Coulomb phase [2, 21]. Below 500 mK experimental systems fall out of equilibrium as time scales rapidly increase.

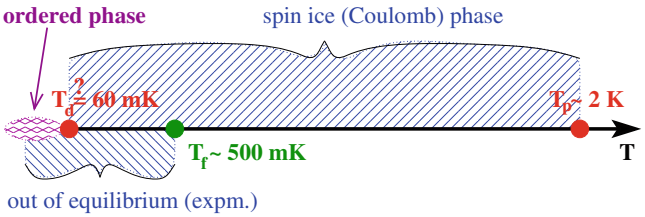

Fig. 7.5 Schematic illustration of the different temperature regimes in spin ice. The theoretically predicted ordering transition at $T_d \ll J, D$ appears to be prevented in experiments by freezing of the magnetic degrees of freedom below a threshold temperature T_f, as evidenced e.g., by a discrepancy between field-cooled and zero-field-cooled magnetisation. The 2in-2out spin ice regime undergoes a continuous crossover to trivial paramagnetic behaviour around $T_p \sim J, D$

At much lower temperatures, between 200 and 60 mK, the DSI model [22] and its variants [16, 17] undergoes a transition to a long range ordered state as the band width of Pauling states comes into play. No such ordering has as yet been observed in experiment, although evidence of a non-trivial low energy landscape has recently been shown for $Dy_2Ti_2O_7$ [25].

By construction, the Pauling states are degenerate in the dumbbell model, thus showing Coulomb phase physics in the spin ice regime, and predicting correctly the evolution of pinch point scattering patterns above 0.5 K [26]. In this approximation there is no ordering down to zero temperature, and the magnetolyte description does not reproduce any of the details coming from the bandwidth of the low energy states, as this is explicitly excluded from the model.

7.2.1 The Magnetolyte as a Model for Spin Ice

The mapping to a grand canonical fluid means that the independent thermodynamic variables are T and μ, which together with the diamond lattice constant r_d and the monopole charge Q completely specify the problem. For each spin ice material, μ (7.4) can be estimated from the parameters of the DSI model, which are themselves extracted from specific heat measurements. Starting from a vacuum configuration, Δ_s is the energy required to flip a spin and create a nearest neighbor monopole-antimonopole pair and $u_d = -u(r_d) = \frac{\mu_0 Q^2}{4\pi r_d}$ is the Coulomb energy required to separate the pair to infinity. Following the sign convention of thermodynamics, $\mu = -(\Delta_s + u_d)/2$. For $Dy_2Ti_2O_7$ and $Ho_2Ti_2O_7$ one finds $\mu = -4.35$ K and -5.8 K respectively [3, 27].

Internal consistency can be tested numerically by driving a slave magnetolyte from a DSI simulation [27]. Here the monopole and Dirac string network configurations were taken directly from the spin configurations of DSI for $Dy_2Ti_2O_7$. At each step that creates or destroys a nearest neighbor pair of monopole defects, a monopole chemical potential can be estimated by comparing the spin and Coulomb energy

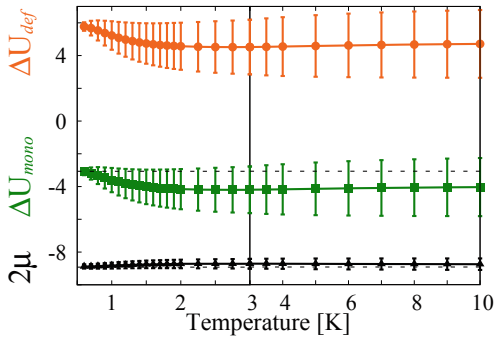

Fig. 7.6 Creation of a pair of quasi-particles: Energy (in Kelvin) required in the dipolar spin ice model (ΔU_{def} , orange ●) or gained in the slave magnetolyte (ΔU_{mono}, green ■) and the resulting chemical potential $2\mu(T) = \Delta U_{mono} - \Delta U_{def}$ (▲) as a function of temperature [27]. The vertical bars are *not* error bars but the standard deviation of these quantities. $2\mu(T)$ tends to the limit $2\mu_1 = -8.92$ K (lower dashed line) at very low temperature. The middle dashed line is the analytical prediction of the energy gained by creating a pair of monopoles in a vacuum $-u_d = -3.07$ K. The temperature scale below 3 K is enlarged for a better display. Note that, neglecting the bandwidth of vacuum states, one can take $\Delta_s = \Delta U_{def}(T = 0)$

changes in the two systems. These quantities fluctuate strongly due to both screening effects from the long range interactions and the bandwidth of Pauling states, but the extracted μ was found to be constant to within 3% error from 0.5 K to 10 K, with mean value $\bar{\mu} = -4.46$ K in close agreement with the calculated value. The small difference can be put down as direct evidence for the small bandwidth of Pauling states present in the DSI but absent in the magnetolyte.

The monopole picture therefore appears robust, with the logical consequence that the emergent magnetostatics of the magnetolyte should provide an accurate account of spin ice thermodynamics. Hence, we expect the magnetolyte to accurately reproduce the thermodynamic properties of either the DSI model, or of experiments on spin ice materials. In Fig. 7.7, we compare specific heat data simulated from the DSI and from the magnetolyte model with parameters J and D taken to model $Dy_2Ti_2O_7$. Results for the magnetolyte are shown for both the calculated values of μ, -4.35 K and the value extracted from the slave magnetolyte simulation, -4.46 K. Excellent agreement is seen between the two model systems for temperatures above 0.6 K confirming that the magnetolyte is an accurate simplification of the DSI above the temperature range in which the DSI undergoes an ordering transition. The slight under estimation of the peak height could reflect the 3% variation of the extracted μ with temperature observed in Fig. 7.6. The data for $\mu = -4.35$ K is slightly shifted from that of the DSI, but allowing μ to shift to -4.46 K gives a quantitative description of the model dipolar system, whose success in describing the specific heat of spin ice materials is well documented [16, 17, 22].

Moving away from holmium and dysprosium titanate, the full phase diagram for DSI has been been mapped out, as a function of T/D and J/D. The Coulomb phase and low temperature ordering (Fig. 7.5) give way to an antiferromagnetic phase

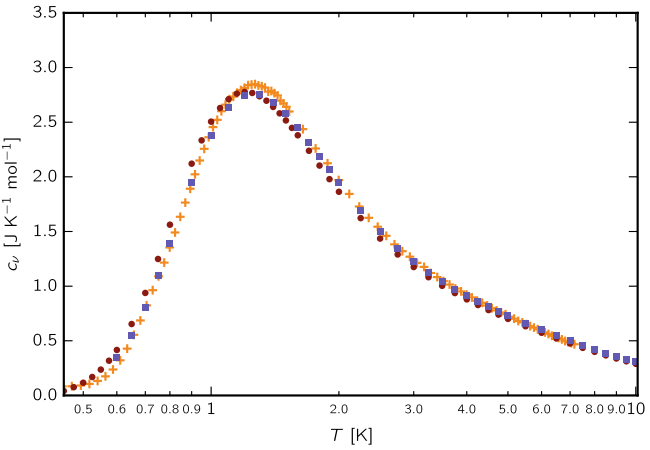

Fig. 7.7 Specific heat: Specific heat vs temperature for models of Dysprosium Titanate: simulation of magnetolyte including double monopoles, $\mu = -4.35$ K (brown circles [28]), $\mu = -4.46$ K (blue squares [28]), dipolar spin ice with $Jm^2 = 3.72$ K and $Dm^2 = 1.41$ K (orange crosses [15])—see text. Data taken from [15, 28] with permission from the American Physical Society

in which alternate tetrahedra have all spins pointing into and all out, for negative J/D [22]. Within the monopole description, the all-in all-out phase corresponds to a double monopole crystal on the diamond lattice—the Zinc blend structure. As a consequence, the all-in-all-out, spin ice phase boundary can be estimated from the emergent magnetotatics [29]. The ground state of the magnetolyte is determined by the trade off between Coulomb energy gain of having an ionic cystal of single or double monopoles (U_{c1}/U_{c2}) and the energy cost of monopole creation ($-\mu N - \mu_2 N_2$). In spin ice materials the energy cost largely outweighs the gain from interactions, so that the ground state is a vacuum—the Coulomb phase. This vacuum energy should be compared with that of both a singly and a doubly charged monopole crystal forming a zinc blend structure on the diamond lattice of N_0 sites:

$$U_{c1} = \left(\frac{N_0}{2}\right) u(r_d)\,\alpha - N_0\mu,\;\; U_{c2} = \left(\frac{N_0}{2}\right) u_2(r_d)\,\alpha - N_0\mu_2\,, \qquad (7.6)$$

where $u_2(r_d) = 4u(r_d)$ is the nearest neighbour Coulomb energy of a pair of double monopoles, and $\alpha = 1.63$ is the Madelung constant for a diamond lattice (Zinc blende). One finds a single threshold $\mu_2/u_2(r_d) = \alpha/2$, below which monopole crystallization is preferred over the vacuum. Above the threshold, the Coulomb energy of the double monopoles wins ensuring that, at zero temperature, the magnetolyte passes from a vacuum to a double monopole crystal. Using the values for μ_2 and $u_2(r_d)$ calculated from the DSI model [3] and applying this criterion [29] one finds the threshold ratio

$$\frac{J_{\rm nn}}{D_{\rm nn}} = -\frac{4}{5}\left[1+\sqrt{\frac{2}{3}}\left(1-\frac{\alpha}{2}\right)\right] = -0.918, \tag{7.7}$$

where $J_{\rm nn} = J/3$ and $D_{\rm nn} = 5D/3$. This magnetostatic estimate is in excellent agreement with numerical results for DSI. Melko et al. [22] find $J_{\rm nn}/D_{\rm nn} = -0.905$ with hysteresis down to $J_{\rm nn}/D_{\rm nn} \simeq -1$. The slight difference is again due to the small bandwidth for the Pauling states arising from the quadrupolar corrections that are neglected in the magnetic charge description [30].

The emergent monopole fluid therefore gives an excellent description of classical spin ice materials over the whole phase diagram. Most importantly, the identification of the emergent quasi-particles renders the otherwise complex problem of frustration in spin ice accessible through the development of effective theories for the emergent degrees of freedom, particularly at low temperature, as we illustrate in the next section.

7.2.2 Debye-Hückel Theory

In this section we use Debye-Hückel theory for the Coulomb interactions, to obtain the monopole density profile and heat capacity of spin ice [24, 31]. We will refer to three different Coulomb fluids: a magnetolyte restricted to single charge monopoles which we refer to as the 14-vertex magnetolyte when distinction is required; the full 16 vertex magnetolyte including double charge sites; and a symmetric, diamond lattice electrolyte in which the constraints imposed by the spin background are neglected.

Starting with the electrolyte, one can construct the grand potential, $\Omega = U_C - ST - \mu N$ for different levels of approximation. Initially we consider the non-interacting case, which is a self avoiding lattice gas of $N/2$ positive and $N/2$ negative quasiparticles on N_0 vertices of the diamond lattice. Each vertex can be in one of three states with charge $Q_\alpha = 0, \pm Q$. The number of configurations is $W_E = N_0!/[(N/2)!(N/2)!(N_0 - N)!]$, giving the well-known entropy of mixing

$$S = -k_B N_0 \left[n \ln(n/2) + (1-n)\ln(1-n)\right], \tag{7.8}$$

where $n = N/N_0$ is the quasiparticle number density. Minimizing $\Omega_0 = -ST - \mu N$ with respect to n gives

$$n = \frac{2\exp(\beta\mu)}{1+2\exp(\beta\mu)} \sim 2\exp(\beta\mu) \qquad \text{for } T \to 0 \qquad (\mu < 0). \tag{7.9}$$

This equation of state is modified by interactions and solving for the Coulomb energy U_C of a charged system is a complex problem. An approximate solution is provided by Debye-Hückel theory (see e.g., [31, 32]) which uses the linearized

Poisson-Boltzmann equation to go beyond mean field theory, predicting a correlation induced electrostatic potential, $\psi(r)$, at distance r from a test charge Q:

$$\psi(r \geq r_d) = \left(\frac{\mu_0 Q}{4\pi r}\right) \frac{\exp\left[-(r - r_d)/\ell_D\right]}{1 + r_d/\ell_D}, \qquad \ell_D = \sqrt{\frac{k_B T}{Q^2 \rho \mu_0}}, \tag{7.10}$$

where ℓ_D is the Debye length. The short distance cut off is, in our case, the lattice spacing r_d of the diamond lattice, and $\rho = N/V$ is the volume density of charges. The test charge induces a charge cloud in its vicinity of opposite sign, whose extension is controlled by ℓ_D. The Coulomb energy is the energy required to place the test charge in the induced potential. It can be calculated using the Debye charging procedure in which the charge on each site is built up adiabatically for fixed particle correlations. Setting $Q(\lambda) = \lambda Q$, the Coulomb energy for infinitesimal λ is defined

$$\delta u(\lambda) = -\lambda Q \psi(r_d, \lambda) = -\left(\frac{\mu_0 Q^2}{4\pi r_d}\right) \frac{\lambda^2}{1 + (r_d \lambda/\ell_D)}. \tag{7.11}$$

This expression can now be integrated from $\lambda = 0$ to $\lambda = 1$ to find the Coulomb energy of the test particle leading to an extensive internal energy U_C^{DH}

$$U_C^{\mathrm{DH}} = N_0 u_{\mathrm{DH}} = -\frac{N_0 k_B T}{6\pi\sqrt{3}} \left[\ln\left(1 + \frac{r_d}{\ell_D}\right) - \left(\frac{r_d}{\ell_D}\right) + \frac{1}{2}\left(\frac{r_d}{\ell_D}\right)^2\right]. \tag{7.12}$$

To convert the extensive variable from volume to N_0 we have used the volume per diamond lattice site, $\tilde{v} = 8r_d^3/3\sqrt{3}$ [24]. Surprisingly, as $\ell_D \propto 1/\sqrt{n}$, $U_C^{\mathrm{DH}} \sim n^{3/2}$ at low monopole density, contrary to the n^2 behaviour typical of mean field descriptions of short range systems.

We now have an expression for the full free energy Ω as a function of the monopole density n and independent thermodynamic variables μ (defined as $-\Delta$ in [24]) and T, as well as the lattice parameter r_d and the monopole charge Q. Minimizing $\Omega(n)$ with respect to n gives an effective chemical potential

$$\mu_{\mathrm{eff}} = \mu + \Delta\mu^{\mathrm{DH}} = \mu + k_B T \frac{\ell_T}{\ell_D + r_d}, \tag{7.13}$$

and zero field activity coefficient,

$$\gamma(0) = \exp\left(-\beta \Delta\mu^{\mathrm{DH}}\right). \tag{7.14}$$

Here, it is convenient to introduce the Bjerrum length, $\ell_T = \frac{\mu_0 Q^2}{8\pi k_B T}$, at which the Coulomb interaction per particle is equal to the thermal energy scale.

Putting μ_{eff} into (7.9) and solving self-consistently for the density [24] gives a Debye-Hückel equation of state $n(\mu, T)$ from which all thermodynamic quantities follow. The interactions reduce the energy scale for the inclusion of monopoles at

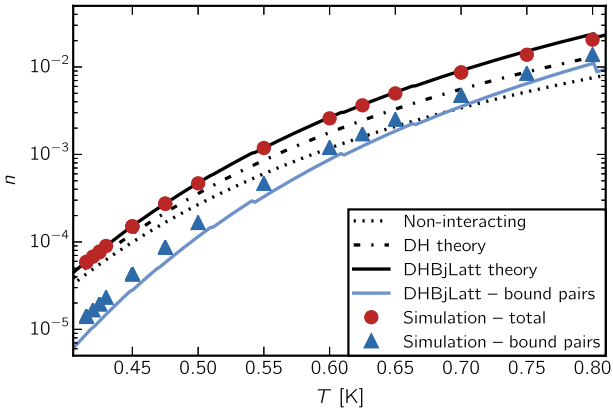

Fig. 7.8 Charge density: Charge vs temperature for a lattice electrolyte, comparing simulation results and self-consistent theories discussed in the text. The parameters of the electrolyte correspond to monopoles in $Dy_2Ti_2O_7$ but the Dirac string constraints are absent. Reprinted figure from [33] with permission from Nature Materials

finite density: $|\mu_{\text{eff}}| < |\mu|$ and $\gamma(0) < 1$, leading to an increased monopole concentration compared to the non-interacting gas, in the ratio $1/\gamma(0)$ [33].

Debye-Hückel theory underestimates this increase, as the linearization is not a good approximation for bound pairs separated by distances $r < \ell_T$. The Bjerrum length provides a threshold, allowing the division of the charge concentration into two categories: free particles, n_f, and neutral (Bjerrum) pairs of charges bound together by the long range Coulomb interaction. We define $n_b = n_b^+ + n_b^-$, the concentration of charge bound into pairs so that the bound pair concentration is $n_b/2$ and the total charge concentration $n = n_f + n_b$. The theory can be improved in certain regimes by employing Bjerrum's correction, which treats bound pairs exactly within a two body approximation, and performing Debye-Hückel theory on the free particles for which $r > \ell_T$ (see [31] for details). The density profile is compared with Debye-Hückel-Bjerrum theory in Fig. 7.8 for a lattice electrolyte with $\mu = -4.35$ K as appropriate for $Dy_2Ti_2O_7$. The agreement is excellent, showing the relevance of this theoretical approach and the importance of interactions even in the low density, low temperature limit.

Moving from the lattice electrolyte to the magnetolyte, the entropy of the vacuum can be included in the non-interacting limit by returning to the vertex problem. Following Ryzhkin [4], one can write an approximate expression for the vertex entropy of the magnetolyte by considering each type of vertex as a species of indistinguishable objects. Restricting to single monopoles, that is, to the 14-vertex magnetolyte, each vertex can again be occupied by magnetic charge 0, $\pm Q$, with 6 2in-2out spin ice configurations corresponding to charge zero, and 4 3in-1out (4 3out-1in) configurations corresponding to charge Q ($-Q$). The total number of microstates is estimated to be

$$W = \left(\frac{1}{2}\right)^{2N_0} \frac{N_0!}{N_1!N_2!\ldots N_{14}!}, \tag{7.15}$$

where N_a is the number of vertices of type $a = 1, \ldots, 14$. The prefactor, $(1/2)^{2N_0}$ takes into account the compatibility of the spins shared between neighboring vertices. Without this the vertex distribution wildly over estimates the number of micro states. Setting $N_1 = N_2 = \cdots N_6 = N_p/6$ and $N_7 = N_8 = \cdots N_{14} = N_m/8$, where $N_p = (1-n)N_0$ is the number of 2in-2out vertices and $N_m = nN_0$ is the number of vertices carrying a monopole, it follows that

$$S = -k_B N_0 \left\{ n \ln\left(\frac{n}{2}\right) + (1-n)\ln(1-n) + (1-n)\ln\left(\frac{2}{3}\right) \right\}. \tag{7.16}$$

This formula elegantly separates the entropy into a monopole term and a vacuum term, and yields the approximate Pauling entropy, $S_p = k_B N_0 \ln(3/2)$ as $n \to 0$. Minimizing the noninteracting free energy with respect to n, including the vacuum term, yields

$$n = \frac{\frac{4}{3}\exp(\beta\mu)}{1 + \frac{4}{3}\exp(\beta\mu)}, \tag{7.17}$$

from which we obtain the correct high temperature limit for the density of the 14 vertex magnetolyte, $n(T \to \infty) = \frac{4}{7}$, the correct entropy limit, $S(\infty) = N_0 k_B \ln\left(\frac{7}{2}\right)$, and the entropy change $\Delta S = S(\infty) - S(0) = \ln\left(\frac{7}{3}\right)$, calculated within a Pauling approximation. The process can easily be extended to include double monopoles in the full 16 vertex magnetolyte.

One can now proceed with Debye-Hückel theory as before, giving a complete self contained description of the magnetolyte fluid in which the spin and magnetic charge degrees of freedom have been included independently, rather in the spirit of the gauge mean field theories used to study quantum spin liquids [34]. The magnetic specific heat transforms, in the monopole representation, to

$$C_\mu = \left(\frac{\partial}{\partial T}\right)_\mu (U_C - \mu N) = -N_0 \mu_{\text{eff}} \left(\frac{\partial n}{\partial T}\right)_\mu. \tag{7.18}$$

Specific heat data are shown in Fig. 7.9 for systems with the chemical potential $\mu = -5.57$ K, corresponding to the value extracted for $Ho_2Ti_2O_7$. The upper panel shows simulation data for the electrolyte and the 14-vertex magnetolyte. One can notice that the areas under the curves are significantly different. This is a consequence of the constrained magnetolyte having a significantly different entropy change going from low to high temperature. The inset shows the effect of including double monopoles, moving from the 14 to 16-vertex magnetolyte. As can be seen, double monopoles modify the specific heat from 2K and above. In the lower panel we show data for the 16-vertex magnetolyte together with the corresponding Debye-Hückel theory, which has been extended accordingly [31]. The theory provides a

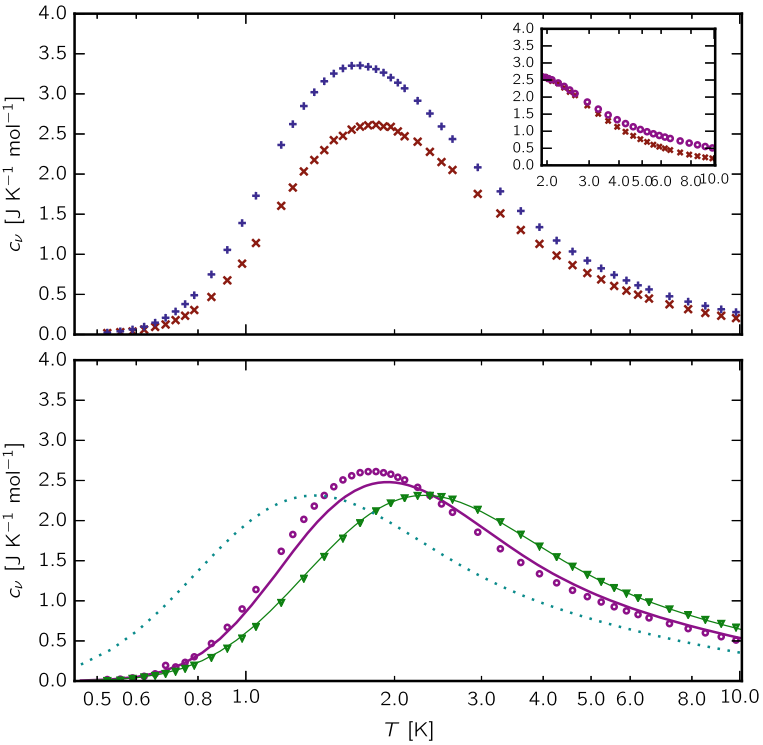

Fig. 7.9 **Specific heat: Top panel**: simulation data for the electrolyte (blue crosses) and 14-vertex magnetolyte (brown crosses) with $\mu = -5.7$ K, as estimated for $Ho_2Ti_2O_7$ [22]. Inset: difference between 14 and 16-vertex (violet circles) magnetolytes above 2 K. **Bottom panel**: simulation data for 16-vertex magnetolyte with $\mu = -5.7$ K (violet circles) and nearest neighbour spin ice with $J_{\text{eff}} = -\mu/2 = 2.85$ K (green triangles), Debye-Hückel theory (violet line), non-interacting magnetolyte (green line) for $\mu = -5.7$ K, and non-interacting magnetolyte for $\mu = -3.4$ K (dotted turquoise line). Data taken from [28] with permission from the American Physical Society

good qualitative description of the simulation data giving a Schottky peak characteristic of monopole excitation out of the vacuum with approximately the correct position and amplitude. The theory becomes quantitatively correct at both high and low temperature. This is to be expected as the theory is accurate for small values of $\frac{r_d}{\ell_d} \propto \sqrt{\frac{u_d n}{k_B T}}$, but it is worth pointing out that model systems against which Debye-Hückel theory can be so extensively compared are rare and spin ice clearly is such a system.

To illustrate the importance of the Coulomb interactions in spin ice, we also show specific heat data for a non-interacting magnetolyte with $\mu = -5.57$ K. The non-interacting model appears in error at both high and low temperature and gives only a poor qualitative description of the Schottky peak. Closer examination at low temperature shows an asymptotic approach towards the simulation results below 0.5 K,

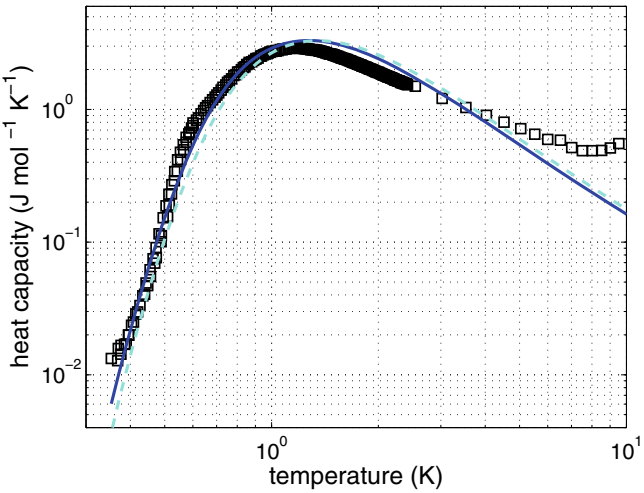

Fig. 7.10 Specific heat: Experimental results for the heat capacity of $Dy_2Ti_2O_7$ (data taken from [35] with permission from AAAS), compared with Debye-Hückel theory of the electrolyte, for $\mu = -4.35$ K, (solid blue line) and $\mu = -4.57$ K (dashed cyan line)

as the monopole density falls to zero [31] (see also Fig. 7.8). At high temperature the data always disagree, illustrating the importance of screening in a Coulombic system even in this limit.

A non-interacting approximation for the magnetolyte is equivalent to a single tetrahedron model for spin ice [31] with $J_{\text{eff}} = -\mu/2$. The specific heat of the NNSI is accurately described by the single tetrahedron model everywhere in the spin ice phase diagram, except close to the boarder with the all-in-all-out phase [30]. Comparing with simulation data for the NNSI for $J_{\text{eff}} = 2.85$ K one can see that this is the case here. Finally, we have also included data for a non-interacting magnetolyte with $\mu = -3.34$ K, which corresponds to $J_{\text{eff}} = 1.7$ K, the estimated value for a NNSI description of $Ho_2Ti_2O_7$ [22]. This model fails to capture the quantitative features of the magnetolyte, even at high temperature where it underestimates the simulation, although the value of J_{eff} could be fine tuned to fit the data in this limit. Specific heat data for $Dy_2Ti_2O_7$ have previously been compared with Debye-Hückel theory for the electrolyte [35]. In Fig. 7.10, reproduced from reference [35] we show the comparison. The data are plotted on a logarithmic scale to accentuate the low temperature region. The overall form of the experimental specific heat is well reproduced. However, there appears to be some structure at low temperature, possibly coming from the fine structure of the low energy band of states, that the theory does not predict. The theory passes above the experimental data through the peak because of the differences between electrolyte and magnetolyte discussed above, while at high temperature the data crosses above the theoretical curve due to the absence of double defects in this Debye-Hückel treatment. As we have seen, both effects can be accounted for in the magnetolyte and the ensuing Debye-Hückel theory, to give a

quantitative agreement between the model, the theory and experiment over the whole temperature range of the spin ice phase above 0.6 K (not shown).

In conclusion, we demonstrated that the monopole picture provides a framework for theoretical modelling beyond mean field approaches, using Debye-Hückel theory and improvements thereof, which gives a semi-quantitive description of spin ice. This kind of development has so far proved beyond the capacity of the spin picture. Hence in this regard, the magnetolyte takes us a step further than the dipolar spin ice model from which it is derived. The price one pays for this step however, is to sweep the finite energy scale of the bandwidth of Pauling states under the carpet. This has important consequences, particularly for the long time scale dynamics at low temperature, as we will see in the next section.

7.3 Monopoles and Dynamics

The benefits of a Coulomb liquid description are not limited to thermodynamic properties. It is also key to understand response and equilibration time scales in these systems.

To estimate time scales, one needs first to identify the energy scales of the dynamical processes. Starting from a vacuum state, the energy required to break the ice rules and create a monopole-antimonopole pair is $\Delta_s = 2\Delta - u_d$, where $\Delta = -\mu > 0$. As shown in Fig. 7.6, this is estimated at around 5.7 K for $Dy_2Ti_2O_7$. This should be compared with the hopping of a free monopole. Three of the four spins next to an isolated monopole can flip at low energy cost. Their reversal results in conservative dynamics in which the monopole hops from one tetrahedron to the next (see Fig. 7.11) with the monopole number unchanged. For finite monopole concentration

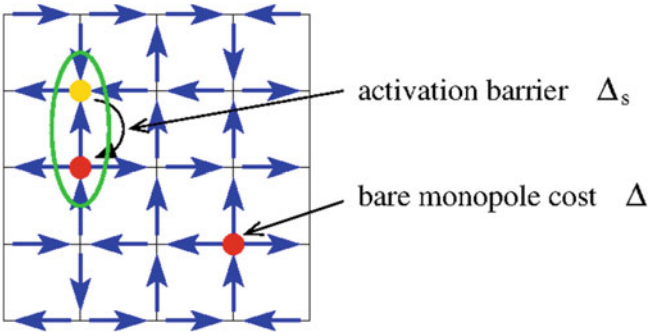

Fig. 7.11 Left side: a generic spin reversal in 2in-2out spin ice incurs a large energy barrier due to the creation of a monopole-antimonopole pair. Right side: a monopole acts as a spin flip facilitator, in that it allows three of the four neighbouring spins to flip without such barrier. Flipping one of those spins results in the monopole hopping to a neighbouring tetrahedron and the energy of the system remains essentially unchanged

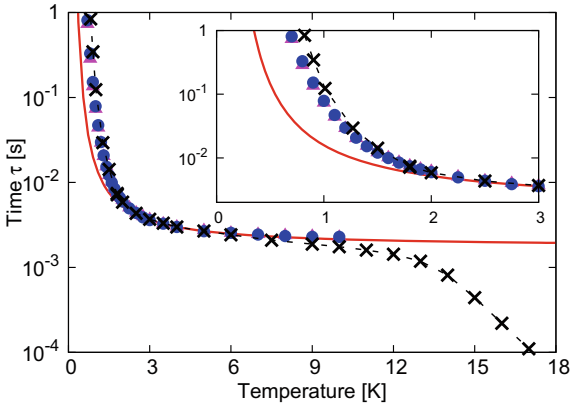

Fig. 7.12 Relaxation time scales τ in $Dy_2Ti_2O_7$ experiment and simulation. The experimental data ($\times$) are from Snyder et al. [36]. The Arrhenius law (red line) represents the free diffusion of topological defects for the nearest neighbour model. The relaxation time scale of the Dirac string network driven by Metropolis dynamics of magnetic monopoles has been obtained for fixed chemical potential and with μ varying slowly to match the defect concentration in dipolar spin ice. The temperature scale is fixed without any free parameters. Inset: Magnification of the same data at the lowest temperatures. Reprinted figure from [5] with permission from Nature Physics

these hops will be dressed by a Coulomb energy coming from monopole—monopole interactions, but these can be neglected as the concentration goes to zero. The density of sites open to the first process scales as f $\sim (1-n)$, suggesting an associated time scale, $\tau_s \sim e^{\Delta_s/T}/(1-n) \sim e^{\Delta_s/T}$, at low temperatures where $n \sim e^{-\Delta/T} \ll 1$. On the contrary, the hopping process involves no or small energy barriers, but it can only occur next to an existing monopole, suggesting a monopole hopping correlation time $\tau_m \sim 1/n \sim e^{\Delta/T}$. Which of the two processes dominates is determined by the smallest of the two energy scales, Δ and $\Delta_s = 2\Delta - u_d$. In known spin ice materials, $\Delta > u_d$ ($\Delta = 4.35$ K and $u_d = 3.07$ K in $Dy_2Ti_2O_7$, for example) so that the dynamics is dominated by monopole hopping and the above arguments suggest an Arrhenius behavior for equilibration times at low temperature. However, this statement must be modified on several counts for a successful encounter with experiment. In a key experiment, Snyder et al. [36] extracted relaxation times from bulk magnetometry measurements in $Dy_2Ti_2O_7$. The data, reproduced in Fig. 7.12, show a quasi-plateau region, followed by a steep increase in time scales that one can interpret as due to a rapid fall in monopole concentration. The data through the upturn cannot be fitted to a simple exponential law, but can be interpreted within the monopole picture, as shown in the same figure, where the data is compared with time scales extracted from simulations of the magnetolyte [5, 37]. These simulations use stochastic Metropolis dynamics with a single, temperature independent monopole hopping, τ_0 [5], as the existence of the plateau region suggests is the case above 2 K. The monopole-monopole interactions considerably modify the relaxation time scales. As discussed in the previous section, screening effects are important when

the monopole concentration is high, so that at high temperature the energy scales are significantly modified, giving relaxation times that are characteristic of a system of non-interacting tetrahedra [5]. Through the region from 3 to 0.7 K there is a continuous evolution of the energies scales (see Fig. 7.6) leading to a non-Arrhenius behaviour which is well reproduced by the simulation data, although the time scales are underestimated at the lowest temperatures.

The observation of a characteristic temperature-independent monopole hopping time scale has been the key to developing a theoretical understanding [38–41] of spin ice dynamics and to the interpretation of experiments on real materials [42–45]—some of which will be reviewed in Sects. 7.3.2, 7.3.3, 7.3.4, and 7.3.5. However, it is clear from subsequent experiments [42, 46–50] that there are important corrections to this picture. A detailed analysis suggests that the evolution does indeed cross over to an Arrhenius law at lower temperature but that the temperature scale corresponds more closely to 2Δ than Δ. One explanation could be that the monopole hopping time scale depends significantly on its local environment [49–51] through for example surface effects or magnetic impurities, leading to a temperature dependent hopping rate at low temperature.

These results promoted further work examining the properties of spin ice away from equilibrium [40, 52–55]. Magnetic impurities in these materials and their relation to response and relaxation properties have only recently started to be investigated systematically [56], suggesting that Oxygen vacancies play a crucial role. Recent experiments [51, 57] suggest that a heterogeneous spread of time scales is present, even at high temperature, when a temperature independent mean times scale appears to be well established. It is too soon to tell definitively which mechanism(s) are at the root of these phenomena, but the challenge is certain to stimulate new and exciting research on spin ice and related materials. Better microscopic modelling and understanding is needed to bring further clarification.

Finally, as we have seen, within the dumbbell approximation the two terms $\mu = -\Delta$ and u_d are functions of the microscopic parameters of the system, so that one could in principle realize the opposite situation for different spin ice materials. Indeed, as shown in Sect. 7.2.1, the criterion for passage from spin ice to the all-in all-out antiferromagnetic phase corresponds, within the monopole picture, to $\Delta/u_d = \alpha/2$ (where α is the Madelung constant for the diamond lattice), leaving a window between monopole crystallization and the threshold, $\Delta = u_d$, in which the dynamics could be dominated by monopole creation rather than diffusion.

In the following sections we illustrate the rich dynamical properties of model spin ice, examining response and relaxation phenomena, transport processes and the behaviour far from equilibrium through both thermal and field driven quenches. This led to the emergence of complex phenomena occurring in diverse fields and contexts, such as the conductivity of electrolytes, reaction diffusion processes, dimer adsorption, and kinetically constrained models, making spin ice a laboratory of choice for the study of tuneable, slow dynamics.

7.3.1 Hydrodynamic Description

A hydrodynamic approach to dynamics was taken in [4] in the approximation of non-interacting monopoles, using the thermodynamics of irreversible processes. Building on Jaccard theory for water ice [58], Ryzhkin identified an entropic correction to an applied magnetic field, **H**, coming from the ordering of the Dirac string network. The configurational entropy of a coarse grained volume element of spin ice depends on the local magnetic moment [1], providing entropic disordering forces. The entropy per unit volume can be estimated quantitatively [1, 58, 59],

$$S[\mathbf{M}(\mathbf{r})] - S(0) \approx -k_B \frac{4r_d}{\sqrt{3}Q^2} |\mathbf{M}(\mathbf{r})|^2. \tag{7.19}$$

Equating monopole flux and entropy production, one can identify a generalized force driving the monopole movement and hence an effective field acting on the thermally excited monopoles

$$\mathbf{H}_{\text{eff}} = \mathbf{H} - \frac{\mathbf{M}}{\chi_T}, \tag{7.20}$$

where $\mathbf{M}(\mathbf{r})$ is the magnetic moment per unit volume and $\chi_T = \frac{\sqrt{3}\mu_0 Q^2}{8k_B T r_d}$ is the magnetic susceptibility of the nearest neighbor spin ice model [60, 61], expressed in terms of the magnetic charge [4]. The effective field drives a magnetic current density $\mathbf{j}(\mathbf{r})$

$$\mathbf{j}(\mathbf{r}) = \frac{\partial \mathbf{M}(\mathbf{r})}{\partial t} = \frac{Q^2 \kappa_m n_f}{\hat{V}} \mu_0 \mathbf{H}_{\mathbf{eff}}(\mathbf{r}), \tag{7.21}$$

where $\hat{V} = \frac{8r_d^3}{3\sqrt{3}}$ is the volume associated with a single tetrahedron (n_f is a number density), and κ_m is the monopole mobility. The latter can be estimated within the linear response regime, using the Einstein relation and the diffusion constant for stochastic monopole dynamics on the diamond lattice; $\kappa_m = \frac{D}{k_B T}$ and $D = \frac{r_d^2}{9\tau_0}$ [24, 31].[1] Normalizing the magnetic moment by its equilibrium value, $m = \frac{|\mathbf{M}|}{|\mathbf{M}_{eq}|}$, leads to the dynamical equation,

$$\frac{dm}{dt} = \frac{1}{\tau_m}(h - m), \tag{7.22}$$

where the dimensionless field $h = \chi_T \frac{|\mathbf{H}|}{|\mathbf{M}_{eq}|}$ and where $\tau_m = \frac{3\tau_0}{2n_f}$ [62] corresponds roughly to the equilibration time scale discussed above, given that for low monopole concentration $n \approx n_f$. Hence, assumming that the free monopole concentration, n_f

[1] The diffusion constant for a random walk on a diamond lattice is $D = \frac{r_d^2}{6\tau_0}$ [24], which is modified to take into account both the spatial [24] and temporal [31] constraints of monopole hopping in the magnetolyte.

and mobility are time and field independent, this non-interacting theory predicts that τ_m indeed diverges exponentially at low temperature, capturing the leading order divergence of magnetic relaxation time scales [5, 36] discussed in the previous section.

7.3.2 Wien Effect

The magnetolyte description of spin ice leads naturally to the study of dynamical properties in the spirit of charge dynamics in an electrolyte. In particular, it has been proposed that spin ice should exhibit the Wien effect in the presence of a magnetic field in analogy with the response of a weak electrolyte to an electric field [63].

The Wien effect [64] is the non-Ohmic contribution to the conductivity of a weak electrolyte due to the field induced change in the number of charge carriers. As only the free charges contribute to the conductivity, the latter is an indirect measure of their concentration, n_f. In the low concentration, or weak electrolyte limit, the effect can be spectacular, with the concentration of charge carriers increasing by up to an order of magnitude. This is due to the fact that the charge increase varies linearly with the modulus of the applied field which is a highly unusual result—a scalar quantity that responds linearly to an applied vector perturbation.

Onsager's famous solution of this problem gives the non-(thermodynamic) equilibrium steady state for a double chemical equilibrium between a vacuum, an ensemble of bound charge pairs treated as a neutral chemical species, and a plasma of free charges: $(0) \rightleftharpoons (+-) \rightleftharpoons (+) + (-)$. The dissociation/association equilibria for the two stages are characterized by the dissociation constants K_0 and K respectively. K_0, the constant determining the balance between the vacuum and the bound pairs, is taken to be field independent. This is a valid approximation, as long as the time scales associated with the first equilibrium are short compared with those of the second [31, 33].

The 'vacuum' (0) is a classical electrolyte of molecules which can dissociate into charges, or other vacua in many chemical and physical processes. Important examples are

$$2H_2O \rightleftharpoons [H_3O^+HO^-] \rightleftharpoons H_3O^+ + OH^-, \tag{7.23}$$

in the case of both water and ice; also, thermal and optical electron-hole generation in semiconductors [65]; to this list one can now add spin ice, a highly original magnetic example [63, 66].

For an electrolyte of charges $\pm q$ and permittivity $\varepsilon = \varepsilon_0 \varepsilon_r$ in the presence of an electric field $E = |\mathbf{E}|$, the evolution of free charges due to the association and dissociation of pairs can be written in the form of a rate equation

$$\frac{dn_f}{dt} = k_D n_b - \frac{k_A}{2} n_f^2, \tag{7.24}$$

where k_D and k_A are the dissociation and association rates and $K = \frac{k_D}{k_A}$. In the non-equilibrium steady state, one finds that, while the association constant remains field independent, the dissociation rate evolves with field leading to Onsager's solution:

$$K(E)/K(0) \equiv F(b) = I_1(\sqrt{8b})/\sqrt{2b} = 1 + b + b^2/3 + \mathcal{O}\left(b^3\right) \quad (7.25)$$

where $b = q^3E/8\pi\varepsilon(k_BT)^2$ and I_1 is a modified Bessel function. The result is universal in that all microscopic details disappear from the dimensionless argument b, which can be cast as the ratio of two lengths: the Bjerrum length $\ell_T = q^2/8\pi\varepsilon k_BT$ and the field length $\ell_E = k_BT/qE$, which defines the scale of thermal fluctuations against the applied field. The leading linear term signals the non-equilibrium nature of the effect, as it would be forbidden by symmetries in equilibrium.

The increase in $K(E)$ relates to the free ion concentration through the steady state solution of the rate equation, (7.24). However, one further caveat is required in that both the chemical kinetics and Onsager's solution are constructed using two body interactions only. As a result, the concentrations occurring in (7.24) are those of a non-interacting system. Including the effects of charge screening increases the concentration by a factor $1/\gamma$, as discussed in Sect. 7.2.2. As a consequence, in the weak electrolyte limit which is of interest for spin ice, the free charge concentration is predicted to evolve in a universal manner:

$$\frac{\Delta n_f(E)}{n_f(0)} = \frac{\gamma(0)}{\gamma(E)}\sqrt{F(\ell_T/\ell_E)} - 1, \quad (7.26)$$

while the bound pair concentration is buffered, i.e., replenished rapidly from the reservoir so that $n_b(E)/n_b(0) = 1$. Consequently the total charge concentration, $n = n_f + n_b$, increases considerably as the field is applied. Outside an initial low field region one assumes that the Debye screening cloud surrounding a charge is destroyed by the applied field, so that $\gamma(E) = 1$, while for intermediate field strengths a phenomenological theory interpolates successfully between the high and low field limits, restoring a regularized E^2 dependence at low fields (see [31, 33] for details).

In Fig. 7.13 we show results from numerical simulations of an electrolyte with parameters equivalent to those of spin ice (diamond lattice, chemical potential equal to that of monopoles in $Dy_2Ti_2O_7$) but without the constraints of the spin degrees of freedom [33]. The data shown are for a temperature equivalent to 0.5 K for $Dy_2Ti_2O_7$ and external field which, when translated into the language of magnetic monopoles, corresponds to a magnetic field in the range, $\mu_0 H = 0 - 150$ mT, with the field aligned along the [100] cubic axis (see Fig. 7.1). The excellent agreement between theory and simulation clearly shows that, putting aside for the moment the kinetic constraints of the Dirac string network, spin ice offers a lattice Coulomb gas at low temperature that falls in the parameter range where the Wien effect is important. We note, for example, that Onsager's theory predicts a five fold increase in monopole density over the above field range. Returning to the magnetolyte, we need to change electric charge $q \to$ magnetic charge Q, $\varepsilon \to 1/\mu_0$ and $E \to H = |\mathbf{H}|$, thus converting the problem from an electrostatic to a magnetostatic one. However,

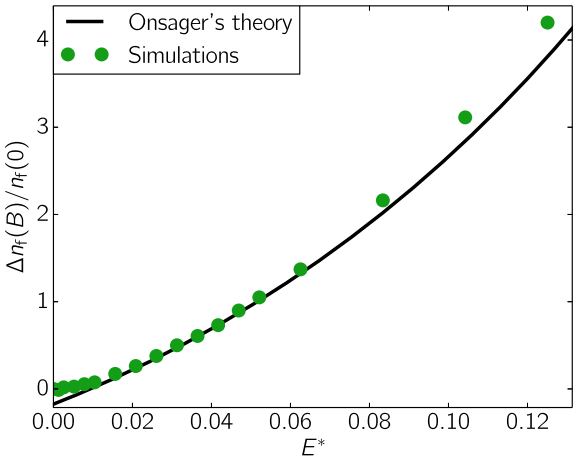

Fig. 7.13 Wien effect for electrolyte: Relative free charge increase as a function of reduced field E^*. The green circles are simulation data from a diamond lattice electrolyte; the continuous line represents Onsager's theory. The data shown parameterize $Dy_2Ti_2O_7$ at $T = 0.5$ K, with reduced field range $E^* = \frac{qE}{\tilde{u}(r_d)} = 0 - 0.12$, where $\tilde{u}(r_d)$ is the nearest neighbor Coulomb interaction for electrical charges q. For spin ice this corresponds to a magnetic field range, $\mu_0 H = 0 - 150$ mT, as discussed in the main text. Reprinted figure from [33] with permission from Nature Materials

things are now complicated by the fact that the magnetolyte does not support a dc current due to the presence of the reaction field. As discussed in Sect. 7.3.1, after applying a field the current decays on a magnetization time scale τ_m [4, 5, 62], because a moving monopole leaves a wake of flipped spins behind it, and a monopole flux inexorably orders the network of Dirac strings, cutting off prospective pathways and stifling the current. However, a transient Wien effect does exist, as can be seen in Fig. 7.14. Here we show simulation results for the evolution of the free charge concentration n_f as a function of time, with an external field applied along [100] at $t = 0$ for an electrolyte and magnetolyte of equivalent chemical potential. While the electric charge builds up from the equilibrium value to a new steady state value on the 'Langevin' time scale τ_L, the monopole concentration increases to an equivalent level, but then dips down, falling eventually below the starting concentration over a time scale τ_m. At the temperature shown, $T = 0.5$ K, the two times scales are very different and this difference increases as the temperature falls, resulting in a time window in which the two systems are equivalent. Therefore, as shown in Fig. 7.15, on applying a square wave ac field for frequencies within this window, an excess monopole concentration can be stabilized, corresponding to the steady state excess for the electrolyte at the given field strength. From Fig. 7.15b one can observe that the agreement between Onsager's theory for the fractional increase in n_f and the results from numerical simulation for a square field pulse of frequency $2\pi/\tau_m < \omega < 2\pi/\tau_L$ is indeed quantitative, confirming the existence of a quasi-steady state Wien effect in the magnetolyte. The steady state response to a field of constant amplitude, but

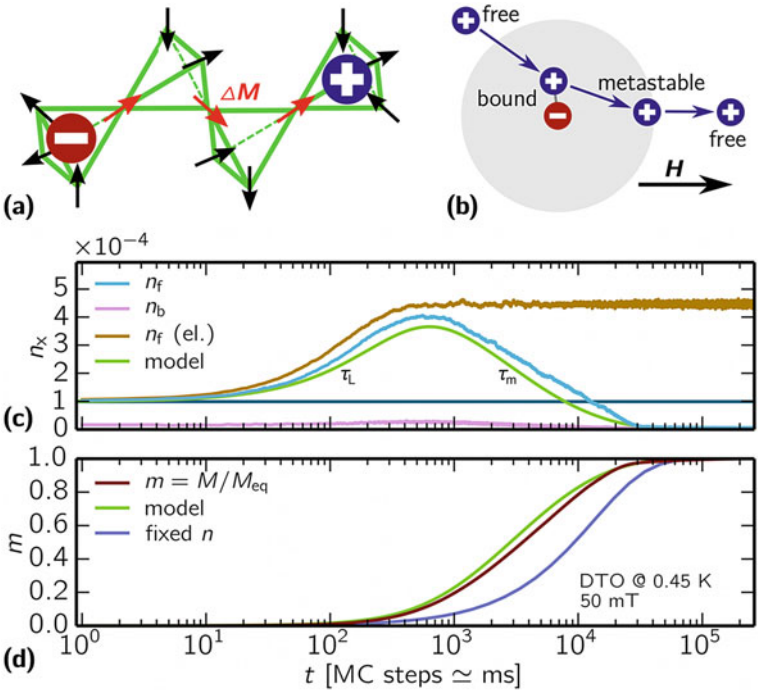

Fig. 7.14 (Color online) **a** Monopoles move via spin flips; their current magnetizes the spin configuration. **b** The second Wien effect involves the field-enhanced dissociation of bound pairs. Nonlinear response: **c** After a field quench, the Wien effect increases the free charge density, n_f, in an electrolyte. In a magnetolyte with the same initial density and temperature, the free monopole density increase is only transient, counteracted by the growing magnetization m of the system (**d**). The increased monopole density is observable in the faster rate of magnetization m compared to a magnetization process at fixed density n. The response is well described by the kinetic model. The bound charge density is only weakly influenced (n_b). The magnetolyte parameters are $T = 0.45$ K, $n_\mathrm{tot}(0) \simeq 1.1 \times 10^{-4}$, $n_\mathrm{f}(0) \simeq 1.0 \times 10^{-4}$, and $\mu_0 H_0 = 50$ mT; the electrolyte parameters are set to obtain the same zero field density. Reprinted figure from [62] with permission from the American Physical Society

alternating directions, illustrates the coupling of the monopole density to the modulus of the applied field. The magnetization reverses with the field as expected, but the moment at each reversal point is far from saturated.

As we have seen, the magnetization time scale depends inversely on the free monopole concentration, $\tau_m \sim 1/n_f$. Hence, going beyond linear response theory, the magnetic response and the monopole response to an applied field are coupled. A nonlinear theory can be developed which encapsulates this coupling. Applying $H(t) = H_0 h(t)$ along [100] and following (7.22), (7.24) and (7.25), one can write

$$\mathrm{d}n_\mathrm{f}/\mathrm{d}t = k_\mathrm{D} F\,(b_0\,|h(t) - m|)\,n_\mathrm{b} - k_\mathrm{A} n_\mathrm{f}^2/2\,, \tag{7.27}$$

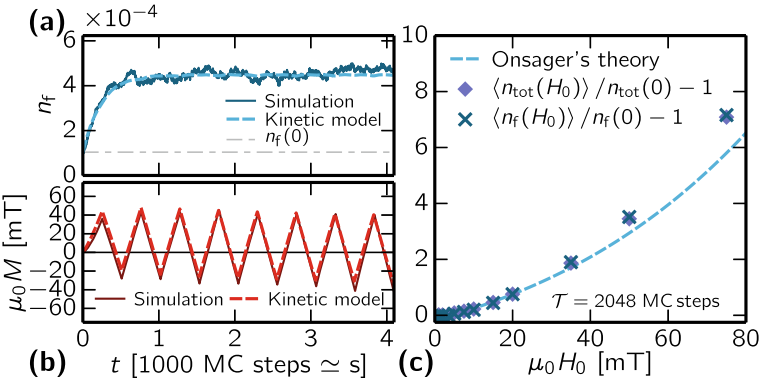

Fig. 7.15 (Color online) Square wave driving stabilizes the free monopole density increase due to the second Wien effect (**a**), provided that the magnetization M stays well below $M_{\rm eq} = \chi_T H_0$ (**b**). The kinetic model captures the response including the transition from equilibrium to a periodic steady state. The amplitude-dependence of the average density increase (**c**) matches the DC Wien effect theory with no free parameters, confirming spin ice's dynamical "window" of electrolyte behavior. Magnetolyte parameters are $T = 0.45$ K, $n_{\rm tot}(0) \simeq 1.1 \times 10^{-4}$, $n_{\rm f}(0) \simeq 1.0 \times 10^{-4}$, and $\mu_0 H_0 = 50$ mT (a–b). Reprinted figure from [62] with permission from the American Physical Society

where, $b_0 = \mu_0^2 Q_{\rm m}^3 H_0 / 8\pi (k_{\rm b} T)^2$. We note again that the evolution of the rate equation depends on the modulus of the field. Linearising in $b_0 |h(t) - m|$ and in $\Delta n_{\rm f} = n_{\rm f} - n_{\rm f}^0$ one finds

$$ {\rm d}\Delta n_{\rm f}/{\rm d}t = k_{\rm D}(0) n_b b_0 \, |h(t) - m| - k_{\rm A} n_{\rm f}^0 \Delta n_{\rm f} \ . \tag{7.28} $$

We now use the key elements of the Wien effect: n_b and $k_{\rm A}$ are unchanged on application of a field and $k_{\rm D}(0) = k_{\rm A} n_f(0)^2/(2n_b)$, so that defining $\zeta(t) = \Delta n_{\rm f}(t)/(b^0 n_{\rm f}(0)/2)$, one obtains the first of two constitutive equations

$$ {\rm d}\zeta/{\rm d}t = \frac{1}{\tau_{\rm L}^{(0)}} \left(|h(t) - m| - \zeta \right) \ , \tag{7.29} $$

where $\tau_{\rm L}^{(0)} = 2\tau_0/(\chi_T n_{\rm f}(0))$ is the zero field Langevin time [64, 67]. The second is the Ryzhkin dynamical equation for the magnetization relaxation, (7.22), taken beyond linear response through the field dependence of the free monopole concentration:

$$ {\rm d}m/{\rm d}t = (1 + b_0 \zeta/2)(h(t) - m)/\tau_{\rm m}^0 \ . \tag{7.30} $$

with $\tau_{\rm m}^0 = (3/2)\tau_0/n_{\rm f}(0)$.

Equations (7.29) and (7.30) form a complete kinetic model which captures the non-equilibrium dynamics observed in simulations: the non-linear behavior comes dominantly from the absolute value in (7.29) and the monopole-spin coupling term

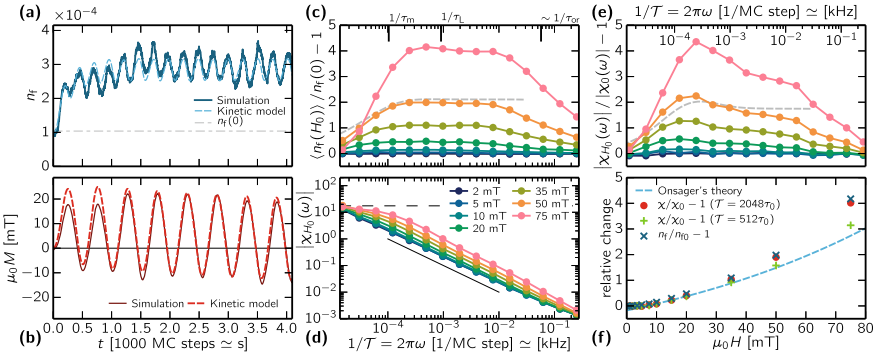

Fig. 7.16 (Color online) The free monopole density increase (**a**) due to sine driving enhances the magnetic response (**b**). The Wien effect persists over a range of frequencies (**c**). The enhanced density leads to an increase in the absolute value of the non-linear susceptibility (**d**), where the dashed line is χ_T and solid line is $\propto 1/\omega$. The relative change in χ_{H_0} is shown in (**e**) revealing additional features in the Wien effect plateau compared to the density increase. The amplitude dependence stays close to Onsager's theory of the DC Wien effect despite the approximations made (**f**). The kinetic model (results for $\mu_0 H_0 = 50$ mT) captures the time evolution of density and magnetization (dashed lines in a–b); the low-frequency transition in density and susceptibility (dashed lines in c and e); and the structure of the susceptibility increase. However, it does not include the high-frequency cutoff due to pair reorientation. Magnetolyte parameters are $T = 0.45$ K, $n_{\rm tot}(0) \simeq 1.1 \times 10^{-4}$, $n_{\rm f}(0) \simeq 1.0 \times 10^{-4}$. Reprinted figure from [62] with permission from the American Physical Society

$b\zeta m/2$ in (7.30). To make quantitative comparisons between this non-linear theory and numerical simulation, one can further replace $b_0\zeta/2$ with the full expression for the Wien effect, (7.26) and $\tau_{\rm L}^{(0)}$ with $\tau_{\rm L} = \tau_{\rm L}^{(0)} n_{\rm f}(b)/n_{\rm f}(0)$. The equations are not generally solvable in closed form, but are readily integrated numerically. As shown in Figs. 7.14, 7.15a, b, 7.16a, b, the dynamical equations give quantitive agreement with numerical data for both magnetization and monopole density, in the case of a constant field applied at $t = 0$ and for a square/sinusoidal field of frequency ω.

The major advantage of spin ice over an electrolyte system is that magnetic response experiments are readily available. The dynamical coupling between monopole concentration and magnetization strongly suggests that Wien effect physics should be apparent in these. From Fig. 7.16 one can see that, as for an electrolyte [67–70], enhanced density is stabilized by harmonic driving of the magnetolyte with field $H(t) = H_0 \sin(\omega t)$. Harmonic driving stabilises a plateau of monopole density increase in a frequency window between $\omega_{\rm low} \simeq 1/\tau_{\rm m}$ and $\omega_{\rm high} \gg 1/\tau_{\rm L}$ (Fig. 7.16c). The magnetization also responds to the applied field and the dynamical equations reproduce the evolution of both these quantities with remarkable accuracy. We notice that the process limiting the AC Wien effect at high ω appears to be the reorientation of bound pairs along the field direction (on a time scale $\tau_{\rm or}$), and not the density relaxation ($\tau_{\rm L}$); see [42] for an early treatment of reorientation.

As a consequence, a signature of the Wien effect can indeed be developed from susceptibility measurements. From (7.22), holding $n_f = n_f(0)$, one finds a Debye-like susceptibility [4, 71], characteristic of a paramagnetic response

$$\chi^0(\omega) = \chi_T/(1 - i\omega\tau_{\rm m}^0), \tag{7.31}$$

although the time scale τ_m^0 corresponds to the collective response of the Dirac strings, rather than of the individual dipoles, and is consequently extremely long at low temperature compared to microscopic time scales. Including the time dependent evolution of the monopole density through the Wien effect, (7.30), introduces a correction to this relaxation which shows up in the non-linear susceptibility.

Spectral analysis of $M(t)$ yields $M(\omega)$, from which one can define $\chi_{H_0}(\omega) = M(\omega)/H_0$, with the non-linear part being the excess, $\delta\chi(\omega) = \chi_{H_0}(\omega) - \chi^0(\omega)$. One finds non-linear contributions both at the frequency of the applied field and for higher harmonics. Both the magnitude of the field response and the occurrence of higher harmonics are characteristic of the Wien effect. Specifically, only odd higher susceptibilities are visible. This is a direct consequence of the coupling of the density to the modulus of an applied vector field [67] and to the occurrence of even harmonics in density.

In Fig. 7.16d, e one can observe the appearance of a significant non-linear susceptibility in the same frequency window for $Dy_2Ti_2O_7$ at $T = 0.45$ K. Throughout the window we have $\omega \gg 1/\tau_m$, so that

$$\frac{|\delta\chi(\omega)|}{|\chi^0(\omega)|} \approx \frac{\Delta\,\langle n_{\rm f}(H_0)\rangle_{\mathscr{T}}}{n_{\rm f}(0)}, \tag{7.32}$$

where the monopole concentration increase is averaged over the period of the applied field, $\mathscr{T} = 2\pi/\omega$. Hence the relative non-linear susceptibility should be given by Onsager's formula, (7.26). From Fig. 7.16f one can see that this is true to a good level of approximation, particularly at frequencies $1/\tau_{\rm m} \lesssim \omega \lesssim 1/\tau_{\rm L}$ (Fig. 7.16e) where the density fully relaxes as the field changes (even from zero field, as in Fig. 7.14c). A reduction in magnetic response is observed between $1/\tau_{\rm L}$ and $1/\tau_{\rm or}$, reflecting the increasing fraction of time the monopoles spend establishing the Wien effect rather than magnetizing the system. The Wien effect vanishes for $\omega \gg 1/\tau_{\rm or}$. The same theory holds at higher temperatures where relaxation time scales are more accessible; we refer the reader to [62] for equivalent results for parameters corresponding to $Dy_2Ti_2O_7$ at $T = 0.7$ K.

From this analysis it appears that the magnetolyte provides a rare example of a model system in which an experimentally relevant non-linear many body response can be treated analytically and numerically in great detail. This luxurious situation is down entirely to the monopole picture, as it is hard to imagine that the complex magnetic response to the field could have been predicted without it. Initial experiments on $Dy_2Ti_2O_7$ show that this kind of protocol works at high fields [45] where the Wien effect, which predicts a monopole current varying as the square root of the applied field, is observed. Onsager's theory is fitted in this limit with an anomalously small

activity coefficient, which could be a signal of non-equilibrium behaviour. Results at lower field are, however less convincing, possibly because of a temperature or disorder dependent monopole mobility, as discussed above. Clearly more experimental work is required to access the Wien effect over a full range of temperatures and fields. This is a great challenge for the future as success in modelling of the AC Wien effect would open the door to a broad range of experiments in which spin ice provides a model system for the study of non-equilibrium and non-linear physics.

For the moment however, there remain open questions for instance about the exact nature of the linear response at $T < T_{\rm f} \simeq 0.6$ K in $Dy_2Ti_2O_7$ [25, 36, 40, 72, 73], when the system is no longer ergodic on experimentally accessible time scales. Here it is convenient that the approach outlined above relies only on measuring relative quantities, eliminating many non-universal contributions. Finally, we note that this model and analysis should contribute to the resolution of open issues concerning the experiment of [63] (see also [74–78], and [79] for a summary).

7.3.3 Behaviour Far From Equilibrium

In general, a system in which point-like excitations freely moving in three dimensions are responsible for bulk magnetic response is bound to exhibit an interesting separation of time scales. This is in contrast with the conventional scenario where the dynamics is dominated by the domain coarsening time scale, characteristic e.g., of ferromagnetic and antiferromagnetic systems [80]. Monopoles are created and annihilated in nearest neighbour pairs, so that monopole density relaxation processes involve monopole motion over distances of the order of the average monopole-monopole separation, $\xi \sim n^{-1/3}$. In a ballistic regime where positive monopoles are driven towards negative monopoles, the corresponding time scale is of the order of ξ monopole hops. At sufficiently high temperatures and / or beyond the screening length, the monopole motion is diffusive and the time scales as $\xi^2 \sim n^{-2/3}$. Finally, any changes in the bulk magnetisation and other observables that depend on the local spin orientations require the monopoles to visit a finite fraction of the spins in the systems. Therefore on average they have to move across a finite fraction of ξ^3 spins per monopole, corresponding to a time scale of the order of $\xi^3 \sim n^{-1}$ (see Sect. 7.3.1 for a more formal discussion of this result).

One further expects a close interplay between the dynamical properties of the monopoles—which are fractionalised point-like excitations—and the properties of the spin-ice vacuum that hosts them. For instance, at a local level each monopole can only ever hop across 3 of the 4 neighbouring spins (see later Fig. 7.18). At a global level the motion of monopoles polarises the vacuum they traverse and therefore two monopoles of the same charge cannot directly follow one another (see also the discussion of the reaction field in Sect. 7.3.2). This interplay is responsible for both local and global (topological) kinematic constraints that play a crucial role in determining the dynamical behaviour of spin ice systems. The fact that we can couple to the vacuum directly using externally applied fields allows for a supripsing

tuneability of the dynamical behaviour, as we have already seen in the case of the Wien effect in Sect. 7.3.2.

As a result, the nature of the fractionalised excitations in spin ice strongly affects its dynamical properties and is reflected in the behaviour of the system when it is brought strongly out of equilibrium. In the following, we shall discuss two examples in some detail. Specifically, we shall consider sudden quenches from a high to a low monopole density state, triggered by either tuning the temperature (Sect. 7.3.4) or an applied magnetic field (Sect. 7.3.5).

We shall discover intriguing connections between the physics of spin ice and other areas of research, including reaction diffusion processes in the presence of long-range Coulomb interactions, dimer adsorption, and kinetically constrained models. This lead to the affirmation of spin ice as a laboratory of choice for the study of tuneable, slow dynamics.

We mention in passing that the phase diagram of spin ice includes a critical end point in presence of a magnetic field. "Slow quenches" (i.e., continuous variations of the parameters as a function of time) to / across the critical point are therefore expected to give rise to out-of-equilibrium scaling behaviour à la Kibble-Zurek, in the novel context of a topological magnet with emergent gauge symmetry and fractionalised Coulomb-interacting quasiparticles [81]. Although experimental evidence for the universal scaling of defect density in Kibble Zurek ramps is available [82, 83], a decisive test of the scaling of dynamical response functions in this context is currently lacking. Spin ice materials offer a unique experimental opportunity owing to their slow microscopic time scales [5, 36], $\tau_0 \sim 1$ ms, in contrast with typical critical phenomena in magnetic materials which occur on much faster time scales, of the order of nanoseconds or even picoseconds. The simulations in [81] suggest that Kibble Zurek scaling in spin ice is within reach of current field sweep experimental capability [40].

7.3.4 Thermal Quenches

One way to cause the system to evolve from a state with high monopole density to a state with low monopole density is to lower its temperature. Here we consider for simplicity the case where the system is initially at infinite temperature (trivial Ising paramagnet) and it is suddenly quenched to a target (low) temperature [38]. In Coulomb liquid terms, this is equivalent to quenching a plasma where positive and negative charges can be created (and annihilated) only in pairs, and each charge costs some finite amount of energy $\Delta = -\mu$.

Immediately after the quench, the system is strongly out of equilibrium (e.g., the monopole density is much larger than its thermodynamic value at the target temperature). When coupled to a thermal bath, it will relax to equilibrium via the available dynamical processes, namely monopole motion and monopole-antimonopole creation/annihilation—this is typical of reaction-diffusion processes and contrasts the behaviour of conventional magnetic systems.

Whereas monopole-antimonopole annihilation events lower the energy of the system, pair creation events face a finite energy cost Δ_s and are hence suppressed by the Boltzmann factor $\exp(-\Delta_s/k_BT)$. We limit ourselves below to the case where the target temperature is much smaller than the pair creation energy so that we can neglect creation processes altogether. In this regime the equilibrium density of monopoles at the target temperature is also vanishingly small and we shall set it to zero. The equations of evolution for the monopole density can be generically written as [84]:

$$\begin{aligned} \frac{\partial n_\pm(r,t)}{\partial t} + \nabla \cdot \mathbf{J}_\pm &= -\kappa\, n_+(r,t) n_-(r,t) \\ \mathbf{J}_\pm &= -D\nabla n_\pm(r,t) - \kappa_m\, q_\pm n_\pm(r,t)\nabla V(r,t)\,, \end{aligned} \tag{7.33}$$

where $n_\pm$ and $\mathbf{J}_\pm$ are the densities and currents of positive and negative monopoles, $\kappa = 2k_A$ is the annihilation reaction constant and where the local monopole current $\mathbf{j}(\mathbf{r}) = Q(\mathbf{J}_+ - \mathbf{J}_-)$. The two current terms are due to diffusion (constant D) and deterministic drift caused by long range interactions (mobility κ_m, interaction potential V). As discussed in Sect. 7.3.1, the relevant constants can be estimated analytically or obtained from independent comparison to simulations or experiments, leaving few or no fitting parameters in the equations [38].

Nearest-neighbour spin ice

Let us focus firstly on the case where spin-spin interactions are truncated at nearest-neighbour distance and correspondingly the charges in the Coulomb liquid language are non-interacting ($V(r) = 0$), so that $u_d = 0$ and $\Delta_s = 2\Delta$.

Within this approximation, and under the quench conditions outlined in Sect. 7.3.4, the dynamical processes in the system are limited to diffusion of non-interacting charges and monopole-antimonopole annihilation events. At the mean field level (uniform system, no spatial dependence), the diffusive term can be dropped and we are left with a straightforward reaction equation:

$$\frac{dn}{dt} = -\kappa\, n^2(t). \tag{7.34}$$

(This is directly related to the chemical kinetics discussed in Sect. 7.3.2, namely (7.24), once Coulomb interactions are suppressed, as appropriate for nearest-neighbour spin ice.) The right hand side is determined by the rate of monopole annihilation events, which is proportional to the probability of finding a monopole-antimonopole pair in the system ($\sim n^2$) divided by the characteristic time scale for a single annihilation event to take place (namely, the characteristic single spin flip time scale τ_0). The constant $\kappa \propto 1/\tau_0$ depends on details of the underlying microscopic lattice through a combinatorial factor accounting for the ways to arrange two monopoles next to one another across a bond of the lattice [38] (see also Sect. 7.3.2).

The mean field (7.34), complemented with the initial condition $n(t = 0) = n_0$, can be solved straightforwardly to find

$$n(t) = \frac{n_0}{1 + \kappa n_0 t} \tag{7.35}$$

such that the long time decay in the monopole density goes as t^{-1}. The accuracy of the mean field solution in describing the behaviour of nearest-neighbour spin ice depends crucially on how uniform the initial charge distribution is, to ensure that diffusion time scales are indeed irrelevant.

Spatial variations in the initial distribution of monopoles and antimonopoles can however alter the behaviour significantly [85]. For instance, if the charges are distributed entirely at random with density n_0, then the net charge fluctuations in a volume of linear size ℓ scale as $\sqrt{n_0 \ell^3}$. Given that annihilation processes conserve the local net charge (they always remove one positive and one negative monopole), they cannot remove these fluctuations. After a time t sufficient for monopoles to diffuse over the length ℓ (i.e., $\ell = \sqrt{Dt}$), all possible annihilation events within the volume of size ℓ will have taken place, leaving behind a number $\sim \sqrt{n_0 \ell^3}$ of monopoles of the same charge due to the statistical net charge fluctuation. The density of leftover monopoles scales as $\sqrt{n_0 \ell^3}/\ell^3 = n_0^{1/2}(Dt)^{-3/4}$; it decays with time more slowly than the mean field behaviour ($\sim t^{-1}$) and therefore dominates at long times. (We refer the reader to [85] for a detailed derivation and discussion of this result.)

However, none of this in fact applies to spin ice. As discussed above, when a monopole travels along a given path across the system, it modifies the underlying spin ice vacuum by polarising the spins along the path. Another monopole of the same charge *cannot* follow the same path in the same direction. Equivalently, we can at most drive ℓ^2 monopoles of equal charge across a system of volume ℓ^3 before the system becomes fully polarised and no more monopoles of the same charge can travel in that direction. This means that the most net charge that can accumulate in a volume ℓ^3 of a spin ice system is of the order ℓ^2. The density of leftover monopoles in spin ice therefore scales as $\sqrt{\ell^2}/\ell^3 = (Dt)^{-1}$ rather than $(Dt)^{-3/4}$, which has the same asymptotic behaviour as the mean field solution.

These observations are confirmed by the excellent agreement between Monte Carlo simulations of thermal quenches in nearest neighbour spin ice and the solution of the mean field equation, (7.35), illustrated in Fig. 7.17. Notice that the agreement is achieved without any fitting parameters [38].

Dipolar spin ice

Let us now consider the case of dipolar spin ice, where monopole excitations are coupled by long range Coulomb interactions. The additional energetic term introduces a bias for positive and negative monopoles to find one another which leads to screening correlations at equilibrium, and it has in general a smoothing effect on spatial fluctuations of the net charge. Therefore, the naive expectation from this coarse grained picture is that the monopole density decay following a thermal quench in DSI is at least as fast as the nearest neighbour case. (We refer the reader to [84] for a discussion of annihilation-diffusion reaction processes in presence of long-range interactions.)

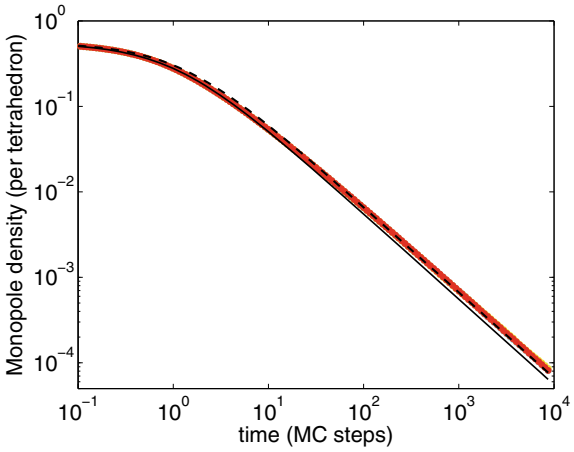

Fig. 7.17 Monopole density evolution in nearest neighbour spin ice, after a thermal quench from $T = 10$ K to $T = 0$ K, for system sizes $L = 32, 64, 128$ (where the total number of spins is $16L^3$). The analytical mean-field result (7.35) is shown for $\kappa = 3/2\tau_0$ (dashed black line) and $\kappa = 9/5\tau_0$ (solid black line)—see [38] for details. Reprinted figure from [38] with permission from the American Physical Society

Monte Carlo (MC) simulations confirm this expectation at short times, as illustrated in Fig. 7.18, right panel. However, for sufficiently low target temperatures, a long-lived metastable plateau develops in the time evolution of the monopole density. This new and unexpected feature is due to a curious interplay between long-range emergent physics (the Coulomb liquid description) and lattice-scale physics (related to how monopole motion changes the underlying spin ice vacuum)—a phenomenon already encountered in the discussion of the Wien effect in Sect. 7.3.2.

When a positive and a negative monopole meet in spin ice, there is a one in four chance that spin between them is a minority spin rather than one of the three majority ones, as illustrated in Fig. 7.18, top left panel. In this case, flipping the spin does not annihilate the two monopoles but rather creates a double monopole pair (a pair of 4in-4out tetrahedra) at high energy cost. At low temperatures, the likelihood of such process is so low that it is effectively forbidden. We shall dub such pairs of monopoles *noncontractible*. Once they meet through a minority spin, the two monopoles of a noncontractible pair are bound together, held by their mutual Coulomb attraction. This is a direct consequence of the long-range nature of the dipole-dipole interaction.

The monopoles forming noncontractible pairs do not need necessarily to separate in order to be able to annihilate. It can also happen that another (free) monopole collides with the pair, whereby it annihilates one of the monopoles in the pair (that with opposite charge to the free monopole) and free up the other one. Pictorially, one can think of this as *radioactive decay*, triggered by the absorption of a monopole, in contrast to *spontaneous decay* of the pair, where the monopole and antimonopole separate and annihilate elsewhere on the lattice. The radioactive process straightfor-

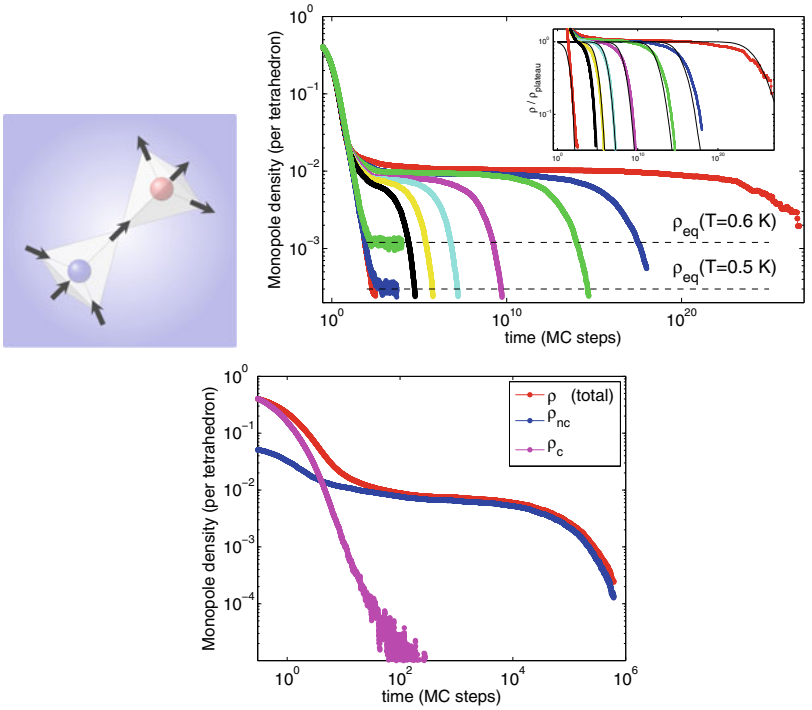

Fig. 7.18 Top left panel: Spin configuration of two adjacent tetrahedra hosting a noncontractible monopole-antimonopole pair. Top right panel: Decay of the total monopole density in Monte Carlo simulations of dipolar spin ice, following thermal quenches from infinite temperature to different finite target temperatures (see Fig.3 in [38] for details). Inset: comparison of the long time tail of the monopole density to the Poissonian modelling of the spontaneous decay of noncontractible pairs discussed in the text. Bottom panel: Monte Carlo simulation of dipolar spin ice, showing the total monopole density (red), noncontractible pair density (blue), and free monopole density (magenta), following a thermal quench from $T = \infty$ to $T = 0.125$ K, with system size $L = 8$ and $Dy_2Ti_2O_7$ parameters. Reprinted figure from [38] with permission from the American Physical Society

wardly reduces the energy of the system, whereas the spontaneous process incurs a finite energy barrier (the Coulomb separation energy).

Which of the two processes controls the long time decay of the monopole density depends on the relative population of free monopoles and noncontractible pairs. If free monopoles are abundant, then nearly all noncontractible pairs decay radioactively (vanishing energy barrier, fast relaxation channel). If instead most monopoles in the system form noncontractible pairs, then their annihilation must occur via spontaneous decay (slow relaxation channel, due to the finite activation energy barrier).

At high-temperature, when the system is nearly paramagnetic and the defects are dense, one can readily verify that the density of free monopoles is statistically larger (by about one order of magnitude) than the density of noncontractible pairs—as reflected in the initial conditions that can be inferred from Fig. 7.18, bottom panel.

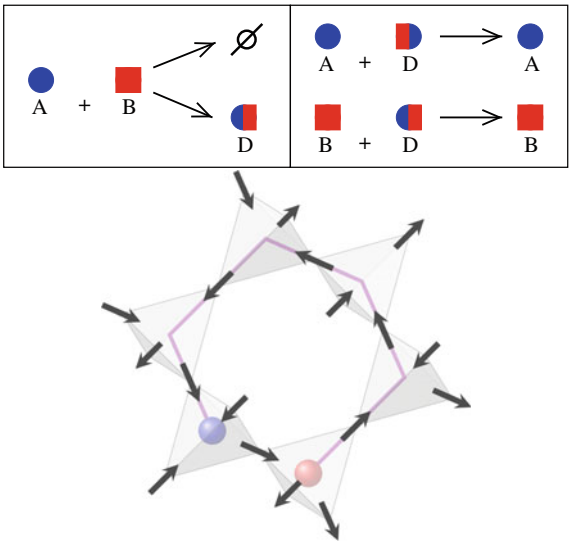

Fig. 7.19 Top panel: Qualitative illustration of the dynamical processes involved in the monopole density evolution following a thermal quench in dipolar spin ice. (A=positive and B=negative monopole; D=noncontractible pair). Bottom panel: Example of a hexagonal path for the spontaneous decay of a noncontractible pair

Therefore, we see that a *population inversion* is required to cause the system to relax via the slow channel and to develop a long-lived metastable plateau at low temperature.

Once again, the long range Coulomb interaction plays a crucial role in determining how the free vs noncontractible monopoles evolve with time. Free monopoles and antimonopoles are drawn together by Coulomb forces which are stronger than the attraction between free monopoles and noncontractible pairs (charge-dipole interaction). Naively, one would thus expect that the long range interactions favour direct annihilation of free monopoles over the radioactive decay of noncontractible pairs. If the bias is sufficiently pronounced, it can eventually cause the density of free monopoles to become vanishingly small with respect to the density of noncontractible pairs, leading to the population inversion and the metastable plateau. MC simulations of DSI seem to confirm this picture, in that they show a population inversion taking place and the density of noncontractible pairs is solely responsible for the long lived metastable plateau (see bottom panel in Fig. 7.18). However, the precise role of the long-range tail of the Coulomb interaction in the population inversion, to verify or reject the naive conjecture about the bias, is subject of ongoing investigation.

As in the case of nearest-neighbour spin ice, one can use differential equations for reaction-diffusion processes to model the evolution of the monopole density following a quench and confirm the qualitative understanding presented above. The processes that ought to be included are:

1. monopole-antimonopole annihilation
2. noncontractible pair formation
3. radioactive and spontaneous decay of noncontractible pairs.

They are qualitatively illustrated (with the exception of the spontaneous decay) in the top panel of Fig. 7.19. In contrast to the nearest neighbour case, one has to introduce an additional density variable to represent noncontractible pairs (a new 'species' of particles whose evolution is directly related to that of the free monopoles).

Here we limit ourselves to modelling in some detail the long time tail of the monopole density decay. As discussed above, it is evident from the bottom panel of Fig. 7.18 that the noncontractible pairs are largely responsible for this tail. In this regime we expect the spontaneous decay of noncontractible pairs to be the leading dynamical process in the system.

Firstly, we ought to estimate the typical energy barrier $\Delta E_{\rm nc}$ of a spontaneous decay process. This is determined by the distance by which a monopole and an antimonopole in a noncontractible pair need to be separated before they are able to annihilate elsewhere in the lattice. The shortest possible path is illustrated in the bottom panel of Fig. 7.19. It requires separating the two monopoles from nearest neighbour ($r_{\rm nn}$) up to third neighbour ($r_{3\rm n}$) distance, before they are brought together again to annihilate:

$$\Delta E_{\rm nc} = -\frac{\mu_0}{4\pi} Q^2 \left(\frac{1}{r_{3\rm n}} - \frac{1}{r_{\rm nn}} \right). \tag{7.36}$$

Now that we have an estimate of the energy barrier, we can proceed with modelling the spontaneous decay of noncontractible pairs. (Notice that the existence of a hexagonal decay path for each noncontractible pair is far from obvious and ought to be regarded as a working assumption at this stage; it will be confirmed a posteriori by comparison with simulations.) We shall assume that the spontaneous decay events are uncorrelated and they obey a Poissonian distribution, with decay probability per unit time $\mathscr{P}(t) = e^{-t/\tau_{\rm nc}}/\tau_{\rm nc}$. The time scale for the activated process is $\tau_{\rm nc} = \tau_0 e^{\Delta E_{\rm nc}/k_B T}$, where τ_0 is the microscopic spin flip time scale ($\tau_0 = 1$ in MC simulations). Finally, the noncontractible pair density at time t is determined by the number of pairs that have not annihilated via spontaneous decay at any $t' \leq t$, i.e.,

$$n(t) \;\propto\; 1 - \int_0^t \mathscr{P}(t')\, dt' \;\propto\; e^{-t/\tau_{\rm nc}}. \tag{7.37}$$

In the magnetolyte Coulomb liquid, $\Delta E_{\rm nc}$ is defined by the Coulomb interaction as in (7.36). However, as we have seen, when mapping from the DSI to the magnetolyte one neglects quadrupolar corrections to self-screening that give the Pauling states a finite bandwidth [3, 15, 20] (see Sect. 7.2.1). These terms lead to many body corrections to $\Delta E_{\rm nc}$ that are well approximated by a Gaussian distribution of mean $\Delta E_{\rm nc} \simeq 1.47$ K and variance 0.01 K^2 [38], obtained from MC simulations of DSI using $Dy_2Ti_2O_7$ parameters. The value of $n(t)$ in (7.37) ought to be averaged over such a Gaussian distribution to compare with simulations:

$$\langle n(t) \rangle_{\rm dis} \propto \int \exp\left[-\frac{(\Delta E - \Delta E_{\rm nc})^2}{2\sigma^2} \right] \exp\left[-\frac{t}{\tau_0 e^{\Delta E/k_B T}} \right] d\Delta E. \tag{7.38}$$

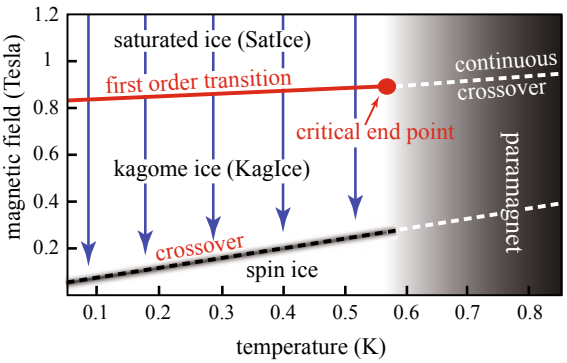

Fig. 7.20 Phase diagram of spin ice in presence of a [111] field. The vertical arrows represent field quenches from saturated ice (high monopole density) to kagome ice (low monopole density), discussed in the text. Reprinted figure from [41] with permission from PNAS

Notice that (7.37), (7.38) have only one fitting parameter left: the proportionality constant, i.e., the height of the metastable plateau induced by the long-lived non-contractible pairs. The comparison between theory and simulations is illustrated in the inset of the right panel in Fig. 7.18. We note the good agreement over *more than 20 orders of magnitude*, demonstrating that the qualitative understanding in terms of Coulomb liquid and noncontractible pairs is indeed correct, and that the choice of single-hexagon paths for the spontaneous decay is justified. (Had we ignored the finite width of the Gaussian distribution and used the mean value of $\Delta E_{\rm nc}$ instead, we would have captured the long time behaviour to leading order, but the agreement between theory and simulations in Fig. 7.18 would have been appreciably worse.)

We close by stressing the role played by the long range Coulomb interactions between the monopoles in determining the strikingly different behaviour in dipolar vs nearest neighbour spin ice. On the one hand, they are responsible (at short range) for the existence of metastable noncontractible pairs. On the other hand—we conjectured—their long range nature contributes to the population inversion that is key to the long time plateau in the monopole density at low temperatures.

(We refer the reader to [38] for a discussion of possible experimental verification in field-quench and field-sweep measurements, and also to [43], [45].)

7.3.5 Field Quenches

An alternative protocol to drive spin ice from high to low monopole density involves the use of an applied magnetic field pointing in one of the global [111] crystallographic directions. Whereas a small field exerts a force driving the monopoles across the system, this effective description breaks down for intermediate and large fields, and their leading effect becomes that of a (staggered) chemical potential for the monopoles [3]. The resulting phase diagram is typical of a liquid-gas system, with a first order transition line ending at a critical end point (see Fig. 7.20).

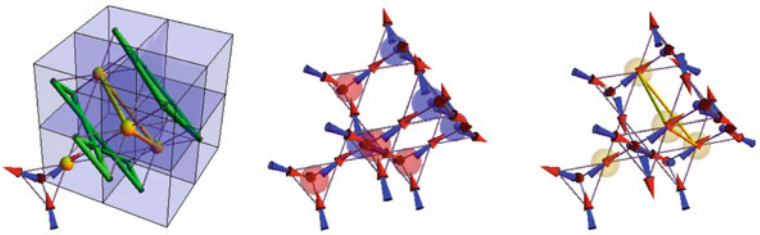

Fig. 7.21 Left panel: With respect to the global [111] direction identified by the field, the pyrochlore lattice can be seen as a stack of triangular (yellow) and kagome (green) layers perpendicular to the field direction. The easy axis of the triangular spins is parallel to the field whereas the kagome easy-axes are canted, all with the same projection factor $1/3$ onto the field direction. Middle panel: Saturated spin ice state. Right panel: An example of a kagome ice spin configuration. Reprinted figure from [41] with permission from PNAS

To understand this phase diagram, it is convenient to divide the pyrochlore spin lattice into alternating kagome and triangular layers perpendicular to the field direction, as illustrated in Fig. 7.21, left panel. In the limit of strong fields (the saturated ice regime), all of the spins point along the field direction while respecting the local easy axes (Fig. 7.21, middle panel). The ice rules are violated everywhere and each tetrahedron hosts a monopole; the monopoles form an 'ionic crystal' of alternating positive and negative charges [29]. As the field strength is reduced, violations of the ice rules are no longer offset by a gain in Zeeman energy and a regime where most tetrahedra obey the ice rules is recovered (at low temperature). This necessarily requires some of the spins to point against the applied field. At intermediate field strengths, these are mostly spins in the kagome planes, because their Zeeman energy is smaller by a factor of three compared to the spins in the triangular planes. This leads to an extensively degenerate regime known as kagome ice [86–88], illustrated in Fig. 7.21, right panel. At low field strengths, the kagome ice regime becomes entropically unstable to the conventional spin ice regime, namely the ensemble of all configurations satisfying the ice rules irrespective of the polarisation of the triangular spins. All of these regimes cross over at sufficiently large temperatures into a conventional paramagnet.

The range of behaviours that can be investigated in quenches involving an applied field is far richer than in thermal quenches [41]. For instance, the fact that triangular and kagome spins couple differently to the applied field can be used to tune the dimensionality of the system (2D $\leftrightarrow$ 3D). Moreover, the ability to tune both temperature and Zeeman energy against the long range Coulomb interaction allows one to control the dynamical processes at play and even to alter the characteristic monopole hopping time scales.

Here we focus for simplicity on field quenches across the first order transition, while the temperature is held constant. Our initial condition is the large field (saturated ice) state, where each spin has positive projection in the direction of the field (Fig. 7.21, middle panel). Every 'upward pointing' tetrahedron is occupied by a pos-

itive monopole and every 'downward pointing' tetrahedron is occupied by a negative monopole. Further, we only consider temperatures and target field values whereby the thermal equilibrium state after the quench is that of kagome ice. Here the Zeeman energy of the triangular spins is sufficiently large with respect to temperature that they remain effectively fully polarised in the field direction. On the other hand, the Zeeman energy of the kagome spins is comparable to the temperature, and they are therefore disordered (indeed, the ice rules due to exchange and dipolar interactions within kagome ice result in a reduced yet extensive degeneracy [89–91]). We note that this choice of temperature and field after the quench typically corresponds to a negligibly small equilibrium monopole density—hence the quenches can be regarded once again to be from high to zero monopole density, albeit the starting configuration is much different from the initial paramagnetic state used in thermal quenches. (For a more detailed discussion of [111] field quenches in spin ice, we refer the reader to [41].)

Initial decay

Immediately following a field quench from saturated ice at low temperature, the monopole density is far greater than its thermodynamic equilibrium value, and dynamical spin flip processes leading to monopole-antimonopole annihilation events occur.

Notice that the triangular spins do not participate in the initial decay of the monopole density. Not only they are pinned by a larger Zeeman energy than the kagome spins, but also—and more importantly—they are akin to the intervening spin in a noncontractible pair. Flipping a triangular spin in saturated ice leads to the creation of a 4in and a 4out defect rather than to the annihilation of two monopoles.

The initial dynamics of a field quench is thus confined to the 2D kagome planes. Here, flipping a spin between two monopoles leads to their straightforward annihilation, which lowers the energy of the system. The process continues so long as there are kagome spins available between two monopoles. With the help of the schematic illustration in Fig. 7.22, one can draw an analogy between the initial decay and a dimer deposition process. To see this, consider the honeycomb lattice formed by the centres of the triangular plaquettes in a kagome plane. Each spin uniquely identifies a bond in the honeycomb lattice. Let us then say that when a spin is flipped and two monopoles are annihilated, the corresponding bond becomes occupied by a dimer. Clearly none of the adjacent spins (bonds) can then be flipped (occupied), according to the process above where only spins between two monopoles can flip. This is equivalent to the hard-core condition typical of dimer models. As time progresses and more spins are flipped, more bonds in the honeycomb lattice become occupied by hard-core dimers.

Notice that dimers can sometimes 'desorb' during the initial decay when thermal fluctuations lead to a second reversal of the same spin, thus creating anew the two monopoles that had been previously annihilated. The desorption rate can be controlled by tuning the value of the target field as well as the temperature. Here we focus for simplicity on the regime where the desorption rate is negligible.

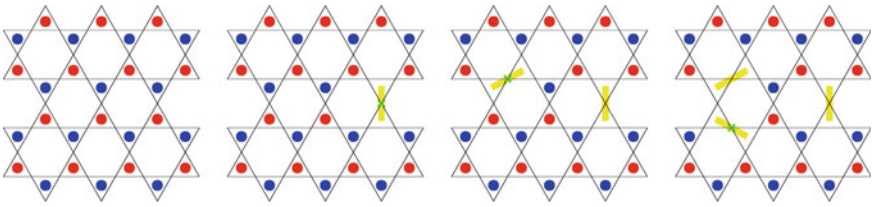

Fig. 7.22 Pictorial representation of the initial monopole annihilation processes within a kagome plane, from left to right. Positive and negative monopoles are represented by red and blue dots; the spins are not shown for simplicity. The green crosses indicate the spins the have flipped in going from one configuration to the next (left to right panels). The flipped spins can be represented as hard core dimers on the dual honeycomb lattice (thick yellow lines)

Ignoring the long-ranged Coulomb interaction between the monopoles, one should expect to be able to model the initial decay process with reasonable accuracy at the mean field level, given the uniformity of the charge distribution in the initial (saturated) state. The equation of motion is thus the same as for nearest-neighbour thermal quenches, (7.34). The agreement with MC simulations of field quenches in DSI is excellent without fitting parameters (Fig. 7.23), suggesting that the Coulomb interactions do not have a measurable effect on the reaction process.

The solution of the mean field equations is temperature independent. As time passes, we see from Fig. 7.23 that the results of the simulations eventually depart from the mean field behaviour and become strongly temperature dependent. This signals the end of the initial (dimer deposition like) regime: randomly selected neighbouring monopoles have straightforwardly annihilated until only isolated ones are left behind and they need to diffuse across the system before their density can decay further.

When the target field value becomes sufficiently large, it is no longer possible to disregard desorption events. This is the likely cause of the departure from mean field behaviour at short times, which begins to appear in the bottom panel of Fig. 7.23.

Intermediate regime

The initial decay ends when there are no more monopoles and antimonopoles next to one another that can be annihilated by flipping the intervening kagome spin. Monopoles are now required to travel across the lattice before their density can be further reduced.

Fig. 7.24 illustrates the behaviour over a large time window, for different fields and temperatures. In general, we observe that the relaxation time scales in the system become substantially longer after the initial decay discussed in the previous section. The new time scales show a clear temperature dependence (the lower the temperature, the slower the decay), as one would expect in presence of activation energy barriers obstructing the relaxation. This scenario is similar to the one observed in thermal quenches in dipolar spin ice (Fig. 7.18). However, we see that the behaviour in field quenches is far richer, with intermediate time regimes that appear to be distinct from both the initial as well as the asymptotically long time decay.

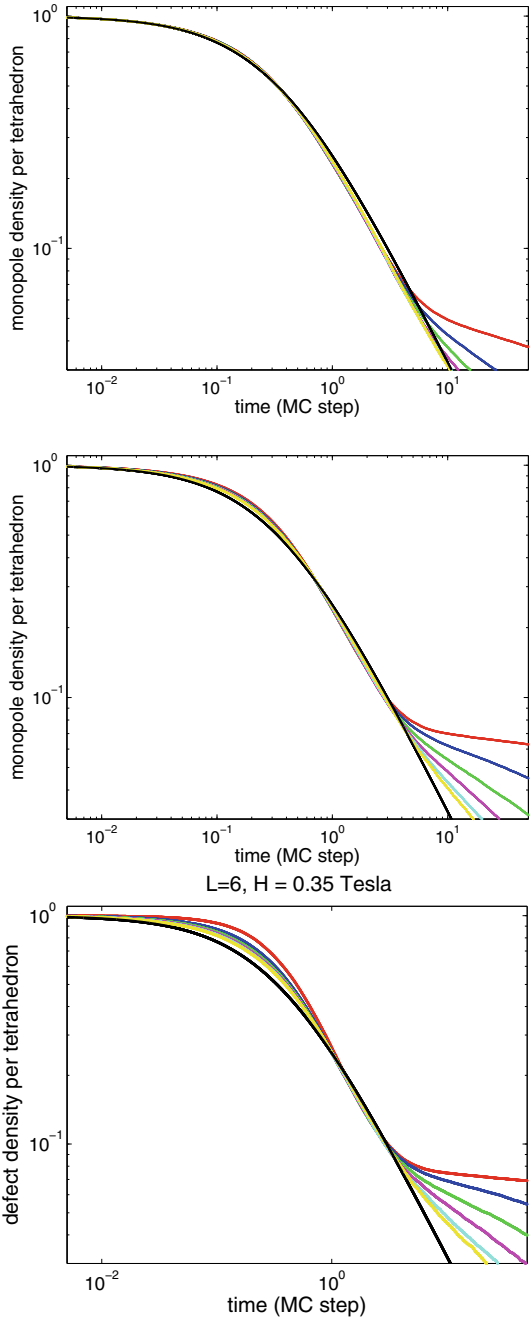

Fig. 7.23 Monte Carlo simulations of field quenches in dipolar spin ice for different values of the target field ($H = 0.2,\ 0.3,\ 0.35$ Tesla, from top to bottom). Only the initial (short time) decay of the monopole density is shown. The different colour curves correspond to different values of the temperature and the superposed black line is the mean field solution (7.34), without any fitting parameters. Reprinted figure from [41] with permission from PNAS

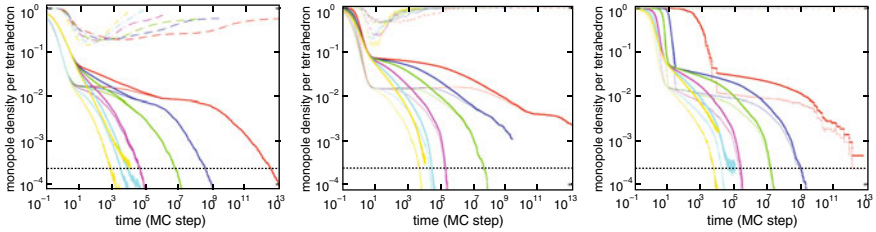

Fig. 7.24 Monopole density (thick lines), density of triangular spins in the direction of the initial magnetisation (thin dotted-dashed lines), and density of noncontractible pairs (thin solid lines) from MC simulations for a system of size $L = 8$ (8192 spins), fields $H = 0.2$, 0.4, and 0.6 Tesla (from left to right panels), and temperatures $T = 0.1$, 0.15, 0.2, 0.3, 0.4, and 0.5 K (red, blue, green, magenta, cyan, and yellow, respectively). At intermediate times, some of the triangular spins reverse, as shown by the dip in their density; the latter has been magnified by a factor of 100 and 1,000 (left and central panels, respectively) for visualisation purposes. In the right panel, the density of triangular spins in the direction of the applied field remains very nearly 1 throughout the simulations; the triangular spins remain polarised throughout the quench and the monopole motion is effectively 2D. (The black dotted horizontal line in each figure indicates the density threshold of one monopole in the entire MC system.) Reprinted figure from [41] with permission from PNAS

The intermediate regimes are controlled by finite size, finite time processes and are rather challenging to model analytically. This interesting and unique regime of an emergent reaction-diffusion process in presence of long-range Coulomb interactions and kinematic constraints, which can in principle be accessed experimentally in spin ice materials [43–45], lacks proper understanding to date.

Long time behaviour

At long times, the monopole density decay becomes increasingly dominated by the longest relaxation time scale in the system. We should therefore be able to capture the physics of this regime by modelling analytically its asymptotic behaviour.

At small and intermediate target field values (left and middle panels in Fig. 7.24) most of the monopoles at long times form noncontractible pairs, and their decay is similar to the case of thermal quenches. This is clearly not the case at larger fields (right panel in Fig. 7.24), and hereafter we shall focus only on this regime.

For large field values, the long relaxation times cannot be ascribed to long-lived noncontractible pairs. Rather, it must be that an energy barrier impedes the diffusion and annihilation of free monopoles. The origin of this barrier can be understood if we recall that monopole diffusion at large fields and low temperatures takes place nearly exclusively within each kagome plane, whilst the triangular spins remain fully polarised (Fig. 7.24, right panel). Under these conditions, a positive monopole in a kagome plane has lower Zeeman energy when it sits in an upward-pointing tetrahedron than in a downward pointing tetrahedron (vice versa for a negative monopole, as illustrated in Fig. 7.25). If we were to make a monopole hop across the kagome lattice, at every other step it would have to overcome a Zeeman energy barrier $dE \simeq 4.48\, H$ K (where H is the value of the target field measured in Tesla) [41].

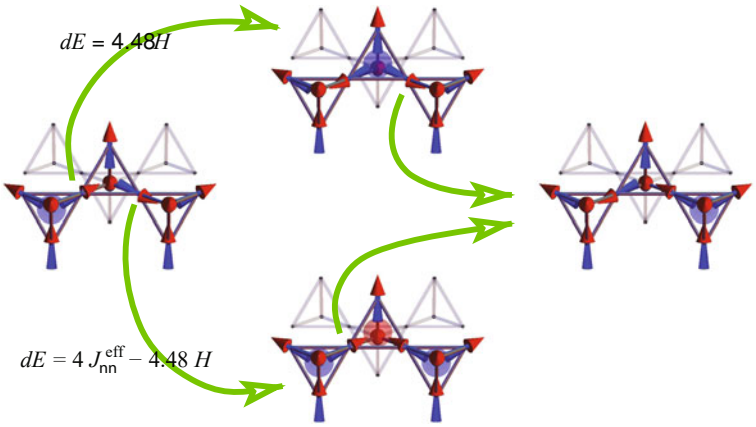

Fig. 7.25 Schematic representation of monopole motion in a kagome plane, via ordinary hopping (upper intermediate diagram) and via pair-assisted hopping (lower intermediate diagram). Both processes result in a negative monopole being transferred from a downward-pointing tetrahedron (left diagram) to one of the four nearest downward-pointing tetrahedra (right diagram). Each process encompasses two spin flips but, according to the order in which they are executed, the two processes face different energy barriers dE with opposite field dependence. The figure shows the value of the barriers for nearest-neighbour spin ice. In the main text we discuss how they are modified in presence of dipolar interactions. The field dependence, however, remains unchanged. The tails of the green arrows originate from the spin being flipped in going from one panel to the next. Only the spins in the front three tetrahedra are drawn for convenience. The triangular spins remain polarised throughout. Reprinted figure from [41] with permission from PNAS

This is the cost of reversing a kagome spin (whose easy axis is canted with respect to the [111] field direction).

Alternatively, the system can create a monopole-antimonopole pair next to the existing monopole and then annihilate the existing monopole with the oppositely charged member of the pair. The outcome is equivalent to moving a monopole from one Zeeman-favoured tetrahedron to another Zeeman-favoured tetrahedron two lattice spacings away from the first (see again Fig. 7.25). This process costs interaction energy (monopole pair creation + Coulomb interactions) but it can be done while gaining Zeeman energy. The corresponding barrier, using the Coulomb liquid description, can be estimated as $dE \simeq 2\Delta - 2u_d + u_{2d} - 4.48\, H$ K, where $u_{2d} = -u(r_{2d})$ is the strength of the Coulomb interaction between next nearest neighbour monopoles.

Notice that the two dynamical processes have opposite dependence on the applied field strength. Using spin ice parameters appropriate for $Dy_2Ti_2O_7$, the second process (pair assisted hopping) becomes energetically favoured with respect to the first one for $H \gtrsim 0.5$ Tesla. When $H = 0.6$ Tesla (right panel in Fig. 7.24), the barrier to pair assisted hopping is of the order of 2 K whereas the barrier to ordinary hopping is approximately 3 K. In order to confirm our understanding of the slowing down of the monopole hopping, we attempt to collapse the long time tails of the MC simulations of DSI by rescaling time using the characteristic activated time scale

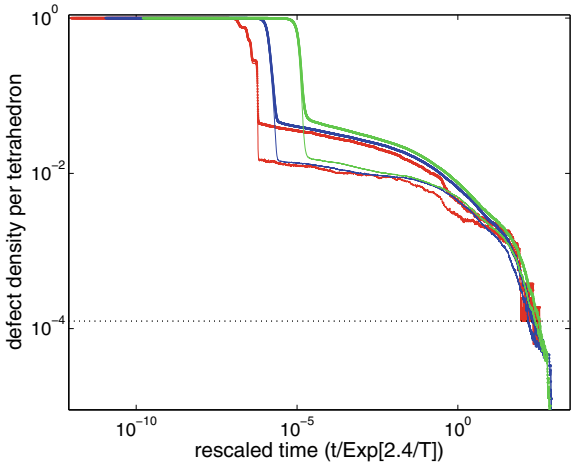

Fig. 7.26 Collapse of the long-time decay of the monopole density (thick lines) and of the noncontractible monopole density (thin lines) after rescaling the time axis by a factor $\exp(-2.4/T)$. The MC simulations are for $L = 10$ with $H = 0.6$ Tesla and $T = 0.13,\ 0.15$, and 0.18 K (red, blue, and green curves, respectively). The good quality of the collapse indicates that the simulated systems are large enough for the energy scale of 2.4 K not to exhibit appreciable system size dependence. Reprinted figure from [41] with permission from PNAS

$e^{dE/T}$. For the target field $H = 0.6$ Tesla, we find a good collapse when we choose $dE = 2.4$ K, in reasonable agreement with the estimated value for the pair assisted hopping (Fig. 7.26). However, larger system sizes and longer simulation times are required for a more discerning and conclusive comparison [41].

Summary and experiments

In summary, field quenches in spin ice offer a realisation of several paradigmatic concepts in nonequilibrium dynamics: dimer adsorption, Coulombic reaction-diffusion physics, and kinetically constrained slow dynamics. There is an unusually high degree of tunability, as one is able to control, say, the time scale of the elementary dynamical move through a Zeeman energy barrier; or the dimensionality of the final state ($d = 2$ kagome vs. $d = 3$ spin ice); or else the relative importance of dimer desorption compared with Coulomb interactions between the monomers.

Given the availability of a range of experimental probes for magnetic systems and the ability to apply time dependent fields of the strength required for spin ice materials, one can expect that it will be possible to study some of these out of equilibrium phenomena experimentally in the near future. (For a discussion of the difference between sudden quenches and fast but continuous field ramps, see for instance [41].)

A range of experimental results on the behaviour of these systems far from equilibrium is already available [40, 42–45, 52–55, 73]. However, these results are not straightforwardly connected to the physics of thermal or field quenches and further theoretical modelling is needed to interpret them.

Amongst other phenomena, it is interesting to point out an intriguing interplay between magnetic and thermal degrees of freedom leading to magnetic deflagration effects [40, 43, 44, 54, 73].

Acknowledgements The work presented in this article covers a cross section of collaborations by both authors. It is a pleasure to thank all our collaborators for these extensive and fruitful projects and in particular S.T. Banks, S.T. Bramwell, J.T. Chalker, T. Fennell, M.J.P. Gingras, V. Kaiser, L.D.C. Jaubert, and R. Moessner. We are grateful to M.J.P Gingras for providing us with the DSI specific heat data and to V. Kaiser for useful comments on the manuscript. This work was supported in part by EPSRC Grant No. EP/K028960/1 and EPSRC Grant No. EP/M007065/1 (CC) and by the Institut Universitaire de France (PCWH).

References

1. S.V. Isakov, K. Gregor, R. Moessner, S.L. Sondhi, Phys. Rev. Lett. **93**, 167204 (2004). https://doi.org/10.1103/PhysRevLett.93.167204
2. C.L. Henley, Annu. Rev. Condens. Matter Phys. **1**, 179 (2010). https://doi.org/10.1146/annurev-conmatphys-070909-104138
3. C. Castelnovo, R. Moessner, S.L. Sondhi, Nature **451**, 42 (2008). https://doi.org/10.1038/nature06433
4. I.A. Ryzhkin, J. Exp. Theor. Phys. **101**, 481–486 (2005). https://doi.org/10.1134/1.2103216
5. L.D.C. Jaubert, P.C.W. Holdsworth, Nat. Phys. **5**, 258 (2009). https://doi.org/10.1038/NPHYS1227
6. C. Castelnovo, R. Moessner, S. Sondhi, Annu. Rev. Condens. Matter Phys. **3**, 35 (2012). https://doi.org/10.1146/annurev-conmatphys-020911-125058
7. S. Powell, Phys. Rev. B **84**, 094437 (2011). https://doi.org/10.1103/PhysRevB.84.094437
8. L.D.C. Jaubert, J.T. Chalker, P.C.W. Holdsworth, R. Moessner, Phys. Rev. Lett. **100**, 067207 (2008). https://doi.org/10.1103/PhysRevLett.100.067207
9. L.D.C. Jaubert, J.T. Chalker, P.C.W. Holdsworth, R. Moessner, Phys. Rev. Lett. **105**, 087201 (2010). https://doi.org/10.1103/PhysRevLett.105.087201
10. M. Hermele, M.P.A. Fisher, L. Balents, Phys. Rev. B **69**, 64404 (2004). https://doi.org/10.1103/PhysRevB.69.64404
11. O. Benton, O. Sikora, N. Shannon, Phys. Rev. B **86**, 075154 (2012). https://doi.org/10.1103/PhysRevB.86.075154
12. L. Balents, Nature **464**, 199 (2010). https://doi.org/10.1038/nature08917
13. M.J. Harris, S.T. Bramwell, D.F. McMorrow, T. Zeiske, K.W. Godfrey, Phys. Rev. Lett. **79**, 2554 (1997). https://doi.org/10.1103/PhysRevLett.79.2554
14. S.T. Bramwell, M.J.P. Gingras, Science **294**, 1495 (2001). https://doi.org/10.1126/science.1064761
15. B.C. den Hertog, M.J. Gingras, Phys. Rev. Lett. **84**, 3430 (2000). https://doi.org/10.1103/PhysRevLett.84.3430
16. T. Yavors'kii, T. Fennell, M.J.P. Gingras, S.T. Bramwell, Phys. Rev. Lett. **101**, 037204 (2008). https://doi.org/10.1103/PhysRevLett.101.037204
17. P. Henelius, T. Lin, M. Enjalran, Z. Hao, J.G. Rau, J. Altosaar, F. Flicker, T. Yavors'kii, M.J.P. Gingras, Phys. Rev. B **93**, 024402 (2016). https://doi.org/10.1103/PhysRevB.93.024402
18. P.W. Anderson, Phys. Rev. **102**, 1008 (1956). https://doi.org/10.1103/PhysRev.102.1008
19. L. Pauling, J. Am. Chem. Soc. **57**, 2680 (1935). https://doi.org/10.1021/ja01315a102
20. S.V. Isakov, R. Moessner, S.L. Sondhi, Phys. Rev. Lett. **95**, 217201 (2005). https://doi.org/10.1103/PhysRevLett.95.217201

21. T. Fennell, P.P. Deen, A.R. Wildes, K. Schmalzl, D. Prabhakaran, A.T. Boothroyd, R.J. Aldus, D.F. McMorrow, S.T. Bramwell, Science **326**, 415 (2009). https://doi.org/10.1126/science.1177582
22. R.G. Melko, M.J.P. Gingras, J. Phys.: Condens. Matter **16**, R1277 (2004). https://doi.org/10.1088/0953-8984/16/43/R02
23. G. Möller, R. Moessner, Phys. Rev. Lett. **96**, 237202 (2006). https://doi.org/10.1103/PhysRevLett.96.237202
24. C. Castelnovo, R. Moessner, S.L. Sondhi, Phys. Rev. B **84**, 144435 (2011). https://doi.org/10.1103/PhysRevB.84.144435
25. D. Pomaranski, L.R. Yaraskavitch, S. Meng, K.A. Ross, H.M.L. Noad, H.A. Dabkowska, B.D. Gaulin, J.B. Kycia, Nat. Phys. **9**, 353 (2013). https://doi.org/10.1038/NPHYS2591
26. A. Sen, R. Moessner, S.L. Sondhi, Phys. Rev. Lett. **110**, 107202 (2013). https://doi.org/10.1103/PhysRevLett.110.107202
27. L.D.C. Jaubert, P.C.W. Holdsworth, J. Phys.: Condens. Matter **23**, 164222 (2011). https://doi.org/10.1088/0953-8984/23/16/164222
28. V. Kaiser, J. Bloxsom, L. Bovo, S.T. Bramwell, P.C.W. Holdsworth, R. Moessner, Phys. Rev. B **98**, 144413 (2018). https://doi.org/10.1103/PhysRevB.98.144413
29. M.E. Brooks-Bartlett, S.T. Banks, L.D.C. Jaubert, A. Harman-Clarke, P.C.W. Holdsworth, Phys. Rev. X **4**, 011007 (2014). https://doi.org/10.1103/PhysRevX.4.011007
30. P.C. Guruciaga, S.A. Grigera, R.A. Borzi, Phys. Rev. B **90**, 184423 (2014). https://doi.org/10.1103/PhysRevB.90.184423
31. V. Kaiser, The Wien effect in electric and magnetic coulomb systems: From electrolytes to spin ice. Ph.D. Thesis, ENS Lyon / TU Dresden (2014)
32. Y. Levin, Reports on Progress in Physics **65**, 1577 (2002). https://doi.org/10.1088/0034-4885/65/11/201
33. V. Kaiser, S.T. Bramwell, P.C.W. Holdsworth, R. Moessner, Nat. Mater. **12**, 1033 (2013). https://doi.org/10.1038/nmat3729
34. L. Savary, L. Balents, Phys. Rev. Lett. **108**, 37202 (2012). https://doi.org/10.1103/PhysRevLett.108.37202
35. D.J.P. Morris, D.A. Tennant, S.A. Grigera, B. Klemke, C. Castelnovo, R. Moessner, C. Czternasty, M. Meissner, K.C. Rule, J. Hoffmann, K. Kiefer, S. Gerischer, D. Slobinsky, R.S. Perry, Science **326**, 411 (2009). https://doi.org/10.1126/science.1178868
36. J. Snyder, B. Ueland, J. Slusky, H. Karunadasa, R. Cava, P. Schiffer, Phys. Rev. B **69**, 064414 (2004). https://doi.org/10.1103/PhysRevB.69.064414
37. L.D.C. Jaubert, M. Haque, R. Moessner, Phys. Rev. Lett. **107**, 177202 (2011). https://doi.org/10.1103/PhysRevLett.107.177202
38. C. Castelnovo, R. Moessner, S.L. Sondhi, Phys. Rev. Lett. **104**, 107201 (2010). https://doi.org/10.1103/PhysRevLett.104.107201
39. D. Levis, L.F. Cugliandolo, Europhys. Lett. **97**, 30002 (2012). https://doi.org/10.1209/0295-5075/97/30002
40. D. Slobinsky, C. Castelnovo, R.A. Borzi, A.S. Gibbs, A.P. Mackenzie, R. Moessner, S.A. Grigera, Phys. Rev. Lett. **105**, 267205 (2010). https://doi.org/10.1103/PhysRevLett.105.267205
41. S. Mostame, C. Castelnovo, R. Moessner, S.L. Sondhi, Proc. Natl. Acad. Sci. **111**, 640 (2014). https://doi.org/10.1073/pnas.1317631111
42. S.R. Giblin, S.T. Bramwell, P.C.W. Holdsworth, D. Prabhakaran, I. Terry, Nat. Phys. **7**, 252 (2011). https://doi.org/10.1038/NPHYS1896
43. C. Paulsen, M.J. Jackson, E. Lhotel, B. Canals, D. Prabhakaran, K. Matsuhira, S.R. Giblin, S.T. Bramwell, Nat. Phys. **10**, 135 (2014). https://doi.org/10.1038/nphys2847
44. M.J. Jackson, E. Lhotel, S.R. Giblin, S.T. Bramwell, D. Prabhakaran, K. Matsuhira, Z. Hiroi, Q. Yu, C. Paulsen, Phys. Rev. B **90**, 064427 (2014). https://doi.org/10.1103/PhysRevB.90.064427
45. C. Paulsen, S.R. Giblin, E. Lhotel, D. Prabhakaran, G. Balakrishnan, K. Matsuhira, S.T. Bramwell, Nat. Phys. **12**, 661 (2016). https://doi.org/10.1038/nphys3704

46. J.A. Quilliam, L.R. Yaraskavitch, H.A. Dabkowska, B.D. Gaulin, J.B. Kycia, Phys. Rev. B **83**, 094424 (2011). https://doi.org/10.1103/PhysRevB.83.094424
47. K. Matsuhira, C. Paulsen, E. Lhotel, C. Sekine, Z. Hiroi, S. Takagi, J. Phys. Soc. Jpn. **80**, 123711 (2011). https://doi.org/10.1143/JPSJ.80.123711
48. L.R. Yaraskavitch, H.M. Revell, S. Meng, K.A. Ross, H.M.L. Noad, H.A. Dabkowska, B.D. Gaulin, J.B. Kycia, Phys. Rev. B **85**, 20410 (2012). https://doi.org/10.1103/PhysRevB.85.20410
49. H.M. Revell, L.R. Yaraskavitch, J.D. Mason, K.A. Ross, H.M.L. Noad, H.A. Dabkowska, B.D. Gaulin, P. Henelius, J.B. Kycia, Nat. Phys. **9**, 34 (2013). https://doi.org/10.1038/nphys2466
50. H. Takatsu, K. Goto, H. Otsuka, R. Higashinaka, K. Matsubayashi, Y. Uwatoko, H. Kadowaki, J. Phys. Soc. Jpn. **82**, 104710 (2013). https://doi.org/10.7566/JPSJ.82.104710
51. L. Bovo, J. Bloxsom, D. Prabhakaran, G. Aeppli, S. Bramwell, Nat. Commun. **4**, 1535 (2013). https://doi.org/10.1038/ncomms2551
52. B. Klemke, M. Meissner, P. Strehlow, K. Kiefer, S.A. Grigera, D.A. Tennant, J. Low Temp. Phys. **163**, 345 (2011). https://doi.org/10.1007/s10909-011-0348-y
53. M.J. Matthews, C. Castelnovo, R. Moessner, S.A. Grigera, D. Prabhakaran, P. Schiffer, Phys. Rev. B **86**, 214419 (2012). https://doi.org/10.1103/PhysRevB.86.214419
54. S. Erfanifam, S. Zherlitsyn, S. Yasin, Y. Skourski, J. Wosnitza, A.A. Zvyagin, P. McClarty, R. Moessner, G. Balakrishnan, O.A. Petrenko, Phys. Rev. B **90**, 064409 (2014). https://doi.org/10.1103/PhysRevB.90.064409
55. G. Kolland, O. Breunig, M. Valldor, M. Hiertz, J. Frielingsdorf, T. Lorenz, Phys. Rev. B **86**, 060402 (2012). https://doi.org/10.1103/PhysRevB.86.060402
56. G. Sala, M.J. Gutmann, D. Prabhakaran, D. Pomaranski, C. Mitchelitis, J.B. Kycia, D.G. Porter, C. Castelnovo, J.P. Goff, Nat. Mater. **13**, 488 (2014). https://doi.org/10.1038/NMAT3924
57. E.R. Kassner, A.B. Eyvazov, B. Pichler, T.J.S. Munsie, H.A. Dabkowska, G.M. Luke, J.C.S. Davis, Proc. Natl. Acad. Sci. **112**, 8549 (2015). https://doi.org/10.1073/pnas.1511006112
58. C. Jaccard, Phys. Kondens. Mater. **3**, 99 (1964). https://doi.org/10.1007/BF02422356
59. I.A. Ryzhkin, R.W. Whitworth, J. Phys.: Condens. Matter **9**, 395 (1997). https://doi.org/10.1088/0953-8984/9/2/008
60. S.V. Isakov, K.S. Raman, R. Moessner, S.L. Sondhi, Phys. Rev. B **70**, 104418 (2004). https://doi.org/10.1103/PhysRevB.70.104418
61. L. Jaubert, M. Harris, T. Fennell, R. Melko, S. Bramwell, P. Holdsworth, Phys. Rev. X **3**, 011014 (2013). https://doi.org/10.1103/PhysRevX.3.011014
62. V. Kaiser, S.T. Bramwell, P.C.W. Holdsworth, R. Moessner, Phys. Rev. Lett. **115**, 037201 (2015). https://doi.org/10.1103/PhysRevLett.115.037201
63. S.T. Bramwell, S.R. Giblin, S. Calder, R. Aldus, D. Prabhakaran, T. Fennell, Nature **461**, 956 (2009). https://doi.org/10.1038/nature08500
64. L. Onsager, J. Chem. Phys. **2**, 599 (1934). https://doi.org/10.1063/1.1749541
65. D.M. Pai, J. Appl. Phys. **46**, 5122 (1975). https://doi.org/10.1063/1.321570
66. C. Castelnovo, Chem. Phys. Chem. **11**, 557 (2010). https://doi.org/10.1002/cphc.200900873
67. R.G. Pearson, Discuss. Faraday Soc. **17**, 187 (1954). https://doi.org/10.1039/DF9541700187
68. D.J. Mead, R.M. Fuoss, J. Am. Chem. Soc. **61**, 2047–2053 (1939). https://doi.org/10.1021/ja01877a028
69. M. Eigen, J. Schoen, Zeitschrift für Elektrochemie, Berichte der Bunsengesellschaft für physikalische. Chemie **59**, 483 (1955). https://doi.org/10.1002/bbpc.19550590604
70. A. Persoons, M.V. Beylen, Pure Appl. Chem. **51**, 887–900 (1979). https://doi.org/10.1351/pac197951040887
71. M.I. Ryzhkin, I.A. Ryzhkin, S.T. Bramwell, Europhys. Lett. **104**, 37005 (2013). https://doi.org/10.1209/0295-5075/104/37005
72. J. Snyder, J.S. Slusky, R.J. Cava, P. Schiffer, Nature **413**, 48 (2001). https://doi.org/10.1038/35092516
73. S. Erfanifam, S. Zherlitsyn, J. Wosnitza, R. Moessner, O. Petrenko, G. Balakrishnan, A. Zvyagin, Phys. Rev. B **84**, 220404 (2011). https://doi.org/10.1103/PhysRevB.84.220404

74. S. Dunsiger, A. Aczel, C. Arguello, H. Dabkowska, A. Dabkowski, M.H. Du, T. Goko, B. Javanparast, T. Lin, F. Ning, H. Noad, D. Singh, T. Williams, Y. Uemura, M. Gingras, G. Luke, Phys. Rev. Lett. **107**, 207207 (2011). https://doi.org/10.1103/PhysRevLett.107.207207
75. S.J. Blundell, Phys. Rev. Lett. **108**, 147601 (2012). https://doi.org/10.1103/PhysRevLett.108.147601
76. G. Sala, C. Castelnovo, R. Moessner, S.L. Sondhi, K. Kitagawa, M. Takigawa, R. Higashinaka, Y. Maeno, Phys. Rev. Lett. **108**, 217203 (2012). https://doi.org/10.1103/PhysRevLett.108.217203
77. P. Quémerais, P. McClarty, R. Moessner, Phys. Rev. Lett. **109**, 127601 (2012). https://doi.org/10.1103/PhysRevLett.109.127601
78. L.J. Chang, M.R. Lees, G. Balakrishnan, Y.J. Kao, A.D. Hillier, Sci. Rep. **3**, 1881 (2013). https://doi.org/10.1038/srep01881
79. L. Nuccio, L. Schulz, A.J. Drew, J. Phys. D: Appl. Phys. **47**, 473001 (2014). https://doi.org/10.1088/0022-3727/47/47/473001
80. A.J. Bray, Adv. Phys. **43**, 357 (1994). https://doi.org//10.1080/00018739400101505
81. J. Hamp, A. Chandran, R. Moessner, C. Castelnovo, Phys. Rev. B **92**, 075142 (2015). https://doi.org/10.1103/PhysRevB.92.075142
82. W.H. Zurek, Nature **317**, 505 (1985). https://doi.org/10.1038/317505a0
83. A. del Campo, W.H. Zurek, Int. J. Mod. Phys. A **29**, 1430018 (2014). https://doi.org/10.1142/S0217751X1430018X
84. V.V. Ginzburg, L. Radzihovsky, N.A. Clark, Phys. Rev. E **55**, 395 (1997). https://doi.org/10.1103/PhysRevE.55.395
85. D. Toussaint, F. Wilczek, J. Chem. Phys. **78**, 2642 (1983). https://doi.org/10.1063/1.445022
86. A.S. Wills, R. Ballou, C. Lacroix, Phys. Rev. B **66**, 144407 (2002). https://doi.org/10.1103/PhysRevB.66.144407
87. G. Möller, R. Moessner, Phys. Rev. B **80**, 140409 (2009). https://doi.org/10.1103/PhysRevB.80.140409
88. G.W. Chern, O. Tchernyshyov, Philos. Trans. R. Soc., A **370**, 5718 (2012). https://doi.org/10.1098/rsta.2011.0388
89. M. Udagawa, M. Ogata, Z. Hiroi, J. Phys. Soc. Jpn. **71**, 2365 (2002). https://doi.org/10.1143/JPSJ.71.2365
90. K. Matsuhira, Z. Hiroi, T. Tayama, S. Takagi, T. Sakakibara, J. Phys.: Condens. Matter **14**, L559 (2002). https://doi.org/10.1088/0953-8984/14/29/101
91. R. Moessner, S.L. Sondhi, Phys. Rev. B **68**, 064411 (2003). https://doi.org/10.1103/PhysRevB.68.064411

Chapter 8
Experimental Observation of Magnetic Monopoles in Spin Ice

Steven T. Bramwell and T. Fennell

Abstract In spin ice, the model of magnetic monopoles arises as a transformation of the dipolar spin ice Hamiltonian developed for materials such as $Dy_2Ti_2O_7$ and $Ho_2Ti_2O_7$. The treatment of spin ice in terms of an effective theory of emergent monopoles presents both theoretical and experimental challenges. In this chapter we give 'monopole theory' a precise definition which allows us to critically assess the extent to which magnetic monopoles have been observed in experiment. We start by answering some basic questions: what magnetic monopoles are, whether or not they are quasiparticles, to what extent they form a 'magnetic electrolyte' and what it means to observe them. We then introduce the main experimental techniques and their relation with the monopole theory, before comparing experimental results on the canonical spin ices $Ho_2Ti_2O_7$ and $Dy_2Ti_2O_7$ with theoretical expectations. We conclude with some comments on different viewpoints on magnetic monopoles, different definitions and disagreements in the literature. Our main conclusion is that the monopole theory is strongly supported by experiment. The Chapter is organised as follows:

8.1 **Introduction** What are magnetic monopoles in spin ice? Magnetic monopoles as quasiparticles. Confirmation or falsification of monopole theory. Spin ice as a magnetic electrolyte. Direct observation of magnetic monopoles.
8.2 **Quantities available to experiment** Equilibrium thermodynamics. Linear response and non-equlibrium thermodynamics.
8.3 **Experiments in weak applied fields** Magnetisation correlations measured by neutron scattering. Specific heat. dc-Susceptibility. ac-Susceptibility. Summary: success and failures of the monopole theory in the weak field regime.

S. T. Bramwell (✉)
Department of Physics and Astronomy and London Centre for Nanotechnology, University College London, London, UK
e-mail: s.t.bramwell@ucl.ac.uk

T. Fennell
Laboratory for Neutron Scattering and Imaging, Paul Scherrer Institute, Villigen, Switzerland
e-mail: tom.fennell@psi.ch

M. Udagawa and L. Jaubert (eds.), *Spin Ice*, Springer Series in Solid-State Sciences 197,
https://doi.org/10.1007/978-3-030-70860-3_8

8.4 **Experiments in strong applied fields** Monopole condensation with applied field along [111]. Strong field correlations. Strong field sweeps and quenches.
8.5 **Monopole derived properties** Thermal Conductivity. Field distribution at point probes. Dielectric response.
8.6 **Future directions for monopole observation** Plasmas. Phonons. New materials. Quantum spin ice.
8.7 **Conclusions** Different viewpoints. Definitions and disagreements. Final word.

8.1 Introduction

8.1.1 What Are Magnetic Monopoles in Spin Ice?

The classical spin ice materials $Ho_2Ti_2O_7$ and $Dy_2Ti_2O_7$ are generally discussed in terms of three model spin Hamiltonians. These are valid at low temperature, where crystal field terms other than the lowest doublet can be neglected. In order of increasing complexity the three models are the near neighbour spin ice model (NNSI) [1, 2], the standard dipolar spin ice model (s-DSM) [3] and the generalised dipolar spin ice model (g-DSM) [4]. NNSI explains spin ice's entropy and general behaviour, but fails to fit properties in fine detail [5]. The s-DSM was originally used to explain the heat capacity and neutron scattering of $Ho_2Ti_2O_7$ [6] and contains only the dipolar interaction and competing first neighbour exchange. It goes beyond NNSI by adding the long range part of the dipole-dipole interaction between spins [5]. The g-DSM, which contains further neighbour exchange constants, was a refinement of the s-DSM that was introduced [4] to account for the detailed spatial correlations between spins, as measured by neutron scattering on $Dy_2Ti_2O_7$ [7].

The long ranged dipole-dipole interaction has been shown to be largely self-screened in the spin ice state, [8, 9], hence the success of NNSI, but it remains important in excited states. These states involve local "three-in–one-out/three-out–one-in' or 'four-in/four-out' spin configurations that are analogous to water ice's ionic defects $H_{2+z}O^{z+}$ and OH^{z-}_{2-z} (here $z = 1, 2$ respectively). The magnetic monopole model of Castelnovo, Moessner and Sondhi (CMS) [10] is an approximate transformation of the s-DSM Hamiltonian that accounts (to within quadrupolar terms) for the remaining dipole-dipole interaction in the excited states. Notably, this turns out to take the form of a magnetostatic Coulomb interaction between the 'ionic' defects.

The monopole model essentially reduces the s-DSM to NNSI, but with defects that interact like magnetic monopoles [11, 12]. Its introduction marked a return to describing spin ice in terms of the water ice analogy, and connected with the work of Ryzhkin [13], who, by directly exploiting the ice analogy, and performing a coarse grained integration of dipolar fields, had inferred the charge-like properties of the defects. Indeed, Ryzhkin has stressed that spin ice and water ice have (essentially) the same properties because they share the same Hamiltonian, which for spin ice is the s-DSM [3], while for water ice it is a pseudo-spin Hamiltonian, developed

a number of years earlier [14]. As we will discuss below, the fact that the 'DSM' approach and the 'water ice' approach to the spin ice materials lead to consistent descriptions, confirms the robust nature of the monopole picture.

The close relationship of NNSI to the monopole model invites a very simple formulation of monopole dynamics. Thus, making the simplest possible assumption, that the spin dynamics of NNSI are spin flip, or Glauber-type [15] dynamics, shows very clearly that magnetic monopoles in spin ice behave just like idealised ionic defects in water ice in the sense that they are created as pairs, can separate ('fractionalise' [10, 16]), diffuse by 'hopping' from site to site and recombine and annihilate - or more generally, they obey quasi-chemical kinetics. Free monopoles are therefore long-lived in the sense that it may take many diffusive hops before the monopole is ultimately annihilated.

A picture of 'NNSI spins plus monopole interactions' creates the 'magnetolyte' model of Jaubert and Holdsworth [11, 12], used in their numerical simulations. This is entirely equivalent to the idealised water ice model and may be described as a generalised Coulomb gas in the grand-canonical ensemble. Here the word 'generalised' refers to the presence of the transverse part of the magnetization field as illustrated in Fig. 8.1. Thus, the solution of the magnetic Gauss' law $\nabla \cdot \mathbf{H} = \rho_m \equiv -\nabla \cdot \mathbf{M}$ generates a magnetisation field $\mathbf{M}(\mathbf{r}, t)$, which has both transverse (divergence-free) and longitudinal (divergence-full) components (for the equivalent electrical analysis see [17]). The monopoles are sources and sinks of the longitudinal field, while the monopole vacuum is described by the transverse field, as discussed further below. In Ryzhkin's theory the coarse-grained magnetization field $\mathbf{M}(\mathbf{r}, t)$ is an auxiliary variable which coexists and interacts with the monopole density field $n_{\pm}(\mathbf{r}, t)$ [13, 18].[1] Properties of the monopole gas arise from the interaction of these two fields.

What we will call 'monopole theory' therefore incorporates two statements:

I Spin ice may be represented as a generalised monopole gas in the grand canonical ensemble.

II Monopoles obey quasi-chemical kinetics and diffusion.

Here statement (I) has been justified theoretically [10, 13], and if taken by itself, offers some advantages over the microscopic approach of *s*-DSM. For example, it allows an analytical approach to the heat capacity that could previously be obtained only by numerical simulation [19]. Statement II on the other hand is a very soundly based hypothesis [13, 18] that provides a means to understand the collective spin dynamics of spin ice. The appeal of this is that it allows one to go far beyond the DSM approach, to treat the spin dynamics of a complex, long range interacting system. A key role of experiment is to test the hypothesis (II) and identify the nature of the diffusion—for example, Brownian or anomalous, with single or multiple relaxation times—and to determine how the monopole mobility depends on temperature or field.

We would like to emphasize that, in both theory and experiment, the monopole picture not only offers a simplification and solves a few problems, but it also *sets*

[1] Strictly the auxiliary variable is $\boldsymbol{\Omega}(\mathbf{r}, t) = \mathbf{M}(\mathbf{r}, t)/Q$, the configuration vector [13].

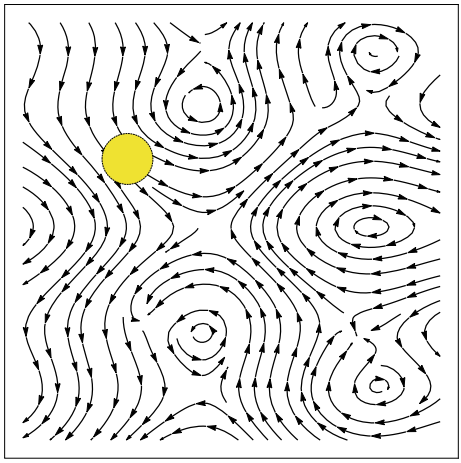

Fig. 8.1 Schematic of the coarse grained magnetisation field in spin ice. The local magnetisation $\mathbf{M}(\mathbf{r}, t)$ can be Helmholtz decomposed into a divergence-free part (reflected here by closed loops) and a divergence-full part (reflected here by sources and sinks). The monopole vacuum is entirely divergence-free, while the thermally excited monopoles are the 'quanta' of the effective magnetic charge density, $\rho_m = -\nabla \cdot \mathbf{M}(\mathbf{r})$. The yellow circle represents a Gaussian surface drawn around a single monopole: the monopolar field crossing the surface *defines* the monopole. Well within the surface there are only spins and the concept of a monopole as an effective point source of the Coulomb field loses its precise meaning. Hence 'direct' observation of a monopole necessarily entails the study of magnetisation textures, $\mathbf{M}(\mathbf{r}, t)$

new problems to be solved. The reason is that the behaviour of a Coulomb gas in the grand canonical ensemble is anything but simple, as two hundred years of research on electrolytes and water ice [20] has most vividly illustrated [21–25]. While much progress can be made by adopting textbook chemical thermodynamics of electrolytes, such as Debye-Hückel theory [21], the general statistical mechanics of Coulomb gases such as electrolytes remains very subtle indeed—and the 'magnetolyte' in spin ice is no exception. Nevertheless, this difficulty is really what drives interest in magnetic monopoles in spin ice. The monopole concept is a rich source of new and interesting theoretical and experimental problems.

8.1.2 Magnetic Monopoles as Quasiparticles

Both the ionic defects of water ice and the magnetic monopoles in spin ice bear close analogy to the quasiparticles of condensed matter, such as quasi-electrons and holes in intrinsic semiconductors. Like electrons and holes, they are thermally excited from a 'quasiparticle vacuum' according to the quasi-chemical reaction scheme:

$$(0) = (+-) = (+) + (-) \tag{8.1}$$

(here and henceforth, unless otherwise stated, we simplify the discussion by considering single charge monopoles only). However, in contrast to the case of electrons and holes, it does not make much sense to talk of an energy-momentum dispersion relation $\varepsilon(p)$ for magnetic monopoles. Our previous statements can alternatively be expressed by saying that the monopole gas is a shorthand for *static* excited state configurations, and the assumption II above is that transitions between these states can be represented as a monopole diffusion. Hence monopoles are quasiparticles only in the general sense that they reduce the problem of treating a strongly-interacting spin system to that of treating a weakly interacting gas of particle-like configurations [13]. They are not derived from an underlying dynamical theory, in contrast to electrons and holes.

What does it mean to 'detect' a quasiparticle? It is immediately apparent that there is a difference between detecting particles and detecting quasiparticles. High energy physicists have invested great efforts in obtaining images of individual particle decay processes, which may be interpreted as clear proof of the existence and properties of the particle in question [26]. This approach is not generally possible in condensed matter (except perhaps for some surface-dwelling examples such as skyrmions in thin films [27]), but we nonetheless accept the existence of a variety of quasiparticles, including phonons, magnons and spinons, Landau quasiparticles and heavy fermions [28], fractional quasiparticles in the fractional quantum Hall effect [29], and an array of boojums, hedgehogs and monopoles in ^{3}He [30].

Let us consider one example from the above list, in order to examine the question of how to detect a quasiparticle. It is widely accepted that conduction in heavy fermion metals is mediated by a quasiparticle with electron-like properties but greatly enhanced mass [28]. Of course these heavy fermions do not exist outside the material in question—they cannot be liberated from the sample and probed directly—because they are actually formed from the underlying valence and conduction electrons and their interactions. Experimental evidence in the form of effective electron masses derived from conductivity and de Haas-van Alphen effect measurements, as well as thermodynamic properties in accord with a gas of free (heavy) fermions, all in accord with theory, are sufficient for us to accept and use the concept of the heavy fermion.

Spin ice is accessible by many probes and the approach to detecting monopoles is no different—comparison of theory and experiment can validate a picture of monopole quasiparticles based on properties that are sensitive to the population, dynamics and interactions of monopoles. However, it is certainly the case that some experiments isolate and expose the monopoles and their properties more directly than others. Below we review which properties of spin ice, thus far, contain distinctive signatures of the monopoles, and how they support (or otherwise) the theory.

8.1.3 Confirmation or Falsification of Monopole Theory

As we have defined it, 'monopole theory' is seen to be an idealised statistical and kinetic theory, developed with respect to the spin ice materials like $Ho_2Ti_2O_7$ and

$Dy_2Ti_2O_7$. The question is, how far is this ideal monopole theory realised in the spin ice materials? It is convenient to consider this question with respect to the statements I and II above.

Regarding statement I, the static monopole model is not an exact transformation of the *s*-DSM, but it is nearly so, and any limitations of the monopole model are essentially limitations of *s*-DSM as well. In the strictest sense, the *s*-DSM has already been falsified as a model for $Dy_2Ti_2O_7$ through the introduction of the *g*-DSM [4]. However the *s*-DSM is nevertheless widely accepted to form the basic description of the static magnetic behaviour of dipolar spin ice, based on the analysis of numerous experimental properties [31]. The monopole model must therefore be accepted as a valid approximate description of spin ice, at the same level as the *s*-DSM, and the question of falsifying statement I does not arise. Departures from the monopole model are most likely to be observed at low fields and low temperatures where the extra terms of the *g*-DSM model become relevant. For example, one established departure from the monopole model is the finite bandwidth of the manifold of Pauling states, as exposed by neutron scattering below 1 K [4]. Although the *s*-DSM has a finite bandwidth [8, 9], only the *g*-DSM captures the effect quantitatively. Possibly the extra terms of the *g*-DSM also modify the Coulomb interaction between magnetic monopoles, but even if such corrections are observed, it is not likely that the monopole picture will have to be completely abandoned.

Statement II, as mentioned above, is equivalent to assuming that the basic dynamics of spin ice are simple spin flips, i.e. Glauber-type [15] dynamics. Such spin flips create and annihilate monopoles and cause them to diffuse. This statement could be falsified in principle, for example, if it were discovered that the dominant spin dynamics in the real materials were propagating (e.g. spin wave—like) modes, rather than diffusive spin flips. However it seems very hard to imagine that spin flip dynamics are completely irrelevant to the classical spin ice materials, which are close to being ideal Ising-like model magnets [31]. Once again, even if corrections to a diffusion picture are found, it seems unlikely that the monopole picture will have to be completely abandoned. Much more likely is that the monopole model will survive as the basic, if approximate, starting model for the discussion of collective spin dynamics in dipolar spin ice.

For these reasons, it is probably unhelpful to talk of the monopole theory being ‘correct’ or ‘incorrect’ as regards a theoretical description of $Dy_2Ti_2O_7$ and $Ho_2Ti_2O_7$. The question is really to what extent can the ideal monopole theory be used immediately to simplify and understand the complex magnetic properties of these strongly interacting materials, and what are the modifications to monopole theory (and their meaning) that are required for more precise descriptions?

8.1.4 Spin Ice as a Magnetic Electrolyte

To conclude this section it is worth identifying to what extent spin ice can be treated as a magnetic electrolyte or ‘magnetolyte’ of single and double charge monopoles. The

analogy is with a 'weak electrolyte' in which free charges coexist with undissociated molecules: for example acetic acid or water. Note that in electrolyte terminology [21], weak/strong refer to degree of dissociation, not to level of dilution. They should not be confused with 'dilute/concentrated' electrolytes (respectively).

As in the case of ions in solution, magnetic monopoles in spin ice are localised, static, Coulombic quasiparticles on which a diffusion theory is based. The theory is most useful when departures from ideal gas behaviour are relatively small and properties can be summarised by an activity coefficient γ[2] and mesoscopic ionic mobilities $u_{\pm}$.[3] This is indeed the case in monopole theory. However there are several differences.

(1) An ion in solution typically carries a solvent cloud and is considered to reside in a polarisable liquid medium. There is no analogue of either property in the spin ice magnetolyte, which is analogous to an idealised lattice electrolyte, with no solvent or liquid mechanical properties. The 'vacuum' in spin ice can be locally polarised (magnetised [13]) and is treated as a divergence-free field. In contrast, in a typical weak electrolyte, the vacuum state is treated as an (possibly non-) ideal gas of molecules embedded in a polarisable medium, described by an effective dielectric constant. In the earlier discussion we distinguished these two idealised cases by referring to the monopole gas as a 'generalised' Coulomb gas.

(2) No real electrolyte can be perfectly charge symmetric but spin ice presents the contrary situation: it is a perfectly symmetric Coulomb gas in which the charges and mobilities of positive and negative monopoles are equal and opposite: $Q^{\pm} = \pm Q$ and $u^{\pm} = \pm u$. The positive-negative charge symmetry is 'protected' by symmetry and topology. Firstly, it is protected by time reversal-symmetry because the spins are axial vectors and if all are reversed, the resulting state must be equivalent in its physical properties to the initial one. It is further protected by topology because the monopoles are topological defects caused by symmetric fractionalisation of dipoles: so local perturbations cannot alter the initial symmetry of the positive and negative charges. Spin ice is remarkable in presenting the only known laboratory example of a perfectly symmetric Coulomb gas.

(3) In the spin ice magnetolyte, conduction is accompanied by magnetisation [13], in the same way that the celebrated 'Grotthus mechanism' [32] leads to polarisation in protonic conductors. However this mechanism is never exclusively realised in protonic systems. Even in water ice [20], so-called D/L defects remove the polarisation and allow normal conduction of ionic defects, for example round a closed loop. There are no analogous defects in spin ice and hence spin ice cannot sustain a direct current round a loop. The expression of this in Ryzhkin's theory is that the magnetic current is $\partial \mathbf{M}/\partial t$, driven by the field $\mathbf{H} - \mathbf{M}/\chi$. The system

[2] In chemical thermodynamics, ideal solution equations involving the concentration or mole fraction x of a species, are applied to non-ideal solutions by replacing the mole fraction with activity a. The activity coefficient is defined as $\gamma = a/x$. Note that γ is always precisely defined and measurable: the theoretical challenge is to calculate it.

[3] Defined here as ratio of monopole drift velocity to local (**H**-) field at zero concentration gradient.

thus reaches equilibrium with $\mathbf{M} = \chi\mathbf{H}$ and zero magnetic current, even though the monopole conductivity κ and mobility u both remain finite.

(4) Ions in solution can be transformed to other particles, for example by electrolysis, in accord with the laws of mass, charge and particle conservation. There is essentially no analogy of this for magnetic monopoles, although certain conservation laws do apply under all circumstances (for example the total monopole charge is zero).

Despite these differences, as explained below, there are many similarities between the properties of the spin ice magnetolyte and those of a simple weak electrolyte, and many instances where electrolyte theory may be applied to spin ice with only small modifications.

8.1.5 Direct Observation of Magnetic Monopoles

The question might reasonably be asked, is it possible to *directly* observe a magnetic monopole? This question gets to the heart of what magnetic monopoles really are. As we have seen, they are local spin configurations that interact like monopoles when viewed over extended length scales. Considering a Gaussian surface drawn in a region of spin ice, the net magnetic charge density $\rho_m \equiv -\nabla \cdot \mathbf{M}$ within the surface may be found by counting the number of positive and negative monopoles within, taking the difference, and multiplying by the charge: $\rho_m = Q(N_+ - N_-)$. What makes spin ice materials different to other magnetic materials in this regard is that the the effective magnetic charge is discretised—one might even say 'quantised'—and hence the following description of a magnetic monopole is essentially an accurate one: *a magnetic monopole is a (non-universal*[4]*) quantum of effective magnetic charge* [33]. However, within the Gaussian surface there is nothing other than certain spin configurations, the existence of which is not in question. From this one can see that even a single monopole can only be 'observed' by means of its associated Gauss' law and the coarse grained magnetisation texture $\mathbf{M}(\mathbf{r}, t)$ that it creates. This is illustrated in Fig. 8.1.

At present there are no probes that allow such direct observation of a single monopole: the thermally averaged properties of $\mathbf{M}(\mathbf{r}, t)$ are the closest one can get. This makes Ryzhkin's theory [13] and its extensions [18, 34, 35], where the basic variables are $\mathbf{M}(\mathbf{r}, t)$ and $n_\pm(\mathbf{r}, t)$, very attractive. Monopole properties ($n_\pm(\mathbf{r}, t)$, Q, μ) influence the magnetisation ($\mathbf{M}(\mathbf{r}, t)$), and monopoles are directly observable in this sense. From the above argument, we would say that strictly speaking, there can be no other sense in which magnetic monopoles are *directly* observable. For this reason, in Sect. 8.2 we treat the question of magnetic response in some detail.

[4] The 'quantum' of charge is material-specific because it depends on the single-ion magnetic moment and lattice spacing of the spin ice under study [10].

Table 8.1 Key parameters and variables in monopole theory: a, Q are microscopic parameters, μ, n are thermodynamic variables and $n(\mathbf{r}, t)$ and $\mathbf{M}(\mathbf{r}, t)$ are mesoscopic variables. See footnote 1 for definition of the configuration vector

Symbol	Meaning	Relations
a	Diamond lattice parameter	$a = \sqrt{3/16} \times$ cubic lattice parameter
Q	Monopole charge	$Q = 2 \times$ rare earth moment$/a$
μ	Monopole chemical potential	$-\mu = 2J_{\text{eff}} + \sqrt{2}C(4\sqrt{6} - 3)/6\pi$ $C =$ Curie constant. $J_{\text{eff}} = J_{\text{nn}} + D_{\text{nn}}$ [5]
n	Equilibrium monopole density	$n = N/V = 2N_{\pm}/V$
$n_{\pm}(\mathbf{r}, t)$	Local densities	
$\mathbf{M}$ (**r**,t)	Local magnetisation	$\mathbf{M} = Q \times$ configuration vector

8.2 Quantities Available to Experiment

In this section, we discuss the main quantities available to experiment in the classical dipolar spin ice materials ($Ho_2Ti_2O_7$, $Dy_2Ti_2O_7$ etc.) and identify how these may be used to probe the properties of magnetic monopoles. We focus attention on properties in weak applied field, returning to the strong field case later. For ease of reference we list some important parameters of monopole theory in Table 8.1.

8.2.1 Equilibrium Thermodynamics

In the simplest case, and neglecting boundary effects, the thermodynamic properties of a magnetic material are summarised by $F = F(T, \mathbf{M})$ or $G = G(T, \mathbf{H})$ (in a familiar notation). That is, there are two independent thermodynamic variables. The monopole model adds a third thermodynamic variable, the monopole number $N = N_+ + N_- = 2N_{\pm}$ or monopole density $n = N/V$, conjugate to the monopole chemical potential μ. Although the chemical potential μ, approximates a material constant in zero and weak fields for any given spin ice material (see Chap. 7), it remains an independent variable in the monopole theory.[5] This allows the monopole theory to describe a whole class of magnetic materials—the classical dipolar spin ices [5].

Consider the case of zero magnetisation (or zero field). In theory, the specific heat and (isothermal) susceptibility need to be written as functions of two variables, for

[5] In principle, it is weakly temperature dependent as a result of thermal expansion, but high precision neutron Larmor diffraction experiments cannot resolve any thermal expansion in the relevant temperature range for either $Dy_2Ti_2O_7$ or $Ho_2Ti_2O_7$ [36].

example $c(\mu, T)$ and $\chi(\mu, T)$ respectively. However, in the low temperature limit, the (isothermal) susceptibility χ of the monopole model turns out to be independent of μ [13], although it still depends on the magnetic charge Q. In spin language the low-temperature susceptibility of the monopole model is twice the Curie susceptibility $\chi = 2\chi_C$ and the product $\chi T/C$ (where C is the Curie constant) is approximately temperature independent, adopting its zero temperature value of 2.[6] Hence the equilibrium susceptibility at low temperature is not a sensitive signature of magnetic monopoles. At higher temperature the susceptibility evolves back towards the Curie susceptibility and this temperature variation does depend on the monopole chemical potential μ [38].

In contrast, the zero field specific heat $c(\mu, T)$ provides a very strong signature of monopole interactions, as the internal energy is a function of the number of excited monopoles and their Coulombic interaction energy. Following electrolyte theory [21], the quantity that controls the specific heat is an effective chemical potential:

$$\mu_{\text{eff}} = \mu + kT \ln \gamma(n, T), \tag{8.2}$$

where γ is the activity coefficient, which here accounts for the screened Coulomb energy of the monopole gas. In the limit of small n/T, the activity coefficient γ may be directly calculated by the 'extended' Debye-Hückel method [21], in which it becomes a function of Q, n, T and a. For a given spin ice material, fitting specific heat to Debye–Hückel theory gives access to the monopole density as a function of temperature, $n(T)$. In general, good agreement between experimental specific heat and Debye–Hückel theory can be obtained, as discussed further below (8.3.2) and in Chap. 7.

It should be noted that boundary (demagnetising) effects are very important in spin ice materials [38, 39], particularly in the usual case that the spin ice sample forms a simply connected domain—let us assume an ellipsoidal shape for simplicity. The bulk magnetic dipole moment and hence the magnetization $\mathbf{M}$, is dependent upon the surface magnetic charge (or monopole) density, which *at equilibrium* in the grand canonical Coulomb gas, is independent of the bulk monopole density to low order in field. Therefore, at weak fields, the sample may be magnetised at constant monopole density.

8.2.2 Linear Response and Non-equilibrium Thermodynamics

Linear response theory [40, 41] formulates the near-to equilibrium response of a magnetic system in terms of position $\mathbf{r}$, wave vector $\mathbf{q}$, time t, and frequency ω.

[6] This behaviour is of interest for another reason: it is a signature of 'topological sector fluctuations' in a harmonic field [37].

Table 8.2 Relationship among response functions and experimental quantities (neglecting corrections from form factor and demagnetising factor). Note that all S, R, χ are really second-rank tensors e.g. $S^{\alpha\beta}$ with $\alpha, \beta = x, y, z$, but the superscripts here are omitted for clarity. It should also be noted that the wavevector $\mathbf{q}$ here is the wavevector that enters the Fourier description of crystal properties. Because of the periodic crystal symmetry, properties are invariant under the transformation $\mathbf{q} + \mathbf{G}$ where $\mathbf{G}$ is a reciprocal lattice vector. For example a general component of the scattering function $S^{\alpha\beta}(\mathbf{q})$ is invariant in this way. Neutron scattering gives a particular way of observing the scattering function in terms of the scattering vector $\mathbf{Q} = \mathbf{q} + \mathbf{G}$. It projects out the components of the scattering function that are perpendicular to $\mathbf{Q}$ by multiplying by the transverse projection operator $\delta_{\alpha\beta} - \hat{Q}_\alpha \hat{Q}_\beta$

Response function	Symbol	Technique	Relations for $\hbar\omega \ll kT$
Correlation function	$S(\mathbf{q}, \omega)$	Neutron scattering	
	$S(\mathbf{q}, t)$	Neutron spin echo	
	S($\mathbf{q}$)	Neutron static approx.	$S(\mathbf{q}) = S(\mathbf{q}, t = 0)$
			$S(\mathbf{q}) \approx \int S(\mathbf{q}, \omega) d\omega$
Relaxation function	$R(\mathbf{q}, t)$		$TR(\mathbf{q}, t) \sim S(\mathbf{q}, t)$
	$R(t)$	dc-magnetization	$R(t) = R(\mathbf{q} = 0, t)$
Susceptibility	$\chi(\mathbf{q}, t)$		$\chi(\mathbf{q}, t) \sim \partial R(\mathbf{q}, t)/\partial t$
	$\chi(t)$		$\chi(t) = \chi(\mathbf{q} = 0, t)$
			$\chi(t) \sim \partial R(t)/\partial t$
	$\chi(\mathbf{q}, \omega)$		$T\mathrm{Im}\chi(\mathbf{q}, \omega) = S(\mathbf{q}, \omega)$
	$\chi(\omega)$	ac-susceptibillity	$\chi(\omega) = \chi(\mathbf{q} = 0, \omega)$
	$\chi(\mathbf{q})$		$\chi(\mathbf{q}) = \chi(\mathbf{q}, \omega = 0)$
			$T\chi(\mathbf{q}) \sim S(\mathbf{q})$
			$\chi(\mathbf{q}) \sim R(\mathbf{q}, t = 0)$

Generalized susceptibilities χ, relaxation functions R, or correlation functions S[7] relate the local, time dependent magnetisation to a local, time dependent applied field. Given say $\chi(\mathbf{q}, \omega)$, all the other functions (χ, R, S) can be derived by standard transformations. Generalized susceptibility is therefore a very powerful tool for comparing experiments on a magnetic system.

Table 8.2 gives a list of which response functions are accessible to which probes. Neutron scattering is, in principle, the preeminent probe for model magnets, as it can measure the whole response function. However, in spin ice the dynamics are so slow that this largely removes the possibility of using neutron scattering to measure dynamics. An exception is neutron spin echo on $Ho_2Ti_2O_7$, which can just about resolve some spin dynamics in the monopole regime [42, 43]. Setting this aside, to a first approximation, we must be content to use neutron scattering to measure $\chi(\mathbf{q}, \omega = 0)$, which may be derived from the diffuse scattering intensity in

[7] Unfortunately both entropy and correlation function are invariably denoted by S, the context should make clear which we are referring to.

the static approximation [40], ac-susceptometry to measure $\chi(\mathbf{q} = 0, \omega)$ and dc-magnetometry to measure $R(\mathbf{q} = \mathbf{0}, t)$ (proportional to the time dependent magnetisation, following sudden field removal or application). This limitation makes a clean break between 'static' properties like $\chi(\mathbf{q})$ and "dynamic" ones like $\chi(\omega)$.

In monopole theory, at fixed temperatures, an extension of the above thermodynamic considerations shows that there are two independent local variables, $\mathbf{M}(\mathbf{r}, t)$ and $n(\mathbf{r}, t)$ [18]. However, because the monopole density is a scalar it does not couple to the applied field to low order, near to equilibrium, and the monopole density may be treated as a constant (although this breaks down for the Wien effect, discussed below). The theory of Ryzhkin [18] calculates the generalised susceptibility of the monopole gas and expresses it in terms of monopole transport parameters. This analytical theory of diffusion and drift is an extension (due to Jaccard in the context of ice physics [44]) to the macroscopic theory of transport in electrolytes (Nernst-Planck-Poisson theory) or semiconductors (Van Roosbroeck theory [45]), and is valid on long length scales only. The theory has been extended to treat far from equilibrium and nonlinear response in Ref. [35]. This response, the second Wien effect, is a universal property of weak electrolytes in the dilute regime (here low temperature). In spin ice it takes the form of a transient, field dependent increase in monopole density in response to an applied dc-field. The ac-response becomes more complex: for example the variation of monopole density doubles the frequency of an applied oscillating field [35].

In experiment, only the magnetisation can be measured directly, the monopole density remaining a 'hidden' variable. Bearing in mind the above discussion, there are essentially three available measurements: (1) measurements of $\chi(\mathbf{q})$ and hence correlations in $\mathbf{M}(\mathbf{q})$, (2) measurement of $\mathbf{M}(t)$ and (3) measurements of $\mathbf{M}(\omega)$.

The wavevector dependent magnetisation, $\mathbf{M}(\mathbf{q})$, accessible through its correlations via the neutron scattering $S(\mathbf{q})$, contains both longitudinal (to $\mathbf{q}$) and transverse contributions, as expressed in the susceptibility tensor $\chi^{\alpha\beta}(\mathbf{q})$. The magnetisation in the monopole 'vacuum' is entirely transverse (divergence free), while the monopole contribution is entirely longitudinal (irrotational). Polarised neutron scattering measurements of $S^{\alpha\beta}(\mathbf{q})$ are able to separate the longitudinal and transverse components and provide information on both the monopole vacuum, via the transverse correlations, and the monopole distribution itself, via the longitudinal correlations. The latter provides direct spatial imaging of magnetic monopole correlations in spin ice. In theory it allows direct access to the monopole diffusion length l_{diff}, closely related to the Debye (screening) length (l_D) of the monopole gas [18].

The time and frequency dependent magnetisations, $\mathbf{M}(t)$ and $\mathbf{M}(\omega)$, are directly accessible in dc-and ac-magetization measurements, respectively, giving access to the relaxation function $R(t)$ and the dynamical susceptibility $\chi(\omega)$. In contrast to the equilibrium susceptibility, these properties provide a sensitive test of the monopole theory. Detailed predictions [13] in the linear approximation are summarised in Table 8.3. Referring to the table, the main quantity that can be extracted by comparing theory with experiment (or with numerical simulation of the s-DSM) is the monopole mobility u, or equivalently, the diffusion constant D or monopole hop-rate $\nu_0(T)$. The nonlinear response (Wien effect) that develops at low temperature additionally

Table 8.3 Results of the linear theory [13], for bulk properties

Symbol	Meaning	Relations
$\mathbf{J}$	Magnetic current density Equation of motion	$\mathbf{J} = \partial\mathbf{M}/\partial t$ $\mathbf{J} = \kappa(\mathbf{H} - \mathbf{M}/\chi)$
χ	Isothermal susceptibility	$\chi(T \to 0) = 2C/T = Q^2/\Phi$ (Φ defined in [13])
κ	Monopole conductivity	$\kappa = \mu_0 Qun$
u	Monopole mobility	$u = DQ/kT$
D	Diffusion constant	$D = 4a^2\nu_0/27$ [19]
$\nu_0(T)$	Monopole hop rate	
ν	Magnetic relaxation rate	$\nu = \kappa/\chi$

Table 8.4 Relationship among response functions and experimental quantities

Response function	Monopole property	Measured	Derived
$S_\perp(\mathbf{q})$	Vacuum correlations		
$S_\parallel(\mathbf{q})$	Monopole correlations	$l_{\text{diff}} \sim a/\sqrt{n}$	$n(T)$
c_μ	Screening energy	$\mu_{\text{eff}} = \mu + kT \ln \gamma$	$n(T)$
$R(t)$, $\chi(\omega)$	Ohmic conductivity	$\kappa/\chi_T = \mu_0 nu Q/\chi_T$	$u(T)$ $\to D(T)$, $\nu_0(T)$
(Nonlinear response)	Wien effect, screening, pairwise Coulomb interaction	κ_0, γ Q	

provides direct access to the monopole charge Q and directly exposes the Coulomb interaction between magnetic monopoles [35].

Summary of magnetic response

Table 8.4 summarises the weak field experimental properties of spin ice, within the monopole theory. There are four experimental properties that probe the monopoles directly: the specific heat, the wavevector dependent susceptibility, and the time and frequency dependent magnetisations. The weak-field magnetic response of the monopole gas is formulated in [13, 18, 19, 34, 35]. The table summarises which monopole properties can be extracted, or verified, by each of these measurements.

8.3 Experiments in Weak Applied Fields

In this section we follow Table 8.4 closely, to examine how the direct predictions of monopole theory are born out in experiment.

8.3.1 Magnetisation Correlations Measured by Neutron Scattering

As discussed above, neutron scattering studies of spin ices produce $S(\mathbf{q}) \sim T\chi(\mathbf{q})$, which provides information about magnetization correlations underlying the monopole theory that are static on the timescale it takes the neutron to pass through the sample. Early diffuse scattering data [6] were used to parameterize the s-DSM and so provide indirect support for the monopole model, insofar as these two models are nearly equivalent. This is the case for $Ho_2Ti_2O_7$, but for $Dy_2Ti_2O_7$ the g-DSM model with additional superexchange interactions was required [4, 7]. The effect on the monopole theory of these additional interactions has not been established, and it would be interesting to do so. There is no suggestion that they dramatically change the Coulombic physics of spin ice, but by giving the spin ice states a finite band width, they could in principle alter the interaction between monopoles, or control an ultimate low temperature ground state which has still not been observed [3, 4, 46, 47, 49, 50].

Transverse versus longitudinal correlations

As already discussed in the caption of Table 8.2, magnetic neutron scattering obeys the selection rule that the scattering function depends only on magnetisation components perpendicular to the scattering vector $\mathbf{Q}$. As shown in Fig. 8.2, these visible components may be parallel or perpendicular to the Fourier wavevector $\mathbf{q}$ in which the properties of the periodic crystal system are analysed. This means that in the first Brillouin zone, neutron scattering 'sees' correlations *only* in the transverse (to $\mathbf{q}$) magnetisation, $\mathbf{M}_\perp$, while in higher order zones, it additionally sees correlations in the longitudinal magnetisation, $\mathbf{M}_\parallel$. Polarised neutron scattering may therefore be used to distinguish the transverse and longitudinal magnetisation correlations.[8]

Analysis into transverse and longitudinal correlations in a sense 'diagonalises' the monopole theory. Thus, correlations in the vacuum state are dictated only by the ice rules, which enforces the divergence-free condition on the local magnetisation (for example if spins are regarded as link variables on a continuous magnetisation flux). This means that the vacuum state is described only by $\mathbf{M}_\perp$. Monopoles, on the other hand, are sources and sinks of magnetisation flux, so the magnetisation associated with them is entirely longitudinal, $\mathbf{M}_\parallel$ [51]. The energetic distinction between the monopole vacuum and the excited monopole states therefore performs a kind of 'physical Helmholtz decomposition' on the magnetisation field by energetically separating the vector field $\mathbf{M}$ into its components $\mathbf{M}_\perp$ and $\mathbf{M}_\parallel$.

Neutron scattering can resolve the correlation functions based on $\mathbf{M}_\perp$ and $\mathbf{M}_\parallel$ respectively, and in this way it can distinguish vacuum correlations from monopole-induced correlations of the magnetisation. Monopoles are thus 'seen' by neutrons through the quasi-static divergence-full magnetisation correlations they induce, as in

[8] If the incident neutron polarisation is perpendicular to the scattering plane then spin flip scattering (which flips the neutron spin) isolates the in-plane component of the fluctuating magnetisation, as in Fig. 8.2, while non-spin flip scattering isolates the out-of-plane component.

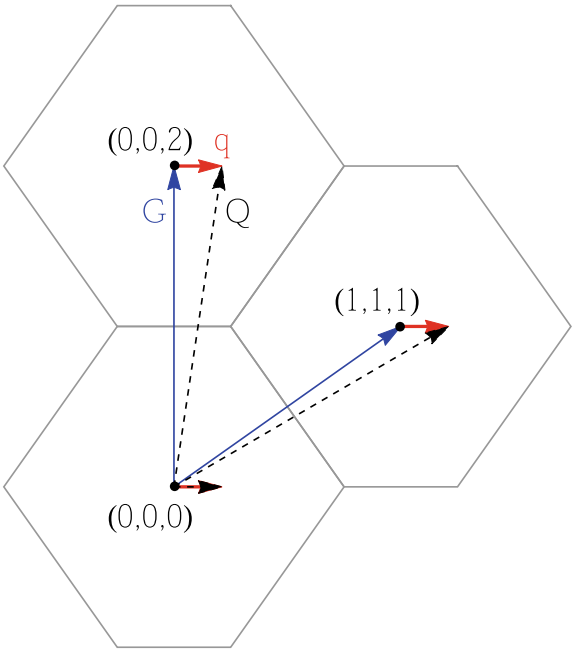

Fig. 8.2 Neutron scattering 'sees' correlated magnetisation components perpendicular to the scattering vector **Q** while physical properties are analysed in terms of the crystal wave vector **q**. The figure shows the first Brillouin zone (lower hexagon) and two second Brillouin zones (upper and right hexagons) for the $[1\bar{1}0]$ plane of spin ice. An example 'physical' wavevector **q** (red) is translated by 'parallel transport' from the origin (0, 0, 0) to the respective zone centres by means of reciprocal lattice vectors **G** (blue). Neutron scattering detects components perpendicular to the scattering vectors (dashed black arrows). In the first zone only, the wave vectors **Q** and **q** are coincident and neutron scattering measures transverse (to **q**) magnetisation components. In the (0, 0, 2) zone (for example) the two wave vectors **Q** and **q** are nearly orthogonal and neutron scattering detects longitudinal in-plane components. Note that out-of-plane components are always transverse to **q** in this scattering plane geometry. The various components may be separated by polarised neutron scattering

Fig. 8.1. It should be noted that neutrons do not directly excite or de-excite monopole states as they do for say spinons in one dimensional magnets [52]. In the classical spin ices, such direct processes are forbidden by the spin selection rule $\Delta S = \pm 1$.

Structure of the monopole vacuum

In its simplest form, monopole theory predicts no correlations in the monopole vacuum state beyond those imposed by the ice rules, so the transverse correlations should be featureless, or paramagnetic, in reciprocal space. The experimental data for $Ho_2Ti_2O_7$, Fig. 8.3, shows that this is only approximately the case. While the measured transverse correlation function $S_\perp(\mathbf{q}) \sim \langle M_\perp(\mathbf{q}) M_\perp(-\mathbf{q}) \rangle$ has intensity across the Brillouin zone, there is a fairly sharp dip at the zone centre, which indicates a correction to monopole theory that has not yet been elucidated theoretically.

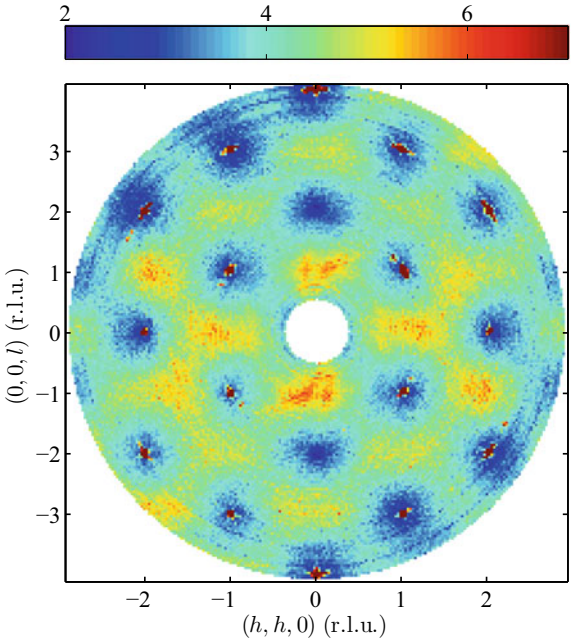

Fig. 8.3 Transverse magnetisation correlations in $Ho_2Ti_2O_7$ measured by polarised neutron scattering in the static approximation [53]. The figure shows the $[1\bar{1}0]$ plane of reciprocal space, with yellow denoting relatively high scattered intensity and blue relatively low scattered intensity. The scattered intensity measures components of the static correlation function $S^{\alpha\beta}(\mathbf{q})$ projected onto the plane perpendicular to the scattering vector, as in Fig. 8.2. Shown here is the out-of-plane scattering, which corresponds to non-spin-flip (NSF) scattering and correlations transverse to the physical wave vector $\mathbf{q}$. Each Brillouin zone centre is marked by a sharp 'dip' in intensity. Reprinted figure from [53] with permission from AAAS

Monopole correlations

As shown in Fig. 8.2 the longitudinal correlation function $S_{\parallel}(\mathbf{q}) \sim \langle M_{\parallel}(\mathbf{q}) M_{\parallel}(-\mathbf{q}) \rangle$ may be measured along a line in reciprocal space that runs perpendicular to the scattering vector, such as $(h, h, 2)$ close to $(0, 0, 2)$. The observed scattering along this line for $Ho_2Ti_2O_7$ can be fitted to a Lorentzian function added to a wavevector-independent ('flat') component [53]—see Fig. 8.4. Monopole theory predicts the Lorentzian function with the width determined by the monopole diffusion length [18]. This allows a direct test of monopole theory as the diffusion length is related to the monopole density. The diffusion length is predicted to go as $l_{\text{diff}} \sim 1/\sqrt{n(T)}$, which for $Ho_2Ti_2O_7$ at high temperatures implies a temperature dependence of

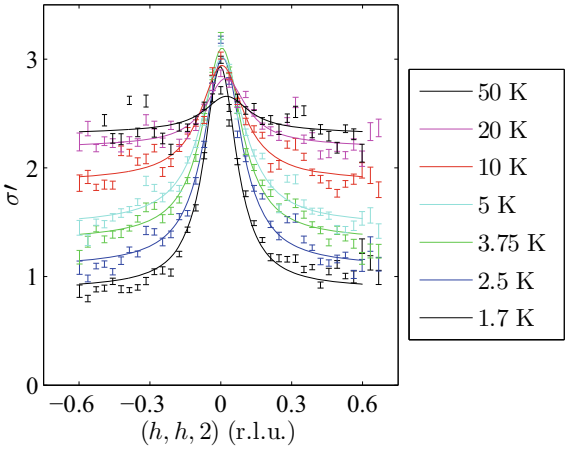

Fig. 8.4 Longitudinal correlations in $Ho_2Ti_2O_7$ measured by polarised neutron scattering in the static approximation. The plot shows scattered intensity versus wavevector q at different temperatures. The wavevectors are chosen to be nearly perpendicular to the scattering vector $\mathbf{Q}$ so that longitudinal correlations are measured by isolating the in-plane component of the correlation function $S^{\alpha\beta}(\mathbf{q})$ as in Fig. 8.2. Experimentally, this corresponds to spin flip scattering (see Fig. 8.5 for the full scattering map). The data show a Lorentzian peak shape superimposed on a flat, temperature-dependent component [53]. Reprinted figure from [53] with permission from AAAS

$\sim \exp(2\ \mathrm{K}/T)$,[9] in accord with experimental observations [53], at least down to about 1.2 K.[10]

There are, however, three discrepancies with the theory that should be noted. First, the flat component of the diffuse scattering is not predicted in current theory, yet its temperature dependence suggests that it is another measure of the monopole density [53] (very recently this discrepancy has been resolved [54]). Second, the experimental width at $T > 1.5$ K [53] is slightly smaller than the predicted width [55], and third, the experimental width fails to diverge below 1 K as predicted theoretically [56]. While there is currently no explanation of these discrepancies, they should not necessarily be regarded as contrary to the monopole model. In particular, the theory is developed at very long wavelength and does not take account of the lattice structure of spin ice, yet for the relatively short diffusion lengths observed in experiment, this must be accounted for. Also, below 1 K, the simple view of the monopole gas as a Debye-Hückel gas starts to break down [35], and this is not accounted for in the theory of magnetic correlations. For this reason, a more sophisticated theory that accounts for the lattice structure (the 'finite size' of monopoles) and the complexities of the Coulomb gas correlations at low temperature, would be desirable.

[9] In $Ho_2Ti_2O_7$ the chemical potential is $\mu/k = 5.7$ K and the Coulomb energy per monopole is 1.5 K; Debye-Hückel screening at high temperature lowers the effective chemical potential to slightly less than $\mu_{\mathrm{eff}}/k = 5.7 - 1.5$ K or approximately 4 K—hence $\sqrt{n}$ varies with an exponential amplitude of ~ 2 K.

[10] Note that in [53] the parameter ξ_{ice} needs to be divided by 2π to get l_{diff}.

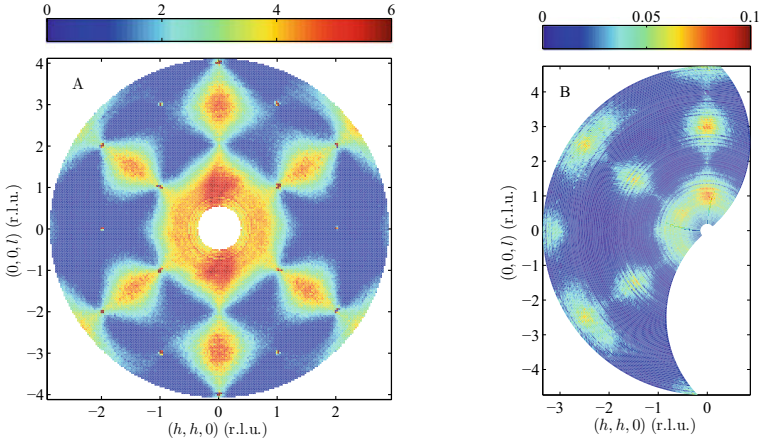

Fig. 8.5 Pinch points measured in $Ho_2Ti_2O_7$ [53] and $Dy_2Ti_2O_7$ [56] using polarized neutron scattering. Reprinted figure from [53] with permission from AAAS

Pinch points

The pinch point [57] is a distinctive bow-tie like form in the diffuse scattering intensity, when measured or presented in a single plane. In essence it arises from viewing a 'mixture' of transverse and longitudinal correlations, for example in an unpolarised neutron scattering experiment, or via 'spin flip' scattering in the case of a polarised experiment on spin ice [53, 58]. Because it is a very striking feature, it has become an iconic signature of a 'Coulomb phase', or vacuum state from which effective magnetic monopoles are the basic excitation. Pinch points in $Ho_2Ti_2O_7$ and $Dy_2Ti_2O_7$ are illustrated in Fig. 8.5.

In general, pinch points arise from either ice rules, which lead to pseudo-dipolar or power-law $(1/r^3)$ spin correlations, or directly from dipolar interactions in a paramagnet [59]. Both mechanisms exclude magnetic charge density, the former on all scales, and the latter on long scales only. In spin ice, both mechanisms are simultaneously active: the divergence free condition is enforced at short scales by the ice rules and reinforced at longer scales by the dipolar interaction (here expressed by the monopole concept) [18, 60]. The different theoretical approaches [18, 60] show that for a particular response function (magnetisation divided by applied field) there should be a 'gap' between the longitudinal and transverse correlation functions at the zone centre. However, such a gap cannot appear in experimental neutron scattering and hence a mechanism must be invoked to remove it. One possible mechanism is instrumental resolution, but this does not appear to explain observations on spin ice. Further work is necessary to clarify the mechanism by which the gap is removed.

Historical observation of pinch points in spin ice

Pinch points were historically observed and discussed in the context of ice-rule ferroelectrics [61–63]. Indeed, a theory based on ice rules and a non-divergent polarization

field was developed, but the relevance of this work to spin ice was only rediscovered later. In spin systems, the pinch point was first identified in Monte Carlo simulations of the pyrochlore Heisenberg antiferromagnet [64], and in analytical calculations for large-N spins on the pyrochlore lattice [65]. The dipolar form of the correlation function was subsequently identified in dimer models on bipartite lattices [66] and the Heisenberg pyrochlore antiferromagnet [67, 68], and then connected with spin ice [9].

Given this, it was therefore somewhat surprising that no pinch points were visible in either $Ho_2Ti_2O_7$ or $Dy_2Ti_2O_7$ when first probed by unpolarised neutron scattering [6, 7]. Although the residual entropy suggested that the ice rules are obeyed in both compounds [6, 69], it might be argued that the entropy confirms only the shortest-range existence of the ice rules, and not their long-range coherence, for which the observation of a pinch point is crucial. Eventually pinch points were unearthed by polarized neutron scattering, confirming the power-law form of the spin correlations. They are now known to exist in $Ho_2Ti_2O_7$ [53, 58] and $Dy_2Ti_2O_7$ [56, 70], see Fig. 8.5. The reason they are not clearly visible by unpolarised neutron scattering is that the zone centre 'dip' in the transverse correlation function (discussed above) largely cancels the Lorentzian peak in the longitudinal one. The theoretical reason for this has not yet been determined, but it goes beyond the equivalent monopole models of [18, 60].

8.3.2 Specific Heat

Two results—the integration of the specific heat to obtain the value of Pauling entropy [6, 69], and the recent report that this residual entropy may not persist to the lowest temperatures [47] (but see [48])—bookend the study of the spin ice specific heat. Before [71], and in between [72–79], the specific heat of $Dy_2Ti_2O_7$ has been reported a number of times. The data in these reports have small quantitative differences, but all have the same generic features. A large asymmetric peak at $T \sim 1.1$ K with (from low temperature upwards) a very steep rise, followed by a long decaying tail. The peak is rather sharper than a Schottky anomaly, but is not indicative of a thermodynamic phase transition.

The specific heat can be reproduced by the *s*-DSM, which implicitly contains the energetic fluctuations represented by creation and annihilation of monopoles, but one may ask if the monopole theory works at least equally well, is more compact and improves understanding. In the case of the specific heat, if one treats only the monopoles (i.e. ignoring the vacuum), textbook Debye-Hückel theory, as formulated by CMS [19], is a very reasonable approximation to the specific heat, as first shown by Morris et al. [72].

Standard Debye-Hückel theory can be significantly improved by accounting for the vacuum and double charge monopoles, as explained in Chap. 7. One important conclusion that comes out of the Debye-Hückel analysis is that the monopole gas may be treated as nearly ideal in two regimes: first at low temperature, where the

monopole density ρ is small, and second at high temperature, where $1/T$ is small. The reason is that Debye-Hückel charge correlations depend on n/T. In the high temperature regime, the dense monopole gas is actually very strongly screened, but it approaches ideal behavior because T is large.

The inclusion of double charge monopoles into the Debye-Hückel theory [80] has resulted in a very close agreement between theory and experiment. The general success of the monopole model in describing the specific heat of spin ice materials is a conspicuous triumph of the theory.

Modification of the chemical potential

An important property of the monopole gas is the chemical potential, which governs the monopole population at a given temperature. In spin ices, the monopole chemical potential has a unique value in each spin ice material, controlled by the lattice parameter, size of the magnetic moment, and the relative strengths of their dipole and exchange interactions (which control the energy of creation of a pair of monopoles). It is not at all easy to modify in-situ, in a particular spin ice material, likely requiring the application of enormously high pressure. However, it can be conveniently modified by chemical pressure, as was done by synthesis of the high pressure pyrochlore phases $Ho_2Ge_2O_7$ and $Dy_2Ge_2O_7$. They have considerably smaller lattice parameters than the titanates, which leads to stronger exchange interactions competing with the dipolar interaction, resulting, at least in $Dy_2Ge_2O_7$, in a much lower chemical potential for monopole creation than the respective titanates. As such, they represent magnetolytes with more strongly interacting monopoles, and this is manifested in the heat capacity, which cannot be reproduced by simple Debye-Hückel theory, but requires the addition of a Bjerrum term to account for the enhanced importance of monopole dimers [81, 82]. The resultant modification analytically captures the heat capacity of $Dy_2Ge_2O_7$ and provides a neat explanation of the difference between the two heat capacities, as shown in Fig. 8.6.

8.3.3 dc-Susceptibility

As discussed above, the dc-susceptibility $\chi = M/H_{\text{internal}}$, obtained by measuring the apparent susceptibility $\chi_a = M/H_{\text{applied}}$ and taking account of the demagnetisation factor [38, 83–85], is not a direct signature of the monopoles. Nevertheless, the temperature dependence of χ can be related to the monopole chemical potential, with satisfactory results [38].

It is worth noting that the fact that the susceptibility $\chi = M/H_{\text{internal}}$ is finite immediately distinguishes spin ice from a true conductor of magnetic monopoles. Thus, if the susceptibility depended only on free charges (monopoles), then the surface charge would completely screen the applied field and the apparent susceptibility $\chi_a = M/H_{\text{applied}}$ would be exactly equal to the reciprocal of the demagnetising factor at all temperatures: $\chi_a = 1/\mathscr{D}$. The usual susceptibility $\chi = M/H_{\text{internal}}$ would then be infinite at all temperatures, like the divergent dielectric constant of an electrical

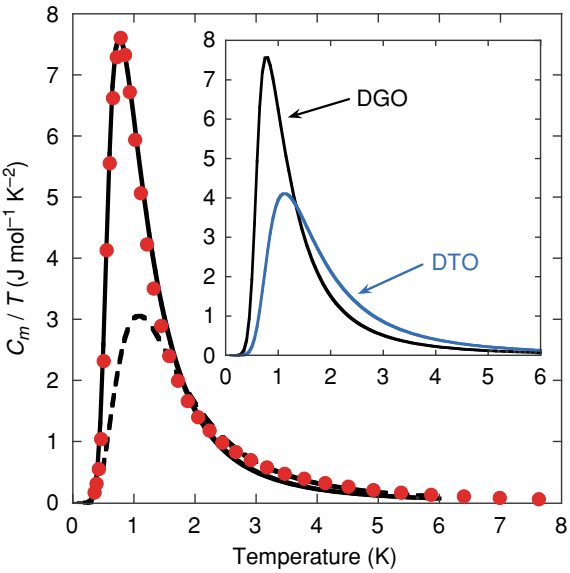

Fig. 8.6 Specific heat of $Dy_2Ge_2O_7$ fitted to an approximate Debye-Hückel theory (full black line) [81]. Dashed line refers to an ideal lattice gas. Inset compares the specific heat of $Dy_2Ge_2O_7$ and $Dy_2Ti_2O_7$. Reprinted from [81] with permission from Nature Communications

conductor. However, in spin ice, the susceptibility χ becomes finite once the vacuum is taken into account, and χ_a is given by:

$$\chi_a^{-1} = \chi^{-1} + \mathscr{D}. \tag{8.3}$$

A detailed theory of the screening of the applied fields by magnetic monopoles is given in [34] (see also [39] for a detailed calculation of the anomalous demagnetisation factor).

8.3.4 *ac*-Susceptibility

The *ac*-susceptibility of $Dy_2Ti_2O_7$ and $Ho_2Ti_2O_7$ has been investigated a number of times [38, 42, 43, 84–94], though most interest has been in $Dy_2Ti_2O_7$. From an experimental point of view, the susceptibility shows a frequency dependent peak in χ'', which shifts to lower frequency at lower temperature. One way to present the complicated behaviour of the *ac*-susceptibility has been to extract a characteristic spin relaxation time, which is taken as $\tau = 1/2\pi f_{\max}$, where $f_{\max}$ is the frequency at which the maximum of the peak in χ'' occurs for a particular temperature.[11]

As observed experimentally in $Ho_2Ti_2O_7$ and $Dy_2Ti_2O_7$, the magnetic relaxation time has four thermal regimes, of which it is sensible to consider only three for comparison with the monopole response functions: high temperatures ($2 < T < 12$

[11] Note the different convention with respect to 2π in the works of Snyder et al. [86].

K), in which the relaxation time is roughly temperature independent; intermediate temperatures ($0.6 < T < 2$ K), in which the relaxation time is getting longer with decreasing temperature; and low temperatures ($T < 0.6$ K), where the spins freeze and the relaxation time becomes too long to measure in these experiments. The distinction between these ranges has both a theoretical and experimental basis, as explained below. The fourth regime is a thermally activated part at $T > 12$ K where the activation energy corresponds roughly to the energy of the first crystal field level. This part can be attributed to a phonon mediated or Orbach mechanism [95] and is not relevant to monopole physics.

High temperatures: $2 < T \lesssim 12$ K

In this region the average relaxation time is roughly temperature-independent [84]. In [42] for $Ho_2Ti_2O_7$ and [86] for $Dy_2Ti_2O_7$, it was argued that the temperature-independence arose from spin tunnelling. By equating a tunnelling spin flip with a monopole 'hop' in numerical simulations of both dipolar spin ice and a magnetic Coulomb gas, Jaubert and Holdsworth produced impressive support for the monopole model [11, 12]. Specifically they reanalyzed the previously published $\chi(\omega)$ data of Snyder et al. [86], using their 'magnetolyte' model and assuming a temperature-independent monopole hop rate. At sufficiently high temperature, the relaxation rate is proportional to the monopole density, but there are corrections [11, 12] associated with the Coulomb interaction. These corrections were discussed by CMS in the context of Debye-Hückel theory [19].

In this regime, although the monopole density is large, the ratio n/T is sufficiently small that monopole screening is well accounted for by Debye-Hückel theory. Hence, the monopole gas may be treated as dense, but weakly interacting. As in the case of electrolytes [96], it is therefore appropriate to apply the usual drift-diffusion theory, which in this case is Ryzhkin's theory of monopole transport (originally derived for the dilute limit). In Ryzhkin's theory, the magnetic relaxation rate is simply the monopole conductivity divided by the isothermal susceptibility: see Table 8.3.

Bovo et al. [94] applied Ryzhkin's theory directly to the average relaxation rate derived from fitting ac-susceptibility measurements to derive the temperature dependence of the monopole mobility. This involved combining accurate experimental measurements of the mean relaxation time, the static susceptibility, and the monopole density derived from fitting the heat capacity to Debye-Hückel theory. They thus established experimentally that the monopole mobility u is inversely proportional to temperature in the high temperature regime, as shown in Fig. 8.7. This conclusion is consistent with a constant monopole hop rate and Brownian diffusion of monopoles to give the Nernst-Einstein relation i.e. $u = DQ/kT$ with temperature-independent diffusion constant D.

The numerical simulations of Jaubert and Holdsworth are equivalent to the Ryzhkin theory in the sense that they treat the long-range dipole interaction entirely through magnetic monopoles, but they also differ in two ways: first, they take into account the lattice nature of spin ice (as in extended Debye-Hückel theory), and second, they assume a constant hop-rate for magnetic monopoles. In the experiment

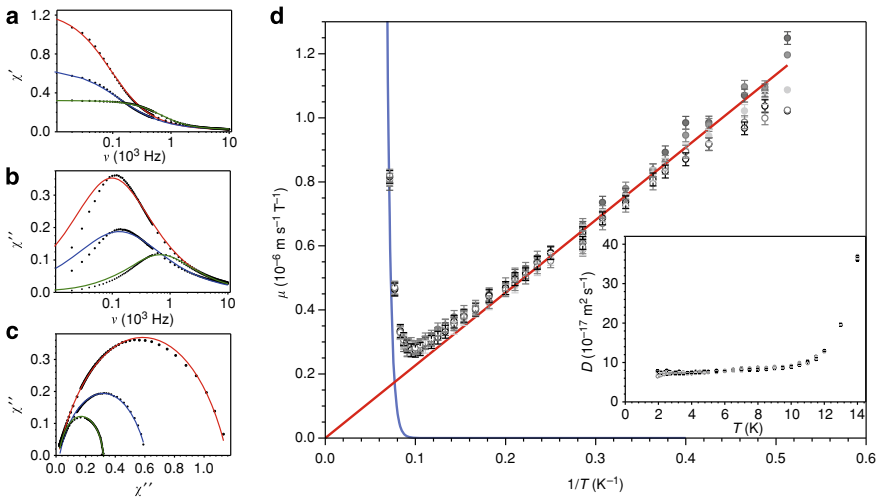

Fig. 8.7 Monopole mobility measured by *ac*-susceptibility measurements [94]. The left panel shows fitted data. The right panel shows the measured monopole mobility (at several weak field values) compared to predictions for a constant hop rate (red line). The inset shows the measured diffusion constant. Reprinted from [94] with permission from Nature Communications

of Bovo et al., the constant hop rate at $T \geq 2$ K is an experimental result rather than a prior assumption.

In a related numerical approach Takatsu et al. [97] used single spin flip dynamics to achieve close agreement with the experimental susceptibility while monitoring a "conversion factor" between Monte Carlo time and real time. In the high temperature regime ($2 < T < 10$ K in their work) this factor is again almost exactly temperature independent. The question of the hop-rate at lower temperatures will be further addressed below.

The consistency of these numerical and analytic approaches to the analysis of the *ac*-susceptibility $\chi(\omega)$ is excellent evidence for the robust and correct nature of the monopole model. In Ryzhkin's formulation the relaxation time depends on three potentially temperature dependent factors: $u(T)$, $\chi(T)$ and $n(T)$. Hence it is somewhat fortuitous that a temperature-independent hop rate leads to a temperature-independent relaxation time. Although they were ultimately correct, the inferences of [42] and [88] (i.e. that spins flip by quantum tunnelling) cannot be fully justified in the absence of the monopole model, since the relaxation implies nothing directly about the spin flip processes. In this way we can see that the monopole model has, at the very least, enabled the experimental observation of spin tunnelling to be put on a much firmer experimental basis.

In summary, the simplest numerical or analytical treatment of monopole dynamics employs a single, temperature independent hop rate, and already matches the measured relaxation time extremely well at $T \geq 2$ K in $Dy_2Ti_2O_7$. In $Ho_2Ti_2O_7$, the

relaxation is much faster than for $Dy_2Ti_2O_7$ in the high temperature regime [42], and similar analysis has not proved feasible.

Intermediate temperatures: 0.6 K $< T <$ 2 K

In the intermediate temperature range, the specific heat peaks and monopole screening becomes strong in the sense that Debye-Hückel theory can no longer describe it. As a consequence, the simple linear theory of Ryzhkin should only be applied with caution in this regime. Indeed, the linear variation of magnetic relaxation rate with monopole density observed at higher temperatures breaks down [93]. However, an interesting observation is that the magnetic relaxation rate seems to vary as the square of the monopole density in this regime [98], which again suggests that monopoles are the natural variables with which to understand the spin dynamics of spin ice. Although the squared law has not yet been explained in detail it is not in any sense contradictory to the monopole model as has been suggested by some authors [93]—unless one insists that the monopole hop rate has to be temperature-independent over the entire temperature range.

Low temperatures: $T <$ 0.6 K

Below $T \sim 0.6$ K, the magnetic relaxation time becomes exceptionally long and spin ice "freezes" on experimental time scales [86]. A natural explanation of spin freezing is a definite triumph of the monopole model. For example, $Ho_2Ti_2O_7$ has slower dynamics than $Dy_2Ti_2O_7$ in this regime because it has fewer monopoles as a consequence of a larger monopole chemical potential (5.7 K as opposed to 4.3 K)—despite its much faster dynamics at higher temperature. In general the freezing temperature should depend on the timescale of the experiment—a slower experiment should maintain equilibrium to a lower temperature with a smaller population of monopoles. However, the freezing temperature observed is always close to 0.6 K, but this is again a consequence of several factors which conspire at about this temperature—the monopole gas is rarifying rapidly and the hop rate is possibly also decreasing rapidly—leading to an exponential suppression in relaxation rate and loss of equilibrium on all reasonable experimental time scales (restoration of dynamics by quenching monopole-rich states to low temperature is discussed below) [92, 98].

Thermal quenches

In a thermal quench, the system, which may be a dipolar spin ice model or Coulomb gas, transitions rapidly from a relatively high temperature, where a large population of monopoles would exist, to a low temperature, where few monopoles would exist at equilibrium. The evolution of the system from the large quenched-in population of monopoles towards the equilibrium population is then studied. In both cases, there is a rapid decay of the monopole density, leading to a plateau which represents a metastable, long-lived monopole population. The importance of so-called non-contractible pairs in maintaining this population of monopoles was stressed [99]. A non-contractible pair of monopoles is a pair of monopoles on adjacent tetrahedra, which cannot annihilate because flipping the intermediate spin would actually create a higher-energy spin configuration (i.e. pair of double-charged monopoles). The

shortest path for annihilation of these monopoles is for one of them to hop around the hexagonal loop which contains an edge of their respective tetrahedra, but in general they have to diffuse away across the lattice and find a new way to annihilate, and there is always a Coulombic energy cost for them to do this. Hence, their removal from the system is thermally activated and, at the low temperatures reached in the quench, is extremely slow.

The onset of non-equilibrium physics (on typical experimental timescales) is at $T \approx 0.6$ K in $Dy_2Ti_2O_7$ and $T \approx 0.7$ K for $Ho_2Ti_2O_7$ (which also corresponds to the low-temperature regime discussed above in Sect. 8.3.4), as signalled by the well-documented splitting of field-cooled and zero-field-cooled susceptibilities at this temperature [87, 100]. The key point to stress, when considering this temperature regime, is that from the point of view of the monopole model, all typical experiments are actually thermal quenches. This is an explicit result of the monopole model that is largely independent of the microscopic nature of the spin dynamics, and occurs as a consequence of the kinetic equations for monopole recombination [51]. Comparing experiments in this temperature regime is therefore extremely difficult, since temperature and field sweep parameters and history must be controlled in a reproducible way. Furthermore, processes existing in non-equilibrium experiments may not appear in ostensibly equilibrated experiments with different techniques. For example, it may not be simple to compare relaxation of the magnetisation after a field pulse in the low-temperature state with an *ac*-susceptibility experiment at the same temperature with a different cooling history.

Reproducible thermal quenching was achieved in [101], which developed a magneto-thermal quench technique for fast and reproducible cooling. Comparison with numerical simulations showed definite evidence of quenched, non-equilibrium monopole density, and its relaxation. It should be stressed that the effective chemical kinetic theory of [35] is a rigorous non-equlibrium theory that naturally accounts for thermal quenches. Hence looking forward, all experiments in the low temperature regime should apply either the protocol of [101] or a similarly reproducible method of thermal quenching. One goal of controlled thermal quenching experiments is to identify the 'noncontractible' monopole pairs, which have been discussed theoretically [99].

The Wien effect in spin ice

In the dilute regime, the response of a Coulomb gas to applied fields may be counterintuitively complex owing to the occurrence of the second Wien effect, as first calculated by Onsager for the case of electrolytes [22]. Onsager solved the problem of electrodiffusion in the combined Coulomb and applied field potentials and the results were very surprising and non-trivial. Kaiser et al. recently extended the analysis to the case of a lattice Coulomb gas and then to magnetic monopoles in spin ice [35, 102].

The essential result is that the rate of production of free charges (as in 8.1) becomes strongly field-dependent. At low applied field $\mathbf{E}$ or $\mathbf{H}$, the increase is linear with the *modulus* of the field while at high field it depends on the exponential of the square root of the field. At very low field, screening regularises the linear dependence to

make it quadratic. Even though spin ice does not sustain a direct monopole current, these effects feed through to increase the charge density at short times, which in turn affects the magnetisation and its rate of relaxation in a striking way.

Although the physics of the Wien effect is very complex, its final result, as summarised by Onsager's function [22], is rather simple and universal, and most importantly, does not depend on the definition of free and bound charges—a consequence of Gauss' divergence theorem [103]. The appeal of measuring the Wien effect for magnetic monopoles in spin ice is first, that it extends this remarkable non-linear and non-equilibrium physics to a magnetic system, and second it can be used to experimentally image the Coulomb interaction between magnetic monopoles and to measure the monopole charge. The reason for this is that Onsager's function is essentially a direct transform of the pairwise interaction between monopoles. Indeed, according to our discussion above, one must conclude that is not possible to conceive of any more direct detection of magnetic monopoles that the observation of the Wien effect.

Figure 8.8 [35] shows a simulation of the monopole density versus time in spin ice when a field is suddenly applied: the increase is the Wien effect, and the subsequent decrease is a return to equilibrium. A very comprehensive set of measurements of out-of-equlibrium monopole response [104], using the reproducible 'avalanche quench protocol' [101] has now unambiguously established the Wien effect for magnetic monopoles in spin ice, consistent with Fig. 8.8. Some of the results are shown in Fig, 8.9. These experiments have finally established the Coulomb interaction between magnetic monopoles in spin ice, have confirmed the expected monopole charge to within about 10 % and have given direct evidence of 'non-contractible' pairs [99]. The only discrepancy between theory and experiment in [104] is an anomalously large screening correction at low field, that needs further investigation.

The experiments of [104] supersede two earlier experimental attempts to measure the Wien effect for magnetic monopoles. In [105] slow relaxation of the magnetization was studied by applying field pulses of different size or duration to the low-temperature state [105], hence measuring the relaxation function (see Table 8.2). The non-exponential decay of the magnetization following a field pulse could be satisfactorily described by a model of monopole kinetics in which the new charges produced by the Wien effect led to polarization (magnetization), as in a capacitor: this is essentially a theory of 'saturation current' for the Wien effect. Although the data seemed consistent with Onsager's universal function, it now seems unlikely that the 'saturation current' approximation is correct, given the results of [104]. The other experimental paper [106], which involves muon spin rotation, μSR, is discussed further below.

The Wien effect accounts for the magnetic response at relatively short times in the low temperature regime (see Fig. 8.8). The long time limit, which probes the near to equilibrium response, is less dominated by the Wien effect, as the field that drives the monopoles, $\mathbf{H} - \mathbf{M}/\chi$ [13] approaches zero [35]. However some progress has been made in connecting the approach to this limit to the monopole model. In particular Revell et al. have shown that monopoles trapped on crystal defects contribute to the slowing of the current at long times [98]. At exceptionally long times ($> 10^6$

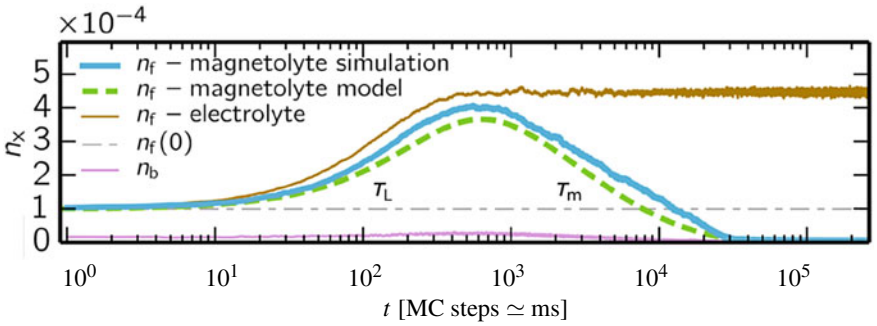

Fig. 8.8 Theoretical Wien effect in spin ice and an analogous lattice electrolyte, following the sudden application of a field (magnetic and electric respectively), from [35]. The brown and blue lines are, respectively the ion or monopole concentration as a function of log time ($Dy_2Ti_2O_7$ parameters at 0.45 K). Dotted line is a kinetic model [35] and n_f, n_b are free and bound monopole concentrations respectively. In spin ice the Wien effect dies away at long times as the field $\mathbf{H} - \mathbf{M}/\chi$ approaches zero, while at short times spin ice behaves like the electrolyte. Reprinted figure from [35] with permission from the American Physical Society

s), it has been argued that the spin ice state may start to rearrange and lower its degeneracy [47], but more experiments and theory are needed to verify this (See [48] for the latest results).

The μSR controversy

The Wien effect [104] is unquestionably *the* signature of magnetic monopoles in spin ice, as it unambiguously exposes their deconfinement and pairwise Coulombic interaction. In particular, measurement of the monopole conductivity κ or density n as a function of field allows a no-parameter measurement of the magnetic charge Q. All of these possibilities were originally developed in [106], in which the authors and colleagues also reported a transverse field μSR experiment in which it was assumed that the muon relaxation rate was a measure of n, and on this basis, they derived an estimate for the magnetic charge, in close agreement with the theoretical value. The experiment was later repeated on both $Dy_2Ti_2O_7$ and $Ho_2Ti_2O_7$ by Chang et al., with a consistent results [107].

There were two comments on [106] by Dunsiger et al. [108] and by Blundell [109], which called into question the interpretation of the μSR data. Following this, the interpretation of extra data offered by Dunsiger et al. [108] has been debated [110], and this study itself also questioned [111]. For detailed discussion of the issues at stake we refer the reader to the paper of Chang et al. [107] and the review by Nuccio et al. [112].

Regardless of all the issues under debate, it is clear that, unlike the magnetisation experiment of [104], the μSR experiment of [106] is not a convincing demonstration of the Wien effect in spin ice. The explanation of the data collapse of [106] and [107] therefore remains an open question of interest from the perspective of μSR methodology. The muons analysed in these experiments were implanted in low-field

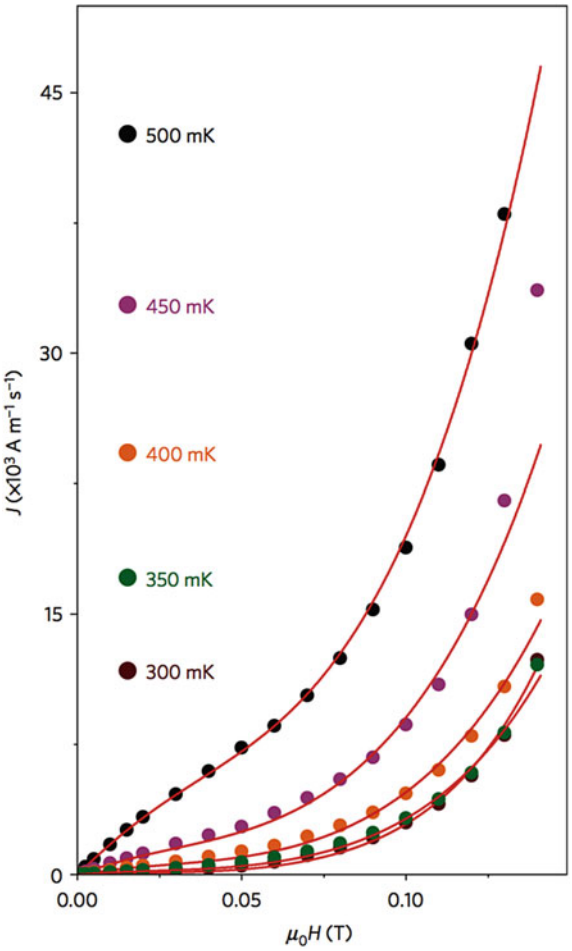

Fig. 8.9 Nonlinear non-equilbrium magnetisation dynamics captured by the monopole model. Experimentally measured magnetic monopole current density ($\partial M/\partial t$, circles) compared with the theory [35] of the Wien effect for magnetic monopoles in spin ice (line), from [104]. Each point on the figure represents the early-time current density after a highly controlled thermal quench, which corresponds roughly to the peak in Fig. 8.8. Reprinted figure from [104] with permission from Nature Physics

sites (whether inside or outside the sample), as shown experimentally [106, 107]. It seems that the question of the data collapse can only be resolved by more detailed calculation of the fields to which these muons were exposed [108, 109, 113, 114].

Distribution of relaxation times

It has long been recognised that the magnetic relaxation times of spin ice materials are broadly distributed [84]. This is a particular area in which observations and interpretations are complicated, and suggests modifications to the simplest version of the monopole theory.

A single relaxation time is usually provided by the treatment of *ac*-susceptibility data, the characteristic time being related to the frequency of the peak in χ''. However, some susceptibility experiments provide evidence for two relaxation processes within the time-window of such experiments, while other techniques also suggest

both slower and faster processes exist. Notably, heat capacity experiments suggest the existence of very slow processes; neutron spin echo [42] and backscattering [115], μSR [116] and dielectric constant measurements [117] suggest processes which have the same general temperature dependence as ac-susceptibility (hence indicative of monopoles), but with faster frequencies, characteristic of the probe. Transformation of both susceptibility and dielectric constant measurements suggest a stretched exponential distribution of timescales.

From the monopole perspective there are at least four causes of this broad distribution of relaxation times and associated non-exponential relaxation.

(1) The hop rate itself may be distributed according to the physical nature of the microscopic spin flip process. As a static representation, monopole theory has nothing to say about this, but it can accommodate it phenomenologically in the same way that electrolyte theory can accommodate the dynamical details of microscopic chemical processes.
(2) The monopolar fields can create a broadening of the relaxation time distribution. Experimental evidence [94] has shown that the variance of the relaxation time distribution is related to the monopole density, suggesting the importance of monopole fields in causing local spin flip processes. Also, the high frequency 'adiabatic' susceptibility is proportional to the monopole density. Further theoretical work is needed to understand those effects.
(3) The Wien effect creates a broad intrinsic distribution of relaxation times in the monopole gas. The theory is set out in [35] and experiments are required to test it.
(4) The dynamical scales of even the most simple Coulomb gas are broadly distributed, in the sense that the hop rate ν_0 and the relaxation rate ν are proportional by a factor of the (dimensionless) monopole density, which, as a function of temperature, varies over many orders of magnitude [51]. Although this latter effect does not lead to a departure from single-exponential relaxation in the bulk magnetisation, it can, of course affect spatially dependent probes.

8.3.5 Summary: Success and Failures of the Monopole Theory in the Weak Field Regime

In the previous sections we have discussed the interface between the monopole theory and extant observations. We have shown many instances where the monopole theory agrees with experimental observations, others where experimental observations agree qualitatively with dynamics mediated by monopoles, and pointed to some instances where developments are required to fully resolve theory and experiment. However, there are no examples where the monopole theory is outright falsified by experimental data.

We want to stress that the monopole theory (or other successful theory of spin ice) should be able to describe the magnetic response across the full range of its

applicability i.e. within the temperature range of the Ising approximation and above any process which releases the spin ice entropy. Within this temperature window, a single, unifying description should be possible, without recourse to too complex a phenomenology.

This raises the question of whether accepting the broad distribution of relaxation times and thermal evolution of the monopole mobility $u(T)$ really goes too far from the most basic monopole dynamical model as formulated by Ryzhkin. We feel that, on balance, it does not, particularly because the broadness of the distribution seems connected to monopole parameters, and the thermal evolution of $u(T)$ is not unexpected in the monopole picture. Nevertheless, a recent paper applied the phenomenology of glasses and supercooling to the magnetic relaxation of $Dy_2Ti_2O_7$, suggesting that this would be a more profitable approach to spin ice dynamics than one based on monopoles [118]. While the results of [118] are interesting, we feel that the approach of that paper is a step backwards: at least the monopole model is well established as the correct static description of spin ice, as the fits to Debye-Hückel theory demonstrate, and the monopole theory is surely the best starting point for understanding spin dynamics. Hence we feel that it is premature to abandon the monopole model and return to a purely phenomenological approach that has no theoretical justification.

8.4 Strong Field Response

With the exception of the work of Shtyk and Feigel'man [119] and Otsuka et al. [120] (see below), the analytical monopole theory has been less comprehensively developed for strong fields than it has in the weak field limit. Nevertheless, the behaviour of spin ice in strong applied fields is very diverse and interesting, and the idea of magnetic monopoles has allowed a number of insights into its behaviour. These are reviewed in this section.

8.4.1 Monopole Condensation with Applied Field Along [111]

Application of the field along the [111] direction of a spin ice corresponds to applying the field parallel to one spin on each tetrahedron, while the remainder make a rather shallow angle with the field. This means that at relatively low fields one spin per tetrahedron will be pinned parallel to the field, but the ice rule can still operate and a subset of the ice rule states are selected. Parallel to the [111] direction, the pyrochlore lattice forms an alternating stack of triangular and kagome planes. The pinned spins occupy the triangular planes, while the competition of field and ice rule means that one spin per tetrahedron (or per triangle in a kagome layer) opposes the field. This creates a magnetisation plateau, known as the kagome ice [78, 121] phase, a quasi-

two dimensional version of spin ice formed by these degenerate 1-down–2-up spin components.[12]

Kagome ice is a 2d Coulomb phase [123–126]. It survives until the field is large enough to flip the 'down' spin, resulting in an ordered 'three-in–one-out' phase. This results in a gigantic peak in the entropy, due to the crossing of energy levels of the ice rule and non-ice rule states [127], which has been observed in $Dy_2Ti_2O_7$ [128]. It was also observed, again in $Dy_2Ti_2O_7$, that this plateau termination has a first-order character at low temperature, leading to a critical point [129, 130]. The existence of a critical point was later confirmed in $Ho_2Ti_2O_7$ [100, 126].

The liquid-gas critical point in spin ice should itself be viewed as a fascinating surprise—no explanation was available when it was originally reported and studied and CMS pointed out that such a critical point is extremely rare in localized spin systems. In the monopole picture the ordered array of 3-in-1-out and 1-in-3-out tetrahedra is a monopole-antimonopole crystal. The monopole theory provides a natural explanation of the existence of the liquid-gas critical point, which is a property of a symmetric Coulombic gas at sufficient density. CMS argued that the field tunes the chemical potential of dipolar pairs of monopoles (here not to be confused with the monopole chemical potential) so as to increase their density sufficiently that such a transition occurs. They thus showed that the existence of the line of first order phase transitions reflects monopole interactions, which explains why it is not a property of a near-neighbour spin ice model, where the analogous defects are non-interacting [10].

Developing Ryzhkin's method, Shtyk and Feigel'man [119] produced a comprehensive monopole-based theory of magnetic response at the critical point that terminates the first order line, showing it to be in the mean field universality class (with logarithmic corrections). However they pointed out that there is no true monopole conductivity at the critical point as monopoles are essentially bound into dipole pairs. This conclusion also applies at much higher temperatures than the critical point, as discussed below.

More recently, Otsuka et al. [120] have considered the susceptibility of kagome ice in terms of the entropic interaction of monopoles in two dimensions, which makes an analogy with the two dimensional Coulomb gas [131]. They have suggested a scaling form in terms of a characteristic frequency which can be identified as the breather excitation of the two dimensional Coulomb gas. This scaling form is expected to be valid within the kagome ice plateau, and limited Monte Carlo simulations in this region do confirm this.

Neutron scattering

An early experiment in this regime was by Kadowaki and collaborators [75]. Close to the liquid-gas critical point, if the analogy to a Coulomb gas holds, the diffuse neutron scattering should show evidence of fluctuations between a phase with sparse monopoles (kagome ice) and a phase with concentrated monopoles (in this case

[12] Another spin model with a type of ice rule constraint on the kagome lattice was orginally studied by Wills et al. [122] and referred to as kagome spin ice. It is topologically distinct to kagome ice in spin ice, as it lacks the constraint on the ice rule introduced by the interlayer spins [123]. However, it is the prototype of many artificial spin ices.

the field induced ordered phase). By examining the diffuse scattering close to the critical point (H_c, T_c) diffuse scattering around (or underlying) certain Bragg peaks was located, and shown to coexist with the pattern characteristic of the kagome ice. The component of the diffuse scattering underlying the Bragg peaks indicates ferromagnetic fluctuations characteristic of the high density phase, while the kagome ice pattern is characteristic of the coexisting low density phase. These observations supported the picture of a liquid-gas critical point originating from monopoles, as postulated by CMS. An interesting aspect of these observations concerns the dimensionality of the fluctuations. The kagome ice scattering pattern is two dimensional, and monopoles are confined to the kagome planes there. However, by employing different out-of-plane resolutions, it was found that the ferromagnetic fluctuations are three dimensional, suggesting that although the monopoles are confined in two dimensions, they interact within and between planes (as would be expected for an isotropic Coulomb interaction). This observation was subsequently confirmed both in theory (see above) and susceptibility experiments (see below).

ac-susceptibility studies

Several investigations of the susceptibility of spin ices with field applied in the [111] direction have been made post-CMS, though unfortunately they have not approached the critical point very closely. At least two distinct measurements are possible: the longitudinal susceptibility, parallel to the main field along the [111] direction [94, 119, 132]; and the transverse susceptibility perpendicular to the main field, parallel to the kagome planes [120, 133]. The former is the conventional measurement, the latter is less common but has an intuitive appeal for studying monopole motion within the kagome planes. In fact, observations by ac-susceptibility in longitudinal [94, 132] and transverse [133] directions are qualitatively similar. Observations of the adiabatic susceptibility [94] focus on the highest frequency part of the response, which has a dramatic field dependence.

Using longitudinal ac-susceptibility, Matthews et al. investigated the field range of the monopole crystallisation transition, but at a temperature much higher than the critical point [132] (i.e. $T > 1.8$ K). They observed a broad peak in the real part of the response, χ' at the crossover field. Bovo et al. [94] observed that the adiabatic susceptibility, which in zero field is directly proportional to the monopole density, is very sharply peaked at the crossover field. The susceptibility on this peak is given almost exactly by the Curie law for the subset of spins that flips at the crossover. This dramatically confirms and generalises the point made by Shtyk and Feigel'man [119] i.e. that monopoles are confined into dipole pairs at the crossover.

Shtyk and Feigel'man predicted that the susceptibility would diverge at the critical point with mean field-like exponents (i.e. $\chi \sim |H - H_C|^{(1/\delta)-1}$ with $\delta = 3$) and logarithmic correction, and that the critical fluctuations would belong to the same universality class as easy-axis ferroelectrics. Bovo et al. [94] tested this on the adiabatic susceptibility peak (albeit well above the critical temperature), and found unusual scaling behavior, characteristic of a zero-dimensional phase transition. We suggest that one possible explanation of this difference is that the extended line of sharp crossovers studied by Bovo et al. might actually be a Widom line for the super-

critical monopole fluid [134], rather than the fluctuations associated with the critical point.

Takatsu et al. applied the main field along the [111] direction to form the kagome ice phase, but then measured the *ac*-susceptibility using a small driving field perpendicular to this direction [133]. With a lowest temperature of 0.5 K, their study approaches the critical point at $T_C \approx 0.36$ K more closely. They also observe a broad peak in χ' at the crossover field. A Monte Carlo analysis confirmed that monopole motion is highly correlated at the crossover, in agreement with the findings of Shtyk and Feigel'man and Bovo et al.

As can be seen from the maps of the field and temperature dependence of both χ' and χ'' presented by Takatsu et al. [133] (see Fig. 8.10), at low frequency peaks in both χ' and χ'' seem to delineate the phase diagram of spin ice/kagome ice (and also therefore, correspond well with regimes of high and low monopole density that they simulate), as well as a fan of fluctuations above the critical point (particularly in χ'). At higher frequency the peaks seem to demarcate crossover lines in the supercritical region (particularly in χ''). Considering only the data at 1 K, again well above the critical region, they found that with increasing frequency the double peak structure seems to narrow about the critical field (H_c), such that the characteristic fluctuation frequency gets faster as H_c is approached from either side, or the relaxation rate diverges—a so-called critical speeding up [133]. This critical speeding up could be simply parameterized in terms of simulated monopole density. Using Monte Carlo simulations of the dipolar spin ice model, the general features in the *ac*-susceptibility were semi-quantitatively reproduced, apart from the speeding up.

8.4.2 Strong Field Correlations

As previously described, the diffuse neutron scattering pattern contains signatures of the spin configurations in a spin ice, both the ice rule manifold and excited/monopole states. The whole pattern contains aspects of both, but certain parts of it may be more readily associated with the former or the latter. Diffuse neutron scattering measurements as a function of field and temperature provided early qualitative support for the monopole picture.

By applying a strong field in the [001] direction, all monopoles are swept out of the system, and the spins form an ordered ice rule state which can be viewed as a well defined configuration of 'Dirac strings' (lines of flipped spins which span the sample at this point). Decreasing the field allows the creation of monopoles within the sample. Although there is a Zeeman energy cost for the string to be extended along the field direction, there is an entropic gain as the string ends make a random walk in successive lattice planes perpendicular to the field, and this can lead to a net free energy gain. Then the system can be viewed as random walking monopoles interacting by a Coulomb interaction, connected by a short section of Dirac string, in which the spins are oppositely oriented to the bulk of spins in the sample, which are still oriented by the field. This ensemble of small, (assumed to

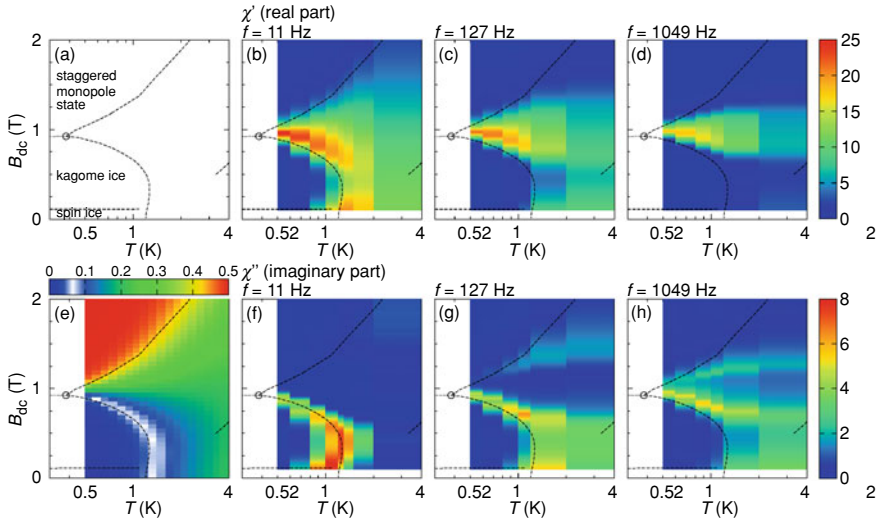

Fig. 8.10 *ac*-$\chi_\perp$ of $Dy_2Ti_2O_7$, showing how the susceptibility peak delimits the phase diagram, which itself is determined by the monopole density. **a** Phase diagram under the [111] field. **b**–**d** real part of the susceptibility. **e** Simulated monopole density. **f**–**h** Imaginary part of the susceptibility. Reprinted figure from [133] with permission from the Journal of the Physical Society of Japan

be) uncorrelated and non-interacting string segments in a ferromagnetic background provides contrast for a diffuse neutron scattering experiment, and Morris et al. [72] showed that diffuse neutron scattering in fields between zero and saturation could be qualitatively reproduced by a model of random walking string ends. They also noted the difficulty of making experiments in applied fields on the large size of single crystal typically used for neutron scattering by showing that strongly tilted fields obtained purely by the demagnetizing factor biased the random walk probabilities in agreement with their calculations.

8.4.3 Strong Field Sweeps and Quenches

Field sweeps starting from different field cooled and zero-field cooled states and heading towards saturation have long been studied for spin ice. As one passes into the low-temperature regime, irreversible processes appear in magnetisation measurements, which show hysteresis and steps [135, 136], sweep rate dependence [135–138], and departure from predicted scaling forms [72]. Although such effects can be seen when the field is parallel to [001] [72, 135] and [110] directions [135], they can be particularly pronounced when the field is parallel to the [111] direction [136, 139].

Slobinsky et al. [136] investigated the magnetisation steps of $Dy_2Ti_2O_7$ in considerable detail. As a magnetic field applied along the [111] direction is swept upward, one expects the magnetisation to increase smoothly to the value expected in the kagome ice plateau. However, in the low-temperature regime, at sweep-rates above a critical value, the magnetization curve has a slow, or even field independent, onset, then jumps up essentially to the equilibrium curve (measured at higher temperature), where it may again lag in an almost temperature independent plateau, before jumping up again. Further observations were made by Jackson et al. [139] , and also for both zero and finite field cooled initial states with the field applied along the [001] direction. When expressed in terms of the internal field, the magnetization has a negative slope, an effect which has also been observed in $Ho_2Ti_2O_7$ [100], though the steps have not been investigated in detail in that material.

Slobinsky et al. [136] suggest that this negative slope means that the magnetization jump is a "triggered" event: "once the process has started, it does not stop even though the internal field falls below the triggering value." Consequently they drew an analogy with deflagration[13] initiated by a spark. They suggested that in the fast-sweep regime, when jumps are produced, that as Zeeman energy evolves by the formation of monopoles at the start of the jump, the lattice is unable to equilibrate the system with the bath so that there is local heating which promotes the creation and unbinding of more monopoles and more Zeeman energy, leading to a thermal runaway. They obtained evidence of this by monitoring the sample temperature, which has a strong spike at the magnetization jump. Interestingly, the maximum of the temperature spike is approximately independent of the starting condition of the magnetization jump—it always reaches ≈ 0.6 K, the temperature at which equilibration becomes efficient.

Jackson et al. [139] obtained further evidence for avalanches, but showed that while the avalanches are very reproducible for a given experiment, the exact sweep rates will depend on the experimental set up, implying that they depend on the degree of coupling between the sample and apparatus, which is similar but not identical in these studies. They also point out that the temperature jumps up to ≈ 0.9 K, around the maximum of the heat capacity. The question of coupling was also addressed in the studies of Erfanifam et al. [137, 138], using ultrasonic techniques. The sample temperature and sound velocity are closely correlated, and peaks in both appear at sufficiently fast field sweep rates. They observed that the decay of the non-equilibrium peak in the sound velocity/temperature resembled that of a system in which heat is leaking to the environment, and were subsequently able to show that the non-equilibrium effects can be completely suppressed with sufficiently strong coupling, in this case by immersing the sample in liquid helium.

These studies are qualitatively consistent with the monopole picture since any magnetisation in spin ice requires spin flips that can be represented in the monopole picture. However as Jackson et al. have pointed out, such magnetothermal processes are the norm, rather than the exception in low temperature magnets, so they are not themselves indicative of monopoles. Nevertheless, the interesting question is

[13] Deflagration is "combustion which propagates through a gas or across the surface of an explosive at subsonic speeds, driven by the transfer of heat."

whether such processes can be represented by the monopole picture to a point that might be useful or quantitative. The strong field magnetisation involves irreversible creation and annihilation of monopoles. Considering annihilation, there must be 'decay products' that carry away the energy, and there must be magnetic reconnection. The energy released in these processes presumably either appears as phonons and is dumped in the lattice, or is transferred directly to neighbouring spins via their interactions i.e. used to create new monopoles. It is interesting to speculate that with highly sensitive apparatus, one might detect monopole annihilations or magnetic reconnection events by measuring the phonons released. The possibilities of imaging avalanches in spin ice are discussed in [139].

We finally mention a field quench protocol that has been investigated theoretically by Mostame et al. [140]. Here the field is applied along [111] as above, and the system is quenched from the low-temperature, monopole-rich, high-field state, across the first order transition, to the low-temperature, monopole-poor, low-field state. However, such field quenches have not yet been studied experimentally.

8.5 Monopole Derived Properties

So far we have viewed monopole theory as essentially a theory of coarse-grained magnetic response. However, in an earlier section we discussed how magnetic monopoles could be viewed as quasiparticles, and as such we might expect them to interact with non-magnetic excitations or fields, or even microscopic probes. In this section we summarise a number of properties that are derived from magnetic monopoles in this spirit.

8.5.1 Thermal Conductivity

In general, measurement of the thermal conductivity of a material can provide important information about its excitations. Usually it is dominated by contributions from phonons, but in materials with spin or other electronic degrees of freedom, these can also contribute—for example, superconducting quasiparticles or magnons. The thermal conductivity of spin ice materials has now been investigated in both $Dy_2Ti_2O_7$ [73, 141–143] and $Ho_2Ti_2O_7$ [144] and it has been shown that there is a magnetic contribution that can be understood to come from discrete, deconfined magnetic monopoles.

That there is a magnetic contribution to the thermal conductivity of a spin ice is agreed by all investigators, but their interpretations are different. In a detailed calorimetric study, Klemke et al. [73] assumed that the magnetic excitations were localized, such that all heat transport is due to phonons. They observed a weak suppression of the thermal conductivity with increasing field (along the [110] direction) at low temperature in $Dy_2Ti_2O_7$ which they attributed to scattering of phonons on

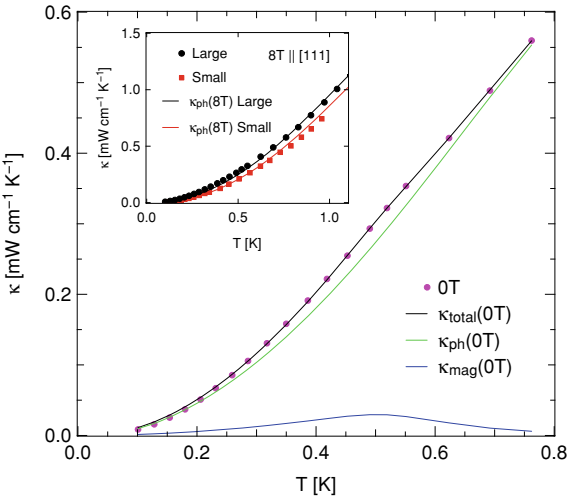

Fig. 8.11 Thermal conductivity of $Ho_2Ti_2O_7$ modeled by monopole and phonon contributions [144].The data are fitted with a kinetic theory. Reprinted figure from [144] with permission from the American Physical Society

localized magnetic excitations. On the other hand, Kolland et al. [141], with the field applied along the [001] direction, observed a strongly field dependent contribution to the thermal conductivity which took the form of a step-like decrease as the field was increased (with hysteresis at sufficiently low temperature). It was concluded that monopoles themselves transport heat, and the decrease corresponds to monopole confinement by the field. A diffusion coefficient was obtained for the monopoles which strongly increases below 0.5 K, when monopoles are expected to be sparse and to have a long free path. However this diffusion constant is orders of magnitude larger than the value obtained from the directly determined monopole mobility [94]. Two more studies [142, 143] report results qualitatively in agreement with a magnetic contribution to the thermal conductivity due to monopoles with their roughly expected properties—confinement by field for example—but with some unexpected and unexplained irreversibility.

In the work of Toews et al. [144] thermal conductivity data, measured with field along [111], is confronted with the monopole theories in the form of Debye-Hückel calculations. These authors used both zero field and strong field data to estimate pure magnetic and phonon contributions, and adopted very simple models of monopole-monopole and monopole-phonon scattering, i.e. that the scattering rate is proportional to the monopole density. They then applied Debye-Hückel theory to calculate the temperature dependence of the monopole density, and in this way, they were able to reproduce the observed temperature dependence of the total zero field thermal conductivity extremely accurately, as shown in Fig. 8.11.

8.5.2 Field Distribution at Point Probes

The possibility of detecting monopolar fields by point probes is an appealing one, although it should be born in mind that on microscopic scale, there are only spins in the system. Hence a point probe can only detect monopolar fields in the sense that the coarse grained or far field has a long range monopolar component that is longitudinal. In the dilute monopole regime this will tend to be dominated by the shorter range fields coming from the transverse part of the magnetisation, or spin structure.

The field distribution inside and around a sample of spin ice has been calculated, with monopoles present and absent [108, 113]. By performing a zero-field NMR experiment on ^{17}O nuclei, the internal field distribution of spin ice could be probed and agreed well with the calculated expectation [113]. The possibility of measuring monopolar fields was discussed.

External field distributions have also been estimated [109] in the context of μSR experiments, although only the surface charge contribution was accounted for. Although it is relatively short range, it would be interesting to calculate the contribution arising from bulk monopoles (volume magnetic charge), as this is potentially relevant to the experiments of [106, 107].

8.5.3 Dielectric Response

Khomskii pointed out another possible consequence of emergent monopoles on the pyrochlore lattice [145]. A redistribution of electric charge depending on the spin configuration can lead to the formation of a spontaneous electric dipole moment. On the pyrochlore lattice, with ⟨111⟩ spins, this is only expected for "1-in–3-out" configurations, i.e. monopoles, as other possible spin configurations on tetrahedra are too symmetric to allow an uncompensated charge redistribution. Sarkar et al. proposed the formation of an electric dipole moment on a magnetic monopole by a different mechanism[146]. As a consequence, monopoles should couple not only to magnetic fields, but also to electric fields. The electric dipole moment of the monopole becomes like the spin of a charged particle—a nice example of duality between electricity and magnetism! Various measurable consequences, which differ in details between the two mechanism, were outlined, e.g. the possibility to separate monopoles and antimonopoles in an electric field.

The most striking consequence of Khomskii's theory, particularly since it already appeared to have been measured, is the contribution to dielectric response functions in monopole-rich parts of the phase diagram. As Khomskii pointed out, the previously unexplained results of Saito et al. [147] contain a strong peak in the dielectic constant of $Dy_2Ti_2O_7$ at $\approx$ 1 T, with the field applied along [111], just as the kagome ice plateau is terminated by the proliferation of monopoles and formation of the monopole crystal phase.

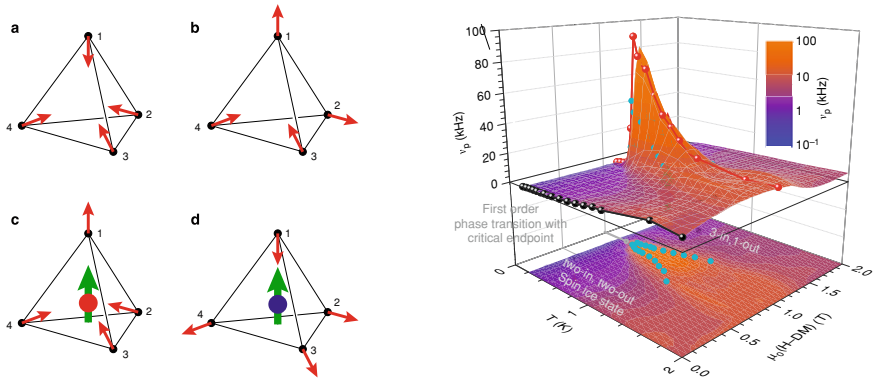

Fig. 8.12 Formation of electric dipole moment on monopole hosting tetrahedra [145], and peak frequency of the dielectric loss function showing critical speeding up of magnetoelectric response as monopoles proliferate at the termination of the kagome ice plateau [117]. Reprinted figures from [117, 145] with permission from Nature Communications

This effect has been examined in considerably more detail by Grams et al. [117] (see Fig. 8.12). They found that the dielectric response is insensitive to the slow relaxation process attributed to Brownian motion of monopoles in magnetic susceptibility studies, but contains another relaxation process that is roughly two orders of magnitude faster, and whose magnetic field dependence confirms it has a magnetic origin. This process leads to a field and temperature dependent relaxation spectrum which is fastest and sharpest at the critical point, and broadens and slows, forming a fan-shaped region above the critical point, whose border follows the scaling predictions of Shytk and Feigel'man. The increased relaxation rate at the critical point implies a negative dynamical critical exponent and critical speeding up, rather than the usual critical slowing down, similar to what has been observed by Takatsu et al. and Bovo et al. in the magnetic susceptibility [94, 133]. Liu et al. have obtained some evidence that $Ho_2Ti_2O_7$ also responds to an electric field at low temperature [148].

8.6 Future Directions for Monopole Observation

8.6.1 Plasmas

As alluded to above, the physics of Coulomb gases is extremely rich, and many phenomena are possible. Current connections between experiment and theory in spin ice are based on casting theories of electrolytes in terms of magnetic monopoles. A gas of charged particles is more generally a plasma, and connections between magnetic monopoles and plasma physics have been proposed [149]. An ambitious future direction would be the exploration of this connection. Indeed, the study of

frequency dependent effects in kagome ice is already somewhat reminiscent of this approach.

Apart from the charge correlations and dynamics, plasma physics has another important ingredient which has an appealing analog in spin ice. Many fascinating plasma properties are regarded as being controlled by magnetic field lines, which essentially gain a real physical quality in such work. Modification of the topology of magnetic field line configurations is known as magnetic reconnection [150], graphically visible in an event such as a coronal mass ejection at the surface of the sun, where huge loops of flux are 'short circuited' at the solar surface as the plasma which carries them is ejected into space [151]. Field lines in spin ice have a similarly appealing physical reality in the form of the Dirac strings which thread the monopole vacuum. Annihilation of a pair of monopoles can be seen directly as a reconnection event, and creation of a pair must be a disconnection.

Magnetic reconnection in material spin ice has yet to be explored, but it may provide a unique way to test the physics of the monopoles. In this context, it is interesting to note that Vedmedenko has proposed a model of artificial spin ices that focusses on Dirac strings and their reconnections: this model potentially goes much further than the monopole model as it naturally accounts for the loss of degeneracy of the Pauling states [152]. A three dimensional version of this theory would be very interesting.

8.6.2 Phonons

At magnetic reconnection, magnetic energy is released. In stellar plasmas this naturally goes toward the acceleration of ejected mass. In spin ice, a rather specific process must accompany the reconnection event. Currently there is interest in decays of quasiparticles such as magnons [153], and one may ask what happens to monopoles. So far there is no suggestion that they decay, indeed since they are fractional topological defects, it does not appear possible for an individual monopole to decay—the annihilation of a pair is required. This process must release energy, and some decay products are to be expected, presumably phonons. Phonon detection experiments are known in other rare earth based materials, and it would be highly interesting to try to detect monopole decay phonons in spin ices.

Generally, the role of phonons in the behaviour of the monopoles is relatively unexplored. It has been implied that the monopoles and phonons scatter on each other [144], and this interaction suggests that the spin ice monopole universe may be more complicated than an idealised magnetic Coulomb gas. The interaction of monopoles with another quasiparticle may be exploitable, perhaps to control the propagation or annihilation/creation of monopoles.

8.6.3 New Materials

As also explained above, the behavior of the magnetic Coulomb gas in a given spin ice, i.e. the trajectory through the (magnetic) Coulomb gas phase diagram, in the space of chemical potential and temperature, is largely fixed by material parameters. It is therefore of interest to identify new spin ices, in which the relevant energy scales can be modified and new magnetic Coulomb gas phenomena may be realized. The high pressure synthesis of $Ho_2Ge_2O_7$ and $Dy_2Ge_2O_7$ provides one example—stronger exchange interactions compete with the dipolar interactions resulting in a lower chemical potential and a denser monopole gas with stronger monopole correlations [81]. With a view to testing the theory of magnetic Coulomb gases by accessing other aspects of their behavior, it will be interesting to develop the study of other spin ices. For example in other crystal structures such as the chalcogenide spinels (e.g. $CdEr_2Se_4$ [154]) the balance of such parameters may be quite different, or differently controllable, to the pyrochlore oxides.

8.6.4 Quantum Spin Ice

Quantum effects in spin ice are an extremely interesting direction for the future. We leave the exploration of so-called quantum spin ices for dedicated chapters, Chaps. 9, 10, 11 and 12, but note that a recent thread of work has begun in which quantum effects in long-thought classical spin ices such as $Dy_2Ti_2O_7$ are explored [49, 155–157]. This is particularly motivated by the possible loss of entropy and possibility of a quantum spin liquid at low temperature. It is interesting to note that the pinch point behaviour calculated in [155] is close to that observed in experiment [7].

8.7 Conclusion

In this section we draw some conclusions and comment on different conceptions of magnetic monopoles in spin ice and on some disagreements in the literature.

8.7.1 Different Viewpoints

In nearly twenty years of research on spin ice there have always been two intertwined approaches that offer complementary viewpoints on the problem.

The first approach may be called the ‘model magnetism’ approach [52], that sees materials such as $Dy_2Ti_2O_7$ and $Ho_2Ti_2O_7$ of interest insofar as they approximately realise idealised statistical mechanical models. In the early days the model of interest

was the ice-type 16-vertex model (NNSI) [1, 2, 158], and it was found that these materials realise it to a remarkable degree. More recently the model of interest has been NNSI embellished with magnetostatic Coulomb interactions—the monopole model discussed in this review. This model has all the rich physics of the 16-vertex model and much more besides—it is a classical statistical mechanical model of enormous interest, which has recently been extended into the quantum mechanical regime [155, 159]. As shown in this chapter, there is no question that $Dy_2Ti_2O_7$ and $Ho_2Ti_2O_7$ are model magnets that realise the classical monopole model to a very considerable degree, and that is sufficient to inspire much interest in these materials and models.

The second approach might be called the 'microscopic' approach, which focusses on the materials $Dy_2Ti_2O_7$ and $Ho_2Ti_2O_7$ and seeks to establish their microscopic Hamiltonian and understand their material properties. Rather remarkably, the basic Hamiltonian that has been established, the *s*-DSM [3], is the same as that put forward for water ice [14]. The fact that the monopole model is an approximation to *s*-DSM explains why both the spin ice materials and water ice realise the elegant statistical mechanical models discussed in the first approach.

Similar 'model' and 'microscopic' approaches are applied to many other condensed matter systems. However, among model magnets, spin ice is remarkable and unusual in that the two approaches are in such close alignment. The classical spin ices are both model magnetic Coulomb gases (or magnetic ice analogues) and interesting magnetic materials. This gives magnetic monopoles in spin ice a particularly broad appeal. Interest focusses not only on identifying the fundamental properties of the magnetic Coulomb gas, but also on understanding material properties such as thermal conductivity, dielectric response and the role of defects [98, 160], in terms of monopole theory.

As the detailed microscopic understanding of spin ice materials improves, it remains to be seen how closely the microscopic description remains in alignment with magnetic monopole theory. Whatever the outcome, it is surely undeniable that magnetic monopole concept has already proved very valuable. An analogy here may be drawn with liquid helium physics, where the question of to what extent helium-II is a Bose condensate taxed the community for many years [161]. However, the immediate adoption of the idea that helium-II is *essentially* a Bose condensate led to much understanding and rich physics [162]. In a similar way, while one might anticipate the monopole description to be more clearly delimited, it is very hard to imagine it being completely overhauled as a description of spin ice materials.

8.7.2 Definitions and Disagreements

Surveying the literature, there has been a tendency of the community to adopt a rather fuzzy and flexible definition of magnetic monopoles in spin ice. Historically, this is

justifiable, as it took several years for the theory to catch up with experiments.[14] However, in this review we have given a precise definition of magnetic monopole theory, which has allowed us to critically assess its successes and limitations. The downside to our present approach is that adoption of a definition might hinder the organic development of the concept, but we feel that this is more than outweighed by the advantage of logical precision.

To illustrate this, we return to the fact that some authors have claimed that there are experimental inconsistencies with monopole theory related to the temperature dependence of the magnetic relaxation time and the non-exponential relaxation (see Sect. 8.3). This argument is valid only if one *insists* that the monopole hop rate or diffusion constant is temperature-independent and non-dispersed. However we see no reason to add such artificial constraints to monopole theory, any more than one should insist on them in the study of water ice or electrolytes, for example. Ryzhkin's original model does not insist on a temperature independent diffusion constant and is clearly a linear approximation to the dynamics, which could be (and in fact are) more complex in detail.

Therefore, while it is important that researchers identify and report any inconsistencies they find with the monopole model, we recommend that they take great care to define exactly what model they are talking about and exactly what the nature of the inconsistency is. This highlights the risks of adopting an imprecise definition of monopole theory: what to some researchers is perfectly consistent, to others is perfectly inconsistent.

By taking this approach, we have shown how many published experiments have revealed magnetic monopoles and their interactions in the classical spin ice compounds.

8.7.3 Final Word

In conclusion, we may call upon various lines of evidence for the existence of monopoles in spin ice. Generally, we must seek the evidence of monopoles in bulk and collective properties. Activity in the field at present divides between looking at the basic magnetic response of monopoles and measuring other properties, to see if they can be understood in terms of monopoles. An overview of the literature shows that there is currently no serious contender to the monopole picture. Since the monopole dynamics are single spin flips, the simplest possible dynamic in an Ising magnet [15], they are extremely reasonable objects to propose. Spin ice as a universe with magnetic monopoles is extremely interesting since one can look over all aspects of it—the quasiparticles and the vacuum from which they emerge.

[14] For example the detailed theory of pinch points [18, 60] post-dated experiments [53, 58] on them.

References

1. M.J. Harris, S.T. Bramwell, D.F. McMorrow, T. Zeiske, K.W. Godfrey, Phys. Rev. Lett. **79**, 2554 (1997). https://doi.org/10.1103/PhysRevLett.79.2554
2. S.T. Bramwell, M.J. Harris, J. Phys.: Condens. Matter **10**, L215 (1998). https://doi.org/10.1088/0953-8984/10/14/002
3. B.C. den Hertog, M.J.P. Gingras, Phys. Rev. Lett. **84**, 3430 (2000). https://doi.org/10.1103/PhysRevLett.84.3430
4. T. Yavors'kii, T. Fennell, M.J.P. Gingras, S.T. Bramwell, Phys. Rev. Lett. **101**, 037204 (2008). https://doi.org/10.1103/PhysRevLett.101.037204
5. S.T. Bramwell, M.J.P. Gingras, Science **294**, 1495 (2001). https://doi.org/10.1126/science.1064761
6. S.T. Bramwell, M.J. Harris, B.C. den Hertog, M.J.P. Gingras, J.S. Gardner, D.F. McMorrow, A.R. Wildes, A.L. Cornelius, J.D.M. Champion, R.G. Melko, T. Fennell, Phys. Rev. Lett. **87**, 047205 (2001). https://doi.org/10.1103/PhysRevLett.87.047205
7. T. Fennell, O.A. Petrenko, B. Fåk, S.T. Bramwell, M. Enjalran, T. Yavors'kii, M.J.P. Gingras, R.G. Melko, G. Balakrishnan, Phys. Rev. B **70**, 134408 (2004). https://doi.org/10.1103/PhysRevB.70.134408
8. M.J.P. Gingras, B.C. den Hertog, Can. J. Phys. **79**, 1339 (2001). https://doi.org/10.1139/p01-099
9. S.V. Isakov, R. Moessner, S.L. Sondhi, Phys. Rev. Lett. **95**, 217201 (2005). https://doi.org/10.1103/PhysRevLett.95.217201
10. C. Castelnovo, R. Moessner, S.L. Sondhi, Nature **451**, 42 (2008). https://doi.org/10.1038/nature06433
11. L.D.C. Jaubert, P.C.W. Holdsworth, Nat. Phys. **5**, 258 (2009). https://doi.org/10.1038/NPHYS1227
12. L.D.C. Jaubert, P.C.W. Holdsworth, J. Phys.: Condens. Matter **23**, 164222 (2011). https://doi.org/10.1088/0953-8984/23/16/164222
13. I.A. Ryzhkin, J. Exp. Theor. Phys. **101**, 481 (2005). https://doi.org/10.1134/1.2103216
14. I.A. Ryzhkin, Solid State Commun. **52**, 49 (1984). https://doi.org/10.1016/0038-1098(84)90716-6
15. R.J. Glauber, J. Math. Phys. **4**, 294 (1963). https://doi.org/10.1063/1.1703954
16. R. Moessner, S.L. Sondhi, Phys. Rev. Lett. **105**, 166401 (2010). https://doi.org/10.1103/PhysRevLett.105.166401
17. A.C. Maggs, V. Rossetto, Phys. Rev. Lett. **88**, 196402 (2002). https://doi.org/10.1103/PhysRevLett.88.196402
18. M.I. Ryzhkin, I.A. Ryzhkin, S.T. Bramwell, Europhys. Lett. **104**, 37005 (2013). https://doi.org/10.1209/0295-5075/104/37005
19. C. Castelnovo, R. Moessner, S.L. Sondhi, Phys. Rev. B **84**, 144435 (2011). https://doi.org/10.1103/PhysRevB.84.144435
20. V.F. Petrenko, R.W. Whitworth, *Physics of Ice* (Oxford University Press, Oxford, 1999). ISBN 9780198518945
21. W.J. Moore, *Physical Chemistry* (Longmans Green and Co., London, 1963)
22. L. Onsager, J. Chem. Phys. **2**, 599 (1934). https://doi.org/10.1063/1.1749541
23. L. Onsager, Science **166**, 1359 (1969). https://doi.org/10.1126/science.166.3911.1359
24. M.E. Fisher, Y. Levin, Phys. Rev. Lett. **71**, 3826 (1993). https://doi.org/10.1103/PhysRevLett.71.3826
25. V. Kobelev, A.B. Kolomeisky, M.E. Fisher, J. Chem. Phys. **116**, 7589 (2002). https://doi.org/10.1063/1.1464827
26. P.L. Galison, *Image and Logic: A Material Culture of Microphysics* (University of Chicago Press, Chicago and London, 1997). ISBN 9780226279176
27. N. Romming, C. Hanneken, M. Menzel, J.E. Bickel, B. Wolter, K. von Bergmann, A. Kubetzka, R. Wiesendanger, Science **341**, 636 (2013). https://doi.org/10.1126/science.1240573

28. A.J. Schofield, Contemp. Phys. **40**, 95 (1999). https://doi.org/10.1080/001075199181602
29. H.L. Stormer, D.C. Tsui, A.C. Gossard, Rev. Mod. Phys. **71**, S298 (1999). https://doi.org/10.1103/RevModPhys.71.S298
30. G.E. Volovik, *The Universe in a Helium Droplet* (Oxford University Press, Oxford, 2009). https://doi.org/10.1093/acprof:oso/9780199564842.001.0001
31. S.T. Bramwell, M.J.P. Gingras, P.C.W. Holdsworth, *Spin ice, chapter in Frustrated Spin Systems*, ed. by H.T. Diep (World Scientific, Singapore, 2005). https://doi.org/10.1142/9789814440745_0007
32. S. Cukierman, Biochim. Biophys. Acta **1757**, 876 (2006). https://doi.org/10.1016/j.bbabio.2005.12.001
33. C. Castelnovo, R. Moessner, S.L. Sondhi, Annu. Rev. Condens. Matter Phys. **3**, 35 (2012). https://doi.org/10.1146/annurev-conmatphys-020911-125058
34. I.A. Ryzhkin, M.I. Ryzhkin, JETP Lett. **93**, 384 (2011). https://doi.org/10.1134/S0021364011070095
35. V. Kaiser, S.T. Bramwell, P.C.W. Holdsworth, R. Moessner, Phys. Rev. Lett. **115**, 037201 (2015). https://doi.org/10.1103/PhysRevLett.115.037201
36. M. Ruminy, F. Groitl, T. Keller, T. Fennell, Phys. Rev. B **94**, 174406 (2016). https://doi.org/10.1103/PhysRevB.94.174406
37. L.D.C. Jaubert, M.J. Harris, T. Fennell, R.G. Melko, S.T. Bramwell, P.C.W. Holdsworth, Phys. Rev. X **3**, 011014 (2013). https://doi.org/10.1103/PhysRevX.3.011014
38. L. Bovo, L.D.C. Jaubert, P.C.W. Holdsworth, S.T. Bramwell, J. Phys.: Condens. Matter **25**, 386002 (2013). https://doi.org/10.1088/0953-8984/25/38/386002
39. M. Twengström, L. Bovo, M.J.P. Gingras, S.T. Bramwell, P. Henelius, Phys. Rev. Mater. **1**, 044406 (2017). https://doi.org/10.1103/PhysRevMaterials.1.044406
40. W. Marshall, R.D. Lowde, Rep. Prog. Phys. **31**, 705 (1968). https://doi.org/10.1088/0034-4885/31/2/305
41. R.W. White, *Quantum Theory of Magnetism* (Springer, Berlin, 1983). ISBN 978-3-540-85416-6
42. G. Ehlers, A.L. Cornelius, M. Orendác, M. Kajnaková, T. Fennell, S.T. Bramwell, J.S. Gardner, J. Phys.: Condens. Matter **15**, L9 (2003). https://doi.org/10.1088/0953-8984/15/2/102
43. G. Ehlers, A.L. Cornelius, T. Fennell, M. Koza, S.T. Bramwell, J.S. Gardner, J. Phys.: Condens. Matter **16**, S635 (2004). https://doi.org/10.1088/0953-8984/16/11/010
44. C. Jaccard, Phys. Kondens. Materie **3**, 99 (1964). https://doi.org/10.1007/BF02422356
45. W. Van Roosbroeck, Bell Systems Technical Journal **29**, 560 (1950). https://archive.org/details/bellsystemtechni00amerrich
46. R.G. Melko, B.C. den Hertog, M.J.P. Gingras, Phys. Rev. Lett. **87**, 067203 (2001). https://doi.org/10.1103/PhysRevLett.87.067203
47. D. Pomaranski, L.R. Yaraskavitch, S. Meng, K.A. Ross, H.M.L. Noad, H.A. Dabkowska, B.D. Gaulin, J.B. Kycia, Nat. Phys. **9**, 353 (2013). https://doi.org/10.1038/NPHYS2591
48. S.R. Giblin, M. Twengström, L. Bovo, M. Ruminy, M. Bartkowiak, P. Manuel, T. Fennell et al., Phys. Rev. Lett. **121**, 067202 (2018). https://doi.org/10.1103/PhysRevLett.121.067202
49. P.A. McClarty, O. Sikora, R. Moessner, K. Penc, F. Pollmann, N. Shannon, Phys. Rev. B **92**, 094418 (2015). https://doi.org/10.1103/PhysRevB.92.094418
50. P. Henelius, T. Lin, M. Enjalran, Z. Hao, J.G. Rau, J. Altosaar, F. Flicker, T. Yavors'kii, M.J.P. Gingras, Phys. Rev. B **93**, 024402 (2016). https://doi.org/10.1103/PhysRevB.93.024402
51. S.T. Bramwell, Phil. Trans. R. Soc. A **370**, 5738 (2012). https://doi.org/10.1098/rsta.2011.0596
52. S.T. Bramwell, B. Keimer, Nat. Mater. **13**, 763 (2014). https://doi.org/10.1038/nmat4045
53. T. Fennell, P.P. Deen, A.R. Wildes, K. Schmalzl, D. Prabhakaran, A.T. Boothroyd, R.J. Aldus, D.F. McMorrow, S.T. Bramwell, Science **326**, 415 (2009). https://doi.org/10.1126/science.1177582
54. S.T. Bramwell, Nat. Commun. **8**, 2088 (2017). https://doi.org/10.1038/s41467-017-02102-1
55. S.T. Bramwell, unpublished
56. T. Fennell, unpublished

57. C. Henley, Annu. Rev. Condens. Matter Phys. **1**, 179 (2010). https://doi.org/10.1146/annurev-conmatphys-070909-104138
58. L.J. Chang, Y. Su, Y.-J. Kao, Y.Z. Chou, R. Mittal, H. Schneider, T. Brueckel, G. Balakrishan, M.R. Lees, Phys. Rev. B **82**, 172403 (2010). https://doi.org/10.1103/PhysRevB.82.172403
59. J. Als-Nielsen, L.M. Holmes, H.J. Guggenheim, Phys. Rev. Lett. **32**, 610 (1974). https://doi.org/10.1103/PhysRevLett.32.610
60. A. Sen, R. Moessner, S.L. Sondhi, Phys. Rev. Lett. **110**, 107202 (2013). https://doi.org/10.1103/PhysRevLett.110.107202
61. R. Youngblood, J.D. Axe, Phys. Rev. B **17**, 3639 (1978). https://doi.org/10.1103/PhysRevB.17.3639
62. R. Youngblood, J.D. Axe, B.M. McCoy, Phys. Rev. B **21**, 5212 (1980). https://doi.org/10.1103/PhysRevB.21.5212
63. R.W. Youngblood, J.D. Axe, Phys. Rev. B **23**, 232 (1981). https://doi.org/10.1103/PhysRevB.23.232
64. M.P. Zinkin, M.J. Harris, T. Zeiske, Phys. Rev. B **56**, 11786 (1997). https://doi.org/10.1103/PhysRevB.56.11786
65. B. Canals, D.A. Garanin, Can. J. Phys. **79**, 1323 (2001). https://doi.org/10.1139/p01-101
66. D.A. Huse, W. Krauth, R. Moessner, S.L. Sondhi, Phys. Rev. Lett. **91**, 167004 (2003). https://doi.org/10.1103/PhysRevLett.91.167004
67. S.V. Isakov, K. Gregor, R. Moessner, S.L. Sondhi, Phys. Rev. Lett. **93**, 167204 (2004). https://doi.org/10.1103/PhysRevLett.93.167204
68. C.L. Henley, Phys. Rev. B **71**, 014424 (2005). https://doi.org/10.1103/PhysRevB.71.014424
69. A.P. Ramirez, A. Hayashi, R.J. Cava, R. Siddharthan, B.S. Shastry, Nature **399**, 333 (1999). https://doi.org/10.1038/20619
70. Y. Su, unpublished
71. H.W.J. Blöte, R.F. Wielinga, W.J. Huiskamp, Physica **43**, 549 (1969). https://doi.org/10.1016/0031-8914(69)90187-6
72. D.J.P. Morris, D.A. Tennant, S.A. Grigera, B. Klemke, C. Castelnovo, R. Moessner, C. Czternasty, M. Meissner, K.C. Rule, J.-U. Hoffmann, K. Kiefer, S. Gerischer, D. Slobinsky, R.S. Perry, Science **326**, 411 (2009). https://doi.org/10.1126/science.1178868
73. B. Klemke, M. Meissner, P. Strehlow, K. Kiefer, S.A. Grigera, D.A. Tennant, J. Low. Temp. Phys. **163**, 345 (2011). https://doi.org/10.1007/s10909-011-0348-y
74. R. Higashinaka, H. Fukazawa, D. Yanagishima, Y. Maeno, J. Phys. Chem. Solids **63**, 1043 (2002). https://doi.org/10.1016/S0022-3697(02)00065-3
75. H. Kadowaki, N. Doi, Y. Aoki, Y. Tabata, T.J. Sato, J.W. Lynn, K. Matsuhira, Z. Hiroi, J. Phys. Soc. Jpn. **78**, 103706 (2009). https://doi.org/10.1143/JPSJ.78.103706
76. R. Higashinaka, H. Fukazawa, Y. Maeno, Phys. Rev. B **68**, 014415 (2003). https://doi.org/10.1103/PhysRevB.68.014415
77. Z. Hiroi, K. Matsuhira, S. Takagi, T. Tayama, T. Sakakibara, J. Phys. Soc. Jpn. **72**, 411 (2003). https://doi.org/10.1143/JPSJ.72.411
78. R. Higashinaka, H. Fukazawa, K. Deguchi, Y. Maeno, J. Phys. Soc. Jpn. **73**, 2845 (2004). https://doi.org/10.1143/JPSJ.73.2845
79. X. Ke, R.S. Freitas, B.G. Ueland, G.C. Lau, M.L. Dahlberg, R.J. Cava, R. Moessner, P. Schiffer, Phys. Rev. Lett. **99**, 137203 (2007). https://doi.org/10.1103/PhysRevLett.99.137203
80. V. Kaiser, J. Bloxsom, L. Bovo, S.T. Bramwell, P.C.W. Holdsworth, R. Moessner, Phys. Rev. B **98**, 144413 (2018). https://doi.org/10.1103/PhysRevB.98.144413
81. H.D. Zhou, S.T. Bramwell, J.G. Cheng, C.R. Wiebe, G. Li, L. Balicas, J.A. Bloxsom, H.J. Silverstein, J.S. Zhou, J.B. Goodenough, J.S. Gardner, Nat. Commun. **2**, 478 (2011). https://doi.org/10.1038/ncomms1483
82. H.D. Zhou, J.G. Cheng, A.M. Hallas, C.R. Wiebe, G. Li, L. Balicas, J.S. Zhou, J.B. Goodenough, J.S. Gardner, E.S. Choi, Phys. Rev. Lett. **108**, 207206 (2012). https://doi.org/10.1103/PhysRevLett.108.207206
83. S.T. Bramwell, M.N. Field, M.J. Harris, I.P. Parkin, J. Phys.: Condens. Matter **12**, 483 (2000). https://doi.org/10.1088/0953-8984/12/4/308

84. K. Matsuhira, Y. Hinatsu, T. Sakakibara, J. Phys.: Condens. Matter **13**, L737 (2001). https://doi.org/10.1088/0953-8984/13/31/101
85. J.A. Quilliam, L.R. Yaraskavitch, H.A. Dabkowska, B.D. Gaulin, J.B. Kycia, Phys. Rev. B **83**, 094424 (2011). https://doi.org/10.1103/PhysRevB.83.094424
86. J. Snyder, B. Ueland, A. Mizel, J.S. Slusky, H. Karunadasa, R.J. Cava, P. Schiffer, Phys. Rev. B **70**, 184431 (2004). https://doi.org/10.1103/PhysRevB.70.184431
87. J. Snyder, B.G. Ueland, J.S. Slusky, H. Karunadasa, R.J. Cava, P. Schiffer, Phys. Rev. B **69**, 064414 (2004). https://doi.org/10.1103/PhysRevB.69.064414
88. J. Snyder, B.G. Ueland, J.S. Slusky, H. Karunadasa, R.J. Cava, A. Mizel, P. Schiffer, Phys. Rev. Lett. **91**, 107201 (2003). https://doi.org/10.1103/PhysRevLett.91.107201
89. J. Snyder, J.S. Slusky, R.J. Cava, P. Schiffer, Phys. Rev. B **66**, 064432 (2002). https://doi.org/10.1103/PhysRevB.66.064432
90. J. Snyder, J.S. Slusky, R.J. Cava, P. Schiffer, Nature **413**, 48 (2001). https://doi.org/10.1038/35092516
91. K. Matsuhira, Y. Hinatsu, K. Tenya, T. Sakakibara, J. Phys.: Condens. Matter **12**, L649 (2000). https://doi.org/10.1088/0953-8984/12/40/103
92. K. Matsuhira, C. Paulsen, E. Lhotel, C. Sekine, Z. Hiroi, S. Takagi, J. Phys. Soc. Jpn. **80**, 123711 (2011). https://doi.org/10.1143/JPSJ.80.123711
93. L.R. Yaraskavitch, H.M. Revell, S. Meng, K.A. Ross, H.M.L. Noad, H.A. Dabkowska, B.D. Gaulin, J.B. Kycia, Phys. Rev. B **85**, 020410(R) (2012). https://doi.org/10.1103/PhysRevB.85.20410
94. L. Bovo, J.A. Bloxsom, D. Prabhakaran, G. Aeppli, S.T. Bramwell, Nat. Commun. **4**, 1535 (2013). https://doi.org/10.1038/ncomms2551
95. M. Ruminy, S. Chi, S. Calder, T. Fennell, Phys. Rev. B **95**, 060414(R) (2017). https://doi.org/10.1103/PhysRevB.95.060414
96. L. Onsager, Ann. N. Y. Acad. Sci. **46**, 241 (1945). https://doi.org/10.1111/j.1749-6632.1945.tb36170.x
97. H. Takatsu, K. Goto, H. Otsuka, R. Higashinaka, K. Matsubayashi, Y. Uwatoko, H. Kadowaki, J. Phys. Soc. Jpn. **82**, 104710 (2013). https://doi.org/10.7566/JPSJ.82.104710
98. H.M. Revell, L.R. Yaraskavitch, J.D. Mason, K.A. Ross, H.M.L. Noad, H.A. Dabkowska, B.D. Gaulin, P. Henelius, J.B. Kycia, Nat. Phys. **9**, 34 (2012). https://doi.org/10.1038/nphys2466
99. C. Castelnovo, R. Moessner, S.L. Sondhi, Phys. Rev. Lett. **104**, 107201 (2010). https://doi.org/10.1103/PhysRevLett.104.107201
100. C. Krey, S. Legl, S.R. Dunsiger, M. Meven, J.S. Gardner, J.M. Roper, C. Pfleiderer, Phys. Rev. Lett. **108**, 257204 (2012). https://doi.org/10.1103/PhysRevLett.108.257204
101. C. Paulsen, M.J. Jackson, E. Lhotel, B. Canals, D. Prabhakaran, K. Matsuhira, S.R. Giblin, S.T. Bramwell, Nat. Phys. **10**, 135 (2014). https://doi.org/10.1038/nphys2847
102. V. Kaiser, S.T. Bramwell, P.C.W. Holdsworth, R. Moessner, Nat. Mater. **12**, 1033 (2013). https://doi.org/10.1038/nmat3729
103. D.P. Mason, D.K. McIlroy, J. Chem. Soc., Faraday Trans. 2 **74**, 2019 (1978).https://doi.org/10.1039/F29787402019
104. C. Paulsen, S.R. Giblin, E. Lhotel, D. Prabhakaran, G. Balakrishnan, K. Matsuhira, S.T. Bramwell, Nat. Phys. **12**, 661 (2016). https://doi.org/10.1038/nphys3704
105. S.R. Giblin, S.T. Bramwell, P.C.W. Holdsworth, D. Prabhakaran, I. Terry, Nat. Phys. **7**, 252 (2011). https://doi.org/10.1038/NPHYS1896
106. S.T. Bramwell, S.R. Giblin, S. Calder, R. Aldus, D. Prabhakaran, T. Fennell, Nature **461**, 956 (2009). https://doi.org/10.1038/nature08500
107. L.J. Chang, M.R. Lees, G. Balakrishnan, Y.J. Kao, A.D. Hillier, Sci. Rep. **3**, 1881 (2013). https://doi.org/10.1038/srep01881
108. S.R. Dunsiger, A.A. Aczel, C. Arguello, H. Dabkowska, A. Dabkowski, M.-H. Du, T. Goko, B. Javanparast, T. Lin, F.L. Ning, H.M.L. Noad, D.J. Singh, T.J. Williams, Y.J. Uemura, M.J.P. Gingras, G.M. Luke, Phys. Rev. Lett. **107**, 207207 (2011). https://doi.org/10.1103/PhysRevLett.107.207207

109. S.J. Blundell, Phys. Rev. Lett. **108**, 147601 (2012). https://doi.org/10.1103/PhysRevLett.108.147601
110. P. Quémerais, P. McClarty, R. Moessner, Phys. Rev. Lett. **109**, 127601 (2012). https://doi.org/10.1103/PhysRevLett.109.127601
111. J.A. Rodriguez, A. Yaouanc, B. Barbara, E. Pomjakushina, P. Quémerais, Z. Salman, Phys. Rev. B **87**, 184427 (2013). https://doi.org/10.1103/PhysRevB.87.184427
112. L. Nuccio, L. Schulz, A.J. Drew, J. Phys. D: Appl. Phys. **47**, 473001 (2014). https://doi.org/10.1088/0022-3727/47/47/473001
113. G. Sala, C. Castelnovo, R. Moessner, S.L. Sondhi, K. Kitagawa, M. Takigawa, R. Higashinaka, Y. Maeno, Phys. Rev. Lett. **108**, 217203 (2012). https://doi.org/10.1103/PhysRevLett.108.217203
114. F.R. Foronda, F. Lang, J.S. Möller, T. Lancaster, A.T. Boothroyd, F.L. Pratt, S.R. Giblin, D. Prabhakaran, S.J. Blundell, Phys. Rev. Lett. **114**, 017602 (2015). https://doi.org/10.1103/PhysRevLett.114.017602
115. J.P. Clancy, J.P.C. Ruff, S.R. Dunsiger, Y. Zhao, H.A. Dabkowska, J.S. Gardner, Y. Qiu, J.R.D. Copley, T. Jenkins, B.D. Gaulin, Phys. Rev. B **79**, 014408 (2009). https://doi.org/10.1103/PhysRevB.79.014408
116. J. Lago, S.J. Blundell, C. Baines, J. Phys.: Condens. Matter **19**, 326210 (2007). https://doi.org/10.1088/0953-8984/19/32/326210
117. C.P. Grams, M. Valldor, M. Garst, J. Hemberger, Nat. Commun. **5**, 4853 (2014). https://doi.org/10.1038/ncomms5853
118. E.R. Kassner, A.B. Eyvazov, B. Pichler, T.J.S. Munsie, H.A. Dabkowska, G.M. Luke, J.C.S. Davis, Proc. Natl. Acad. Sci. **112**, 8549 (2015). https://doi.org/10.1073/pnas.1511006112
119. A.V. Shtyk, M.V. Feigel'man, JETP Letters **92**, 799 (2010). https://doi.org/10.1134/S0021364010240045
120. H. Otsuka, H. Takatsu, K. Goto, H. Kadowaki, Phys. Rev. B **90**, 144428 (2014). https://doi.org/10.1103/PhysRevB.90.144428
121. K. Matsuhira, Z. Hiroi, T. Tayama, S. Takagi, T. Sakakibara, J. Phys.: Condens. Matter **14**, L559 (2002). https://doi.org/10.1088/0953-8984/14/29/101
122. A.S. Wills, R. Ballou, C. Lacroix, Phys. Rev. B **66**, 144407 (2002). https://doi.org/10.1103/PhysRevB.66.144407
123. A.J. Macdonald, P.C.W. Holdsworth, R.G. Melko, J. Phys.: Condens. Matter **23**, 164208 (2011). https://doi.org/10.1088/0953-8984/23/16/164208
124. R. Moessner, S.L. Sondhi, Phys. Rev. B **68**, 064411 (2003). https://doi.org/10.1103/PhysRevB.68.064411
125. Y. Tabata, H. Kadowaki, K. Matsuhira, Z. Hiroi, N. Aso, E. Ressouche, B. Fåk, Phys. Rev. Lett. **97**, 257205 (2006). https://doi.org/10.1103/PhysRevLett.97.257205
126. T. Fennell, S.T. Bramwell, D.F. Mcmorrow, P. Manuel, A.R. Wildes, Nat. Phys. **3**, 566 (2007). https://doi.org/10.1038/nphys632
127. S.V. Isakov, K.S. Raman, R. Moessner, S.L. Sondhi, Phys. Rev. B **70**, 104418 (2004). https://doi.org/10.1103/PhysRevB.70.104418
128. H. Aoki, T. Sakakibara, K. Matsuhira, Z. Hiroi, J. Phys. Soc. Jpn. **73**, 2851 (2004). https://doi.org/10.1143/JPSJ.73.2851
129. T. Sakakibara, T. Tayama, Z. Hiroi, K. Matsuhira, S. Takagi, Phys. Rev. Lett. **90**, 207205 (2003). https://doi.org/10.1103/PhysRevLett.90.207205
130. T. Sakakibara, T. Tayama, K. Matsuhira, S. Takagi, Z. Hiroi, J. Magn. Magn. Mater. **272**, 1312 (2004). https://doi.org/10.1016/j.jmmm.2003.12.1215
131. P. Minnhagen, Rev. Mod. Phys. **59**, 1001 (1987). https://doi.org/10.1103/RevModPhys.59.1001
132. M.J. Matthews, C. Castelnovo, R. Moessner, S.A. Grigera, D. Prabhakaran, P. Schiffer, Phys. Rev. B **86**, 214419 (2012). https://doi.org/10.1103/PhysRevB.86.214419
133. H. Takatsu, K. Goto, H. Otsuka, R. Higashinaka, K. Matsubayashi, Y. Uwatoko, H. Kadowaki, J. Phys. Soc. Jpn. **82**, 073707 (2013). https://doi.org/10.7566/JPSJ.82.073707

134. G.G. Simeoni, T. Bryk, F.A. Gorelli, M. Krisch, G. Ruocco, M. Santoro, T. Scopigno, Nat. Phys. **6**, 503 (2010). https://doi.org/10.1038/nphys1683
135. T. Fennell, O.A. Petrenko, B. Fåk, J.S. Gardner, S.T. Bramwell, B. Ouladdiaf, Phys. Rev. B **72**, 224411 (2005). https://doi.org/10.1103/PhysRevB.72.224411
136. D. Slobinsky, C. Castelnovo, R.A. Borzi, A.S. Gibbs, A.P. Mackenzie, R. Moessner, S.A. Grigera, Phys. Rev. Lett. **105**, 267205 (2010). https://doi.org/10.1103/PhysRevLett.105.267205
137. S. Erfanifam, S. Zherlitsyn, J. Wosnitza, R. Moessner, O.A. Petrenko, G. Balakrishnan, A.A. Zvyagin, Phys. Rev. B **84**, 220404(R) (2011). https://doi.org/10.1103/PhysRevB.84.220404
138. S. Erfanifam, S. Zherlitsyn, S. Yasin, Y. Skourski, J. Wosnitza, A.A. Zvyagin, P. McClarty, R. Moessner, G. Balakrishnan, O.A. Petrenko, Phys. Rev. B **90**, 064409 (2014). https://doi.org/10.1103/PhysRevB.90.064409
139. M.J. Jackson, E. Lhotel, S.R. Giblin, S.T. Bramwell, D. Prabhakaran, K. Matsuhira, Z. Hiroi, Q. Yu, C. Paulsen, Phys. Rev. B **90**, 064427 (2014). https://doi.org/10.1103/PhysRevB.90.064427
140. S. Mostame, C. Castelnovo, R. Moessner, S.L. Sondhi, Proc. Natl. Acad. Sci. **111**, 640 (2014). https://doi.org/10.1073/pnas.1317631111
141. G. Kolland, O. Breunig, M. Valldor, M. Hiertz, J. Frielingsdorf, T. Lorenz, Phys. Rev. B **86**, 060402(R) (2012). https://doi.org/10.1103/PhysRevB.86.060402
142. G. Kolland, M. Valldor, M. Hiertz, J. Frielingsdorf, T. Lorenz, Phys. Rev. B **88**, 054406 (2013). https://doi.org/10.1103/PhysRevB.88.054406
143. C. Fan, Z.Y. Zhao, H.D. Zhou, X.M. Wang, Q.J. Li, F.B. Zhang, X. Zhao, X.F. Sun, Phys. Rev. B **87**, 144404 (2013). https://doi.org/10.1103/PhysRevB.87.144404
144. W.H. Toews, S.S. Zhang, K.A. Ross, H.A. Dabkowska, B.D. Gaulin, R.W. Hill, Phys. Rev. Lett. **110**, 217209 (2013). https://doi.org/10.1103/PhysRevLett.110.217209
145. D.I. Khomskii, Nat. Commun. **3**, 904 (2012). https://doi.org/10.1038/ncomms1904
146. A. Sarkar, S. Mukhopadhyay, Phys. Rev. B **90**, 165129 (2014). https://doi.org/10.1103/PhysRevB.90.165129
147. M. Saito, R. Higashinaka, Y. Maeno, Phys. Rev. B **72**, 144422 (2005). https://doi.org/10.1103/PhysRevB.72.144422
148. D. Liu, L. Lin, M.F. Liu, Z.B. Yan, S. Dong, J.M. Liu, J. Appl. Phys. **113**, 17D901 (2013). https://doi.org/10.1063/1.4793704
149. M. Bonitz, Nat. Phys. **7**, 192 (2011). https://doi.org/10.1038/nphys1935
150. M. Yamada, R. Kulsrud, H. Ji, Rev. Mod. Phys. **82**, 603 (2010). https://doi.org/10.1103/RevModPhys.82.603
151. J.B. Zirker, *The Magnetic Universe* (Johns Hopkins University Press, Baltimore, 2009). ISBN 9780801893025
152. E.Y. Vedmedenko, Phys. Rev. Lett. **116**, 077202 (2016). https://doi.org/10.1103/PhysRevLett.116.077202
153. M.E. Zhitomirsky, A.L. Chernyshev, Rev. Mod. Phys. **85**, 219 (2013). https://doi.org/10.1103/RevModPhys.85.219
154. J. Lago, I. Živković, B.Z. Malkin, J. Rodriguez Fernandez, P. Ghigna, P. Dalmas de Réotier, A. Yaouanc, T. Rojo, Phys. Rev. Lett. **104**, 247203 (2010). https://doi.org/10.1103/PhysRevLett.104.247203
155. O. Benton, O. Sikora, N. Shannon, Phys. Rev. B **86**, 075154 (2012). https://doi.org/10.1103/PhysRevB.86.075154
156. B. Tomasello, C. Castelnovo, R. Moessner, J. Quintanilla, Phys. Rev. B **92**, 155120 (2015). https://doi.org/10.1103/PhysRevB.92.155120
157. J.G. Rau, M.J.P. Gingras, Phys. Rev. B **92**, 144417 (2015). https://doi.org/10.1103/PhysRevB.92.144417
158. M.J. Harris, S.T. Bramwell, P.C.W. Holdsworth, J.D.M. Champion, Phys. Rev. Lett. **81**, 4496 (1998). https://doi.org/10.1103/PhysRevLett.81.4496
159. M.J.P. Gingras, P.A. McClarty, Rep. Prog. Phys. **77**, 056501 (2014). https://doi.org/10.1088/0034-4885/77/5/056501

160. G. Sala, M.J. Gutmann, D. Prabhakaran, D. Pomaranski, C. Mitchelitis, J.B. Kycia, D.G. Porter, C. Castelnovo, J.P. Goff, Nat. Mater. **13**(5), 488 (2014). https://doi.org/10.1038/nmat3924
161. S. Balibar, Séminaire Poincaré **1**, 11 (2003). https://doi.org/10.1007/978-3-0348-7932-3_2
162. F. London, Nature **141**, 643 (1938). https://doi.org/10.1038/141643a0

Chapter 9
Quantum Coherence: Quantum Spin Ice and Lattice Gauge Theory

Lucile Savary and Leon Balents

Abstract In this chapter, we address the effects of symmetry-allowed terms which induce quantum dynamics in a range of models close to the classical spin ice point. Specifically, we focus on Coulombic quantum spin liquid states, in which a highly entangled massive superposition of spin ice states is formed, allowing for dramatic quantum effects. In the perturbative limit near classical spin ice, a compact $U(1)$ lattice gauge theory applies, and affords a direct description of the simplest such state. Supplementing the gauge theory with matter fields provides the key to a physically-motivated non-perturbative parton approach, which allows a description of the phase diagram more broadly. Throughout the presentation we use and discuss how results from lattice gauge theory translate to the context of quantum spin ice. We include a somewhat pedagogical presentation of duality and of the excitations of Coulombic spin liquids, and a new discussion of the wavefunctions of the various phases of quantum spin ice, not previously published in the literature. The latter provides some intuitive insight and may be a useful reference point for future variational approaches. Finally, we draw a thorough comparison between classical and quantum spin ice, before addressing some frontier topics such as the more frustrated version of quantum spin ice, quantum phase transitions, numerics and disorder.

9.1 What Is Quantum Spin Ice?

Prior chapters have discussed the canonical spin ice problem and corresponding materials. There, spins are regarded as purely classical Ising variables, and a (long-range) classical Ising model is the proper Hamiltonian for the system. The physics is that of dynamics and statistical mechanics within the macroscopically degenerate but constrained manifold of spin ice ground states. A large amount of entropy remains

L. Savary (✉)
Université de Lyon, ENS de Lyon, Université Claude Bernard, CNRS, Laboratoire de Physique, 69342 Lyon, France

L. Balents (✉)
Kavli Institute of Theoretical Physics, University of California, Santa Barbara, USA
e-mail: balents@kitp.ucsb.edu

M. Udagawa and L. Jaubert (eds.), *Spin Ice*, Springer Series in Solid-State Sciences 197,
https://doi.org/10.1007/978-3-030-70860-3_9

present in the system, and many distinct states are accessed over time. The dynamics itself is very slow, requiring thermal activation to achieve actual, not virtual, transitions between states. The slow nature of the dynamics furthermore implies that it is incoherent, and can be thus described simply by classical stochastic models, or even rate equations.

In this chapter, we will discuss a class of systems in which the basic spin ice physics is still present, but where quantum effects play a major role. The quantum dynamics is generated by substantial non-Ising exchange terms in the Hamiltonian, which we will specify below. In general such terms break the spin ice degeneracy, though not in an explicit and obvious way, since they are non-classical. Thus at sufficiently low temperatures, the entropy of the system becomes fully quenched, and the system does *not* explore many distinct states. Rather we will see that, in a certain limit, the low energy quantum states are *superpositions* of many of the classical spin ice states. It should be emphasized that superposition is fundamentally different from fluctuation. The former does not imply any large entropy. Furthermore, the superposition state, by virtue of quantum entanglement (which the classical spin ice states lack), can support a variety of novel excitations. All this will be discussed below.

9.1.1 Hamiltonian

As mentioned in Chap. 1, The majority of rare earth pyrochlores have single ion physics described by a doublet ground state. Provided mixing with higher multiplets can be considered small, which is usually an excellent approximation, the two-level system of the on-site doublet can be regarded as an effective spin-1/2, and described by spin operators $\mathsf{S}_i^\mu = \sigma_i^\mu/2$, where σ_i^μ are Pauli matrices. When nearest-neighbor interactions dominate, symmetry strongly restricts the form of allowed couplings between these spins. If we assume that the spins transform as dipolar doublets, i.e. like angular momentum operators under the restricted set of symmetry operations of the pyrochlore lattice, the most general nearest-neighbor Hamiltonian involves four distinct interactions [1–3]:

$$\begin{aligned} H = \sum_{\langle ij \rangle} \Big\{ & J_{zz} \mathsf{S}_i^z \mathsf{S}_j^z - J_\pm (\mathsf{S}_i^+ \mathsf{S}_j^- + \mathsf{S}_i^- \mathsf{S}_j^+) \\ & + J_{z\pm} \left[\mathsf{S}_i^z (\zeta_{ij} \mathsf{S}_j^+ + \zeta_{ij}^* \mathsf{S}_j^-) + i \leftrightarrow j \right] \\ & + J_{\pm\pm} \left[\gamma_{ij} \mathsf{S}_i^+ \mathsf{S}_j^+ + \gamma_{ij}^* \mathsf{S}_i^- \mathsf{S}_j^- \right] \Big\}. \end{aligned} \tag{9.1}$$

Here we have written the spins in a *local* basis, so that S_i^z is proportional to the moment along the local Ising axis of the spin at site i. The matrices γ_{ij}, ζ_{ij} consist of unimodular complex numbers (see Chap. 11). Since this Hamiltonian is based on

symmetries, the parameters include all nearest-neighbor contributions, regardless of their origin.

The Hamiltonian in (9.1) applies to many real materials. This includes the "classical spin ices," for which J_{zz} is positive and the other three "quantum" couplings are negligible in comparison. In that limit, (9.1) is the Hamiltonian for classical nearest-neighbor spin ice. Equation (9.1) has also been shown to be a good description of $Er_2Ti_2O_7$ [4] and $Yb_2Ti_2O_7$ [2, 5–7], both of which have dipolar doublet ground states with substantial quantum dynamics. It also describes $Pr_2Sn_2O_7$ and $Pr_2Zr_2O_7$ [3, 8], where Pr^{3+} has a non-Kramers doublet ground state which forces $J_{z\pm} = 0$ above. Relying only upon the symmetry of the pyrochlore lattice, (9.1) is also appropriate for rare earth ions on the B-site of the spinel lattice, such as for example $CdEr_2Se_4$.

It should be noted that there are situations where (9.1) does not apply. This can happen in several ways. Rare earth ions on the pyrochlore lattice can have an octupolar rather than dipolar doublet ground state. This is described by a different effective Hamiltonian written in [9], and appropriate to, for example, $Nd_2Zr_2O_7$. Equation (9.1) *may* also fail even in the presence of a symmetry appropriate ground state doublet, if the mixing to higher multiplets cannot be neglected. This may be the case in $Tb_2Ti_2O_7$, where Tb^{3+} has the same non-Kramers doublet ground state as Pr^{3+}, but a very small gap to the next excited doublet [10]. Also, in general, non-Kramers doublets can couple strongly to the lattice, and this coupling, not included in (9.1), may play a crucial role. Finally, longer distance interactions might be important. This is obviously the case in the classical spin ice materials. We expect it is much less important in the quantum systems, since there is much less degeneracy when the non-Ising exchange terms are significant.

For the remainder of this chapter, we will consider the Hamiltonian in (9.1) as a working definition of "quantum spin ice", with the requirement that $J_{zz} > 0$, which enforces the spin ice ground state manifold in the classical limit, and the somewhat vague proviso that the remaining couplings are "not too large". Later sections will clarify unambiguously sharp criteria to define *phases* which are the most "spin ice like".

9.1.2 Near the Spin Ice Point

If the quantum terms are small, $0 < |J_\pm|, |J_{\pm\pm}|, |J_{z\pm}| \ll J_{zz}$, the system is "close" to classical spin ice, and can be described by perturbation theory around that point [2, 11]. Since the spin ice point, $J_\pm = J_{\pm\pm} = J_{z\pm} = 0$ is highly degenerate, degenerate perturbation theory is the appropriate formalism, and the result of this exercise is an effective Hamiltonian *projected* onto the classical ground state manifold of nearest-neighbor spin ice. In the present notation, these are the states for which

$$\sum_{i\in t} \mathsf{S}_i^z = 0, \tag{9.2}$$

where the sum is taken over the four sites of any tetrahedron t. This corresponds to the "two-in-two-out" condition familiar from previous chapters.

The effective Hamiltonian is highly constrained by the requirement that it operates in the spin ice manifold of states. This requirement in particular prohibits any single spin-flip processes, which would violate the two-in-two-out constraint. The terms in the effective Hamiltonian must either be diagonal, i.e. flip no spins, or act in such a way that spins are flipped always pairwise on tetrahedra. This necessitates at least six spin flips, around the smallest hexagonal ring of the pyrochlore lattice. The physical meaning of this will become apparent below.

The form of the perturbative effective Hamiltonian is, to leading order [2],

$$H_{\text{eff}} = -K \sum_{\{i,j,k,l,m,n\}=\hexagon} \left(\mathsf{S}_i^+ \mathsf{S}_j^- \mathsf{S}_k^+ \mathsf{S}_l^- \mathsf{S}_m^+ \mathsf{S}_n^- + \text{h.c.} \right) - J_{(3)} \sum_{\langle\langle\langle i,j \rangle\rangle\rangle} \mathsf{S}_i^z \mathsf{S}_j^z. \quad (9.3)$$

Here $K = 12 J_\pm^3 / J_{zz}^2$ is the six-site "ring exchange" term alluded to above, and $J_{(3)} = 3 J_{z\pm}^2 / J_{zz}$ is an Ising exchange between the third-neighbor sites which share one common nearest-neighbor and are symmetric with respect to the latter (in particular, they are *not* on opposite sides of a hexagon). Note that, to leading order, $J_{\pm\pm}$ does not generate any additional terms, and its leading contribution to K and $J_{(3)}$ above is subdominant to those from $J_{z\pm}$ and $J_\pm$ given above if $J_{\pm\pm}$ is of the same order as the other quantum exchanges [2, 11].

The effective Hamiltonian in (9.3) was first introduced, for $J_{(3)} = 0$, in [11]. There, H_{eff} was derived for the XXZ model with $J_{z\pm} = J_{\pm\pm} = 0$, and it was furthermore shown that it is actually a form of $U(1)$ *lattice gauge theory*. We will discuss this gauge theory much further in Sect. 9.2. For the moment, we simply note that the full H_{eff} contains just one dimensionless parameter, the ratio of $J_{(3)}$ to K. When $J_{(3)} = 0$, the Hamiltonian is entirely off-diagonal in the S_i^z basis. In the limit $J_{(3)}/K \ll 1$, fluctuations are strong, and the description as a gauge theory is essential. We will argue in Sect. 9.2 that this describes a quantum spin liquid phase.

For $K = 0$ (or large $J_{(3)}$), the Hamiltonian is diagonal in the S_i^z basis, and hence can be treated classically. Since $J_{(3)} > 0$, a state in which all third neighbor spins are parallel, if any exist, must be a ground state. The set of all sites connected by third neighbor moves from a given site is simply the fourth of the sites of a single sublattice. Thus any configuration which does not enlarge the unit cell is a ground state. Since there are six 2in-2out states of a single tetrahedron, these are the six global ground states (see Fig. 9.1). Physically, these are ferromagnetic states with total moment $\sum_i \mathbf{S}_i$ aligned along one of the six $\langle 100 \rangle$ axes.

9.1.3 Mean Field Limit

Far from the spin ice point, and far from any phase boundaries, the general Hamiltonian in (9.1) is not very frustrated, and being three-dimensional, is expected to

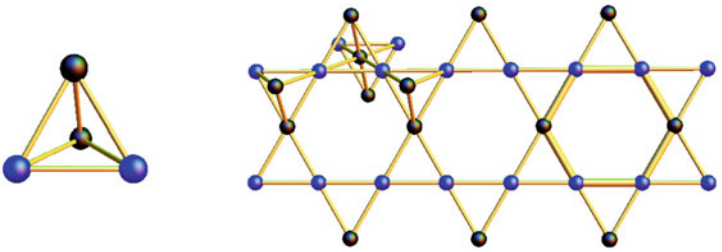

Fig. 9.1 A "two-in-two-out" tetrahedron, and the $\mathbf{Q} = \mathbf{0}$ state obtained by repeating this structure. Such a state contains no "flippable" hexagons. Reprinted from [2] with permission from the American Physical Society

be only weakly affected by fluctuations, including quantum ones. Thus we expect that a mean-field or classical ground state analysis is a good starting point. This contains four generic ordered states: a non-collinear ferromagnet with net magnetization along the $\langle 100 \rangle$ axes, and three antiferromagnetic phases with zero net magnetization [12]. As there are four exchange couplings and the overall scale of energy is unimportant at zero temperature, in general the ground state phase diagram, classical or otherwise, is three-dimensional. A representative cut of the classical result is shown in Fig. 9.2 [5]. A complete classical analysis can be found in [12]. Near the spin ice point, and also near some phase boundaries, quantum fluctuations become large and the classical result is unreliable. The quantum spin ice state which is the focus of this chapter is the ultimate outcome of these fluctuations when J_{zz} dominates.

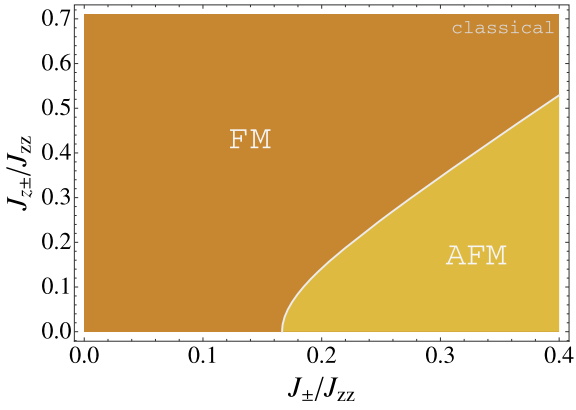

Fig. 9.2 Classical phase diagram in the $J_{\pm}/J_{zz} - J_{z\pm}/J_{zz}$ plane for $J_{zz} > 0$ close to the spin ice point. Reprinted from [5] with permission from the American Physical Society

9.2 Perturbative Gauge Theory

9.2.1 Derivation and Formulation

As remarked in Sect. 9.1.2, the effective Hamiltonian in the vicinity of the spin ice point is a $U(1)$ lattice gauge theory. In a certain sense this is inevitable from the nature of the spin ice constraint itself. Since the effective Hamiltonian operates within the space with $\sum_{i\in t} \mathsf{S}_i^z = 0$, it necessarily commutes with the left-hand-side of this equation *for every tetrahedron t separately*. Since the operator $\sum_{i\in t} \mathsf{S}_i^z$ is integer-valued, this is a local $U(1)$ symmetry of (9.3).

More formally, we may define

$$Q_t = \varepsilon_t \sum_{i\in t} \mathsf{S}_i^z =_0 0, \tag{9.4}$$

where for convenience we included the factor ε_t which assigns a sign that discriminates two orientations of tetrahedra: $\varepsilon_t = +1(-1)$ for up (down) oriented tetrahedra (see Fig. 9.3). The equality on the right hand side of (9.4) holds in the ground state sector (as indicated by the subscript 0 on the equality sign). The "charge" Q_t commutes with H_{eff}. It follows that H_{eff} is invariant under the $U(1)$ symmetry generated by the unitary operator $U = e^{i\chi Q_t}$, for any t and any χ.

Noting that the charge Q_t is defined on the sites t of a diamond lattice (the tetrahedron centers), we can recast the effective Hamiltonian entirely as a diamond lattice gauge theory. To do so, we define

$$\mathsf{S}^{\pm}_{t,t'} = \mathsf{S}^{\pm\varepsilon_t}_{i(t,t')}, \tag{9.5}$$

$$\mathsf{S}^{z}_{t,t'} = \varepsilon_t \mathsf{S}^{z}_{i(t,t')}, \tag{9.6}$$

where $i(t,t')$ is the pyrochlore site shared by neighboring tetrahedra t and t'. This definition gives a "vectorial" sense to the operators on the diamond lattice, so that $\mathsf{S}^{\pm}_{t,t'} = \mathsf{S}^{\mp}_{t',t}$ and $\mathsf{S}^{z}_{t,t'} = -\mathsf{S}^{z}_{t',t}$. Then the gauge charge becomes

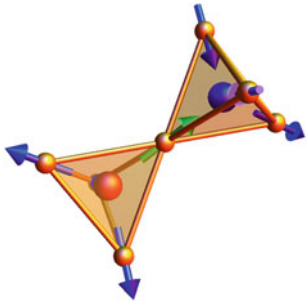

Fig. 9.3 Classical representation of a spinon-antispinon pair (spinons and antispinons correspond to the monopoles in other chapters). The red and blue spheres are located on "up" and "down" tetrahedra, respectively

$$Q_t = \varepsilon_t \sum_{t' \in \partial t} \mathsf{S}^z_{t,t'} \equiv \varepsilon_t \left(\operatorname{div} \mathsf{S}^z\right)_t =_0 0, \tag{9.7}$$

where the sum indicates nearest neighbor sites of t, and the result is the lattice divergence at t of the vector field $\mathsf{S}^z_{t,t'}$. We recognize therefore $\mathsf{S}^z_{t,t'}$ as the lattice analog of a "magnetic field". The quantity Q_t is a magnetic "charge", so that a state with non-zero Q_t is analogous to a magnetic monopole. Such states in the earliest works on QSI were called "spinons", which is a term widely used in the literature on quantum spin liquids, more generally. In this chapter we use the term magnetic monopole and spinon interchangeably. In the classical context, magnetic monopoles in spin ice are discussed extensively in other chapters of this book.

Here we should note that we are departing from most prior literature on *quantum* spin ice, in which Q_t was called an "electric" charge, and $\mathsf{S}^z_{t,t'}$ an "electric" field. The ambiguity in terminology reflects an element of the physics of 3+1-dimensional quantum electrodynamics: *self-duality*. In electrodynamics, electric and magnetic variables (fields, charges, currents) can be exchanged leaving the theory invariant. Prior work on QSI fixed the convention based on the convention for compactness: in most literature on compact U(1) gauge theory, the electric field is regarded as discrete and magnetic vector potential as periodic. This, unfortunately, is opposite to the usual spin ice conventions, and so in this article, to keep in closer agreement with the rest of the book, we choose the opposite convention. There is one particular merit to the spin ice convention we take here: the emergent electro-magnetic fields transform in the same way as their fundamental counterparts under time reversal symmetry. It is because of this that a magnetic monopole in spin ice can be "really" magnetic, in the sense that it carries a divergence of physical magnetization.

The Hamiltonian becomes

$$H_{\text{eff}} = -K \sum_{\hexagon} \left(\prod_{t \in \hexagon = 1}^{6} \mathsf{S}^+_{t,t+1} + \text{h.c.} \right) - J_{(3)} \sum_{t_1,t_2,t_3,t_4}{}' \mathsf{S}^z_{t_1,t_2} \mathsf{S}^z_{t_3,t_4}. \tag{9.8}$$

The prime on the sum in the latter term indicates it represents a complicated form which simply reproduces the third-neighbor condition in (9.3).

This Hamiltonian now has a manifest gauge invariance, under local phase rotations by angle χ_t on each diamond site, for which

$$\mathsf{S}^{\pm}_{t,t'} \to e^{\pm i(\chi_{t'} - \chi_t)} \mathsf{S}^{\pm}_{t,t'}. \tag{9.9}$$

We can recognize from (9.9) that $\mathsf{S}^{\pm}_{t,t'}$ behaves as a *gauge connection*, i.e. the exponential of a gauge field or vector potential.

9.2.2 Relation to Compact QED

One may make this more explicit, following [11], by representing the spin-1/2 operators S_i by rotors. We can write

$$\mathsf{S}^z_{t,t'} \to B_{t,t'}, \tag{9.10}$$

where $B_{t,t'}$ is a half-integral valued angular momentum, and

$$\mathsf{S}^{\pm}_{t,t'} \to e^{\pm i\mathscr{A}_{t,t'}}, \tag{9.11}$$

where $\mathscr{A}_{t,t'} = -\mathscr{A}_{t',t}$ is a 2π-periodic angular variable. If we impose the canonical commutation relations $[B_{t,t'}, \mathscr{A}_{t,t'}] = i$ then $\mathsf{S}^{\pm}_{t,t'}$ acts as the desired spin raising/lowering operator, except that it can raise/lower "outside" the physical space with $B_{t,t'} = \pm 1/2$. To fix this problem, we add a term $+U(B^2_{t,t'} - 1/4)$ to the Hamiltonian and remember that in the end we must take the limit $U \to \infty$, which projects out the unphysical states. After these manipulations, $H_{\text{eff}} \to H_{cQED}$, with

$$H_{cQED} = -2K \sum_{\hexagon} \cos(\text{curl}\mathscr{A}) + U \sum_{\langle t,t' \rangle} \left(B^2_{t,t'} - \frac{1}{4} \right) - J_{(3)} {\sum_{t_1,t_2,t_3,t_4}}' B_{t_1,t_2} B_{t_3,t_4}. \tag{9.12}$$

Here $(\text{curl}\mathscr{A})_{\hexagon} = \sum_{t \in \hexagon = 1}^{6} \mathscr{A}_{t,t+1}$ defines a "electric flux" E through a plaquette. Now (9.12) is very recognizable (though written in variables dual to standard compact gauge theory conventions) as a quantum model of compact electromagnetism on the lattice. It is compact because $\mathscr{A}$ is 2π-periodic, so that the space of gauge connections $e^{i\mathscr{A}}$ is the compact $U(1)$ group.

9.2.3 Phases of Compact QED

This problem with $J_{(3)} = 0$ and *integer* (rather than half-integer) $B_{t,t'}$ was studied in detail in [13] in the context of lattice gauge theories. In this model there are two phases: the "confining" phase which occurs for $U \gg K$, and the "Coulomb" phase, which occurs at $U \ll K$. In the confining phase B has very small fluctuations away from the $U = \infty$ ground state which, is simply a product wavefunction $|\psi\rangle = \otimes_{\langle tt' \rangle} |B_{t,t'} = 0\rangle$. The smallest excitation away from the ground state costs a non-zero energy, since B is discrete. If a test charge is introduced, i.e. we require that $\text{div}B$ is non-zero at some single lattice site, the magnetic field emanating from this site is concentrated into a line in order to minimize the U term. This field line costs an energy proportional to its length, which extends over the full system width or the distance to a compensating opposite charge. This linear energy cost is a characteristic of confinement. More generally, we may consider a confined phase as one in which the elementary excitations are all "local", i.e. can be created by local operators. The

magnetic monopoles of spin ice (i.e. the magnetic charges of the gauge theory) are non-local, and are not elementary excitations in the confined phase of quantum spin ice because they cost an infinite energy.

In the Coulomb phase, B fluctuates wildly due to small U, while $\mathscr{A}$ fluctuates enormously because the large K term constrains only the curl but not the average $\mathscr{A}$. In this phase, at low energy $E = \text{curl}\mathscr{A}$ is constrained to be small, so it is legitimate to expand the cosine term, which leads, up to a constant, to the quadratic effective Hamiltonian,

$$H_{EM} = K \sum_{\hexagon} (\text{curl}\mathscr{A})^2 + U \sum_{\langle t,t' \rangle} B_{t,t'}^2. \tag{9.13}$$

The normal modes of this quadratic Hamiltonian contain a gapless "photon", with linear dispersion at small momentum. This is a standard calculation in the continuum, in which it corresponds to a textbook quantization of vacuum electromagnetism. On the lattice, it is only slightly more involved. Please see Chap. 11, or [5, 14]

At the most fundamental level, the difference between the Coulomb and confined phases has to do with the support of the wavefunction in Hilbert space. In the confined phase, the wavefunction amplitude is substantial only on a very small region of this space, in which $B_{t,t'} = 0$ for most t, t'. Conversely, in the Coulomb phase, the wavefunction is "delocalized" in the magnetic field basis. Moreover, there is actually *no* local basis for which the wavefunction is not a massive superposition. We say that the Coulomb phase exhibits massive or long-range entanglement. It is this entanglement which is responsible for the ability of this state to support novel emergent excitations such as the photon and magnetic charges.

9.2.4 Electric Charges and Duality

A somewhat more subtle feature of the Coulomb phase is the presence of another gapped excitation apart from the magnetic charges: a dual electric charge. The presence of *both* electric and magnetic charges is a feature of *compact* electrodynamics, due to the periodicity of $\mathscr{A}$ (famously Dirac postulated the existence of a magnetic monopole to explain the quantization of electric charge). Physically, a finite energy configuration can arise in which E is small almost everywere, except in the vicinity of some cell of the lattice which acts as a source of electric flux. From the outside of this cell, this appears as a monopole configuration of E, and the flux, $\sum_{\hexagon \in \mathscr{S}} E_{\hexagon} = \pm 2\pi$, if the sum is taken over the surface $\mathscr{S}$ of hexagons enclosing the source cell.

It is instructive to bring out the electric charges explicitly by what is known as a *duality* transformation [15–17]. We follow a Hamiltonian formulation as in [18]. To do so, we solve the Gauss' law constraint $\text{div} B = 0$ (which is (9.7) rewritten from (9.10)) according to

$$B_{t,t'} = (\text{curl}\, A)_{t,t'} + B^{(0)}_{t,t'}, \tag{9.14}$$

where $B^{(0)}_{t,t'}$ is a fixed classical half-integer configuration satisfying the Gauss' law constraint, and $A_{a,a'}$ is an integer-valued vector field on a dual lattice whose sites a, a' are centered on the "voids" of the original one. In trading B for A, we at the same time trade the $\mathscr{A}_{t,t'}$ variables for $E_{a,a'}$, with

$$E_{a,a'} = (\mathrm{curl}\, \mathscr{A})_{a,a'}\,, \tag{9.15}$$

which is just the electric flux of the original gauge field. One can readily check that

$$\left[E_{a,a'}, A_{a,a'}\right] = i. \tag{9.16}$$

and that these variables commute on different bonds. So the E and A variables have the same commutation relations as the B and $\mathscr{A}$ variables in the original formulation. Then the Hamiltonian is simply rewritten as

$$H_{cQED} = -2K \sum_{\langle a,a'\rangle} \cos E + U \sum_{\langle t,t'\rangle} \left[(\mathrm{curl}\, A)_{t,t'} + B^0_{t,t'}\right]^2, \tag{9.17}$$

up to a constant, and neglecting $J_{(3)}$. Now a standard manipulation is to "relax" the integer constraint on $A_{a,a'}$ by making it continuous and at the same time adding a term to favor integer values. After these manipulations, we arrive at

$$H_{dual} = K \sum_{\langle a,a'\rangle} E^2 + U \sum_{\langle t,t'\rangle} \left[(\mathrm{curl}\, A)_{t,t'} + B^0_{t,t'}\right]^2 - \upsilon \sum_{\langle a,a'\rangle} \cos(\vartheta_a - \vartheta_{a'} - 2\pi A_{a,a'}), \tag{9.18}$$

where now E and A are continuous variables, and the υ term "remembers" the discreteness of the original A (or B) fields. Comparing to (9.13), we see that magnetic and electric fields have changed roles, as have $\mathscr{A}$ and A. This is why this is called a duality transformation. Indeed, the vacuum Maxwell equations have such a symmetry under interchange of magnetic and electric fields (up to signs related to time-reversal). From the point of view of low energy physics in the Coulomb phase, the magnetic charges are on the same footing as the electric ones, and indeed a duality transformation exists which interchanges them, taking $E \leftrightarrow B$. However, the electric charges are non-local in the spin basis natural to QSI, and have no analog in classical spin ice.

The additional ingredient in (9.18) is the final, υ term, which appears like an XY ferromagnetic interaction of "spins" with phase ϑ coupled to the gauge field A. This reflects the promised presence of electric charges in the compact electromagnetism from which we started. We can identify the operator $e^{i\vartheta_a}$ as creating such an electric charge at the dual site a. Such a charge must be accompanied by an electric field configuration $\mathrm{div}\, E = \pm 2\pi$, reflecting the dual Gauss' law. The dual Hamiltonian in (9.18) is in fact the same as that of a charge boson coupled to a gauge field, as is familiar in condensed matter from the theory of superconductivity.

All the effects of compactness are captured by the υ term. We can use (9.18) to make a few observations. First, if υ is small (or K is large and U is small), then we may perturbatively integrate out the ϑ_a fields in an expansion in υ. Since the theory with $\upsilon = 0$ has a continuous gauge invariance under $A_{a,a'} \to A_{a,a'} + \mu_a - \mu_{a'}$, with arbitary μ_a, by Elitzur's theorem [19], all non gauge-invariant expectation values in this theory vanish, and consequently, the effective action *to all orders in* υ is gauge invariant, and these terms only renormalize the coefficients of E^2 and $(\text{curl } A)^2$. This demonstrates the stability of the Coulomb phase. The physical interpretation is that so long as the electric charges are gapped (which they are in this limit), then they can be integrated out and they only renormalize the Coulomb phase quantitatively.

Second, if we increase υ sufficiently, or at fixed non-zero υ increase U/K enough, then the XY phase variables ϑ order. We can say that by e.g. increasing υ, the gap for electric monopoles lowers until they "condense". When this happens, we can expect a "Meissner" effect for the flux of the dual gauge field A. That is, the flux, curl A, is concentrated into lines like the magnetic field in a superconductor is concentrated into vortex lines. Recall from (9.14) that this flux is the original emergent magnetic field strength B. This phenomenon is nothing but the confinement of magnetic field into lines discussed directly in the previous subsection. Thus we conclude that, remarkably, *the confined phase and the condensate of electric charges are one and the same!* [13] Indeed, it is common to view condensation of charges as the mechanism of confinement.

9.2.5 Application to Quantum Spin Ice

This same picture largely applies to the case relevant for quantum spin ice, in which B takes half-integer rather than integer values, and $J_{(3)}$ is non-zero. In the half-integer case, the limit $U \to \infty$ remains non-trivial, as $B = \pm 1/2$ states remain degenerate. However, it is a strongly coupled limit, and we must rely upon numerical methods to evaluate even the $J_{(3)} = 0$ case. There is strong evidence that in this limit, the system remains in the Coulomb phase despite $U = \infty$ [14, 20]. In this regime the magnetic charges (spin ice monopoles) have a gap of order J_{zz}, the electric charges have a gap of order K, and the "speed of light" of the emergent photon is also of order K. With increasing $J_{(3)}$, however, the magnetic degeneracy is broken, and we expect a transition to a confined phase. This transition can actually be thought of as condensation/proliferation of the electric charges.

Finally, we ask a question: what makes the gauge theory a useful description when neither B nor $\mathscr{A}$ are "good quantum numbers?" Certainly, one answer comes from the identification to the well-studied theory of quantum electromagnetism, and more generally from the experience accumulated treating lattice gauge theory in general. In Sect. 9.3.1, the appropriateness of the gauge fields will become more transparent as we include "matter fields" whose particles will represent "defects" of the pure

gauge theory. The (gauge invariant!) gauge field fluxes will then quantify the number of enclosed defects, which will be nothing but the electric charges and magnetic monopoles. Therefore, the gauge theory description, while not providing an explicit ground state wavefunction, does shed light on the nature of the massive excitations above the ground state. Moreover, the identification of the theory with a $U(1)$ (continuous) gauge theory also informs us on the existence of gapless excitations.

9.3 A Global View

In the previous section, we discussed the perturbative treatment around the degenerate spin ice point. In this limit, the ground state can be fully represented within the degenerate spin ice manifold, with corrections outside that manifold included perturbatively by the systematic machinery of degenerate perturbation theory. Thus H_{eff} in (9.3) acts entirely within the constrained subspace of the full spin-1/2 Hilbert space. In this description, there are really just two distinct ways the wavefunction can behave: it can delocalize across the spin ice states, which is the case in the Coulomb phase, or it can localize to one or a few specific spin ice states, which describes confining phases, such as the ordered $\langle 100 \rangle$ ferromagnet.

Outside the perturbative regime, it is no longer obvious that one can fully describe the dynamics within the spin ice manifold. Specifically, we may wonder if a third type of phase, in which violations of the spin ice constraint become important, might be possible. In this section, we will describe a formalism which allows one to capture both the spin ice physics and emergent $U(1)$ gauge theory, but without invoking perturbative projection into the spin ice manifold [5]. Such a formalism is especially useful for describing transitions out of the Coulomb spin liquid phase. From it, we can ascribe a precise meaning to the notion of when the ground state "violates" the spin ice constraints.

9.3.1 Slave Spinon Formulation

As mentioned above, the perturbation theory described in Sects. 9.1.2 and 9.2 acts only within the manifold which preserves the spin ice constraints, and is therefore inappropriate to treat terms in the Hamiltonian which take one out of this manifold and wavefunctions with terms that violate the spin ice constraints. The identification of the projected Hamiltonian as a (pure) gauge theory, however, guides us on how to proceed. Indeed, we will turn the pure gauge theory in which $\mathsf{S}^{\pm}_{t,t'} \to e^{\pm i(\chi_{t'}-\chi_t)}\mathsf{S}^{\pm}_{t,t'}$ (9.9), to a full gauge theory *with matter* where now it is the combined transformation of matter fields Φ_t and $\Phi_t^\dagger$ and gauge field which will leave the theory invariant.

The "matter" fields Φ_t and $\Phi_t^\dagger$ are lowering and raising operators of the charge Q_t defined in Sect. 9.2, (9.4), and can be formally defined to be $\Phi_t^\dagger = e^{i\varphi_t}$, where φ_t is a real and compact operator canonically conjugate to Q_t, i.e. $[\varphi_t, Q_t] = i$, and the new gauge transformation is given by:

$$\mathsf{s}^{\pm}_{t,t'} \to e^{\pm i(\chi_{t'}-\chi_t)}\mathsf{s}^{\pm}_{t,t'} \quad \text{and} \quad \Phi_t \to \Phi_t e^{-i\chi_t}, \tag{9.19}$$

where $\mathbf{s}$ is the gauge field for this theory with matter, which replaces $\mathbf{S}$. In other words, one allows for "defects" in the pure gauge theory where the absence of symmetry under $\mathsf{s}^{\pm}_{t,t'} \to e^{\pm i(\chi_{t'}-\chi_t)}\mathsf{s}^{\pm}_{t,t'}$ at some points (ends of strings) may be compensated by an appropriate transformation of the matter fields. In that sense, the latter are "slaved" to the gauge fields. In more pedestrian terms, and as applied to the problem of quantum spin ice, the action of a spin raising or lowering operator on a diamond bond (t, t') should be associated with the action of charge raising and lowering operators on t and t'. We can call Φ and $\Phi^\dagger$ spinon/magnetic monopole annihation and creation operators, respectively.

We now proceed to this formal construction, introduced in [5]. We first consider an enlarged Hilbert space $\mathscr{H}_{\mathsf{S}} \to \mathscr{H}_{\mathsf{S}} \otimes \mathscr{H}_Q = \mathscr{H}_g$, where $\mathscr{H}_{\mathsf{S}}$ is the 2^N dimensional space of states of the N spins $\mathbf{S}_i$, and $\mathscr{H}_Q$ is the space of possible superpositions of integer charge states for each tetrahedon, $\mathscr{H}_Q \sim \mathbb{Z}^{N_t}$, with N_t the number of tetrahedra. The idea is to embed the physical states in $\mathscr{H}_{\mathsf{S}}$ into $\mathscr{H}_g$ so that $Q_t - \varepsilon_t \sum_{i\in t} \mathsf{S}^z_i = 0$. We denote the subspace of $\mathscr{H}_g$ which satisfies this constraint $\check{\mathscr{H}}_g$. This is a "projection" of the enlarged Hilbert space back to a physical one. It is isomorphic to the original space $\mathscr{H}_{\mathsf{S}}$, and indeed we can map states in $\mathscr{H}_{\mathsf{S}}$ one to one to states in $\check{\mathscr{H}}_g$ (see Sect. 9.3.4). With this mapping, there is a corresponding mapping of operators. Specifically, $\mathsf{S}^+_{t,t'} \to \mathsf{s}^+_{t,t'} \otimes \Phi_t^\dagger \Phi_{t'} \equiv \Phi_t^\dagger \mathsf{s}^+_{t,t'} \Phi_{t'}$ and $\mathsf{S}^z_{t,t'} \to \mathsf{s}^z_{t,t'} \otimes 1$, where $\mathsf{s}_{t,t'}$ acts in the copy of $\mathscr{H}_{\mathsf{S}}$ in $\mathscr{H}_g$. By construction, the operators on the right hand side of these transformations have the same matrix elements in $\check{\mathscr{H}}_g$ as the operators on the left hand side do in $\mathscr{H}_{\mathsf{S}}$. A thorougher discussion of the differences between the Hilbert spaces defined here is given in Sect. 9.3.4.

So, finally, with the replacements

$$\mathsf{S}^+_{t,t'} = \Phi_t^\dagger \mathsf{s}^+_{t,t'} \Phi_{t'} \quad \text{and} \quad \mathsf{S}^z_{t,t'} = \mathsf{s}^z_{t,t'} \tag{9.20}$$

the gauge constraint commutes with the Hamiltonian, and all the matrix elements of the original Hamiltonian are reproduced. We obtain:

$$
\begin{aligned}
H = \sum_{t\in \mathrm{I,II}} \frac{J_{zz}}{2} Q_t^2 - J_{\pm} \Bigg\{ & \sum_{t\in \mathrm{I}} \sum_{\mu,\nu\neq\mu} \Phi^{\dagger}_{t+\mathbf{e}_\mu} \Phi_{t+\mathbf{e}_\nu} \mathsf{S}^{-}_{t,t+\mathbf{e}_\mu} \mathsf{S}^{+}_{t,t+\mathbf{e}_\nu} \\
& + \sum_{t\in \mathrm{II}} \sum_{\mu,\nu\neq\mu} \Phi^{\dagger}_{t-\mathbf{e}_\mu} \Phi_{t-\mathbf{e}_\nu} \mathsf{S}^{+}_{t,t-\mathbf{e}_\mu} \mathsf{S}^{-}_{t,t-\mathbf{e}_\nu} \Bigg\} \\
- J_{z\pm} \Bigg\{ & \sum_{t\in \mathrm{I}} \sum_{\mu,\nu\neq\mu} \left(\gamma^{*}_{\mu\nu} \Phi^{\dagger}_{t} \Phi_{t+\mathbf{e}_\nu} \mathsf{S}^{z}_{t,t+\mathbf{e}_\mu} \mathsf{S}^{+}_{t,t+\mathbf{e}_\nu} + \mathrm{h.c.} \right) \\
& + \sum_{t\in \mathrm{II}} \sum_{\mu,\nu\neq\mu} \left(\gamma^{*}_{\mu\nu} \Phi^{\dagger}_{t-\mathbf{e}_\nu} \Phi_{t} \mathsf{S}^{z}_{t,t-\mathbf{e}_\mu} \mathsf{S}^{+}_{t,t-\mathbf{e}_\nu} + \mathrm{h.c.} \right) \Bigg\} \\
+ J_{\pm\pm} \Bigg\{ & \sum_{t\in \mathrm{I}} \sum_{\mu,\nu\neq\mu} \gamma_{\mu\nu} \Phi^{\dagger}_{t} \Phi^{\dagger}_{t+\mathbf{e}_\mu-\mathbf{e}_\nu} \Phi^{2}_{t+\mathbf{e}_\mu} \mathsf{S}^{+}_{t,t+\mathbf{e}_\mu} \mathsf{S}^{+}_{t+\mathbf{e}_\mu-\mathbf{e}_\nu,t+\mathbf{e}_\mu} + \mathrm{h.c.} \\
& + \sum_{t\in \mathrm{II}} \sum_{\mu,\nu\neq\mu} \gamma_{\mu\nu} \Phi^{\dagger}_{t-\mathbf{e}_\mu} \Phi^{\dagger}_{t-\mathbf{e}_\nu} \Phi^{2}_{t} \mathsf{S}^{+}_{t-\mathbf{e}_\mu,t} \mathsf{S}^{+}_{t-\mathbf{e}_\nu,t} + \mathrm{h.c.} \Bigg\} + \mathrm{const.},
\end{aligned}
\tag{9.21}
$$

where the $\mathbf{e}_\mu$ are the nearest-neighbor vectors of the dual diamond lattice. The Hamiltonian (9.21) thereby obtained is an *exact* rewriting of the original Hamiltonian expressed in terms of the spin variables, (9.1). The terms proportional to $J_{\pm}$ and $J_{z\pm}$ appear as spinons hopping in a fluctuating background. More precisely, $J_{\pm}$ introduces same-diamond-sublattice hopping, while $J_{z\pm}$ is the parameter for a "nearest-diamond-neighbor" hopping Hamiltonian. (Note that the mean field decoupling discussed in Sect. 9.3.2 will decouple the spinon and gauge field Hamiltonians, which will then be solved self-consistently.) The term proportional to $J_{\pm\pm}$ [8] introduces interactions *directly* between the spinons themselves.

We now make a number of important remarks. Parton constructions based on Schwinger bosons and Abrikosov fermions have been extensively studied [21]. The partons used here are different, and have the merit of a much more transparent physical interpretation. This is thanks to the degeneracy of the spin ice manifold and the fact that this construction has the spinons live at the centers of the tetrahedra. Moreover, when $J_{z\pm} = J_{\pm\pm} = 0$, the Hamiltonian (9.1) is (accidentally) spin-conserving. S^z is then a good quantum number, which the spinons can carry. Since a spin flip, i.e. a $\mathsf{S}^z = \pm 1$ "excitation," excites two spinons, and since the spinons can separate to an arbitrarily large distance in the deconfined phases, one may see each spinon as a $\mathsf{S}^z = \pm 1/2$ (i.e. "fractional") excitation. When $J_{z\pm}$ and/or $J_{\pm\pm}$ are non-zero, while this picture is valid in spirit, S^z is not conserved, and the spinons therefore do not rigorously carry $\mathsf{S}^z = \pm 1/2$. However, they are still "fractional" in the sense that a single spinon is "half" of what can be created by any local operator. It may be better to say that the spinons are non-local excitations.

This construction, while appearing natural for a number of reasons, is of course not unique, and one may well imagine that other parton constructions based on (9.1) will lead to quantum spin liquid phases in the phase diagram, which may be different in nature, or not, from those which we describe in the bulk of this chapter. In fact, a field theoretic classification of possible time-reversal symmetric $U(1)$ QSLs on the pyrochlore lattice exists and indicates the potential existence of six other QSL states which would require other parton constructions [22]. However, it is unclear whether any of these pertain to (9.1), or indeed in what, if any, microscopic situations they may arise.

Finally, we address why the electric particles do not appear explicitly like the magnetic particles described by Φ_t operators. This is fundamentally because the electric and magnetic particles are dual to one another, and have long-range statistical interactions, which makes it difficult to include both particles explicitly in the Hamiltonian. Nevertheless, they are necessarily present since the rewriting is exact. In these variables, as for the gauge-field-only Hamiltonians in (9.8) or (9.12), the electric charge is implicit as a non-local texture in the dual vector potential $\mathscr{A}$. For a crude intuition, one might think thus, given the correspondence in (9.20), of a texture in the x-y components of the spins (however in reality these spins are strongly fluctuating even in the absence of the electric particle).

9.3.2 Gauge Mean Field Theory

The usual Curie-Weiss mean field theory applied to spin systems is useful when the order parameter is a local moment. This assumes small fluctuations of the spins and the spins, directly, to provide a fairly good description of the system. In a quantum spin liquid, like that of quantum spin ice, such an approach is doomed to failure. Indeed, the spins are wildly fluctuating, and their expectation values are nowhere close to the right quantities to describe the system well. The exact rewriting above, however, can provide a good starting point to a mean field like treatment, where it is meaningful to perform a decoupling in the natural variables of the quantum spin liquid state.

So, using the formalism developed in the section above, we proceed to the following mean field decoupling,

$$\Phi^\dagger \Phi \, \mathsf{s}\,\mathsf{s} \to \Phi^\dagger \Phi \langle \mathsf{s} \rangle \langle \mathsf{s} \rangle + \langle \Phi^\dagger \Phi \rangle \mathsf{s} \langle \mathsf{s} \rangle + \langle \Phi^\dagger \Phi \rangle \langle \mathsf{s} \rangle \mathsf{s} - 2 \langle \Phi^\dagger \Phi \rangle \langle \mathsf{s} \rangle \langle \mathsf{s} \rangle, \tag{9.22}$$

and

$$\begin{aligned} &\Phi^\dagger \Phi^\dagger \Phi \, \Phi \, \mathsf{s}\,\mathsf{s} \to \langle \mathsf{s} \rangle \langle \mathsf{s} \rangle \\ &\times \left(\langle \Phi^\dagger \Phi^\dagger \rangle \Phi \Phi + \Phi^\dagger \Phi^\dagger \langle \Phi \Phi \rangle + \langle \Phi^\dagger \Phi \rangle \Phi^\dagger \Phi + \Phi^\dagger \Phi \langle \Phi^\dagger \Phi \rangle + \langle \Phi^\dagger \Phi \rangle \Phi^\dagger \Phi + \Phi^\dagger \Phi \langle \Phi^\dagger \Phi \rangle \right) \\ &+ \left(\langle \mathsf{s} \rangle \mathsf{s} + \mathsf{s} \langle \mathsf{s} \rangle \right) \left(\langle \Phi^\dagger \Phi^\dagger \rangle \langle \Phi \Phi \rangle + \langle \Phi^\dagger \Phi \rangle \langle \Phi^\dagger \Phi \rangle + \langle \Phi^\dagger \Phi \rangle \langle \Phi^\dagger \Phi \rangle \right) \\ &- 4 \langle \mathsf{s} \rangle \langle \mathsf{s} \rangle \langle \Phi^\dagger \Phi^\dagger \rangle \langle \Phi \Phi \rangle - 4 \langle \mathsf{s} \rangle \langle \mathsf{s} \rangle \langle \Phi^\dagger \Phi \rangle \langle \Phi^\dagger \Phi \rangle - 4 \langle \mathsf{s} \rangle \langle \mathsf{s} \rangle \langle \Phi^\dagger \Phi \rangle \langle \Phi^\dagger \Phi \rangle. \end{aligned} \tag{9.23}$$

The goal of this decoupling is to separate the gauge field s and particle Φ sectors, and reduce the mean field Hamiltonian to a sum of individual gauge spins $\mathsf{s}^{\mu}_{t,t'}$ each in its own self-consistent Zeeman field, and a quadratic Hamiltonian for the $\Phi_t^\dagger$, Φ_t and Q_t operators. Thus, at the mean field level, solutions are determined by the state of the gauge spin and spinon subsystems. In the former, the state is specified by the orientation of the gauge spins, which may be along the z axis, or normal to it, or at some angle. The latter spinon part, if written in terms of the fundamental φ_t operators, becomes a type of quantum XY model. Consequently we expect that it contains two types of states: a "paramagnet" in which $\langle \Phi_t \rangle = 0$, and an XY ordered state, in which $\langle \Phi_t \rangle \neq 0$. A third possibility, mentioned briefly below, is an intermediate "nematic" state in which $\langle \Phi_t \rangle = 0$ but $\langle \Phi_t^2 \rangle \neq 0$. Each combination of states in the spinon and gauge subsystems constitutes a possible phase of the system. We say *possible* phases because all combinations may not occur in the actual mean field solution, and because, since some of these quantities are not gauge invariant, their interpretation as order parameters is somewhat subtle. We will first discuss the solution, and then elucidate the meaning.

A technical complication arises because the mean field spinon part, while quadratic and decoupled from the gauge fields, is not in general exactly soluble because the Φ_t are not canonical fields. Rather, it is a quantum XY model containing cosine terms of the φ_t variables. Hence some further approximation, not related to the emergent gauge structure, is required to solve the spinon sector. The simplest approach comprises a spherical approximation [5] which converts Φ_t to fundamental fields at the cost of introducing a Lagrange multiplier λ to enforce $\langle \Phi_t^\dagger \Phi_t \rangle = 1$ on average. Other approaches are possible [23].

To solve the mean field problem, we resort to Ansätze. We focus on the situation where $J_\pm > 0$. In that case, by dint of the perturbative approach, we choose a zero "flux" solution on all the hexagonal plaquettes. (Conversely, the situation where $J_\pm < 0$ introduces complications due the requirement of a non-zero flux on hexagonal plaquettes. This issue is discussed in Sect. 9.6.) When $J_{\pm\pm} = 0$ we use:

$$\langle \mathsf{s}^-_\mu \rangle = \bar{\mathsf{s}} \cos\theta, \qquad \langle \mathsf{s}^z_\mu \rangle = \bar{\mathsf{s}}\, \varepsilon_\mu \sin\theta \quad \text{with} \quad \varepsilon = (1, 1, -1, -1). \tag{9.24}$$

At $T = 0$, $\bar{\mathsf{s}} = 1/2$, while at $T > 0$ we allow for $\bar{\mathsf{s}} \leq 1/2$. The latter Ansatz is meant to capture $\mathbf{Q} = \mathbf{0}$ ferromagnetic order with net moment along the $\langle 100 \rangle$ axis. Here there are three general cases: (i) $\theta = 0$, for which Ising component of the gauge spin vanishes $\langle \mathsf{s}^z \rangle = 0$; (ii) $0 < \theta < \pi/2$, for which both in-plane and Ising components are non-zero; and (iii) $\theta = \pi/2$, for which the gauge spin has zero transverse component. We note that $\mathsf{s}^z = \mathsf{S}^z$ is gauge invariant, so this component is a true order parameter in the usual sense, while $\mathsf{s}^\pm$ should really be interpreted as a gauge connection, and $\langle \mathsf{s}^\pm \rangle \neq 0$ in gMFT does not imply $\langle \mathsf{S}^\pm \rangle \neq 0$.

For each of these possibilities, we must self-consistently solve the spinon sector. One constraint is immediately apparent: if $\theta = \pi/2$ so that $\langle \mathsf{s}^\pm \rangle = 0$, then the spinon hopping vanishes, i.e. there is no exchange in the effective XY model. Clearly in this limit there is no XY magnetism, i.e. $\langle \Phi_t \rangle = \langle \Phi_t^2 \rangle = 0$. In fact, this type of solution is

Table 9.1 Order parameters for phases within gMFT. The last four columns are related to the Ansätze we give in the text. In particular, the ferromagnetic state chosen in (9.24), related to $\langle \mathsf{S}^z \rangle$ is one of the classical $\mathbf{Q} = 0$ spin ice states. The entries FM/FQ (ferromagnetic/ferroquadrupolar) and AFM/AFQ (antiferromagnetic/antiferroquadrupolar) describe the physical meaning of the broken symmetries in the Kramers/non-Kramers cases. TSL stands for Thermal Spin Liquid. Note that $\mathsf{S}^z = \mathsf{s}^z$

	$\langle \Phi \rangle$	$\langle \Phi\Phi \rangle$	$\langle \mathsf{s}^z \rangle$	$\langle \mathsf{s}^- \rangle$	$\langle \mathsf{S}^z \rangle$	$\langle \mathsf{S}^- \rangle$
$U(1)$ QSL	0	0	0	$\neq 0$	0	0
Coulomb FM	0	0	$\neq 0$	$\neq 0$	$\neq 0$	$\neq 0$
$\mathbb{Z}_2$ QSL	0	$\neq 0$	0	$\neq 0$	0	0
FM/FQ	$\neq 0$	$\neq 0$	$\neq 0$	$\neq 0$	$\neq 0$	$\neq 0$
AFM/AFQ	$\neq 0$	$\neq 0$	0	$\neq 0$	0	$\neq 0$
Confined	0	0	$\neq 0$	0	$\neq 0$	0
TSL	0	0	0	0	0	0

never obtained at zero temperature in the nearest-neighbor model within gMFT, but it would occur with additional interactions such as for example next-nearest-neighbor Ising exchange. Combining these possibilities for the gauge sector with those for the spinons mentioned above, we arrive at a set of phases summarized in Table 9.1.

We are now armed to solve the gMFT. There are in fact two possible approaches. One consists in solving self-consistent equations, choosing the lowest-energy solution, when there are several, and the other is to minimize a *variational* energy. Depending on the details, one approach might be simpler than another.

Taking the self-consistent route for $J_{\pm\pm} = 0$ and the Ansatz (9.24) at $T = 0$, one obtains self-consistent equations on $\langle \Phi_t^\dagger \Phi_t \rangle$, $|\mathsf{h}^z_{\mathrm{eff},\mu}|$, and $|\mathsf{h}^-_{\mathrm{eff},\mu}|$, where $\mathsf{h}^\nu_{\mathrm{eff},\mu}$ are the effective mean fields which act on the "spins" s^ν. These equations allow to solve for λ, θ and a parameter ρ, which, when nonzero, signals $\langle \Phi \rangle \neq 0$. Because there may exist several solutions to the self-consistency equations with different energies, the energy must be calculated for each one of them. The mean field rules for $J_{\pm\pm} = 0$, (9.22), yield:

$$H^{\mathrm{MF}} = H_\Phi^{\mathrm{MF}} + H_\mathsf{s}^{\mathrm{MF}} - E_{\mathrm{MF}}. \tag{9.25}$$

The energy E_{MF} is simply given by the constant term in (9.22). The energies from the spinons $E_\Phi = \langle H_\Phi^{\mathrm{MF}} \rangle$ and the s fields $E_\mathsf{s} = \langle H_\mathsf{s}^{\mathrm{MF}} \rangle$ are given by:

$$E_\Phi = \int_\mathbf{k} (\omega_\mathbf{k}^+ + \omega_\mathbf{k}^-) - 2N_{u.c.}\lambda, \qquad E_\mathsf{s} = -\frac{N_{u.c.}}{2} \sum_\mu \sqrt{(\mathsf{h}^z_{\mathrm{eff},\mu})^2 + |\mathsf{h}^-_{\mathrm{eff},\mu}|^2}, \tag{9.26}$$

where $\omega_\mathbf{k}^\pm$ are the spinon dispersion relations. Another calculation for the energy consists in a "variational" formulation. Then, one looks at $\langle H - H_0 \rangle_0$ ($F_v = F_0 + \langle H - H_0 \rangle_0$ at finite temperature) where 0 denotes a trial wavefunction (taken here to be the mean field wavefunction).

9.3.3 Phases of gMFT and Their Interpretation

The result of the gMFT solution is the assignment of one of the entries of Table 9.1 to each set of physical parameters, along with of course various quantitative results. Now we discuss the interpretation of these solutions. The most obvious quantity is $\langle \mathsf{s}^z_t \rangle$, which is gauge invariant and equal to the local spin expectation value. If this is non-zero, the spins have some Ising order and time-reversal symmetry is broken. This, however, does not address the entanglement and emergent gauge structure of the phase.

First let us consider the states in which the spinon sector is fully gapped, i.e. $\langle \Phi_t \rangle = \langle \Phi_t^2 \rangle = 0$. This corresponds to the situation in the perturbative limit discussed in Sect. 9.2, where the ground state is in the spin ice sector. Then the key distinguishing feature is whether $\langle \mathsf{s}^\pm_t \rangle$ is zero or non-zero. In the actual gMFT solution, we always find it to be non-vanishing, i.e. $\theta < \pi/2$. What is the interpretation?

The non-vanishing $\langle \mathsf{s}^\pm \rangle$ may seem confusing at two levels. First, as mentioned above, $\mathsf{s}^\pm$ acts as a gauge connection, and Elitzur's theorem imposes that local gauge invariance cannot be spontaneously broken [19], so that a non-zero expectation value may seem to contradict the absence of gauge symmetry breaking in the Coulomb phases. Second, it might seem to immediately give a nonzero expectation value to the spins $\langle \mathsf{S}^\pm \rangle$. The first concern in fact appeared in the early days of the application of mean field approximations to gauge theories and was soon resolved by the realization that ascribing a non-zero value to the expectation value of the gauge field corresponded to a gauge-fixing choice, leaving all gauge-invariant quantities unmodified [24, 25]. In fact, $\langle \mathsf{s}^\pm \rangle \neq 0$ is the signature (when $\langle \Phi_t \rangle = \langle \Phi_t^2 \rangle = 0$ as assumed) of the deconfined Coulomb phase. At the mean field level, we can see that $\langle \mathsf{s}^\pm \rangle \neq 0$ is necessary for the spinons to be able to propagate, which is consistent with the basic property of the Coulomb phase that magnetically charged quasiparticles exist. Furthermore, on including quadratic phase fluctuations around the uniform saddle point for $\langle \mathsf{s}^\pm \rangle$, the gapless linear photon mode is recovered. Specifically, if one replaces $\mathsf{s}^\pm_{tt'} \to \overline{\mathsf{s}} \cos\theta e^{\pm i \mathscr{A}_{tt'}}$, and integrates out the spinons to quadratic order in $\mathscr{A}$ in a path integral formulation, one obtains a leading Maxwell action, proportional to $(\varepsilon_{\mu\nu\lambda}\partial_\nu \mathscr{A}_\lambda)^2$, at low energy.

Returning to the second issue, the spin expectation value may or may not be non-zero, as via (9.20), $\mathsf{s}^\pm$ and $\mathsf{S}^\pm$ are not equal. In fact, in gMFT two Coulombic phases arise, one with $\langle \mathsf{s}^z \rangle = 0$ ($\theta = 0$), corresponding to the QSL, and another with $0 < \langle \mathsf{s}^\pm \rangle < 1/2$ ($0 < \theta < \pi/2$), which we denote the Coulomb ferromagnet . In the latter, indeed $\langle \mathsf{S}^\pm \rangle \neq 0$ [23], but as we discuss in Sect. 9.3.4.3, this does not destroy or fundamentally modify the deconfined (entangled) nature of the associated phase.

Having established the specification of the Coulomb phases in gMFT, we can ask: what would it mean if, instead, $\langle \mathsf{s}^\pm \rangle = 0$ (i.e. $\theta = \pi/2$)? In that case, the phase of $\mathsf{s}^\pm$ is not well-defined, and so there is no low energy gauge field. Moreover, the spinons are unable to propagate and cannot be coherent quasiparticles. Thus we are led to interpret $\langle \mathsf{s}^\pm \rangle = 0$ as the signature of the confined phase within gMFT. This indeed occurs if we add further neighbor Ising interactions which classically break

the frustration of the spin ice manifold. As explained in Sect. 9.2.4, the confined phase may be thought of as a condensation of the emergent electric charges, though this is not evident without a duality transformation.

Now we turn to the "order parameters" in the spinon sector. Unlike the electric charges, the magnetic charges of the Coulombic phases are explicit: they *are* the spinons. Hence gMFT can directly describe condensates of magnetic charges. Due to the duality between electric and magnetic charges and fields, the effect of such magnetic condensation is directly analogous to electric condensation: it too destroys the emergent U(1) gauge structure of the Coulomb phases. Condensation of charged particles is known as a *Higgs* transition. The bosonic spinon theory developed here proves particularly convenient to describe Higgs transitions. Condensation of the "fundamental" Higgs field $\langle \Phi_t \rangle \neq 0$ fully destroys the gauge structure. As in a superconductor, a gap is induced for the gauge field $\mathscr{A}$ (i.e. for the photon), and the consequent Meissner effect implies the confinement of emergent electric fields into lines with a non-zero line tension, removing the electric charges as quasiparticles. The magnetic charge is no longer a good quantum number as the Higgs condensation makes it uncertain. Hence neither spinons nor electric charges nor photon remain in the spectrum. Thus we may correctly regard any state with $\langle \Phi_t \rangle \neq 0$ as a conventional phase. We will show in Sect. 9.3.4.4 that the corresponding wavefunction is short range entangled, i.e. essentially a product state. Note that the Higgs *transition* itself occurs at the point at which the spinon gap vanishes (if the transition is a second order one), so that at the mean field level both gapless spinons and a gapless gauge field are present.

When $J_{\pm\pm} \neq 0$, one must also allow for the spinons to condense in *pairs*, $\langle \Phi\Phi \rangle \neq 0$, yielding a $\mathbb{Z}_2$ QSL when $\langle \Phi \rangle = 0$ [26], and again a conventional phase for $\langle \Phi \rangle \neq 0$. The $\mathbb{Z}_2$ QSL is a distinct QSL for which the magnetic charge is not a good quantum number but its *parity* remains well-defined. It can rightly be considered a *topological phase*: it hosts gapped fractional excitations and supports non-zero topological entanglement entropy, and is fully gapped [27–29]. However, while such a solution is a priori allowed in gMFT, in the phase space explored so far, it was not found to be realized as a ground state.

Additional details do not distinguish between conventional and deconfined phases, but, rather, aspects of symmetry. A summary is in Table 9.1. They depend somewhat on the Ansätze chosen, and the latter should be motivated by physical arguments relative to the magnitudes of the couplings. Concretely, when $J_{\pm\pm} = 0$, the "angle" θ acts as an order parameter distinguishing between phases with (for $\theta > 0$) and without (for $\theta = 0$) a local polarization along the local z axes (which leads to a global polarization along one of the $\langle 100 \rangle$ axes), induced by a nonzero $J_{z\pm}$. The state with $\theta = 0$ and $\langle \Phi_t \rangle \neq 0$ describes antiferromagnet planar ordering of pseudospins $\mathsf{S}_i^{\pm}$: ψ_2 and ψ_3 states in the nomenclature of [12], denoted AFM here. The state with $\theta > 0$ is a canted ferromagnetic (FM) state. When $J_{z\pm} = 0$ but $J_{\pm\pm} \neq 0$, the ground states are found by minimizing a variational energy, which yields, throughout the phase diagram the same $U(1)$ Coulombic QSL, discussed throughout this paper, and two conventional ordered phases. These states correspond to FM and the AFM

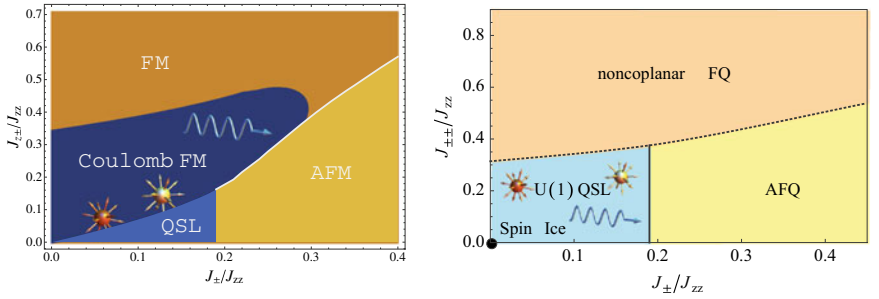

Fig. 9.4 gMFT phase diagrams in the $J_{\pm}/J_{zz} - J_{z\pm}/J_{zz}$ (left [5, 30]) and $J_{\pm}/J_{zz} - J_{\pm\pm}/J_{zz}$ (right [8]) planes at $J_{\pm\pm} = 0$ and $J_{z\pm} = 0$, respectively. Reprinted from [8, 30] with permission from the American Physical Society

states of the pseudospins. With $J_{z\pm} = 0$ there is no canting, and the ferromagnetism due to $J_{\pm\pm}$ is purely in-plane.

The physical meaning of these states is quite distinct in the case of dipolar Kramers doublets and magnetic non-Kramers doublets. In the former case, the magnetic moment is proportional to the pseudospin, and the above interpretation is literal. For non-Kramers magnetic doublets, the same model holds except that $J_{z\pm} = 0$ is required by symmetry. However, the in-plane pseudospin components describe not magnetic moments but quadrupole moments. Hence these states describe "ferro-quadrupolar" (FQ) and "antiferroquadrupolar" (AFQ) phases [8].

Finally, we remark that at non-zero temperature, a first-order phase transition to a thermal spin liquid (TSL) state, akin to classical spin ice, is found within gMFT [30]. At the transition, entropy is released, and in this thermal state, coherent hopping of the spinons is entirely suppressed, $\overline{\mathsf{s}} = 0$. There is no sharp distinction between the Coulomb QSL and high temperature TSL at non-zero temperature, so there is no need for such a phase transition beyond mean field theory. Numerical studies of the XXZ model [20] suggest the transition itself is an artifact of gMFT, though a rapid crossover may be considered a remnant of it (Fig. 9.4).

9.3.4 Wavefunction

It is interesting to construct a wavefunction which corresponds to the gMFT approximation. This is helpful not only in understanding the physical meaning of gMFT, but for comparison to more standard variational wavefunctions used to describe other highly entangled spin systems. Moreover, a wavefunction can be a useful jumping off point for numerical investigations.

9.3.4.1 Three Hilbert Spaces

It is amusing to compare the Hilbert spaces of three Hamiltonians: the original quantum spin ice model, (9.1), the effective model near the classical spin ice point, (9.3), and the slave spinon Hamiltonian in (9.21). In the first, the Hilbert space $\mathscr{H}$ is that of the original pseudo-spin 1/2 problem, and has dimension 2^N, where N is the number of pyrochlore sites. In the effective Hamiltonian of (9.3), we have projected to the 2in-2out manifold, which has a smaller dimension, approximately 1.22^N. In the slave spinon approach, we have *enlarged* the Hilbert space to $\mathscr{H}_g$ with additional boson states, on top of the spin-1/2 states of the original model—unless we truncate the Hilbert space of the bosons, the third model has an infinite dimensional Hilbert space! A physical wavefunction for the spin Hamiltonian must live in the first of these spaces.

To obtain this from the gMFT Hamiltonian, we must apply the gauge constraints, which define a projection. In particular, we require that the constraint in (9.7) be imposed for each t, with Q_t equal to the spinon charge on the diamond site t. It is easy to confuse the physical spins S_i^μ and the "small" spins s_i^μ which play the role of gauge fields. These seem to be almost the same! Understanding how to relate them at the wavefunction level helps to clarify the difference.

The slave spinon formulation is really a mapping between the original spin Hilbert space $\mathscr{H}$ and a *subspace* $\check{\mathscr{H}}_g$ of the larger $\mathscr{H}_g$ one of the small spins plus spinons. We can make this completely concrete by defining an operator M which maps a physical state in $\mathscr{H}$ to one in $\check{\mathscr{H}}_g$:

$$M = \sum_{\{\sigma_i = \pm 1/2\}} \left(\otimes_t |Q_t = \varepsilon_t \sum_{t' \in t} \sigma_{i(t,t')} \rangle \right) |\{\mathsf{s}_i^z = \sigma_i\}\rangle\langle\{\mathsf{S}_i^z = \sigma_i\}|. \tag{9.27}$$

Similarly, we can define the "left inverse" M^{-1}, which takes a state in $\check{\mathscr{H}}_g$ into a physical one in $\mathscr{H}$:

$$M^{-1} = \sum_{\{\sigma_i = \pm 1/2\}} |\{\mathsf{S}_i^z = \sigma_i\}\rangle\langle\{\mathsf{s}_i^z = \sigma_i\}| \left(\otimes_t \langle Q_t = \varepsilon_t \sum_{t' \in t} \sigma_{i(t,t')}| \right). \tag{9.28}$$

These operators have the property that, $M^{-1}M = 1$ acts as the identify in $\mathscr{H}$. However, $MM^{-1} = 1$ only within $\mathscr{H}_g$, not within $\mathscr{H}_g$. Actually, MM^{-1} is the projector to $\check{\mathscr{H}}_g$ within $\mathscr{H}_g$.

The operator M^{-1} is what we need to produce a physical spin state from a gMFT calculation, that is

$$|\psi\rangle_{\text{var}} = M^{-1}|\Psi\rangle_{\text{gMFT}}, \tag{9.29}$$

where $|\psi\rangle_{\text{var}}$ is the desired physical—variational – wavefunction. Let us consider what the wavefunctions look like in the different phases obtained by gMFT.

9.3.4.2 Coulomb QSL Phase

First consider the most interesting case of the Coulombic QSL phase. There we took the "spins" s_i to be fully polarized in the X direction. That is $|\Psi\rangle_{\text{gMFT}} = |\Psi\rangle_{\text{spinon}} \otimes |\Psi\rangle_{\mathsf{s}}$, with

$$|\Psi\rangle_{\mathsf{s}} = \otimes_i |\mathsf{s}_i^x = \frac{1}{2}\rangle. \tag{9.30}$$

To evaluate the action of M^{-1}, we need to express this in the s_i^z basis, using $|\mathsf{s}_i^x = \frac{1}{2}\rangle = \frac{1}{\sqrt{2}}(|\mathsf{s}_i^z = +\frac{1}{2}\rangle + |\mathsf{s}_i^z = -\frac{1}{2}\rangle)$:

$$|\Psi\rangle_{\mathsf{s}} = 2^{-N/2} \sum_{\{s_i = \pm\frac{1}{2}\}} |\{\mathsf{s}_i^z = s_i\}\rangle, \tag{9.31}$$

which is an equal-weight superposition of all possible Ising spin states. Next, we need the spinon wavefunction, which in general is more non-trivial. Without further approximations (i.e. the spherical model approximation used in some calculations), this is the ground state of a quantum XY model, in its paramagnetic "Mott insulating" state. Deep in the Mott phase, this is just a product state, $|\Psi\rangle_{\text{spinon}} \approx \otimes_t |Q_t = 0\rangle$, i.e. the trivial spinon vacuum. However, as the spinon hopping increases, the ground state of the XY model increasingly mixes in virtual pairs of *nearby* spinons and anti-spinons. A reasonable approximate wavefunction capturing this is the Jastrow form (recall that by construction $[\varphi_t, Q_t] = i$, see Sect. 9.3)

$$|\Psi\rangle_{\text{spinon}} \approx \exp\left[\sum_{t,t'} v_{t,t'} \cos(\varphi_t - \varphi_{t'})\right] \otimes_t |Q_t = 0\rangle, \tag{9.32}$$

where $v_{t,t'}$ are amplitudes which: (1) are translationally invariant, (2) decay exponentially for large $|t - t'|$, and (3) are non-zero only when t and t' are on the same sublattice. The first condition is a consequence of symmetry, the second is due to the gap in the spinon excitation spectrum, and the latter condition arises because in the QSL, the inter-sublattice hopping vanishes at the mean field level. This in turn implies that the total charge on each sublattice separately *exactly vanishes*, i.e. $\sum_{t\in A} Q_t = 0$ exactly.

This is a good wavefunction when the $v_{t,t'}$ are not too large. How do we use it? Again, we should express (9.32) in the same basis as M^{-1}, in this case the spinon number Q_t basis. Essentially the exponential in (9.32) acts to create oppositely charged pairs on sites t, t' connected by $v_{t,t'}$, with small amplitude $v_{t,t'}$. So we can think that $|\Psi\rangle_{\text{spinon}}$ is just the $Q_t = 0$ vacuum plus a sprinkling of superimposed randomly placed dipoles with $Q_t = -Q_{t'} = \pm 1$ on nearby t, t' on the same sublattice.

Now we form the product of this state with the spin wavefunction $|\Psi\rangle_{\mathsf{s}}$ in (9.31), and act on it with M^{-1}. The result is that we copy every configuration of s_i^z spins to the physical S_i^z spins with an amplitude given by calculating the charge Q_t of that spin configuration according to (9.7), and taking the corresponding amplitude

from $|\Psi\rangle_{\text{spinon}}$. For the "deep Mott" limit $v_{t,t'} = 0$, this amounts to a projection to the spin ice manifold. The result is that this "deep Mott" wavefunction for the QSL is just a uniform sum over all the ice rule states. This is the exact ground state of the Rokhsar-Kivelson point model discussed in Chap. 10.

More generally, when $v_{t,t'} \neq 0$, violations of the ice rules are allowed, with reduced weight, but only when the defects—the "spinons" or "monopoles"—arise in neutral nearby pairs on the same sublattice. Physical spin configurations therefore occur in $|\psi\rangle_{\text{var}}$ for which the associated monopole charges are non-zero, provided those charges form nearby dipoles independently on each sublattice. It is possible to construct wavefunctions of this type and use them variationally [31]. Most importantly, the fact that only allowed configurations are those with *bound* dipoles of Q_t charges on each sublattice means that the wavefunction obtained by flipping a single spin, $\mathsf{S}_i^+|\psi\rangle_{\text{var}}$ is necessarily orthogonal to $|\psi\rangle_{\text{var}}$. This is because the action of S_i^+ creates a state with $\sum_{t\in A} Q_t = 1$. Moreover, the state $|\psi\rangle_{\text{var}}$ is obviously invariant under $\mathsf{S}_i^z \to -\mathsf{S}_i^z$, and together we see that

$$ {}_{\text{var}}\langle\psi|\, \mathsf{S}_i^\mu |\psi\rangle_{\text{var}} = 0, \tag{9.33}$$

as expected in a fully disordered QSL state.

9.3.4.3 Coulomb Ferromagnet Phase

Let us now consider the modification to the wavefunction in the Coulomb ferromagnet state. There are two modifications: the spins s_i are now polarized at an angle in the X-Z plane, and, consequently, the spinons now have a non-zero amplitude to hop between opposite sublattices. The former leads to a modified "spin" wavefunction (c.f. (9.31))

$$|\Psi\rangle_{\mathsf{s}} \propto 2^{-N/2} \sum_{\{s_i=\pm\frac{1}{2}\}} \prod_i \sqrt{1+\eta_i s_i}\,|\{\mathsf{s}_i^z = s_i\}\rangle, \tag{9.34}$$

where $\eta_i = \pm\eta$, with the sign depending upon the sublattice of the site i, and $0 < \eta < 1$. The limit $\eta \to 0$ recovers the QSL phase, while increasing η introduces a preference for up (down) spins on site i when η_i is positive (negative).

In the Coulomb ferromagnet phase, the spinons remain gapped, so that a wavefunction of the form of (9.32) is still a good approximation. However, the non-zero amplitude for spinon hopping between different sublattices means that the restriction that $v_{t,t'} = 0$ when t, t' are on different sublattices should be lifted. Consequently, the physical wavefunction now includes terms in which dipoles form across the two sublattices, for example with a positive and negative charge on neighboring tetrahedra. The net charge on each sublattice thereby no longer exactly vanishes, and indeed is uncertain.

From the point of view of entanglement and gauge theory, none of these changes are truly significant. The variational wavefunction $|\psi\rangle_{\text{var}}$ is still highly entangled,

and the fluctuations of monopolar charges are very small on long scales. In this sense it retains the "Coulombic" nature of the QSL phase. However, the modifications to the wavefunction alter its symmetry completely. The asymmetry between up and down spins and the violation of the sublattice charge conservation means that both S_i^z and $\mathsf{S}_i^{\pm}$ develop non-zero expectation values. While $\langle \mathsf{S}_i^z \rangle \neq 0$ was pointed out already in [5], the fact that $\langle \mathsf{S}_i^{\pm} \rangle \neq 0$ in the Coulomb ferromagnet was noticed only recently [23].

9.3.4.4 Higgs Phases: "XY" Ferromagnet and Antiferromagnet

We now consider the "Higgs" phases in the gMFT phase diagram, in which spinons have condensed. The wavefunction $|\Psi\rangle_{\mathsf{s}}$ has the same form as in the Coulomb ferromagnet above. The difference is in the spinon wavefunction, which now must be that of an XY ordered phase. That is, we should take a wavefunction $|\Psi\rangle_{\text{spinon}}$ such that

$$ {}_{\text{spinon}}\langle \Psi | \ \Phi_t | \Psi \rangle_{\text{spinon}} \neq 0. \tag{9.35}$$

This means that states in which the charge configuration differs by $\Delta Q_t = \pm 1$ on a single tetrahedron must be contained in $|\Psi\rangle_{\text{spinon}}$, when expressed in the charge basis. Contrary to the Mott insulating spinon wavefunction, this "superfluid" spinon wavefunction contains therefore isolated spinon/monopole charges, not just tightly bound dipoles.

It is instructive to consider the extreme limit (opposite to the deep Mott limit in Sect. 9.3.4.2) of an ideal superfluid. This is the limit of the rotor model as $J_{zz} \to 0$, and the phase φ_t becomes a definite variable. The spinon hopping prefers equal values of φ_t on all diamond sites t, so

$$ |\Psi\rangle_{\text{spinon}}^{\text{ideal sf}} = \otimes_t |\varphi_t = 0\rangle, \tag{9.36}$$

where we chose the global phase $\varphi = 0$ arbitrarily. Expressing this in the Q_t basis, we have

$$ |\Psi\rangle_{\text{spinon}}^{\text{ideal sf}} = \sum_{\{n_t\} \in \mathbb{Z}} \otimes_t |Q_t = n_t\rangle. \tag{9.37}$$

Here all Q_t configurations have equal weight, and so, acting with M^{-1}, one sees that the state of the physical spins is identical to that of the gauge spins s_t in this limit. It is as though, in the gMFT, we replace $\Phi_t \to 1$ everywhere.

9.4 Comparison of Classical and Quantum Spin Ice

Some of the physics of quantum spin ice seems very similar to its classical counterpart. Obviously, in the perturbative limit discussed in Sect. 9.1.2, the low energy physics of QSI can be understood entirely in the two-in-two-out manifold of classical

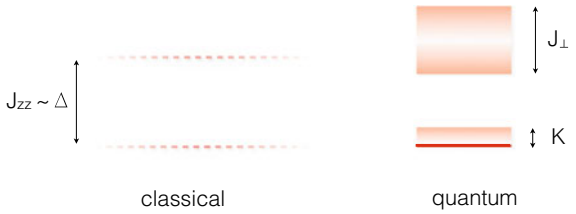

Fig. 9.5 Difference in the structure of energy levels in classical and quantum spin ice

spin ice. Going further, the emergent magnetic fields and monopoles, which feature throughout the discussion of classical spin ice, appear very close to the emergent gauge theory of the Coulomb QSL (and Coulomb ferromagnet). In this section we will try to clarify the similarities and differences.

A basic difference is in the structure of energy levels, as shown in Fig. 9.5. In ideal models of classical spin ice, say the nearest-neighbor spin ice model with coupling J_{zz}, the energy depends *only* upon the net spin on each tetrahedron. Thus there is an extensively degenerate set of ground states, and additional highly degenerate "monopolar" states at energy J_{zz} and above. It has been argued that this remains a good approximation for dipolar spin ice [32, 33] (but see below). In QSI, there is no extensive degeneracy of ground or excited states. Very generally, large ground state degeneracies are forbidden by level repulsion of quantum mechanics, which dictates that many more parameters must be tuned to achieve degeneracies quantum mechanically than classically. The situation *closest* to classical spin ice in QSI is the QSL in the perturbative regime as discussed in Sect. 9.1.2. In this case, the classically degenerate spin ice ground states are broadening into a "band" with characteristic energy $K \ll J_{zz}$. These correspond to the excitations of electric and magnetic fields of the emergent gauge theory. Magnetic monopolar states form additional bands beginning at around J_{zz}, and these states are more highly dispersive (of order $J_\pm$ rather than K) than the electromagnetic field states. When temperature is lowered within the low energy band, $k_B T \ll K$, the entropy vanishes as $S(T) \sim T^3$.

The phase structure of classical and quantum spin ice is quite different. The Coulomb behavior of classical spin ice is *not* a phase, in the thermodynamic sense: on increasing temperature, the Coulomb regime crosses over smoothly to a trivial paramagnet. Physically, this is because the spin ice constraint is never perfectly imposed: though monopoles have a non-zero energy cost Δ (=J_{zz} in the nearest-neighbor model), they always exist at a non-zero thermal activated density for any non-zero temperature, and at a length scale beyond their typical separation, properties of spin ice are qualitatively those of a usual paramagnet. We cannot properly take classical spin ice to $T = 0$, as the ground state is not defined due to degeneracy. QSI has a proper $T = 0$ ground state, and the Coulomb QSL is a distinct phase of matter at $T = 0$. A non-zero gap Δ for monopoles is sufficient to ensure that there are no unbound monopoles (spinons) in the QSL ground state, only virtual bound dipoles. A more formal view of this is that the quantum problem is described by an imaginary time partition function in $3 + 1$ dimensions with a length of the imaginary time τ direction equal to $\beta = \hbar / k_B T$. In this problem the monopoles become lines in

space-time, and an unbound monopole exists for the full τ interval and thereby has an *action* proportional to β which diverges at $T = 0$. Small finite loops of the monopole world-lines describe virtual dipole fluctuations which do not disrupt the Coulomb phase. The latter being a distinct phase, a quantum phase transition *unavoidably* occurs on tuning from the QSL to any trivial ordered state by changing exchange parameters, applying a magnetic field, etc.

If we do insist on taking the $T \to 0$ limit of classical spin ice (strictly $T = 0$ is not defined), then we see that it is extremely fine-tuned, even at the classical level. An arbitrarily weak generic additional exchange interaction, for example between second or third neighbor spins, splits the degeneracy of the two-in-two-out manifold, and immediately orders the system at low enough temperature. Indeed, it was shown long ago that this was the case for the physical dipolar interaction [34]. This ordering has not been widely observed, presumably because spin ice tends to fall out of equilibrium before order can set in. The very low energy difference between spin ice states and the very slow intrinsic timescale of spin dynamics in the classical spin ice materials makes equilibration difficult. Recent experiments have nonetheless observed quenching of the magnetic entropy below the spin ice value in $Dy_2Ti_2O_7$ [35]. Because of the lack of degeneracy in quantum spin ice, and the substantial off-diagonal terms in the Hamiltonian, the dynamics in QSI is much faster, and much less susceptible to disequilibrium.

The Coulomb QSL is a highly entangled, coherent quantum ground state. As such, it supports additional emergent excitations not found in classical spin ice, beyond the spin ice monopoles, which are the spinons of the QSL. Most spectacularly, there are gapless emergent photons, discussed extensively in Chaps. 10 and 11, with the properties of real photons but ultimately composed entirely of microscopic spins. Unlike the more familiar Goldstone modes of ordered magnetic systems with continuous symmetries, the photon cannot be gapped by any small perturbation: it is a robust feature of the Coulombic phases, and is removed at low energy only if a transition occurs to an entirely different ground state. Furthermore, the QSL supports a "dual" electric monopole which behaves similarly to the spinon but is associated with transverse spin configurations rather than Ising ones—see Sect. 9.2.3. The existence of a particle that acts like an electric charge in a purely magnetic system (i.e. microscopically composed of spins) is remarkable, and perhaps it is even more striking than the photon. It is a purely quantum object, not present at all in classical spin ice, arising solely due to the uncertainty relation between electric and magnetic variables.

Although spinons/monopoles occur both in classical and quantum spin ice, there is an important difference between them. In classical spin ice, a monopole is not a "state" of the system. Consistent with any single assignment of monopolar charges are many spin micro-states. Motion of a monopole changes these states. For example, if we consider a classical spin ice state with a single monopole in, we can move that monopole in a loop by a certain series of spin flips, and return the monopole to the original position. Although the monopole charges of the final and original

configuration are identical, the final state is different from the original. In this sense *the monopole in classical spin ice is not a quasiparticle*. The set of flipped spins left behind from the monopole's motion is called a "string", and this string is observable in principle. The change of the spin background with the monopole's motion means that in ordinary spin ice it is not possible to form superpositions of monopoles over extended spatial regions, which would require a superposition of an extensive number of degenerate spins. Another consequence of the degenerate spin background is that the monopole is easily confined by perturbations. As remarked earlier, arbitrarily small perturbations should order spin ice at low temperature. This lifts the degeneracy of the spin background, and once the order has set in, the string acquires a non-zero free energy cost per unit length.

By contrast, a monopole or spinon in the QSL phase of spin ice *is* a quasiparticle. The analog of the spin micro-states in classical spin ice is the background magnetic field of the spinon. However there is a unique magnetic field state of the spinon in its ground state, so this does not bring any degeneracy. Indeed, the spinon has essentially an identical description to that of an electron in vacuum, which is clearly a "quasiparticle". What about the "string"? To move the monopole still requires acting with spin flip operators over a line along the path of motion: a string *operator*. So why does a string operator not disrupt the state of the system? The answer is that the massive superposition of quantum spin ice is essential. Since the low energy states are already superpositions of all the ice rule states, flipping spins consistent with the ice rules simply reshuffles the states within the superposition, and does not actually change the wavefunction, except near the ends of the string operator, where of course it *should* be disrupted if the monopole is to move. Because the QSL is a robust quantum phase of matter, the monopole is also a robust quasiparticle.

What the quantum monopole has in common with the classical one is that it is non-local: it cannot be created one at a time by any local operator. In the classical case, this may be considered due to the "string". In the quantum case, it is due to the magnetic field of the monopole. To create a monopole, one must also create its field configuration, which is extended around it. Any other phenomena related to the non-locality of the monopole can be understood, just as for an electron, by thinking of the physics of the surrounding (in this case emergent) electro-magnetic field. For example, like an electron, an accelerating monopole would be expected to radiate (emergent) photons. One could imagine somehow separating a finite density of positive monopoles/spinons on one side of the sample from an equal density of negative monopoles/spinons on the other. This is like a (dual) capacitor, and would produce a net magnetic field between the two sides. If the density is low, however, so that the QSL is weakly perturbed in the interior, then the field will be uniform, i.e. it will not be resolved into any sort of string-like observable. This is all perfectly consistent with regarding the monopole as a quasiparticle, and the strings as unobservable: there are magnetic (and electric) fields but no strings in the QSL.

9.5 Observing Quantum Spin Ice

The construction has at least provided us with the right class of materials where the phenomena described here may appear. We will not discuss specific materials here, leaving that for Chap. 12. If we have a candidate material in hand, how can we tell whether its ground state is one of the quantum spin liquid states of the phase diagram? This same question arises in all situations where a material is identified as a "possible quantum spin liquid candidate." In the case of quantum spin ice, one is in the unique situation where the quantum spin liquid candidate is theoretically completely understood, with a well-identified (and general) Hamiltonian and many specific predictions as regards the expected experimental signatures. Moreover, in the class of systems where one looks for quantum spin ice behavior, high field neutron scattering experiments on single crystals are possible and allow for a complete, *quantitative* and precise determination of the Hamiltonian [2, 4].

What are these experimental signatures? Certainly, a common hallmark of quantum spin liquids is the fractional excitations they support, in the case of quantum spin ice, the spinons/magnetic monopoles and electric charges. However, precisely because of their fractional nature, sharp signals in conventional probes are not readily obtained. Here, while the spinons nicely couple directly to neutrons, only diffuse scattering is expected, whose origin is tricky to trace back precisely to spinons. More quantitative modeling, specific to a candidate material and its parameters, would be necessary to make such a case. The quantum spin liquids in quantum spin ice, however, also feature a photon, which, despite tracing back directly to a gauge field, couples nevertheless directly to neutrons as well. The corresponding structure factor $\langle \mathsf{S}^z_{-\mathbf{k}-\omega} \mathsf{S}^z_{\mathbf{k}\omega} \rangle$ may be readily calculated upon including fluctuations beyond mean field theory [5]. It presents a sharp signal for potential experiments, though it is certainly challenging due to the low energy required and small spectral weight expected from theory. The photon, however, provides an additional feature: because it is a linear mode near $\mathbf{q} = \mathbf{0}$, it contributes (in 3d) by a $B_{phot} T^3$ term in the specific heat. This temperature dependence is identical to that of phonons, but a quick estimation of its coefficient B shows that it is expected to be a thousand times larger than B_{phonon} [5]. While this should in principle provide convincing evidence of the existence of a photon mode, the quantum spin liquid phases only survive at very low temperatures, a condition in which it is often challenging to perform accurate specific heat measurements. In general many other low energy experiments might probe the photon—e.g. NMR $1/T_1$ relaxation, ultrasound attenuation, thermal conductivity, etc.—and would be worthwhile to pursue if a strong candidate is found.

9.6 Frontier Topics

9.6.1 Antiferromagnetic XY Coupling

Most of the work on the QSI model in (9.1) has concentrated on the case of $J_\pm > 0$, which corresponds to unfrustrated "ferromagnetic" (in the local basis) XY coupling. It is indeed known that $J_\pm > 0$ in $Yb_2Ti_2O_7$ and $Er_2Ti_2O_7$. Not only does $J_\pm > 0$ simplify analytic approaches, it also allows sign-free quantum Monte Carlo (QMC) simulation in the case $J_{z\pm} = J_{\pm\pm} = 0$, which places the phase diagram of the model in this case on a quite rigorous footing. By contrast, the "antiferromagnetic" sign $J_\pm < 0$, which has been speculated to apply to some Pr compounds, is frustrated and complicates analytic approaches while generating a sign problem in QMC.

The antiferromagnetic case is, however, both interesting theoretically and promising physically. The QMC simulations for $J_\pm > 0$ show that the Coulomb QSL occupies only a very small region of phase space, giving way to an XY ordered phase (an antiferromagnet in the global spin basis) at the small value $J_\pm/J_{zz} \gtrsim 1/40$ (for $J_{z\pm} = J_{\pm\pm} = 0$) [20]. The dominance of the XY ordered phase can be ascribed to its unfrustrated nature, which gives it a very low energy. By contrast, the frustrated antiferromagnetic interaction $J_\pm < 0$ has no obvious energetically competitive ground state, and indeed even the pure antiferromagnetic XY model on the pyrochlore lattice has an extensive classical degeneracy, and so we expect strong quantum fluctuations to persist regardless of the ratio of $J_\pm/J_{zz}$ in this case.

For $|J_\pm/J_{zz}| \ll 1$, the perturbative analysis discussed in Sect. 9.1.2 implies that the effective model of (9.3) applies with $K < 0$ in the antiferromagnetic case. The effective model with $K < 0$ can be rigorously mapped to the one with $K > 0$, and so in the perturbative regime we know that a Coulomb QSL exists also on this side. The mapping that changes the sign of K changes the sign of the "electric" flux through the hexagons, so the state for $0 < -J_\pm/J_{zz} \ll 1$ is in fact a π-flux QSL, which is a distinct phase from the QSL with the opposite sign. For example, the spinons/monopoles of this π-flux QSL have a drastically altered and more narrow dispersion, i.e. are expected to be much "heavier" than those of the unfrustrated QSL state.

Due to the frustration of XY ordering, we expect this Coulomb QSL to be stable to larger $|J_\pm/J_{zz}|$ than on the ferromagnetic side. Indeed, a naïve application of gMFT to this case [8] already supports this conclusion. However, an exhausting search for ground states even at the gMFT level has not been carried out, and is probably necessary, since competing ordered states are likely quite complex in this case. The evolution from the QSI limit to the Heisenberg point $J_\pm = -\frac{1}{2}J_{zz}$ is particularly interesting, since the Heisenberg model has enhanced $SU(2)$ symmetry which may be incompatible with the spin-ice-inspired QSL state. It is widely suspected that the Heisenberg antiferromagnetic model, however, has some sort of QSL ground state, which would imply multiple distinct QSL states along the antiferromagnetic XXZ line, and the prospect of interesting quantum phase transitions between these states. This is an interesting subject for future investigations.

9.6.2 Quantum Phase Transitions

While the focus of this paper has primarily been on the Coulombic QSL states, there are also many interesting phase transitions in the model. Within the gMFT formalism, several distinct quantum phase transitions, for example between the QSL and AFM, and QSL and Coulomb FM, were obtained. These are driven by the onset of local order parameters (e.g. $\langle \mathsf{s}_i^z \rangle$) or by "Higgs" condensation of gauge charged particles (e.g. spinons). There has been very limited theoretical work addressing the nature of these transitions beyond the mean field approximation. However, Higgs transitions in 3+1 dimensions are at their upper critical dimension in the sense of critical phenomena, and are amenable to renormalization group methods. It is typically the case that these transitions are driven weakly first order by feedback effects between the gauge field and gapless Higgs field [18].

Furthermore, even outside the QSI regime when $J_{zz} > 0$ dominates, there can be transitions between different classically ordered states of (9.1). Even though the ordered states themselves typically are adequately described classically, with sometimes semi-classical corrections (for example order-by-disorder in the XY AFM [4]), the transitions between states can exhibit enhanced quantum fluctuations.

9.6.3 Numerics

Computational studies of quantum spin ice have already proven quite fruitful, and are discussed in Chap. 10 of this book. The majority of studies focus on QMC approaches, and are thereby tied to sign-free limits of the problem. This includes several studies of the perturbative regime, and of the XXZ model on the $J_{\pm} > 0$ side [20].

There are many motivations to go beyond these limits. The best characterized QSI material experimentally, $Yb_2Ti_2O_7$, has strong $J_{z\pm}$ exchange, which cannot be treated directly by QMC methods. The $J_{\pm\pm}$ interaction may favor a gapped $\mathbb{Z}_2$ QSL state (see Sect. 9.3.2), which so far however has not been supported by analytic calculations. As discussed in the previous subsection, the case $J_{\pm} < 0$ also raises many interesting issues that cannot be addressed by QMC.

Beyond QMC, established numerical methods for frustrated quantum spin models include exact diagonalization (ED), series expansions, density matrix renormalization group, tensor network approaches, and variational wavefunctions. The application of such methods up to now for QSI is very limited. Following early ED work on the isotropic Heisenberg antiferromagnet [36], some exploration of the more general Hamiltonian was carried out in [3]. Series and coupled cluster expansions have been used to successfully calculate intermediate temperature thermodynamics [6, 7]. Variational wavefunctions have been very little explored [37], but seem a promising direction for future exploration, following the discussion in Sect. 9.3.4 and other standard Ansätze.

9.6.4 Disorder

Some imperfections are inevitable in real materials, and this disorder can of course affect the subtle competition of phases in QSI. For example (see Chap. 12), many rare earth pyrochlores suffer a tendency to "inversion", the placement of A or B site atoms on the wrong sublattice and "stuffing," off-stoichiometric replacements of, e.g., A-sites by B-site atoms. This can lead to missing or extra spins, as well as changes to the environment that give rise to modified crystal field splittings and modified exchange couplings. The effect of these various types of disorder are largely unknown, theoretically or experimentally, though enormous sample to sample variations in the specific heat of materials such as $Yb_2Ti_2O_7$ point to a strong influence on the physical properties.

Do such disorder effects spell doom for QSI physics? There are several reasons for hope. First, and most importantly, the Coulomb QSL state is in fact *immune* at least to weak disorder. Fundamentally, this is because the long range entanglement of the Coulomb phase is entirely independent of any symmetry, including translational, time-reversal, and spin-rotation symmetries which might be broken by various impurities. So there is no a priori reason to suppose that the QSL physics is washed out by defects. However, *strong*, even dilute, defects, which may well be relevant to some samples, can alter or destabilize highly entangled states. It may be that particular types of disorder actually *stabilize* a QSL state. The actual consequences for simple and/or realistic models of defective QSI should be an interesting subject for future work.

Acknowledgements This chapter was based on research supported by the National Science Foundation, grant NSF-DMR1506119, the Department of Energy Office of Basic Energy Sciences, grant DE-FG02-08ER46524 (L.B.) and by the Gordon and Betty Moore Foundation through a postdoctoral fellowship of the EPiQS initiative, grant GBMF4303 (L.S.). We benefitted from the facilities of the KITP, supported by the National Science Foundation under Grant No. NSF PHY11-25915, and meetings of the Quantum Materials program of the Canadian Institute for Advanced Research. We thank Bruce Gaulin, Kate Ross, SungBin Lee, and Shigeki Onoda for collaborations and discussions.

References

1. S.H. Curnoe, Phys. Rev. B **78**, 094418 (2008). https://doi.org/10.1103/PhysRevB
2. K.A. Ross, L. Savary, B.D. Gaulin, L. Balents, Phys. Rev. X **1**, 021002 (2011). https://doi.org/10.1103/PhysRevX.1.021002
3. S. Onoda, Y. Tanaka, Phys. Rev. B **83**, 09441 (2011). https://doi.org/10.1103/PhysRevB.83.094411
4. L. Savary, K.A. Ross, B.D. Gaulin, J.P.C. Ruff, L. Balents, Phys. Rev. Lett. **109**, 167201 (2012). https://doi.org/10.1103/PhysRevLett.109.167201
5. L. Savary, L. Balents, Phys. Rev. Lett. **108**, 037202 (2012). https://doi.org/10.1103/PhysRevLett.108.037202

6. N. Hayre, K. Ross, R. Applegate, T. Lin, R. Singh, B. Gaulin, M. Gingras, Phys. Rev. B **87**, 184423 (2013). https://doi.org/10.1103/PhysRevB.87.184423
7. R. Applegate, N. Hayre, R. Singh, T. Lin, A. Day, M. Gingras, Phys. Rev. Lett. **109**, 097205 (2012). https://doi.org/10.1103/PhysRevLett.109.097205
8. S. Lee, S. Onoda, L. Balents, Phys. Rev. B **86**, 104412 (2012). https://doi.org/10.1103/PhysRevB.86.104412
9. Y.P. Huang, G. Chen, M. Hermele, Phys. Rev. Lett. **112**, 167203 (2014). https://doi.org/10.1103/PhysRevLett.112.167203
10. H.R. Molavian, M.J. Gingras, B. Canals, Phys. Rev. Lett. **98**, 157204 (2007). https://doi.org/10.1103/PhysRevLett.98.157204
11. M. Hermele, M.P. Fisher, L. Balents, Phys. Rev. B **69**, 064404 (2004). https://doi.org/10.1103/PhysRevB.69.064404
12. H. Yan, O. Benton, L. Jaubert, N. Shannon, Phys. Rev. B **95**, 094422 (2017). https://doi.org/10.1103/PhysRevB.95.094422
13. E. Fradkin, S.H. Shenker, Phys. Rev. D **19**, 3682 (1979). https://doi.org/10.1103/PhysRevD.19.3682
14. N. Shannon, O. Sikora, F. Pollmann, K. Penc, P. Fulde, Phys. Rev. Lett. **108**, 067204 (2012). https://doi.org/10.1103/PhysRevLett.108.067204
15. T. Banks, R. Myerson, J. Kogut, Nucl. Phys. B **129**, 493 (1977). https://doi.org/10.1016/0550-3213(77)90129-8
16. M.E. Peskin, Ann. Phys. **113**, 122 (1978). https://doi.org/10.1016/0003-4916(78)90252-X
17. J.L. Cardy, Nucl. Phys. B **205**, 17 (1982). https://doi.org/10.1016/0550-3213(82)90464-3
18. D.L. Bergman, G.A. Fiete, L. Balents, Phys. Rev. B **73**, 134402 (2006). https://doi.org/10.1103/PhysRevB.73.134402
19. S. Elitzur, Phys. Rev. D **12**, 3978 (1975). https://doi.org/10.1103/PhysRevD.12.3978
20. A. Banerjee, S.V. Isakov, K. Damle, Y.B. Kim, Phys. Rev. Lett. **100**, 047208 (2008). https://doi.org/10.1103/PhysRevLett.100.047208
21. P.A. Lee, N. Nagaosa, X.G. Wen, Rev. Mod. Phys. **78**, 17 (2006). https://doi.org/10.1103/RevModPhys.78.17
22. C. Wang, T. Senthil, Phys. Rev. X **6**, 011034 (2016). https://doi.org/10.1103/PhysRevX.6.011034
23. Z. Hao, A.G.R. Day, M.J.P. Gingras, Phys. Rev. B **90**, 214430 (2014). https://doi.org/10.1103/PhysRevB.90.214430
24. B. Pendleton, Phys. Lett. B **118**, 121 (1982). https://doi.org/10.1016/0370-2693(82)90613-X
25. V. Alessandrini, V. Hakim, A. Krzywicki, Nucl. Phys. B **215**, 109 (1983). https://doi.org/10.1016/0550-3213(83)90269-9
26. X.G. Wen, Phys. Rev. B **44**, 2664 (1991). https://doi.org/10.1103/PhysRevB.44.2664
27. A. Kitaev, J. Preskill, Phys. Rev. Lett. **96**, 110404 (2006). https://doi.org/10.1103/PhysRevLett.96.110404
28. A.Y. Kitaev, Ann. Phys. **303**, 2 (2003). https://doi.org/10.1016/S0003-4916(02)00018-0
29. M. Levin, X.G. Wen, Phys. Rev. Lett. **96**, 110405 (2006). https://doi.org/10.1103/PhysRevLett.96.110405
30. L. Savary, L. Balents, Phys. Rev. B **87**, 205130 (2013). https://doi.org/10.1103/PhysRevB.87.205130
31. B. Clark, L. Savary, L. Balents, Variational methods for quantum spin ice. Unpublished
32. S.V. Isakov, R. Moessner, S. Sondhi, Phys. Rev. Lett. **95**, 217201 (2005). https://doi.org/10.1103/PhysRevLett.95.217201
33. B.C. den Hertog, M.J. Gingras, Phys. Rev. Lett. **84**, 3430 (2000). https://doi.org/10.1103/PhysRevLett.84.3430
34. R.G. Melko, B.C. den Hertog, M.J. Gingras, Phys. Rev. Lett. **87**, 3430 (2001). https://doi.org/10.1103/PhysRevLett.87.067203
35. D. Pomaranski, L. Yaraskavitch, S. Meng, K. Ross, H. Noad, H. Dabkowska, B. Gaulin, J. Kycia, Nat. Phys. **9**, 353 (2013). https://doi.org/10.1038/NPHYS2591

36. B. Canals, C. Lacroix, Phys. Rev. Lett. **80**, 2933 (1998). https://doi.org/10.1103/PhysRevLett.80.2933
37. F. Burnell, S. Chakravarty, S. Sondhi, Phys. Rev. B **79**, 144432 (2009). https://doi.org/10.1103/PhysRevB.79.144432

Chapter 10
Quantum Monte Carlo Simulations of Quantum Spin Ice

Nic Shannon

Abstract One of the strongest reasons for studying "quantum spin–ice" materials is the possibility that quantum tunnelling between different ice states could convert the classical magnetostatics of spin ice into a lattice analogue of quantum electrodynamics, with both magnetic and electric charges, and emergent "photon" excitations. In this Chapter we review what Quantum Monte Carlo simulations have taught us about this exotic quantum spin liquid state, and how this might help us to understand real materials.

10.1 Introduction

10.1.1 Preamble—Why Try to Simulate a Quantum Spin Ice?

Quantum Monte Carlo simulation of frustrated magnets can be a unrewarding business, since the very frustration which makes these systems interesting, frequently leads to fatal "sign problems" in simulation. Quantum spin ice offers a rare exception to this rule, since many of the most important questions can be asked in the context of models which are "sign–free". And as a result, quantum Monte Carlo simulation has been central to progress in understanding quantum spin ice.

The purpose of this chapter is to explore what numerical simulation, and in particular quantum Monte Carlo (QMC), has taught us about quantum effects in spin–ice like magnets. We begin by introducing the idea of a "quantum ice", as a natural treatment of quantum tunnelling between ice–like states, whether in proton–bonded ferroelectrics, spin ice, or water ice. Models of this type find a natural description in terms of lattice–gauge theories, and we provide a concise overview of some of key predictions of this approach, identifying those questions where simulation could play a decisive role.

N. Shannon (✉)
Theory of Quantum Matter Unit, Okinawa Institute of Science and Technology Graduate University, Okinawa, Japan
e-mail: nic.shannon@oist.jp

M. Udagawa and L. Jaubert (eds.), *Spin Ice*, Springer Series in Solid-State Sciences 197,
https://doi.org/10.1007/978-3-030-70860-3_10

We then turn to simulation, considering first the ground–state properties of an idealised "Rokshar–Kivelson" model of a quantum ice, of the type introduced by Hermele et al. [1]. We review evidence, from zero–temperature Green's function Monte Carlo simulation, for a robust quantum spin–liquid ground state, with excitations described by a quantum U(1) lattice gauge theory [2]. And we explore how simulation informs us about some of the features which would distinguish this spin–liquid in experiment [3].

We then consider simulation of a microscopic model of anisotropic exchange on the pyrochlore lattice, more directly motivated by experiment, at finite temperature. Here path-integral QMC simulation, pioneered by Banerjee et al. [4], provide strong evidence for a quantum spin–liquid, described by the same U(1) lattice gauge theory [4, 5]. Simulations at finite temperature also offer valuable insight into what such a spin–liquid would look like in experiment.

We conclude the chapter with a brief survey of simulation of problems which closely parallel quantum spin ice, including its two–dimensional anaglogue, quantum square ice [6–9], three–dimensional quantum dimer models [10–15], and quantum effects in dipolar spin ice [16], before discussing some of the open issues in simulation of quantum spin ice.

10.1.2 So What Is a Quantum Spin Ice, Anyway ?

The term *quantum spin ice* naturally suggests a spin ice in which quantum fluctuations play an important role. As such, the most obvious place to look for a quantum spin ice might be in a conventional spin ice such as $Dy_2Ti_2O_7$, at very low temperatures. In practice, however, things are not quite this simple. The magnetic ions in $Dy_2Ti_2O_7$ have strong single–ion anisotropy, which inhibits dynamics, and are subject to long–range, dipolar interactions. As a result, they tend to fall out of equilibrium at low temperatures [17–20] (see also Chap. 4), and attempts to understand quantum effects in dipolar spin ice remain in their infancy [16, 21, 22]. Meanwhile, the epiphet "quantum spin ice", has been applied to a range of different pyrochlore magnets, based on different rare-earth ions, all of which have been argued to show spin–liquid behaviour in the presence of significant quantum dynamics [23–25]. And, to add to the confusion, spin ice is just one example of a wide class of materials, including common water ice, with ice–like degeneracies. Quantum effects could, in principle, play a role in any of these systems.

Concrete simulations require a concrete model, and for the purposes of this chapter, we will consider a quantum spin ice to be a magnet in which spin configurations are governed by the same "two–in, two–out" constraint as in a conventional spin ice, but in which quantum fluctuations permit tunnelling between different spin configurations obeying these "ice rules". (An example of this type of tunnelling in illustrated in Fig. 10.1). Fortunately, this common–sense definition of a quantum spin ice is exactly what is needed to obtain a model described by a lattice gauge theory, and accessible to simulation. And since exactly the same considerations apply to

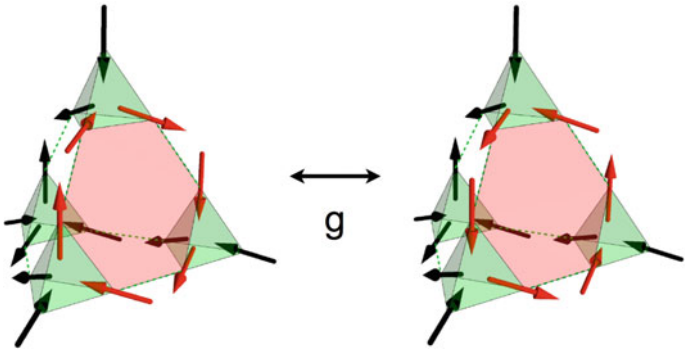

Fig. 10.1 (Color online). Illustration of the simplest form of quantum tunnelling in a spin ice. The ice rules dictate that two spins point into, and two spins point out of, every tetrahedron on the lattice. Where these spins form a closed loop, the sense of each spin within the loop can be reversed without violating the ice rules. The shortest such loop in the pyrochlore lattice occurs on an hexagonal plaquette, and the minimal model of a quantum spin ice, $\mathscr{H}_{\text{tunnelling}}$ (10.6) describes quantum tunnelling between the two "flippable" configurations of this plaquette, here shaded pink. Reprinted from [3] with permission from the American Physical Society

common water ice [26–29], and other proton–bonded systems [8, 30], we can view it as a paradigm for a more general "quantum ice".

Given a model, the most urgent question will be "what is its equilibrium ground state ?" Ice–like systems exhibit an extensive classical ground–state degeneracy [31], leading to the celebrated Pauling residual ice entropy [32, 33]. This residual entropy stands in clear violation of the third law of thermodynamics, and at low temperatures, the effect of quantum fluctuations must ultimately be to lift the extensive degeneracy of the classical ground–state manifold. But how this happens is far less obvious. It could be that quantum fluctuations drive the system to order, for example by selecting one particular spin–ice configuration as a ground state. Alternatively, fluctuations could blend an extensive set of classical spin–ice configurations into a single, unique, ground–state wave function. It is this second possibility—of a quantum spin liquid (QSL) in a well–motivated model of a three–dimensional quantum magnet—which makes simulations of quantum spin ice so interesting. And the goal of this chapter is to explore what QMC has taught us about the possible ground states of a quantum spin ice, and what the associated phases might look like in experiment.

As a first step, in Sect. 10.1.3 we briefly review the passage from a minimal microscopic model of a quantum spin ice, to an effective model of tunnelling between different spin ice configurations, and from that to a description of quantum spin ice in terms of a U(1) lattice gauge theory. Doing so, we arrive at a more precise formulation of our question about the nature of ground state of a quantum spin ice, in a form which can be answered directly by simulation. Our account will closely parallel the treatment of Hermele et al. [1], since this has most directly influenced published results for simulation [2–5]. None the less, we note that there are alternative routes to a gauge theory of quantum spin ice [34], and that quantum spin ice is by no means

the only way of obtaining a U(1) spin liquid [35]. Readers already familiar with the relevant lattice gauge theory are encouraged to turn directly to the account of simulation in Sect. 10.2. Those less familiar might also like to refer to Chaps. 9 and 11 of this book.

10.1.3 A Short Tour of Models, and the Maths Used to Describe Them

The simplest, microscopic, model satisfying our working definition of a quantum ice is a simplified model of anisotropic exchange interactions on the pyrochlore lattice

$$\mathscr{H}_{\mathsf{xxz}} = -J_{\pm} \sum_{\langle ij \rangle} \left(\mathsf{S}_i^+ \mathsf{S}_j^- + \mathsf{S}_i^- \mathsf{S}_j^+ \right) + J_{zz} \sum_{\langle ij \rangle} \mathsf{S}_i^z \mathsf{S}_j^z \,, \tag{10.1}$$

where, following the notation of [24], S_i describes a (pseudo) spin-1/2

$$[\mathsf{S}_i^+, \mathsf{S}_j^-] = 2\mathsf{S}_i^z \delta_{ij} \,. \tag{10.2}$$

with the local z–axis chosen to be parallel to the [111] axis at site i. Both exchange interactions are taken to be positive, $J_{zz},\ J_{\pm} > 0$. In the limit $J_{zz} \gg J_{\pm}$, the "Ising" term J_{zz} selects the manifold of ground states where each tetrahedron obeys the ice rule

$$\sum_{i \in \mathsf{tet.}} \mathsf{S}_i^z = 0 \,, \tag{10.3}$$

while the transverse term $J_{\pm}$ introduces fluctuations about these spin configurations and, ultimately, makes it possible for the system to tunnel from one spin–ice configuration to another.

So far as real pyrochlore magnets are concerned, the anisotropic exchange model $\mathscr{H}_{\mathsf{xxz}}$ (10.1) is an idealisation, since it neglects both Dzyaloshinski–Moriya and pseudo–dipolar interactions permitted by the symmetry of the lattice [24, 36, 37]. None the less, it remains a useful approximation to materials such as $Yb_2Ti_2O_7$ [24, 38, 39]. And, crucially, it is a model which does not present any sign problem in simulation.

Studies of quantum ice can also be motived from models of Fermions [40] or hard–core Bosons [4] with strong nearest–neighbour interactions on the pyrochlore lattice

$$\mathscr{H}_{\mathsf{tV}} = -t \sum_{\langle ij \rangle} \left(b_i^\dagger b_j + b_j^\dagger b_i \right) + V \sum_{\langle ij \rangle} \left(n_i - \frac{1}{2} \right) \left(n_j - \frac{1}{2} \right) - \mu \sum_i n_i \tag{10.4}$$

For $V \gg t$, at half–filling, interactions enforce the ice–rule constraint, (10.3), which become the condition that there should be exactly two particles in each tetrahedron on the lattice. For Bosons, $[b_i\,,\,b_j^\dagger] = \delta_{ij}$, and $\mathscr{H}_{\mathsf{tV}}$ can be mapped onto $\mathscr{H}_{\mathsf{xxz}}$ (10.1) through the quantum lattice–gas mapping

$$\mathsf{S}_i^z = n_i - \frac{1}{2} \quad , \quad J_{zz} = V \quad , \quad J_\pm = t \; . \tag{10.5}$$

Just as the form of exchange interactions in a Mott insulator are dictated by the symmetry of the lattice and wave function, so the form of tunnelling between different ice configurations is controlled by the topology of the ice states. Within our model of a quantum spin ice, quantum fluctuations take the form of short–lived virtual pairs of magnetic monopoles [41, 42], created by transverse exchange $J_\pm$. These can propagate through the lattice, reversing the sense of a closed loop of spins before annihilating. On a pyrochlore lattice, the shortest such loop occurs on a hexagon [cf. Fig. 10.1], and tunnelling can be represented by the effective Hamiltonian

$$\mathscr{H}_{\mathsf{tunnelling}} = -g \sum_{\hexagon} \mathsf{S}_1^+ \mathsf{S}_2^- \mathsf{S}_3^+ \mathsf{S}_4^- \mathsf{S}_5^+ \mathsf{S}_6^- + \text{H.c.} \; , \tag{10.6}$$

acting on the space of spin–ice configurations [1, 16]. Within degenerate perturbation theory for $\mathscr{H}_{\mathsf{xxz}}$ (10.1),

$$g = \frac{12 J_\pm^3}{J_{zz}^2} > 0 \; , \tag{10.7}$$

cf. [1]. In principle (10.6) could be extended to include tunnelling on loops of 8, 10, 12,… spins. However tunnelling on a loop of six spins is sufficient to connect all but a vanishing fraction of spin–ice configurations within a given topological sector, and so represents the minimum model of a quantum spin ice [2].

It is important to note that $\mathscr{H}_{\mathsf{tunnelling}}$ (10.6) is not tied to $\mathscr{H}_{\mathsf{xxz}}$ (10.1), but could be derived from any microscopic model which described fluctuations about spin–ice configurations. In particular, equivalent forms of tunnelling can be derived for protons in water ice [26, 29], or for hard–core bosons described by $\mathscr{H}_{\mathsf{tV}}$ (10.4). To emphasise this point, as well as for compactness, it can be helpful to represent (10.6) symbolically as

$$\mathscr{H}_{\mathsf{tunnelling}} = -g \sum_{\hexagon} |\circlearrowleft\rangle\langle\circlearrowright| + |\circlearrowright\rangle\langle\circlearrowleft| \; , \tag{10.8}$$

where $\circlearrowleft$ and $\circlearrowright$ represent the two "flippable" configurations of the hexagonal plaquette in Fig. 10.1.

Written in terms of spins, our model of a quantum ice reduces to a constraint imposing the ice rules, (10.3), and a term introducing dynamics within the extensive set of states which satisfy that constraint, (10.6). Following Hermele et al. [1], we can resolve both of these terms by interpreting the z–component of spin as an electric field, and writing

$$\mathsf{S}^{z}_{\mathbf{r}\mathbf{r}'} \to E_{\mathbf{r}\mathbf{r}'} \quad , \quad \mathsf{S}^{\pm}_{\mathbf{r}\mathbf{r}'} \to e^{\pm i A_{\mathbf{r}\mathbf{r}'}} \tag{10.9}$$

where $A_{\mathbf{r}\mathbf{r}'}$ is a real–valued field with canonical commutation relation

$$[E_{\mathbf{r}\mathbf{r}'}, A_{\mathbf{r}''\mathbf{r}'''}] = i\delta_{\mathbf{r}\mathbf{r}''}\delta_{\mathbf{r}'\mathbf{r}'''} \tag{10.10}$$

(Here both $E_{\mathbf{r}\mathbf{r}'}$ and $A_{\mathbf{r}\mathbf{r}'}$ are directed variables, defined on the bonds of a diamond lattice, as described in [1, 3], see also Chap. 9). Following this prescription, the constraint (10.3) becomes a zero–divergence condition on the electric field $E_{\mathbf{r}\mathbf{r}'}$, while the tunnelling term (10.6) takes on the Villain form [43]

$$\mathscr{H}_{\text{tunnelling}} = -2\,g \sum_{\hexagon} \cos\left(A_{12} - A_{23} + A_{34} - A_{45} + A_{56} - A_{61}\right) \ . \tag{10.11}$$

This theory is invariant under the U(1) gauge transformation

$$A_{nm} \to A_{nm} + \chi_n - \chi_m \tag{10.12}$$

and is *compact*, since the Hamiltonian is periodic in χ. It is also said to be *frustrated*, since the electric field is required to take on half–integer values $E_{\mathbf{r}\mathbf{r}'} = \pm 1/2$, and we cannot resolve (10.3) simply by setting $E_{\mathbf{r}\mathbf{r}'} \equiv 0$.

Lattice gauge theories of this form have a long history [44–47], and are known to undergo a phase transition between a "confined" phase in which there are no free charges, and a "deconfined" phase in which charges interact through Coulomb interactions [45]. These two phases correspond to the two scenarios which we discussed, on general grounds, for a quantum spin ice. Viewed in terms of spins, the electric charges of the gauge theory are magnetic monopoles [41, 42] (see also Chaps. 3, 9), and the deconfined phase is a QSL, with emergent photon excitations, in which magnetic monopoles are free to propagate. Meanwhile the confined phase would corresponds to one or more competing forms of magnetic order [34].

Lattice gauge theories have also been widely studied in the context of the quantum dimer model (QDM) introduced by Rokhsar and Kivelson [48]. And by analogy with work on the QDM, it is instructive to introduce an additional interaction term μ_{RK} which counts the number of "flippable" plaquettes

$$\mathscr{H}_{\mathsf{RK}} = -g \sum_{\hexagon} |\hexagon\rangle\langle\hexagon| + |\hexagon\rangle\langle\hexagon| + \mu_{\mathsf{RK}} \sum_{\hexagon} |\hexagon\rangle\langle\hexagon| + |\hexagon\rangle\langle\hexagon| \ , \tag{10.13}$$

in a given spin–ice configuration or, equivalently, the fluctuations of magnetic field in the compact, frustrated lattice gauge theory described above. Since the off–diagonal matrix elements of $\mathscr{H}_{\mathsf{RK}}$ (10.13) have a definite sign, which can always be chosen to be negative [1], its ground state must be real, coherent superposition of spin–ice configurations with definite flux

$$|0\rangle = \sum_{\lambda} c_\lambda |\lambda\rangle \quad , \quad c_\lambda \geq 0 \ . \tag{10.14}$$

This means that $\mathscr{H}_{\mathsf{RK}}$ is accessible to quantum Monte Carlo simulation. Moreover, at the "RK–point", $g = \mu_{\mathsf{RK}}$, (10.13) takes the form of a projection operator,

$$\mathscr{H}'_{\mathsf{RK}} = g \sum_{\hexagon} [|\circlearrowleft\rangle - |\circlearrowright\rangle][\langle\circlearrowleft| - \langle\circlearrowright|] \ , \tag{10.15}$$

for which the ground state is known exactly [48]—it is the equally–weighted superposition of all states within a given topological sector, with energy

$$\mathscr{H}'_{\mathsf{RK}}|0\rangle'_0 = E'_0|0\rangle'_0 \equiv 0 \ . \tag{10.16}$$

This simple result has a very profound consequence—the ground state of the *quantum* model $\mathscr{H}_{\mathsf{RK}}$, for $g = \mu_{\mathsf{RK}}$, is a spin liquid whose correlations are identical to those of a *classical* spin ice.

By continuity, Hermele et al. [1] argued that the ground state of $\mathscr{H}_{\mathsf{RK}}$ should be a quantum spin liquid, described by the deconfined phase of the lattice gauge theory—cf. Fig. 10.2. Exactly same argument was advanced by Moessner and Sondhi, in the context of three–dimensional quantum dimer models [10]. Both sets of authors further argued that low–energy correlations in the spin–liquid phase should be described by the *non-compact* form of the lattice gauge theory

$$\mathscr{H}_{\mathrm{U}(1)} = \frac{\mathscr{U}}{2} \sum_{\langle rr' \rangle} E^2_{\mathbf{r}\mathbf{r}'} + \frac{\mathscr{K}}{2} \sum_{\hexagon} [\nabla_{\hexagon} \times A]^2 + \frac{\mathscr{W}}{2} \sum_{\hexagon} [\nabla_{\hexagon} \times \nabla_{\hexagon} \times A]^2 \tag{10.17}$$

where $E_{\mathbf{r}\mathbf{r}'}$ can take on any value, and $\nabla_{\hexagon}\times$ denotes a lattice curl. The term proportional to $\mathscr{U}$ in (10.17) reflects the ice–rule constraint, while the term proportional to $\mathscr{K}$, describes tunnelling between different spin–ice configurations. The third term, proportional to $\mathscr{W}$, is needed to describe the correlations at the RK point, where $\mathscr{K} = 0$ [1, 3, 10]. Naively, $\mathscr{U} \propto J_{zz}$, while $\mathscr{K} \propto g - \mu$. However, since $\mathscr{H}_{\mathrm{U}(1)}$ (10.17) is an effective low–energy theory, the values of these parameters are strongly renormalised by fluctuations.

After this long series of manipulations we have finally arrived at a form of theory which looks very familiar. Introducing a magnetic field

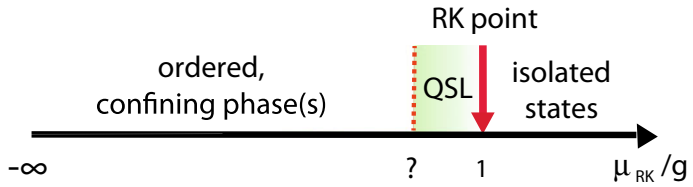

Fig. 10.2 Schematic ground–state phase diagram diagram of the Rokshar–Kivelson (RK) model, $\mathscr{H}_{\mathsf{RK}}$ (10.13), following [1, 10]. A quantum spin-liquid (QSL), described by the deconfined phase of the $U(1)$ lattice gauge theory $\mathscr{H}_{\mathrm{U}(1)}$ (10.17), abuts the exactly–soluble RK point $\mu_{\mathsf{RK}} = g$

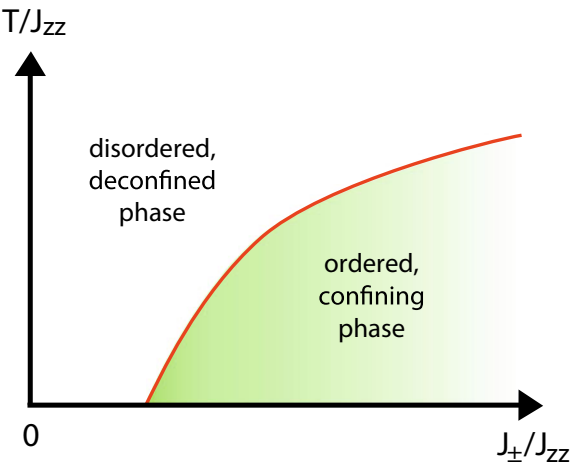

Fig. 10.3 Schematic finite–temperature phase diagram of the anisotropic exchange model $\mathscr{H}_{\text{xxz}}$ (10.1), adapted from a study of proton disorder in water ice [26]. On the basis of earlier work on lattice gauge theories [47, 49], the ground state for small values of the XY interaction $J_{\pm}/J_{zz}$ is conjectured to be a quantum liquid described by the deconfined phase of the lattice gauge theory $\mathscr{H}_{\text{U(1)}}$ (10.17)

$$\mathbf{B} = \nabla_{\hexagon} \times A \tag{10.18}$$

we recognise the first two terms in (10.17) as a lattice version of the Maxwell Hamiltonian

$$\mathscr{H}_{\text{Maxwell}} = \int d\mathbf{r}\, \frac{1}{2}\left[\varepsilon_0 \mathbf{E}^2 + \frac{1}{\mu_0}\mathbf{B}^2\right] . \tag{10.19}$$

By analogy, the excitations of (10.17) should be transverse excitations of the gauge field $\mathbf{A}$, i.e. photons, with long–wavelength dispersion

$$\omega(\mathbf{k}) = c|\mathbf{k}| , \tag{10.20}$$

with effective speed of light

$$c = \sqrt{\mathscr{U}\mathscr{K}}\; a_0\, \hbar^{-1} . \tag{10.21}$$

where a_0 is the linear dimension of the cubic unit cell of the pyrochlore lattice [3, 4].

We will not attempt to review the steps which lead to the non–compact lattice theory $\mathscr{H}_{\text{U(1)}}$ (10.17), or its solution in terms of photons, and refer the interested reader instead to the original papers [1, 3, 10], and the related discussion in Chaps. 9 and 11 of this book. None the less, we will make extensive use of $\mathscr{H}_{\text{U(1)}}$ below, in comparison with simulation of the microscopic models $\mathscr{H}_{\text{xxz}}$ (10.1) and $\mathscr{H}_{\text{RK}}$ (10.13). And it is important to note that this lattice gauge theory applies to a much wider range of systems than just a quantum spin ice—the arguments leading up to $\mathscr{H}_{\text{U(1)}}$ could equally have been presented in terms of a three–dimensional quantum dimer model [10], frustrated charge order on the pyrochlore lattice [4, 40], or protons in water ice [26, 29]—cf. Fig. 10.3.

10.1.4 How Can Simulations Help ?

So what have we learned, and how has it brought us closer to understanding a quantum spin liquid ?

We have seen that a physically motivated model of a quantum spin ice, $\mathscr{H}_{\mathsf{xxz}}$ (10.1) reduces both to a familiar problem in lattice gauge theory $\mathscr{H}_{\mathrm{U(1)}}$ (10.17), and to a simple effective model which could support a spin–liquid ground state, $\mathscr{H}_{\mathsf{RK}}$ (10.13).

Simulations of classical models of ice have a long history, and efficient algorithms, based on "loop" updates make it possible to simulate very large systems [50]. The simulation of classical spin ice, where long–range dipolar interactions must also be taken into account, has also been raised to high art [42, 51]. However for a quantum ice, at $T = 0$, the choices are much more limited. Exact diagonalisation (ED) offers exact and unbiased answers, regardless of the model considered, but is limited to small cluster sizes (for these models, 108 sites [52]), and so provides limited information about long–wavelength excitations. Furthermore, since both of the microscopic models $\mathscr{H}_{\mathsf{xxz}}$ (10.1) and $\mathscr{H}_{\mathsf{RK}}$ (10.13) are "sign–free", both are, in principle, acesssible to quantum Monte Carlo simulation.

Our first goal therefore is to determine whether the quantum spin liquid phase proposed in Figs. 10.2 and 10.3 is really seen in simulation. And since it is relatively easy to carry out analytic calculations for the lattice gauge theory (10.17), we can compare the results of simulations directly with the predictions of theory. Happily this has been accomplished, first for the anisotropic exchange model $\mathscr{H}_{\mathsf{xxz}}$ [4], and then for the RK–model $\mathscr{H}_{\mathsf{RK}}$ [2]. In what follows we review what simulations have taught us about each of these models. For pedagogical reasons, we consider first the ground–state properties of $\mathscr{H}_{\mathsf{RK}}$, before turning to finite–temperature simulations of $\mathscr{H}_{\mathsf{xxz}}$.

10.2 Simulation of Quantum Spin Ice at Zero Temperature

10.2.1 Overview of Section

In what follows we explore the evidence for a quantum spin–liquid ground state in the Rokhsar–Kivelson (RK) model $\mathscr{H}_{\mathsf{RK}}$ (10.13) introduced by Hermele et al. [1]. Our main tool will be Green's function Monte Carlo (GFMC) simulation, a form of zero–temperature quantum Monte Carlo simulation which preserves quantum numbers [53]. Since GFMC gives us access to ground states in different topological sectors, we begin by considering the structure of spin ice states, and the way in which their degeneracy is lifted by quantum tunnelling. Comparing the results of simulation with the predictions of the lattice gauge theory $\mathscr{H}_{\mathrm{U(1)}}$ (10.17), we find clear evidence of a quantum spin–liquid, and a ground state phase diagram of the form shown in Fig. 10.4, confirming the predictions of Hermele et al. [cf. Fig. 10.2].

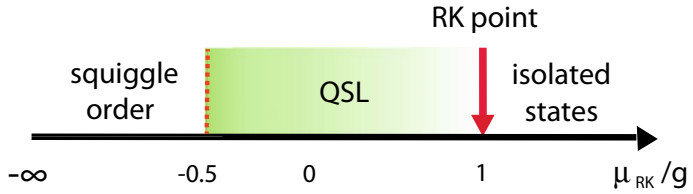

Fig. 10.4 Ground–state phase diagram diagram of the Rokshar–Kivelson (RK) model, $\mathscr{H}_{\mathsf{RK}}$ (10.13) from simulation, following [2, 3]. For a wide range of parameters, bordering the exactly–soluble RK point, the ground state is a quantum spin-liquid (QSL) described by the lattice gauge theory $\mathscr{H}_{\mathrm{U}(1)}$ (10.17). This competes with an ordered, confining "squiggle" phase, described in [2]. The minimal model of a quantum spin ice, $\mathscr{H}_{\mathsf{tunnelling}}$ (10.6), corresponds to $\mu_{\mathsf{RK}} = 0$

We go on to examine the correlations of this quantum spin liquid, and explore how simulation informs us about the different length scales over which quantum, and classical, effects predominate.

10.2.2 Topology, Quantum Numbers and Simulation

The key to successful simulation of $\mathscr{H}_{\mathsf{RK}}$ (10.13) at $T = 0$ is understanding the topology of spin–ice states, and the quantum numbers which follow from it. All spin–ice configurations can be classified according to the flux of the electric field

$$\phi_S = \int_S d\mathbf{S} \cdot \mathbf{E} \tag{10.22}$$

through a closed surface S, as illustrated in Fig. 10.5a. The flux ϕ_S is a topological property, conserved under *all* local operations which respect the ice rules [cf. Fig. 10.5b]. And since the dynamics of $\mathscr{H}_{\mathsf{RK}}$ are purely local, we can define a set of topological quantum numbers

$$\boldsymbol{\phi} = (\phi_x, \phi_y, \phi_z) \tag{10.23}$$

which are conserved under the action of this Hamiltonian. For this reason, the QSL formed through the coherent superposition of ice–configurations can be considered to have topological order [1].

The topological sector with the greatest number of spin ice configurations is the zero–flux sector $\boldsymbol{\phi} = 0$, and all of the low–lying topological sectors contains an extensive number of states [54]. Spin–ice configurations in other topological sectors can be systematically constructed by reversing the sense of a closed loop of spins which traverse the periodic boundaries of the cluster (cf. Fig. 10.5c, and discussion in [14]). In the language of the lattice gauge theory, this is equivalent to creating a point source of electric field (in a spin ice, a magnetic monopole), moving it through the

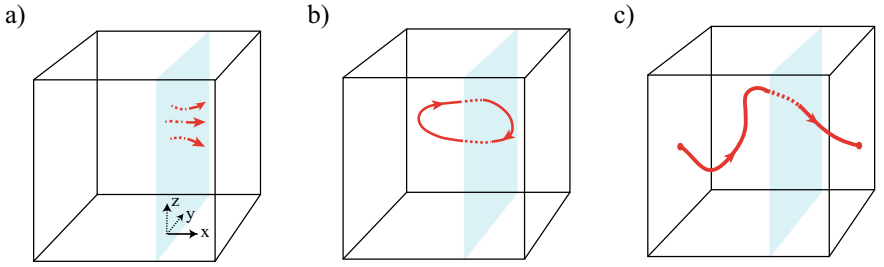

Fig. 10.5 Flux of electric field **E** as a topological quantum number. **a** Surface S used to define the flux ϕ_x associated with a particular spin–ice configuration, for a cluster with periodic boundary conditions. **b** A closed loop of spins within the cluster. Reversing the sense of these spins leaves the flux through the surface S unchanged. **c** A closed loop of spins which traverses the periodic boundaries of the cluster. The flux can be changed by reversing the sense of the spins in this loop

periodic boundary of the cluster, and then annihilating it. Fortunately, in the case of quantum spin ice, all but a vanishing fraction of states within low–lying topological sectors are connected by the matrix elements of $\mathscr{H}_{\mathsf{RK}}$ [2].

To directly probe the structure of this topologically–ordered ground state, simulations should be carried out in a way which preserves topological quantum numbers. This is automatically true in ED. However ED studies are limited to clusters of 108 sites [52], far too small to reveal the long–wavelength behaviour of any QSL. Fortunately, GFMC, a form of diffusion Monte Carlo simulation provides a means of evaluating ground state properties which respects all quantum numbers, including topological ones. GFMC simulation proceeds by using matrix elements of the Hamiltonian to tunnel, at random, from one spin–ice configuration to another [53]. However, since there is no way to sample all of the extensive number of spin–ice configurations which contribute to a spin–liquid ground state, importance–sampling must be used to guide this process of diffusion through "Hamiltonian graph" (the network of spin–ice configurations connected by 10.6). In practice, this means identifying a good variational wave function, carrying out variational Monte Carlo (VMC) simulations to optimise this variational wave function for a given parameter set, and then using the optimised wave function to guide GFMC simulations. In this sense GFMC can be thought of as a systematic way of improving on VMC simulations. It is numerically exact, where simulations converge, however simulations are not guaranteed to converge in finite time.

The most important step in GFMC simulation, therefore, is identifying a suitable variational wave function, and here our physical intuition can help. The QSL is adiabatically connected with the ground state at the RK point, which is the uniform superposition of the set of states $\{\mathsf{c}\}_{\boldsymbol{\phi}}$, within in a given topological sector $\boldsymbol{\phi}$, which are connected by matrix elements of $\mathscr{H}_{\mathsf{RK}}$ (10.13)

$$|\boldsymbol{\phi}\rangle = \frac{1}{\sqrt{N_{\mathsf{c}}}} \sum_{\lambda \in \{\mathsf{c}\}_{\boldsymbol{\phi}}} |\lambda\rangle \tag{10.24}$$

The Frobenius–Perron theorem implies that, away from the RK point, the ground state must still be a superposition of spin–ice configurations with positive coefficients. We can therefore construct a variational wave function for the ground state within a given topological sector by acting on $|\boldsymbol{\phi}\rangle$ with an operator which re–weights the spin–ice configurations within $\{\mathtt{c}\}$ so as to minimise the energy.

A variational wave function which has proved effective in practice [2, 3, 13, 14] is

$$|\psi_{\mathsf{var}}\rangle_{\boldsymbol{\phi}} = \exp\left[\alpha N_{\mathsf{f}} + \sum_{ij} \gamma_{ij}\tau_i\tau_j\right]|\boldsymbol{\phi}\rangle \ , \tag{10.25}$$

where sum on ij runs over pairs of hexagonal plaquettes within the pyrochlore lattice and $\tau_i = 0{,}1$ is an Ising-like variable which takes on the value $\tau_i = 1$ when the hexagonal plaquette i is "flippable" [cf. Fig. 10.1]. Meanwhile $N_{\mathsf{f}} = \sum_i \tau_i$ counts the total number of flippable plaquettes. For large lattices there are many different pairs of hexagonal plaquettes, and the variational parameters α, γ_{ij} are minimized using a stochastic reconfiguration algorithm [55, 56]. In practice, a good wave function can be obtained using a set of approximately 40 inequivalent γ_{ij}. We note that in parallel work on the QDM, described in Sect. 10.4.1, it is useful to add an additional variational parameter associated with the order parameter m_{R} of the competing ordered ground state [13, 14].

10.2.3 Evidence for a Spin–Liquid from Finite–Size Scaling of Energy Spectra

Armed with a simulation method, and a suitable guide wave function, we are now in a position to determine the ground state phase diagram of $\mathscr{H}_{\mathsf{RK}}$ (10.13). The first point of business is to identify any competing ordered phases—cf. Fig. 10.2. This is easiest to accomplish for $\mu_{\mathsf{RK}} \to -\infty$, where the ground state is the spin–ice configuration with the maximum number of flippable plaquettes N_{f}. This can be determined by using classical Monte Carlo simulation techniques, and was found to be the ordered, "squiggle state" described in [2]. The squiggle state has a 20–site unit cell, is 60–fold degenerate, has finite magnetisation parallel to the [100] axis, and belongs to a topological sector with flux

$$\boldsymbol{\phi}_{\mathsf{squiggle}} = (\phi_{\mathsf{squiggle}}, 0, 0) \quad , \quad \phi_{\mathsf{squiggle}} = N/5 \tag{10.26}$$

where N is the number of sites in the cluster. GFMC simulations find a crossing between a ground state in the squiggle–flux sector, and a ground state in the zero–flux sector, for $\mu_{\mathsf{RK}} = (-0.50 \pm 0.03) \times g$, suggesting that the squiggle state remains a ground state for $-\infty < \mu_{\mathsf{RK}} < -0.5\ g$ [2].

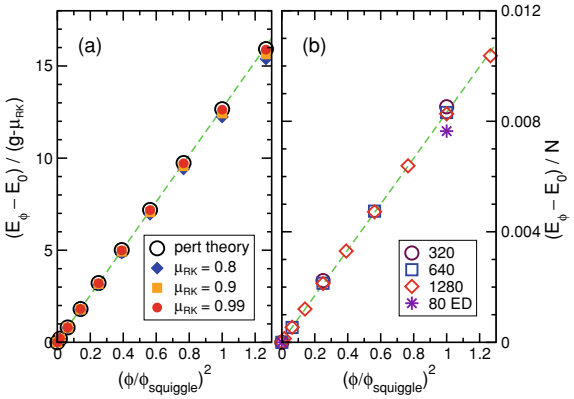

Fig. 10.6 Evidence for the existence of a quantum spin liquid (QSL) ground state in the Rokhsar–Kivelson (RK) model $\mathscr{H}_{\mathsf{RK}}$ (10.13). **a** Scaling of finite–size energy gap $E_{\boldsymbol{\phi}} - E_0$, as a function of topological sector $\boldsymbol{\phi}$, for parameters approaching the RK point $\mu_{\mathsf{RK}} = g$. **b** Scaling of $E_{\boldsymbol{\phi}} - E_0$ for $\mu_{\mathsf{RK}} = 0$, corresponding to the minimal model of a quantum spin ice. The dashed lines show the scaling expected from the U(1) lattice gauge theory, (10.28). Results are taken from Green's function Monte Carlo simulation of 320-site, 640-site and 1280-site clusters, and exact diagonalization for an 80-site cluster. Flux $\boldsymbol{\phi}$ is measured relative to the flux $\boldsymbol{\phi}_{\mathsf{squiggle}}$ of the competing ordered ground state [10.26]. Reprinted from [2] with permission from the American Physical Society.

The best way to approach any simulation of a finite size system, is to use finite–size effects to your advantage. Happily, the lattice gauge theory, $\mathscr{H}_{\mathrm{U(1)}}$ (10.17), makes a prediction for the finite–size scaling of energy gaps within its deconfined phase, which uniquely identify the QSL in question. In the thermodynamic limit, the ground states of $\mathscr{H}_{\mathsf{RK}}$ in all topological sectors are degenerate. However this is not true for a finite–size cluster [10], where a flux $\boldsymbol{\phi}$ through a cluster of volume L^3 corresponds to an average electric field

$$\mathbf{E} = \boldsymbol{\phi}/L^2 \tag{10.27}$$

and, in a spin–liquid described by (10.17), the ground states in different topological sectors with different values of electric field are split by an energy gap

$$E_{\boldsymbol{\phi}} - E_0 \propto c^2 \boldsymbol{\phi}^2 / L \propto c^2\, N \left(\phi/\phi_{\mathsf{squiggle}}\right)^2 \ . \tag{10.28}$$

The energy gap $E_{\boldsymbol{\phi}} - E_0$ can be calculated directly in GFMC simulation [2] and, for $g - \mu_{\mathsf{RK}} \to 0$, in perturbation theory about the the RK point [1, 2]. As shown in Fig. 10.6, both perturbation theory and simulation are found to be in excellent agreement with (10.28), for a wide range of parameters bordering the RK point.

As no evidence is found in simulation of any other state besides the QSL for $\mu_{\mathsf{RK}} > -0.5\, g$, the ground state phase digram of $\mathscr{H}_{\mathsf{RK}}$ (10.13) is believed to have the form shown in Fig. 10.4, confirming the form predicted by Hermele et al. [1]—cf. Fig. 10.2.

10.2.4 Evidence for a QSL Ground State from Correlation Functions

Simulation also allows us to probe the phenomenology of the QSL ground state in a way more directly linked to experiment. Spin correlations in classical spin ice exhibit dipolar correlations in 3 dimensions, for which $S(\mathbf{r}) \propto 1/r^3$ [54, 57]. This leads to characteristic "pinch points" in polarised neutron scattering experiments [58], with structure factor

$$S_{\alpha\beta}(\mathbf{q}) \propto \left(\delta_{\alpha\beta} - \frac{q_\alpha q_\beta}{q^2}\right) . \tag{10.29}$$

In the QSL ground state, on the other hand, quantum fluctuations lead to dipolar correlations in (3 +1) dimensions, with $S(\mathbf{r}) \propto 1/r^4$ [1]. At long–wavelength the corresponding equal–time structure factor has the form [3]

$$S_{\alpha\beta}(\mathbf{q}) = \int d\omega \; S_{\alpha\beta}(\mathbf{q}, \omega) \propto \frac{q}{\sqrt{c^2 + \mathscr{W}^2 q^2}} \left(\delta_{\alpha\beta} - \frac{q_\alpha q_\beta}{q^2}\right) . \tag{10.30}$$

In the limit $c \to 0$ (i.e. at the RK point), the properties of the QSL are controlled by the term proportional to $\mathscr{W}$ in $\mathscr{H}_{\mathrm{U(1)}}$ (10.17), and the correlations are identical to those of a classical spin ice, (10.29). However, away from the RK point, $c \neq 0$, and sharp pinch–points for $\mathbf{q} \to 0$ are eliminated by the the additional factor of q in the numerator of (10.30).

As shown in Fig. 10.7, this phenomenology finds strong support in simulation. It is possible to calculate the equal–time structure factor for a finite–size cluster, both within GFMC simulation of $\mathscr{H}_{\mathsf{RK}}$ (10.13), and using the lattice gauge theory $\mathscr{H}_{\mathrm{U(1)}}$ (10.17), with parameters $\mathscr{U}$, $\mathscr{K}$, $\mathscr{W}$, extracted from simulation, as described in [2]. Comparing the two, we find essentially perfect agreement, validating the use of the non–compact form of the lattice gauge theory $\mathscr{H}_{\mathrm{U(1)}}$ to describe the ground state properties of the microscopic mode, $\mathscr{H}_{\mathsf{RK}}$. And this, in turn, suggests that, much as in conventional electrodynamics, the photons of a quantum spin ice do not interact in the absence of charge.

For $\mu_{\mathsf{RK}}/g = 0$—where the microscopic model corresponds to the minimal model of a quantum spin ice, $\mathscr{H}_{\mathsf{tunnelling}}$ (10.6)—quantum fluctuations have a dramatic effect, eliminating the zone–center pinch points entirely. However, away from the zone center, simulations reveal that correlations are very similar for all values of μ_{RK}/g—cf. Fig. 10.7. This evolution of correlations with $\mathbf{q}$ highlights another feature of the phenomenology of the QSL. While the term proportional to $\mathscr{W}$ in $\mathscr{H}_{\mathrm{U(1)}}$ is an irrelevant perturbation, in the RG sense [1], it sets a length scale

$$\lambda_{\mathscr{W}} \propto \frac{\sqrt{\mathscr{W}}}{c} , \tag{10.31}$$

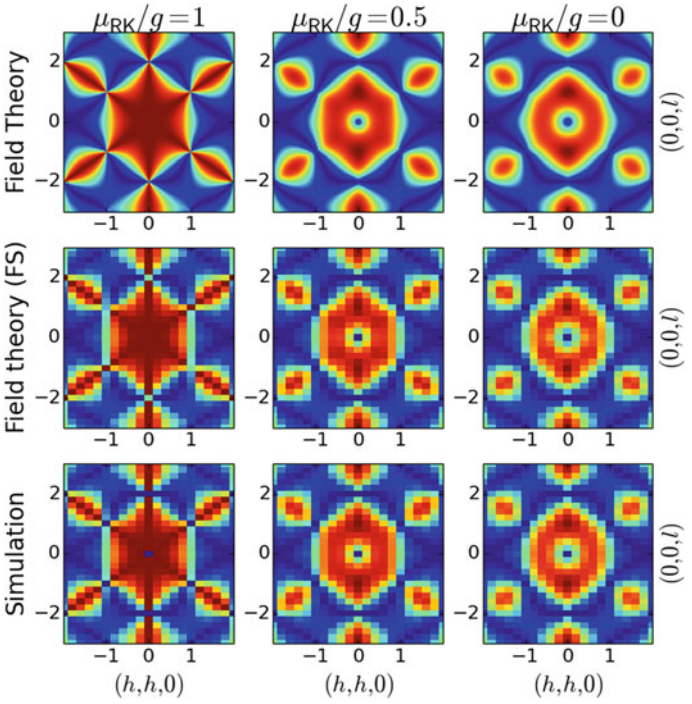

Fig. 10.7 Evolution of spin correlations in the Rokhsar–Kivelson (RK) model of a quantum spin ice, $\mathscr{H}_{\mathsf{RK}}$ (10.13), following [3]. First row—predictions of the lattice gauge theory $\mathscr{H}_{\mathrm{U}(1)}$ (10.17) for the equal–time structure factor $S(\mathbf{q})$, as a function of μ_{RK}/g, in the thermodynamic limit $N \to \infty$. At the RK point, $\mu_{\mathsf{RK}}/g = 1$, correlations exactly reproduce those of a classical spin ice. Second row—predictions of the lattice gauge theory for a finite–size (FS) cluster of $N = 2000$ sites. Third row—results of Green's function Monte Carlo (GFMC) simulations for cluster of $N = 2000$ sites. Correlations are shown in the spin–flip channel measured by Fennel et al. [58]. Reprinted from [3] with permission from the American Physical Society

and correlations for distances $r < \lambda_{\mathscr{W}}$ retain their classical character, while correlations for $r > \lambda_{\mathscr{W}}$ are strongly renormalised by quantum fluctuations. And as we will see in Sect. 10.3, the thermal excitation of photons introduces another length–scale into the problem, λ_T, restoring classical correlations at long distance.

10.3 Simulation of Quantum Spin Ice at Finite Temperature

10.3.1 Overview of Section

While the ground–state properties of the RK model $\mathscr{H}_{\mathsf{RK}}$ (10.13) demonstrate the quantum aspects of ice in their purest form, making comparison with experiment

means getting to grips with the properties of the anisotropic exchange model $\mathscr{H}_{\mathsf{xxz}}$ (10.1), at finite temperature. Historically, quantum Monte Carlo simulations at finite temperature predate studies of quantum ice at $T = 0$, and they provide a powerful tool for exploring the phenomenology of a quantum spin ice, particularly when combined with analytic results for the lattice gauge theory [3–5].

Besides bringing us closer to experiment, the finite–temperature physics of $\mathscr{H}_{\mathsf{xxz}}$ contains a number of new features not present in $\mathscr{H}_{\mathsf{RK}}$. Firstly, any QSL ground state must interpolate, presumably through a classical spin–ice regime, to the high–temperature paramagnet. How this happens is an interesting question. Secondly, for large values of $J_{\pm}$, $\mathscr{H}_{\mathsf{xxz}}$ need not support a QSL ground state, and its phase diagram should include at least one competing ordered phase, as proposed in Fig. 10.3. And thirdly, while $\mathscr{H}_{\mathsf{RK}}$ represents a pure lattice gauge theory, the Hilbert space of $\mathscr{H}_{\mathsf{xxz}}$ includes the charges of the gauge field. Given that the electric charges of the gauge theory correspond to the magnetic monopoles of a spin ice, this is of both experimental and theoretical interest.

Continuing the theme developed in Sect. 10.2.4, we start by exploring evidence for a QSL from quantum Monte Carlo simulations carried out at finite temperatures. We then consider the way in which this QSL evolves into a paramagnet at finite temperature, before turning to competing ordered phases, and the global phase diagram of $\mathscr{H}_{\mathsf{xxz}}$ as a function of interactions and temperature.

10.3.2 *Evidence for a QSL from Correlations at Finite Temperature*

At low temperatures, within the QSL regime, the evolution of spin correlations is controlled by the thermal excitation of photons. These modify the $T = 0$ prediction of the lattice gauge theory $\mathscr{H}_{\mathrm{U}(1)}$ (10.17) for the equal–time structure factor, (10.30), to give [3]

$$S_{\alpha\beta}(\mathbf{q}) \propto \frac{q}{\sqrt{c^2 + \mathscr{W}^2 q^2}} \left(\delta_{\alpha\beta} - \frac{q_\alpha q_\beta}{q^2} \right) \coth \left(\frac{q\sqrt{c^2 + \mathscr{W}^2 q^2}}{2T} \right) . \quad (10.32)$$

For $T \gg cq$, we can apoximate the thermal factor as

$$\coth \left(\frac{q\sqrt{c^2 + \mathscr{W}^2 q^2}}{2T} \right) \approx \frac{2T}{q\sqrt{c^2 + \mathscr{W}^2 q^2}} + \mathscr{O}\left(\frac{cq}{T} \right) , \quad (10.33)$$

and, for $\mathscr{W} q \ll c$, (10.32) interpolates to the result for a classical spin ice, (10.29). More generally, the thermal de Broglie wavelength for photons,

$$\lambda_{\mathsf{T}} = \frac{\pi c}{T} , \quad (10.34)$$

sets an intermediate length scale, beyond which thermal fluctuations destroy the quantum coherence of a quantum spin ice, restoring classical spin–ice correlations. Thus, we expect the pinch points of a quantum spin ice to slowly "switch back on" as the QSL is heated from $T = 0$ and, at least in the pure gauge theory $\mathscr{H}_{\mathrm{U(1)}}$, the transition from quantum to classical spin ice can be accomplished through a crossover [3]. Simulation at finite temperatures provides the opportunity to check whether this is true.

The first QMC simulations of correlations in a quantum ice were carried out by Banerjee et al. [4], who considered the model of hard–core Bosons on the pyrochlore lattice, $\mathscr{H}_{\mathsf{tV}}$ (10.4), equivalent to $\mathscr{H}_{\mathsf{xxz}}$ (10.1). Simulations were performed within the path–integral formulation of QMC, using a stochastic series expansion (SSE) [59], in a version tailored to the simulation of frustrated spin systems [60, 61]. Great care was taken to ensure thermalisation of simulations at low temperatures, with cross–checks made between two, independently–written, codes [62].

Following the conjectured form of the phase diagram [1, 26], a QSL state should be found at low temperature, for small $J_{\pm}$. For $J_{\pm} = 0.103\ J_{zz}$, and $T = 0.0017\ J_{zz}$, Banerjee et al. found good agreement between the results of simulations and their own analytic calculations, from the lattice gauge theory, $\mathscr{H}_{\mathrm{U(1)}}$ (10.17), of both the equal time,

$$C^{\alpha\alpha'}(\mathbf{q}, \tau = 0) = \langle n_{\alpha}(\mathbf{q}) n_{\alpha'}(-\mathbf{q}) \rangle \tag{10.35}$$

and the zero–frequency correlations of

$$S^{\alpha\alpha'}(\mathbf{q}, \omega_n = 0) = \int_0^{\beta} d\tau\ C^{\alpha\alpha'}(\mathbf{q}, \tau) \tag{10.36}$$

Bosons on the sublattice $\alpha = 0, 1, 2, 3$—cf. Fig. 10.8—demonstrating the existence of a quantum liquid state. And, to underwrite the quantum nature of this liquid state, they developed a scaling argument, relating equal–time and zero–frequency correlations at different temperatures through scaling functions derived from $\mathscr{H}_{\mathrm{U(1)}}$. Once again, excellent agreement was found between theory and simulation [4].

For $J_{\pm}/J_{zz} \gtrsim 0.1$, Banerjee et al. found evidence of a first–order transition into a superfluid state of Bosons [4]. Viewed in terms of the lattice gauge theory, such a superfluid is a confined state, and within a quantum lattice–gas mapping, (10.5), it has the interpretation of easy–plane magnetic order. Overall, the finite–temperature phase diagram found by in these simulations closely matches the expectation shown in Fig. 10.3.

The QMC simulation of $\mathscr{H}_{\mathsf{xxz}}$ (10.1) at finite temperatures was subsequently revisited by Kato and Onoda [5], using a continuous (imaginary) time formulation of world–line QMC [63], with directed loop updates [59], modified so as to deal efficiently with the hard–core constraint [64]. The results of Kato and Onoda are entirely consistent with the earlier findings of Banerjee et al. [4], and lead to the phase diagram shown in Fig. 10.9. For $J_{\pm} > 0.052\ J_{zz}$, the ground state of $\mathscr{H}_{\mathsf{xxz}}$ is

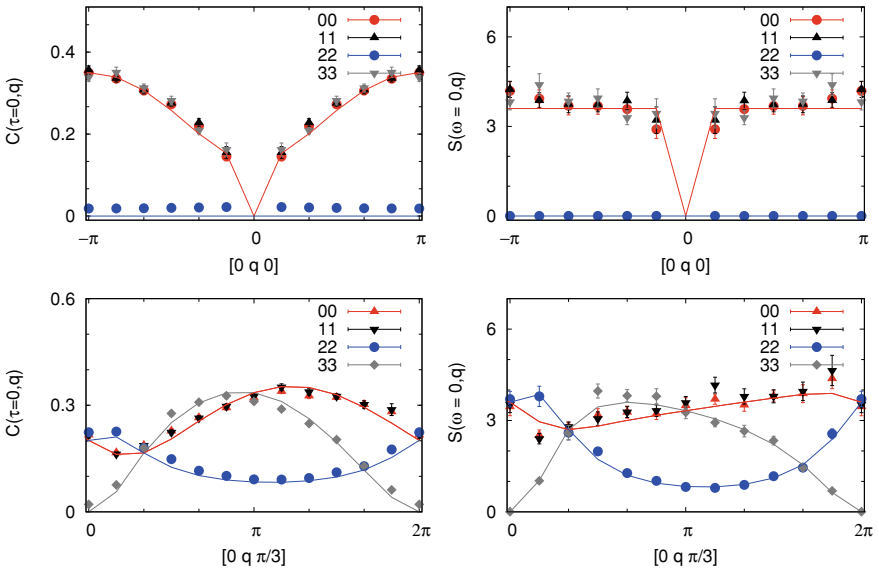

Fig. 10.8 Numerical evidence for the existence of a quantum liquid in a model of hard–core bosons on the pyrochlore lattice. Both the equal–time structure factor $C^{\alpha\alpha}(\mathbf{q}, \tau = 0)$ [left column] and the zero–frequency structure factor for $S^{\alpha\alpha}(\mathbf{q}, \omega = 0)$ [right column], are well described by the predictions of a non-compact U(1) lattice gauge theory, $\mathscr{H}_{\mathrm{U(1)}}$ (10.17). Results are taken from quantum Monte Carlo simulations carried out for $T = 0.0017\ J_{zz}$, $J_{\pm} = 0.103\ J_{zz}$. Reprinted from [4] with permission from the American Physical Society

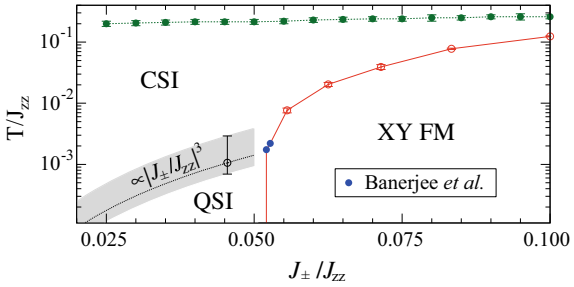

Fig. 10.9 Finite–temperature phase diagram quantum spin ice, showing the crossover between classical (CSI) and quantum (QSI) spin–ice regimes. For $T \lesssim 0.2\ J_{zz}$ spin configurations obey the "ice rules". A dotted line marks the crossover into a low–temperature quantum spin–ice (QSI) regime [cf. Fig. 10.10b]. The crossover temperature is taken to scale $\propto g \sim J_{\pm}^3/J_{zz}^2$ [cf. (10.7)]. A solid red line marks the onset of easy–plane ferromagnetic order (XY FM) at low temperatures, for $J_{\pm} \gtrsim 0.05\ J_{zz}$. Results are taken from quantum Monte Carlo (QMC) simulations of $\mathscr{H}_{\mathrm{XXZ}}$ (10.1), as described in [4, 5], with notation adjusted to be consistent with usage in this chapter. Adapted figure from [5] with permission from the American Physical Society

found to be an easy–plane ferromagnet; for $J_{\pm} < 0.052\ J_{zz}$ the ground state is a QSL, described by the deconfined phase of $\mathscr{H}_{\mathrm{U(1)}}$ (10.17).

Kato and Onoda also present extensive results for the equal–time spin structure factor $S_{\alpha\beta}(\mathbf{q})$. At low temperatures, within the QSL, the evolution of correlations is found to be well–described by the predictions of the lattice gauge theory $\mathscr{H}_{\mathrm{U(1)}}$ (10.17)—cf. (10.32)—suggesting that the transition into the classical spin–ice (CSI) regime occurs through a smooth crossover, as described in [3]. Unsurprisingly, the pure gauge theory $\mathscr{H}_{\mathrm{U(1)}}$ does not give such a good account of the subsequent crossover from the CSI regime into the high–temperature paramagnet, for $T \approx 0.2 J_{zz}$, where the ice–rules begin to break down. Within this high–temperature paramagnet, the structure factor $S_{\alpha\beta}(\mathbf{q})$ is dominated by strong "rods" of scattering along [111] directions, similar to those observed in $Yb_2Ti_2O_7$ [38, 39, 65–67].

10.3.3 Thermodynamics of Quantum Spin Ice

The two crossovers seen in the correlations of quantum spin ice, from high–temperature paramagnet to CSI, and from CSI to QSL, also have thermodynamic signatures. Simulation results for the heat capacity $c_V(T)$ of $\mathscr{H}_{\mathsf{xxz}}$ (10.1), evaluated for $J_{\pm} = 0.045\ J_{zz}$, are shown in Fig. 10.10. A pronounced peak in c_V for $T \approx 0.2\ J_{zz}$ marks the onset of classical spin–ice behaviour. Below this peak, the entropy remaining in the system is found to be very close to the residual entropy $S = 1/2 \ln(3/2)$ predicted by the ice rules [32, 68].

Since the QSL has a unique quantum mechanical ground state, this residual entropy must also be lost on cooling to $T = 0$. And on general grounds, the crossover from CSI to QSL is expected to be accompanied by a Shottky–like anomaly in the specific heat. For $T \to 0$, this second peak in $c_V(T)$ should merge with the simple power law

$$c_V(T \to 0) = B\ T^3 + \ldots \tag{10.37}$$

controlled by the thermal excitation of photons [1, 34], with the dimensional coefficient B given by [3]

$$B = \left(\frac{\pi^2}{30}\right) k_B \left(\frac{k_B a_0}{\hbar c}\right)^3 J\ K^{-4}\ \mathrm{mol}^{-1}\ , \tag{10.38}$$

where mol^{-1} refers one mole of the formula unit. Unfortunately, at present, no simulation results are available at the temperatures $T \lesssim 0.001\ J_{zz}$ needed to confirm these predictions. None the less, Kato and Onoda [5] have used a cubic spline interpolation to extrapolate their numerical data for $c_V(T)$ into the QSL regime, and these interpolations suggest the existence of a second specific heat anomaly, shown in Fig. 10.10b.

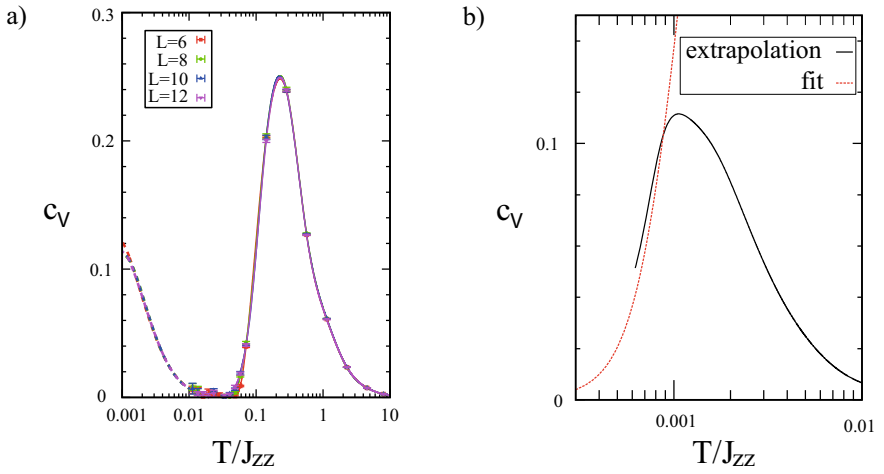

Fig. 10.10 Heat capacity of a quantum spin ice. **a** Heat capacity per spin, $c_V(T)$, showing a peak at $T \approx 0.2\ J_{zz}$, signalling the onset of classical spin ice (CSI) correlations. The dashed line shows an interpolation to low temperatures, where a second peak associated with the onset of quantum coherence is anticipated. **b** Detail of extrapolation to low temperatures—the dashed line shows a fit to the anticipated low–temperature behaviour $c_V(T) \propto (T/c)^3$ [cf. (10.37), based on an independent estimate of the speed of light c. Results are taken from QMC simulations of $\mathscr{H}_{\mathsf{xxz}}$ (10.1) for $J_\pm = 0.045\ J_{zz}$, as described in [5]. Adapted figure from [5] with permission from the American Physical Society

Moreover, it is possible to extract the speed of light c, and thereby the behaviour of the heat capacity for $T \to 0$, from the finite size scaling of the ground–state energy of the QSL [3, 14]. Doing so, for $J_\pm = 0.045\ J_{zz}$, Kato and Onoda find

$$c = 1.49(4)\ g\ a_0\ \hbar^{-1} \tag{10.39}$$

in good agreement with their interpolation of c_V [cf. Fig. 10.10]. It is interesting to compare this value with the estimate

$$c = 1.8(1)\ g\ a_0\ \hbar^{-1} \tag{10.40}$$

obtained in the earlier quantum Monte Carlo simulations of Banerjee et al.. [4] for $J_\pm = 0.103\ J_{zz}$, and the value

$$c = (0.6\ \pm\ 0.1)\ g\ a_0\ \hbar^{-1}\ , \tag{10.41}$$

obtained in Greens function Monte Carlo simulations of the effective low–energy model $\mathscr{H}_{\mathsf{tunnelling}}$ (10.6), valid in the limit $J_\pm/J_{zz} \to 0$ [3]. A similar, if slightly lower, estimate for the speed of light

$$c \approx 0.41\ g\ a_0\ \hbar^{-1}\ , \tag{10.42}$$

was also obtained in a recent semi–classical treatment of quantum spin ice [69].

The trend which emerges is an enhancement of the speed of light, as measured in units of g, with increasing $J_{\pm}/J_{zz}$. This is consistent with degenerate perturbation theory, where tunnelling on longer loops becomes possible with increasing $J_{\pm}/J_{zz}$. Since the tunnelling matrix elements associated with these longer loops all have the same (negative) sign, they do not change the ground state, but lead to faster fluctuations of the gauge field, and so to a higher speed of light.

10.4 An Honourable Mention—Work on Related Models

10.4.1 The Quantum Dimer Model on a Diamond Lattice

While it remains the most visible example, quantum spin ice is by no means the only three–dimensional system to be described by by an effective low–energy model of the form $\mathscr{H}_{\text{tunnelling}}$ (10.6), acting on an extensive manifold of states. Quantum dimer models (QDM's), on bipartite lattices, in three dimensions, have also been proposed to support quantum liquid ground states, analagous to those found in quantum spin ice [1, 10–12]. And in the case of the QDM on a diamond lattice, this proposal has found strong support in simulation [13–15].

The ground state phase diagram of the Rokshar–Kivelson (RK) model $\mathscr{H}_{\text{RK}}$ (10.13), acting on the dimer coverings of a diamond lattice, has been studied using the methods described in Sect. 10.2, leading to the phase diagram shown in Fig. 10.11 [13, 14]. A quantum liquid, described by the deconfined phase of $\mathscr{H}_{\text{U(1)}}$ (10.17), is indeed found bordering the RK point, $\mu_{\text{RK}} = g$, confirming the original conjecture of Moessner and Sondhi [10]. However the extent of this quantum liquid is notably smaller than that found in the RK model of a quantum spin ice, [cf. Fig. 10.4], and does not include the point $\mu_{\text{RK}} = 0$. Moreover, the QDM on a diamond lattice exhibits hidden quantum numbers which can adversly effect the ergodicity of simulation [14].

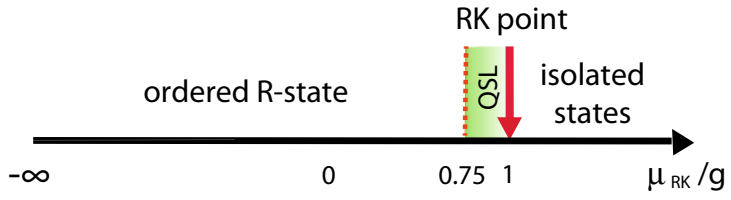

Fig. 10.11 Ground–state phase diagram of the Rokshar–Kivelson (RK) model $\mathscr{H}_{\text{RK}}$ (10.13), acting on the dimer coverings of a diamond lattice, following [13, 14]. Strong evidence is found for a quantum liquid ground state, described by the deconfined phase of $\mathscr{H}_{\text{U(1)}}$ (10.17), bordering the RK point $\mu_{\text{RK}} = g$. This competes with an ordered "R–state", described in [11, 12]

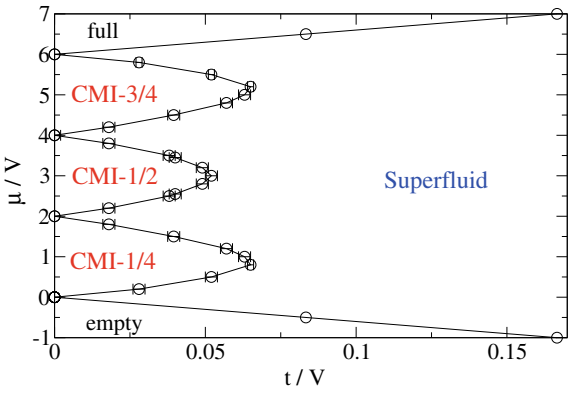

Fig. 10.12 Ground–state phase diagram for hard–core bosons on the pyrochlore lattice $\mathscr{H}_{\mathsf{tV}}$ (10.4), as a function of chemical potential μ. The phase CMI-1/2, found at half–filling, is equivalent to the spin liquid in a quantum spin ice [2–5]. The phases CMI-1/4 and CMI-1/4 both correspond to the quantum liquid found in the quantum dimer model on a diamond lattice, previously studied in [11–14]. Phase boundaries are estimated from finite–temperature QMC simulation, as described in [15]. Reprinted figure from [15] with permission from the American Physical Society

More recently, Lv et al. [15] have also presented evidence for a quantum liquid phases in QMC simulations of hard–core bosons on the pyrochlore lattice, $\mathscr{H}_{\mathsf{tV}}$ (10.4), at filling factors which correspond to the QDM on a diamond lattice. Working in the grand canonical ensemble, using a finite–temperature, continuous–time QMC method based on a worm algorithm [70–72], Lv et al. revisited the model considered by Banerjee et al. [4], considering a range of values of chemical potential which span 1/4–, 1/2– and 3/4–filling—cf. Fig. 10.12. At 1/2–filling, these simulations reproduce earlier results for quantum spin ice [4, 5], while new liquid phases for 1/4– and 3/4–filling correspond to tunnelling between states with exactly one, or three, bosons per tetrahedron, which can be mapped onto dimer coverings of the diamond lattice, previously studied in [11–14]. The residual entropy associated with these phases is found to be similar to the known value $S/N = 0.13$ for dimer coverings of the diamond lattice [73].

10.4.2 Quantum Square Ice, Also Known as the Quantum Six–Vertex Model

A two–dimensional analogue of water ice, often referred to as "square ice", occurs in certain proton–bonded ferroelectrics [30], and has a long and venerable history as a problem in statistical mechanics, where it is known as the 6–vertex model [74]. Quantum versions of square ice, analagous to quantum spin ice, have been motivated by models of cuprate high–temperature superconductivity [75], and hard–core bosons on the checkerboard lattice [6, 9]. Meanwhile a very similar, quantum 8–vertex model, arises in models of layered anti–ferroelectrics known as "square

acid" [8]. And a square ice built of water molecules was also recently realised for the first time [76]. Here too, experiments on rings of water molecules hint that quantum tunnelling could play a role [77].

Just as in three–dimensional quantum spin ice, quantum tunnelling between different two–dimensional ice configurations can be described by a compact U(1) lattice gauge theory. However, in two dimensions, this is expected to be confining [26, 47, 78], and early exact diagonalisation studies of quantum square ice found clear evidence of a plaquette–ordered ground state [6]. None the less, the properties of the model remain of interest, and considerable ingenuity has been brought to bear on simulations of quantum square ice. Ground–state properties have been investigated using continuous–time diffusion Monte Carlo [7], and a tailor–made "membrane algorithm" was used to explore phases at finite–temperature [9]. QMC simulations have also been carried out for the closely–related quantum 8–vertex model [8]. In all cases, ground states are found to be ordered [7], but with a very low transition temperature [9, 26]. Quantum effects remain significant at finite temperature, even in the disordered phase [8, 9].

10.5 Where Next ?

Viewed in terms of all the things which don't happen, the ground state of a quantum spin ice is not a very interesting state. Breaking no symmetries, and possessing only hidden, topological order, it evolves quietly out of the classical, high–temperature paramagnet without so much as a phase transition. What makes this massively–entangled, but seemingly inert, spin–liquid so interesting is the range of different excitations which it can support—the elementary excitations of the lattice gauge theory $\mathscr{H}_{\mathrm{U}(1)}$ (10.17) include emergent photons, as well as both electric and magnetic charges. However, while QMC has contributed enormously to our understanding of the ground–state and thermodynamic properties of quantum spin ice, to date simulations offer only an indirect portrait of the photons [cf. Fig. 10.13], and the electric charges of the lattice gauge theory (the magnetic monopoles of spin ice). As yet, no evidence has been found for the magnetic charges of (10.17).

So far as simulation is concerned, this lack of a clear portrait of excitations has to be viewed as unfinished business. However some information is now available from other sources—estimates of the dispersion of the electric gauge–charges (magnetic monopoles) can be gleaned from mean–field theory [34, 79], calculations on a Bethe lattice [80], and an analysis of spinon diffusion [81] And in the case of two–dimensional quantum square ice, estimates of the associated bandwidth have been made from QMC for bosons [9] and ED for fermions [40, 82].

Another promising avenue for future investigation is the generalisation of the quantum ice to new contexts, such as Rydberg atoms in an optical lattice [83]. And there is growing evidence that the collective quantum tunnelling of protons [26–29, 84, 85], may play an important role in the low–temperature physics of the original ice—common, hexagonal water ice [31–33, 86–88]. But given its importance as a

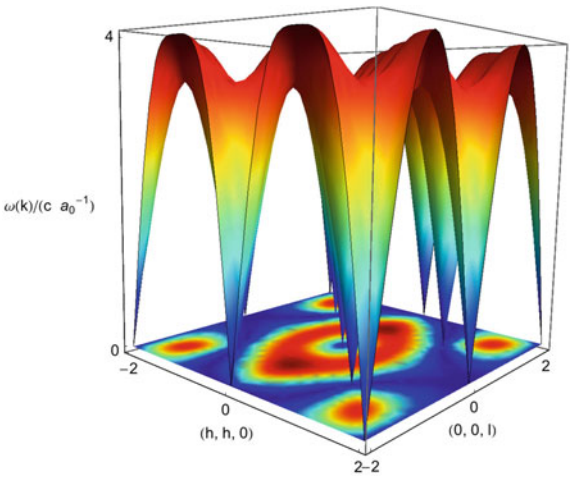

Fig. 10.13 Figure illustrating the connection between the photons of the lattice gauge theory $\mathscr{H}_{\mathrm{U}(1)}$ (10.17) and the equal–time structure factor $S(\mathbf{q})$, in a quantum spin ice. The vanishing spectral weight in the zone center (absent pinch point) can be understood in terms of the vanishing intensity of the photon for $\omega \to 0$, [3, 34]. Reprinted figure from [3] with permission from the American Physical Society

model system, perhaps the most glaring omission is the lack of a clear picture of how quantum mechanics enters into the theory of conventional, dipolar spin ice.

Conventional spin ice materials, such as $Dy_2Ti_2O_7$, differ in important ways from the idealised quantum spin ice considered in this chapter. Magnetic moments interact through strong, long–range, dipolar interactions [51, 89–93]. In the absence of quantum fluctuations, these interactions are known to favour ordered ground states [51, 89–91, 94]. For a long time, experiment did not reveal any sign of an ordering transition down to 300 mK [17–19, 95]. But recent experiments, which observe an upturn in the heat capacity of $Dy_2Ti_2O_7$ below 500 mK [20], provide a strong motivation to reexamine the ground state of dipolar spin ice. And since it is clear that spin ice still has dynamics at this temperature, albeit a very slow dynamics, it is worth asking whether quantum effects could play a role ?

As yet, there is no universally agreed picture, at a microscopic level, of how quantum effects enter in a dipolar spin ice [21, 22]. However, if quantum fluctuations lead to tunnelling between different spin configurations obeying the ice rules, the form of tunnelling is subject to exactly the same topological constraints as in a quantum spin ice. We can therefore take $\mathscr{H}_{\mathsf{tunnelling}}$ (10.6) as a minimal, effective model of quantum effects in a dipolar spin ice. Carrying out QMC simulations of a system with frustrated, long–range interactions is a challenging proposition. None the less, the ground–state properties of dipolar spin ice, in the presence of quantum tunnelling $\mathscr{H}_{\mathsf{tunnelling}}$, were recently investigated using the same GFMC methods as previously applied to quantum spin ice [2, 3]. These simulations [16] reveal that even a small amount of quantum tunnelling $g \approx 0.1\ D$ can stabilise a QSL ground state of the same type as found in quantum spin ice (here D is the bare scale of dipolar interactions)—cf. Fig. 10.14. While this is a long way from being the end of the story, these results leaves open the possibility that the equilbrium ground state of a dipolar spin ice could be a quantum spin liquid.

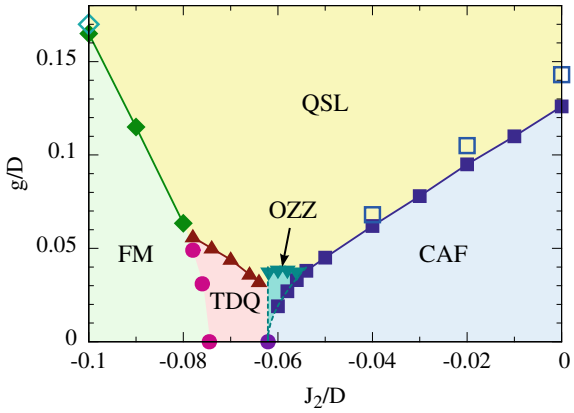

Fig. 10.14 Ground–state phase diagram of a spin ice with long range dipolar interactions D, quantum tunnelling g (10.6), and 2^{nd}–neighbour exchange, J_2. For $g \gtrsim 0.1\ D$, the ground state is a quantum spin liquid (QSL), described by the deconfined phase of the U(1) lattice gauge theory, $\mathscr{H}_{U(1)}$ (10.17). The competing phases, marked FM, TDQ, OZZ and CAF, exhibit chain–based order, of the type discussed in [16]. Phase boundaries are taken from Green's function Monte Carlo (GFMC) simulation, as described in [16]. Reprinted figure from [16] with permission from the American Physical Society

10.6 Conclusions

In this chapter we have explored some of the recent progress in understanding quantum spin ice which has come from quantum Monte Carlo simulation. This work has brought a number of rewards. Crucially, it has given us reason to believe that a quantum spin–liquid of the type described in Chap. 9 and 11 [1, 34], can occur in a realistic microscopic model of a three–dimensional magnet [2, 4]. It has also taught us to trust in the lattice–gauge theory description of this quantum spin–liquid, at its simplest, non–compact level [2–5], opening the route to a clear phenomenology for comparison with experiment [2, 3, 5]. And, by allowing us to pose questions in new ways, simulation has brought alive many of the subtle and exotic features of this spin–liquid state.

Note added in proof:
Two very recent publications are worth remark in context of this Chapter. The first, by Huang et al., presents dynamical structure factors for a model quantum spin ice found from QMC simulations, showing the dynamics of topological excitations [96]. The second by Sibille et al., reports the possible observation of emergent electrodynamics in the quantum spin ice candidate, $Pr_2Hf_2O_7$ [97].

References

1. M. Hermele, M.P.A. Fisher, L. Balents, Phys. Rev. B **69**, 064404 (2004). https://doi.org/10.1103/PhysRevB.69.064404
2. N. Shannon, O. Sikora, F. Pollmann, K. Penc, P. Fulde, Phys. Rev. Lett. **108**, 067204 (2012). https://doi.org/10.1103/PhysRevLett.108.067204
3. O. Benton, O. Sikora, N. Shannon, Phys. Rev. B **86**, 075154 (2012). https://doi.org/10.1103/PhysRevB.86.075154
4. A. Banerjee, S.V. Isakov, K. Damle, Y.B. Kim, Phys. Rev. Lett. **100**, 047208 (2008). https://doi.org/10.1103/PhysRevLett.100.047208
5. Y. Kato, S. Onoda, Phys. Rev. Lett **115**, 077202 (2015). https://doi.org/10.1103/PhysRevLett.115.077202
6. N. Shannon, G. Misguich, K. Penc, Phys. Rev. B **69**, 220403(R) (2004). https://doi.org/10.1103/PhysRevB.69.220403
7. O.F. Syljusen, S. Chakravarty, Phys. Rev. Lett. **96**, 147004 (2006). https://doi.org/10.1103/PhysRevLett.96.147004
8. C.-H. Chern, N. Nagaosa, Phys. Rev. Lett. **112**, 247602 (2014). https://doi.org/10.1103/PhysRevLett.112.247602
9. L.-P. Henry, T. Roscilde, Phys. Rev. Lett. **113**, 027204 (2014). https://doi.org/10.1103/PhysRevLett.113.027204
10. R. Moessner, S. Sondhi, Phys. Rev. B **68**, 184512 (2003). https://doi.org/10.1103/PhysRevB.68.184512
11. D. L. Bergman, R. Shindou, G. A. Fiete, and L. Balents, Phys. Rev. Lett **96**, 097207 (2006); erratum ibid **97**, 139906 (2006). https://doi.org/10.1103/PhysRevLett.96.097207
12. D.L. Bergman, G.A. Fiete, L. Balents, Phys. Rev. B **73**, 134402 (2006). https://doi.org/10.1103/PhysRevB.73.134402
13. O. Sikora, F. Pollmann, N. Shannon, K. Penc, P. Fulde, Phys. Rev. Lett. **103**, 247001 (2009). https://doi.org/10.1103/PhysRevLett.103.247001
14. O. Sikora, N. Shannon, F. Pollmann, K. Penc, P. Fulde, Phys. Rev. B **84**, 115129 (2011). https://doi.org/10.1103/PhysRevB.84.115129
15. J.-P. Lv, G. Chen, Y. Deng, Z.Y. Meng, Phys. Rev. Lett. **115**, 037202 (2015). https://doi.org/10.1103/PhysRevLett.115.037202
16. P.A. McClarty, O. Sikora, R. Moessner, K. Penc, F. Pollmann, N. Shannon, Phys. Rev. B **92**, 094418 (2015). https://doi.org/10.1103/PhysRevB.92.094418
17. J. Snyder, J.S. Slusky, R.J. Cava, P. Schiffer, Nature **413**, 48 (2001). https://doi.org/10.1038/35092516
18. K. Matsuhira, Y. Hinatsu, T. Sakakibara, J. Phys.: Condens. Matter **13**, L737 (2001). https://doi.org/10.1088/0953-8984/13/31/101
19. B. Klemke, M. Meissner, P. Strehlow, K. Kiefer, S.A. Grigera, D.A. Tennant, J. Low Temp. Phys. **163**, 345 (2011). https://doi.org/10.1007/s10909-011-0348-y
20. see e.g. D. Pomaranski, L. R. Yaraskavitch, S. Meng, K. A. Ross, H. M. L. Noad, H. A. Dabkowska, B. D. Gaulin and J. B. Kycia, Nat. Phys. **9**, 353 (2013) and references therein. https://doi.org/10.1038/NPHYS2591
21. B. Tomasello, C. Castelnovo, R. Moessner, J. Quintanilla, Phys. Rev. B **92**, 155120 (2015). https://doi.org/10.1103/PhysRevB.92.155120
22. J.G. Rau, M.J.P. Gingras, Phys. Rev. B **92**, 144417 (2015). https://doi.org/10.1103/PhysRevB.92.144417
23. Hamid R. Molavian, Michel J. P. Gingras and Benjamin Canals Phys. Rev. Lett. **98**, 157204 (2007). https://doi.org/10.1103/PhysRevLett.98.157204
24. K.A. Ross, L. Savary, B.D. Gaulin, L. Balents, Phys. Rev. X **1**, 021002 (2011). https://doi.org/10.1103/PhysRevX.1.021002
25. A.J. Princep, D. Prabhakaran, A.T. Boothroyd, D.T. Adroja, Phys. Rev. B **88**, 104421 (2013). https://doi.org/10.1103/PhysRevB.88.104421

26. A. H. Castro Neto, P. Pujol and E. Fradkin, Phys. Rev. B 74, 024302 (2006). https://doi.org/10.1103/PhysRevB.74.024302
27. L.E. Bove, S. Klotz, A. Paciaroni, F. Sacchetti, Phys. Rev. Lett. **103**, 165901 (2009). https://doi.org/10.1103/PhysRevLett.103.165901
28. C. Drechsel-Grau, D. Marx, Phys. Rev. Lett. **112**, 148302 (2014). https://doi.org/10.1103/PhysRevLett.112.148302
29. O. Benton, O. Sikora, N. Shannon, Phys. Rev. B **93**, 125143 (2016). https://doi.org/10.1103/PhysRevB.93.125143
30. R. Youngblood, J.D. Axe, B.M. McCoy, Phys. Rev. B **21**, 5212 (1980). https://doi.org/10.1103/PhysRevB.21.5212
31. J.D. Bernal, R.H. Fowler, J. Chem. Phys. **1**, 515 (1933). https://doi.org/10.1063/1.1749327
32. L. Pauling, J. Am. Chem. Soc. **57**, 2680 (1935). https://doi.org/10.1021/ja01315a102
33. W.F. Giauque, J.W. Stout, Am. J. Chem. Phys **58**, 1144–1150 (1936). https://doi.org/10.1021/ja01298a023
34. L. Savary, L. Balents, Phys. Rev. Lett. **108**, 037202 (2012). https://doi.org/10.1103/PhysRevLett.108.037202
35. S.-S. Lee and P. A. Lee Phys. Rev. B **74**, 035107 (2006). https://doi.org/10.1103/PhysRevB.74.035107
36. S. H. Curnoe, Phys. Rev. B **75**, 212404 (2007); erratum ibid **76**, 139903(E) (2007). https://doi.org/10.1103/PhysRevB.75.212404
37. H. Yan, O. Benton, L. Jaubert, N. Shannon, Phys. Rev. B **95**, 094422 (2017). https://doi.org/10.1103/PhysRevB.95.094422
38. J.D. Thompson, P.A. McClarty, H.M. Ronnow, L.P. Regnault, A. Sorge, M.J.P. Gingras, Phys. Rev. Lett. **106**, 187202 (2011). https://doi.org/10.1103/PhysRevLett.106.187202
39. L.J. Chang, S. Onoda, Y. Su, Y.-J. Kao, K.-D. Tsuei, Y. Yasui, K. Kakurai, M.R. Lees, Nat. Commun. **3**, 992 (2012). https://doi.org/10.1038/ncomms1989
40. P. Fulde, K. Penc, N. Shannon, Ann. Phys. **11**, 892 (2002). https://doi.org/10.1002/1521-3889
41. C. Castelnovo, R. Moessner, S.L. Sondhi, Nature **451**, 42 (2008). https://doi.org/10.1038/nature06433
42. L. D. C. Jaubert and P. C. W. Holdsworth Nat. Phys. **5**, 258 (2009). https://doi.org/10.1038/NPHYS1227
43. J. Villain, J. Phys. France **36**, 581 (1975). https://doi.org/10.1051/jphys:01975003606058100
44. K. Wilson, Phys. Rev. D **10**, 2445 (1974). https://doi.org/10.1103/PhysRevD.10.2445
45. J.B. Kogut, Rev. Mod. Phys. **51**, 659 (1979). https://doi.org/10.1103/RevModPhys.51.659
46. A.H. Guth, Phys. Rev. D **21**, 2291 (1980). https://doi.org/10.1103/PhysRevD.21.2291
47. E. Fradkin, S.H. Shenker, Phys. Rev. D **19**, 3682 (1979). https://doi.org/10.1103/PhysRevD.19.3682
48. D.S. Rokhsar, S.A. Kivelson, Phys. Rev. Lett. **61**, 2376 (1988). https://doi.org/10.1103/PhysRevLett.61.2376
49. B. Lautrup, M. Nauenberg, Phys. Rev. Lett. **45**, 1755 (1980). https://doi.org/10.1103/PhysRevLett.45.1755
50. M. E. J. Newman and G.T. Barkema, Monte Carlo Methods in Statistical Physics, (Oxford University Press, Oxford New York, 1999), pp. 179–209. https://doi.org/10.1007/978-3-642-03163-2
51. R.G. Melko, B.C. den Hertog, M.J.P. Gingras, Phys. Rev. Lett. **87**, 067203 (2001). https://doi.org/10.1103/PhysRevLett.87.067203
52. F. Pollmann, PhD. Thesis, Technical University of Dresden (2006)
53. M. Calandra Buonaura and S. Sorella, Phys. Rev. B **57**, 11446 (1998). https://doi.org/10.1103/PhysRevB.57.11446
54. C.L. Henley, Phys. Rev. B **71**, 014424 (2005). https://doi.org/10.1103/PhysRevB.71.014424
55. S. Sorella, Phys. Rev. B **64**, 024512 (2001). https://doi.org/10.1103/PhysRevB.64.024512
56. M. Capello, F. Becca, M. Fabrizio, S. Sorella, E. Tosatti, Phys. Rev. Lett. **94**, 026406 (2005). https://doi.org/10.1103/PhysRevLett.94.026406

57. D.A. Huse, W. Krauth, R. Moessner, S.L. Sondhi, Phys. Rev. Lett. **91**, 167004 (2003). https://doi.org/10.1103/PhysRevLett.91.167004
58. T. Fennell, P.P. Deen, A.R. Wildes, K. Schmalzl, D. Prabhakaran, A.T. Boothroyd, R.J. Aldus, D.F. McMorrow, S.T. Bramwell, Science **326**, 415 (2009). https://doi.org/10.1126/science.1177582
59. O.F. Syljuasen, A.W. Sandvik, Phys. Rev. E **66**, 046701 (2002). https://doi.org/10.1103/PhysRevE.66.046701
60. K. Louis and C. Gros, Phys. Rev. B **70**, 100410(R) (2004). https://doi.org/10.1103/PhysRevB.70.100410 K. Damle et al. (unpublished)
61. Roger G Melko, J. Phys.: Condens. Matter **19**, 145203 (2007). https://doi.org/10.1088/0953-8984/19/14/145203
62. Y.-B. Kim, private communication
63. N. Kawashima, K. Harada, J. Phys. Soc. Jpn. **73**, 1379 (2004). https://doi.org/10.1143/JPSJ.73.1379
64. Y. Kato, T. Suzuki, N. Kawashima, Phys. Rev. E **75**, 066703 (2007). https://doi.org/10.1103/PhysRevE.75.066703
65. P. Bonville, J. A. Hodges, E. Bertin, J.-P. Bouchaud, P. Dalmas de Reotier, L.-P. Regnault, H. M. Ronnow, J.-P. Sanchez, S. Sosin, and A. Yaouanc, Hyperfine Interact. **156**, 103 (2004). https://doi.org/10.1023/B:HYPE.0000043235.21257.13
66. K.A. Ross, J.P.C. Ruff, C.P. Adams, J.S. Gardner, H.A. Dabkowska, Y. Qiu, J.R.D. Copley, B.D. Gaulin, Phys. Rev. Lett. **103**, 227202 (2009). https://doi.org/10.1103/PhysRevLett.103.227202
67. K.A. Ross, L.R. Yaraskavitch, M. Laver, J.S. Gardner, J.A. Quilliam, S. Meng, J.B. Kycia, D.K. Singh, T. Proffen, H.A. Dabkowska, B.D. Gaulin, Phys. Rev. B **84**, 174442 (2011). https://doi.org/10.1103/PhysRevB.84.174442
68. J.F. Nagle, J. Math. Phys. **7**, 1484 (1966). https://doi.org/10.1063/1.1705058
69. M.P. Kwasigroch, B. Douçot, C. Castelnovo, Phys. Rev. B **95**, 1484 (2017). https://doi.org/10.1103/PhysRevB.95.134439
70. N.V. Prokofev, B.V. Svistunov, I.S. Tupitsyn, J. Exp. Theor. Phys. **87**, 310 (1998). https://doi.org/10.1134/1.558661
71. N.V. Prokofev, B.V. Svistunov, I.S. Tupitsyn, Phys. Lett. A **238**, 253 (1998). https://doi.org/10.1016/S0375-9601(97)00957-2
72. L. Pollet, Rep. Prog. Phys. **75**, 094501 (2012). https://doi.org/10.1088/0034-4885/75/9/094501
73. J.F. Nagle, Phys. Rev. **152**, 190 (1966). https://doi.org/10.1103/PhysRev.152.190
74. R. J. Baxter Exactly solved models in statistical mechanics, reprinted, 3rd edition. (Dover, Mineloa, 2007) ISBN 10 : 0486462714
75. S. Chakravarty, Phys. Rev. B **66**, 224505 (2002). https://doi.org/10.1103/PhysRevB.66.224505
76. G. Algara-Siller, O. Lehtinen, F. C. Wang, R. R. Nair, U. Kaiser, H. A. Wu, A. K. Geim and I. V. Grigorieva Nature **519**, 443 (2015). https://doi.org/10.1038/nature14295
77. X. Meng, J. Guo, J. Peng, J. Chen, Z. Wang, J.-R. Shi, X.-Z. Li, E.-G. Wang, Y. Jiang, Nat. Phys. **11**, 235 (2015). https://doi.org/10.1038/nphys3225
78. A.M. Polyakov, Nucl. Phys. B **120**, 429 (1977). https://doi.org/10.1016/0550-3213(77)90086-4
79. Z.H. Hao, A.G.R. Day, M.J.P. Gingras, Phys. Rev. B **90**, 214430 (2014). https://doi.org/10.1103/PhysRevB.90.214430
80. O. Petrova, R. Moessner and S. L. Sondhi, Phys. Rev. B **92**, 100401(R) (2015). https://doi.org/10.1103/PhysRevB.92.100401
81. Y. Wan, J. Carrasquilla and R. G. Melko, Phys. Rev. Lett. **116**, 167202 (2016). https://doi.org/10.1103/PhysRevLett.116.167202
82. D. Poilblanc, K. Penc, N. Shannon, Phys. Rev. B **75**, 220503(R) (2007). https://doi.org/10.1103/PhysRevB.75.220503
83. A.W. Glaetzle, M. Dalmonte, R. Nath, I. Rousochatzakis, R. Moessner, and P. Zoller, Phys. Rev. X **4**, 041037 (2014). https://doi.org/10.1103/PhysRevX.4.041037
84. J. Ihm, J. Phys. A **29**, L1 (1996). https://doi.org/10.1088/0305-4470/29/1/001

85. F. Yen, T. Gao, J. Phys. Chem. Lett. **6**, 2822 (2015). https://doi.org/10.1021/acs.jpclett.5b00797
86. N. Bjerrum, Science **115**, 385 (1952). https://doi.org/10.1126/science.115.2989.385
87. V.F. Petrenko, R.W. Whitworth, *Physics of Ice* (Oxford University Press, Oxford, 1999). ISBN 9780198518945
88. S.V. Isakov, R. Moessner, S.L. Sondhi, D.A. Tennant, Phys. Rev. B **91**, 245152 (2015). https://doi.org/10.1103/PhysRevB.91.245152
89. R. Siddharthan, B.S. Shastry, A.P. Ramirez, A. Hayashi, R.J. Cava, S. Rosenkranz, Phys. Rev. Lett. **83**, 1854 (1999). https://doi.org/10.1103/PhysRevLett.83.1854
90. B.C. den Hertog, M.J.P. Gingras, Phys. Rev. Lett. **84**, 3430 (2000). https://doi.org/10.1103/PhysRevLett.84.3430
91. R. Siddharthan, B.S. Shastry, A.P. Ramirez, Phys. Rev. B **63**, 184412 (2001). https://doi.org/10.1103/PhysRevLett.63.184412
92. S.T. Bramwell, M.J. Harris, B.C. den Hertog, M.J.P. Gingras, J.S. Gardner, D.F. McMorrow, A.R. Wildes, A.L. Cornelius, J.D.M. Champion, R.G. Melko, T. Fennell, Phys. Rev. Lett. **87**, 047205 (2001). https://doi.org/10.1103/PhysRevLett.87.047205
93. T. Yavors'kii, T. Fennell, M.J.P. Gingras, S.T. Bramwell, Phys. Rev. Lett. **101**, 037204 (2008). https://doi.org/10.1103/PhysRevLett.101.037204
94. S.V. Isakov, R. Moessner, S.L. Sondhi, Phys. Rev. Lett. **95**, 217201 (2005). https://doi.org/10.1103/PhysRevLett.95.217201
95. A.P. Ramirez, A. Hayashi, R.J. Cava, R. Siddharthan, B.S. Shastry, Nature **399**, 333 (1999). https://doi.org/10.1038/20619
96. C.-J. Huang, Y. Deng, Y. Wan, Z.Y. Meng, Phys. Rev. Lett. **120**, 167202 (2018). https://doi.org/10.1103/PhysRevLett.120.167202
97. R. Sibille, N. Gauthier, H. Yan, M.C. Hatnean, J. Ollivier, B. Winn, U. Filges, G. Balakrishnan, M. Kenzelmann, N. Shannon, T. Fennell, Nat. Phys. **14**, 711 (2018). https://doi.org/10.1038/s41567-018-0116-x

Chapter 11
Analytical Approaches to Quantum Spin Ice

Owen Benton

Abstract In this chapter we introduce some analytical approaches which are useful for the description of quantum spin ice systems. Firstly, we will show how to obtain the dispersion relation of the emergent photons in the U(1) spin liquid phase of quantum spin ice, starting from a lattice field theory. We will see how this can be used to calculate the structure factor for neutron scattering experiments. Secondly, we will introduce a method which allows us to derive the general Hamiltonian for pyrochlore spin systems and to find its classical phase diagram purely from symmetry considerations. This enables us to express the conditions for a pyrochlore magnet to be in its ground state in terms of a general local constraint, of which the "ice rule" known from spin ice is a special case.

11.1 Emergent Photons in Quantum Spin Ice

One of the most intriguing features of the $U(1)$ quantum spin liquid state on the phase diagram of quantum spin ice materials is the predicted existence of gapless, linearly dispersing, emergent photons as excitations of this state [1]. For exchange parameters falling within the quantum spin liquid regime, one can describe the low temperature physics in terms of a "photon gas". This approach has been very successful in describing simulation results for quantum ice models on the pyrochlore lattice, both with regard to thermodyamic properties and spin correlations [2–5]. A detailed discussion on the gauge theory and numerics of quantum spin ice is given in Chaps. 9 and 10.

In what follows, will we derive the photons as the excitations of a non-compact, lattice gauge theory, Hamiltonian

$$\mathscr{H}_{\mathrm{U}(1)} = \frac{\mathscr{U}}{2} \sum_{\langle rr' \rangle} E^2_{\mathbf{r}\mathbf{r}'} + \frac{\mathscr{K}}{2} \sum_{\hexagon} [\nabla_{\hexagon} \times A]^2 \tag{11.1}$$

O. Benton (✉)
Max Planck Institute for the Physics of Complex Systems, Dresden, Germany
e-mail: benton@pks.mpg.de

M. Udagawa and L. Jaubert (eds.), *Spin Ice*, Springer Series in Solid-State Sciences 197,
https://doi.org/10.1007/978-3-030-70860-3_11

defined on the diamond lattice.

The electromagnetic fields E and A live on the links $\mathbf{r}\mathbf{r}'$ of the diamond lattice. They are directed variables, i.e.

$$E_{\mathbf{r}\mathbf{r}'} = -E_{\mathbf{r}'\mathbf{r}} \tag{11.2}$$

$$A_{\mathbf{r}\mathbf{r}'} = -A_{\mathbf{r}'\mathbf{r}} \tag{11.3}$$

The lattice curl ($\nabla_{\hexagon} \times$) in (11.1) is defined on the hexagonal plaquettes of the diamond lattice. As in conventional electromagnetism, the electric field E and the vector potential A are canonically conjugate and have a commutation relationship

$$[E_{\mathbf{r}\mathbf{r}'}, A_{\mathbf{r}''\mathbf{r}'''}] = i(\delta_{\mathbf{r}\mathbf{r}''}\delta_{\mathbf{r}'\mathbf{r}'''} - \delta_{\mathbf{r}'\mathbf{r}''}\delta_{\mathbf{r}\mathbf{r}'''}). \tag{11.4}$$

This lattice field theory describes the low energy physics of the $U(1)$ quantum spin liquid phase of a quantum spin ice [1, 4, 7]. One can view this description as phenomenological, with the parameters being fixed by comparison with numerics for a given microscopic model [4]. Alternatively, one can derive this description from a microscopic model of tunnelling between ice-rule obeying states using a novel $1/S$ approximation [6].

Remembering that a bond on the diamond lattice maps to a site of the pyrochlore lattice, the electric field $E_{\mathbf{r}\mathbf{r}'}$ on each bond relates directly to the direction of the flux carried by the spin on each pyrochlore site, in the classical spin ice problem. The spin structure factor thus relates directly to the correlation functions of the electric field.

In Sect. 11.1.1 we will show how (11.1) may be diagonalized in terms of photon operators and calculate the photon dispersion on the lattice. In Sect. 11.1.2 we will show how to calculate the correlation functions of the electric field, and how these are related to the spin-spin correlation functions which one could measure in a neutron scattering experiment on a quantum spin ice.

11.1.1 Constructing the Photon

The quantisation of the electromagnetic potential $A_{\mathbf{r}\mathbf{r}'}$ proceeds in analogy with conventional quantum electromagnetism by introducing a bosonic operator

$$[a_\lambda(\mathbf{q}), a^\dagger_{\lambda'}(\mathbf{q}')] = \delta_{\lambda\lambda'}\delta_{\mathbf{q}\mathbf{q}'} \tag{11.5}$$

where the band index λ runs from 1 to 4, because there are four sites in the primitive unit cell of the pyrochlore lattice.

We adopt a labelling convention in which the bonds $\mathbf{r}, \mathbf{r}'$ of the diamond lattice are labelled by a single site $\mathbf{r}$, belonging to the 'A' sublattice of the diamond lattice, and a direction index m

$$\mathbf{r}, \mathbf{r}' = \mathbf{r}, \mathbf{r} + \mathbf{e}_m \rightarrow \mathbf{r}, m \tag{11.6}$$

where the bond vectors $\mathbf{e}_m$ are

$$\mathbf{e}_0 = \frac{a_0}{4}(1, 1, 1) \tag{11.7}$$

$$\mathbf{e}_1 = \frac{a_0}{4}(1, -1, -1) \tag{11.8}$$

$$\mathbf{e}_2 = \frac{a_0}{4}(-1, 1, -1) \tag{11.9}$$

$$\mathbf{e}_3 = \frac{a_0}{4}(-1, -1, 1) \tag{11.10}$$

and a_0 is the linear dimension of the cubic unit cell of the lattice.

The electromagnetic potential written in terms of the operators $a_\lambda(\mathbf{q}), a_\lambda(\mathbf{q})^\dagger$ becomes

$$A_{(\mathbf{r},m)} = \sqrt{\frac{2}{N}} \sum_{\mathbf{q}} \sum_{\lambda=1}^{4} \sqrt{\frac{\mathscr{U}}{\omega_\lambda(\mathbf{q})}} \big[\exp(-i\mathbf{q} \cdot (\mathbf{r} + \mathbf{e}_m/2)) \eta_{m\lambda}(\mathbf{q}) a_\lambda(\mathbf{q}) + \exp(i\mathbf{q} \cdot (\mathbf{r} + \mathbf{e}_m/2)) \eta^*_{m\lambda}(\mathbf{q}) a^\dagger_\lambda(\mathbf{q}) \big] \tag{11.11}$$

where the $\eta_{m\lambda}(\mathbf{q})$ are the elements of a unitary 4×4 matrix whose columns $\eta_\lambda(\mathbf{q})$ play the same role as the polarisation vector in conventional electromagnetism. The function $\omega_\lambda(\mathbf{q})$ will be determined below. The electric field is then

$$E_{(\mathbf{r},m)} = i\sqrt{\frac{2}{N}} \sum_{\mathbf{q}} \sum_{\lambda=1}^{4} \sqrt{\frac{\omega_\lambda(\mathbf{q})}{\mathscr{U}}} \big[\exp(-i\mathbf{q} \cdot (\mathbf{r} + \mathbf{e}_m/2)) \eta_{m\lambda} a_\lambda(\mathbf{q}) - \exp(i\mathbf{q} \cdot (\mathbf{r} + \mathbf{e}_m/2)) \eta^*_{m\lambda} a^\dagger_\lambda(\mathbf{q}) \big] \tag{11.12}$$

Inserting these definitions into (11.1) we obtain a Hamiltonian which is bilinear $a_\lambda(\mathbf{q}), a^\dagger_\lambda(\mathbf{q})$. All we need to do to diagonalise (11.1) is to choose the function $\omega_\lambda(\mathbf{q})$ such that terms which do not conserve photon number are eliminated. In order to do this, we need to evaluate the Fourier transform of the lattice curl operator on hexagonal plaquettes ($\nabla_{\hexagon} \times$), illustrated in Fig. 11.1.

The centres of the hexagonal plaquettes form an additional pyrochlore lattice, dual to the 'original' one. The lattice of plaquette centres therefore has four sublattices and we denote the position of any plaquette as

$$\mathbf{p} - \mathbf{e}_n/2$$

where the set of points $\mathbf{p}$ forms an FCC lattice.

Each six-bond plaquette is composed of pairs of bonds which enter with opposite signs in the directed sum around the plaquette. These bonds have midpoints located

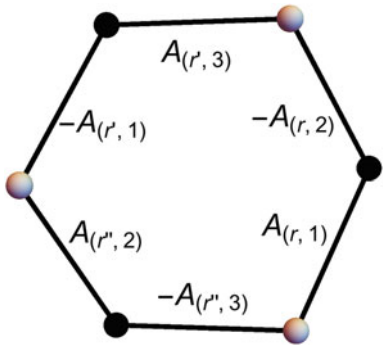

Fig. 11.1 Lattice curl taken around a hexagonal plaquette. The black (gray) sites are the A (B) sites of the diamond lattice. The lattice curl is given by the sum of terms $\pm A_{(\mathbf{r},m)}$ with alternating signs as indicated

at

$$\mathbf{p} - \mathbf{e}_n/2 \pm \mathbf{h}_{nm}$$

where

$$\mathbf{h}_{nm} = \frac{a_0}{\sqrt{8}} \frac{\mathbf{e}_n \times \mathbf{e}_m}{|\mathbf{e}_n \times \mathbf{e}_m|} \tag{11.13}$$

Therefore, we obtain for the lattice curl of A evaluated around a plaquette located at $\mathbf{p} - \mathbf{e}_n/2$

$$\begin{aligned}(\nabla_{\hexagon} \times A)_{(\mathbf{p},n)} = \sqrt{\frac{2}{N}} \sum_{\mathbf{q}} \sum_{\lambda=1}^{4} \sqrt{\frac{\mathscr{U}}{\omega_\lambda(\mathbf{q})}} \\ \Big\{ \exp[-i\mathbf{q}\cdot(\mathbf{p} - \mathbf{e}_n/2)] a_\lambda(\mathbf{q}) \sum_m (-2i \sin(\mathbf{q}\cdot\mathbf{h}_{nm})) \eta_{m\lambda}(\mathbf{q}) + \\ \exp[i\mathbf{q}\cdot(\mathbf{p} - \mathbf{e}_n/2)] a^\dagger_\lambda(\mathbf{q}) \sum_m (2i \sin(\mathbf{q}\cdot\mathbf{h}_{nm})) \eta^*_{m\lambda}(\mathbf{q}) \Big\}\end{aligned} \tag{11.14}$$

The $\sum_m$ in (11.14) may be written in a more convenient form by introducing an Hermitan, anti-symmetric matrix

$$Z(\mathbf{q}) = -2i \begin{pmatrix} 0 & \sin(\mathbf{q}\cdot\mathbf{h}_{01}) & \sin(\mathbf{q}\cdot\mathbf{h}_{02}) & \sin(\mathbf{q}\cdot\mathbf{h}_{03}) \\ -\sin(\mathbf{q}\cdot\mathbf{h}_{01}) & 0 & \sin(\mathbf{q}\cdot\mathbf{h}_{12}) & \sin(\mathbf{q}\cdot\mathbf{h}_{13}) \\ -\sin(\mathbf{q}\cdot\mathbf{h}_{02}) & -\sin(\mathbf{q}\cdot\mathbf{h}_{12}) & 0 & \sin(\mathbf{q}\cdot\mathbf{h}_{23}) \\ -\sin(\mathbf{q}\cdot\mathbf{h}_{03}) & -\sin(\mathbf{q}\cdot\mathbf{h}_{13}) & -\sin(\mathbf{q}\cdot\mathbf{h}_{23}) & 0 \end{pmatrix} \tag{11.15}$$

The matrix $Z(\mathbf{q})$ is Hermitian, and therefore a complete, orthonormal, basis may be constructed from its eigenvectors. We choose the "polarisation" vectors $\eta_\lambda(\mathbf{q})$ to be the eigenvectors of $Z(\mathbf{q})$, i.e.

$$Z(\mathbf{q}) \cdot \begin{pmatrix} \eta_{0\lambda}(\mathbf{q}) \\ \eta_{1\lambda}(\mathbf{q}) \\ \eta_{2\lambda}(\mathbf{q}) \\ \eta_{3\lambda}(\mathbf{q}) \end{pmatrix} = \zeta_\lambda(\mathbf{q}) \begin{pmatrix} \eta_{0\lambda}(\mathbf{q}) \\ \eta_{1\lambda}(\mathbf{q}) \\ \eta_{2\lambda}(\mathbf{q}) \\ \eta_{3\lambda}(\mathbf{q}) \end{pmatrix}. \tag{11.16}$$

This choice corresponds to a specific choice of gauge, which we have made for maximum convenience in constructing the photon dispersion. It corresponds to the Coulomb, or radiation, gauge

$$\nabla \cdot A = 0 \tag{11.17}$$

Using (11.16), (11.14) becomes

$$\begin{aligned}(\nabla_{\hexagon} \times A)_{(\mathbf{p},n)} = \sqrt{\frac{2}{N}} \sum_{\mathbf{q}} \sum_{\lambda=1}^{4} \sqrt{\frac{\mathscr{U}}{\omega_\lambda(\mathbf{q})}} \\ \Big\{ \exp[-i\mathbf{q} \cdot (\mathbf{p} - \mathbf{e}_n/2)] a_\lambda(\mathbf{q}) \zeta_\lambda(\mathbf{q}) \eta_{n\lambda}(\mathbf{q}) + \\ \exp[i\mathbf{q} \cdot (\mathbf{p} - \mathbf{e}_n/2)] a_\lambda^\dagger(\mathbf{q}) \zeta_\lambda(\mathbf{q}) \eta_{n\lambda}^*(\mathbf{q}) \Big\}\end{aligned} \tag{11.18}$$

Inserting this into (11.1) gives

$$\begin{aligned}\mathscr{H}_{\mathrm{U}(1)} = \sum_{\mathbf{q}} \sum_{\lambda=1}^{4} \Bigg[\left(\frac{\mathscr{U}\mathscr{K}\zeta_\lambda(\mathbf{q})^2}{4\omega_\lambda(\mathbf{q})} + \frac{\omega_\lambda(\mathbf{q})}{4} \right) (a_\lambda(\mathbf{q}) a_\lambda^\dagger(\mathbf{q}) + a_\lambda^\dagger(\mathbf{q}) a_\lambda(\mathbf{q})) + \\ \left(\frac{\mathscr{U}\mathscr{K}\zeta_\lambda(\mathbf{q})^2}{4\omega_\lambda(\mathbf{q})} - \frac{\omega_\lambda(\mathbf{q})}{4} \right) (a_\lambda^\dagger(-\mathbf{q}) a_\lambda^\dagger(\mathbf{q}) + a_\lambda(\mathbf{q}) a_\lambda(-\mathbf{q})) \Bigg].\end{aligned} \tag{11.19}$$

To diagonalize the Hamiltonian we require

$$\frac{\mathscr{U}\mathscr{K}\zeta_\lambda(\mathbf{q})^2}{4\omega_\lambda(\mathbf{q})} = \frac{\omega_\lambda(\mathbf{q})}{4} \tag{11.20}$$

$$\implies \omega_\lambda(\mathbf{q}) = \sqrt{\mathscr{U}\mathscr{K}} |\zeta_\lambda(\mathbf{q})|. \tag{11.21}$$

This gives us four bands of non-interacting modes, with dispersion $\omega_\lambda(\mathbf{q})$

$$\mathscr{H}_{\mathrm{U}(1)} = \sum_{\mathbf{q}} \sum_{\lambda=1}^{4} \omega_\lambda(\mathbf{q}) \left(a_\lambda^\dagger(\mathbf{q}) a_\lambda(\mathbf{q}) + \frac{1}{2} \right) \tag{11.22}$$

To find the dispersions $\omega_\lambda(\mathbf{q})$ we need to know the eigenvalues of the matrix $Z(\mathbf{q})$, $\zeta_\lambda(\mathbf{q})$. These are

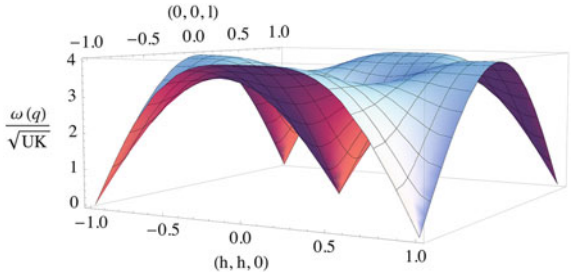

Fig. 11.2 Dispersion of the photon excitations of the gauge theory $\mathscr{H}_{\mathsf{U}(1)}$ (11.1). The dispersion is given by (11.23) and (11.26), and is shown here in the (h, h, l) plane of reciprocal space. Close to reciprocal lattice vectors the photons are linearly dispersing (11.27)

$$\zeta_1(\mathbf{q}) = -\zeta_2(\mathbf{q}) = \sqrt{2}\sqrt{\sum_{mn} \sin(\mathbf{q}\cdot\mathbf{h}_{nm})^2} \equiv \zeta(\mathbf{q}) \tag{11.23}$$

$$\zeta_3(\mathbf{q}) = \zeta_4(\mathbf{q}) = 0 \tag{11.24}$$

Thus, the four bands of excitations correspond to two, degenerate, physical, photon modes and two unphysical zero energy modes. The unphysical modes arise as a result of the gauge redundancy in A and make no contribution to either the Hamiltonian or any gauge invariant correlation function.

We can therefore drop the unphysical modes from the sum in (11.22) and write

$$\mathscr{H}_{\mathsf{U}(1)} = \sum_{\mathbf{q}} \sum_{\lambda=1}^{2} \omega(\mathbf{q}) \left(a_\lambda^\dagger(\mathbf{q}) a_\lambda(\mathbf{q}) + \frac{1}{2} \right) \tag{11.25}$$

where the sum over λ now runs over two, transverse, photons and both physical modes have dispersion

$$\omega(\mathbf{q}) = \sqrt{\mathscr{U}\mathscr{K}}\,\zeta(\mathbf{q}). \tag{11.26}$$

This dispersion relation is illustrated in Fig. 11.2.

The photon dispersion is linear and isotropic in the long wavelength limit

$$\omega(\mathbf{q} \approx \mathbf{0}) \approx c|\mathbf{q}| \tag{11.27}$$

with a "speed of light"

$$c = \sqrt{\mathscr{U}\mathscr{K}}\, a_0. \tag{11.28}$$

11.1.2 Correlation Functions of the Electromagnetic Fields

The electric fields of our gauge theory, are directly related to the ⟨111⟩ components of the spin in a quantum spin ice. Therefore their correlation functions may be accessed in neutron scattering experiments.

We define the correlation function

$$S_E^{mn}(\mathbf{q},\omega) = \frac{1}{2\pi}\int dt e^{i\omega t}\langle E_m(\mathbf{q},t)E_n(-\mathbf{q},0)\rangle \tag{11.29}$$

where m, n are sublattice indices, indexing the four pyrochlore sublattices (or four inequivalent sets of bonds on the diamond lattice). $E_m(\mathbf{q},t)$ is simply the spatial Fourier transform of the electric field at time t

$$E_m(\mathbf{q},t) = \sqrt{\frac{1}{N_{\text{u.c.}}}}\sum_{\mathbf{r}} \exp[-i\mathbf{q}\cdot(\mathbf{r}+\mathbf{e}_n/2)]E_m(\mathbf{r},t) \tag{11.30}$$

where $N_{\text{u.c.}} = \frac{N}{4}$ is the number of primitive unit cells. The time evolution of the electromagnetic fields is given by the time evolution of the photon operators $a_\lambda(\mathbf{q})$, $a_\lambda^\dagger(\mathbf{q})$, which, since the photons are eigenstates of $\mathscr{H}_{\mathsf{U}(1)}$, is simply

$$a_\lambda^\dagger(\mathbf{q})(t) = e^{i\omega_\lambda(\mathbf{q})t}a_{\mathbf{q}}^\dagger(0) \quad a_\lambda(\mathbf{q})(t) = e^{-i\omega_\lambda(\mathbf{q})t}a_{\mathbf{q}}(0). \tag{11.31}$$

Therefore

$$E_m(\mathbf{q},t) = \frac{i}{\sqrt{2}}\sum_{\lambda=1}^{4}\sqrt{\frac{\omega_\lambda(\mathbf{q})}{\mathscr{U}}}\left(\eta_{m\lambda}(\mathbf{q})a_\lambda(-\mathbf{q})e^{-i\omega_\lambda(\mathbf{q})t} - \eta_{m\lambda}^*(\mathbf{q})e^{i\omega_\lambda(\mathbf{q})t}a_\lambda^\dagger(\mathbf{q})\right). \tag{11.32}$$

Inserting this into (11.29) we obtain

$$S_E^{mn}(\mathbf{q},\omega) = \frac{1}{2}\sum_{\lambda=1}^{2}\frac{\omega_\lambda(\mathbf{q})}{\mathscr{U}}\eta_{m\lambda}\eta_{n\lambda}^* \left[\delta(\omega-\omega_\lambda(\mathbf{q}))\langle a_\lambda(\mathbf{q})a_\lambda^\dagger(\mathbf{q})\rangle + \delta(\omega+\omega_\lambda(\mathbf{q}))\langle a_\lambda^\dagger(\mathbf{q})a_\lambda(\mathbf{q})\rangle\right]. \tag{11.33}$$

In writing (11.33) we have used the fact that the operators which do not conserve photon number have vanishing expectation values

$$\langle a_\lambda(\mathbf{q})a_{\lambda'}(-\mathbf{q})\rangle = \langle a_\lambda^\dagger(\mathbf{q})a_{\lambda'}^\dagger(-\mathbf{q})\rangle = 0. \tag{11.34}$$

For the physical polarisations $\lambda = 1, 2$

$$\langle a_\lambda(\mathbf{q}) a^\dagger_{\lambda'}(\mathbf{q})\rangle = \delta_{\lambda\lambda'} + \langle a^\dagger_\lambda(\mathbf{q}) a_{\lambda'}(\mathbf{q})\rangle$$
$$= \delta_{\lambda\lambda'}\left(1 + \frac{1}{\exp(\omega(\mathbf{q})/T) - 1}\right) \equiv \delta_{\lambda\lambda'}\,(1 + n_B(\omega(\mathbf{q}))) \quad (11.35)$$

and thus

$$S^{mn}_E(\mathbf{q},\omega) = \frac{1}{2}\left[\delta(\omega - \omega(\mathbf{q}))(1 + n_B(\omega(\mathbf{q}))) + \delta(\omega + \omega(\mathbf{q}))n_B(\omega(\mathbf{q}))\right] \times$$
$$\sum_{\lambda=1}^{2} \frac{\omega_\lambda(\mathbf{q})}{\mathscr{U}} \eta_{m\lambda}\eta^*_{n\lambda}. \quad (11.36)$$

The sum over polarisations can be simplified by extending the sum to include the unphysical polarisations $\lambda = 3, 4$ (they make no contribution since $\omega_{3,4}(\mathbf{q}) = 0$) and using the fact that for all bands λ (including the unphysical $\zeta_\lambda(\mathbf{q}) = 0$ bands)

$$\omega_\lambda(\mathbf{q}) = \sqrt{\mathscr{U}\mathscr{K}}\,|\zeta_\lambda(\mathbf{q})| \quad (11.37)$$
$$|\zeta_\lambda(\mathbf{q})| = \zeta_\lambda(\mathbf{q})^2/\zeta(\mathbf{q}) \quad (11.38)$$

with $\zeta(\mathbf{q})$ defined by (11.23).

We can now use the spectral theorem to note that

$$\sum_{\lambda=1}^{4} \zeta_\lambda(\mathbf{q})^2 \eta_{m\lambda}\eta^*_{n\lambda} = (Z(\mathbf{q})^2)_{mn}. \quad (11.39)$$

Thus, the dynamical correlation function for the electric fields is

$$S^{mn}_E(\mathbf{q},\omega) = 2\frac{\mathscr{K}}{\omega(\mathbf{q})}\left(\sum_l \sin(\mathbf{q}\cdot\mathbf{h}_{ml})\sin(\mathbf{q}\cdot\mathbf{h}_{nl})\right)$$
$$\times\left[\delta(\omega - \omega(\mathbf{q}))(1 + n_B(\omega(\mathbf{q}))) + \delta(\omega + \omega(\mathbf{q}))n_B(\omega(\mathbf{q}))\right] \quad (11.40)$$

Integrating over energy gives the equal-time correlation function

$$S^{mn}_E(\mathbf{q}, t = 0) = 2\frac{\mathscr{K}}{\omega(\mathbf{q})}\coth\left(\frac{\omega(\mathbf{q})}{2T}\right)\left(\sum_l \sin(\mathbf{q}\cdot\mathbf{h}_{ml})\sin(\mathbf{q}\cdot\mathbf{h}_{nl})\right) \quad (11.41)$$

The contribution this makes to the physical spin structure factor of a quantum spin ice, as might be measured in a neutron scattering experiment, is given by projecting on to the local easy axes

$$S^{\alpha\beta}(\mathbf{q},\omega) = \sum_{mn}(\hat{\mathbf{e}}_n.\hat{\alpha})(\hat{\mathbf{e}}_m.\hat{\beta})S^{mn}_E(\mathbf{q},\omega). \quad (11.42)$$

where α and β index different spin components in the crystal coordinate frame. By using polarised neutron scattering one can probe different combinations of the components of $S^{\alpha\beta}(\mathbf{q}, \omega)$.

From (11.41) we can see how the correlations of a quantum spin ice in the $U(1)$ liquid phase differ from those of a classical spin ice and how one can cross over to the other as a function of temperature. In a classical spin ice, we expect to see pinch points at reciprocal lattice vectors, reflecting the dipolar nature of the correlations. In the $U(1)$ spin liquid at $T = 0$, these pinch points disappear and are replaced by suppressions of the scattering, with the intensity vanishing as $|\mathbf{q} - \mathbf{K}|$ approaching a reciprocal lattice vector $\mathbf{K}$. This multiplicative factor effectively "hollows out" the pinch point.

At small but finite temperature the pinch point is restored, with a height growing linearly with T, due to the thermal excitation of photons. This can be seen using the fact that at small $\mathbf{q}$

$$\coth\left(\frac{\omega(\mathbf{q})}{2T}\right) \approx \coth\left(\frac{cq}{2T}\right) \approx \frac{2\,T}{cq}. \tag{11.43}$$

The extra factor of q in the demoninator cancels the linear suppression of the scattering and restores the pinch point. This makes clear the existence of a thermal length scale in the problem

$$\lambda_T = \frac{\pi c}{T} \tag{11.44}$$

which defines a wavelength scale over which correlations cross over from their classical to quantum form [4].

11.2 Point Group Symmetries of the Pyrochlore Lattice and Anisotropic Exchange Interactions

Symmetry has long been a foundational concept in theoretical physics and the study of pyrochlore magnets, including the spin ices, is no exception to this. In this section, we enumerate the point group symmetries of the pyrochlore lattice and use these to consider the problem of nearest-neighbour anisotropic exchange in pyrochlore magnets. These symmetry considerations will enable us to derive the four-parameter Hamiltonian [8–10] studied in Chaps. 9 and 12.

A full consideration of the symmetries, however, allows us to do more than simply constrain the form of the Hamiltonian. Using some elementary representation theory we will see that one can re-write this Hamiltonian in terms of local order parameters for the different types of four-sublattice magnetic order which are found in magnetic pyrochlores [17, 18]. Once this simplification is obtained, it becomes a simple matter to identify the classical ground state of the model for arbitrary exchange parameters.

11.2.1 Classical Vector Spins on the Corners of a Tetrahedron

We begin by considering a single tetrahedron with a spin at each vertex. Initially, we consider the spins to be classical, axial vectors.

We wish to consider nearest neighbour interactions on the pyrochlore lattice. All nearest neighbour bonds belong uniquely to a single tetrahedron, so quite generically we may write our exchange Hamiltonian, H_{ex}, as a sum over tetrahedra of single tetrahedron Hamiltonians

$$H_{\text{ex}} = \sum_{\text{tet},i} H_{\text{tet},i} = \sum_{\text{tet}\in\text{A}} H_{\text{tet,A}} + \sum_{\text{tet}\in\text{B}} H_{\text{tet,B}}. \tag{11.45}$$

On the RHS of (11.45) we have split the sum over tetrahedra into two sums, one running over the A sublattice tetrahedra of the lattice and the other running over the B sublattice tetrahedra. Translational symmetry guarantees that all tetrahedra of one sublattice have the same Hamiltonian.

The operations under which a tetrahedron is unchanged form a 24 element group, T_d. This group is a subgroup of O_h, which contains the full set of point group operations of the pyrochlore lattice. O_h differs from T_d by the inclusion of inversion symmetry which swaps the A sublattice and B sublattice tetrahedra.

We can thus derive the appropriate nearest neighbour Hamiltonian on the pyrochlore lattice by using T_d to derive the Hamiltonian of a single tetrahedron, with the inversion symmetry being satisfied by the fact that the 'A' and 'B' tetrahedra have the same Hamiltonian

$$H_{\text{tet,A}} = H_{\text{tet,B}} = H_{\text{tet}}. \tag{11.46}$$

Since we consider bilinear exchange we may write H_{tet} as

$$H_{\text{tet}} = \frac{1}{2}\sum_{i,j=0}^{3} \mathbf{S}_i \cdot \mathbf{J}_{ij} \cdot \mathbf{S}_j \tag{11.47}$$

where

$$\mathbf{J}_{ij} = (\mathbf{J}_{ji})^T, \quad \mathbf{J}_{ii} = \begin{pmatrix} 0 & 0 & 0 \\ 0 & 0 & 0 \\ 0 & 0 & 0 \end{pmatrix}. \tag{11.48}$$

We now proceed to use the operations of T_d to constrain the form of H_{tet}. The group T_d has five conjugacy classes:

1. The identity element (e)
2. $8 \times \frac{2n\pi}{3}$ around $\langle 111\rangle$ axes (8 C_3)
3. $3 \times \pi$ rotations around $\langle 100\rangle$ axes (3 C_2)
4. $6 \times \frac{2(n+1)\pi}{2}$ rotations around $\langle 100\rangle$ axes combined with reflection in the plane normal to the rotation axis (rotoreflection) (6 S_4)

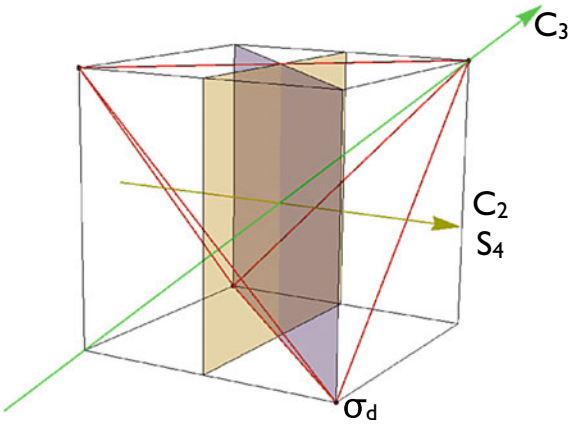

Fig. 11.3 The symmetries of a tetrahedron. There are 8 three-fold rotations around ⟨111⟩ axes (green), 3 two-fold rotations and 6 four-fold rotoreflections around ⟨100⟩ axes (yellow) and 6 reflections in [011] planes (blue)

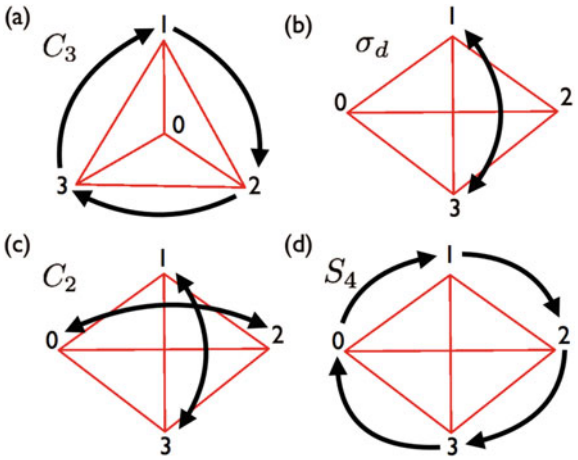

Fig. 11.4 The operations of T_d represented as permutations of the four vertices of a tetrahedron. **a** The conjugacy class 8 C_3: one site remains fixed while the other three are cyclically permuted. **b** 6 σ_d: two sites are swapped. **c** 3 C_2: two pairs of sites are swapped. **d** 6 S_4: all four sites are cyclically permuted

5. 6× reflections in [011] planes (6 σ_d)

These are illustrated in Fig. 11.3.

Any symmetry operation of T_d both permutes the sites of a tetrahedron (as illustrated in Fig. 11.4) and rotates the spins. The spins transform as axial vectors. The action of reflecting a vector in a plane with normal $\hat{\mathbf{n}}$ may in general be written

$$A(\hat{\mathbf{n}}) = R(\hat{\mathbf{n}}, \pi)\mathscr{I} \tag{11.49}$$

where $\mathscr{I}$ is spatial inversion and $R(\hat{\mathbf{n}}, \pi)$ is a π rotation around $\hat{\mathbf{n}}$. Axial vectors don't transform under spatial inversion, and hence the action of the reflection operations is to simply rotate the spin by π around the normal vector of the reflection plane (in addition to the relevant permutation of the site indices).

First off we consider the coupling matrix between $\mathbf{S}_0$ and $\mathbf{S}_1$, initially allowing all nine elements of the matrix to be independent

$$\mathbf{J}_{01} = \begin{pmatrix} J_a & J_b & J_c \\ J_d & J_e & J_f \\ J_g & J_h & J_i. \end{pmatrix} \tag{11.50}$$

Reflecting the system in the $[01\bar{1}]$ plane swaps sites 2 and 3 but leaves sites 0 and 1 where they are, so $\mathbf{J}_{01}$ is affected only by the rotation by π around $(0, -1, 1)$. Imposing invariance under this transformation gives us

$$\mathbf{R}((0,-1,1),\pi)^T \cdot \mathbf{J}_{01} \cdot \mathbf{R}((0,-1,1),\pi) = \begin{pmatrix} J_a & J_c & J_b \\ J_g & J_i & J_h \\ J_d & J_f & J_e \end{pmatrix} = \begin{pmatrix} J_a & J_b & J_c \\ J_d & J_e & J_f \\ J_g & J_h & J_i \end{pmatrix} \tag{11.51}$$

$$\implies J_b = J_c, \quad J_g = J_d, \quad J_i = J_e, \quad J_f = J_h \tag{11.52}$$

Applying a π rotation around the [100] axis swaps sites 2 and 3 and sites 0 and 1, so using (11.48)

$$\mathbf{R}((1,0,0),\pi)^T \cdot \mathbf{J}_{10} \cdot \mathbf{R}((1,0,0),\pi) = \begin{pmatrix} J_a & -J_d & -J_d \\ -J_b & J_e & J_f \\ -J_b & J_f & J_e \end{pmatrix} = \begin{pmatrix} J_a & J_b & J_b \\ J_d & J_e & J_f \\ J_d & J_f & J_e \end{pmatrix} \tag{11.53}$$

$$\implies J_b = -J_d, \tag{11.54}$$

which finally leaves us with a matrix with only four parameters

$$\mathbf{J}_{01} = \begin{pmatrix} J_2 & J_4 & J_4 \\ -J_4 & J_1 & J_3 \\ -J_4 & J_3 & J_1. \end{pmatrix} \tag{11.55}$$

All the remaining exchange matrices may be generated by applying combinations of $\frac{2\pi}{3}$ rotations around the various $\langle 111 \rangle$ axes to (11.55). This gives the full Hamiltonian in the global, crystal, co-ordinate frame.

It is quite common in the literature to present the Hamiltonian in a local co-ordinate frame, with the z-axis on each site pointing along the local C_3 axis. Writing the Hamiltonian in this co-ordinate frame, and using ladder operators $\mathsf{S}^{\pm} = \mathsf{S}^x \pm i\mathsf{S}^y$ gives

$$H_{\text{tet}} = \sum_{\langle ij \rangle} \Big\{ J_{zz} \mathsf{S}_i^z \mathsf{S}_j^z - J_{\pm} (\mathsf{S}_i^+ \mathsf{S}_j^- + \mathsf{S}_i^- \mathsf{S}_j^+) + J_{\pm\pm} \left[\gamma_{ij} \mathsf{S}_i^+ \mathsf{S}_j^+ + \gamma_{ij}^* \mathsf{S}_i^- \mathsf{S}_j^- \right] + J_{z\pm} \left[\mathsf{S}_i^z (\zeta_{ij} \mathsf{S}_j^+ + \zeta_{ij}^* \mathsf{S}_j^-) + i \leftrightarrow j \right] \Big\} \tag{11.56}$$

where the complex, unimodular, 4×4 matrices γ and ζ are given by

$$\gamma = -\zeta^* = \begin{pmatrix} 0 & 1 & \exp\left(\frac{2\pi i}{3}\right) & \exp\left(\frac{-2\pi i}{3}\right) \\ 1 & 0 & \exp\left(\frac{-2\pi i}{3}\right) & \exp\left(\frac{2\pi i}{3}\right) \\ \exp\left(\frac{2\pi i}{3}\right) & \exp\left(\frac{-2\pi i}{3}\right) & 0 & 1 \\ \exp\left(\frac{-2\pi i}{3}\right) & \exp\left(\frac{2\pi i}{3}\right) & 1 & 0 \end{pmatrix} \tag{11.57}$$

and occur due to the rotation of the local co-ordinate frame between different sites.

The relationships between the exchange co-efficients $\{J_1, J_2, J_3, J_4\}$ and $\{J_{zz}, J_{\pm}, J_{\pm\pm}, J_{z\pm}\}$ are

$$J_{zz} = -\frac{1}{3}(2J_1 - J_2 + 2(J_3 + 2J_4)) \tag{11.58}$$

$$J_{\pm} = \frac{1}{6}(2J_1 - J_2 - J_3 - 2J_4) \tag{11.59}$$

$$J_{\pm\pm} = \frac{1}{6}(J_1 + J_2 - 2J_3 + 2J_4) \tag{11.60}$$

$$J_{z\pm} = \frac{1}{3\sqrt{2}}(J_1 + J_2 + J_3 - J_4). \tag{11.61}$$

11.2.2 Rewriting the Hamiltonian in Terms of Local Order Parameter Fields

A useful rewriting of H_{ex} can be obtained which allows us to directly obtain the classical ground state for any set of exchange parameters [17, 18]. In this section we will obtain that rewriting by finding objects, defined on a single tetrahedron, which transform according to the different irreducible representations (irreps) of the point group.

Rewriting the Hamiltonian in terms of the order parameters of four sublattice order is attractive because for any set of exchange parameters $\{J_i\}$ it is possible to find a $\mathbf{q} = 0$, four-sublattice, state which minimises the classical energy of H_{ex}. One can convince oneself of this by the following argument: the full Hamiltonian can be written as a sum over the Hamiltonians of the tetrahedra. Taking a classical ground state of the A sublattice tetrahedra and tiling it over all A tetrahedra obviously minimises the total energy of the A sublattice tetrahedra. Since the 'A' and 'B' tetrahedra are related by inversion symmetry, and thus have the same Hamiltonian

(11.46), this state also minimises the energy of the B tetrahedra. Since the energy of each individual tetrahedron is minimal in such a state, it is clear that the total energy of the system must be.

This demonstrates the existence of a $\mathbf{q} = 0$, four-sublattice, classical ground state but of course does not preclude the existence of degenerate, finite $\mathbf{q}$ states. Generally speaking, however, this will only occur at the $T = 0$ classical phase boundaries [18].

11.2.3 Irreducible Representations of T_d

The dominance of four sublattice orders on the phase diagram leads us to consider the different symmetries of local order parameter which may be constructed from the four spins on a tetrahedron. By saying that these objects have "different symmetries" we mean that they transform according to different irreducible representations of the group T_d. Below, we give a brief explanation of the meaning of this statement. For a fuller explanation of the concept of irreducible representations and their use in solving physics problems we invite the reader to consult one of the many textbooks on the subject (e.g. [19, 20]).

Consider some linear combination of the different components of the four spins on a tetrahedron

$$\varphi_1 = \sum_{i=0}^{3} \sum_{\alpha=x,y,z} c_{i\alpha} S_i^{\alpha}. \tag{11.62}$$

We could apply all the symmetry operations of T_d to this object and in this way generate some number, d, of linearly independent objects $\{\varphi_1 ... \varphi_d\}$. This set of objects would, by construction, transform only amongst each other under the operations of T_d, i.e. for each group operation g acting on any φ_n we could write

$$g\varphi_n = \sum_{m=1}^{d} \Gamma_{nm}(g)\varphi_m \tag{11.63}$$

and we can therefore associate with each group element g a $d \times d$ matrix $\Gamma(g)$ in the d-dimensional basis $\{\varphi_1 ... \varphi_d\}$.

The set of matrices $\Gamma(g)$ form a d-dimensional representation of T_d. Two representations of a group are equivalent if they are related by a unitary transformation

$$\Gamma(g) \rightarrow U\Gamma(g)U^{\dagger} \tag{11.64}$$

$$U^{\dagger} = U^{-1}. \tag{11.65}$$

If we can find some unitary transformation which simultaneously block diagonalises all the $\Gamma(g)$ then we have decomposed the d-dimensional representation into a series

of lower dimensional representations. For example, if we have

$$U\Gamma(g)U^{\dagger} = \begin{pmatrix} \Gamma_1(g) & 0 \\ 0 & \Gamma_2(g) \end{pmatrix} \tag{11.66}$$

then the matrices $\Gamma_1(g)$ and the matrices $\Gamma_2(g)$ seperately form representations of T_d. If the matrices $\Gamma_1(g)$ have size $d_1 \times d_1$ and the matrices $\Gamma_2(g)$ have size $d_2 \times d_2$ then we have decomposed the d-dimensional representation into one d_1-dimensional and one d_2-dimensional representation, where $d = d_1 + d_2$. If there exists no unitary transformation which block diagonalises all the $\Gamma(g)$ then $\Gamma(g)$ form an *irreducible representation*.

A general method for decomposing reducible representations into irreducible ones is obtained by considering the "characters" $\chi(g)$ in a given representation, which are given by

$$\chi(g) = \mathrm{Tr}[\Gamma(g)]. \tag{11.67}$$

The characters of any two group elements belonging to the same conjugacy class will be equal, so we need only calculate $\chi(g)$ for one element from each class. If a representation Γ may be decomposed into two representations Γ_1 and Γ_2 then it follows the characters may also be decomposed as

$$\chi(g) = \chi_1(g) + \chi_2(g). \tag{11.68}$$

More generally, the character of a general reducible representation χ can be expressed as a sum over characters of the irreducible representations $\chi_j(g)$ with integer coefficients h_j

$$\chi(g) = \sum_j h_j \chi_j(g). \tag{11.69}$$

The meaning of the coefficients h_j is that irreducible representation j occurs h_j times in the decomposition of the reducible representation.

The characters of the irreducible representations obey an orthogonality theorem [19]

$$\sum_g \chi_i^*(g)\chi_j(g) = \mathscr{N}\delta_{ij}. \tag{11.70}$$

where $\mathscr{N}$ is the number of group elements ($\mathscr{N} = 24$ in the case of T_d). The characters of each conjugacy class within the irreducible representations may be looked up in a book for commonly occurring symmetry groups.

The character table of T_d is reproduced in Table 11.1. The group T_d has two one dimensional representations (A_1 and A_2), one two dimensional representation (E) and two three dimensional representations (T_1 and T_2).

Table 11.1 The character table of the irreducible representations of T_d. Each row corresponds to one of the irreducible representations and each column to one of the conjugacy classes. Each entry in the table shows the character χ_j of a given conjugacy class within a given irreducible representation. This information can be used in conjuction with (11.71) to decompose a given reducible representation into a direct sum of irreducible representations

	$\mathscr{E}$	$8C_3$	$3C_2$	$6S_4$	$6\sigma_d$
A_1	1	1	1	1	1
A_2	1	1	1	−1	−1
E	2	−1	2	0	0
T_1	3	0	−1	1	−1
T_2	3	0	−1	−1	1

Armed with this information, we can use (11.69) and (11.70) to find the coefficients h_j

$$h_j = \frac{1}{\mathscr{N}} \sum_g \chi_j^*(g)\chi(g) \tag{11.71}$$

where the sum is over group elements, $\chi_j(g)$ is the character of the group element g within irreducible representation j and can be found in Table 11.1 and $\chi(g)$ is the character of g within the (reducible) representation which we are trying to decompose.

11.2.4 Local Order Parameter Fields

We may uniquely write any spin configuration on a tetrahedron as a 12 component vector

$$\tilde{S} = (S_0^x, S_0^y, S_0^z, S_1^x, S_1^y, S_1^z, S_2^x, S_2^y, S_2^z, S_3^x, S_3^y, S_3^z). \tag{11.72}$$

All of the operations of T_d become 12×12 matrices which act on $\tilde{S}$. These matrices thus form a 12-dimensional representation of T_d. One may readily construct these matrices, by considering each symmetry as a combination of rotation operations on the spins and permutations of the sites, as discussed in Sect. 11.2.1. Once this is done, one simply takes the trace of these matrices to find the characters of our 12 dimensional representation and uses Table 11.1 and (11.71). We find

$$h_{A_1} = 0, \quad h_{A_2} = 1, \quad h_E = 1, \quad h_{T_1} = 2, \quad h_{T_2} = 1. \tag{11.73}$$

Table 11.2 Local order parameters $\mathbf{m}_\gamma$ appearing in (11.74). When summed over the lattice these become the order parameters of the $\mathbf{q} = 0$, 4-sublattice ordered phases of the model (11.47)

Local order parameter	Definition in terms of spin components
m_{A_2}	$\frac{1}{2\sqrt{3}}\left(S_0^x + S_0^y + S_0^z + S_1^x - S_1^y - S_1^z - S_2^x + S_2^y - S_2^z - S_3^x - S_3^y + S_3^z\right)$
$\mathbf{m}_{\mathsf{E}}$	$\begin{pmatrix} \frac{1}{2\sqrt{6}}\left(-2S_0^x + S_0^y + S_0^z - 2S_1^x - S_1^y - S_1^z + 2S_2^x + S_2^y - S_2^z + 2S_3^x - S_3^y + S_3^z\right) \\ \frac{1}{2\sqrt{2}}\left(-S_0^y + S_0^z + S_1^y - S_1^z - S_2^y - S_2^z + S_3^y + S_3^z\right) \end{pmatrix}$
$\mathbf{m}_{\mathsf{T}_2}$	$\begin{pmatrix} \frac{1}{2\sqrt{2}}\left(-S_0^y + S_0^z + S_1^y - S_1^z + S_2^y + S_2^z - S_3^y - S_3^z\right) \\ \frac{1}{2\sqrt{2}}\left(S_0^x - S_0^z - S_1^x - S_1^z - S_2^x + S_2^z + S_3^x + S_3^z\right) \\ \frac{1}{2\sqrt{2}}\left(-S_0^x + S_0^y + S_1^x + S_1^y - S_2^x - S_2^y + S_3^x - S_3^y\right) \end{pmatrix}$
$\mathbf{m}_{\mathsf{T}_{1,\mathrm{ice}}}$	$\begin{pmatrix} \frac{1}{2\sqrt{3}}(S_0^x + S_0^y + S_0^z + S_1^x - S_1^y - S_1^z + S_2^x - S_2^y + S_2^z + S_3^x + S_3^y - S_3^z) \\ \frac{1}{2\sqrt{3}}(S_0^x + S_0^y + S_0^z - S_1^x + S_1^y + S_1^z - S_2^x + S_2^y - S_2^z + S_3^x + S_3^y - S_3^z) \\ \frac{1}{2\sqrt{3}}(S_0^x + S_0^y + S_0^z - S_1^x + S_1^y + S_1^z + S_2^x - S_2^y + S_2^z - S_3^x - S_3^y + S_3^z) \end{pmatrix}$
$\mathbf{m}_{\mathsf{T}_{1,\mathrm{pl}}}$	$\begin{pmatrix} \frac{1}{2\sqrt{6}}(-2S_0^x + S_0^y + S_0^z - 2S_1^x - S_1^y - S_1^z - 2S_2^x - S_2^y + S_2^z - 2S_3^x + S_3^y - S_3^z) \\ \frac{1}{2\sqrt{6}}(S_0^x - 2S_0^y + S_0^z - S_1^x - 2S_1^y + S_1^z - S_2^x - 2S_2^y - S_2^z + S_3^x - 2S_3^y - S_3^z) \\ \frac{1}{2\sqrt{6}}(S_0^x + S_0^y - 2S_0^z - S_1^x + S_1^y - 2S_1^z + S_2^x - S_2^y - 2S_2^z - S_3^x - S_3^y - 2S_3^z) \end{pmatrix}$

This tells us that, from linear combinations of the 12 spin components S_i^α we can form one local order parameter transforming according to each of the representations A_2, E and T_2 and two which transform according to T_1. Since these objects are linear in the spin components, and the Hamiltonian is bilinear in the spins the Hamiltonian must also be bilinear in the local order parameters. Furthermore, since the Hamiltonian is symmetric under the operations of T_d it *cannot* couple objects transforming according to different irreducible representations. Thus, when written in terms of the local order parameter fields the Hamiltonian of one tetrahedron must take the form

$$H_{\mathrm{ex}}^{\mathrm{tet}} = \frac{1}{2}\Big[a_{\mathsf{A}_2} m_{\mathsf{A}_2}^2 + a_{\mathsf{E}}\mathbf{m}_{\mathsf{E}}^2 + a_{\mathsf{T}_2}\mathbf{m}_{\mathsf{T}_2}^2 + a_{\mathsf{T}_{1,\mathsf{A}}}\mathbf{m}_{\mathsf{T}_{1,\mathsf{A}}}^2 + a_{\mathsf{T}_{1,\mathsf{B}}}\mathbf{m}_{\mathsf{T}_{1,\mathsf{B}}}^2 + a_{\mathsf{T}_{1,\mathsf{AB}}}\mathbf{m}_{\mathsf{T}_{1,\mathsf{A}}} \cdot \mathbf{m}_{\mathsf{T}_{1,\mathsf{B}}}\Big]. \tag{11.74}$$

If we can identify the objects $\mathbf{m}_\gamma$ which transform according to the irreducible representations $\{A_2, E, T_1, T_2\}$ then we can find explicit expressions for the coefficients a_γ by comparison of (11.74) with (11.47).

Such a set of fields is defined in Table 11.2. These fields are the local order parameters for the different kinds of four-sublattice order which can occur on the pyrochlore lattice.

The scalar object m_{A_2} is the order parameter for the Ising-like, two-fold degenerate,"all in, all out" ordered state. The two-component vector $\mathbf{m}_{\mathsf{E}}$ serves as a local

Table 11.3 Definitions of the coefficients a_γ appearing in $H_{\text{ex}}^{\text{tet}}$ (11.74) in terms of the exchange parameters J_i

Coefficient	Definition in terms of exchange parameters $\{J_1, J_2, J_3, J_4, D\}$	Definition in terms of exchange parameters $\{J_{zz}, J_\pm, J_{\pm\pm}, J_{z\pm}\}$
a_{A_2}	$-2J_1 + J_2 - 2(J_3 + 2J_4)$	$3J_{zz}$
a_{E}	$-2J_1 + J_2 + J_3 + 2J_4$	$-6J_\pm$
a_{T_2}	$-J_2 + J_3 - 2J_4$	$2J_\pm - 4J_{\pm\pm}$
$a_{\mathsf{T}_1,\text{ice}}$	$\frac{1}{3}(2J_1 - J_2 + 2J_3 + 4J_4)$	$-J_{zz}$
$a_{\mathsf{T}_1,\text{pl}}$	$\frac{1}{3}(4J_1 + J_2 - 5J_3 + 2J_4)$	$2J_\pm + 4J_{\pm\pm}$
$a_{\mathsf{T}_1,\text{mixing}}$	$-\frac{4\sqrt{2}}{3}(J_1 + J_2 + J_3 - J_4)$	$-8J_{z\pm}$

order parameter for the XY-like order observed in $Er_2Ti_2O_7$. There is a $U(1)$ manifold of states which maximises $\mathbf{m}_{\mathsf{E}}$, the degeneracy of which can only be lifted by terms at sixth order in the free energy. The lifting of this degeneracy by the mechanism of order-by-disorder has attracted a lot of attention in the context of experiments on $Er_2Ti_2O_7$ [11, 12]. The vector $\mathbf{m}_{\mathsf{T}_2}$ is associated with the Palmer-Chalker ordered state, which was originally identified as a ground state in a model describing competition between antiferromagnetic Heisenberg and long range dipolar interactions [13].

Since we can define two independent fields which transform according to the T_1 representation, there will generally exist a term which couples them. We have some choice about how to define these fields. In Table 11.2 we show one convenient choice in which one field, $(\mathbf{m}_{\mathsf{T}_1,\text{ice}})$ is maximised by an 'ice' configuration and the other $(\mathbf{m}_{\mathsf{T}_1,\text{pl}})$ is maximised by a ferromagnetic state in which all spins are perpendicular to the local $\langle 111\rangle$ axes. With this choice of co-ordinates the Hamiltonian of a single tetrahedron is

$$H_{\text{ex}}^{\text{tet}} = \frac{1}{2}\Big[a_{\mathsf{A}_2} m_{\mathsf{A}_2}^2 + a_{\mathsf{E}}\mathbf{m}_{\mathsf{E}}^2 + a_{\mathsf{T}_2}\mathbf{m}_{\mathsf{T}_2}^2 + a_{\mathsf{T}_1,\text{ice}}\mathbf{m}_{\mathsf{T}_1,\text{ice}}^2 + a_{\mathsf{T}_1,\text{pl}}\mathbf{m}_{\mathsf{T}_1,\text{pl}}^2 + a_{\mathsf{T}_1,\text{mixing}}\mathbf{m}_{\mathsf{T}_1,\text{ice}} \cdot \mathbf{m}_{\mathsf{T}_1,\text{pl}}\Big]. \quad (11.75)$$

The coefficients a_γ are shown in terms of the exchange parameters in Table 11.3.

The term which couples the two T_1 fields may be removed by a parameter dependent, orthogonal transformation

$$\begin{pmatrix}\mathbf{m}_{\mathsf{T}_1 1}\\ \mathbf{m}_{\mathsf{T}_1 2}\end{pmatrix} = \begin{pmatrix}\cos(\phi_{\mathsf{T}_1}) & \sin(\phi_{\mathsf{T}_1})\\ -\sin(\phi_{\mathsf{T}_1}) & \cos(\phi_{\mathsf{T}_1})\end{pmatrix} \cdot \begin{pmatrix}\mathbf{m}_{\mathsf{T}_1,\text{ice}}\\ \mathbf{m}_{\mathsf{T}_1,\text{pl}}\end{pmatrix} \quad (11.76)$$

$$\tan(2\phi_{\mathsf{T}_1}) = \frac{a_{\mathsf{T}_1\text{mixing}}}{a_{\mathsf{T}_1,\text{ice}} - a_{\mathsf{T}_1,\text{pl}}}. \quad (11.77)$$

The fields $\mathbf{m}_{\mathsf{T}_1 1}$ and $\mathbf{m}_{\mathsf{T}_1 2}$ are linear combinations of $\mathbf{m}_{\mathsf{T}_1,\mathsf{ice}}$ and $\mathbf{m}_{\mathsf{T}_1,\mathsf{pl}}$ and will be maximal in the "splayed ferromagnet" configurations which have been proposed ground states for $Yb_2Ti_2O_7$ [14, 15] and $Yb_2Sn_2O_7$ [16].

The Hamiltonian of the whole system thus becomes a sum of five quadratic terms, defined on each tetrahedron, summed over all tetrahedra

$$H = \frac{1}{2}\sum_{\mathsf{tet}} \left[a_{\mathsf{A}_2} m_{\mathsf{A}_2}^2 + a_{\mathsf{E}} \mathbf{m}_{\mathsf{E}}^2 + a_{\mathsf{T}_2} \mathbf{m}_{\mathsf{T}_2}^2 + a_{\mathsf{T}_1,1} \mathbf{m}_{\mathsf{T}_1,1}^2 + a_{\mathsf{T}_1,2} \mathbf{m}_{\mathsf{T}_1,2}^2 \right]. \tag{11.78}$$

There is a simple way to identify the ground state from (11.78). We define

$$\mathscr{E}_0 = \min(a_{\mathsf{A}_2}, a_{\mathsf{E}}, a_{\mathsf{T}_2}, a_{\mathsf{T}_1 1}, a_{\mathsf{T}_1 2}) \tag{11.79}$$

and make use of the identity

$$m_{\mathsf{A}_2}^2 + \mathbf{m}_{\mathsf{E}}^2 + \mathbf{m}_{\mathsf{T}_2}^2 + \mathbf{m}_{\mathsf{T}_1,1}^2 + \mathbf{m}_{\mathsf{T}_1,2}^2 = \mathbf{S}_0^2 + \mathbf{S}_1^2 + \mathbf{S}_2^2 + \mathbf{S}_3^2 = 4S^2. \tag{11.80}$$

by adding and subtracting $NS^2\mathscr{E}_0$ from 11.78.

This gives us

$$\begin{aligned} H = \frac{1}{2}\sum_{tet} \big[&(a_{\mathsf{A}_2} - \mathscr{E}_0) m_{\mathsf{A}_2}^2 + (a_{\mathsf{E}} - \mathscr{E}_0)\mathbf{m}_{\mathsf{E}}^2 + (a_{\mathsf{T}_2} - \mathscr{E}_0)\mathbf{m}_{\mathsf{T}_2}^2 + \\ &(a_{\mathsf{T}_1,1} - \mathscr{E}_0)\mathbf{m}_{\mathsf{T}_1,1}^2 + (a_{\mathsf{T}_1,2} - \mathscr{E}_0)\mathbf{m}_{\mathsf{T}_1,2}^2 \big] + NS^2\mathscr{E}_0. \end{aligned} \tag{11.81}$$

The local order parameter (or *parameters* in the case of a degeneracy) for which $a_\gamma = \mathscr{E}_0$ is eliminated from the Hamiltonian, while the others now occur quadratically with positive coefficients. Thus the condition

$$\mathbf{m}_\gamma = 0 \ \forall \ \gamma \ \text{ such that } \ a_\gamma > \mathscr{E}_0 \tag{11.82}$$

applying to every tetrahedron in the lattice is both a sufficient and necessary condition to be in a ground state.

The problem of finding the classical ground state for the nearest neighbour anisotropic exchange model on the pyrochlore lattice, can therefore always be reduced to the problem of satisfying local constraints, defined on each tetrahedron in the lattice.

The nearest neighbour spin ice model is a special case in which the constraints are

$$\mathbf{m}_{\mathsf{E}} = \mathbf{m}_{\mathsf{T}_1,\mathsf{pl}} = \mathbf{m}_{\mathsf{T}_2} = 0 \tag{11.83}$$

which forces all spins onto their $\langle 111 \rangle$ axes and

$$m_{\mathsf{A}_2} = 0 \tag{11.84}$$

which enforces the "2 in, 2 out" rule on every tetrahedron.

While in the case of spin ice there is an exponentially large set of degenerate ground states, for more general sets of exchange parameters the constraints will usually only be satisified by a discrete set of $\mathbf{q} = 0$ configurations with degeneracy $\mathcal{O}(1)$. Greater freedom is obtained when $\mathscr{E}_0$ is equal to two or more coefficients a_γ, which occurs at the classical $T = 0$ phase boundaries of the model. These degeneracies can be associated with many interesting phenomena including dimensionally reduced states, spin nematics and spin liquids [18, 21, 22].

References

1. M. Hermele, M. P. A. Fisher and L. Balents, Phys. Rev. B **69**, 064404 (2004). https://doi.org/10.1103/PhysRevB.69.064404
2. A. Banerjee, S. V. Isakov, K. Damle and Y. B. Kim, Phys. Rev. Lett. **100**, 047208 (2008). https://doi.org/10.1103/PhysRevLett.100.047208
3. N. Shannon, O. Sikora, F. Pollmann, K. Penc and P. Fulde, Phys. Rev. Lett. **108**, 067204 (2012). https://doi.org/10.1103/PhysRevLett.108.067204
4. O. Benton, O. Sikora and N. Shannon, Phys. Rev. B **86**, 075154, (2012). https://doi.org/10.1103/PhysRevB.86.075154
5. Y. Kato and S. Onoda, Phys. Rev. Lett. **115**, 077202 (2015). https://doi.org/10.1103/PhysRevLett.115.077202
6. M. P. Kwasigroch, B. Doucot and C. Castelnovo, Phys. Rev. B **95**, 134439, (2017). https://doi.org/10.1103/PhysRevB.95.134439
7. Z. Hao, A. G. R. Day and M. J. P. Gingras, Phys. Rev. B **90**, 214430, (2014). https://doi.org/10.1103/PhysRevB.90.214430
8. S. H. Curnoe, Phys. Rev. B **75**, 212404 (2007); Phys. Rev. B **76**, 139903(E) (2007). https://doi.org/10.1103/PhysRevB.75.212404
9. S. Onoda and Y. Tanaka, Phys. Rev. B **83**, 094411 (2011). https://doi.org/10.1103/PhysRevB.83.094411
10. K. A. Ross, L. Savary, B. D. Gaulin and L. Balents, Phys. Rev X **1**, 021002 (2011). https://doi.org/10.1103/PhysRevX.1.021002
11. L. Savary, K. A. Ross, B. D. Gaulin, J. P. C. Ruff and L. Balents, Phys. Rev. Lett. **109**, 167201 (2012). https://doi.org/10.1103/PhysRevLett.109.167201
12. M. E. Zhitomirsky, M. V. Gvozdika, P. C. W. Holdsworth and R. Moessner, Phys. Rev. Lett. **109**, 077204 (2012). https://doi.org/10.1103/PhysRevLett.109.077204
13. S. E. Palmer and J. T. Chalker, Phys. Rev. B **62**, 488-492 (2000). https://doi.org/10.1103/PhysRevB.62.488
14. L. J. Chang, S. Onoda, Y. Su, Y. J. Kao, K. D. Tsuei, Y. K. Yasui, K. Kakurai and M. R. Lees, Nat. Commun. **3**, 992 (2012). https://doi.org/10.1038/ncomms1989
15. J. Gaudet, K. A. Ross, E. Kermarrec, N. P. Butch, G. Ehlers, H. A. Dabkowska and B. D. Gaulin, Phys. Rev. B **93**, 064406 (2016). https://doi.org/10.1103/PhysRevB.93.064406
16. A. Yaouanc, P. Dalmas de Reotier, P. Bonville, J. A. Hodges, V. Glazkov, L. Keller, V. Sikolenko, M. Bartkowiak, A. Amato, C. Baines, P. J. C. King, P. C. M. Gubbens and A. Forget, Phys. Rev. Lett. **110**, 127207 (2013). https://doi.org/10.1103/PhysRevLett.110.127207
17. P. A. McClarty, S. H. Curnoe and M. J. P. Gingras, J. Phys.: Conf. Series, **145**, 021032 (2009). https://doi.org/10.1088/1742-6596/145/1/012032

18. H. Yan, O. Benton, L. Jaubert and N. Shannon, Phys. Rev. B **95**, 094422 (2017). https://doi.org/10.1103/PhysRevB.95.094422
19. H. F. Jones, *Groups, Representations and Physics*, 2nd ed. (Taylor and Francis, New York, 1998). https://doi.org/10.1201/9780367805791
20. M. Tinkham, *Group Theory and Quantum Mechanics* (Dover Publications, New York, 2003). ISBN -10 0-486-43247-5
21. O. Benton, Ph.D. thesis, University of Bristol (2015)
22. O. Benton, L. D. C. Jaubert, H. Yan and N. Shannon, Nat. Commun. **7**, 11572 (2016). https://doi.org/10.1038/ncomms11572

Chapter 12
Experimental Search for Quantum Spin Ice

Kate A. Ross

Abstract At the most general level, Quantum Spin Ice refers to a pyrochlore system in which ice-rule obeying configurations are endowed with dynamics from quantum fluctuations. To generate such a state experimentally, material candidates must support anisotropic exchange interactions between localized spins on the pyrochlore lattice. Quantum fluctuations result from smaller XY-like interactions that compete with the dominant ferromagnetic Ising interactions required for classical spin ice. These quantum fluctuations modify the experimental signatures associated with classical spin ice, and may also generate novel ground states, such as a U(1) Quantum Spin Liquid. In the search for such exotic phases there have arisen several material candidates; $Yb_2B_2O_7$ (B = Sn, Ti), $Tb_2B_2O_7$ (B = Sn, Ti) and $Pr_2B_2O_7$ (B = Sn, Zr, Ir, Hf) all display properties consistent with a dynamic version of spin ice, but their lowest temperature properties are not yet understood. The status of the current literature on these materials is reviewed here.

12.1 Introduction

Classical Spin Ice (CSI) has the intriguing characteristic of supporting emergent excitations that can be identified as magnetic monopoles. These monopole excitations are the result of a fractionalization of a single spin flip out of a macroscopically degenerate manifold of disordered ground states—the monopole "vacuum". The constraints imposed by the ice rules can be re-written in terms of an emergent gauge field, with the monopoles as the gauge charges. In CSI, to generate new ice states from a starting configuration, loops of at least 6 spins must be flipped. This process becomes extremely unfavorable at temperatures below the nearest neighbor exchange energy, and the spin system freezes. In Quantum Spin Ice (QSI), quantum fluctuations promote *tunneling* between ice states, potentially resulting in coherent motion of monopoles.

K. A. Ross (✉)
Colorado State University, Fort Collins, CO, USA
e-mail: kate.ross@colostate.edu

M. Udagawa and L. Jaubert (eds.), *Spin Ice*, Springer Series in Solid-State Sciences 197,
https://doi.org/10.1007/978-3-030-70860-3_12

One of the most appealing aspects of QSI is that it offers the possibility of extending the monopole picture of CSI by inducing dynamics in the gauge field, effectively producing a full emergent electrodynamics; the fundamental quasi-particles would be spin-based analogs to electrons, magnetic monopoles, and photons. This phase of matter is called a U(1) Quantum Spin Liquid (QSL), and related to it is a partially polarized spin liquid called the Coulomb Ferromagnet (CFM). The unique excitations of these phases, in particular the gapless, linearly dispersing magnetic photon modes, can lead to identifiable experimental signatures. If they were to be observed, this would constitute the long-sought "smoking gun" for an experimental example of a QSL. Since the early days of QSL research, material candidates could only be described in terms of what they were *not*; i.e. not magnetically ordered, and not valence bond crystals [1, 2]. It is of enormous interest to find experimental realizations of QSI, which could support the "smoking gun" photons; these could finally provide a positive signature for QSL physics in a real material.

Experimental Quantum Spin Ice is a rapidly advancing area. This chapter discusses the status of the field as of December 2016. At the time of writing, an observation of emergent photons has not yet been claimed in any material. However, there are several candidate QSI compounds that deserve attention in the quest for this exotic physics. Primarily, the goal of this chapter is to review the body of knowledge on current QSI candidate materials. The theoretical background is presented earlier in the book, and has also been comprehensively reviewed in [3]. Prior to an exposition of the experimental behavior of QSI materials, the expected experimental signatures of QSI physics will be reviewed and compared to CSI. At the end of the chapter, a review of useful single-ion properties as well as a perspective for the future of QSI materials is provided. This may provide a guide for the search for new QSI materials.

12.1.1 Experimental Signatures of Classical Spin Ice

Taken in the most literal sense, QSI starts from the CSI ground state manifold of ice-rule obeying states and adds quantum fluctuations. Therefore, it is reasonable to expect that experimental signatures for QSI may be similar to CSI, with some modifications. The CSI signatures are reviewed here for comparison.

The pyrochlore lattice consists of an array of corner-sharing tetrahedra. Ising-like moments on this lattice, when coupled solely by a ferromagnetic nearest neighbor interaction (called J_{zz} here, in anticipation of the QSI case), will lead to CSI. In real materials, the necessary Ising anisotropy is generated by spin-orbit coupling. The single-ion angular momentum eigenstates of strongly spin-orbit coupled moments (for example in rare earth based materials) can be split by the Crystal Electric Field (CEF) generated by the surrounding ions, leading to moment anisotropy at the single-ion level that can be characterized by the g-tensor. In pyrochlore materials, the symmetry of the lattice dictates that any anisotropy of the g-tensor must be defined

with respect to the local $< 111 >$ direction; g_z (Ising) and g_{xy} (XY) components point respectively parallel and perpendicular to the axis connecting the corner of the tetrahedron to its center.

The ground states of CSI are characterized by the "ice rule", which refers to the constraint that each tetrahedron must have two spins pointing in and two spins pointing out, a 6-fold degenerate configuration for a single tetrahedron. On the pyrochlore lattice, the two-in-two-out rule does not fully constrain the choice for each tetrahedron. This leads to a macroscopic manifold of degenerate *disordered* ground states having emergent dipolar spin correlations. With the addition of dipolar *interactions*, as in the dipolar spin ices $Ho_2Ti_2O_7$ and $Dy_2Ti_2O_7$, the model retains the same ground state manifold, but the dynamical properties are richer. Although some degree of single-ion quantum tunneling seems to be necessary to explain the dynamics of dipolar spin ice, the coherent multi-spin moves allowed in QSI are not appreciable, and in this sense dipolar spin ice should still be considered a CSI. Dipolar spin ice is discussed extensively in the first half of this book.

How do you tell if your pyrochlore material is a spin ice? First, the Ising nature of the g-tensor (i.e. $g_z >> g_{xy}$) required for CSI can be determined from knowledge of the crystal field Hamiltonian (deduced, for example, through analysis of neutron or optical spectroscopy [4, 5]), or it can be directly measured by ESR or Mössbauer spectroscopy [6]. Meanwhile, the sign of the dominant exchange interaction can be determined from inverse susceptibility through Curie-Weiss analysis, although this represents only an average interaction energy and does not usually tell the whole story. Sometimes the existence of dominant Ising-like ferromagnetic interactions is inferred based on other experimental signatures of CSI, which we now describe.

The experimental signatures of CSI are exemplified by the materials $Dy_2Ti_2O_7$ and $Ho_2Ti_2O_7$. First, the freezing of the system into one particular choice of ice rule obeying states produces a residual molar entropy approximately equal to $S_p = \frac{1}{2}R\ln(3/2)$, the same residual entropy that was first estimated by Pauling in relation to water ice. This residual entropy has been observed in $Dy_2Ti_2O_7$ and $Ho_2Ti_2O_7$, via low temperature specific heat measurements [7, 8]. Secondly, magnetization measurements on single crystals of spin ice show a plateau at 2/3 of the saturation magnetization (which itself occurs at 1/3 of the full moment) when the field is applied along the $< 111 >$ direction (see Chap. 5) [9, 10]. This plateau indicates the formation of a partially polarized ice rule obeying state known as Kagome ice. Third, the freezing of the moments manifests as a very long relaxation time, measurable via the frequency dependence of ac susceptibility, for example. The timescale for relaxation diverges as the temperature is lowered beyond the energy required to thermally excite a spin flip. For example, the relaxation time in $Dy_2Ti_2O_7$ begins to diverge at about 1 K [11, 12], which is on the same order as $J_{zz} = 1.1$ K [13]. However it should be noted that a simple activation process is not observed in CSI and understanding the monopole dynamics in CSI is still a subject of active research.

Another distinguishing characteristic of CSI is the dipolar form of the spin correlations, $< S_i(0) \cdot S_j(\mathbf{r}) > \propto \frac{1}{r^3}$, leading to "pinch points" observable by diffuse neutron scattering from a single crystal. It should be noted that the presence of pinch points generally indicates dipolar spin correlations (see Chap. 3) but these can arise

in other models on the pyrochlore lattice (for example, the Heisenberg AFM model [14, 15]). Therefore, the presence of pinch points alone does not guarantee spin ice. The details of the structure factor, as could be observed by diffuse single crystal neutron scattering, have been calculated for the nearest neighbor CSI model, both with and without the inclusion of dipolar interactions, and the results agree well with polarized neutron scattering experiments on $Ho_2Ti_2O_7$ [16]. Although pinch points can not be directly observed in polycrystalline samples, the powder average of this structure factor can be compared to diffuse scattering to identify spin ice correlations, as was done for $Ho_2Ge_2O_7$ [17], $Ho_2Sn_2O_7$ [18], and $Pr_2Sn_2O_7$ (see Fig. 11) [19].

12.1.2 Experimental Signatures of Quantum Spin Ice

The most basic requirement of QSI is that, despite dominant spin ice type interactions, there is retention of spin dynamics at temperatures well below the energy scale of the nearest neighbor spin ice interaction J_{zz}. Although the most general interpretation of QSI, that of CSI with the addition of quantum fluctuations, allows for *ordered* $T = 0$ ground states, one may still expect a finite temperature region of *dynamic* spin ice behavior [20, 21] above the temperature at which the quantum ground state sets in. Spin dynamics in such a fluctuating spin ice regime can be probed by several experimental methods; ac and dc susceptibility, μSR, Mössbauer spectroscopy, specific heat, thermal transport, and inelastic neutron scattering have all been employed to show this property in the case of the known QSI candidates.

Great insight on the nature of QSI has come from the application of an anisotropic exchange pseudo-spin $\frac{1}{2}$ Hamiltonian (see Chap. 11).

$$\begin{aligned} H = \sum_{\langle ij \rangle} \Big\{ & J_{zz} \mathsf{S}_i^z \mathsf{S}_j^z - J_{\pm} (\mathsf{S}_i^+ \mathsf{S}_j^- + \mathsf{S}_i^- \mathsf{S}_j^+) \\ & + J_{\pm\pm} \left[\gamma_{ij} \mathsf{S}_i^+ \mathsf{S}_j^+ + \gamma_{ij}^* \mathsf{S}_i^- \mathsf{S}_j^- \right] \\ & + J_{z\pm} \left[\mathsf{S}_i^z (\zeta_{ij} \mathsf{S}_j^+ + \zeta_{ij}^* \mathsf{S}_j^-) + i \leftrightarrow j \right] \Big\}, \end{aligned} \tag{12.1}$$

where S_i^μ are *local* spin coordinates, with z defined along the local $< 111 >$ direction (Fig. 12.1a). The matrices γ and ζ consist of unimodular complex numbers (see Chap. 11 and the Appendix of [22]). The four exchange constants of this Hamiltonian represent the full symmetry-allowed exchange tensor for the pyrochlore lattice, as first developed by Curnoe [23]. J_{zz} is the nearest neighbor Ising exchange; retaining *only* this term would produce either the nearest neighbor CSI model for positive J_{zz} or a long range ordered "all-in all-out" (AIAO) state for negative J_{zz}. The additional interactions ($J_{\pm}$, $J_{\pm\pm}$, and $J_{z\pm}$) introduce some XY character, and when they are small compared to a positive J_{zz} they act to introduce quantum fluctuations to the spin ice.

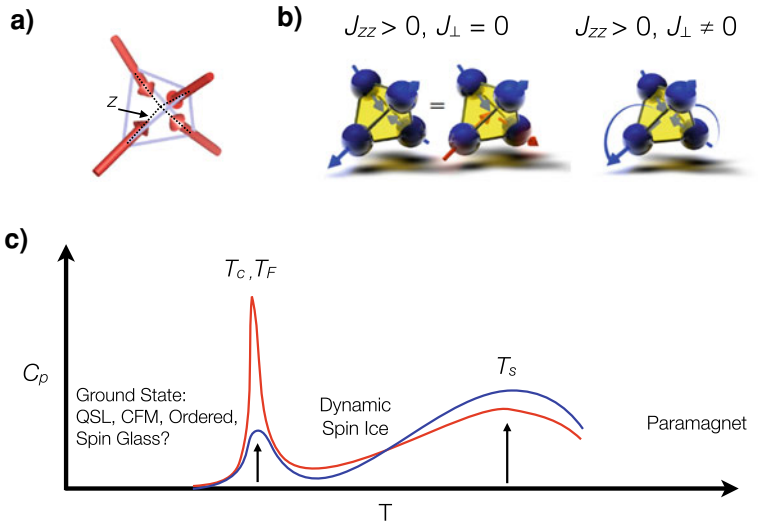

Fig. 12.1 **a** Definition of the local z axis in spin ice; each spin on the corner of a tetrahedron points in or out of the center of the tetrahedron. **b** Classical spin ice is characterized by ferromagnetic exchange that couples the spins along the local z directions, $J_{zz} > 0$. The ground state is a macroscopically degenerate manifold of states in which each tetrahedron obeys the ice rule: "2-in-2-out". When smaller planar exchange terms are introduced, $J_\perp \neq 0$, the spin ice states are endowed with dynamics and can tunnel between ice-rules obeying configurations. **c** A general zero-field phase diagram for Quantum Spin Ice materials. The specific heat typically shows either one or two features at low temperatures. The first is a Schottky-like hump at $T_s \sim J_{zz}$, signaling the entrance to ice rule obeying states which retain significant dynamics. In some materials, there is then a lower temperature feature such as a sharp anomaly at T_c, signaling a phase transition, or small peak at T_F, signaling spin freezing or a crossover. The ground state below T_c or T_F could be exotic, such as the Quantum Spin Liquid (QSL) or Coulomb Ferromagnet (CFM), or it could be more conventional. The region between T_s and T_c is called "dynamic spin ice" in this chapter

There are several ground state phases of this model which have been identified for dominant positive J_{zz}. Two of these phases are conventional ferromagnetic and antiferromagnetic orders (or ferroquadrupolar and antiferroquadrupolar phases in the case that the pseudo-spin is constructed from a non-Kramers ion [24]), and two are exotic phases: the U(1) QSL and the Coulomb Ferromagnet (CFM). In the two latter phases, the fundamental excitations are not magnons, as would be expected from conventionally ordered states, but are instead analogs of magnetic monopoles, electric monopoles (electrons), and gauge photons leading to a complete "lattice electrodynamics" [25–29].

In what follows, we first outline some experimental signatures of *dynamic* spin ice systems which exist at temperatures *above a phase transition* to any of the relevant ground states of the model, but below the crossover to ice rule dominated spin states at T_s (see Fig. 12.1c). Then we outline the predicted experimental signatures for the exotic phases of the QSI model described above.

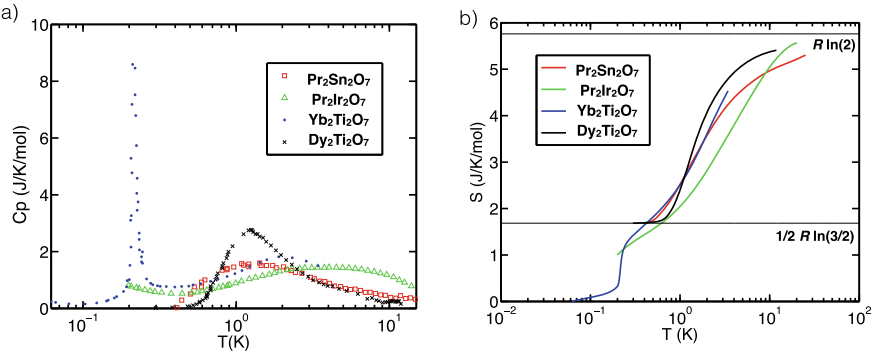

Fig. 12.2 **a** Specific heat of several QSI materials compared to $Dy_2Ti_2O_7$. QSI materials sometimes show a "double peak" structure, with a broad peak higher temperature signaling the entrance to ice-rule-dominated states, and a lower temperature transition, or upturn in C_p vs. T. **b** The molar entropy associated with the C_p curves; all materials shown here (aside from $Dy_2Ti_2O_7$) approach a total entropy change of $R\ln(2)$ which is taken as the limiting high temperature value. In several QSI materials there is a slight entropy plateau near the Pauling value, $1/2R\ln(3/2)$, suggesting ice-rules-dominated spin correlations. The lower temperature transition will act to remove the residual entropy associated with CSI, potentially forming a quantum superposition of ice rule states, the QSL. (Source of data: $Pr_2Sn_2O_7$ [19], $Pr_2Ir_2O_7$ [30], $Yb_2Ti_2O_7$ [31], and $Dy_2Ti_2O_7$ [7], with permission from Nature Materials, the American Physical Society and Elsevier.)

Dynamic Spin Ice Signatures

The freezing behavior of CSI is controlled by the interaction J_{zz}. When temperature is low enough that the strong spin ice correlations prevent the spin flips necessary to create and move the monopoles, the relaxation time increases dramatically [12]. In a QSI material, quantum fluctuations allowing multi-spin moves are expected, and the monopoles can therefore propagate more easily at temperatures below this energy scale. In this case, if a magnetization plateau is observed in a $< 111 >$ field, it is likely to be less sharply defined (in some cases, it may look more like an inflection point: see, for example, theoretical estimates in [32]). Furthermore, the entropy associated with the dynamic spin ice regime may be near to Pauling's entropy, but in QSI the system can more easily release the excess entropy through a phase transition, or crossover, at a lower temperature. This scenario results in an entropy plateau near the Pauling value (Fig. 12.2). Note that this eventual release of the Pauling entropy has also been shown to occur in the CSI material $Dy_2Ti_2O_7$, but on experimentally impractical timescales [33]; thus for all practical purposes, $Dy_2Ti_2O_7$ goes out of equilibrium and stays a spin ice to the lowest temperatures.

In QSI, the signatures of the residual fast spin dynamics can be observed by several experimental techniques. μSR may show a quickly relaxing asymmetry, indicating fluctuating moments. Meanwhile, if any spin freezing is detected by ac or dc susceptibility, it would be expected to occur at temperatures lower than $\sim J_{zz}/k_B$, and the deduced timescale for spin flips will be relatively fast. Furthermore, inelastic

neutron scattering may reveal a large fraction of quasi-elastic scattering (relative to elastic scattering) at low temperatures, indicative of enhanced fluctuations in the spin system.

The application of a magnetic field at low temperatures in the dynamic spin ice regime may be revealing. A weak magnetic field applied along the $< 100 >$ direction could also be used to reveal the monopole-like nature of the excitations in the the QSI phase, through the detection of quantized "string excitations" [34]. These excitations result from a field-induced tension of the Dirac strings that connect magnetic monopoles in the quantum system, resulting in quantized energies for different Dirac string lengths. Experimental signatures of such a scenario may have been seen in one QSI candidate, $Yb_2Ti_2O_7$, in its dynamic spin ice regime [35].

Signatures of U(1) QSL-related Phases

Theoretically, QSI materials may support exotic physics in their ground states. The ground states may be reached from the dynamic spin ice regime by a phase transition [36] or a thermal crossover [20], at which the residual entropy of the system is removed. If the ground state is a QSL or CFM phase, the fundamental excitations would lead to unique experimental signatures. The gapless and linearly dispersing photon modes are expected to dominate the very low temperature thermodynamic properties, for example as a large T^3 dependence of the low temperature specific heat [28, 29]. Furthermore, these photons are actually composed of spin degrees of freedom and could therefore be detected by neutron scattering. In one minimal model of QSI based on retaining only J_{zz} and a perturbative $J_{\pm}$ term in Eqn. (12.1), the neutron scattering response from these photon modes is predicted [29]. A distinguishing characteristic is that, in contrast to magnon excitations, the intensity of the photon modes is expected to vanish as as energy approaches zero ($I(\omega) \propto 1/\omega$ as $\omega \to 0$) [29].

The CFM phase, while predicted to support emergent electrodynamics, might simultaneously display signatures of a conventionally ordered ferromagnet, including magnetic Bragg peaks, finite magnetization, and perhaps even magnon excitations, coexisting with a quantum Coulomb phase supporting the other more exotic signatures. This could be understood as a kind of moment fragmentation [37], where the Ising component of the spin degree of freedom on each site becomes polarized in an ordered fashion, while the remaining XY component is responsible for the QSL type physics. It is worth noting that although the CFM phase is stable in gauge mean field theory (gMFT) for Kramers ion systems [27], this approach ignores fluctuations of the gauge field and the interaction of the gauge field with the spinons, and may not capture the true phase stability of the model. In another approach in which the gauge fluctuations are phenomenologically considered, it appears that the CFM phase is replaced by a *fully ordered* phase with conventional excitations [38]. It is currently not well-understood whether the CFM phase is a stable phase of the model when *both* gauge fluctuations *and* interactions with spinons are included. However, the idea of a phase with coexisting spin polarization and exotic excitations (e.g. deconfined

spinons) appears to be plausible, particularly in the context of recent experimental findings on QSI materials (particularly $Yb_2B_2O_7$) as discussed later in this chapter.

In contrast to the gauge photons, the emergent electrons and magnetic monopoles of the QSL and CFM phases are gapped, and would contribute an exponential temperature dependence to the low temperature specific heat, and would produce low-lying gapped modes in neutron scattering. Thus, even in the QSL phase, there are multiple signatures that could compete in a single measurement. Therefore, as a first step, a departure from conventional CSI behavior in the low temperature phases of QSI materials is promising.

While direct signatures of QSL physics and emergent electrodynamics such as those mentioned above have not yet been conclusively shown in any particular material, there are several promising material candidates, which we discuss below.

12.2 Quantum Spin Ice Materials

The known QSI materials all come from the rare-earth pyrochlore family of compounds. Their general chemical formula is $R_2B_2O_7$, with R a trivalent rare earth ion (e.g. Pr^{3+}, Tb^{3+} or Yb^{3+}), and B a tetravalent cation (e.g. Sn^{4+}, Ti^{4+}, Zr^{4+}, Hf^{4+} or Ir^{4+}). The magnetism arises solely from the R pyrochlore sublattice, which is strongly influenced by the CEF imposed by the nonmagnetic ions forming the local environment. The CEF in the pyrochlore lattice allows magnetic dipole moments that are in general described by a g-tensor with two independent components, g_z and g_{xy}. Some CEF doublets will also support significant quadrupole or octupole moments, and these play a role in determining the symmetry-allowed terms in Eqn. (12.1) and the physical ground state phases of the model [24, 39–41]. Depending on the type of rare-earth ion (Kramers vs. non-Kramers) as well as the details of the CEF Hamiltonian, each pyrochlore material has varying degrees of single-ion anisotropy. CSI materials have strong Ising dipole moments with essentially no XY dipole or quadrupole moments, while QSI materials usually have significant XY moments. Additionally, the intrinsic exchange interactions may be anisotropic and have varying Ising and XY contributions. Substituting different non-magnetic B cations can change the weight of relevant exchange interactions between the R ions. Thus, materials which differ only by the B site cations can display different ground states (see, for example, $Yb_2Ge_2O_7$ versus $Yb_2Ti_2O_7$ [42]). The QSI materials are part of an extensive family of isostructural magnetic pyrochlore oxides; an excellent review of the more general behavior of these materials can be found in [43].

In the QSI materials there is a distinct departure from the classical "dipolar spin ice" materials such as $Ho_2Ti_2O_7$ and $Dy_2Ti_2O_7$. In part, the difference arises because the size of the magnetic moments are much smaller (~ 2 to $5\mu_B$ rather than $\sim 10\mu_B$), strongly diminishing the relative importance of the dipolar interactions in the QSI materials. The resulting dominance of the exchange interactions encourages quantum dynamics, since in many cases there are sizable *transverse* exchange terms that couple the XY components of the ground state CEF doublets.

In each QSI material outlined in this chapter, the nature of the magnetic ground state is not net fully understood; some of them form partially ordered states, while others display partial spin freezing at very low temperatures. In many of the materials there is a sample-to-sample variation of the lowest temperature properties, the understanding of which is currently the subject of much experimental effort. However, in each material there appears to exist a temperature regime in which spin ice correlations form, but resist freezing; i.e. the "dynamic spin ice" regime outlined above (Fig. 12.1), which exists *between* the Schottky-like peak in the specific heat (T_s) and a lower temperature anomaly that signals the entrance to the ground state (T_c, T_N or T_F or another crossover). Both the ground state properties as well as the properties in this dynamic spin ice regime, which could host monopoles excitations experiencing much faster dynamics than CSI allows.

The remainder of this chapter is organized by families of pyrochlores defined by the relevant rare earth cation, since the CEF ground states of these ions control the anisotropy and symmetry properties of the resulting pseudo-spin.

12.2.1 Yb^{3+}-Based Pyrochlores

The known Yb^{3+}-based magnetic pyrochlores are $Yb_2B_2O_7$, with B = Ti, Sn and more recently synthesized Ge, and Pt. Each $Yb_2B_2O_7$ compound is expected to have a well-isolated Kramers CEF ground state doublet that is composed mainly of $J_z = \pm\frac{1}{2}$ eigenstates, as shown explicitly for $Yb_2Ti_2O_7$ [4–6, 44]. This CEF scheme allows for a pseudo-spin 1/2 description with XY-like moments and strong transverse exchange interactions. If combined with strongly Ising-like superexchange interactions, this could lead to QSI. The pyrochlore structural phases of B = Ge, Pt have so far only been obtained through high pressure synthesis [45–47], which has limited the sample sizes and number of studies on these members. Accordingly, most studies have focussed on $Yb_2Ti_2O_7$ and $Yb_2Sn_2O_7$, while only the former can be produced as large single crystals by the floating zone method, and thus has been the most widely studied. Therefore, the following discussion mainly emphasizes results in $Yb_2Ti_2O_7$, which has been proposed as a QSI material. However, a recent comparison between $Yb_2Ti_2O_7$, $Yb_2Sn_2O_7$, and $Yb_2Ge_2O_7$ shows that they have similar unusual excitations despite having different magnetically ordered ground states [48]. Much less is known about $Yb_2Pt_2O_7$, but its heat capacity signatures are similar to the three aforementioned materials, and therefore it may be expected to provide an additional point of comparison in the future [47]. This similarity between the Yb^{3+}-based pyrochlores despite their different ground states suggests a new direction for the understanding of this enigmatic pyrochlore family.

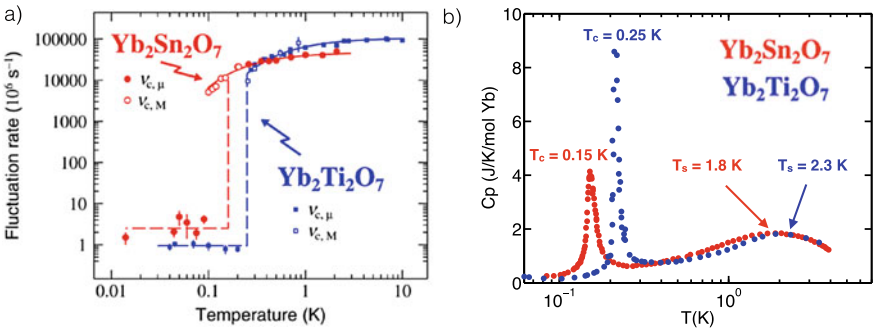

Fig. 12.3 Comparison of μSR and specific heat results on powder samples of $Yb_2Ti_2O_7$ and $Yb_2Sn_2O_7$. **a** Spin fluctuation rates as measured by μSR, reprinted from [57] with permission from the American Physical Society **b** specific heat of powder samples, adapted from [57] with permission from the American Physical Society and from [31] with permission from Elsevier. Arrows show the temperatures of the transitions (T_c) and the Schottky-like peaks (T_s)

$Yb_2Ti_2O_7$

The XY-like g-tensor in $Yb_2Ti_2O_7$ (g_z =1.92; g_{xy} =3.69 [44]) combined with its overall ferromagnetic interactions ($\theta_{CW} \sim 0.3$ K) [31, 49] should naively lead to a magnetically long range ordered state. However, the story is richer than this. The anisotropic exchange described in Eqn. (12.1) with dominant couplings involving the Ising direction (positive J_{zz} and negative $J_{z\pm}$) has been found to be appropriate to this material, suggesting a connection to spin ice.

The specific heat shows two features of interest (Fig. 12.3); a broad Schottky-like anomaly with a peak at T_s = 2.6 K, and a sharper anomaly at a temperature that depends on the detailed preparation of the sample, between $T_c = 200$ and 265 mK [22, 31, 50–52]. Despite the sharp anomaly, results of μSR [49, 53, 54], Mössbauer spectroscopy [49], and several neutron scattering experiments [22, 49, 55, 56] seem to be inconsistent with static long range magnetic order (LRO) below this temperature. An early μSR study revealed that the spin fluctuation rate undergoes a dramatic decrease at T_c in a first order transition, but with persistent spin fluctuations below T_c [49] (Fig. 12.3), prompting the initial suggestion that $Yb_2Ti_2O_7$ hosts a kind of spin liquid state below T_c.

There is a known sample-to-sample variation in the properties of this material, including even the μSR result just mentioned. Some samples are seen to magnetically order below T_c, while others are not. For this reason, it is important to carefully discuss the results in different classes of samples, namely single crystals versus powder samples. The high sensitivity to structural disorder in $Yb_2Ti_2O_7$ may be the result of a delicate competition between competing classical phases, a situation not uncommon to frustrated materials in general. After several years of experimental study, it now seems clear that the most structurally ideal samples of $Yb_2Ti_2O_7$ form a long range ordered state below T_c. However, the nature of the excitations in all samples,

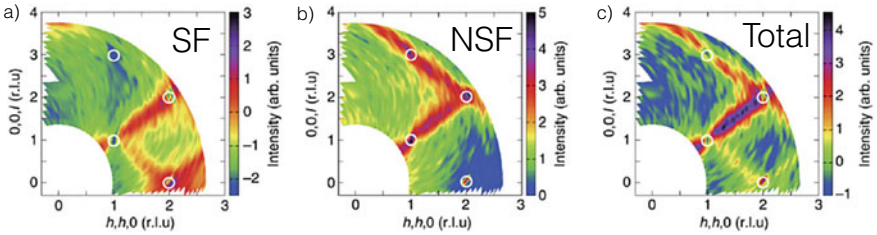

Fig. 12.4 Energy integrated polarized diffuse neutron scattering from single crystal $Yb_2Ti_2O_7$. Rods of scattering along $< 111 >$ are visible in both spin flip (SF) and non-spin flip (NSF) channels, making them the strongest features in the total neutron scattering (as observed in [55]). Near the zone centers, the scattering appears to sharpen, a feature reminiscent of pinch points from a coulomb phase. White circles indicate the position of nuclear Bragg peaks which were subtracted. Reprinted figure from [59] with permission from Nature Communications

whether those samples are long range ordered or not, seems to be unconventional. Furthermore, the temperature regime between T_s and T_c is an unusual correlated regime, which may be related to a dynamic version of spin ice in which monopole excitations propagate freely due to quantum fluctuations.

Large single crystals of $Yb_2Ti_2O_7$ can be prepared via the optical floating zone method of crystal growth, and are thus quite amenable to neutron scattering studies. Such studies have been reported by several authors, and some inconsistencies surrounding the nature of the magnetic state in different crystals at the lowest accessible temperatures were noted. Above T_c, neutron scattering studies appear to be consistent with one another, revealing "rods" of magnetic diffuse scattering extending along the $< 111 >$ directions (Fig. 12.4) [55, 58, 59]. In at least one single crystal sample, these "rods" were found to be the result of dynamic correlations, appearing as quasi-elastic neutron scattering [22, 55].

Below T_c there have been varying reports. Several single crystals of $Yb_2Ti_2O_7$ do not seem to undergo a transition to LRO [22, 55, 56]. In those samples, the low energy continuum-like diffuse scattering persists to temperatures well below T_c. However, there exists one crystal reported to display a long range ordered state below T_c, revealed through the development of magnetic Bragg peaks in neutron diffraction [59, 60] and magnetization measurements [61]. The discrepancy likely relates to inconsistencies in the magnetic specific heat of different samples of $Yb_2Ti_2O_7$ [22, 50, 52]. A survey of the literature reveals that single crystal samples are less likely to display sharp specific heat peaks than powders: their heat capacity anomalies are broader and occur at low temperature (typically 200 mK). This variation in heat capacity must arise from extrinsic effects like non-stoichiometry ("stuffing", Yb deficiency, or oxygen non-stoichiometry have all been proposed) induced by the crystal growth process [51, 59, 62]. The polycrystalline (powder) samples are less prone to sample variability than the crystals, and it is by now accepted that these high quality samples show signs of magnetic LRO below T_c with a reduced moment reported to be between 0.8 to 1.2 μ_B [58, 61, 63, 64]. However, the ground state of

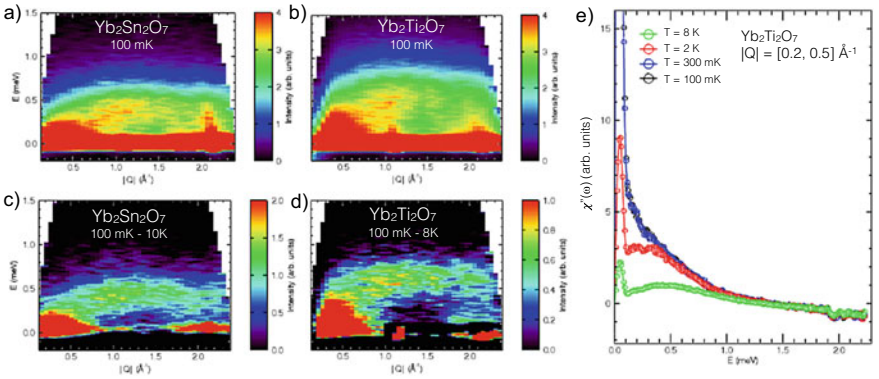

Fig. 12.5 Inelastic neutron scattering from $Yb_2Sn_2O_7$ and $Yb_2Ti_2O_7$ powder samples, taken on the Disk Chopper Spectrometer at the NIST Center for Neutron Research, with $\lambda = 5$Å incident neutrons. The $Yb_2Ti_2O_7$ sample is the same one previously characterized by neutron diffraction and found to be fully stoichiometric [51]. The $Yb_2Sn_2O_7$ results have been previously presented in [73]. **a**, **b** Inelastic neutron scattering from $Yb_2Sn_2O_7$ and $Yb_2Ti_2O_7$ at $T = 100$ mK. Broad incoherent inelastic scattering is seen in both samples even at the lowest temperatures. This broad feature is present at higher temperatures, and when data at 8 K or 10 K is subtracted **c**, **d** the low temperature inelastic features are revealed to be dispersive excitations with no gap to within the energy resolution (0.1 meV). **e** $\chi''(\omega)$ at low $|Q|$ (0.2 to 0.5 $Å^{-1}$), showing that no gap in the excitation spectrum is opening upon crossing T_c

the powder samples still apparently lacks the ability to depolarize neutrons, contrary to what would be expected for a conventional ferromagnet [63], while μSR experiments show persistent spin dynamics in some cases [49, 54], though not in others [52]. Finally, in at least one powder sample there remains a broad dynamic structure factor as measured by inelastic neutron scattering, inconsistent with magnon excitations despite confirmed LRO in that same sample (see Fig. 12.5) [64].

Despite the XY nature of the dipole moment anisotropy, which arises from the g-tensor for the lowest CEF Kramers doublet, $Yb_2Ti_2O_7$ has strong exchange coupling involving the z components of the pseudo-spins (i.e., sizable J_{zz} or $J_{z\pm}$ in Eqn. 12.1). A large Ising-like exchange in $Yb_2Ti_2O_7$ was first reported by Cao et al. on the basis of local susceptibility measurements [66], and further insight has come from studying the spin dynamics induced by the application of a magnetic field. The spin wave dispersions measured by inelastic neutron scattering in the field-polarized regime have been fit in order to extract of the four constants in (12.1). Two sets of exchange interactions have been obtained this way [27, 56] with a similarly good description of the measured spin wave excitations that were reported in [27]. However, these parameter sets are not mutually consistent, and it can be noted that while one set reproduces zero-field thermodynamic quantities at intermediate temperatures [21, 67], the other seems to capture features of diffuse scattering more accurately [56] but has not yet been tested against the thermodynamic measurements. Further, two additional sets of exchange interactions were initially extracted by concentrating solely on matching the details of the diffuse scattering above T_c in the cooperative

Table 12.1 Exchange parameters that have been proposed for $Yb_2Ti_2O_7$ (in meV). The values which best reproduce the field polarized spin wave spectrum are distinguished by boldface

Exchange constant[a]	Reference [56]	Reference [27]	Reference [65]	Reference [59]
J_{zz}	**0.07**	**0.17(4)**	0.023	0.059
$J_{\pm}$	**0.085**	**0.05(1)**	0.038	0.023
$J_{\pm\pm}$	**0.07**	**0.05(1)**	0.007	0.006
$J_{z\pm}$	**−0.15**	**− 0.14(1)**	−0.040	−0.029

[a]terms defined based on (12.1)

paramagnetic regime, but the values so-obtained do not reproduce the thermodynamic measurements [21]. The sets of exchange parameters that have been proposed for $Yb_2Ti_2O_7$ are summarized in Table 12.1, and the two most robust sets are emphasized in bold.

Considering first the exchange parameter set, from [27], J_{zz} is dominant and positive, as expected for CSI, but the additional presence of transverse terms could be expected to produce quantum fluctuations amongst the spin ice states. Within this model $Yb_2Ti_2O_7$ would thus have the necessary ingredients for QSI. This phenomenology could possibly explain some of the puzzling experimental features in $Yb_2Ti_2O_7$, for instance the lack of conventional spin wave excitations below T_c [55, 56] even in spite of the confirmed presence of LRO in the powders [64], while also providing a natural explanation for some of the low energy dynamical phenomena above T_c [59, 68, 69]. This leads to the tantalizing possibility of the exotic QSL or CFM phases being realized by this material.

The suggestion that $Yb_2Ti_2O_7$ may support QSI physics begs the question as to whether $Yb_2Ti_2O_7$ hosts "ice rule" correlations in any temperature regime. This question has not yet been definitively answered, however some indirect evidence favors such correlations in the temperature regime between T_c and T_s (what might be considered the "dynamic spin ice" regime, Fig. 12.1); notably the observed pinch points in diffuse neutron scattering in one experiment (Fig. 12.4, [59]) and a smoothed entropy plateau near the Pauling value [21]. Intriguingly, terahertz spectroscopy measurements performed at $T = 1.6$ K (below T_s) on a single crystal of $Yb_2Ti_2O_7$ have revealed an unusual field-dependence of the g-factor for small magnetic fields applied along the [100] direction [35], possibly arising from excitations similar to the quantum strings predicted for QSI [34]. Furthermore, the zero-field dynamics measured by the same technique [68] as well as thermal conductivity [69] may be consistent with monopole dynamics above T_c. Finally, the temperature dependence of ultrasound velocity measurements above T_c can be qualitatively reproduced within the single tetrahedron model of spin ice [70].

The more recently proposed exchange parameter set from [56] includes a fit to both the field polarized spin wave excitations from [27] as well as the paramagnetic diffuse neutron scattering in zero field, most importantly the diffuse scattering intensity near the (220) position. This scattering, as well as the diffuse rods along ⟨111⟩ can be

accounted for by the presence of both AFM and FM correlations [56, 71], and this parameter set places $Yb_2Ti_2O_7$ very close to a classical phase boundary between the splayed ferromagnet and the XY AFM ordered states called ψ_2 and ψ_3. Furthermore, the ice-like J_{zz} does not dominate; $J_{z\pm}$ is larger by a factor of two. This raises a new question: what effect does the proximity to this phase boundary between competing classical phases have? Could it be responsible for the extreme sample dependence of the low temperature properties? This line of questioning has been pursued in recent theoretical works [71, 72].

The "splayed ferromagnet", which is the mean field LRO ground state for large enough $J_{z\pm}$ [21, 28, 71], supports nearly collinear moments oriented approximately along the [100] direction with a small canting that is thought to be either "ice-like" [59, 64] or "all-in-all-out like" [74] in $Yb_2Ti_2O_7$. Within the QSI phenomenology, the presence of this ordered state was proposed to arise through a Higgs mechanism, in which the free spinons (monopoles) condense into conventional excitations [59], again suggesting that temperature regime between T_s and T_c could be related to dynamic spin ice physics. However, the nature of the spin excitations in the ordered state in the best powder samples are strikingly inconsistent with a conventionally ordered state (or equivalently, a "Higgs phase"), even in samples where magnetic Bragg peaks from the splayed ferromagnet arise in neutron diffraction [64]. There are no sharp magnon modes; instead, continuum-like excitations persist below T_c with no sign of the spin wave gap predicted for the conventionally ordered state (see Fig. 12.5). Furthermore, the ordering transition appears to have no effect on this spectrum; it is identical above and below T_c.

The reported ordered moment in samples of $Yb_2Ti_2O_7$ that display LRO ranges from 0.87 μ_B to 1.2 μ_B [49, 61, 63, 64] which is 50 to 70% of the total moment of 1.7 μ_B [6, 61]. The reduction is presumably due to quantum fluctuations. The fluctuating part of the moments may be free to engage in unusual behavior, such as the emergent electrodynamics predicted for the polarized CFM phase, or possibly another quantum effect arising from proximity of a classical phase boundary. Whatever viewpoint is taken, any successful theory will have to account for the simultaneous presence of LRO with a reduced moment and continuum-like inelastic scattering in $Yb_2Ti_2O_7$.

$Yb_2Sn_2O_7$ and $Yb_2Ge_2O_7$

In terms of both static and dynamic properties, $Yb_2Sn_2O_7$ bears a remarkable resemblance to $Yb_2Ti_2O_7$; the sharp transition observed in the specific heat at $T_c = 150$ mK also does not appear to lead to a completely ordered state in $Yb_2Sn_2O_7$. The same discontinuous drop in spin fluctuation rate is observed with μSR [57] (Fig. 12.3). Low temperature neutron diffraction reveals a splayed ferromagnetic LRO state with an ordered moment of only 1.1 μ_B, and inelastic neutron scattering reveals persistent spin dynamics [73] with a constant relaxation rate below $\sim T_s$. Glassy dynamics coexisting with magnetic order were observed by ac susceptibility, μSR, and neutron diffraction, and was compared to a percolating cluster glass with possible quantum Griffiths behavior [75]. ac susceptibilty measurements on both $Yb_2Sn_2O_7$

and $Yb_2Ti_2O_7$ revealed similar frequency and field dependences, which are consistent with a spontaneous moment below T_c, but are not consistent with conventional ferromagnetism [42]. Finally, inelastic neutron scattering on powders of both materials displays a combination of correlated and uncorrelated behavior down to 60 mK (Fig. 12.5), and the inelastic spectra do not change appreciably at T_c [64].

Strikingly, the pyrochlore $Yb_2Ge_2O_7$ [46, 48, 76], while having similar heat capacity signatures to the stannate and titanate, shows AFM order below T_N = 570 mK. Despite this qualitatively different ground state, this Yb pyrochlore supports spin excitations that are nevertheless nearly identical to $Yb_2Ti_2O_7$ and $Yb_2Sn_2O_7$, resembling damped FM spin waves (as in Fig. 12.5) [48]. Again, the inelastic neutron scattering signatures are not modified on passing through T_N. This apparent insensitivity of the excitations to the type of ordered ground state, and indeed also to the thermal transition, is perhaps the result of very close proximity to a quantum critical point in the exchange parameter phase space. Whatever the explanation, it is clear that the $Yb_2B_2O_7$ compounds are quite unusual frustrated magnets. The apparent lack of connection between the ordered ground states and the spin excitations is an important outstanding issue in the $Yb_2B_2O_7$ compounds; how this observation is eventually explained will also speak to the relevance of QSI physics to these materials.

12.2.2 Tb^{3+}-Based Pyrochlores

$Tb_2Ti_2O_7$

$Tb_2Ti_2O_7$ was the first material to be suggested as a quantum spin ice, but this designation is not yet agreed upon in the literature. Since 1999 the material has been intensely studied owing to its spin liquid behavior down to temperatures well below the mean interaction strength, $\theta_{cw} = -13$ K [77]. The spin dynamics at temperatures down to 30 mK have been probed by neutron scattering and neutron spin echo [78–81], μSR [78, 82, 83], and ac susceptibility [80, 84–86], with no LRO or complete spin freezing detected.

However, the disorder and persistent spin fluctuations in $Tb_2Ti_2O_7$ are quite surprising when considering the CEF scheme and average exchange interactions. Considering only the non-Kramers CEF ground state doublet of Tb^{3+} in this material, the moments are strictly Ising with no possibility of dynamics at the single ion level, since there are no matrix elements of the angular momentum raising and lowering operators $\mathbf{J}_+$ or $\mathbf{J}_-$ between the two states [77, 87]. Furthermore, the Curie-Weiss temperature indicates an *antiferromagnetic* mean field interaction strength of 13 K [77]. The combination of Ising spins and antiferromagnetic exchange should lead to an *ordered* "all-in-all-out" (AIAO) configuration that is the complement of spin ice [13, 88]. Yet $Tb_2Ti_2O_7$ is famed for its persistently dynamic and disordered magnetism down to millikelvin temperatures, indicating that the simple picture of Ising spins with antiferromagnetic exchange is not sufficient to describe its behavior.

What is the mechanism for the persistent fluctuations in $Tb_2Ti_2O_7$? One route to understanding this might be to try to extract the symmetry-allowed anisotropic exchange parameters for $Tb_2Ti_2O_7$, as was done for $Yb_2Ti_2O_7$. An attempt has been made to extract the exchange parameters for the pseudo-spin 1/2 model (12.1) judiciously applied to the unique case of the symmetries allowed by the non-Kramers doublet coupled to a very low-lying excited CEF level which sits at 1.5 meV (i.e. 18 K) in $Tb_2Ti_2O_7$ [23, 91]. Exchange parameters within this model were extracted for $Tb_2Ti_2O_7$ based on energy integrated diffuse neutron scattering at 1.4 K [91], and they do have QSI character. However, as was shown for $Yb_2Ti_2O_7$, fitting the diffuse scattering in the correlated paramagnetic regime does not always lead to a unique solution for these parameters. And although $Tb_2Ti_2O_7$ can be field-polarized and supports spin wave excitations observable with inelastic neutron scattering [92], the analysis of these modes is complicated by the strong field-induced mixing of the low lying crystal field level into the ground state.

Instead of analyzing a Hamiltonian such as (12.1), two alternative theoretical models have been proposed to explain the persistent spin dynamics and lack of LRO in $Tb_2Ti_2O_7$. One proposal is that the CEF ground state non-Kramers doublet is split by local lattice distortions. Such a Jahn Teller (JT) distortion, either static or dynamic, would produce two singlet levels with a small energy splitting. Such a splitting is conceivable; strong magneto-elastic coupling in $Tb_2Ti_2O_7$ is well documented [93–98] (Fig. 12.7) and an incipient *dynamic* tetragonal distortion was observed at 300 mK by x-ray scattering in a single crystal sample [95]. If such a distortion were occurring, the low temperature magnetic dynamics could result from the newly allowed transitions between the two low energy states [99]. An observed splitting consistent with a static JT scenario has not been definitively resolved experimentally, except in samples known to be non-stoichiometric [100], although a low energy feature revealed by inelastic neutron scattering in most samples has been proposed as evidence for this scenario in the past [101–103]. More recently, however, other studies have shown that the low energy feature coexists with elastic scattering, and thus cannot be due to a simple doublet splitting [89, 104, 105]. The *dynamic* JT distortion scenario seems to be more plausible and has been explored recently though the introduction of quadrupolar interactions to the effective Hamiltonian [87], which may induce dynamics as has been proposed in the Pr-based pyrochlores [39] discussed later in this chapter.

A second possibility for the origin of the dynamics in $Tb_2Ti_2O_7$ arises from the details of the known CEF eigenstates. Because the lowest excited crystal field level is only 18 K above the ground state (compare this to a ∼900 K separation of the ground state to first excited doublet in the CEF scheme for $Yb_2Ti_2O_7$ [44]), there will be appreciable second order effects, i.e. virtual crystal field excitations, occurring even at very low temperatures. Molavian et al. [106] have shown that by including the effects of virtual excitations to the next highest crystal field doublet the interactions between Ising moments in $Tb_2Ti_2O_7$ become effectively *ferromagnetic*, while also inducing transverse coupling terms, leading to the possibility of QSI physics. Polarized neutron diffraction experiments on single-crystal $Tb_2Ti_2O_7$ may be taken as evidence supporting QSI-like physics. The measurements reveal pinch points in

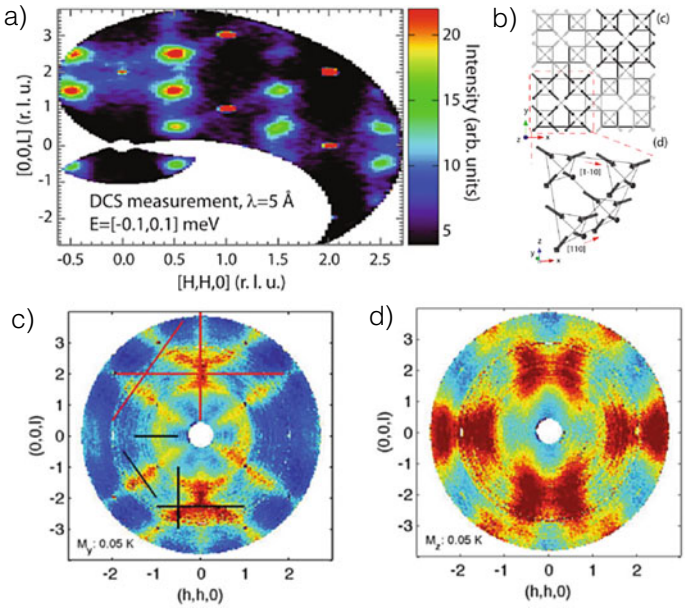

Fig. 12.6 Diffuse neutron scattering from single crystals of $Tb_2Ti_2O_7$. **a** unpolarized *elastic* ($\delta E = \pm 0.1$ meV) scattering at 66 mK, showing strong peaks at (1/2,1/2,1/2) positions [89]. **b** proposed short range correlations in $Tb_2Ti_2O_7$ based on the data in (**a**); an "ordered spin ice" structure is modified by tilting spins away from local $< 111 >$ axes by 12° (resembling the longer-ranged ordered structure in $Tb_2Sn_2O_7$), and the pattern is reversed every other unit cell [89]. **c**, **d** polarized neutron diffraction (energy integrated) in $Tb_2Ti_2O_7$ from spin correlations in the scattering plane (M_y) and perpendicular to the scattering plane (M_z). The maps reveal detailed anisotropic spin correlations with "pinch points" at 50 mK [90]. Red and black lines refer to additional data shown in [90]. Reprinted figures from [89] and from [90] with permission from the American Physical Society

the diffuse scattering from $Tb_2Ti_2O_7$ indicating a Coulomb phase with dipolar spin correlations (Fig. 12.6c, d) [90, 105]. However, since Coulomb phases can also arise in non-spin ice models, such as the Heisenberg AFM pyrochlore model [14, 15], this does not by itself settle the debate. Further evidence for spin ice correlations in $Tb_2Ti_2O_7$ comes from the form of the diffuse scattering seen in the partially frozen state below 400 mK observed in some samples; the correlations produce neutron scattering intensity at (1/2/,1/2,1/2) type positions; this pattern of diffuse scattering can be modeled by a *short range ordered* spin ice with AFM correlations between unit cells (Fig. 12.6a, b) [89]. At the time of writing, it is not yet clear whether this short range correlated state proposed in [89] could also be consistent with the pinch points and the other details of the polarized neutron diffraction experiment [90].

The proposal of quantum spin ice in $Tb_2Ti_2O_7$ came with the prediction of a rounded magnetization plateau in a $< 111 >$ field [32]. The theory predicts a plateau, which would be due to the formation of a dynamic version of Kagome ice, ending

at fields of ∼0.1 T. However, the experimental search for this plateau has turned up conflicting results [85, 108–110]. What this effort has shown so far is that there are several low field regimes possible in different samples of $Tb_2Ti_2O_7$ at the lowest temperatures, which have been discussed both in terms of the predicted plateau [85] as well as multiple other field-induced transitions [84, 108, 109], all at fields lower than 0.5 T. The presence of such very low field features indicates that there is a delicate balance of energetic terms responsible for the low temperature behavior of this material. This may be consistent with the observation of sample-dependent properties for extremely small variations in stoichiometry, as discussed below.

Many studies have been devoted to understanding which of the two pictures put forward for spin dynamics in $Tb_2Ti_2O_7$ are correct, and unfortunately the experimental literature on $Tb_2Ti_2O_7$ can seem contradictory. Not until recently was it appreciated that small deviations from ideal stoichiometry in different $Tb_2Ti_2O_7$ samples can have a strong influence in the lowest temperature magnetic properties. This was shown by Taniguichi et al. by varying the nominal Tb content in powder samples by $\sim 0.25\%$. This study revealed that the low temperature specific heat can be dramatically changed by such a small change in stoichiometry. A specific heat anomaly at 400 mK was observed for slightly stuffed $Tb_{2+x}Ti_{2-x}O_7$ ($x = 0.005$) which was accompanied by an apparent splitting of the ground state doublet [100]. As the composition was varied towards nominal full stoichiometry (i.e. $x = 0$), the specific heat anomaly evolved towards something resembling a freezing transition at lower temperatures. Signatures of this low temperature freezing at various temperatures between 100 mK and 400 mK have been observed in many previous studies [80–86, 89, 108] and the magnetic behavior below the freezing transition seems to show slightly different properties from sample to sample, indicating that each has slightly different stoichiometry. Further investigation of the cause of sample dependence is warranted, with the study by Taniguchi et al. offering the first road map [100].

One reason for the apparent sensitivity of $Tb_2Ti_2O_7$ to small structural details may be attributable to the strong magnetoelastic coupling that has been clearly observed in this material. This has been demonstrated directly from x-ray diffraction in a magnetic field (Fig. 12.7b) [96], low-temperature x-ray diffraction [95], pressure-induced LRO (Fig. 12.7c) [107], as well as from the striking observation of a sharp magnetoelastic mode [98] which couples the lattice vibrations to the low lying crystal field level [105] (Fig. 12.7a). Thus, the eventually successful microscopic description of $Tb_2Ti_2O_7$ may require a combination of QSI type interactions [91, 106], and a dynamic JT distortion that couples to them via the magnetoelastic modes [87]. Recently, effective magnetoelastic parameters in $Tb_2Ti_2O_7$ were proposed which may be used to predict the interplay of magnetic and lattice degrees of freedom [111, 112]. The dynamic nature of the magnetic ground state, made even richer by coupling to the lattice, is unprecedented and promises a new direction in the search for exotic phases.

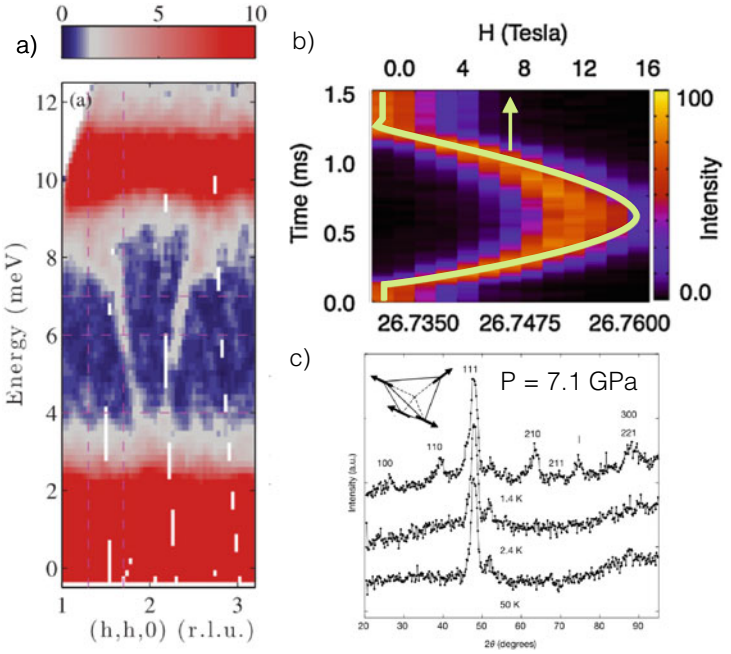

Fig. 12.7 Evidence for magnetoelastic coupling in $Tb_2Ti_2O_7$. **a** A sharp magneto-elastic mode was observed by inelastic neutron scattering; the phonon-like mode hybridizes with the magnetic CEF level at 10 meV, and its partial magnetic character has been confirmed by polarized neutron scattering. Reprinted figure from [98] with permission from the American Physical Society. **b** The time vs. θ (Bragg angle) dependence of a structural peak measured by synchrotron diffraction in a pulsed magnetic field. Adapted figure from [96] with permission from the American Physical Society. The overlaid line shows the time dependence of the magnetic field strength. The lattice contracts upon application of magnetic fields and a strong field of ~ 30 T can lower the symmetry of the crystal structure. **c** Pressure-induced long range order in polycrystalline $Tb_2Ti_2O_7$. Inset shows the proposed ordered structure, which consists of a partially collinear structure in which only two spins point parallel to their local $< 111 >$ axes. Reprinted figure from [107] with permission from Nature

$Tb_2Sn_2O_7$

Replacing Ti on the non-magnetic B-site with Sn in $Tb_2B_2O_7$ has the seemingly innocuous effect of increasing the lattice constant (10.426 Å [113] compared to 10.1694 Å in $Tb_2Ti_2O_7$ [114]) as well as modifying the shape of the oxygen environment around Tb^{3+}, making it slightly more of an isotropic cube with $x = 0.336$ [113] vs. $x = 0.329$ in $Tb_2Ti_2O_7$ [114] (see Chap. 1 for the definition of x). These slight changes in lattice structure appear to bring about a rather dramatic change in the magnetic properties at low temperatures.

In contrast to $Tb_2Ti_2O_7$, all samples of $Tb_2Sn_2O_7$ have been reported to undergo a transition below $T_c = 0.87$ K, where a large anomaly in the specific heat is observed [113, 115]. Above this temperature, there is a broad peak in specific heat around 1.3 K

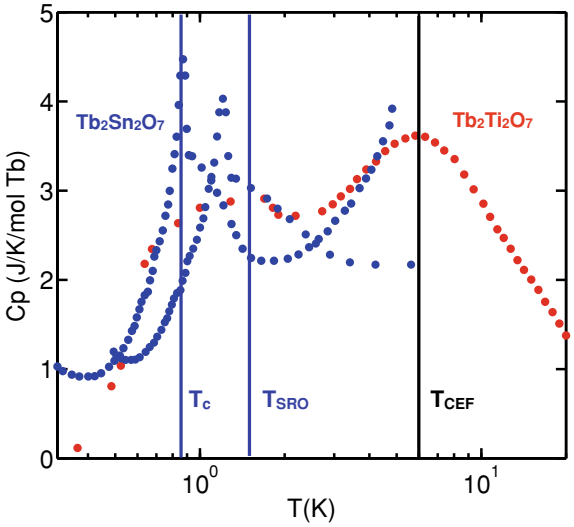

Fig. 12.8 Specific heat of $Tb_2Sn_2O_7$ (blue points) [113] and $Tb_2Ti_2O_7$ (red points) [77]. Both compounds show a broad peak around $T_{CEF} \sim 6$ K that can be attributed to thermally populating a low-lying excited CEF doublet. The features at lower temperatures in $Tb_2Ti_2O_7$ are relatively featureless, depending on the sample [100]. In $Tb_2Sn_2O_7$ there are two low temperature features, a broad feature starting at $T_{SRO} = 1.3$ K, and a sharp anomaly at $T_c = 0.87$ K. Data digitized from [113] and [77] with permission from the American Physical Society

[113], and yet another broad feature at ~6 K which can be ascribed to thermal population of a low-lying CEF level (Fig. 12.8). It is noteworthy that sample-to-sample variation of the specific heat of $Tb_2Sn_2O_7$ does not appear to be an issue. Elastic neutron scattering has revealed broad magnetic diffuse scattering below 10 K, indicative of AFM correlations with a similar form to that in $Tb_2Ti_2O_7$ [78] (Fig. 12.9). Below 1.3 K, FM correlations begin to form, as indicated by the development of scattering near $|Q| = 0$. The widths of the peaks increase sharply below T_c, but do not become resolution limited, maintaining a correlation length of $\xi \sim 180$ Å at all T<600 mK [113]. The magnetic structure is related to spin ice in the following way: the Ising components of the moments follow a two-in-two-out rule as in spin ice, but each tetrahedron satisfies it in the same way, forming what is known as "ordered spin ice" with a net moment along [001]. Due to the cubic symmetry, six magnetic domains of this structure are expected in a zero field cooled sample. It should be expected that by applying a magnetic field while cooling, a net moment could be induced by aligning domains of this structure, as was observed with dc magnetization and μSR [116]. Note that the "ordered spin ice" structure has an ordering wave vector of $k = (000)$, which differs from the ordered state predicted for *dipolar* spin ice having $k = (001)$ [117]. However, in $Tb_2Sn_2O_7$, the ordered spin ice structure described above is not exact; finite transverse components of the moments exist, and they produce a total canting of 13.3° from the local Ising axis (Fig. 12.9) [113].

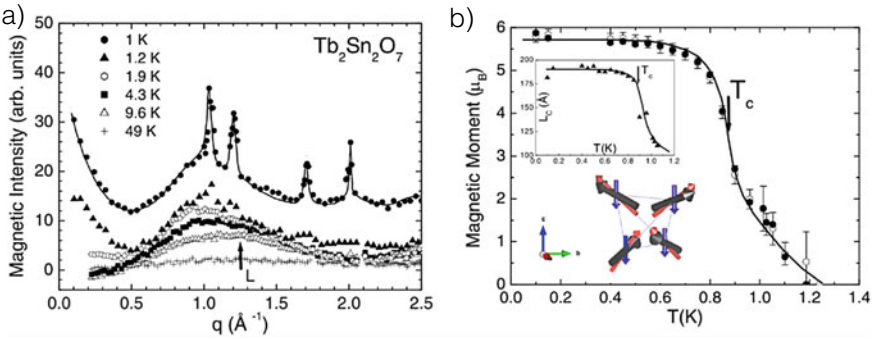

Fig. 12.9 **a** Neutron diffraction from $Tb_2Sn_2O_7$ at different temperatures, showing the development of AFM correlations below about 10 K with a typical length scale of 1 nearest neighbor (the inverse of that length is indicated by L). At 1.3 K there is a shift to FM correlations, indicated by an upturn at low $|Q|$, and below $T_c = 0.87$ K a short range ordered structure appears. **b** The derived magnetic moment as a function of temperature from the data in panel (**a**), based on a $\mathbf{k} = (0,0,0)$ magnetic structure shown in the inset. Top inset: the correlation length of the SRO structure does not exceed 180 Å at the lowest temperatures [113]. Bottom inset: The magnetic structure of $Tb_2Sn_2O_7$ below $T_c = 0.87$ K, shown for a single tetrahedron. Red components represent the ordered spin ice configuration, and blue components are the deviation from an ordered spin ice. The actual direction of the short range ordered moments in $Tb_2Sn_2O_7$ are shown as black arrows. Reprinted figures from [113] with permission from the American Physical Society

The presence of an ordered structure based on the two-in-two-out rule indicates that the effective nearest neighbor interaction in $Tb_2Sn_2O_7$ is ferromagnetic, despite an antiferromagnetic Curie-Weiss temperature (~ -12 K [118]). Some of the ferromagnetic coupling comes from a sizable dipolar interaction between the large moments expected in the ground state CEF doublet, $\mu = 5.9\mu_B$ [119], which as in the CSIs, could overwhelm the AFM exchange to produce overall effective FM coupling. Furthermore, an isolated non-Kramers doublet arising from Tb^{3+} would necessarily be Ising-like, just as in $Tb_2Ti_2O_7$, and we therefore have the basic ingredients for spin ice behavior. Given the non-Kramers ground state doublet, it is natural to ask where the *finite* anisotropy comes from that allows transverse moments in the partially ordered structure. One answer is that, just as in $Tb_2Ti_2O_7$, some *exchange field induced* XY spin susceptibility can arise from virtual excitations to a low-lying CEF level, which lies at $\sim$1.2 meV in $Tb_2Sn_2O_7$. These virtual excitations can mix in transverse components to the CEF ground state doublet.

Thus there appears to be a microscopic basis for spin ice physics in $Tb_2Sn_2O_7$. Intriguingly, the moments in the ordered state in $Tb_2Sn_2O_7$ are only *short range* ordered spatially, and it supports spin dynamics that appear to span several *decades* of frequency [113, 115, 120–123]. This has been shown experimentally in several ways. For example, analysis of the nuclear hyperfine splitting in specific heat has shown that the static moment on the timescale of 10^{-5} to 10^{-6} s is only $\sim$50% of the static moment observed by neutron diffraction [119] (the latter was 5.9 μ_B, comparable to the full moment allowed by the CEF ground state). Polarized neutron

diffraction has also shown a static component of only 60 % on the neutron timescale [121]. μSR results initially led to the conclusion that the *whole* spin system retains dynamics [115, 120], but later a study in which muons were implanted outside of the sample found an external magnetic field static on the timescale of 10^{-9} to 1 s, which was correlated with the two transitions and was argued to arise from a net magnetization of the ordered spin ice state.

Results of a neutron spin echo experiment may be able to explain the apparent discrepancy between inferred spin fluctuation timescales. Rule et al. found that the spin dynamics vary as a function of $|Q|$, spanning fluctuation time scales on the order of 10^{-8}s at $|Q| \sim 0.1$ Å^{-1} to 10^{-11} at higher $|Q|$ [123]. This gives a hint as to why such different timescales can be observed in this material; the slowest response is governed by the ferromagnetic correlations at low $|Q|$ (i.e. the ordered spin ice component), which manifest as a static signal in macroscopic probes like dc magnetometry and external muon implantation. The fast response, observed by internally implanted muons and other probes that average over $|Q|$, is then either associated with AFM correlations, or could be totally incoherent. This coexistence of an ordered and disordered component calls to mind the exotic CFM phase proposed for the nearest neighbor quantum spin ice. Perhaps in support of such a scenario, a T^3 dependence of specific heat below T_c [113], normally observed for *antiferromagnetic* spin waves, shows that the low energy spin excitations (E <0.1 meV) may be of an unusual character in this material and calls to mind the photon modes predicted for the theoretically proposed CFM state.

In comparison to the AFM correlations observed in $Tb_2Ti_2O_7$, the ferromagnetic nature of the spin correlations in $Tb_2Sn_2O_7$ may be understood based on the larger moment afforded by the CEF ground state (~6.0 μ_B in the stannate [119, 124], versus 4 μ_B [124] or 5 μ_B [77, 119, 125] in the titanate), which increases the importance of the ferromagnetic near neighbor dipolar coupling. Yet despite the obvious differences between $Tb_2Ti_2O_7$ and $Tb_2Sn_2O_7$, i.e. the partially ordered spin ice state in the latter in contrast to the liquid-like or partially frozen state in the former, there are many similarities between the two compounds. The spin excitations for E >0.1 meV in the partially ordered state in $Tb_2Sn_2O_7$ have been measured using time-of-flight inelastic neutron scattering [123] and show a remarkable similarity to the excitations in the *magnetic field induced* state of $Tb_2Ti_2O_7$ [92]. Furthermore, the short range spin structure inferred in some samples of $Tb_2Ti_2O_7$ based on (1/2,1/2,1/2) peaks shows the same "ordered spin ice" character for a single unit cell (although in $Tb_2Ti_2O_7$, the sign of this ordered spin ice structure changes every other unit cell along < 111 >, indicating the increased importance of AFM interactions). The presence and persistence of spin dynamics spanning a large range of timescales is intriguing in both materials. The CEF eigenstates of both compounds have received renewed attention recently, and have been suggested [124] to be even more similar than previously thought [119], though the details of the $Tb_2Ti_2O_7$ CEF levels are still not completely agreed upon [125]. It is clear that both compounds have a low lying CEF level around 1.2 to 1.5 meV. The origin of the spin dynamics in both compounds may therefore be the same, whether it be related to virtual crystal field excitations, a dynamic JT distortion, or both. The magnetoelastic properties of $Tb_2Sn_2O_7$ are also likely to

be of importance in its microscopic description. The coupling of the magnetism to the lattice is already hinted at by the long range AFM ordered state induced by hydrostatic pressure [126], which also occurs in $Tb_2Ti_2O_7$ [107].

In $Tb_2Sn_2O_7$ there is clear evidence for a spin ice type correlations ("ordered spin ice") that supports unusual spin dynamics at the lowest measurable temperatures. Thus the stannate is in some ways more likely to be directly related to exotic phases predicted for QSI than the titanate. This, combined with less variation from sample to sample of its low temperature magnetic properties means that, despite the lack of single crystal samples, $Tb_2Sn_2O_7$ should be a fruitful source of interesting comparisons to QSI models.

12.2.3 Pr^{3+}-Based Pyrochlores

Pyrochlores with the non-Kramers Pr^{3+} ion ($Pr_2B_2O_7$, B = Hf, Zr, Ir, Sn, and the metastable pyrochlore $Pr_2Pb_2O_7$ [127]) have attracted attention as candidates for QSI behavior for the following reasons; (1) they have Ising-like dipole moments, (2) the well-isolated non-Kramers CEF doublets allow for fewer exchange interactions in (12.1), and (3) strong quadrupolar interactions were predicted to "melt" the spin ice state by introducing quantum fluctuations in the pseudo-spin 1/2 model [39, 40]. Analysis of possible ground states of the model described by (12.1) for non-Kramers pyrochlores with well-isolated ground state doublets was carried out, and the QSL phase was found to have increased stability compared to the Kramers case due to the requirement that $J_{z\pm} = 0$ [24]. Mean field theory can capture the classical ordered phases of the model, some of which are quadrupolar-ordered phases involving the XY part of the non Kramers pseudo-spin [24, 40, 128].

$Pr_2Zr_2O_7$

$Pr_2Zr_2O_7$ can be grown as large single crystals by the floating zone method [129–131]. This has enabled many detailed measurements, and there is ample evidence for some version of dynamic spin ice. Crystal field analyses based on an inelastic neutron scattering measurement confirm a well-isolated (by 9.5 meV ∼110 K) non-Kramers doublet, which by symmetry is required to have Ising character [132, 133]. The Ising character is confirmed by magnetization measurements [131, 134]. A Curie-Weiss (CW) analysis of the susceptibility gives an effective moment of 2.5 μ_B and a *negative* CW temperature ranging from -2.4 K [131] to -0.4K [132] depending on the temperature range considered. Despite the negative CW temperature, which indicates overall AFM exchange, there is no sign of an AIAO long range dipole ordered state down to 20 mK [129, 132]; instead there are signs for *partial* freezing of the moments near 300 mK [128, 129, 132]. The freezing may be expected to lead to some residual entropy, and indeed the change in magnetic entropy, estimated by subtracting lattice and nuclear contributions of the specific heat, shows good

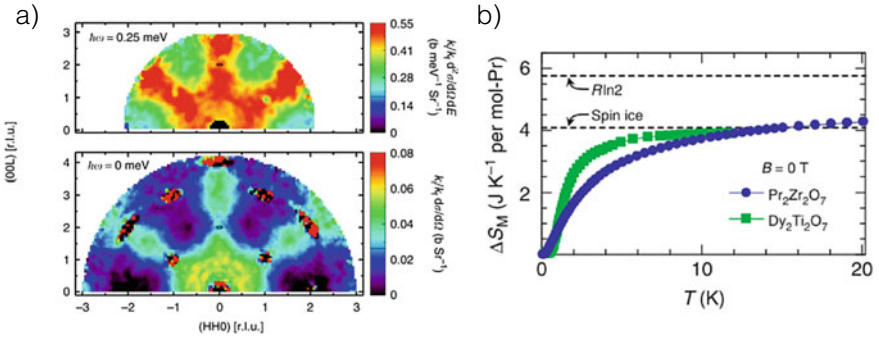

Fig. 12.10 **a** Elastic (bottom) and inelastic (top) neutron scattering from single crystal $Pr_2Zr_2O_7$ at $T = 0.1$ K. The elastic scattering, which due to the energy resolution of the measurement probes spins with fluctuation timescales longer than 2 ps, accounts for only 10% of the moment in $Pr_2Zr_2O_7$. Pinch point scattering is observed near zone centers, which is strongly reminiscent of the nearest neighbor CSI. The inelastic scattering, however, is very strong even at the lowest temperatures, and the absence of pinch points at finite energy transfer indicates a monopole-rich spin ice correlation for the spin fluctuations. **b** Magnetic entropy of $Pr_2Zr_2O_7$ estimated based on lattice and nuclear subtractions of the specific heat. The entropy released from 0.1 K to 10 K is approximately the Pauling value, similar to the CSI $Dy_2Ti_2O_7$. Reprinted figures from [132] with permission from Nature Communications

agreement with a Pauling residual entropy over the range of 0.1 to 10 K (Fig. 12.10b)) [132]. However, ac susceptibility measurements of $Pr_2Zr_2O_7$ show that the "spin flip attempt frequency" is orders of magnitude faster than in $Dy_2Ti_2O_7$ and $Ho_2Ti_2O_7$, suggesting that monopole dynamics are faster in this spin ice-like system [132].

Single crystal neutron scattering provides the best indication of a connection to spin ice, but also an interesting departure from it. Using unpolarized neutrons, Kimura et al. showed that $Pr_2Zr_2O_7$ has *weak* diffuse elastic scattering taking the same form as predicted for the nearest neighbor spin ice model (Fig. 12.10) [132]. The presence of pinch points in the elastic scattering pattern identifies dipolar correlations arising from a spin ice ground state. However, the pinch points are not resolution limited, indicating that the dipolar correlations are cut off at some length scale. The effective length scale for the correlations seems to be limited by the density of defects ($\sim$1% Pr vacancies) in the single crystal used in [132]. Intriguingly, most of the scattering ($> 90\%$) is *inelastic*. Gapless excitations (to within the energy resolution of 0.2 meV) forming a continuum were observed to extend up to at least 1.5 meV. These excitations are strongly Q-dependent; the pattern of inelastic scattering resembles the nearest neighbor spin ice model, but with a high density of magnetic monopoles. The monopole defects destroy the algebraic correlations and remove the pinch points.

In an Ising system, including spin ice, spin flips are expected to be gapped due to the absence of a continuous degree of freedom. An estimate of the size of the energy gap to monopole excitations can be made based on the thermal activation barrier for spin flips determined by ac susceptibility, 1.6 K $\sim$ 0.1 meV. Thus the energy resolution of the measurement in [132] ($\delta E = 0.2$ meV) may not be fine

enough to resolve the expected gap to the monopole-dense excitations. Although gapless photon excitations are predicted for the QSL phase of QSI, these transverse fluctuations would primarily correspond to fluctuations in the *quadrupolar* part of the pseudo-spin in a non-Kramers spin ice, and therefore may not be observable with neutron scattering. Instead they may be observable by thermodynamic probes.

Recently, a similar inelastic neutron scattering signature from $Pr_2Zr_2O_7$ was interpreted in a different manner [128]. In one single crystal sample, the inelastic spectrum a $T = 60$ mK was found to be well-described by an overdamped mode at 0.4 meV. The Q-dependence of this mode is similar to that in [132], including the pinch point structure and ice-like pattern (Fig. 12.10a). This was explained in terms of a liquid-like antiferro-quadrupolar correlated ground state [128]. Within this scenario, *inelastic* spin ice scattering is explained by spin ice correlations between the precessing part of the pseudo-spin around locally ordered quadrupole moments. This brings to mind another possible meaning of the term "dynamic spin ice"; that is, literally, the dynamics themselves have spin ice correlations. This is not quite the same as the QSI picture presented earlier in this chapter. For the quadrupolar ordered state that is proposed in [128] to be relevant to $Pr_2Zr_2O_7$, the important term in Eqn. (12.1) is not J_{zz} but rather $J_{\pm}$. In fact J_{zz} could even be zero or negative, and the same spin ice-like excitations would be present. This may explain the apparent discrepancy between negative CW temperature in $Pr_2Zr_2O_7$ and the spin ice-like dynamics.

The Role of Disorder in Non-Kramers Pyrochlores: Relevance to $Pr_2Zr_2O_7$

Recently, a new route to QSI in non-Kramers pyrochlores was proposed based on the presence of *local* structural disorder [135]. Since the ground CEF doublets are not protected by time reversal symmetry, they can be split by random crystal strains. Savary and Balents showed that small enough distortions could induce quantum entanglement and lead to the U(1) QSL phase in these non-Kramers pyrochlores, in an analogy to the random transverse field Ising model [135]. This picture is of great interest in the context of $Pr_2Zr_2O_7$, as there is evidence for local structural disorder that depends on crystal growth parameters [130], and evidence for random splittings of the non-Kramers doublet has recently emerged [136]. This type of random splitting of the non-Kramers doublet is similar to that observed in $Pr_2Ru_2O_7$ [137] and postulated for the Tb-based pyrochlores [99]. This seems to be an unavoidable question for all QSI candidates based on non-Kramers ions, and therefore studying the effects of dynamic and static lattice distortions will be an important route to pursue in Tb^{3+}, Pr^{3+}, and even Ho^{3+} pyrochlores.

$Pr_2Hf_2O_7$

The non-magnetic cation Hf^{4+} is chemically very similar to Zr^{4+}, making $Pr_2Hf_2O_7$ a natural system to explore in light of the dynamic spin ice behavior observed in

$Pr_2Zr_2O_7$. Large single crystals can be produced [138]. Two recent reports on the magnetic properties single crystals and powders of $Pr_2Hf_2O_7$ have indicated many similarities to $Pr_2Zr_2O_7$, including a well isolated Ising CEF ground doublet [139, 140], a crossover to a correlated state for $T < 0.5$ K with a broad inelastic neutron scattering spectrum peaked at ∼0.4 meV [139], and partial spin freezing near 0.2 K [139, 140]. Magnetization measurements of one crystal [139] reveal a smoothed plateau-like feature for fields oriented along $< 111 >$, consistent with QSI phenomenology. Such a metamagnetic feature has not been clearly observed in $Pr_2Zr_2O_7$, and is not reported in another crystal of $Pr_2Hf_2O_7$ [140]. These differences might be due to different levels of structural disorder in the samples; $Pr_2Hf_2O_7$ generally appears to be more structurally pristine than $Pr_2Zr_2O_7$ [138, 140]. Inelastic neutron scattering from single crystals is not yet reported, but should be expected to appear soon after the time of writing, given the availability of large crystals.

$Pr_2Sn_2O_7$

The Pr^{3+} based stannate pyrochlore, so far only available as powder samples, is known to form spin ice correlations with some spin freezing in addition to persistent fluctuations. Like $Pr_2Zr_2O_7$ and $Pr_2Hf_2O_7$, the CEF ground state of Pr^{3+} is a non-Kramers doublet with a significant quadrupole moment [141], which may provide a mechanism for quantum fluctuations in a spin ice ground state. Although there is no evidence for magnetic order down to 90 mK (from specific heat [19], ac susceptibility [142], or neutron scattering [19]) there is a frequency-dependent peak near 0.3 K in the ac susceptibility which is consistent with spin freezing [142]. Unlike $Pr_2Zr_2O_7$, however, the ac susceptibility *does* seem to vanish as $T \to 0$ [142], consistent with a static frozen state like CSI, and the relaxation time is expected to diverge. The magnetic specific heat shows a broad Schottky-like peak around 1 K, but the integrated entropy only approaches 25% of the Pauling entropy. This has been used as an argument for a *dynamic* spin ice state in $Pr_2Sn_2O_7$ [19]. In support of this claim, inelastic neutron scattering reveals a quasi-elastic signal that persists down to at least 200 mK, with a spin relaxation rate that is much faster than observed in the frozen spin ice state of $Dy_2Ti_2O_7$ (0.02 ns compared to 1000 ns) [19]. Although only powder samples are available, the $|Q|$ dependence of this quasi-elastic neutron scattering resembles that of dipolar spin ice, but with small differences. The pattern is better described by the anisotropic exchange model proposed by Onoda et al. [39], in which quadrupolar interactions are argued to create quantum fluctuations in the spin ice ground state, and a different weighting of ice rules states compared to the dipolar spin ice model is expected (Fig. 12.11a). Furthermore, the observed linear decrease of $S(|Q|)$ as $|Q|$ goes to zero has been shown to be consistent with quantum spin ice [143].

The similarities between the reported properties of $Pr_2Sn_2O_7$ and $Pr_2Zr_2O_7$ are striking. However, there are some differences: the ac susceptibility does not vanish in $Pr_2Zr_2O_7$, and by best estimates of nuclear Schottky contributions, the magnetic entropy in $Pr_2Zr_2O_7$ reaches approximately the *full* Pauling value [132]. Some questions remain, namely, what fraction of the spins are static in the low temperature

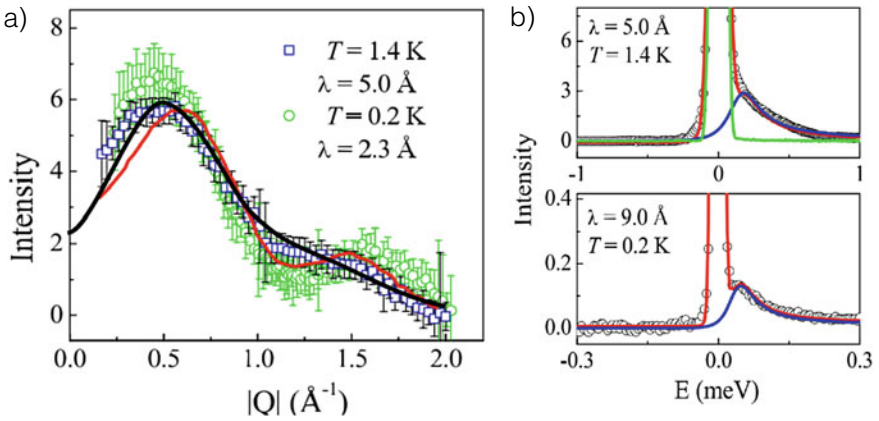

Fig. 12.11 **a** Elastic magnetic diffuse scattering in $Pr_2Sn_2O_7$ at 1.4 K (blue) and 0.2 K (green) (50 K data subtracted). The red line is the form of the diffuse scattering predicted for dipolar CSI [18], and the black line results from a model based on a pseudo-spin 1/2 Hamiltonian for Pr-based pyrochlores that predicts QSI behavior [39]. **b** Energy dependence of the dynamic structure factor in $Pr_2Sn_2O_7$. At 1.4 K the dynamic spin response can be fit to a Lorentzian (blue solid line) and a timescale of 4×10^{-4} ns for the spin fluctuations can be extracted. At 200 mK (bottom panel) the spin fluctuations persist, and a timescale of 0.02 ns can be extracted. These spin relaxation times are much shorter than those found in the dipolar spin ice materials, which are on the order of 10 to 1000 ms in the spin ice regime. Reprinted figure from [19] with permission from the American Physical Society

phase of $Pr_2Sn_2O_7$ (this was found to be less than 10 % in $Pr_2Zr_2O_7$)? How does the magnetic entropy compare to CSI if it is measured to lower temperatures and the nuclear contributions are removed? Such questions can be investigated even in powder samples and therefore we should expect to see more progress on $Pr_2Sn_2O_7$ in the near future.

Metallic Spin Ice, $Pr_2Ir_2O_7$

The concept of QSI requires localized magnetic moments on the pyrochlore lattice. The metallic pyrochlore $Pr_2Ir_2O_7$ is a fascinating example of QSI in which the localized moments forming the dynamic spin ice *coexist* with conduction electrons. The Ir^{4+} cation on the pyrochlore B-site forms mobile electron bands while Pr^{3+} gives a localized Ising moment as in the other Pr-based pyrochlores described above, and these seem to form spin ice configurations.

In $Pr_2Ir_2O_7$, the Ir conduction electrons experience the strongly correlated yet disordered local fields generated by the spin ice. The interplay between the conduction electrons and the spin ice state gives rise to novel properties, namely an anomalous hall effect (AHE) below $T = 1.5$ K even in the absence of time-reversal symmetry breaking from magnetic dipole ordering or freezing [144, 145]. The AHE

and other aspects of the conduction electron behavior in $Pr_2Ir_2O_7$ are discussed in another chapter in this book, Chaps. 13 and 14, so here attention is limited to the local moments.

The local moments in $Pr_2Ir_2O_7$ are formed by a well-isolated non-Kramers doublet ground state of the CEF split Pr^{3+} levels [146]. Despite an AFM low-temperature Curie-Weiss temperature ($\theta_{CW} = -1.8$ K), evidence for ferromagnetic coupling in $Pr_2Ir_2O_7$ is inferred from the presence of a magnetization plateau when the field is applied along the $< 111 >$ direction in the partially frozen state of single crystal samples. As in other Pr-based pyrochlores, the non-Kramers doublet gives strict Ising anisotropy to the dipole moments, meanwhile the planar components transform as quadrupoles. And, as in the other Pr based systems, the "quantum melting of spin ice" might be expected based on interactions between these quadrupole parts of the pseudo-spin [39].

The spin ice state that is formed by the Pr moments remains dynamic, at least down to ~400 mK. This conclusion may be drawn from dc susceptibility, which does not show any field cooled vs. zero field cooled splitting until ~ 0.3 K, and which maintains a constant value of the susceptibility below this freezing transition indicating remaining unfrozen moments [146]. The dynamic nature of the spin ice is also inferred based on the temperature independent dynamic relaxation rate observed down to 20 mK in μSR [147] (note, however, that both [147, 148] have inferred the presence of a local distortion caused by the muons which influences μSR results on Pr-based materials). Finally, quantum critical behavior was observed down to 400 mK, implying that quantum fluctuations are strong in this system [30]. This may be due to the conduction electrons, as postulated in a quantum critical theory describing the pyrochlore iridate family [149, 150], or from the local Pr moments forming a QSI state near a quantum critical point, or most likely the unique physics arising from their interplay.

12.2.4 Summary and Outlook

This chapter has been primarily devoted to a review of the known QSI candidate materials. In each material, the dominant interactions have been proposed to be ferromagnetic and locally Ising, just as in CSI. The major difference between CSI and these materials, however, is the introduction of additional interactions which promote quantum fluctuations within the spin ice manifold. As a result, the systems discussed here do not freeze and fall out of equilibrium at temperatures set by the spin ice interaction energy, J_{zz}, as the classical dipolar spin ice materials do. Instead, these materials remain in equilibrium and support persistent spin fluctuations down to very low temperatures relative to the dominant interaction strength. Their magnetic entropy sometimes makes a brief visit at the Pauling entropy, in a temperature regime called "dynamic spin ice" in this chapter, before carrying on further towards $S = 0$ in their ground states. In some cases, whether the ground states of these materials are conventionally long range ordered or are more exotic, such as a U(1) QSL or CFM

phases with emergent electrodynamics, is presently debated. The future observation of such emergent excitations in the QSI materials discussed here is a tantalizing possibility.

Experimentally, a key step towards understanding the ground states of these materials will be to gain a better understanding of the presence and effects of structural imperfections. For example, lattice defects on the order of 0.25% have been shown to generate grossly varying low temperature behavior in $Tb_2Ti_2O_7$ [100]. Although phase competition likely plays a role, particularly in the $Yb_2B_2O_7$ materials, another reason for the sensitivity of the QSI materials to such low levels of disorder is the overall low energy scales associated with their interactions. This is due to the magnetism being generated by rare earth ions, which have very well localized $4f$ orbitals, and thus weak exchange. This sensitivity to disorder could perhaps be thought of as a "feature" rather than a "bug" in non-Kramers systems, where it could actually promote entanglement [135]. This idea may be applicable to $Pr_2Zr_2O_7$ [136], as briefly discussed in this chapter, and perhaps also the recently reported anion-defective pyrochlore $Tb_2Hf_2O_7$ [151].

Given the extreme sensitivity to disorder in several of the QSI candidates, one hope for the future is the discovery of a high temperature version of spin ice, perhaps incorporating magnetic $3d$ transition metal ions as in the recently synthesized series of fluoride-pyrochlores $NaA'M_2F_7$ (A' = Ca, Sr; M = Co, Mn, Fe, Ni) [152–155]. However, this path is not without its challenges, since spatial anisotropy generated by spin-orbit coupling is a key to the spin ice story. In this regard, pyrochlores or spinels based on Co^{2+} in a distorted octahedral environment could provide the required anisotropy, similar in spirit (but opposite in anisotropy) to the XY fluoride pyrochlores $NaCaCo_2F_7$ and $NaSrCo_2F_7$ [156, 157].

Another consequence of their relatively weak interactions is that rare earth based QSI materials can display rather different behavior depending on the details of the *non-magnetic* ions in the lattice. For example, $Tb_2Sn_2O_7$ forms a quasi-long range ordered ground state, while $Tb_2Ti_2O_7$ remains liquid-like, but can be easily driven to long range order by applied pressure, as discussed earlier in this chapter. The effect of such modifications of the lattice is a very informative route to pursue in understanding the QSI materials; this is already beginning to be explored in solid solutions of $Tb_2Sn_{2-x}Ti_xO_7$ [158], and in the recent comparative study of $Yb_2B_2O_7$ (B = Sn, Ti, Ge) [42, 48]. These types of studies may guide the field towards an understanding of the structure–property relationships in QSI. Simply put, the relevant question is: how can we tune the interactions in Eqn. (12.1) by tuning the non-magnetic sublattices?

Much of the promise of QSI materials lies in the possibility of producing a U(1) QSL phase. In this regard it is interesting that a distinct version of this U(1) QSL exists, which is not based on spin ice-like dipole correlations, but rather octupole correlations [41, 159]. This could occur in materials with so-called "dipolar-octupolar" CEF ground state doublets, such as $Ce_2Sn_2O_7$ and $Nd_2Zr_2O_7$. Experimentally, the former has been shown to be a QSL candidate [160], and the latter was proposed as an example of moment fragmentation in spin ice [161]. In this regard, the experimental QSI signatures discussed in this chapter, which are often based on ice-correlations

forming amongst *dipole* moments, should not be taken too strictly, and the transformation properties of CEF doublets in each rare earth pyrochlore should be considered.

Although this chapter has discussed only pyrochlore materials $R_2B_2O_7$, the spinel structure with general chemical formula AB_2X_4 also hosts a pyrochlore sublattice on the B site. Although there are many examples of magnetic spinels, only a few reported compounds have magnetic rare-earth B-sublattices and non-magnetic A-sites [162–164]. In principle, these could lead to the required Ising anisotropy and a similar anisotropic exchange Hamiltonian to Eqn. (12.1). Towards this end, it is promising that the compounds $CdEr_2Se_4$ and $CdEr_2S_4$ are reported to display signatures for *classical* spin ice [165, 166], yet the Yb^{3+}-based spinels MYb_2X_4 (M =Mg, Cd, X =Se, S) appear to be more Heisenberg-like [164]. This variation in anisotropy suggests that it might be possible to extend the materials space of rare earth B-site spinels to find new QSI candidates.

In the search for new QSI materials, some guiding principles may be useful. First, the materials must be able to support anisotropic exchange interactions, which are generated by spin-orbit coupling—heavier magnetic ions are therefore generally more desirable (although Co^{2+} should not be ignored, as mentioned above). Second, a source for quantum fluctuations is required. In Kramers ion systems, such as $Yb_2B_2O_7$, the fluctuation-generating XY exchange terms in the effective Hamiltonian can come from the planar nature of the g-tensor. In non-Kramers systems, such as $Tb_2B_2O_7$ and $Pr_2B_2O_7$, the spin dynamics must come from another route; coupling to low lying CEF levels, quadrupolar interactions, and coupling to the lattice degrees of freedom or structural defects have all been proposed as mechanisms to generate these quantum fluctuations.

With these principles in mind, it may be possible to design new QSI materials. Such an effort combined with the continued intense experimental effort on the current QSI materials may bring us to definitive observations of truly novel phases of matter.

Acknowledgements KAR gratefully acknowledges funding from NSERC of Canada during the initial phase of writing of this chapter.

References

1. L. Balents, Nature **464**, 199 (2010). https://doi.org/10.1038/nature08917
2. B. Normand, Contemp. Phys. **50**, 533 (2009). https://doi.org/10.1080/00107510902850361
3. M.J.P. Gingras, P.A. McClarty, Rep. Prog. Phys. **77**, 056501 (2014). https://doi.org/10.1088/0034-4885/77/5/056501
4. B. Malkin, A. Zakirov, M. Popova, S. Klimin, E. Chukalina, E. Antic-Fidancev, P. Goldner, P. Aschehoug, G. Dhalenne, Phys. Rev. B **70**, 075112 (2004). https://doi.org/10.1103/PhysRevB.70.075112
5. B. Malkin, T. Lummen, P. Van Loosdrecht, G. Dhalenne, A. Zakirov, J. Phys.: Condens. Matter **22**, 276003 (2010). https://doi.org/10.1088/0953-8984/22/27/276003
6. J. Hodges, P. Bonville, A. Forget, M. Rams, K. Królas, G. Dhalenne, J. Phys.: Condens. Matter **13**, 9301 (2001). https://doi.org/10.1088/0953-8984/13/41/318
7. A.P. Ramirez, A. Hayashi, R. Cava, R. Siddharthan, B. Shastry, Nature **399**, 333 (1999). https://doi.org/10.1038/20619

8. S.T. Bramwell, M. Harris, B. Den Hertog, M.J.P. Gingras, J. Gardner, D. McMorrow, A. Wildes, A. Cornelius, J. Champion, R. Melko et al., Phys. Rev. Lett. **87**, 047205 (2001). https://doi.org/10.1103/PhysRevLett.87.047205
9. O. Petrenko, M. Lees, G. Balakrishnan, Phys. Rev. B **68**, 012406 (2003). https://doi.org/10.1103/PhysRevB.68.012406
10. H. Fukazawa, R. Melko, R. Higashinaka, Y. Maeno, M.J.P. Gingras, Phys. Rev. B **65**, 054410 (2002). https://doi.org/10.1103/PhysRevB.65.054410
11. J. Snyder, B. Ueland, J. Slusky, H. Karunadasa, R. Cava, P. Schiffer, Phys. Rev. B **69**, 064414 (2004). https://doi.org/10.1103/PhysRevB.69.064414
12. L.D. Jaubert, P.C. Holdsworth, J. Phys.: Condens. Matter **23**, 164222 (2011). https://doi.org/10.1088/0953-8984/23/16/164222
13. B.C. den Hertog, M.J.P. Gingras, Phys. Rev. Lett. **84**, 3430 (2000). https://doi.org/10.1103/PhysRevLett.84.3430
14. R. Moessner, J. Chalker, Phys. Rev. B **58**, 12049 (1998). https://doi.org/10.1103/PhysRevB.58.12049
15. C.L. Henley, Annu. Rev. Condens. Matter Phys. **1**, 179 (2010). https://doi.org/10.1146/annurev-conmatphys-070909-104138
16. T. Fennell, P. Deen, A. Wildes, K. Schmalzl, D. Prabhakaran, A. Boothroyd, R. Aldus, D. McMorrow, S.T. Bramwell, Science **326**, 415 (2009). https://doi.org/10.1126/science.1178868
17. A. Hallas, J. Paddison, H. Silverstein, A. Goodwin, J. Stewart, A. Wildes, J. Cheng, J. Zhou, J. Goodenough, E. Choi et al., Phys. Rev. B **86**, 134431 (2012). https://doi.org/10.1103/PhysRevB.86.134431
18. H. Kadowaki, Y. Ishii, K. Matsuhira, Y. Hinatsu, Phys. Rev. B **65**, 144421 (2002). https://doi.org/10.1103/PhysRevB.65.144421
19. H. Zhou, C. Wiebe, J. Janik, L. Balicas, Y. Yo, Y. Qiu, J. Copley, J. Gardner, Phys. Rev. Lett. **101**, 227204 (2008). https://doi.org/10.1103/PhysRevLett.101.227204
20. Y. Kato, S. Onoda, Phys. Rev. Lett. **115**, 077202 (2015). https://doi.org/10.1103/PhysRevLett.115.077202
21. R. Applegate, N. Hayre, R. Singh, T. Lin, A. Day, M.J.P. Gingras, Phys. Rev. Lett. **109**, 097205 (2012). https://doi.org/10.1103/PhysRevLett.109.097205
22. K. Ross, L. Yaraskavitch, M. Laver, J. Gardner, J. Quilliam, S. Meng, J. Kycia, D. Singh, T. Proffen, H. Dabkowska et al., Phys. Rev. B **84**, 174442 (2011). https://doi.org/10.1103/PhysRevB.84.174442
23. S.H. Curnoe, Phys. Rev. B **75**, 212404 (2007). https://doi.org/10.1103/PhysRevB.75.212404
24. S. Lee, S. Onoda, L. Balents, Phys. Rev. B **86**, 104412 (2012). https://doi.org/10.1103/PhysRevB.86.104412
25. M. Hermele, M.P. Fisher, L. Balents, Phys. Rev. B **69**, 064404 (2004). https://doi.org/10.1103/PhysRevB.69.064404
26. A. Banerjee, S.V. Isakov, K. Damle, Y.B. Kim, Phys. Rev. Lett. **100**, 047208 (2008). https://doi.org/10.1103/PhysRevLett.100.047208
27. K.A. Ross, L. Savary, B.D. Gaulin, L. Balents, Phys. Rev. X **1**, 021002 (2011). https://doi.org/10.1103/PhysRevX.1.021002
28. L. Savary, L. Balents, Phys. Rev. Lett. **108**, 037202 (2012). https://doi.org/10.1103/PhysRevLett.108.037202
29. O. Benton, O. Sikora, N. Shannon, Phys. Rev. B **86**, 075154 (2012). https://doi.org/10.1103/PhysRevB.86.075154
30. Y. Tokiwa, J. Ishikawa, S. Nakatsuji, P. Gegenwart, Nat. Mater. **13**, 356 (2014). https://doi.org/10.1038/nmat3900
31. H. Blöte, R. Wielinga, W. Huiskamp, Physica **43**, 549 (1969). https://doi.org/10.1016/0031-8914(69)90187-6
32. H.R. Molavian, M.J.P. Gingras, J. Phys.: Condens. Matter **21**, 172201 (2009). https://doi.org/10.1088/0953-8984/21/17/172201

33. D. Pomaranski, L. Yaraskavitch, S. Meng, K. Ross, H. Noad, H. Dabkowska, B. Gaulin, J. Kycia, Nat. Phys. **9**, 353 (2013). https://doi.org/10.1038/NPHYS2591
34. Y. Wan, O. Tchernyshyov, Phys. Rev. Lett. **108**, 247210 (2012). https://doi.org/10.1103/PhysRevLett.108.247210
35. L. Pan, S.K. Kim, A. Ghosh, C.M. Morris, K.A. Ross, E. Kermarrec, B.D. Gaulin, S. Koohpayeh, O. Tchernyshyov, N. Armitage, Nat. Commun. **5**, 4970 (2014). https://doi.org/10.1038/ncomms5970
36. L. Savary, L. Balents, Phys. Rev. B **87**, 205130 (2013). https://doi.org/10.1103/PhysRevB.87.205130
37. M. Brooks-Bartlett, S. Banks, L. Jaubert, A. Harman-Clarke, P. Holdsworth, Phys. Rev. X **4**, 011007 (2014). https://doi.org/10.1103/PhysRevX.4.011007
38. Z. Hao, A.G. Day, M.J.P. Gingras, Phys. Rev. B **90**, 214430 (2014). https://doi.org/10.1103/PhysRevB.90.214430
39. S. Onoda, Y. Tanaka, Phys. Rev. Lett. **105**, 047201 (2010). https://doi.org/10.1103/PhysRevLett.105.047201
40. S. Onoda, Y. Tanaka, Phys. Rev. B **83**, 094411 (2011). https://doi.org/10.1103/PhysRevB.83.094411
41. Y.P. Huang, G. Chen, M. Hermele, Phys. Rev. Lett. **112**, 167203 (2014). https://doi.org/10.1103/PhysRevLett.112.167203
42. Z. Dun, M. Lee, E. Choi, A. Hallas, C. Wiebe, J. Gardner, E. Arrighi, R. Freitas, A. Arevalo-Lopez, J. Attfield et al., Phys. Rev. B **89**, 064401 (2014). https://doi.org/10.1103/PhysRevB.89.064401
43. J.S. Gardner, M.J.P. Gingras, J.E. Greedan, Rev. Mod. Phys. **82**, 53 (2010). https://doi.org/10.1103/RevModPhys.82.53
44. J. Gaudet, D. Maharaj, G. Sala, E. Kermarrec, K. Ross, H. Dabkowska, A. Kolesnikov, G. Granroth, B. Gaulin, Phys. Rev. B **92**, 134420 (2015). https://doi.org/10.1103/PhysRevB.92.134420
45. R. Shannon, A. Sleight, Inorg. Chem. **7**, 1649 (1968). https://doi.org/10.1021/ic50066a038
46. Z.L. Dun, X. Li, R.S. Freitas, E. Arrighi, C.R.D. Cruz, M. Lee, E.S. Choi, H.B. Cao, H.J. Silverstein, C.R. Wiebe et al., Phys. Rev. B **92**, 140407 (2015). https://doi.org/10.1103/PhysRevB.92.140407
47. Y. Cai, Q. Cui, X. Li, Z. Dun, J. Ma, C. dela Cruz, Y. Jiao, J. Liao, P. Sun, Y. Li, et al., Phys. Rev. B **93**, 014443 (2016). https://doi.org/10.1103/PhysRevB.93.014443
48. A. Hallas, J. Gaudet, N. Butch, M. Tachibana, R. Freitas, G. Luke, C. Wiebe, B. Gaulin, Phys. Rev. B **93**, 100403 (2016). https://doi.org/10.1103/PhysRevB.93.100403
49. J. Hodges, P. Bonville, A. Forget, A. Yaouanc, P.D. De Réotier, G. André, M. Rams, K. Królas, C. Ritter, P. Gubbens et al., Phys. Rev. Lett. **88**, 077204 (2002). https://doi.org/10.1103/PhysRevLett.88.077204
50. A. Yaouanc, P.D. de Réotier, C. Marin, V. Glazkov, Phys. Rev. B **84**, 172408 (2011). https://doi.org/10.1103/PhysRevB.84.172408
51. K. Ross, T. Proffen, H. Dabkowska, J. Quilliam, L. Yaraskavitch, J. Kycia, B. Gaulin, Phys. Rev. B **86**, 174424 (2012). https://doi.org/10.1103/PhysRevB.86.174424
52. L.J. Chang, M.R. Lees, I. Watanabe, A.D. Hillier, Y. Yasui, S. Onoda, Phys. Rev. B **89**, 184416 (2014). https://doi.org/10.1103/PhysRevB.89.184416
53. A. Yaouanc, A. Maisuradze, P.D. de Réotier, Phys. Rev. B **87**, 134405 (2013). https://doi.org/10.1103/PhysRevB.87.134405
54. R. D'Ortenzio, H. Dabkowska, S. Dunsiger, B. Gaulin, M.J.P. Gingras, T. Goko, J. Kycia, L. Liu, T. Medina, T. Munsie et al., Phys. Rev. B **88**, 134428 (2013). https://doi.org/10.1103/PhysRevB.88.134428
55. K. Ross, J. Ruff, C. Adams, J. Gardner, H. Dabkowska, Y. Qiu, J. Copley, B. Gaulin, Phys. Rev. Lett. **103**, 227202 (2009). https://doi.org/10.1103/PhysRevLett.103.227202
56. J. Robert, E. Lhotel, G. Remenyi, S. Sahling, I. Mirebeau, C. Decorse, B. Canals, S. Petit, Phys. Rev. B **92**, 064425 (2015). https://doi.org/10.1103/PhysRevB.92.064425

57. A. Yaouanc, P.D. de Réotier, P. Bonville, J. Hodges, V. Glazkov, L. Keller, V. Sikolenko, M. Bartkowiak, A. Amato, C. Baines et al., Phys. Rev. Lett. **110**, 127207 (2013). https://doi.org/10.1103/PhysRevLett.110.127207
58. P. Bonville, J. Hodges, E. Bertin, J.P. Bouchaud, P.D. De Réotier, L.P. Regnault, H. Rønnow, J.P. Sanchez, S. Sosin, A. Yaouanc, in *ICAME 2003* (Springer, 2004), pp. 103–111 https://doi.org/10.1007/978-1-4020-2852-6_17
59. L.J. Chang, S. Onoda, Y. Su, Y.J. Kao, K.D. Tsuei, Y. Yasui, K. Kakurai, M.R. Lees, Nat. Commun. **3**, 992 (2012). https://doi.org/10.1038/ncomms1989
60. Y. Yasui, M. Soda, S. Iikubo, M. Ito, M. Sato, N. Hamaguchi, T. Matsushita, N. Wada, T. Takeuchi, N. Aso et al., J. Phys. Soc. Jpn. **72**, 3014 (2003). https://doi.org/10.1143/JPSJ.72.3014
61. E. Lhotel, S. Giblin, M.R. Lees, G. Balakrishnan, L. Chang, Y. Yasui, Phys. Rev. B **89**, 224419 (2014). https://doi.org/10.1103/PhysRevB.89.224419
62. G. Sala, M. Gutmann, D. Prabhakaran, D. Pomaranski, C. Mitchelitis, J. Kycia, D. Porter, C. Castelnovo, J. Goff, Nat. Mater. **13**, 488 (2014). https://doi.org/10.1038/NMAT3924
63. J. Gardner, G. Ehlers, N. Rosov, R. Erwin, C. Petrovic, Phys. Rev. B **70**, 180404 (2004). https://doi.org/10.1103/PhysRevB.70.180404
64. J. Gaudet, K. Ross, E. Kermarrec, N. Butch, G. Ehlers, H. Dabkowska, B. Gaulin, Phys. Rev. B **93**, 064406 (2016). https://doi.org/10.1103/PhysRevB.93.064406
65. J.D. Thompson, P.A. McClarty, H.M. Rønnow, L.P. Regnault, A. Sorge, M.J. Gingras, Phys. Rev. Lett. **106**, 187202 (2011). https://doi.org/10.1103/PhysRevLett.106.187202
66. H. Cao, A. Gukasov, I. Mirebeau, P. Bonville, C. Decorse, G. Dhalenne, Phys. Rev. Lett. **103**, 056402 (2009). https://doi.org/10.1103/PhysRevLett.103.056402
67. N. Hayre, K. Ross, R. Applegate, T. Lin, R. Singh, B. Gaulin, M.J.P. Gingras, Phys. Rev. B **87**, 184423 (2013). https://doi.org/10.1103/PhysRevB.87.184423
68. L. Pan, N. Laurita, K.A. Ross, B.D. Gaulin, N. Armitage, Nat. Phys. **12**, 361 (2016). https://doi.org/10.1038/nphys3608
69. Y. Tokiwa, T. Yamashita, M. Udagawa, S. Kittaka, T. Sakakibara, D. Terazawa, Y. Shimoyama, T. Terashima, Y. Yasui, T. Shibauchi et al., Nat. Commun. **7**, 10807 (2016). https://doi.org/10.1038/ncomms10807
70. S. Bhattacharjee, S. Erfanifam, E. Green, M. Naumann, Z. Wang, S. Granovsky, M. Doerr, J. Wosnitza, A. Zvyagin, R. Moessner et al., Phys. Rev. B **93**, 144412 (2016). https://doi.org/10.1103/PhysRevB.93.144412
71. L.D.C. Jaubert, O. Benton, J.G. Rau, J. Oitmaa, R.R.P. Singh, N. Shannon, M.J.P. Gingras, Phys. Rev. Lett. **115**, 267208 (2015). https://doi.org/10.1103/PhysRevLett.115.267208
72. H. Yan, O. Benton, L. Jaubert, N. Shannon, Phys. Rev. B **95**, 094422 (2017). https://doi.org/10.1103/PhysRevB.95.094422
73. Z. Dun, E. Choi, H. Zhou, A. Hallas, H. Silverstein, Y. Qiu, J. Copley, J. Gardner, C. Wiebe, Phys. Rev. B **87**, 134408 (2013). https://doi.org/10.1103/PhysRevB.87.134408
74. A. Yaouanc, P.D. de Réotier, L. Keller, B. Roessli, A. Forget, J. Phys.: Condens. Matter **28**, 426002 (2016). https://doi.org/10.1088/0953-8984/28/42/426002
75. J. Lago, I. Živković, J. Piatek, P. Álvarez, D. Hüvonen, F. Pratt, M. Díaz, T. Rojo, Phys. Rev. B **89**, 024421 (2014). https://doi.org/10.1103/PhysRevB.89.024421
76. A. Hallas, J. Gaudet, M. Wilson, T. Munsie, A. Aczel, M. Stone, R. Freitas, A. Arevalo-Lopez, J. Attfield, M. Tachibana et al., Phys. Rev. B **93**, 104405 (2016). https://doi.org/10.1103/PhysRevB.93.104405
77. M.J.P. Gingras, B. Den Hertog, M. Faucher, J. Gardner, S. Dunsiger, L. Chang, B. Gaulin, N. Raju, J. Greedan, Phys. Rev. B **62**, 6496 (2000). https://doi.org/10.1103/PhysRevB.62.6496
78. J.S. Gardner, S.R. Dunsiger, B.D. Gaulin, M.J.P. Gingras, J. Greedan, R. Kiefl, M.D. Lumsden, W.A. MacFarlane, N.P. Raju, J.E. Sonier et al., Phys. Rev. Lett. **82**, 1012 (1999). https://doi.org/10.1103/PhysRevLett.82.1012
79. J. Gardner, B. Gaulin, A. Berlinsky, P. Waldron, S. Dunsiger, N. Raju, J. Greedan, Phys. Rev. B **64**, 224416 (2001). https://doi.org/10.1103/PhysRevB.64.224416

80. J. Gardner, A. Keren, G. Ehlers, C. Stock, E. Segal, J. Roper, B. Fåk, M. Stone, P. Hammar, D. Reich et al., Phys. Rev. B **68**, 180401 (2003). https://doi.org/10.1103/PhysRevB.68.180401
81. H. Takatsu, H. Kadowaki, T.J. Sato, J.W. Lynn, Y. Tabata, T. Yamazaki, K. Matsuhira, J. Phys.: Condens. Matter **24**, 052201 (2012). https://doi.org/10.1088/0953-8984/24/5/052201
82. A. Yaouanc, P.D. de Réotier, Y. Chapuis, C. Marin, S. Vanishri, D. Aoki, B. Fåk, L.P. Regnault, C. Buisson, A. Amato et al., Phys. Rev. B **84**, 184403 (2011). https://doi.org/10.1103/PhysRevB.84.184403
83. P. Baker, M. Matthews, S. Giblin, P. Schiffer, C. Baines, D. Prabhakaran, Phys. Rev. B **86**, 094424 (2012). https://doi.org/10.1103/PhysRevB.86.094424
84. E. Lhotel, C. Paulsen, P.D. De Réotier, A. Yaouanc, C. Marin, S. Vanishri, Phys. Rev. B **86**, 020410 (2012). https://doi.org/10.1103/PhysRevB.86.020410
85. L. Yin, J.S. Xia, Y. Takano, N. Sullivan, Q.J. Li, X.F. Sun, Phys. Rev. Lett. **110**, 137201 (2013). https://doi.org/10.1103/PhysRevLett.110.137201
86. N. Hamaguchi, T. Matsushita, N. Wada, Y. Yasui, M. Sato, Phys. Rev. B **69**, 132413 (2004). https://doi.org/10.1103/PhysRevB.69.132413
87. P. Bonville, A. Gukasov, I. Mirebeau, S. Petit, Phys. Rev. B **89**, 085115 (2014). https://doi.org/10.1103/PhysRevB.89.085115
88. Y.J. Kao, M. Enjalran, A. Del Maestro, H.R. Molavian, M.J.P. Gingras, Phys. Rev. B **68**, 172407 (2003). https://doi.org/10.1103/PhysRevB.68.172407
89. K. Fritsch, K. Ross, Y. Qiu, J. Copley, T. Guidi, R. Bewley, H. Dabkowska, B. Gaulin, Phys. Rev. B **87**, 094410 (2013). https://doi.org/10.1103/PhysRevB.87.094410
90. T. Fennell, M. Kenzelmann, B. Roessli, M.K. Haas, R.J. Cava, Phys. Rev. Lett. **109**, 017201 (2012). https://doi.org/10.1103/PhysRevLett.109.017201
91. S.H. Curnoe, Phys. Rev. B **88**, 014429 (2013). https://doi.org/10.1103/PhysRevB.88.014429
92. K. Rule, J. Ruff, B. Gaulin, S. Dunsiger, J. Gardner, J. Clancy, M. Lewis, H. Dabkowska, I. Mirebeau, P. Manuel et al., Phys. Rev. Lett. **96**, 177201 (2006). https://doi.org/10.1103/PhysRevLett.96.177201
93. I. Aleksandrov, B. Lidskii, L. Mamsurova, M. Neigauz, K. Pigal'skii, K. Pukhov, N. Trusevich, L. Shcherbakova, J. Exp. Theor. Phys. **62**, 1287 (1985). https://www.jetp.ac.ru/cgi-bin/e/index/e/62/6/p1287?a=list
94. L. Mamsurova, K. Pigal'Skii, K. Pukhov, J. Exp. Theor. Phys. Lett. **43**, 755 (1986). http://www.jetpletters.ru/ps/1413/article_21511.shtml
95. J. Ruff, B. Gaulin, J. Castellan, K. Rule, J. Clancy, J. Rodriguez, H. Dabkowska, Phys. Rev. Lett. **99**, 237202 (2007). https://doi.org/10.1103/PhysRevLett.99.237202
96. J. Ruff, Z. Islam, J. Clancy, K. Ross, H. Nojiri, Y. Matsuda, H. Dabkowska, A. Dabkowski, B. Gaulin, Phys. Rev. Lett. **105**, 077203 (2010). https://doi.org/10.1103/PhysRevLett.105.077203
97. Y. Nakanishi, T. Kumagai, M. Yoshizawa, K. Matsuhira, S. Takagi, Z. Hiroi, Phys. Rev. B **83**, 184434 (2011). https://doi.org/10.1103/PhysRevB.83.184434
98. T. Fennell, M. Kenzelmann, B. Roessli, H. Mutka, J. Ollivier, M. Ruminy, U. Stuhr, O. Zaharko, L. Bovo, A. Cervellino et al., Phys. Rev. Lett. **112**, 017203 (2014). https://doi.org/10.1103/PhysRevLett.112.017203
99. Y. Chapuis, A. Yaouanc, P.D. de Réotier, C. Marin, S. Vanishri, S. Curnoe, C. Vâju, A. Forget, Phys. Rev. B **82**, 100402 (2010). https://doi.org/10.1103/PhysRevB.82.100402
100. T. Taniguchi, H. Kadowaki, H. Takatsu, B. Fåk, J. Ollivier, T. Yamazaki, T. Sato, H. Yoshizawa, Y. Shimura, T. Sakakibara et al., Phys. Rev. B **87**, 060408 (2013). https://doi.org/10.1103/PhysRevB.87.060408
101. P. Bonville, I. Mirebeau, A. Gukasov, S. Petit, J. Robert, Phys. Rev. B **84**, 184409 (2011). https://doi.org/10.1103/PhysRevB.84.184409
102. P. Bonville, I. Mirebeau, A. Gukasov, S. Petit, J. Robert, J. Phys: Conf. Ser. **320**, 012006 (2011). https://doi.org/10.1088/1742-6596/320/1/012006
103. S. Petit, P. Bonville, J. Robert, C. Decorse, I. Mirebeau, Phys. Rev. B **86**, 174403 (2012). https://doi.org/10.1103/PhysRevB.86.174403

104. B. Gaulin, J. Gardner, P. McClarty, M.J.P. Gingras, Phys. Rev. B **84**, 140402 (2011). https://doi.org/10.1103/PhysRevB.84.140402
105. S. Guitteny, J. Robert, P. Bonville, J. Ollivier, C. Decorse, P. Steffens, M. Boehm, H. Mutka, I. Mirebeau, S. Petit, Phys. Rev. Lett. **111**, 087201 (2013). https://doi.org/10.1103/PhysRevLett.111.087201
106. H.R. Molavian, M.J.P. Gingras, B. Canals, Phys. Rev. Lett. **98**, 157204 (2007). https://doi.org/10.1103/PhysRevLett.98.157204
107. I. Mirebeau, I. Goncharenko, P. Cadavez-Peres, S.T. Bramwell, M.J.P. Gingras, J. Gardner, Nature **420**, 54 (2002). https://doi.org/10.1038/nature01157
108. S. Legl, C. Krey, S. Dunsiger, H. Dabkowska, J. Rodriguez, G. Luke, C. Pfleiderer, Phys. Rev. Lett. **109**, 047201 (2012). https://doi.org/10.1103/PhysRevLett.109.047201
109. A. Sazonov, A. Gukasov, H. Cao, P. Bonville, E. Ressouche, C. Decorse, I. Mirebeau, Phys. Rev. B **88**, 184428 (2013). https://doi.org/10.1103/PhysRevB.88.184428
110. P.D. de Réotier, A. Yaouanc, A. Bertin, C. Marin, S. Vanishri, D. Sheptyakov, A. Cervellino, B. Roessli, C. Baines, J. Phys: Conf. Ser. **551**, 012021 (2014). https://doi.org/10.1088/1742-6596/551/1/012021
111. V. Klekovkina, B. Malkin, Opt. Spectrosc. **116**, 849 (2014). https://doi.org/10.1134/S0030400X14060137
112. V. Klekovkina, A. Zakirov, B. Malkin, L. Kasatkina, J. Phys.: Conf. Ser. **324**, 012036 (2011). https://doi.org/10.1088/1742-6596/324/1/012036
113. I. Mirebeau, A. Apetrei, J. Rodriguez-Carvajal, P. Bonville, A. Forget, D. Colson, V. Glazkov, J. Sanchez, O. Isnard, E. Suard, Phys. Rev. Lett. **94**, 246402 (2005). https://doi.org/10.1103/PhysRevLett.94.246402
114. G. Lau, B. Muegge, T. McQueen, E. Duncan, R. Cava, J. Solid State Chem. **179**, 3126 (2006). https://doi.org/10.1016/j.jssc.2006.06.007
115. P.D. De Reotier, A. Yaouanc, L. Keller, A. Cervellino, B. Roessli, C. Baines, A. Forget, C. Vaju, P. Gubbens, A. Amato et al., Phys. Rev. Lett. **96**, 127202 (2006). https://doi.org/10.1103/PhysRevLett.96.127202
116. S. Giblin, J. Champion, H. Zhou, C. Wiebe, J. Gardner, I. Terry, S. Calder, T. Fennell, S.T. Bramwell, Phys. Rev. Lett. **101**, 237201 (2008). https://doi.org/10.1103/PhysRevLett.101.237201
117. R.G. Melko, B.C. den Hertog, M.J.P. Gingras, Phys. Rev. Lett. **87**, 067203 (2001). https://doi.org/10.1103/PhysRevLett.87.067203
118. K. Matsuhira, Y. Hinatsu, K. Tenya, H. Amitsuka, T. Sakakibara, J. Phys. Soc. Jpn. **71**, 1576 (2002). https://doi.org/10.1143/JPSJ.71.1576
119. I. Mirebeau, P. Bonville, M. Hennion, Phys. Rev. B **76**, 184436 (2007). https://doi.org/10.1103/PhysRevB.76.184436
120. F. Bert, P. Mendels, A. Olariu, N. Blanchard, G. Collin, A. Amato, C. Baines, A. Hillier, Phys. Rev. Lett. **97**, 117203 (2006). https://doi.org/10.1103/PhysRevLett.97.117203
121. K.C. Rule, G. Ehlers, J.R. Stewart, A.L. Cornelius, P.P. Deen, Y. Qiu, C.R. Wiebe, J.A. Janik, H. Zhou, D. Antonio et al., Phys. Rev. B **76**, 212405 (2007). https://doi.org/10.1103/PhysRevB.76.212405
122. I. Mirebeau, H. Mutka, P. Bonville, A. Apetrei, A. Forget, Phys. Rev. B **78**, 174416 (2008). https://doi.org/10.1103/PhysRevB.78.174416
123. K. Rule, G. Ehlers, J. Gardner, Y. Qiu, E. Moskvin, K. Kiefer, S. Gerischer, J. Phys.: Condens. Matter **21**, 486005 (2009). https://doi.org/10.1088/0953-8984/21/48/486005
124. J. Zhang, K. Fritsch, Z. Hao, B. Bagheri, M.J.P. Gingras, G. Granroth, P. Jiramongkolchai, R. Cava, B. Gaulin, Phys. Rev. B **89**, 134410 (2014). https://doi.org/10.1103/PhysRevB.89.134410
125. A. Princep, H. Walker, D. Adroja, D. Prabhakaran, A. Boothroyd, Phys. Rev. B **91**, 224430 (2015). https://doi.org/10.1103/PhysRevB.91.224430
126. I. Mirebeau, I. Goncharenko, H. Cao, A. Forget, Phys. Rev. B **80**, 220407 (2009). https://doi.org/10.1103/PhysRevB.80.220407

127. A. Hallas, A. Arevalo-Lopez, A. Sharma, T. Munsie, J. Attfield, C. Wiebe, G. Luke, Phys. Rev. B **91**, 104417 (2015). https://doi.org/10.1103/PhysRevB.91.104417
128. S. Petit, E. Lhotel, S.n. Guitteny, O. Florea, J. Robert, P. Bonville, I. Mirebeau, J. Ollivier, H. Mutka, E. Ressouche, et al., Phys. Rev. B **94**, 165153 (2016). https://doi.org/10.1103/PhysRevB.94.165153
129. K. Matsuhira, C. Sekine, C. Paulsen, M. Wakeshima, Y. Hinatsu, T. Kitazawa, Y. Kiuchi, Z. Hiroi, S. Takagi, J. Phys: Conf. Ser. **145**, 012031 (2009). https://doi.org/10.1088/1742-6596/145/1/012031
130. S. Koohpayeh, J.J. Wen, B. Trump, C. Broholm, T. McQueen, J. Cryst. Growth **402**, 291 (2014). https://doi.org/10.1016/j.jcrysgro.2014.06.037
131. M.C. Hatnean, C. Decorse, M. Lees, O. Petrenko, D. Keeble, G. Balakrishnan, Mater. Res. Express **1**, 026109 (2014). https://doi.org/10.1088/2053-1591/1/2/026109
132. K. Kimura, S. Nakatsuji, J. Wen, C. Broholm, M. Stone, E. Nishibori, H. Sawa, Nat. Commun. **4**, 1934 (2013). https://doi.org/10.1038/ncomms2914
133. P. Bonville, S. Guitteny, A. Gukasov, I. Mirebeau, S. Petit, C. Decorse, M.C. Hatnean, G. Balakrishnan, Phys. Rev. B **94**, 134428 (2016). https://doi.org/10.1103/PhysRevB.94.134428
134. K. Kimura, S. Nakatsuji, A.A. Nugroho, J. Korean Phys. Soc. **63**, 719 (2013). https://doi.org/10.3938/jkps.63.719
135. L. Savary, L. Balents, Phys. Rev. Lett. **118**, 087203 (2017). https://doi.org/10.1103/PhysRevLett.118.087203
136. J.J. Wen, S. Koohpayeh, K. Ross, B. Trump, T. McQueen, K. Kimura, S. Nakatsuji, Y. Qiu, D. Pajerowski, J. Copley et al., Phys. Rev. Lett. **118**, 107206 (2017). https://doi.org/10.1103/PhysRevLett.118.107206
137. J. Van Duijn, K. Kim, N. Hur, D. Adroja, M. Adams, Q. Huang, M. Jaime, S.W. Cheong, C. Broholm, T. Perring, Phys. Rev. Lett. **94**, 177201 (2005). https://doi.org/10.1103/PhysRevLett.94.177201
138. M.C. Hatnean, R. Sibille, M.R. Lees, M. Kenzelmann, V. Ban, V. Pomjakushin, G. Balakrishnan, J. Phys.: Condens. Matter **29**, 075902 (2017). https://doi.org/10.1088/1361-648X/29/7/075902
139. R. Sibille, E. Lhotel, M.C. Hatnean, G. Balakrishnan, B. Fåk, N. Gauthier, T. Fennell, M. Kenzelmann, Phys. Rev. B **94**, 024436 (2016). https://doi.org/10.1103/PhysRevB.94.024436
140. V. Anand, L. Opherden, J. Xu, D. Adroja, A. Islam, T. Herrmannsdörfer, J. Hornung, R. Schönemann, M. Uhlarz, H. Walker et al., Phys. Rev. B **94**, 144415 (2016). https://doi.org/10.1103/PhysRevB.94.144415
141. A. Princep, D. Prabhakaran, A. Boothroyd, D. Adroja, Phys. Rev. B **88**, 104421 (2013). https://doi.org/10.1103/PhysRevB.88.104421
142. K. Matsuhira, C. Sekine, C. Paulsen, Y. Hinatsu, J. Magn. Magn. Mater. **272**, E981 (2004). https://doi.org/10.1016/j.jmmm.2003.12.500
143. N. Shannon, O. Sikora, F. Pollmann, K. Penc, P. Fulde, Phys. Rev. Lett. **108**, 067204 (2012). https://doi.org/10.1103/PhysRevLett.108.067204
144. Y. Machida, S. Nakatsuji, S. Onoda, T. Tayama, T. Sakakibara, Nature **463**, 210 (2010). https://doi.org/10.1038/nature08680
145. L. Balicas, S. Nakatsuji, Y. Machida, S. Onoda, Phys. Rev. Lett. **106**, 217204 (2011). https://doi.org/10.1103/PhysRevLett.106.217204
146. S. Nakatsuji, Y. Machida, Y. Maeno, T. Tayama, T. Sakakibara, J. van Duijn, L. Balicas, J. Millican, R. Macaluso, J.Y. Chan, Phys. Rev. Lett. **96**, 087204 (2006). https://doi.org/10.1103/PhysRevLett.96.087204
147. D. MacLaughlin, Y. Ohta, Y. Machida, S. Nakatsuji, G. Luke, K. Ishida, R. Heffner, L. Shu, O. Bernal, Phys. B **404**, 667 (2009). https://doi.org/10.1016/j.physb.2008.11.167
148. F. Foronda, F. Lang, J. Möller, T. Lancaster, A. Boothroyd, F. Pratt, S. Giblin, D. Prabhakaran, S. Blundell, Phys. Rev. Lett. **114**, 017602 (2015). https://doi.org/10.1103/PhysRevLett.114.017602
149. E.G. Moon, C. Xu, Y.B. Kim, L. Balents, Phys. Rev. Lett. **111**, 206401 (2013). https://doi.org/10.1103/PhysRevLett.111.206401

150. L. Savary, E.G. Moon, L. Balents, Phys. Rev. X **4**, 041027 (2014). https://doi.org/10.1103/PhysRevX.4.041027
151. R. Sibille et al., Nat. Commun. **8**, 892 (2017). https://doi.org/10.1038/s41467-017-00905-w
152. J.W. Krizan, R.J. Cava, Phys. Rev. B **89**, 214401 (2014). https://doi.org/10.1103/PhysRevB.89.214401
153. J. Krizan, R. Cava, J. Phys.: Condens. Matter **27**, 296002 (2015). https://doi.org/10.1088/0953-8984/27/29/296002
154. J. Krizan, R. Cava, Phys. Rev. B **92**, 014406 (2015). https://doi.org/10.1103/PhysRevB.92.014406
155. M. Sanders, J. Krizan, K. Plumb, T. McQueen, R. Cava, J. Phys.: Condens. Matter **29**, 045801 (2016). https://doi.org/10.1088/1361-648X/29/4/045801
156. K.A. Ross, J.W. Krizan, J.A. Rodriguez-Rivera, R.J. Cava, C.L. Broholm, Phys. Rev. B **93**, 014433 (2016). https://doi.org/10.1103/PhysRevB.93.014433
157. K. Ross, J. Brown, R. Cava, J. Krizan, S. Nagler, J. Rodriguez-Rivera, M. Stone, Phys. Rev. B **95**, 144414 (2017). https://doi.org/10.1103/PhysRevB.95.144414
158. M. Dahlberg, M. Matthews, P. Jiramongkolchai, R. Cava, P. Schiffer, Phys. Rev. B **83**, 140410 (2011). https://doi.org/10.1103/PhysRevB.83.140410
159. Y.D. Li, G. Chen, Phys. Rev. B **95**, 041106 (2017). https://doi.org/10.1103/PhysRevB.95.041106
160. R. Sibille, E. Lhotel, V. Pomjakushin, C. Baines, T. Fennell, M. Kenzelmann, Phys. Rev. Lett. **115**, 097202 (2015). https://doi.org/10.1103/PhysRevLett.115.097202
161. S. Petit, E. Lhotel, B. Canals, M.C. Hatnean, J. Ollivier, H. Mutka, E. Ressouche, A. Wildes, M. Lees, G. Balakrishnan, Nat. Phys. **12**, 746 (2016). https://doi.org/10.1038/nphys3710
162. L. Pawlak, M. Duczmal, A. Zygmunt, J. Magn. Magn. Mater. **76**, 199 (1988). https://doi.org/10.1016/0304-8853(88)90367-8
163. G. Lau, R. Freitas, B. Ueland, P. Schiffer, R. Cava, Phys. Rev. B **72**, 054411 (2005). https://doi.org/10.1103/PhysRevB.72.054411
164. T. Higo, K. Iritani, M. Halim, W. Higemoto, T.U. Ito, K. Kuga, K. Kimura, S. Nakatsuji, Phys. Rev. B **95**, 174443 (2017). https://doi.org/10.1103/PhysRevB.95.174443
165. J. Lago, I. Živković, B. Malkin, J.R. Fernandez, P. Ghigna, P.D. de Réotier, A. Yaouanc, T. Rojo, Phys. Rev. Lett. **104**, 247203 (2010). https://doi.org/10.1103/PhysRevLett.104.247203
166. A. Legros, D. Ryan, P.D. de Réotier, A. Yaouanc, C. Marin, J. Appl. Phys. **117**, 17C701 (2015). https://doi.org/10.1063/1.4906182

Chapter 13
Novel Electronic Phases of Matter: Coupling to Itinerant Electrons

Masafumi Udagawa

Abstract In this chapter, we will address the properties of itinerant electrons coupled with spin ice, which we call "itinerant spin ice". In a broader scope, this system serves as a prototypical example of the itinerant electrons interacting with geometrically frustrated magnet. To describe the nature of this frustrated itinerant systems, we firstly introduce the classical Kondo lattice model, and discuss its basic properties. After that, equipped with the knowledge of the model, we consider the thermodynamic and transport properties of itinerant spin ice, with reference to the experimental data of $Pr_2Ir_2O_7$. Finally, we end this chapter with the discussion on several on-going topics and future perspectives for the frustrated itinerant systems.

13.1 Spin Ice Meets Mobile Carriers

Spin ice belongs to a large family of magnetic systems, termed "geometrically frustrated magnet". Geometrical frustration is a concept, associated with the local structure of the lattice on which the system is defined; if a lattice is composed of triangular units, we call the system frustrated, having in mind the difficulty of energy optimization for the antiferromagnetically coupled magnetic moments (Fig. 13.1a). As this example shows, geometrical frustration is usually considered for localized magnetic systems, in which the local nature of magnetic moments makes the system sensitive to the local structure of lattice. In contrast, it is unclear how geometrical frustration affects the itinerant electron systems.

At first glance, it seems unlikely that properties of itinerant electrons are considerably affected by geometrical frustration. In itinerant systems, electrons behave as plane waves extended over the system, apparently insensitive to the small difference in the shape of local lattice structure (Fig. 13.1b). Nevertheless, contrary to this naive expectation, we sometimes come across unusual phenomena in itinerant systems defined on highly frustrated lattice structure.

M. Udagawa (✉)
Department of Physics, Gakushuin University, Tokyo, Japan
e-mail: masafumi.udagawa@gakushuin.ac.jp

M. Udagawa and L. Jaubert (eds.), *Spin Ice*, Springer Series in Solid-State Sciences 197,
https://doi.org/10.1007/978-3-030-70860-3_13

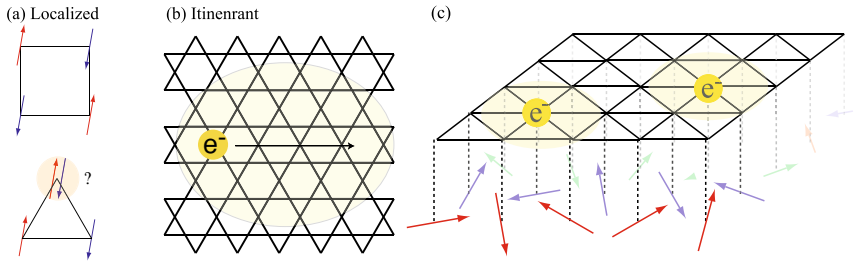

Fig. 13.1 Schematic pictures of the role of geometrical frustration in **a** localized spin systems, **b** itinerant electrons systems, and **c** the hybrid model

To give a few examples, in magnetites, Fe_3O_4, its metal insulator transition was originally attributed to a variant of ice rule imposed on charge degrees of freedom [1]. In LiV_2O_4, it was reported that electrons have 200 times as large mass as those in normal metals [2]. Similar heavy-fermion behavior is also observed for YMn_2 [3], β-Mn [4], Molybdates [5], and many other frustrated conductors. In rare-earth molybdates and iridates, anomalous transport properties have been observed, such as resistivity minimum, unconventional Hall response, and spontaneous Hall effect [6–9].

How does geometrical frustration bring about anomalous phenomena in these materials? To give a hint to this problem, we focus on one important class of systems, namely the composite systems, where itinerant electrons interact with a localized subsystem, such as magnetic moments (Fig. 13.1c). Localized moments are sensitive to the frustrated lattice structure, due to their local nature, and sometimes develop unusual spatial structure, e.g., spin ice. Through the interaction with the anomalous spatial structure developed in the local subsystem, itinerant electrons may also acquire nontrivial properties. In this review, we will focus on this kind of "hybrid" systems, with itinerant spin ice as a prototypical example.

The organization of this article is as follows. In Sect. 13.2, we will introduce the classical Kondo lattice model, as a representative model to describe this hybrid system, followed by a detailed discussion on the basic properties of this model in Sect. 13.3. Section 13.4 will be devoted to the summary of experimental data of $Pr_2Ir_2O_7$, and theoretical perspectives of itinerant spin ice. We will introduce several on-going topics about frustrated itinerant systems in Sect. 13.5, and summarize in Sect. 13.6.

13.2 Classical Kondo Lattice Model

As a basic model to describe the hybrid system, we consider the classical Kondo lattice (CKL) model,

$$\mathscr{H}_{\rm ck}[J] = -t \sum_{(i,j),s} (c_{is}^{\dagger} c_{js} + c_{js}^{\dagger} c_{is}) - J \sum_{i} \mathbf{s}_i \cdot \mathbf{S}_i^{\rm cl} \equiv \mathscr{H}_{\rm kin} + \mathscr{H}_{\rm int}, \quad (13.1)$$

where $c_{is}^{\dagger}(c_{is})$ is a creation (annihilation) operator of electron at site i and spin s, $\mathbf{s}_i \equiv \frac{1}{2} c_{is}^{\dagger} \boldsymbol{\sigma}_{ss'} c_{is'}$ means an electron spin, with $\boldsymbol{\sigma}_{ss'}$, the vector notation of Pauli matrices. $\mathbf{S}_i^{\rm cl} = (S_{ix}^{\rm cl}, S_{iy}^{\rm cl}, S_{iz}^{\rm cl})$ is a vector with three c-number components, representing a classical localized moment defined at site i. The summation over the site pairs, (i, j) defines the lattice structure. This is the simplest possible model to describe the interaction between itinerant electrons and classical localized moments, with only two independent parameters: electron density ($n \equiv \frac{1}{2N} \sum_{i,s} \langle c_{is}^{\dagger} c_{is} \rangle$, N: the number of sites), and the exchange coupling (J/t).

What kind of physical systems can be described by this Hamiltonian, $\mathscr{H}_{\rm ck}[J]$? In fact, the study of CKL model has a long history. Starting from 1950s, the magnetism and conduction properties of manganites [10] have been studied, based on the ferromagnetic CKL model by assuming large coupling constant, J [11–16]. In manganites, the partially filled $3d$ orbitals, subject to crystal field splitting, exhibits a dual nature of itinerancy and localization. As a typical example, in the perovskite manganites, $La_{1-x}Sr_xMnO_3$, the localized $S = 3/2$ magnetic moments in the t_{2g} orbitals interact with itinerant electrons in the conduction band formed by e_g orbitals, through the strong Hund's rule coupling. This picture is well captured by the CKL model (13.1), by assuming large positive J due to the Hund's rule coupling. And, as a result, the magnetic and conduction properties of the manganites have been successfully explained.

Rare-earth compounds are another class of systems represented by this model, and its quantum counterpart, where the classical moment $\mathbf{S}_i^{\rm cl}$ is replaced with a quantum spin operator, $\mathbf{S}_i^{\rm q}$. In rare-earth compounds, localized magnetic moments due to the f-orbitals of rare-earth ions, interact with itinerant electrons due to other, often lighter, ions contained in the compounds [17]. The coexistence of itinerant and localized electrons are well described by Kondo lattice model, however, in quite different parameter region from the manganites mentioned above. In rare-earth compounds, the magnetic interaction is usually originated from superexchange interaction between rare-earth and "light" ions, which is smaller, compared with the energy scale of band width. Accordingly, in the analysis of rare-earth systems, $J \ll t$ is usually assumed in Hamiltonian, $\mathscr{H}_{\rm ck}[J]$, in contrast to $J \gg t$ for Manganites, where J is connected to strong Hund's rule coupling, as mentioned above.

In these two cases, the CKL model naturally appears as a relevant model to describe actual compounds. Meanwhile, in the analysis of more formidable models, the CKL model often serves as an effective model to give reliable approximate results. Starting from the quantum version of Kondo lattice model with $\mathbf{S}_i^{\rm q}$, the CKL model can be obtained through a sort of static approximation, which ignores the quantum dynamics of localized moments, and leads to the replacement, $\mathbf{S}_i^{\rm q} \to \mathbf{S}_i^{\rm cl}$. The CKL Hamiltonian $\mathscr{H}_{\rm ck}[J]$ can also be related to Hubbard model, where electrons interact through the on-site interaction:

$$\mathscr{H}_{\rm Hub} = -t \sum_{(i,j),s} (c_{is}^{\dagger} c_{js} + c_{js}^{\dagger} c_{is}) + U \sum_{i} n_{i\uparrow} n_{i\downarrow}. \tag{13.2}$$

The key to the derivation of $\mathscr{H}_{\rm ck}[J]$ from the Hubbard model is the replacement:

$$n_{i\uparrow} n_{i\downarrow} = -\frac{2}{3} \mathbf{s}_i \cdot \mathbf{s}_i + \frac{1}{2}(n_{i\uparrow} + n_{i\downarrow}) \simeq -\frac{2}{3} \langle \mathbf{s}_i \rangle \cdot \mathbf{s}_i + \frac{1}{2}(n_{i\uparrow} + n_{i\downarrow}). \tag{13.3}$$

The first equality in (13.3) is the operator identity, while the second equality is the replacement of the operator $\mathbf{s}_i$ with its (site-dependent) thermal average, $\langle \mathbf{s}_i \rangle$. If one identifies $\langle \mathbf{s}_i \rangle$ with the classical localized moment, $\mathbf{S}_i^{\rm cl}$, one can recover the Hamiltonian, (13.1), with the constraint that $\mathbf{S}_i^{\rm cl}$ should be connected to the thermal average, $\langle \mathbf{s}_i \rangle$. For a systematic derivation of static approximation, see, for example, [18] These treatments, the replacement of quantum spin operator with classical variables or thermal average, can be allowed in high temperature regions, where thermal fluctuation dominates the quantum fluctuation. In addition to the high temperature region, the CKL model can be justified at much lower temperature, where the magnetic order is well developed, and both thermal and quantum fluctuations are suppressed, accordingly.

Summarizing so far, the CKL model stands as useful phenomenological models on its own, as well as it is connected to various microscopic models. In the subsequent chapter, we will introduce the basic properties of classical Kondo lattice model, together with useful numerical/analytical techniques for this model.

13.3 Basic Properties of Classical Kondo Lattice Model

In this section, we will discuss the basic properties of the CKL model, defined with the Hamiltonian, $\mathscr{H}_{\rm ck}[J]$, given in (13.1).

13.3.1 Ground State

The CKL model belongs to a class of models, where non-interacting fermions are coupled to macroscopic number of classical degrees of freedom, or more generally, conserved quantities. Since $\mathbf{S}_i^{\rm cl}$ is composed of c-numbers, it trivially commutes with Hamiltonian $\mathscr{H}_{\rm ck}[J]$, and can be regarded as continuous-valued conserved quantity. This class of models also includes Falicov-Kimball model [20, 21], in which fermions are coupled to discrete classical charge degrees of freedom. Kitaev model gives an example, in which conserved quantities take more non-trivial form. In this model, the Hamiltonian can be mapped into the free Majorana fermions coupled to conserved Z_2 degrees of freedom [22].

Common through the models in this class, once the values of conserved quantities are fixed, the Hamiltonian takes quadratic form in terms of fermion operators, and can be diagonalized easily. This means that the determination of the ground state of CKL model is nothing but to find the configuration of $\{\mathbf{S}_i^{\mathrm{cl}}\}$, which minimizes the ground-state energy of descendant free fermion Hamiltonian. However, since the number of configurations for $\{\mathbf{S}_i^{\mathrm{cl}}\}$ grows exponentially with system size, brute-force search for the optimal configuration is possible only for small-size cluster. For large systems, one has to resort to approximate analytical or numerical techniques, which we will introduce later in Sect. 13.3.4.

13.3.2 Finite-Temperature Properties

In order to study finite-temperature properties, in the first place, it is necessary to calculate Boltzmann weight, $\exp(-\mathscr{H}_{\mathrm{ck}}[J;\{\mathbf{S}_i^{\mathrm{cl}}\}]/T)$, corresponding to each fixed configuration, $\{\mathbf{S}_i^{\mathrm{cl}}\}$. Once $\{\mathbf{S}_i^{\mathrm{cl}}\}$ is fixed, this quantity can be obtained easily, through the diagonalization of quadratic Hamiltonian. However, to obtain the expectation value of observable, $\mathscr{O}$, we have to make summation over the configurations, $\{\mathbf{S}_i^{\mathrm{cl}}\}$:

$$\langle\mathscr{O}\rangle = \frac{1}{Z}\mathrm{Tr}_{\{\mathbf{S}_i^{\mathrm{cl}}\}}\mathrm{Tr}_{c,c^\dagger}\Big[\mathscr{O}\exp(-\mathscr{H}_{\mathrm{ck}}[J;\{\mathbf{S}_i^{\mathrm{cl}}\}]/T)\Big]. \tag{13.4}$$

Here, $\mathrm{Tr}_{\{\mathbf{S}_i^{\mathrm{cl}}\}}$ means taking trace in terms of classical magnetic moments, while $\mathrm{Tr}_{c,c^\dagger}$ means the trace by fermionic degrees of freedom. To evaluate the summation (13.4) exactly, one has to generate all possible configurations of $\{\mathbf{S}_i^{\mathrm{cl}}\}$, and make summation over them. This is again, an exponentially formidable task as increasing the system size.

13.3.3 Rigorous Results

While it is difficult to evaluate the observables exactly, several rigorous properties are known for the CKL model. We'll introduce some of them, in this subsection.

Time-Reversal Symmetry

From time-reversal symmetry, one can show that the sign of J does not affect the energy spectrum of the CKL model. For the Hamiltonian $\mathscr{H}_{\mathrm{ck}}[J]$ given in (13.1), one can construct a time-reversal operator acting only on electronic degrees of freedom, $\mathscr{T} = \mathscr{R}_y\mathscr{K}$, where $\mathscr{K}$ is the anti-unitary operator taking complex conjugate, and

$\mathscr{R}_y = \exp(i\pi \sum_i s_i^y)$ is the 180° rotation around the y-axis. If the kinetic part of the Hamiltonian, $\mathscr{H}_{\rm kin}$ is time-reversal invariant, i.e., t is real, $\mathscr{T}^{-1}\mathscr{H}_{\rm ck}[J]\mathscr{T} = \mathscr{H}_{\rm ck}[-J]$. Accordingly, $\mathscr{H}_{\rm ck}[J]$ and $\mathscr{H}_{\rm ck}[-J]$ have the identical energy spectrum. We note that the quantum version of Kondo lattice model, with quantum spin $\mathbf{S}^{\rm q}$ instead of $\mathbf{S}^{\rm cl}$, does not have this property. The argument above relies on the fact that $\mathscr{R}_y$ maps $(S_{ix}^{\rm cl}, S_{iy}^{\rm cl}, S_{iz}^{\rm cl}) \to (-S_{ix}^{\rm cl}, S_{iy}^{\rm cl}, -S_{iz}^{\rm cl})$, while $\mathscr{K}$ maps $s_{iy}S_{iy}^{\rm cl} \to -s_{iy}S_{iy}^{\rm cl}$, so $\mathscr{T}$ reverses the sign of interaction term, $\mathscr{H}_{\rm int}$, in total. However, for quantum case, $\mathscr{K}$ maps $s_{iy}S_{iy}^{\rm q}$ into itself, invalidating the argument.

Limit of $d \to \infty$

Remarkably, exact solution is available for the classical Kondo lattice model at the limit of infinite dimension, $d \to \infty$ [23]. At this limit, various thermodynamic quantities and even transport coefficients can be obtained exactly. These results are described in the language of many-body Green's function, and it shares practically the same structure with the exact solution of Falicov-Kimball model [24–29]. The simplification at $d \to \infty$ has been pointed out for many other problems [30], and forms a basis of dynamical mean-field theory, which has been extensively used for the analysis of many-body systems [31].

In many-body perturbation theories, the effect of interaction is taken into account, through the self-energy, $\Sigma_{ij}(\omega)$. The key observation at infinite dimension is that the self-energy is completely local, $\Sigma_{ij}(\omega) = \Sigma_i(\omega)\delta_{ij}$, which simplifies the mathematical structure of the formulation considerably, and make the exact solutions available.

Absence of Spontaneous Symmetry Breaking for Small d

For localized spin systems with continuous symmetry, it is well known that spontaneous symmetry breaking is forbidden in the system dimension $d \leq 2$ for any finite temperature. This Mermin-Wagner's theorem [32] also seems to forbid spontaneous symmetry breaking for the CKL model, since it has continuous symmetry as to the global rotation of spin.

Actually, there is a subtle point in the application of Mermin-Wagner's theorem, since the theorem assumes that the magnetic interaction decays faster than $1/r^{2+d}$. However, the effective spin interaction derived from $\mathscr{H}_{\rm ck}[J]$ is usually long-ranged, as discussed in Sect. 13.3.4. Despite this subtlety, the Mermin-Wagner's theorem was proved for quantum Kondo lattice model with the use of Bogoliubov's inequality [33], and recently reconsidered, taking account of the effect of spin-orbit interaction [34].

13.3.4 Basic Analytical/Numerical Techniques

Apart from the exactly solvable points, the analysis of classical Kondo lattice model requires rather involved calculations. In this section, we introduce popular numerical/analytical methods for the analysis of this model.

Monte Carlo Simulation

A reliable numerical method to accomplish the summation in (13.4) is the determinantial Monte Carlo method. In this method, one replaces the outer trace, $\mathrm{Tr}_{\{\mathbf{S}_i^{\mathrm{cl}}\}}$ in (13.4) with stochastic average, by generating a Markov chain process, and evaluates the inner trace, $\mathrm{Tr}_{c,c^\dagger}$, exactly by diagonalizing the free fermion Hamiltonian. To construct Markov chain process, one can use, e.g., single spin flip dynamics combined with standard Metropolis algorithm. This method is free from negative sign problem, which can be a serious obstacle in the application of quantum Monte Carlo simulation.

The bottleneck in the numerical cost lies in the diagonalization of free fermionic part. In contrast to classical spin systems, the energy change accompanied with local update requires the diagonalization of fermionic Hamiltonian on the whole lattice. The numerical cost for the diagonalization scales as $\mathcal{O}(N^3)$ with the number of spins, N. This means one Monte Carlo step, composed of N spin flips, requires the computation scaled as $\mathcal{O}(N^4)$, imposing a severe computational cost for large systems. To remedy this problem, several efficient algorithms have been proposed [35, 36]. Recently, the application of machine learning was proposed to reduce the computational cost [37].

Dynamical Mean-Field Theory

Given the numerical cost of Monte Carlo simulation, it is desirable to have a well-controlled analytical technique. In this light, dynamical mean-field theory (DMFT) is quite useful. This method is based on the exact solution at infinite dimension, $d \to \infty$, which we introduced in Sect. 13.3.3. DMFT assumes that self-energy is local: $\Sigma_{ij}(\omega) = \Sigma_i(\omega)\delta_{ij}$, and provides a scheme to determine $\Sigma_i(\omega)$ in a self-consistent way. This assumption is justified only at $d \to \infty$, but nevertheless, various aspects of low-dimensional systems remain well described by DMFT [31].

DMFT was applied to the CKL model in the study of colossal magneto-resistance [40], accounting for the behavior of resistivity observed for Mn perovskites [23, 38, 39]. (In this context, the model is often termed as double-exchange model.)

The disadvantage of DMFT lies in the technical difficulty in taking the spatial correlations into account. At the cost of simplification, the off-site components of self-energy are ignored in this scheme. This shortcoming can be serious, when it comes to considering the spatial character of the system, such as geometrical frustration.

To remedy this disadvantage, cluster extension of DMFT (CDMFT) is sometimes adopted, in which not only the on-site component, $\Sigma_{ii}(\omega)$, but all the components of self-energy within a certain size of cluster are taken into account. In particular, by choosing fundamental unit of geometrical frustration, such as triangle and tetrahedron, as a cluster, one can take account of the minimal effect of frustration [41, 42].

Perturbation Expansion

In weakly interacting regimes, it is useful to consider perturbation expansion in terms of J. For this purpose, we firstly fix the configuration of localized moments, $\{\mathbf{S}_i\}$, and then, expand the free energy, $\mathscr{F}$, in terms of $\mathscr{H}_{\rm int}$ in CKL Hamiltonian (13.1):

$$\mathscr{F} - \mathscr{F}_0 = -T \log\Big\langle \mathscr{T}_\tau \exp\Big[-\int_0^\beta d\tau \mathscr{H}_{\rm int}(\tau)\Big]\Big\rangle_0 = \mathscr{F}_2 + \mathscr{F}_4 + \cdots, \quad (13.5)$$

where $\langle\cdots\rangle_0$ means the thermal average in terms of $\mathscr{H}_{\rm kin}$ in (13.1). Here, J^nth order term of the free energy is denoted as $\mathscr{F}_n$. The odd-order terms are absent, under the time-reversal symmetry, which we implicitly assumed. The remaining even-order terms, $\mathscr{F}_n$, are composed of the products of $\mathbf{S}_{\mathbf{q}_1}$, $\mathbf{S}_{\mathbf{q}_2}$, $\ldots$ $\mathbf{S}_{\mathbf{q}_n}$, which satisfy $\mathbf{q}_1 + \mathbf{q}_2 + \cdots \mathbf{q}_n = 0$ (modulo reciprocal vectors). Here, $\mathbf{S}_{\mathbf{q}} = \frac{1}{N}\sum_i \mathbf{S}_i e^{i\mathbf{q}\cdot\mathbf{r}_i} (= \mathbf{S}^*_{-\mathbf{q}})$ is the Fourier transform of the localized moments. To write down the first few terms, we have

$$\mathscr{F}_2 = -J^2 \sum_{\mathbf{q}} \chi^0(\mathbf{q}) |\mathbf{S}_{\mathbf{q}}|^2, \quad (13.6)$$

$$\mathscr{F}_4 = -J^4 \sum_{\mathbf{q}_1+\mathbf{q}_2+\mathbf{q}_3+\mathbf{q}_4=0} \big[A_{\mathbf{q}_1\mathbf{q}_2,\mathbf{q}_3\mathbf{q}_4}(\mathbf{S}_{\mathbf{q}_1}\cdot\mathbf{S}_{\mathbf{q}_2})(\mathbf{S}_{\mathbf{q}_3}\cdot\mathbf{S}_{\mathbf{q}_4}) + B_{\mathbf{q}_1\mathbf{q}_2,\mathbf{q}_3\mathbf{q}_4}(\mathbf{S}_{\mathbf{q}_1}\times\mathbf{S}_{\mathbf{q}_2})\cdot(\mathbf{S}_{\mathbf{q}_3}\times\mathbf{S}_{\mathbf{q}_4})$$
$$+ C_{\mathbf{q}_1\mathbf{q}_2,\mathbf{q}_3\mathbf{q}_4}\Big(S^\alpha_{\mathbf{q}_1}S^\beta_{\mathbf{q}_2} + S^\beta_{\mathbf{q}_1}S^\alpha_{\mathbf{q}_2} - \frac{2}{3}\mathbf{S}_{\mathbf{q}_1}\cdot\mathbf{S}_{\mathbf{q}_2}\delta_{\alpha\beta}\Big)\Big(S^\alpha_{\mathbf{q}_3}S^\beta_{\mathbf{q}_4} + S^\beta_{\mathbf{q}_3}S^\alpha_{\mathbf{q}_4} - \frac{2}{3}\mathbf{S}_{\mathbf{q}_3}\cdot\mathbf{S}_{\mathbf{q}_4}\delta_{\alpha\beta}\Big)\big]. \quad (13.7)$$

The coefficients: $\chi^0(\mathbf{q})$, $A_{\mathbf{q}_1\mathbf{q}_2,\mathbf{q}_3\mathbf{q}_4}$, $B_{\mathbf{q}_1\mathbf{q}_2,\mathbf{q}_3\mathbf{q}_4}$ and $C_{\mathbf{q}_1\mathbf{q}_2,\mathbf{q}_3\mathbf{q}_4}$ are expressed with the multiple correlation functions of fermionic creation/annihilation operators evaluated at $J = 0$. In particular, $\chi^0(\mathbf{q})$ has a special meaning as a susceptibility for the formation of spin density wave with wave number $\mathbf{q}$. If J is small, the lowest order term, $\mathscr{F}_2$, dominates in the expansion, (13.5). Consequently, the configuration of localized moments, $\{\mathbf{S}_i\}$, which minimizes $\mathscr{F}_2$, or equivalently maximizes $\chi^0(\mathbf{q})$, will be realized as the most stable magnetic structure. We will discuss this point in more detail, in Sect. 13.3.5.

Expressing $\mathscr{F}_2$ in a real-space basis, we obtain

$$\mathscr{F}_2 = -J^2 \sum_{i,j} \chi^0_{i,j} \mathbf{S}_i \cdot \mathbf{S}_j. \quad (13.8)$$

This form is known as the Rudermann-Kittel-Kasuya-Yoshida (RKKY) interaction. $\chi^0_{i,j} = \sum_{\mathbf{q}} e^{-i\mathbf{q}\cdot(\mathbf{r}_i - \mathbf{r}_j)}\chi^0(\mathbf{q})$ is the Fourier transform of the $\chi^0(\mathbf{q})$, and it usually decays algebraically, as $\propto 1/|\mathbf{r}_i - \mathbf{r}_j|^3$ with oscillation, in three-dimensional normal metallic systems. Interpreting $\mathscr{F}_2$ as an effective Hamiltonian, χ_{ij} serves as long-ranged effective interaction between localized moments at the limit of small J.

13.3.5 Dual Property of Classical Kondo Lattice Model

The analysis of classical Kondo lattice model can be divided into two steps. At zero temperature, first, one has to determine the magnetic structure, which minimizes the energy of itinerant electrons. After that, one calculates electronic response, given the optimized magnetic structure. This division is possible due to the static nature of the localized moments. Any eigenstate of CKL model can be described as a direct product of Slater determinant of itinerant electrons and one particular configuration of localized moments. This is true only for "classical" Kondo lattice model. In the quantum counterpart of the model, the eigenstates are superposition of direct products, which disables treating magnetic part and electronic part separately.

This separability simplifies the analysis of the model, considerably. It also facilitates to set up phenomenology that connects theory and experiment. If the information of magnetic structure can be obtained from different sources, such as neutron scattering experiment, one can directly calculate the electronic response, by treating the magnetic structure as an "input parameter". This flexibility makes the CKL model stands as a powerful phenomenological model.

Effective Interaction Between Localized Moments

Although it is difficult to determine magnetic structure by taking trace in (13.4), at limiting cases, one can understand the optimized magnetic structure intuitively. At the limit of $J/t \gg 1$ in (13.1), the spins of itinerant electrons are oriented parallel to the localized moments at each site. Consequently, if the electron density is less than half-filling ($n < 1$), the CKL Hamiltonian (13.1) can be rewritten as

$$\mathscr{H}_{\mathrm{ck}}[J] \to \mathscr{H}_{\mathrm{DE}} = -t \sum_{\langle i,j \rangle} (\langle \mathbf{S}_i | \mathbf{S}_j \rangle \alpha_i^\dagger \alpha_j + \mathrm{H.c.}), \tag{13.9}$$

considering only the low-energy sector at $\varepsilon \sim -J + \mathscr{O}(t)$. Here, $|\mathbf{S}_i\rangle$ is the one-particle eigenstate, which satisfies $-\mathbf{S}_i \cdot \boldsymbol{\sigma}|\mathbf{S}_i\rangle = -|\mathbf{S}_i\rangle$, corresponding to the fixed distribution of localized moments, $\{\mathbf{S}_i\}$. $\alpha_i^\dagger$ creates an electron in $|\mathbf{S}_i\rangle$. This limiting case: $J/t \gg 1$ is realized in e.g. Manganese oxides, where J is attributed to Hund's rule coupling as noted in Sect. 13.1.

In this limit, the magnetic structure can be determined by minimizing the energy $\langle \mathscr{H}_{\rm DE} \rangle$. This procedure can be easily carried out, if the electron density, n, is small. In the dilute case, the energy, $\langle \mathscr{H}_{\rm DE} \rangle$, is determined as $\langle \mathscr{H}_{\rm DE} \rangle \propto n\varepsilon_b$, where ε_b is the lowest one-particle eigenenergy of Hamiltonian, $\mathscr{H}_{\rm DE}$. Accordingly, the minimization of energy can be achieved by aligning all the magnetic moments ferromagnetically, which gives $\langle \mathbf{S}_i | \mathbf{S}_j \rangle = 1$ in (13.9), leading to the lowest possible band bottom at $-zt$, with the coordination number of lattice, z. Physically, this alignment of magnetic moments comes from the optimization of kinetic energy, and this mechanism is called "double-exchange mechanism" (Fig. 13.2).

In the opposite limit of $J/t \ll 1$, a quite different mechanism works. In this region, the perturbative treatment introduced in Sect. 13.3.4 works very well. According to (13.8), the localized moments interact through the RKKY interaction, and the system energy can be minimized by forming the magnetic structure, which maximizes the susceptibility, $\chi^0(\mathbf{q})$, as far as the lowest-order term, $\mathscr{F}_2$, is considered. $\chi^0(\mathbf{q})$ is particularly enhanced, if the wave vector, $\mathbf{q} = \mathbf{Q}$, connects the two points on Fermi surface. In this case, the degeneracy of the two points, connected by the vector $\mathbf{Q}$, is lifted, leading to the formation of a local gap $\propto J|\mathbf{S}_\mathbf{q}|^2$ (Fig. 13.2), favoring the formation of spin density wave with wave number $\mathbf{Q}$ [45]. In particular, if the non-interacting band structure has nesting, i.e., a finite fraction of Fermi surface is connected by a single wave vector, $\chi^0(\mathbf{q})$ shows a singularity, signaling the strong instability toward the magnetic ordering.

While $\mathscr{F}_2$ plays an important role in magnetic ordering, $\chi^0(\mathbf{q})$ does not solely give sufficient information to determine the magnetic structure. The magnetic structure cannot be uniquely determined from wave vector, $\mathbf{q}$. One can make various magnetic patterns, using the three components of $\mathbf{S}_\mathbf{q}$. Furthermore, in most systems, due to the point-group symmetry, $\chi^0(\mathbf{q})$ takes the same value for a set of momenta, connected by point-group operation. In this case, superpositions of magnetic density waves with several $\mathbf{q}$ will give the same energy, as far as only $\mathscr{F}_2$ is considered.

To lift the degeneracy, one has to consider non-linear contributions. Some superpositions are automatically eliminated due to the fixed magnitude for localized moment, $|\mathbf{S}_i| = 1$. Moreover, the fourth-order term, $\mathscr{F}_4$ usually makes difference between the degenerate magnetic structures. For example, as is clear from (13.7), $\mathscr{F}_4$ involves the term $\propto A_{\mathbf{q}_1-\mathbf{q}_1,\mathbf{q}_2-\mathbf{q}_2}|\mathbf{S}_{\mathbf{q}_1}|^2|\mathbf{S}_{\mathbf{q}_2}|^2$. This term works to stabilize magnetic structure of single wave number (multiple wave numbers) for $A_{\mathbf{q}_1-\mathbf{q}_1,\mathbf{q}_2-\mathbf{q}_2} > 0\ (< 0)$, depending on the details of a non-interacting band structure.

The superposition of magnetic density waves leads to the possibility of stabilizing non-coplanar magnetic structures, where all the magnetic moments cannot be placed in a plane. This non-coplanar magnetic ordering accompanies finite spin scalar chirality, and leads to finite Hall response, as we discuss below. Regarding this magnetic pattern, several theoretical analyses have shown the realization of integer Hall effect [43–45], and the possibility of chiral spin liquid formation was also pointed out [46].

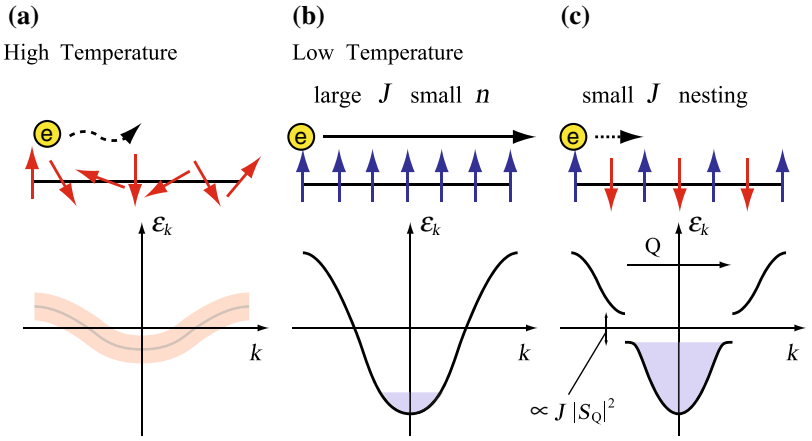

Fig. 13.2 Mechanisms of magnetic ordering in classical Kondo lattice model. **a** At high temperature, due to the thermally disordered spin configurations, itinerant electrons form a quite narrow band with large damping. **b** As lowering temperatures, the localized spins show ferromagnetic ordering for small n, which facilitates the electron motion, leading to the formation of a wide band. The small number of electrons are populated around the band bottom, gaining large kinetic energy. **c** If the electron density is tuned so that Fermi surface develops nesting, or large $\chi_0(\mathbf{q})$, a magnetic ordering characterized by the corresponding wave vector $\mathbf{Q}$ is stabilized. As regards, the system gains energy by opening a gap at the Fermi level

Impact of Magnetic Structure on Itinerant Electrons

Once the magnetic structure is fixed, the localized moments affect the itinerant electrons as a site-dependent magnetic field. Among the various effects on itinerant electrons, particularly interesting is the influence on transport properties. If anomalous correlation is developed among the localized moments, as in spin ice, it gives peculiar scattering effects on itinerant electrons. An another interesting effect comes from the geometrical phase the localized moments impose on the electronic wave function. At the strong coupling limit ($J \gg t$), the electron spins perfectly follow the directions of localized moments at each sites, as described by the strong coupling Hamiltonian (13.9). To describe the effect, assuming the spatial variation of magnetic structure is slow enough, we switch to the continuum picture: $\mathbf{S}_i \to \mathbf{S}(\mathbf{R})$. Then, along the motion from $\mathbf{R}_i \to \mathbf{R}_f$, the electron wave function acquires an additional phase, called Berry phase:

$$|\psi\rangle \to \exp\Big[-i\int_{\mathbf{R}_i}^{\mathbf{R}_f} \mathbf{A}(\mathbf{R})\cdot d\mathbf{R}\Big]|\psi\rangle, \quad \mathbf{A}(\mathbf{R}) = -i\langle \mathbf{S}(\mathbf{R})|\nabla|\mathbf{S}(\mathbf{R})\rangle. \tag{13.10}$$

This expression is interesting in that the magnetic structure $\mathbf{S}(\mathbf{R})$ seems to produce effective vector potential, $\mathbf{A}(\mathbf{R})$. In fact, the non-coplanar magnetic structure gives rise to a non-vanishing effective "magnetic field".

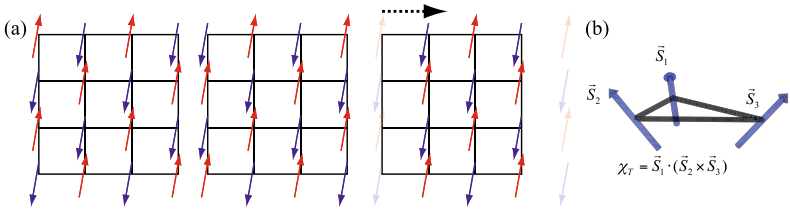

Fig. 13.3 **a** Antiferromagnetic spin configuration. Starting from the left figure, (middle) time-reversal, followed by (right) translation with one lattice space maps the spin state into the original configuration. **b** An example of spin triplets forming a non-coplanar configuration, spanning a finite spin scalar chirality

In fact, this fictitious magnetic field works as real magnetic field, and gives rise to Aharonov Bohm effect for itinerant electrons. Especially well studied transport quantity in this context is the Hall conductivity [50–52]. In the conventional theory of metal, Hall conductivity, σ_{xy} is proportional to magnetic field. In the 60s, the concept of anomalous Hall effect was proposed, in which σ_{xy} is proportional to magnetization [47–49]. These conventional theories expect that σ_{xy} should behave as a monotonic function of magnetic field. However, in contrast to them, the coupling to background magnetic structure leads to fertile behaviors of Hall response.

Then, which type of magnetic structure leads to finite Hall response? We would like to start with a simple criterion to identify the magnetic structure which **does not** contribute to finite Hall conductivity. To start with, the Hall conductivity σ_{xy} connects electric current $\mathbf{J}$ and electric field $\mathbf{E}$, as $J_x = \sigma_{xy} E_y$. Under time-reversal operation, these quantities transform like $J_x \to -J_x$ and $E_y \to E_y$. As to the Hall conductivity itself, if time-reversal symmetry is preserved for a system, any observables should not change under this operation, hence $\sigma_{xy} \to \sigma_{xy}$. This means that σ_{xy} has to be identically zero, if time-reversal symmetry is preserved.

In fact, more strict condition has to be satisfied to obtain finite Hall conductivity. If time-reversal + finite spatial translation maps the system into itself, the Hall conductivity will be absent. This is almost obvious, since a slight translation never changes macroscopic response of the system. This extended criterion is, however, quite useful to judge whether the Hall conductivity is finite or not, given a certain magnetic structure. For example, in the antiferromagnet on square lattice, obviously time-reversal + translation by one lattice space maps the system into itself (Fig. 13.3a). Consequently, the Hall conductivity must be zero.

To check with this criterion, a convenient quantity is the spin scalar chirality, $\mathbf{S}_1 \cdot (\mathbf{S}_2 \times \mathbf{S}_3)$, defined for spin triplet, $(\mathbf{S}_1, \mathbf{S}_2, \mathbf{S}_3)$ (Fig. 13.3b). This quantity takes finite value for non-coplanar magnetic ordering, and reverses its sign under time-reversal operation. This means that the uniform ordering of spin scalar chirality guarantees that a system avoids the "no-go theorem". In fact, finite Hall response has been reported for magnetic structure with uniformly ordered spin scalar chirality [43, 44].

Given that this no-go theorem does not hold for a certain magnetic structure, how can one evaluate the Hall conductivity quantitatively? The Hall conductivity can be obtained through the Kubo formula,

$$\sigma_{xy} = \frac{i}{N} \sum_{m,m'} \frac{f(E_{m'}) - f(E_m)}{E_m - E_{m'}} \frac{\langle m|J_x|m'\rangle\langle m'|J_y|m\rangle}{E_m - E_{m'} + \frac{i}{\tau}}. \tag{13.11}$$

$|m\rangle$ and E_m are the mth one-particle eigenstate and corresponding eigenenergy of the Hamiltonian (13.1) (with fixed spin configuration), J_ν is the current operator in ν direction, and $1/\tau$ is a phenomenologically introduced damping rate due to non-magnetic impurities.

If the magnetic structure has a periodic spatial pattern, the formula (13.11) can be rewritten as an integral of Berry curvature, $B_z(\mathbf{k})$ over the Brillouin zone. At zero temperature,

$$\sigma_{xy} = \frac{e^2}{h} \frac{1}{N} \sum_{\mathbf{k}} B_z(\mathbf{k}), \qquad \mathbf{B}(\mathbf{k}) = \sum_{n\in \mathrm{occ}} \nabla_k \times \frac{1}{i} \langle \psi_{\mathbf{k}}^{(n)} | \nabla_k | \psi_{\mathbf{k}}^{(n)} \rangle, \tag{13.12}$$

where the $|\psi_{\mathbf{k}}^{(n)}\rangle$ is the one-particle electron wave function with momentum, $\mathbf{k}$, in the nth band. ∇_k is the gradient in the momentum space, and $\sum_{n\in \mathrm{occ}}$ is the summation over the occupied bands. $\mathbf{B}(\mathbf{k})$ is called Berry curvature, and its structure determines the Hall conductivity as a function of electron density. In particular, this expression shows that if the system is insulating, i.e., the chemical potential is within a gap, the Hall conductivity is quantized to be the integer multiple of e^2/h.

If the magnetic structure does not have a periodic pattern, the analysis of σ_{xy} will be more involved. However, in the perturbative regime as to J/t and $J\tau$, one can expand the equation (13.11), and the Hall conductivity can be written as a weighted summation of spin scalar chirality [53]:

$$\sigma_{xy} = \sum_{(i,j,k)} g_{ijk} (\mathbf{S}_i \times \mathbf{S}_j) \cdot \mathbf{S}_k. \tag{13.13}$$

Here, the summation is taken over any triplets of spins, as shown in Fig. 13.4. The weight g_{ijk} is anti-symmetric with respect to the site indices, i, j, and k, and decays as site i, j and k are separated. The formula (13.13) means that third-order scattering process contributes to finite Hall response at the lowest order. This comes from the fact that itinerant electrons acquire different phases between two scattering processes: $i \to j \to k$ and $i \to k \to j$. This is a remnant of Berry phase effect introduced in (13.10): the magnetic structure imposes a path-dependent phase on the electron wave function, leading to Aharonov-Bohm effect. This picture holds even in the weakly interacting regime, and leads to finite Hall response.

This picture naturally explains the τ dependence of the coefficients, g_{ijk}: if $t\tau$ is small, only the nearby spin triplets contribute to σ_{xy}, (e.g. triplets with $m = 3$, compared with $m = 9$ in Fig. 13.4b). For the phase difference between paths to make

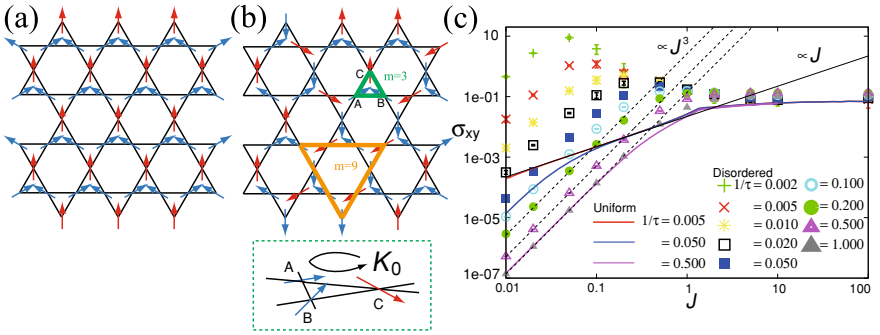

Fig. 13.4 The crossover of Hall conductivity from real-space picture to the momentum-space picture on the basis of the kagome ice model. One of the **a** uniformly ordered and **b** disordered spin configuration on a kagome lattice. The spins take non-coplanar configurations, as shown at the bottom of (**b**). The closed graphs used in the expansion (13.13) are depicted in (**b**) for the total path lengths of $m = 3$ and 9. **c** The J dependence of Hall conductivity, obtained by applying Kubo formula (13.11) to the Kagome ice model for the system size: 32×32 unit cells at $n \sim 0.1$, both for the **a** uniform and **b** disordered configurations. For the disordered case, sample average is taken for 100 configurations. In the disordered case, for $J\tau \ll 1$, σ_{xy} scales as $\sigma_{xy} \propto J^3$, while converges to a constant value for $J \gg t$. Meanwhile in the uniform case, $\sigma_{xy} \propto J^3$ for $J\tau \ll 1$, $\sigma_{xy} \propto J$ for $\frac{1}{\tau} \ll J \ll t$, and $\sigma_{xy} \sim Const.$ for $J \gg t$. Figures adapted from [64] with permission from the American Physical Society

sense, an electron has to keep its phase without being scattered by nonmagnetic impurities, during the third-order scattering.

In Fig. 13.4c, we plot σ_{xy} obtained from the general Kubo formula (13.11) for the ordered (Fig. 13.4a) and disordered (Fig. 13.4b) non-coplanar configurations of magnetic moments [64]. For both configurations, $\sigma_{xy} \propto J^3$ is obtained for small J. This scaling breaks down at $J\tau \sim 1$ or $J/t \sim 1$, and in particular, for ordered configurations, $\sigma_{xy} \propto J$ is obtained for $\frac{1}{\tau} \ll J \ll t$ [54, 64], indicating σ_{xy} is described by the momentum space picture, (13.12). For $J \gg t$, σ_{xy} takes almost a constant value, where the system is described by strong-coupling effective Hamiltonian, $\mathscr{H}_{\mathrm{DE}}$.

13.4 Itinerant Spin Ice

Equipped with the basic knowledge we have introduced so far, now, we would like to tackle on the itinerant spin ice. This setting is actually realized in pyrochlore oxides, $Pr_2Ir_2O_7$. Also the signature of 2-in 2-out type spin ice correlation is observed at high temperature region of $Nd_2Ir_2O_7$. We would like to start with a brief summary of experimental results of these compounds. For detailed introduction of these materials, and more generally, a family of compounds, $Ln_2Ir_2O_7$ (Ln =rare earth), See the Chap. 14.

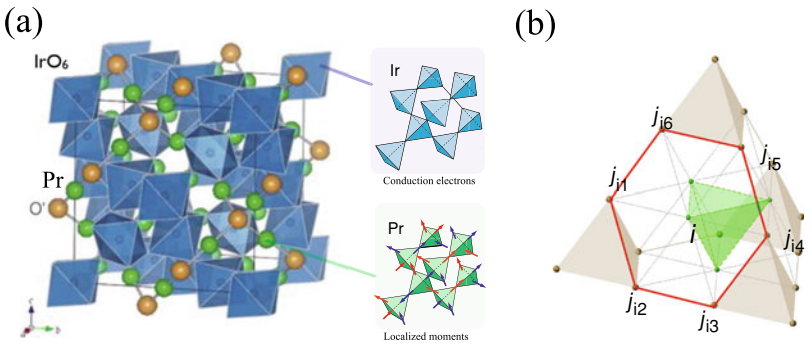

Fig. 13.5 **a** The crystal structure of $Ln_2Ir_2O_7$ (Ln = rare earth), which includes $Pr_2Ir_2O_7$ as one of the members. The green balls are Ln ions, while the blue objects stand for the IrO_6 octahedra. If only the Ir ions are connected, it gives a pyrochlore lattice. Similarly, Ln ions constitute another pyrochlore network, i.e., $Ln_2Ir_2O_7$ is composed of two interpenetrating pyrochlore lattices. Localized magnetic moments exist on the Ln pyrochlore network, except for Ln = Eu and Sm. **b** Relative configuration of Ln and Ir ions. One Ir ion (located at site i) is surrounded by six Ln ions (at $j_{i1} \cdots j_{i6}$), and vice versa

13.4.1 Brief Summary of Experiments

The crystal structure of $Pr_2Ir_2O_7$ is shown in Fig. 13.5. This compound is a member of a more general class of materials, $Ln_2Ir_2O_7$. In this compound, Ir ions and Pr ions constitute pyrochlore networks separately, and the two pyrochlore lattices interpenetrate with each other. Each Ir (Pr) ion is located in the center of hexagonal ring of Pr (Ir) pyrochlore lattice, and is surrounded by six Pr (Ir) ions, respectively.

As to the electronic state of this compound, the 5d orbitals of Ir ions form a conduction band, according to the first-principle calculation [55, 56]. These calculations also shows that only a small number of carriers exist in this system, which is estimated to be less than 2% of total number of Pr ions, consistent with the observed value of the normal component of the Hall coefficient. Furthermore, it was recently proposed by photoemission spectroscopy measurement that the Fermi level is located at quadratic band touching point [57].

On the other hand, the electrons originated from the f-orbitals of Pr ions are well localized. A well-defined magnetic moment of 3.0 Bohr magneton exists in Pr sites. The local ground state levels are formed by the non-Kramers Ising doublet with dominant components of total angular momentum $J = 4$ [58]. The easy axes of Ising moments are parallel to the direction connecting the centers of neighboring tetrahedra, which is an important prerequisite for the formation of spin ice.

Inelastic neutron scattering also gives information on local excited levels. For Pr ions, the first excited states are separated by 160 K from the lowest level. This level splitting is larger, compared with the energy scale of interaction between magnetic moments, which is estimated to be $\sim$20 K, from Curie-Weiss temperature. So, the

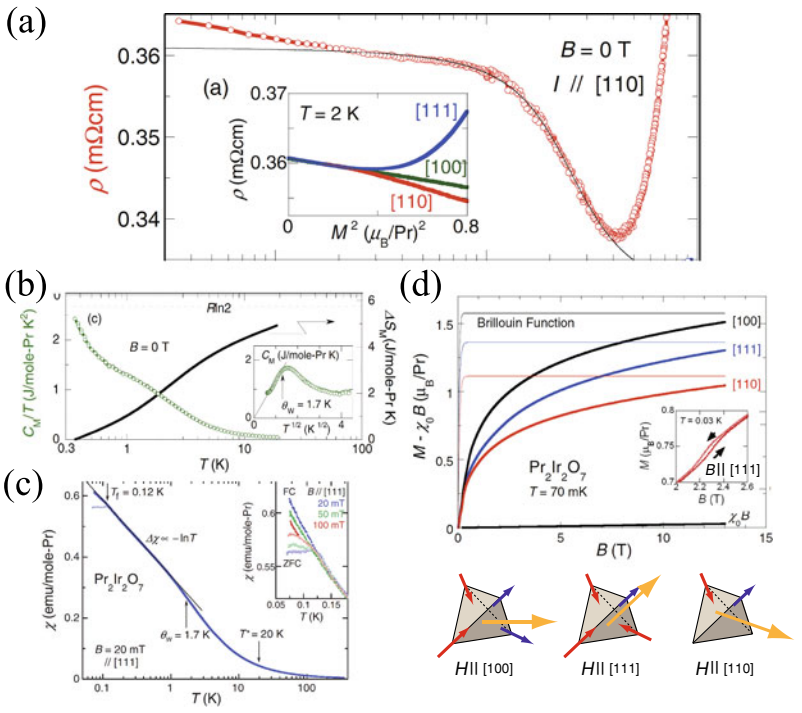

Fig. 13.6 **a** The temperature dependence of electrical resistivity of $Pr_2Ir_2O_7$. The inset shows the magneto-resistivity for three field directions, [100], [110], and [111]. **b** The specific heat **c** The magnetic susceptibility, and **d** Magnetization process for the three field directions. The relative relations between the field directions and orientation of tetrahedra are schematically shown. Figures reprinted from [7] with permission from the American Physical Society

local excited states can be safely neglected and Pr magnetic moment is well described as a classical two-component Ising spin.

Actually, the strong Ising anisotropy of magnetic moments can be confirmed also in the magnetization process. Magnetization curve is strongly dependent on the field direction. In particular, at high magnetic fields, the magnetization approaches different saturation values depending on the field directions. For example, if magnetic field is applied in the [111] direction, the magnetization approaches the half of full moment for large magnetic field, as shown with the blue horizontal line in Fig. 13.6d, as is expected from the strong easy-axis anisotropy. For other field directions, the magnetizations approach the saturation values expected for Ising limit at each field directions. In other words, these data provide the firm evidence that Pr magnetic moments behave as Ising moments with strong anisotropy.

However, do these Ising moments truly lead to the formation of spin ice? Signatures of spin ice formation can be seen in the thermodynamic behavior of this compound. Firstly, as shown in Fig. 13.6c, the magnetic susceptibility, χ is well fitted with Curie-Weiss law at high temperature region, with Curie-Weiss temper-

ature, $\theta_{CW} \sim -20\,K$. However, as decreasing temperature, χ shows no singularity much below the temperature scale given by $|\theta_{CW}|$. χ only shows slight bifurcation at 0.12 K, implying the freezing. The absence of phase transition is also obvious in specific heat, C (Fig. 13.6b), for which the measurement was recently extended down to 0.3 K, however, C shows no singularity down to this lowest temperature [59].

The close inspection of these quantities reveals several evidence in support of the development of spin ice correlation. As shown in Fig. 13.6b, C/T becomes enhanced as decreasing temperature, showing $C \propto \sqrt{T}$ behavior. This enhancement suggests that a large amount of entropy remains unreleased at low temperatures implying the spin ice degeneracy. Moreover, χ does not show any saturation at low temperatures, as well as it shows no divergence. As decreasing temperature, χ simply continues to go up, suggesting that the system remains a cooperative paramagnet. These features give indirect, but rather convincing evidence that spin-ice-like states are realized at low temperature regions.

Then, how does the enhanced spin ice correlation affect the transport properties of this system? In this compound, several unusual transport phenomena have been reported. The first is resistivity minimum. As shown in Fig. 13.6a, the resistivity shows quite non-monotonic behavior in this compound, taking minimum around 40 K and shows upturn below that temperature. At low temperatures, negative magnetoresistivity is also observed. What brings about this resistivity minimum?

One of the well-known mechanism which causes resistivity minimum, is Kondo effect [60]. As lowering temperature, itinerant electrons and a magnetic impurity tend to form a spin singlet, which leads to stronger scattering effects, resulting in a resistivity upturn. In addition to the resistivity minimum, however, Kondo effect gives rise to several characteristic features in thermodynamic quantities, which seem to contradict the experimental data of $Pr_2Ir_2O_7$. As to specific heat, if Kondo effect happened, there would be a peak around the temperature of the resistivity minimum, since the entropy release due to spin-singlet formation should leave a signature in the specific heat. However, in $Pr_2Ir_2O_7$, there is no feature in specific heat around the temperature of resistivity minimum, 40 K. There is a peak around 2 K, but this temperature is too low, compared with 40 K. Secondly, magnetic susceptibility should saturate and takes a finite value at low temperatures, if Kondo effect takes place. However, there is no saturation, and the susceptibility continues to increase much below the temperature of resistivity minimum. This also contradicts the typical Kondo behavior. Considering these discrepancies, Kondo effect seems quite unlikely as an origin of the resistivity minimum.

Another transport quantity, which shows anomalous behavior, is the Hall conductivity. In conventional theory of metallic transport, the Hall conductivity should behave as a monotonic function of magnetic field, as noted in Sect. 13.3.5. In $Pr_2Ir_2O_7$, however, the Hall conductivity is anisotropic, and shows highly non-monotonic behavior (Fig. 13.7a). Obviously, this Hall conductivity cannot be explained by conventional mechanisms.

The most striking phenomenon observed in this system is the spontaneous Hall effect. In order to obtain finite Hall signal, one usually needs to apply a magnetic field, or the system needs to develop finite magnetization. To be precise, time-reversal

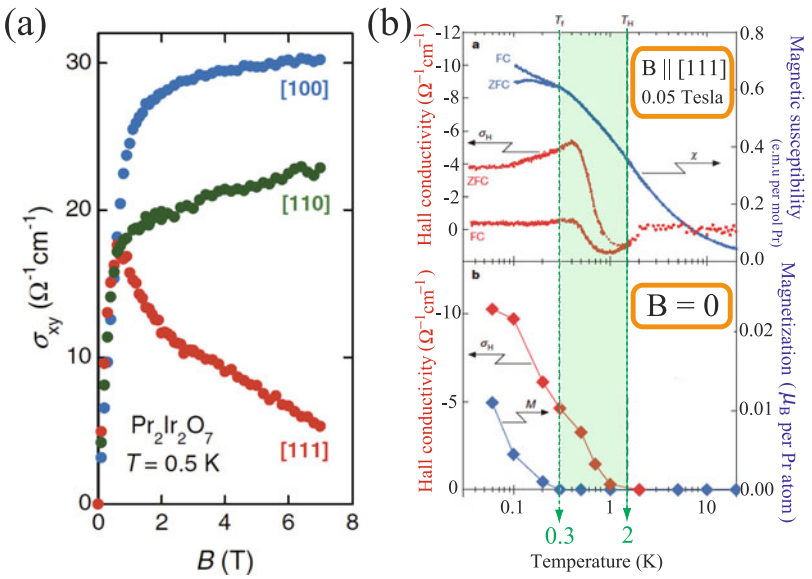

Fig. 13.7 **a** Magnetic field dependence of Hall conductivity, σ_{xy}, of $Pr_2Ir_2O_7$ for [100], [110], and [111] field directions, reprinted from [8] with permission from the American Physical Society. **b** The T dependence of Hall conductivity, σ_H is shown. (Upper) σ_H is plotted, together with the magnetic susceptibility, χ for field cooling and zero field cooling condition for $B \parallel [111]$ at 0.05 T. (Lower) σ_H and magnetization M are plotted at zero magnetic field, which are obtained by setting the system at 7 T for $B \parallel [111]$ at first, and by removing the field. In the shaded region, even after removing the magnetic field, σ_H shows finite value, while M drops to zero, i.e. the spontaneous Hall effect is observed. Figure adapted from [9] with permission from Nature

symmetry must be broken as a prerequisite for the finite Hall response, as we noted in Sect. 13.3.5. And, in most cases, external magnetic field or magnetization are responsible for broken time-reversal symmetry.

However, this compound exhibits finite Hall signal at zero magnetic field, even in the absence of magnetization [9]. To describe the experimental setting more clearly, suppose the system is placed in the magnetic field of 7 T, in the first place. Then you decrease magnetic field gradually to zero, and for this temperature range, from 0.3 to 2.0 K, Hall conductivity shows hysteresis, and exhibits finite value even at zero magnetic field, meanwhile the magnetization behaves continuously, and drops to zero at vanishing magnetic field (Fig. 13.7b). So, in this temperature range, even after the magnetic field is removed, the system remains time-reversal broken, however, without net magnetization. What is the hidden origin, which breaks the time-reversal symmetry?

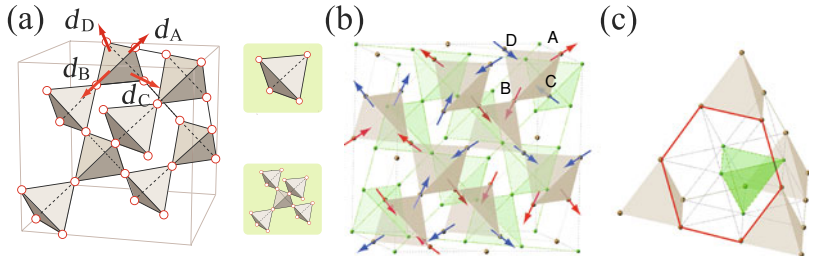

Fig. 13.8 **a** A pyrochlore lattice shown with sublattice-dependent easy axes, $\mathbf{d}_\alpha$ (α = A, B, C, D). Schematic picture of 4- and 16-site clusters used in CDMFT are also shown. **b** The double pyrochlore lattice. On gold tetrahedra, localized moments reside, as shown with arrows, meanwhile itinerant electrons are defined on the green tetrahedra. **c** A tetrahedron for itinerant electrons, surrounded by a quartet of tetrahedra for localized moments. A site on one tetrahedron is surrounded by six sites on the other tetrahedra, as shown with thick red hexagon

13.4.2 *Theoretical Formulation with Classical Kondo Lattice Model*

The Ising Kondo lattice model provides a good starting point to account for the thermodynamic and transport properties of $Pr_2Ir_2O_7$. Here, we introduce a series of theoretical works to address this system from this viewpoint. This is a variant of classical Kondo lattice model introduced in equation (13.1), which we write in a generalized form:

$$\mathscr{H} = -t \sum_{\langle i,j\rangle,s} (c^\dagger_{is} c_{js} + \text{H.c.}) - \sum_{i,s,s'} c^\dagger_{is} \boldsymbol{\sigma}_{ss'} c_{is'} \cdot \mathbf{h}_i . \tag{13.14}$$

Here, $\mathbf{h}_i$ means the effective field coupled to itinerant electrons at site i, originating from the localized moments, $\{\mathbf{S}_j\}$.

We consider this Hamiltonian on two types of lattices shown in Fig. 13.8. One is the pyrochlore lattice (Fig. 13.8a), and we take $\mathbf{h}_i = J\mathbf{S}_i$, i.e., electrons couple to the localized moments at the same site. To reflect the strong Ising nature of Pr moments, we set $\mathbf{S}_i = \eta_i \mathbf{d}_\alpha$ ($\eta_i = \pm 1$, α =A, B, C, D), assuming that $\mathbf{S}_i$ is an Ising moment with anisotropy axis, $\mathbf{d}_\alpha$, with i, belonging to the sublattice α (Fig. 13.8a).

Alternatively, we can define the Hamiltonian on "double pyrochlore lattices", faithful to the crystal structure of $Pr_2Ir_2O_7$ (Fig. 13.8b). In this case, we distinguish the two pyrochlore lattices which itinerant electrons and localized moments belong to, respectively. As the effective field, $\mathbf{h}_i$, we most naturally adopt the form: $\mathbf{h}_i = J \sum_{k\in \text{n.n.of } i} \mathbf{S}_k$, i.e. the sum of six surrounding sites of site i (Fig. 13.8c). For this choice, we also set $\mathbf{S}_k = \eta_k \mathbf{d}_\alpha$ ($\eta_k = \pm 1$), to assume that $\mathbf{S}_k$ is an Ising moment with [111] easy axes.

This model has been studied with various methods we have introduced in this chapter [61, 64, 65, 78]. Among them, CDMFT provided a coherent description of the phase diagram, thermodynamic and transport quantities. In this problem, in

particular, a mapping to 4- and 16-site clusters was used to obtain reliable information, as well as check the cluster-size dependence of the obtained results [61, 65].

As to the determination of magnetic ordering patterns, however, CDMFT has its own limitation due to the tractable cluster size. For this problem, Monte Carlo simulation has given more reliable results. While CDMFT can treat up to 16-site magnetic unit cell, the Monte Carlo method enables to analyze ordering structure with longer period. In fact, existence of up-to-32-site magnetic order was identified for this model [78], as we introduce later.

Accurate description of Hall conductivity requires an analysis of a larger-size system, even compared with the maximal size one can treat with Monte Carlo method. Due to this size limitation, the perturbative method was adopted, combined with the effective spin model for localized moments. In this scheme, spin scalar chirality distribution was sampled with Monte Carlo simulation for effective classical spin model, and the obtained information is used as an input to the formula (13.13) to obtain Hall conductivity [64].

13.4.3 Comparison with Experiments

In this section, we aim at explaining the experimental data of $Pr_2Ir_2O_7$ in a unified way, starting from the Hamiltonian (13.14), mainly on the basis of CDMFT.

Phase Diagram

To start with, we show the phase diagram, in terms of J and n, obtained by CDMFT, in Fig. 13.9. Here, we plot the transition temperatures to ordered states. In the dilute region, the $\mathbf{q} = 0$ ordering of 2-in 2-out tetrahedra takes place, while in higher density region, $n \sim 0.5$, the all-in all-out tetrahedra make the $\mathbf{q} = 0$ order. In the intermediate density region, we cannot find any ordering down to low temperature 0.001 t in CDMFT. The absence of ordering is partly due to the limitation of cluster size available in CDMFT, i.e., only the magnetic order accommodated in the adopted size of cluster can be tractable. The stability of the above two phases were, however, also confirmed by extensive Monte Carlo simulation, in similar regions of J and n [66]. The Monte Carlo analysis revealed two more phases, the $\mathbf{q} = [0, 0, 2\pi]$ order of 2-in 2-out tetrahedra, which is the same ordering pattern as that found for the dipolar spin ice model [67], and a 32-site magnetic order, in the intermediate density, where no order was obtained by CDMFT. These two phases have too large magnetic unit cells to be treated in CDMFT, in which up to 16-site cluster was examined.

How can we understand the structure of this phase diagram? For this purpose, the three energy scales: transition temperature (T_c), Curie-Weiss temperature (T_{CW}), and the nearest-neighbor (n.n.) component of RKKY interaction (J_{RKKY}), are compared at each particle density, in Fig. 13.9b. Let us first discuss the behavior of T_{CW}, which is obtained by fitting the inverse of magnetic susceptibility as $\chi^{-1} = \frac{1}{C}(T - T_{\mathrm{CW}})$

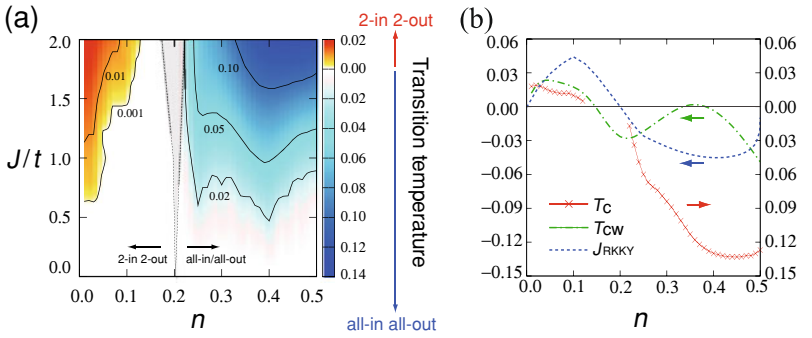

Fig. 13.9 **a** The transition temperature in terms of electron density (n) and the exchange coupling (J). The thin dashed lines show the phase boundaries at $T = 0$. The gray area means the region where phase separation takes place. **b** n dependences of the nearest-neighbor component of RKKY interaction (J_{RKKY}), Curie-Weiss temperature (T_{CW}), and T_c obtained at $J = 2$. T_c is plotted above (below) the horizontal line at 0.00 for two-in two-out (all-in/all-out) order. Figures reprinted from [61] with permission from the American Physical Society

at $0.5 < T/t < 1.0$. As is clear from this plot, T_{CW} has small correlation with T_c. In particular, at higher density region, while T_{CW} is nearly equal to zero, or even slightly positive, the magnetic order has antiferromagnetic tendency (all-in/all-out, in this case). This discrepancy may be attributed to the long-range nature of RKKY interaction: T_{CW} is determined by summing up all the long-range components of the RKKY interaction, however, the sign of n.n. interaction is dominant in the determination of ordering patterns.

In fact, J_{RKKY} shows a good correlation with T_c, as is shown in Fig. 13.9b. J_{RKKY} is estimated from the non-interacting band structure (at $J = 0$). It is ferromagnetic (antiferromagnetic) in the low (high) density region, well consistent with the ordering pattern. The sign of J_{RKKY} can be understood from the relation of $\chi_0(\mathbf{q})$ and the shape of Fermi surface, mentioned in Sect. 13.5. $\chi_0(\mathbf{q})$, as a function of wave vector, $\mathbf{q}$, shows strong enhancement, if $\mathbf{q}$ transverses the Fermi surface. Accordingly, in the small density region, $\chi_0(\mathbf{q})$ takes large value at smaller $|\mathbf{q}|$, which transverses small Fermi surface, i.e. the RKKY interaction is nearly ferromagnetic. As a result, the 2-in 2-out order is favored in this region. Similar result is obtained by the analysis assuming spherical Fermi surface [68]. Meanwhile, as the particle density is increased, the Fermi volume increases. This leads to the enhancement of $\chi_0(\mathbf{q})$ at large $|\mathbf{q}|$, resulting in antiferromagnetic tendency in RKKY interaction, which stabilizes all-in/all-out type order.

Suppression of Magnetic Order

The remarkable feature of this phase diagram is the asymmetry of transition temperatures. For all-in/all-out ordering, the transition takes place around $T \sim 0.1t$. Mean-

while for 2-in 2-out ordering, the T_c is $\sim 0.01t$, one order of magnitude smaller. In the first place, this asymmetry of the transition temperatures is ascribed to the stability of high-temperature paramagnetic phase. For small n, the 2-in 2-out correlation already starts growing at high temperature, accompanying a huge degeneracy. As a result, the associated large entropy stabilizes the paramagnetic phase, leading to the suppression of the transition temperature.

The second reason is a somewhat unexpected protection mechanism of spin ice against the short-ranged perturbation. At first sight, the massive degeneracy of spin ice implies extreme fragility against external perturbations. However, it is well known that the mechanism called "projective equivalence" protects spin ice from long-ranged dipolar interaction in $Ho_2Ti_2O_7$ and $Dy_2Ti_2O_7$ [69]. Surprisingly, it turns out that spin ice is similarly protected from short-ranged perturbations [62].

For small J, the localized moments interact with each other, through the RKKY interaction, and its effective Hamiltonian may be written as

$$\begin{aligned}\mathscr{H}_{\text{eff}}[J_1, J_2, J_3] &= \tilde{J}_1 \sum_{n.n.} \mathbf{S}_i \cdot \mathbf{S}_j + \tilde{J}_2 \sum_{2nd.} \mathbf{S}_i \cdot \mathbf{S}_j + \tilde{J}_3 \sum_{3rd.} \mathbf{S}_i \cdot \mathbf{S}_j \\ &= J_1 \sum_{n.n.} \eta_i \eta_j + J_2 \sum_{2nd.} \eta_i \eta_j + J_3 \sum_{3rd.} \eta_i \eta_j, \end{aligned} \tag{13.15}$$

with truncating the long-ranged exchange couplings further than 3rd neighbors. Actually, this effective Hamiltonian rather faithfully reproduces the phase diagram obtained with Monte Carlo simulation fully taking account of the effect of itinerant electrons [62].

This form of Hamiltonian, surprisingly, turns out to preserve the spin ice state as the ground state, even in the presence of 2nd- (J_2) and 3rd-neighbor (J_3) exchanging couplings, if $J_2 = J_3 \equiv J'$ is satisfied, in an analogous way to projective equivalence, as detailed in Chap. 3. This stability can be proved [62] by rewriting the Hamiltonian (13.15) in the charge representation [89], or by noting that the exchange matrix of $\mathscr{H}[J, J', J']$ can be expressed as a polynomial of the nearest-neighbor Hamiltonian, $\mathscr{H}[J, 0, 0]$: $\mathscr{H}[1, J', J'] = \frac{J'}{2}(\mathscr{H}[1, 0, 0])^2 + (1 - 2J')\mathscr{H}[1, 0, 0] - 3NJ'$. This polynomial expression shows that the 2nd- and 3rd-neighbor perturbations are essentially proportional to $(\mathscr{H}[1, 0, 0])^2$, which can be minimized simultaneously with the nearest-neighbor Hamiltonian, $\mathscr{H}[1, 0, 0]$, by assuming the spin ice ground state, for moderately small J'. In other words, the relevant perturbation to spin ice is given by the energy scale, $|J_2 - J_3|$, which might be smaller than J_2 or J_3 themselves. This fact may underlie the stability of spin-ice-like state in $Pr_2Ir_2O_7$, as well as the canonical spin ice, $Ho(Dy)_2Ti_2O_7$.

The combination of two reasons suppress the transition temperature at low density, and makes this region quite interesting. In Fig. 13.10b, we show the fraction of 2-in 2-out tetrahedra at $J = 1.0$ and $n = 0.05$. At this density, ordering does not happen down to temperature equal to 0.001t. Nevertheless, 2-in 2-out short-range correlation starts to develop at some higher temperature, and the fraction of 2-in 2-out tetrahedra reaches almost 100%, close to absolute zero, even in the absence of long-range

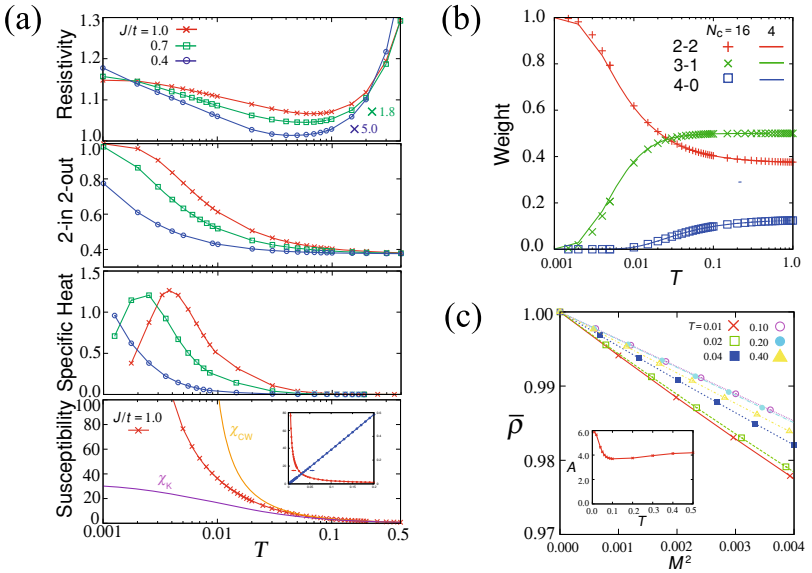

Fig. 13.10 **a** Temperature dependences of resistivity ρ, the rate of 2-in 2-out configuration, specific heat, and magnetic susceptibility, from top to bottom. The data are obtained at $n = 0.05$ by CDMFT with 4-site cluster. ρ is measured in unit of $h/8\pi e^2$, where h is the Planck constant and e is the elementary electronic charge. For comparison, the data for $J = 0.7$ and 0.4 are multiplied by 1.8 and 5.0, respectively. In the plot of χ, the Curie-Weiss fitting $\chi_{\rm CW}$ and "Kondo" susceptibility $\chi_{\rm K}$ are shown for comparison. The inset of the bottom figure shows the plot of χ and χ^{-1} in the linear T scale. Figures reprinted from [61] with permission from the American Physical Society. **b** The temperature dependence of the rate of 2-in 2-out, 3-in 1-out/1-in 3-out and all-in/all-out configurations at $n = 0.05$ and $J = 1.0$. Figure reprinted from [61] with permission from the American Physical Society. **c** The magneto-resistivity scaled at its zero-field value, $\bar{\rho}(H) = \rho(H)/\rho(H = 0) = 1 - AM^2 + \cdots$. The inset shows the temperature dependence of the quadratic coefficient, A. Figure reprinted from [65] with permission from World Scientific Publishing Co

ordering. So, in this broad temperature range, conduction electrons interact with enhanced spin ice correlation.

Resistivity Minimum

The growing spin ice correlation evidently affects the transport properties of the system. In Fig. 13.10a, we show the temperature dependence of resistivity, together with several thermodynamic quantities. Resistivity goes down from high temperature as in normal metals, and takes a minimum at $T = T^* \sim 0.1t$, with successive upturn towards lower temperatures. Roughly speaking, the resistivity takes minimum around the temperature where the 2-in 2-out short-range correlation starts to develop, i.e. the enhanced spin correlation acts as a rather stronger scatterers for electrons, resulting in

resistivity upturn at low temperatures. The relation between the resistivity minimum and the enhanced spin ice correlation is also discussed in the context of its cousin compound, $Nd_2Ir_2O_7$ [70]. Accordingly, the magneto-resistivity becomes negative, insensitive to the magnetic field direction, as shown in Fig. 13.10c. This behavior is reasonable, since the magnetic field aligns 2-in 2-out tetrahedra, and reduces scattering. In fact, the normalized resistivity, $\bar{\rho} \equiv \rho(H)/\rho_0$, scaled with the zero-field resistivity at each temperature, ρ_0, can be well fitted with the square of magnetization, as $\bar{\rho} = 1 - A(T)M^2$, and its coefficient $A(T)$ shows uprise around $T = T^* \sim 0.1t$, below which the resistivity shows upturn, together with the enhancement of spin ice correlation.

While the growing spin ice correlation leads to the resistivity minimum, as discussed above, how is this scenario compatible with other thermodynamic quantities? As regards the Kondo effect, we found obvious discrepancies with experimental data as noted in Sect. 13.4.1: one is that the peak of specific heat is located at much lower temperature compared with resistivity minimum, and the other one is a diverging magnetic susceptibility.

Firstly, as to specific heat, we actually obtain the peak at much lower temperature than resistivity minimum, as shown in Fig. 13.10a. While the resistivity takes minimum around the temperature where the spin ice correlation starts to develop, the specific heat shows a peak when the spin ice correlation saturates. Or more precisely, where the weight of 2-in 2-out tetrahedra has an inflection point, in the sense that entropy release is maximized at this point. These two energy scales: starting point and saturation of spin ice correlation can be considerably different. Moreover, in contrast to the Kondo-like susceptibility, T_K, the obtained magnetic susceptibility shows diverging behavior, consistent with experiment (Fig. 13.10a). This behavior can also be understood by considering that spin ice is a sort of cooperative paramagnet.

Hall Response

At low temperatures, the enhanced spin ice correlation affects the Hall response, considerably. Roughly speaking, we have two main problems as to the Hall response in $Pr_2Ir_2O_7$. Firstly, how can one account for the anisotropic and non-monotonic magnetic field dependence of Hall conductivity? And secondly, what is the origin of spontaneous Hall effect?

Regarding the first question, the conventional theories obviously cannot account for the non-monotonicity of Hall conductivity, as is noted in Sect. 13.4.1. One possible mechanism is the effect of spin scalar chirality discussed in Sect. 13.3.5. In particular, the spin ice forms a non-trivial spin scalar chirality distribution, due to its site-dependent anisotropy axes, which may affect the motion of itinerant electrons, and bring about nontrivial Hall response.

To describe the effect of spin scalar chirality on the Hall conductivity, one has to describe the direction of local field, $\mathbf{h}_i$ in the Hamiltonian (13.14), precisely. Accordingly, we consider the double pyrochlore lattice instead of the single one, faithful to the crystal structure of $Pr_2Ir_2O_7$. Another crucial point is that the spatial

distribution of spin scalar chirality has to be taken into account accurately. For this purpose, we give up CDMFT due to its inadequacy to consider spatial correlation, and adopt a phenomenological analysis based on the effective spin model. Firstly, considering the spin ice correlation is sufficiently developed at low temperatures, we adopt the effective nearest-neighbor spin Hamiltonian $\mathscr{H}_{\rm eff}[J_{\rm spin}, 0, 0]$ in (13.15), and generate the spin configuration by classical Monte Carlo simulation by introducing a phenomenological temperature, $T_{\rm eff}$, which describes the partial violation of spin ice state due to the long-range component of RKKY interaction. Then, we couple the generated spin configuration to itinerant electrons, by inserting it into the local field, $\mathbf{h}_i$, in the Ising Kondo lattice Hamiltonian (13.14). For the calculation of Hall conductivity $\sigma_{\rm H}$, the small exchange coupling in $Pr_2Ir_2O_7$, inherent in rare-earth systems, allow us to use the third-order perturbation formula given in (13.13), for a large-size system. This strategy is based on the separability of classical Kondo lattice model, which is useful to construct a phenomenological model by extracting the information of localized moments from reliable sources, as introduced in Sect. 13.3.5.

The result is plotted in Fig. 13.11b. Here, we consider only [100] and [111] field directions. For [110] direction, our phenomenological nearest-neighbor spin ice model does not work, since the semi-macroscopic degeneracy remains in the ground state, and further perturbation plays an important role in the ground state selection (see Chap. 5). However, for the other two directions, the calculation seems to reproduce the experiential result, Fig. 13.7a, quite well.

Firstly, for small magnetic field, $\sigma_{\rm H}$ has the same value irrespectively of the field direction. This should be attributed to the cubic symmetry of the system. If magnetic field is small enough to be within the linear response region, the Hall response should be isotropic, reflecting the cubic symmetry.

Secondly, at high magnetic field, $\sigma_{\rm H}$ takes different signs between $\mathbf{H} \parallel [100]$ and [111]. This sign reversal may be understood by assuming that only the spin scalar chirality defined for the smallest triangles contributes [8].

And thirdly, a conspicuous peak in the intermediate field range appears for [111] field. In fact, the [111] magnetic field provides a fertile research field for canonical spin ice, as discussed in detail in Chap. 5. Summarizing the main points here, as increasing magnetic field in [111] direction, firstly the spin ice state shows a crossover to the so-called kagome ice state, in which the spins on the triangular plane are aligned in the field direction, while letting the other spins on the kagome plane follow the ice rule [71]. This state persists for finite magnetic field regions, making the kagome ice plateau for $Dy_2Ti_2O_7$. Then as increasing the magnetic field further, the kagome ice state eventually surrenders to spin flip, and the fully polarized 3-in 1-out/1-in 3-out state takes over. These characteristic changes of spin state may affect the Hall response.

To make the connection between $\sigma_{\rm H}$ and these spin ice physics, the ratio of 2-in 2-out (P_{22}) and 3-in 1-out/1-in 3-out tetrahedra (P_{31}) , and the fraction of upward spins on the triangular plane ($P_{\rm triangle}$) are plotted in Fig. 13.11c. As is evident from the figure, the peak of $\sigma_{\rm H}$ corresponds to saturation of $P_{\rm triangle}$, which is an indicator of the spin-ice to kagome-ice crossover. In contrast, the sign reversal of $\sigma_{\rm H}$ roughly corresponds to the interchange of P_{22} and P_{31}, showing that the reversal can be

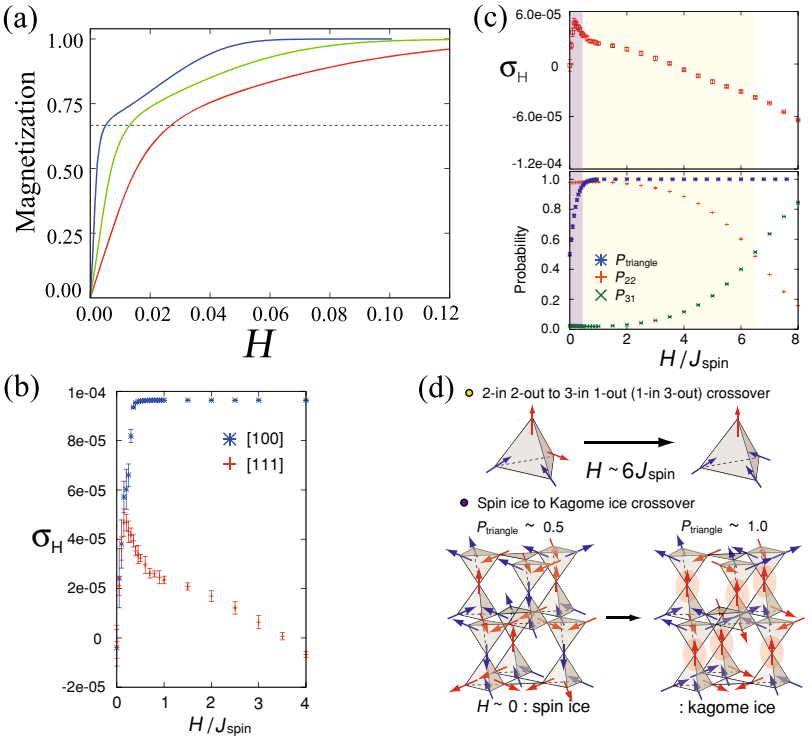

Fig. 13.11 **a** The magnetization curves for $T = 0.02$, 0.01 and 0.004 from bottom to top, obtained by CDMFT for the Hamiltonian (13.14), reprinted from [65] with permission from World Scientific Publishing Co. **b**, **c** The magnetic field dependence of Hall conductivity for **H** ∥ [100] and [111], obtained by phenomenological analysis (see the main text). **c** Shows the Hall conductivity in a wider field range, together with the rate of 2-in 2-out (P_{22}) and 3-in 1-out/1-in 3-out tetrahedra (P_{31}), and the fraction of upward spins on the triangular plane (P_{triangle}). Depending on the behavior of these quantities, the field range can be divided into three regions, as colored differently. **d** Schematic figures of (upper) the spin flip crossover from 2-in 2-out dominant state to 3-in 1-out/1-in 3-out state, and (lower) the spin ice to kagome ice crossover. Figures reprinted from [64] with permission from the American Physical Society

ascribed to the spin flip crossover to the saturated state (Fig. 13.11d). We note that this peak cannot be obtained in the analysis taking account only of the smallest triangles [64]. The spin scalar chirality from spatially extended spin triplets play a relevant role [64].

The relation of the peak and the spin ice to kagome ice crossover is rather surprising. The experimental magnetization curve (Fig. 14.16) is rather smooth, with only a kink-like weak singularity, in contrast to $Dy_2Ti_2O_7$, and this behavior is also reproduced theoretically by CDMFT (Fig. 13.11a). Nevertheless this result implies that the existence of peak in σ_H means substantial kagome ice correlation is developed at

the intermediate field range beyond the peak. It is desired to check this kagome ice correlation through a different experimental probe, such as neutron scattering.

Spontaneous Hall Effect

Another mystery concerning the Hall response, namely the spontaneous Hall effect, has stimulated many theorists and several proposals have been made as to its origin. Roughly speaking, these theories can be divided into two groups. Some people ascribe this phenomenon to the magnetic structure formed by Pr moments, while others seek the origin in the anomalous electronic band structure of this compound.

In the former group, Flint et al. proposed the scenario of ferromagnetic chirality ordering [72]. They derived the effective interaction between chirality degrees of freedom, by mimicking the RKKY interaction between magnetic moments. They suggested that this interaction leads to uniform chirality order at $\sim$1.5 K, below which the spontaneous Hall effect sets in, with a caveat that symmetry-allowed linear coupling between chirality and magnetization causes only a slight amount of uniform magnetization.

Lee et al. proposed another scenario based on the spatially modulated magnetic order [73]. They start from the effective pseudospin$-1/2$ model describing the interaction between ground state-doublets of Pr moments, and found that incommensurate pseudospin order is stabilized in a wide parameter region spanned by exchange coupling constants. By coupling to the pseudospin order, the modulated electronic state gives rise to substantial Hall response, however, with undetectably small magnetization.

In the latter group, Moon et al. proposed a quadratic band touching in the electronic state, as a possible origin of spontaneous Hall effect, combined with long-ranged Coulomb interaction [74]. Referring to the classic theory by Abrikosov [75, 76], they showed that the peculiar electronic state leads to the Hall conductivity sensitive to magnetic field: $\sigma_{xy} \propto H^{0.51}$, by renormalization group analysis, which may account for finite Hall response with undectectably small magnetization, as observed in the experiment. In fact, the recent fully-relativistic first-principle calculation based on LSDA $+U$ ansatz with non-collinear magnetization supports the existence of electronic structure with quadratic band touching in the weakly interacting region [56]. This band structure was also experimentally confirmed recently [57].

Despite all these efforts, however, the definite understanding has not been established for the spontaneous Hall effect. The theories in the former group relies on the existence of chirality/magnetic order. To justify these scenarios, it is crucial to detect these orders by, e.g. neutron scattering experiments, or at least by identifying the existence of sharp signals of phase transition in sufficiently clean samples free of broadening. The theories in the latter group proposed a fascinating story based on the exotic electronic state. However, σ_{xy} shows hysteresis, rather than $H^{0.51}$ behavior, still casting some doubts on the applicability of the theory. Theoretical breakthrough is still awaited for the understanding of this fascinating phenomenon.

13.5 Other Frustrated Itinerant Systems

In this section, we discuss several front-line topics associated with frustrated itinerant systems, and briefly introduce them. We note that the choice of topics is rather subjective. Due to the limitation of pages, we have to give up many important subjects.

13.5.1 Charge Ice

Ice rule is not an idea limited to spin ice, but can be defined for any Ising-like degrees of freedom defined on tetrahedra, or other complete graphs. In fact, ice rule comes from the polarization of hydrogen atom in ice. As another classic example, Anderson proposed that ice rule defined for charge degrees of freedom [1] plays an important role in the metal-insulator transition of Fe_3O_4 [77].

In the context of this "charge ice", it is interesting to consider the Falicov-Kimball model with ice-rule constraint, instead of the classical Kondo lattice model considered in this text. This problem may be regarded as a charge version of itinerant spin ice, which we considered in the previous section. In fact, this model and its equivalent models have been considered on a pyrochlore, checkerboard and kagome lattices, and its transport properties have been well studied [78–80]. Furthermore, it was found that this model is exactly solvable on a loopless variant of the pyrochlore lattice, a tetrahedron Husimi cactus [81]. With the exact solution, the ground-state phase diagram was found to involve two insulating regions separated by a quantum critical point (QCP) where the excitation gap closes. Moreover, novel non-Fermi liquid behavior is obtained right at the QCP, where the self-energy shows anomalous exponents.

13.5.2 Heavy Fermion Behavior

In geometrically frustrated systems represented by spin ice, a large amount of entropy sometimes remains unreleased down to very low temperatures, due to the macroscopic degeneracy in low-energy degrees of freedom. If this residual entropy is transferred to itinerant electrons, we could expect that electrons acquire a large effective mass. In Fermi liquid theory, electronic entropy S is proportional to temperature: $S \propto C = \gamma T$, and it is directly related to effective mass m^*, as $m^* \propto \gamma$.

In fact, heavy fermion behaviors are observed for LiV_2O_4 [2], Molybdates [5], and other frustrated conductors [3, 4]. The role of frustration in heavy-fermion behavior was also pointed out in the theoretical analysis [82]. Does the itinerant spin ice have heavy electrons? In fact, a large specific heat is observed for $Pr_2Ir_2O_7$ [7]. However, to show the large effective mass experimentally, one has to prove that the large entropy is associated with itinerant electrons, not localized moments, by observing e.g. a

sharp coherence peak with photoemission spectroscopy. Theoretical description of large electron mass also requires an involved analysis. The classical Kondo lattice model describes the many-body state only as a direct product of Slater determinant of itinerant electrons and one specific configuration of localized moments. In this description, the effective mass of electrons is given by a thermal average of that in each configuration, and accordingly, it remains more or less the same value as the non-interacting band mass. To describe the large effective mass, one needs to go beyond the classical Kondo lattice model by taking account of the quantum nature of the exchange coupling, which brings quantum coherency between the macroscopic number of direct product states. However, such an analysis inevitably needs treating a huge number of quantum states, which will be a formidable task.

13.5.3 Magnetic Chern Insulator and Dynamics

In Sect. 13.2, we discussed the stable magnetic structure in the classical Kondo lattice model, depending on the electron density and electronic structure. We further discussed the possibility of non-coplanar magnetic ordering, and associated quantized Hall response in the insulating phase. This magnetic Chern insulator is interesting as a variant of integer quantum Hall system, however, can one find essentially new physics beyond IQHE?

We would like to answer this question positively. The crucial difference between the integer quantum Hall system and magnetic Chern insulator is that while the former is induced by external magnetic field, the latter is caused by ordered magnetic moments. While the magnetic field is static external field, the magnetic moments have their own dynamics. Accordingly, one can expect that though there are little difference in the "static" properties like equilibrium Hall current, the dynamical properties should be considerably different between these two systems.

Indeed, the fluctuation of non-coplanar magnetic order can also show topological transport [83–85]. This may be understood as a bosonic analogy of itinerant electrons interacting with frustrated magnets, since the fluctuation around the ordered moments can be regarded as bosonic magnons coupled to the background ordered magnetic moments.

What is more, the topological defects of magnetic Chern insulator shows a quite non-trivial property. For instance, it is proposed that the Z_2 vortex excitation of the four-sublattice magnetic order on a triangular lattice accumulates fractional charge associated with Chern number at its core, and behave as an Abelian anyon [86]. In this regard, while the magnetic Chern insulator is similar to integer quantum Hall system in its static property, it may be closer to fractional quantum Hall system in its dynamical property.

13.5.4 Tight-Binding Model on Line Graphs

In this section, we discuss the motion of non-interacting electrons on a class of geometrically frustrated lattices, called line graph. This topic is different from the problems described by e.g. classical Kondo lattice model. Nevertheless, we would like to discuss this topic, since the mathematical structure of this problem appears in a broad range of geometrically frustrated systems. A line graph is the name of graphs constructed by the following procedures: (a) putting new sites on edges of an original graph, (b) draw new edges between the new sites which are connected to a common site of the original graph, (c) then removing the old sites, as schematically shown in Fig. 13.12a–c.

The popular frustrated lattices, such as pyrochlore, kagome and checkerboard lattices belong to this category, and can be constructed with the procedure above, from diamond, honeycomb and square lattices, respectively. The fundamental unit of the line graph is a complete graph, like a triangle or a tetrahedron, in which all the sites are connected with all the others. In other words, the line graph is the network on which a variant of ice rule can be defined, if proper Ising variables, e.g. charges or Ising spins, are placed on that.

We consider a tight-binding model defined on a line graph,

$$\mathscr{H} = -t \sum_{\langle i,j \rangle} (c_i^\dagger c_j + \text{H.c.}). \tag{13.16}$$

The energy spectrum of this model has N_l bands, corresponding to the number of sites within the unit cell, N_l. Then one can find a common interesting property that there appears $N_l - N_o$ completely flat bands, with the number of sites within the unit cell in the original graph, N_o. This property can be proved based on an elegant mathematical tool, analogous to the concept of supersymmetry. Interestingly, similar arguments lead to the existence of invariant energy levels in the classical Kondo lattice model [88], and anomalous localized modes associated with disordered spin-ice-like magnetic structure [89, 90]. It is also worth pointing out that this argument simplifies the analysis of large-$\mathscr{N}$ analysis of spin model on line graphs, which gives a quite accurate description for the spin correlation of spin ice at zero temperature [69], and at finite temperature [91], as detailed in Chap. 3.

An intuitive proof for the existence of flat bands is available, by focusing on the real-space structure of the flat modes. As is obvious from the construction rule above, a line graph is made of complete graphs, and several complete graphs make a "loop". In the example in Fig. 13.12d, six triangles make hexagonal loops. By focusing on a loop, one can explicitly construct a localized mode belonging to a flat band, by assigning staggered signs as coefficients of an eigenstate wave function. Specifically, in the example in Fig. 13.12d, the state $\frac{1}{\sqrt{6}}(c_1^\dagger - c_2^\dagger + c_3^\dagger - c_4^\dagger + c_5^\dagger - c_6^\dagger)$ creates a localized one-particle eigenmode of Hamiltonian (13.16), with energy $2t$. On time evolution with (13.16), this state makes destructive interference at e.g. site 7 in

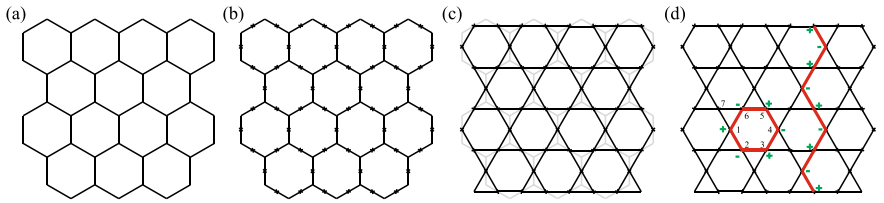

Fig. 13.12 **a–c** Schematic figure of the line-graph correspondence between honeycomb and kagome lattices. **a** Honeycomb lattice. **b** Extended honeycomb lattice, in which sites are located on each edge of honeycomb lattice, in addition to the original honeycomb sites. **c** The Kagome lattice obtained by removing the honeycomb site from the extended honeycomb lattice, then by connecting the edge sites. **d** Schematic figure of the modes consisting the flat band

Fig. 13.12d, and the state cannot go out of the loop. Accordingly, this state stays as the completely localized eigenmode.

Similar flat band structure is also found in different types of lattices, such as the Lieb lattice. However, there is a crucial difference between the flat bands on these two classes of lattices. The flat band of line graph inevitably touches one of the dispersive bands, i.e., no energy gap appears between the flat and dispersive bands. This fact can be understood from the real-space argument in the kagome lattice (Fig. 13.12d) above. There, we insisted that one localized mode exists per one loop. Since the number of loops, $\mathcal{N}_{\text{loop}}$, is equal to that of triangles, i.e., unit cells, this means that the number of localized modes is precisely equal to the number of one-particle states contained in one band.

However, there is a subtle point in this argument. While it appears there are exactly $\mathcal{N}_{\text{loop}}$ localized modes, the localized modes are not linearly independent, but their rank is $\mathcal{N}_{\text{loop}} - 1$, rather than $\mathcal{N}_{\text{loop}}$. One can understand this fact by checking that the eigenmodes of the type, $\frac{1}{\sqrt{6}}(c_1^\dagger - c_2^\dagger + c_3^\dagger - c_4^\dagger + c_5^\dagger - c_6^\dagger)$, summed up over all the loops to vanish. However, this is not the whole story. Under periodic boundary conditions, there are two more modes with the same energy, $2t$, which cannot be expressed as linear combinations of localized modes around loops. These exceptional modes are "string modes", which can be obtained by assigning staggered sign along a string crossing the system, globally. We have two such modes, modulo superposition with additional hexagonal modes. Consequently, there are $\mathcal{N}_{\text{ring}} + 1$ modes with equal energy, 1 mode excess of the number of modes accommodated in a single band. This means that a flat band has to be degenerate with one of the other bands to share this excess mode [92]. This mode counting argument is reminiscent of the structure of Homology group on two-dimensional torus, in which the counterparts of the string modes construct Z_2 component of the group. Similar argument is also used to count topological degeneracy in toric code model.

13.6 Summary

In this review, we have discussed the property of itinerant electrons coupled to localized magnetic moments on geometrically frustrated lattice structures. To explore the physics of frustrated itinerant electron systems, the classical Kondo lattice model provides a good starting point. Even without frustration, this model has various important properties, and has drawn considerable attention for a long time, as was detailed in Sect. 13.3. This model has dual properties. Itinerant electrons mediate effective interaction between localized moments, and give rise to ordered magnetic structures, depending on the carrier density and electronic structure. The stabilized magnetic structure, in turn, affects thermodynamic as well as transport properties of itinerant electrons. The separability of these two actions makes the analysis of this model considerably easier, compared with fully quantum mechanical models, and help understanding the physics of this model to a quite deep level. The role of geometrical frustration in this model is two-fold, accordingly. It brings about peculiar structure in localized moments, e.g. spin ice correlation, which leads to anomalous electron transport. One can see the best example of this process through the analysis of itinerant spin ice, in Sect. 13.4.

There are still many on-going problems in the area of frustrated itinerant systems. Or, we should say, on the basis of a rather firm understanding of purely localized frustrated systems, this area is growing rapidly. In the specific example of itinerant spin ice, the spontaneous Hall effect stands as yet unsolved problem. We have also listed part of the problems left for future, in Sect. 13.5. Ice rule on charge degrees of freedom has provided interesting problems. Among recent topics, this viewpoint may give a clue to the glassy behavior observed in organic compounds [93]. The relation between frustration and glass is a historical problem. The classical Kondo lattice model provides an anchor point, which enables detailed theoretical analysis. However, of course, it sacrifices some essential physics for the sake of simplification. Departure from the classical limit is another important direction, and the description of large electron mass may give a good target for this direction. Incorporation of quantum fluctuation also enables one to examine the dynamics and carrier doping effect of frustrated magnets, especially those comprising non-trivial topological state. we hope that this article will help solving these problems, and further exploring this fertile research field.

References

1. P. W. Anderson, Phys. Rev. **102**, 1008 (1956) https://doi.org/10.1103/PhysRev.102.1008
2. S. Kondo et al., Phys. Rev. Lett. **78**, 3729 (1997) https://doi.org/10.1103/PhysRevLett.78.3729
3. H. Wada et al., J. Magn. Magn. Mater. **70**, 17-19 (1987) https://doi.org/10.1016/0304-8853(87)90350-7
4. T. Shinkoda, K. Kumagai, and K. Asayama, J. Phys. Soc. Jpn. **46**, 1754 (1979) https://doi.org/10.1143/JPSJ.46.1754

5. S. Iguchi, Y. Kumano, K. Ueda, S. Kumakura, and Y. Tokura, Phys. Rev. B **84**, 174416 (2011) https://doi.org/10.1103/PhysRevB.84.174416
6. Y. Taguchi et al., Science **291**, 2573 (2001) https://doi.org/10.1126/science.1058161
7. S. Nakatsuji et al., Phys. Rev. Lett. **96**, 087204 (2006) https://doi.org/10.1103/PhysRevLett.96.087204
8. Y. Machida et al., Phys. Rev. Lett. **98**, 057203 (2007) https://doi.org/10.1103/PhysRevLett.98.057203
9. Y. Machida et al., Nature **463**, 210 (2010) https://doi.org/10.1038/nature08680
10. G. H. Jonker and J. H. Van Santen, Physica **16**, 337 (1950); J. H. Van Santen and G. H. Jonker, *ibid*. **16**, 599 (1950) https://doi.org/10.1016/0031-8914(50)90104-2 https://doi.org/10.1016/0031-8914(50)90033-4
11. C. Zener, Phys. Rev. **82**, 403 (1951) https://doi.org/10.1103/PhysRev.82.403
12. C. Zener, Phys. Rev. **81**, 440 (1951) https://doi.org/10.1103/PhysRev.81.440
13. P. W. Anderson and H. Hasegawa, Phys. Rev. **100**, 675 (1955) https://doi.org/10.1103/PhysRev.100.675
14. P. G. de Gennes, Phys. Rev. **118**, 141 (1960) https://doi.org/10.1103/PhysRev.118.141
15. K. Kubo and N. Ohata, J. Phys. Soc. Jpn. **33**, 21 (1972) https://doi.org/10.1143/JPSJ.33.21
16. N. Furukawa, "Thermodynamics of the double exchange systems Physics of Manganites", In: Kaplan T.A., Mahanti S.D. (eds) Physics of Manganites. Fundamental Materials Research. Springer, Boston, MA. https://doi.org/10.1007/0-306-47091-8
17. G. R. Stewart, Rev. Mod. Phys. **73**, 797 (2001) https://doi.org/10.1103/RevModPhys.73.797
18. N. Macris and J. L. Lebowitz, J. Math. Phys. **38**, 2084 (1997) https://doi.org/10.1063/1.531923
19. H. Tsunetsugu, M. Sigrist, and K. Ueda, Rev. Mod. Phys. **69**, 809 (1997) https://doi.org/10.1103/RevModPhys.69.809
20. J. Hubbard, Proc. R. Soc. London, Ser. A **276**, 238 (1963) https://doi.org/10.1098/rspa.1967.0007
21. L. M. Falicov and J. C. Kimball, Phys. Rev. Lett. **22**, 997 (1969) https://doi.org/10.1103/PhysRevLett.22.997
22. A. Kitaev, Ann. Phys. **321**, 2 (2006) https://doi.org/10.1016/j.aop.2005.10.005
23. N. Furukawa, J. Phys. Soc. Jpn. **63**, 3214 (1994) https://doi.org/10.1143/JPSJ.63.3214
24. U. Brandt and C. Mielsch, Z. Phys. B: Condens. Matter **75**, 365 (1989) https://doi.org/10.1007/BF01321824
25. U. Brandt and C. Mielsch, Z. Phys. B: Condens. Matter **79**, 295 (1990) https://doi.org/10.1007/BF01406598
26. U. Brandt and C. Mielsch, Z. Phys. B: Condens. Matter **82**, 37 (1991) https://doi.org/10.1007/BF01313984
27. U. Brandt, A. Fledderjohann, and G. Hulsenbeck, Z. Phys. B: Condens. Matter **81**, 409 (1990) https://doi.org/10.1007/BF01390822
28. U. Brandt and A. Fledderjohann, Z. Phys. B: Condens. Matter **87**, 111 (1992) https://doi.org/10.1007/BF01308265
29. U. Brandt and M. P. Urbanek, Z. Phys. B: Condens. Matter **89**, 297 (1992) https://doi.org/10.1007/BF01318160
30. W. Metzner and D. Vollhardt, Phys. Rev. Lett. **62**, 324 (1989) https://doi.org/10.1103/PhysRevLett.62.324
31. A. Georges, G. Kotliar, W. Krauth and M. J. Rozenberg, Rev. Mod. Phys. **68**, 13 (1996) https://doi.org/10.1103/RevModPhys.68.13
32. N. D. Mermin and H. Wagner, Phys. Rev. Lett. **17**, 1133 (1966) https://doi.org/10.1103/PhysRevLett.17.1133
33. C. Proetto and A. Lopez, J. Physique Lett. **44**, L635 (1983) https://doi.org/10.1051/jphyslet:019830044015063500
34. D. Loss, F. L. Pedrocchi and A. J. Leggett, Phys. Rev. Lett. **107**, 107201 (2011) https://doi.org/10.1103/PhysRevLett.107.107201
35. A. Weise, G. Wellein, A. Alvermann, and H. Fehske, Rev. Mod. Phys. **78**, 275 (2006) https://doi.org/10.1103/RevModPhys.78.275

36. K. Barros and Y. Kato, Phys. Rev. B **88**, 235101 (2013) https://doi.org/10.1103/PhysRevB.88.235101
37. X. Y. Xu, Y. Qi, J. Liu, L. Fu, Z. Y. Meng, Phys. Rev. B **96**, 041119 (2017) https://doi.org/10.1103/PhysRevB.96.041119
38. N. Furukawa, J. Phys. Soc. Jpn. **64**, 2734 (1995) https://doi.org/10.1143/JPSJ.64.2734
39. N. Furukawa, J. Phys. Soc. Jpn. **64**, 2754 (1995) https://doi.org/10.1143/JPSJ.64.2754
40. For a review, "Colossal Magnetoresistive Oxides", edited by Y. Tokura (Gordon & Breach Science Publisher, 2000) ISBN 90-5699-231-7
41. T. Ohashi, N. Kawakami and H. Tsunetsugu, Phys. Rev. Lett. **97**, 066401 (2006) https://doi.org/10.1103/PhysRevLett.97.066401
42. T. Ohashi, T. Momoi, H. Tsunetsugu and N. Kawakami, Phys. Rev. Lett., **100**, 076402 (2008) https://doi.org/10.1103/PhysRevLett.100.076402
43. I. Martin and C. D. Batista: Phys. Rev. Lett. **101**, 156402 (2008) https://doi.org/10.1103/PhysRevLett.101.156402
44. Y. Akagi and Y. Motome: J. Phys. Soc. Jpn. **79**, 083711 (2010) https://doi.org/10.1143/JPSJ.79.083711
45. Y. Akagi, M. Udagawa and Y. Motome, Phys. Rev. Lett. **108**, 096401 (2012) https://doi.org/10.1103/PhysRevLett.108.096401
46. Y. Kato, I. Martin and C. D. Batista, Phys. Rev. Lett. **105**, 266405 (2010) https://doi.org/10.1103/PhysRevLett.105.266405
47. R. Karplus and J. M. Luttinger, Phys. Rev. **95**, 1154 (1954) https://doi.org/10.1103/PhysRev.95.1154
48. J. Smit, Physica **21**, 877 (1955) https://doi.org/10.1016/S0031-8914(55)92596-9
49. L. Berger, Phys. Rev. B, **2**, 4559 (1970) https://doi.org/10.1103/PhysRevB.2.4559
50. K. Ohgushi, S. Murakami and N. Nagaosa, Phys. Rev. B, **62**, R6065 (2000) https://doi.org/10.1103/PhysRevB.62.R6065
51. M. Taillefumier *et al.*, Phys. Rev. B, **74**, 085105 (2006) https://doi.org/10.1103/PhysRevB.74.085105
52. For a recent review, N. Nagaosa *et al.*, Rev. Mod. Phys. **82**, 1539 (2010) https://doi.org/10.1103/RevModPhys.82.1539
53. G. Tatara and H. Kawamura, J. Phys. Soc. Jpn. **71**, 2613 (2002) https://doi.org/10.1143/JPSJ.71.2613
54. M. Onoda, G. Tatara and N. Nagaosa, J. Phys. Soc. Jpn., **73**, 2624 (2004) https://doi.org/10.1143/JPSJ.73.2624
55. S. K. Pandey and L. Maiti, Phys. Rev. B **82**, 035110 (2010) https://doi.org/10.1103/PhysRevB.82.035110
56. F. Ishii et al., J. Phys. Soc. Jpn. **84**, 073703 (2015) https://doi.org/10.1143/JPSJ.84.073703
57. T. Kondo et al., Nat. Commun. **6**, 10042 (2015) https://doi.org/10.1038/ncomms10042
58. Y. Machida et al., J. Phys. Chem. Solids **66**, 1435 (2005) https://doi.org/10.1016/j.jpcs.2005.05.026
59. Y. Tokiwa, J. J. Ishikawa, S. Nakatsuji, P. Gegenwart, Nat. Mater. **13**, 356 (2014) https://doi.org/10.1038/nmat3900
60. J. Kondo, Prog. Theor. Phys. **32**, 37 (1964) https://doi.org/10.1143/PTP.32.37
61. M. Udagawa, H. Ishizuka and Y. Motome, Phys. Rev. Lett. **108**, 066406 (2012) https://doi.org/10.1103/PhysRevLett.108.066406
62. H. Ishizuka, M. Udagawa and Y. Motome, JPS Conf. Proc. **3**, 014013 (2014) https://doi.org/10.7566/JPSCP.3.014013
63. H. Ishizuka, Y. Motome, Phys. Rev. B **88**, 100402(R) (2013). https://doi.org/10.1103/PhysRevB.88.100402
64. M. Udagawa and R. Moessner, Phys. Rev. Lett. **111**, 036602 (2013) https://doi.org/10.1103/PhysRevLett.111.036602
65. M. Udagawa, Spin **5**(02), 1540004 (2015). https://doi.org/10.1142/S2010324715400044
66. H. Ishizuka, M. Udagawa and M. Motome, J. Phys.: Conf. Ser. **400**, 032027 (2012) https://doi.org/10.1088/1742-6596/400/3/032027

67. R.G. Melko, M.J.P. Gingras, J. Phys.: Cond. Matter **16**, R1277 (2004). https://doi.org/10.1088/0953-8984/16/43/R02
68. A. Ikeda and H. Kawamura, J. Phys. Soc. Jpn. **77**, 073707 (2008) https://doi.org/10.1143/JPSJ.77.073707
69. S. V. Isakov, R. Moessner and S. L. Sondhi, Phys. Rev. Lett., **95**, 217201 (2005) https://doi.org/10.1103/PhysRevLett.95.217201
70. Gia-Wei Chern, Saurabh Maiti, Rafael M. Fernandes, Peter Wölfle, Phys. Rev. Lett. **110**, 146602 (2013) https://doi.org/10.1103/PhysRevLett.110.146602
71. M. Udagawa, M. Ogata and Z. Hiroi, J. Phys. Soc. Jpn. **71**, 2365 (2002) https://doi.org/10.1143/JPSJ.71.2365
72. R. Flint and T. Senthil, Phys. Rev. B **87**, 125147 (2013) https://doi.org/10.1103/PhysRevB.87.125147
73. SungBin Lee, A. Paramekanti and Y. B. Kim, Phys. Rev. Lett. **111**, 196601 (2013) https://doi.org/10.1103/PhysRevLett.111.196601
74. Eun-Gook Moon, C. Xu, Y. B. Kim, L. Balents, Phys. Rev. Lett. **111**, 206401 (2013) https://doi.org/10.1103/PhysRevLett.111.206401
75. A. A. Abrikosov and S. D. Beneslavskii, J. Exp. Theor. Phys. **32**, 699 (1971) www.jetp.ac.ru/cgi-bin/e/index/e/32/4/p699?a=list
76. A. A. Abrikosov, J. Exp. Theor. Phys. **39**, 709 (1974) www.jetp.ac.ru/cgi-bin/e/index/e/39/4/p709?a=list
77. E. Verwey, Nature **144**, 327 (1939) https://doi.org/10.1038/144327b0
78. H. Ishizuka, M. Udagawa and Y. Motome, Phys. Rev. B **83**, 125101 (2011) https://doi.org/10.1103/PhysRevB.83.125101
79. L. D. C. Jaubert, M. Haque, R. Moessner, Phys. Rev. Lett. **107**, 177202 (2011) https://doi.org/10.1103/PhysRevLett.107.177202
80. L. D. C. Jaubert, Swann Piatecki, Masudul Haque, R. Moessner, Phys. Rev. B, **85**, 054425 (2012) https://doi.org/10.1103/PhysRevB.85.054425
81. M. Udagawa and Y. Motome, Phys. Rev. Lett. **104**, 106409 (2010) https://doi.org/10.1103/PhysRevLett.104.106409
82. M. Udagawa, H. Ishizuka and Y. Motome, Phys. Rev. Lett. **104**, 226405 (2010) https://doi.org/10.1103/PhysRevLett.104.226405
83. S. Fujimoto, Phys. Rev. Lett. **103**, 047203 (2009) https://doi.org/10.1103/PhysRevLett.103.047203
84. H. Katsura, N. Nagaosa, and P. A. Lee, Phys. Rev. Lett. **104**, 066403 (2010) https://doi.org/10.1103/PhysRevLett.104.066403
85. R. Matsumoto and S. Murakami, Phys. Rev. B **84**, 184406, (2011) https://doi.org/10.1103/PhysRevB.84.184406
86. A. Rahmani, R. A. Muniz and I. Martin, Phys. Rev. X **3**, 031008 (2013) https://doi.org/10.1103/PhysRevX.3.031008
87. H. Katsura, I. Maruyama, A. Tanaka, Hal Tasaki, Europhys. Lett. **91**, 57007 (2010) https://doi.org/10.1209/0295-5075/91/57007
88. M. Udagawa, H. Ishizuka and Y. Motome, JPS Conf. Proc. **3**, 014009 (2014) https://doi.org/10.7566/JPSCP.3.014009
89. H. Ishizuka, Y. Motome, Phys. Rev. B **87**, 081105(R) (2013). https://doi.org/10.1103/PhysRevB.87.081105
90. Gia-Wei Chern, Armin Rahmani, Ivar Martin, Cristian D. Batista, Phys. Rev. B **90**, 241102 (2014) https://doi.org/10.1103/PhysRevB.90.241102
91. Arnab Sen, R. Moessner, S. L. Sondhi, Phys. Rev. Lett. **110**, 107202 (2013) https://doi.org/10.1103/PhysRevLett.110.107202
92. D. L. Bergman, C. Wu and L. Balents, Phys. Rev. B **78**, 125104 (2008) https://doi.org/10.1103/PhysRevB.78.125104
93. F. Kagawa et al., Nat. Phys. **9**, 419 (2013) https://doi.org/10.1038/nphys2642

Chapter 14
Anomalous Transport Properties of Pyrochlore Iridates

K. Matsuhira and S. Nakatsuji

Abstract Pyrochlore rare-earth iridates $Ln_2Ir_2O_7$ (*Ln*: lanthanides) is a unique frustrated Kondo lattice system composed of localized $4f$ moments and Ir $5d$ conduction electrons. Recent active research has revealed that the Kondo coupling between the $4f$ electron and the Ir $5d$ bands leads to novel transport properties. First, we will make an overview of the phase diagram of pyrochlore rare-earth iridates $Ln_2Ir_2O_7$. Next, we focus on the phenomena associated with spin ice physics. $Ln_2Ir_2O_7$ (*Ln* = Nd, Sm, Eu, ...) exhibits a metal-insulator transition, while $Pr_2Ir_2O_7$ does not show any sign of long range ordering. Both Pr and Nd moments have a local ⟨111⟩ Ising anisotropy. In the metallic state, localized $4f$ moments are coupled through the RKKY interaction. For $Pr_2Ir_2O_7$, a ferromagnetic correlation between Pr moments is developed on cooling. On the other hand, $Nd_2Ir_2O_7$ exhibits a metal-insulator transition at 33 K, and then, all-in all-out magnetic structure of Nd moments emerges below 10 K, as observed in the neutron scattering experiments. For $Nd_2Ir_2O_7$, antiferromagnetic correlation between Nd moments is dominant. Metal insulator transition of $Nd_2Ir_2O_7$ can be suppressed by the application of pressure. The insulating phase disappears above 10 GPa. In the pressure induced metallic state, a new phase transition emerges around 3 K. This phase transition is likely due to ferromagnetic ordering, suggesting an ordered spin ice of Nd moment. In the metallic frustrated magnet $Pr_2Ir_2O_7$, a spontaneous Hall effect is observed at zero field in the absence of uniform magnetization, suggesting an emergence of a chiral spin liquid. The origin of this spontaneous Hall effect is ascribed to chiral spin textures, which are inferred from the magnetic measurements indicating the spin ice-rule formation.

K. Matsuhira (✉)
Kyushu Institute of Technology, Kitakyushu, Japan

S. Nakatsuji (✉)
Institute for Solid State Physics, University of Tokyo, Chiba, Japan
e-mail: satoru@issp.u-tokyo.ac.jp

M. Udagawa and L. Jaubert (eds.), *Spin Ice*, Springer Series in Solid-State Sciences 197,
https://doi.org/10.1007/978-3-030-70860-3_14

14.1 Pyrochlore Rare-Earth Iridates

Recently, 4*d* and 5*d* transition metal pyrochlore oxides have been attracting much interest because of their novel transport properties [1–7]. An important problem that has yet to be solved is to clarify how the geometrical frustration influences the ground states of strongly correlated electron systems in triangle-based lattices.[1] As the pyrochlore rare earth iridates $Ln_2Ir_2O_7$ is a good candidate for the purpose, an active investigation has been carried out. As the *Ln* ion is trivalent, the $(5d)^5$ electrons from Ir^{4+} form an unfilled t_{2g} band. As the 4*f* electrons are generally well localized, only the 5*d* electrons contribute to the electrical conductivity. Therefore, pyrochlore rare-earth iridates $Ln_2Ir_2O_7$ form frustrated Kondo lattice systems composed of localized 4*f* moments and Ir 5*d* conduction electrons (Fig. 14.1).

Figure 14.2 shows the temperature dependence of electrical resistivity of $Ln_2Ir_2O_7$ for *Ln* = Pr, Nd, Sm, Eu, Gd, Tb, Dy, and Ho [9], in the decreasing order of ionic radius. The electrical resistivity ρ of $Ln_2Ir_2O_7$ strongly depends on the ionic radius of Ln^{3+} [5, 10]. As the ionic radius of Ln^{3+} becomes smaller, the electrical conductivities change from metallic to semiconducting with a small energy gap. As the ionic radius of Ln^{3+} is reduced, the Ir-O-Ir bond angle decreases, consequently, the t_{2g} bandwidth becomes narrower. For *Ln* = Nd, Sm, Eu, Gd, Tb, Dy, and Ho, $Ln_2Ir_2O_7$ exhibits metal-insulator transition (MIT) at 33, 117, 120, 127, 132, 134, and 141 K, respectively. In this MIT, no thermal hysteresis and no discontinuous change are observed at MIT temperature T_{MI}. Therefore, these MITs are second-order transitions. For $Pr_2Ir_2O_7$, no MIT was observed, and the compound remains metallic.

Figure 14.3 shows the phase diagram of $Ln_2Ir_2O_7$, which is based on the Ln^{3+} ionic radius dependence of T_{MI}; the ionic radius of Ln^{3+} is for an 8-coordination-number site [9]. T_{MI} monotonically increases as the ionic radius of Ln^{3+} decreases. Obviously, the trend of T_{MI} does not depend on the de-Gennes factor: $(g-1)^2J(J+1)$ or on the magnetism of Ln^{3+}. This fact means that the origin of MITs comes from Ir 5*d* electrons.

At room temperature, *Ln* = Pr and Nd are metallic with low carrier density. In contrast, *Ln* = Sm, Eu and Gd are semimetals, and *Ln* = Tb, Dy, and Ho are semiconductors with small band gaps. In recent theoretical studies, for this insulating state of $Ln_2Ir_2O_7$, the possibility of realizing a topological Mott insulator state and Weyl semimetal state have been discussed. Furthermore, $Pr_2Ir_2O_7$ and $Nd_2Ir_2O_7$ are unique metal near the critical point of MIT [11]. Moreover, a new type of quantum critical phenomena is theoretically predicted, accompanied with a disappearance of MIT [12].

Next, we will discuss the crystalline electric field (CEF) ground state (GS) of Pr^{3+} in $Pr_2Ir_2O_7$ and Nd^{3+} in $Nd_2Ir_2O_7$. The CEF analyses from neutron inelastic scattering experiments reveal that the CEF GS of both Pr^{3+} and Nd^{3+} has a local Ising anisotropy along the ⟨111⟩ directions [4, 13]. In addition, from the magnetic

[1] A tetrahedron, a building block of pyrochlore lattice, is a triangle-based object.

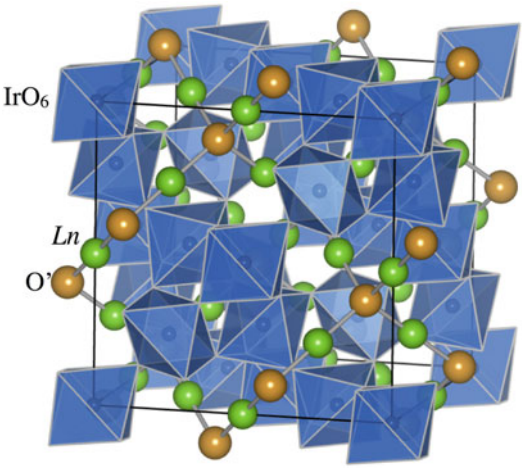

Fig. 14.1 Crystal structure of $Ln_2Ir_2O_7$. This image is produced by VESTA [8]

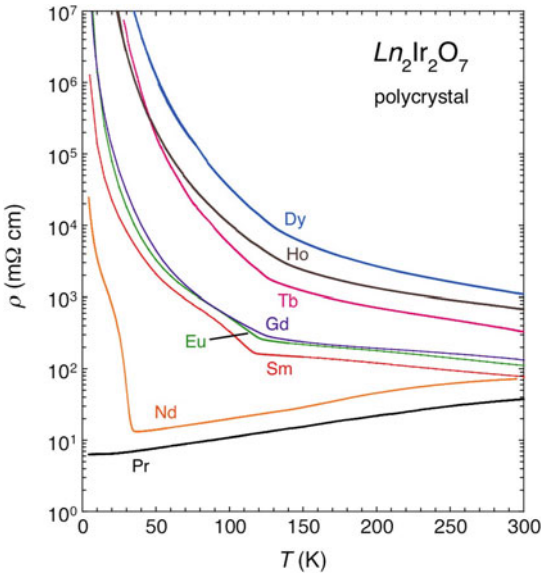

Fig. 14.2 Temperature dependence of electrical resistivity of $Ln_2Ir_2O_7$ (Ln = Pr-Ho), reprinted from [9] from the Journal of the Physical Society of Japan

susceptibility data at low temperature, the effective magnetic moments of $Pr_2Ir_2O_7$ and $Nd_2Ir_2O_7$ are estimated to be 2.68 and 2.73 μ_B, respectively. Figure 14.4 shows these CEF level schemes.

The CEF GS of Pr^{3+} in $Pr_2Ir_2O_7$ is a non-Kramers doublet, which is mainly composed of $\sim|\ J_z = \pm 4\rangle$. Now z-direction corresponds to the trigonal axis in the tetrahedron. The magnetic moment of GS has a component only along the $\langle 111 \rangle$ directions. The other degrees of freedom are two quadrupole moments of O_{zx} and O_{yz} [14]. The CEF GS is well separated from other levels, as the 1st excited CEF state is 162 K above. Therefore, this doublet has an Ising magnetic anisotropy along

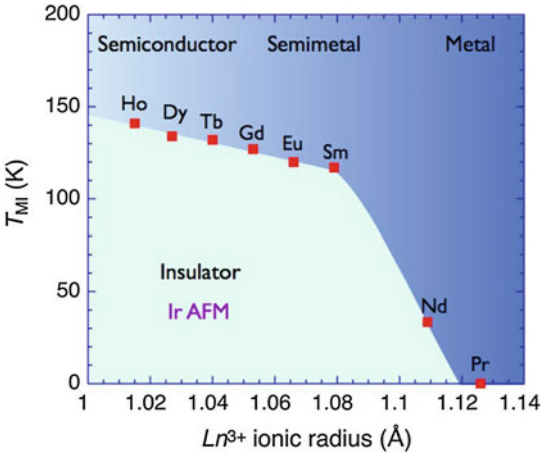

Fig. 14.3 Phase diagram of $Ln_2Ir_2O_7$, reprinted from [9] from the Journal of the Physical Society of Japan. The ionic radius of Ln^{3+} is for an 8-coordination-number site

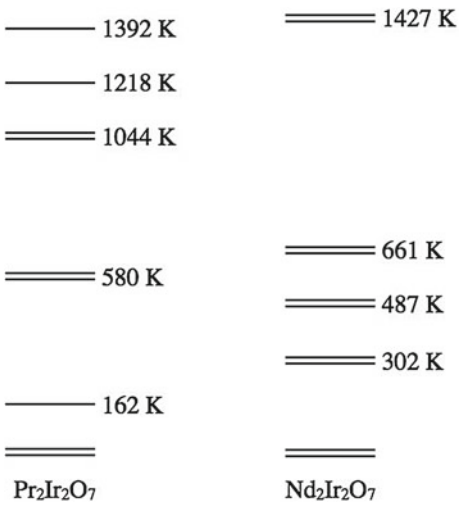

Fig. 14.4 CEF level scheme of Pr^{3+} in $Pr_2Ir_2O_7$ and Nd^{3+} in $Nd_2Ir_2O_7$

the trigonal axis at low temperature. In contrast, the CEF GS of Nd^{3+} in $Nd_2Ir_2O_7$ is a Kramers doublet;

$$|\pm 0\rangle = \alpha \mid J_z = \pm 9/2\rangle \pm \beta \mid J_z = \pm 3/2\rangle + \gamma \mid J_z = \mp 3/2\rangle \pm \delta \mid J_z = \mp 9/2\rangle \tag{14.1}$$

where $\alpha = 0.822$, $\beta = 0.489$, $\gamma = 0.286$ and $\delta = 0.057$. The value of magnetic moment of GS doublet is obtained from $g_J\langle \pm 0 \mid \mathbf{J} \mid \pm 0\rangle = (0, 0, \pm 2.37)$. Then, this doublet has a magnetic moment along the $\langle 111\rangle$ directions. As is shown in Fig. 14.4, the CEF GS is again, well separated from the other levels, as the 1st excited CEF state is 302 K above, which suppresses the transverse component ($\langle 1 \mid J_x \mid 0\rangle$) where $\mid 1\rangle$ is 1st excited CEF state. Therefore, this doublet has an Ising magnetic anisotropy along the trigonal axis at low temperature.

As explained above, their 4f moments of both $Pr_2Ir_2O_7$ and $Nd_2Ir_2O_7$ have Ising anisotropies at low temperature. Therefore, these pyrochlore iridates form frustrated Kondo lattice systems composed of localized $4f$ moments and Ir $5d$ conduction electrons. The magnetic ground states of pyrochlore iridates have been theoretically discussed [15–18]. They propose an emergence of ordered spin ice state and all-in all-out ordering as well as more complicated magnetic structure. These theoretical studies imply that various ground states are in competition, in comparison with simpler insulating Ising systems. In addition, non-Kondo mechanism for resistivity minimum is also proposed [19]. Further studies to reveal the new ground states and phenomena are desirable.

14.2 Metal-Insulator Transition of Pyrochlore Iridate

We will address the characteristics of MIT in pyrochlore rare-earth iridates $Ln_2Ir_2O_7$ in this section. Figure 14.5 shows the magnetic susceptibility M/H of $Eu_2Ir_2O_7$ measured under the zero-field-cooled (ZFC) and the field-cooled (FC) conditions.

ZFC curve above T_{MI} is explained by a summation of Van Vleck paramagnetism of Eu^{3+} and Pauli paramagnetism from Ir 5d electrons. M/H exhibits a Van Vleck paramagnetism at low temperature as Eu^{3+} has the ground state $J = 0$ multiplet. In the case of Eu^{3+} ($4f^5$), the energy splitting between the ground state ($J = 0$) and the 1st excited states ($J = 1$) corresponds to the spin-orbit coupling constant λ. Furthermore, a low carrier density from the t_{2g} band, indicating a semi-metallic behavior, shows Pauli paramagnetism above T_{MI}. From the result of fitting M/H curve above T_{MI}, the parameters of spin-orbit coupling constant $\lambda = 375\,\mathrm{K}$ and constant Pauli paramagnetism $\chi_0 = 1.3 \times 10^{-3}$ emu/mole are obtained.

M/H measured under the ZFC condition shows a tiny peak at T_{MI}. A difference in the M/H appears below T_{MI} between ZFC and FC conditions. This is caused by a tiny ferromagnetic component ($10^{-3}\mu_B$) below T_{MI}. The difference in M/H gives clear evidence that this MIT originates from Ir 5d electrons; Eu^{3+} ($4f^5$: $J = 0$) has no magnetic degree of freedom at low temperature [9]. The slight upturn observed in both curves below 10 K may be caused by a small amount of magnetic impurity.

The difference in the M/H measured under the ZFC and FC conditions is attributed to the very weak ferromagnetic components. The present result indicates that the observed emergence of very weak ferromagnetic components is intrinsic. However, it is very difficult to consider the very weak ferromagnetic ordering as the origin of MIT because the observed ferromagnetic moment is too small to cause magnetic ordering.

Figure 14.6 shows the specific heat divided by temperature C/T of polycrystalline $Eu_2Ir_2O_7$ [9]. A sharp anomaly is clearly observed at T_{MI} [20]. The lattice contribution was subtracted from the raw data; the electronic portions of the C/T ($\Delta C/T$) are shown in the inset. By integrating $\Delta C/T$, we obtained $\Delta S = 1.4\,\mathrm{J/K\ mole}$. ΔS is much smaller than a change in entropy of $2R \ln 2$ ($= 11.5\,\mathrm{J/K\ mole}$), which we

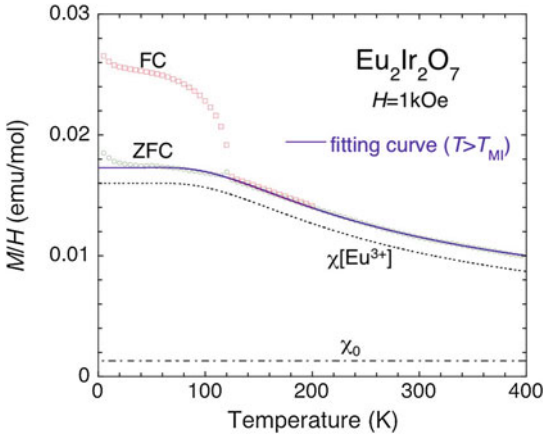

Fig. 14.5 Magnetic susceptibility M/H of $Eu_2Ir_2O_7$ in a magnetic field of 1 kOe. The dotted line indicates the contribution of the Van Vleck susceptibility due to Eu^{3+} with a spin-orbit coupling constant $\lambda = 375\,\mathrm{K}$. The dash-dotted line shows a constant Pauli contribution $\chi_0 = 1.3 \times 10^{-3}$ emu/mole. Solid line shows the fitting curve above T_{MI}, which is obtained by the summation of above-mentioned contributions. Figure reprinted from [9] from the Journal of the Physical Society of Japan

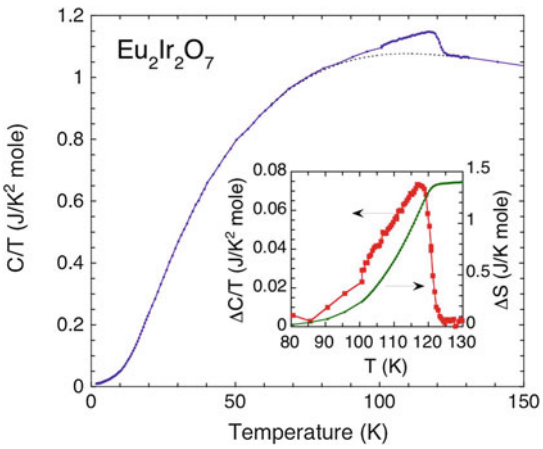

Fig. 14.6 Specific heat divided by temperature of polycrystalline $Eu_2Ir_2O_7$. The broken line shows a smooth polynomial fitted to the data outside the region of the peak. The inset shows the electronic portion of C/T ($\Delta C/T$) and the entropy ΔS estimated from $\Delta C/T$. Figure reprinted from [9] from the Journal of the Physical Society of Japan

would have expected if $5d$ electrons from Ir^{4+} ions with $S = 1/2$ had shown perfect ordering. The small ΔS implies the ordered moment is reduced due to the itinerancy of $5d$ electrons.

MIT of $Eu_2Ir_2O_7$ is confirmed in a single crystal sample. Figure 14.7 shows the temperature dependence of electrical resistivity and the magnetic susceptibility M/H of single crystal $Eu_2Ir_2O_7$. The electrical resistivity clearly exhibits MIT at 120 K which is the same transition temperature in polycrystalline sample although the positive $d\rho/dT$ is observed above T_{MI} in contrast with the negative $d\rho/dT$ observed in

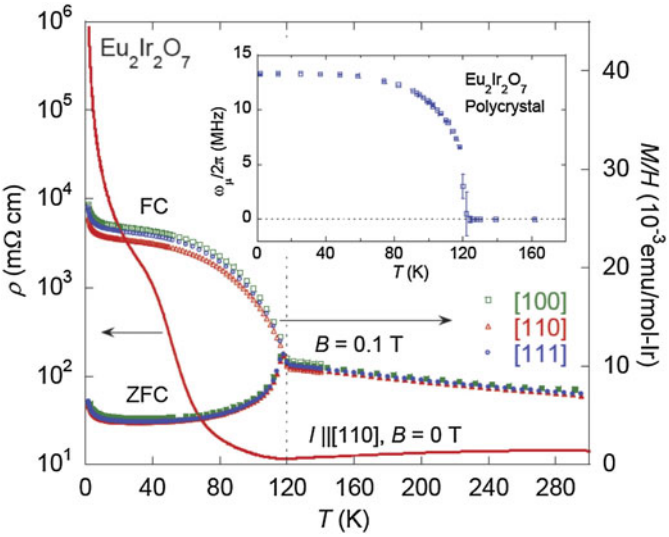

Fig. 14.7 Temperature dependence of electrical resistivity and magnetic susceptibility M/H of single crystal $Eu_2Ir_2O_7$, reprinted from [21] with permission from the American Physical Society. Inset: Temperature dependence of muon spin precession frequency in polycrystalline $Eu_2Ir_2O_7$, reprinted from [22] with permission from the American Physical Society

polycrystalline sample (Fig. 14.2) [21]. In addition, very weak ferromagnetic components emerges below $T_{MI} = 120\,K$ as the difference in the M/H measured under the ZFC and FC conditions is observed. The inset shows the temperature dependence of muon spin precession frequency in polycrystalline $Eu_2Ir_2O_7$. The result indicates the appearance of internal field below $T_{MI} = 120\,K$, which supports a long range magnetic ordering of Ir moment [22].

Next, Fig. 14.8 shows the C/T of $Nd_2Ir_2O_7$ below 40 K [9]. An anomaly due to MIT is observed at T_{MI}, which is consistent with the anomalies in the resistivity, thermoelectric power, and magnetization. The entropy release associated with the MIT is estimated to be 0.47 J/K mole. C/T also shows a broad peak at 4 K and a shoulder at 1 K. From the entropy variation, this broad peak is caused by the CEF ground state doublet in Nd^{3+}. Then, we can fit the data using the Schottky specific heat of two levels with energy splitting $\Delta = 13\,K$; the lattice contribution estimated from the data of $Eu_2Ir_2O_7$ is also considered in this fitting. A good fitting is obtained above 5 K. Because Nd^{3+} is a Kramers ion, the splitting is caused by the internal field due to a *d-f* interaction. This indicates the appearance of an internal field due to MIT below T_{MI}.

From the results of magnetization and specific heat measurements, we may consider that the MIT originates from antiferromagnetic ordering of Ir moments. Furthermore, because the trend of T_{MI} is independent of the magnetism of Ln^{3+}, it is speculated that the magnetic structure of Ir moments is common in insulating state of $Ln_2Ir_2O_7$. As Ir moments are not large, Ir moments seem subject to strong frustration

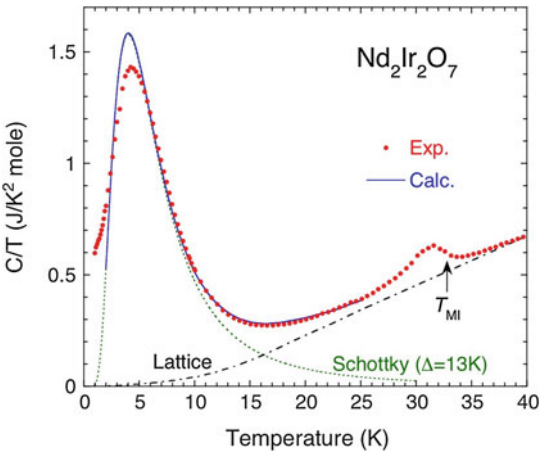

Fig. 14.8 Specific heat divided by temperature of polycrystalline $Nd_2Ir_2O_7$. The broken line (green) shows the Schottky specific heat with energy splitting $\Delta = 13$ K. The dash-dotted line (black) shows the lattice contribution estimated from the data of $Eu_2Ir_2O_7$. The solid line (blue) shows the sum of these contributions. Figure reprinted from [9] from the Journal of the Physical Society of Japan

on the pyrochlore lattice. However, contrary to the expectations, some microscopic measurements (powder neutron scattering and resonant magnetic X-ray scattering) reveal all-in all-out (AIAO) structure with $\mathbf{Q} = 0$ which has no macroscopic degeneracy in the ground state. The AIAO structure is observed for the first time in $Nd_2Ir_2O_7$, among the pyrochlore oxides. Figure 14.9 shows measured neutron diffraction data for powder $Nd_2Ir_2O_7$ [23]. The magnetic scattering in this data is mainly originated from Nd magnetic moments. Bragg reflection lines around (220) reciprocal lattice point at 9, 40, and 102 K are shown in Fig. 14.9a. On cooling, the intensity at 9 K becomes clearly bigger than those above T_{MI}. Figure 14.9b shows the temperature dependence of summation of the integrated intensities for Bragg reflection lines (113) and (222). As temperature decreases, this summation of integrated intensities begins to increase below 15 ± 5 K. Furthermore, a significant peak begins to appear below $T_{MI} = 33$ K in the inelastic scattering data as shown in Fig. 14.9c. The peak position gradually shifts to high energy side on cooling and becomes 1.2 meV at 3 K; this energy is nearly equal to the energy splitting of CEF ground state doublet in Nd^{3+} ($\Delta = 13$ K) in specific heat as discussed above. The results suggest that Nd magnetic moments are in a magnetic ordered state with $\mathbf{Q} = 0$.

From these experimental results, the ordered Ir moments at T_{MI} align the Nd moments through the *d-f* interaction below 15 ± 5 K; the magnetic ordering of Ir moment at T_{MI} is a *true* phase transition because the specific heat shows sharp anomaly, but the magnetic ordering of Nd moment is not a phase transition and there is only a broad peak in the specific heat. As is discussed later, the crystal structure keeps cubic symmetry even below T_{MI}. Therefore, it is quite reasonable that the magnetic structure of Ir moment is AIAO structure, which keeps the cubic symmetry, as shown in Fig. 14.10 [23]. From the analysis on the basis of the AIAO structure in both Nd and Ir moments, the values of magnetic moments of Nd and Ir are estimated to be 2.3 μ_B and 0.2 μ_B at 0.7 K, respectively. Figure 14.11 shows the temperature dependence of the internal field H_{int} by μSR measurement for polycrystalline $Nd_2Ir_2O_7$. On cooling,

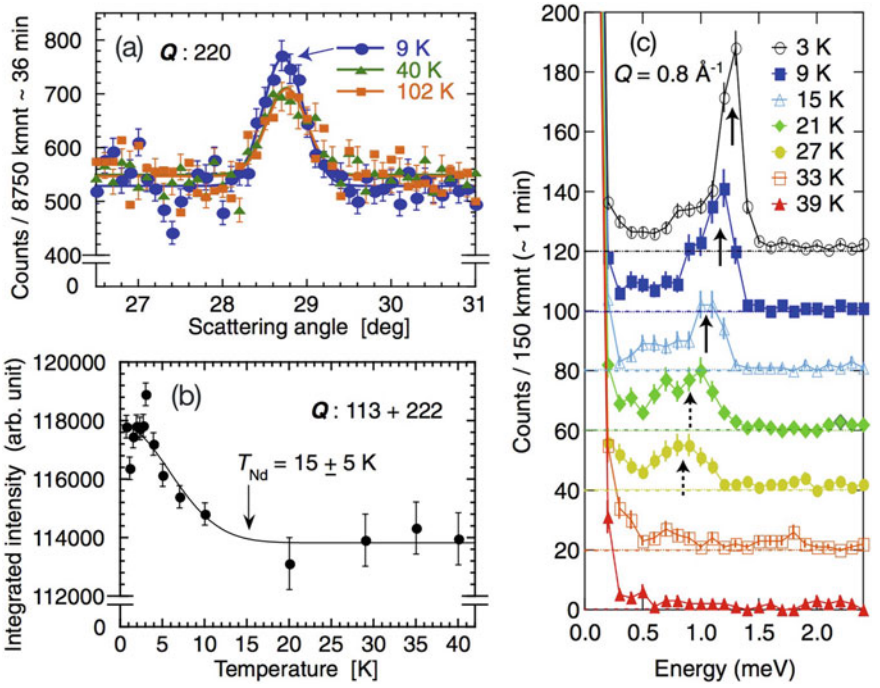

Fig. 14.9 Measured neutron diffraction data for powder $Nd_2Ir_2O_7$ [23]. **a** Bragg reflection lines around (220) reciprocal lattice point at 9, 40, and 102 K. **b** Temperature dependence of summation of the integrated intensities for Bragg reflection lines (113) and (222) **c** Energy scan data measured at constant Q of 0.8 at various temperatures below 39 K. The vertical origins shift to the height indicated by the horizontal dotted lines. Figures reprinted from [23] with permission from the Journal of the Physical Society of Japan

H_{int} appeared below T_{MI}, which indicates a magnetic ordering of Ir moments [24]. Furthermore, on cooling, the internal field tends to a constant but begins to increase again below 10 K. This increase corresponds to the gradual ordering of Nd magnetic moments.

The magnetic ordering of Ir moments with $\mathbf{Q} = 0$ below T_{MI} is clearly confirmed by the resonant magnetic X-ray scattering for $Eu_2Ir_2O_7$ as Eu^{3+} ion is non-magnetic [25]. Furthermore, the AIAO ordering is also realized in the MIT of $Cd_2Os_2O_7$ ($T_{\text{MI}} = 225$ K) [26]. It should be noticed that this AIAO ordering appears in MIT of *5d* electrons systems. It suggests that this Ising magnetic anisotropy is caused by strong spin-orbit interaction in *5d* electrons systems.

AIAO ordering can relieve the magnetic frustration in pyrochlore lattice with no change of cubic symmetry. In the case of long range ordering with "2-in 2-out" configuration, the symmetry may change to tetragonal. Actually, by using X-ray diffraction (XRD) measurements, the single crystal structure analyses for $Nd_2Ir_2O_7$ and $Eu_2Ir_2O_7$ reveal that the lattice keeps its FCC structure below T_{MI}. Figure 14.12

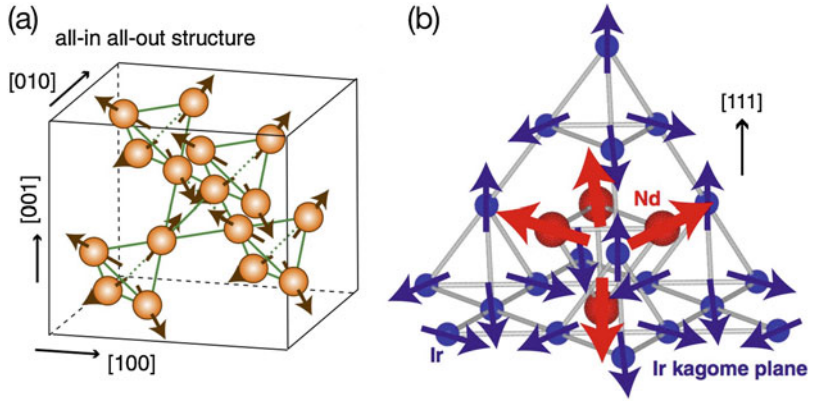

Fig. 14.10 **a** All-in all-out magnetic structure in pyrochlore lattice [23]. **b** Relation between magnetic moments (blue thin arrows) of Ir^{4+} ions (blue small balls) and magnetic moments (red thick arrows) of Nd^{3+} ions (red large balls) [23]. Both the Ir and the Nd moments form the all-in all-out structures. In this figure, the directions of Nd moments are described in the case of a ferromagnetic Nd-Ir interaction. Figures reprinted from [23] with permission from the Journal of the Physical Society of Japan

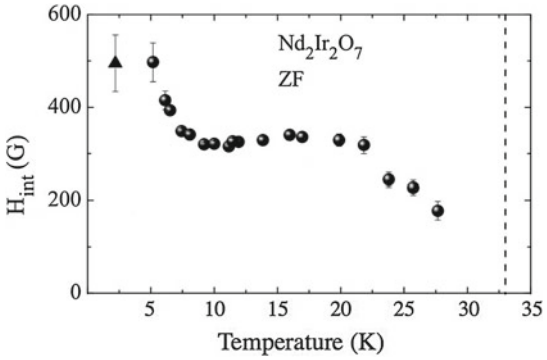

Fig. 14.11 For $Nd_2Ir_2O_7$, temperature dependence of the internal field at the muon site H_{int} observed in the μSR measurement, adapted from [24] with permission from the American Physical Society. The H_{int} at the base temperature is estimated by the LF measurement

shows the temperature dependence of Bragg reflection for $Nd_2Ir_2O_7$ ($T_{MI} = 33$ K) and $Eu_2Ir_2O_7$ (T_{MI}) by XRD measurements. No peak splitting and no superlattice reflections are observed below T_{MI} within the present experimental accuracy [25, 27]. This fact strongly supports the AIAO ordering in MIT of $Nd_2Ir_2O_7$ and $Eu_2Ir_2O_7$. From the result of Raman scattering for $Nd_2Ir_2O_7$, as no peak splitting and no new peak in the spectra are observed below T_{MI}, the lattice keeps its FCC structure [28]. However, Raman scattering experiments of $Eu_2Ir_2O_7$ and $Sm_2Ir_2O_7$ suggest that the symmetry could be lowered below T_{MI} as new peaks emerge at low temperature [28]; even if the symmetry change occurs below T_{MI}, the lattice deformation may be

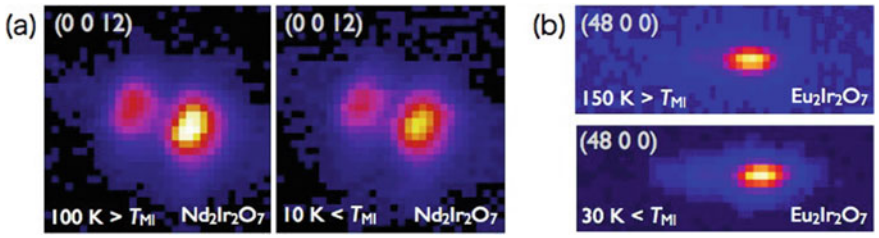

Fig. 14.12 Temperature dependence of Bragg reflection for **a** $Nd_2Ir_2O_7$ ($T_{MI} = 33$ K) and **b** $Eu_2Ir_2O_7$ (T_{MI}) by XRD measurements, adapted from [25] with permission from the American Physical Society

very tiny. The contradiction between XRD and Raman scattering measurements is an open problem. The further study on the low temperature structure is significant in order to clarify the mechanism of MIT.

14.3 Pressure-Induced Magnetic Ordering in $Nd_2Ir_2O_7$

The application of pressure is an effective method to lead to a dramatic change of ground state through the change of various physical parameters such as magnetic interactions, band width, and electronic correlations. The pressure effect of $Nd_2Ir_2O_7$ is shown in this section. Figure 14.13 shows the resistance of single crystal $Nd_2Ir_2O_7$ up to 15 GPa by using a diamond anvil cell [29]. The resistance $R(T)$ at room temperature decreases with increasing pressure [30]. The metal insulator transition of $Nd_2Ir_2O_7$ can be suppressed by the application of pressure. With increasing pressure, T_{MI} and $R(T)$ in the insulating phase also decrease. Only a tiny change of slope in $R(T)$ is observed at $T_{MI}(\sim 3.5\text{K})$ at 9 GPa, suggesting an incomplete opening of band gap. Furthermore, with increasing pressure, $R(T)$ at 10 GPa drops at 3.5 K and increases slightly at 3 K; this slight increase may be considered as the MIT observed at lower pressures. In addition, it should be noticed that $R(T)$ above 11 GPa drops at T_O; $T_O = 3$ K at 11 GPa. The insulating phase almost disappears above 10 GPa. The results clearly indicate the emergence of different phase transition from MIT.

It should be noted that a minimum in $R(T)$ is observed in the metallic phase above, at a temperature denoted as T_{min}, although no minimum in $R(T)$ is observed at ambient pressure as shown in Fig. 14.2. This minimum is observable for the first time by the suppression of the MIT under pressure. With increasing pressure, T_{min} shifts toward high temperature up to 13 GPa. Similar minimum in resistivity is observed in $Pr_2Ir_2O_7$ at ambient pressure [4]. Furthermore, $Eu_2Ir_2O_7$, which has no localized 4*f* moments, also shows a resistivity minimum above 6 GPa [31]. In the case of $Eu_2Ir_2O_7$, Kondo effect is ruled out, due to the absence of magnetic moments in Eu^{3+}. As the possible origin for resistivity minimum in $Pr_2Ir_2O_7$, Kondo effect and new mechanism caused by spin ice correlation are discussed [4, 19]. However, the origin of resistivity minimum in $Ln_2Ir_2O_7$ is still not clear.

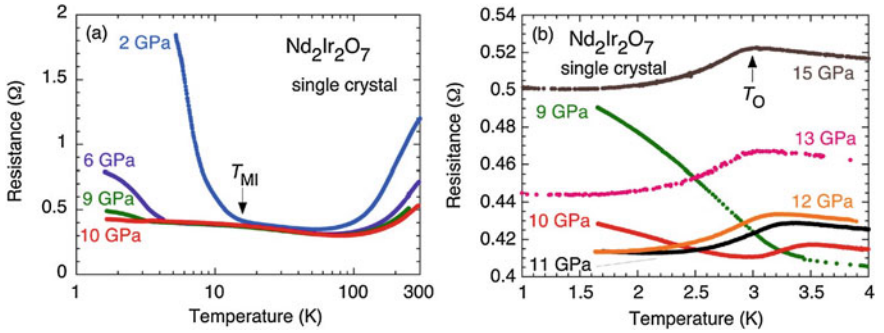

Fig. 14.13 **a** $R(T)$ of single crystal $Nd_2Ir_2O_7$ up to 10 GPa [29]. **b** $R(T)$ of single crystal $Nd_2Ir_2O_7$ in the pressure range of 9 and 15 GPa below 4 K. Figures reprinted from [29] with permission from the American Physical Society

Figure 14.14a shows $R(T)$ at 11 GPa under magnetic fields of 0, 0.5, and 1 T. With increasing magnetic field, the peak of $R(T)$ becomes broader and the $R(T)$ begins to decrease at higher temperature. These features are consistent with ferromagnetic (FM) transition. Now we will discuss the origin of the pressure-induced FM ordering in a pyrochlore lattice in the metallic state. There are three possibilities: ordering of the Ir moment, the Nd moment, or both Ir and Nd moments. Nd moments has a magnetic entropy from the ground state Kramers doublet. Therefore, the ground-state entropy of Nd moments has to be relieved down to 0 K. However, as is shown in Fig. 14.14b, no additional phase transition is observed at 15 GPa down to 40 mK. If the FM ordering originates from only the Ir moment, the ground-state entropy of the Nd moment is not relieved down to near 0 K. Furthermore, it is difficult to consider the FM magnetic ordering of Ir 5*d* conduction electrons because the change of $R(T)$ is not large; the drop of $R(T)$ is only 4%. Therefore, it is highly possible that the FM ordering is mainly driven by the Nd moments originated from RKKY interaction. $Nd_2Ir_2O_7$ under high pressure is considered frustrated Kondo lattice systems composed of localized ⟨111⟩ Ising 4*f* moments and 5*d* conduction electrons. According to theoretical study, the ordered phase of "two-in two-out" with the wave vector $\mathbf{Q} = (0,0,0)$ or $(0,0,2\pi/a)$ is found to be realized in metallic state [15, 17]. Consequently, it is speculated that the present pressure-induced transition of $Nd_2Ir_2O_7$ at 3 K is the FM ordering of "two-in two-out" with $\mathbf{Q} = (0,0,0)$; this corresponds to an "Ice-ferro" phase [17].

Figure 14.15 shows the pressure-temperature phase diagram for $Nd_2Ir_2O_7$. With increasing pressure, the "AIAO" insulator phase is rapidly suppressed. The AIAO insulator phase disappears above 11 GPa. Instead, a new magnetic ordered phase emerges in the metallic state. The feature of magnetic ordered phase is consistent with FM transition which is caused by Nd-moments originated from RKKY interaction. It is suggested that this pressure-induced phase corresponds to "Ice-ferro" phase which is theoretically predicted [15, 17]. Consequently, the application of pressure for $Nd_2Ir_2O_7$ can change the ground state from AFM AIAO insulator to FM metal

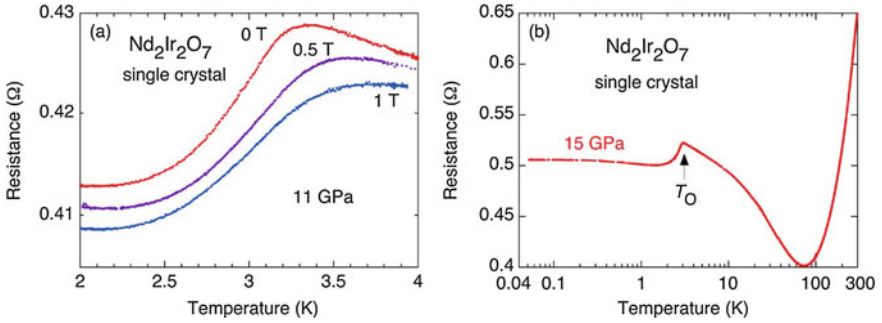

Fig. 14.14 **a** $R(T)$ at 11 GPa under several magnetic fields for $Nd_2Ir_2O_7$, adapted from [29] with permission from the American Physical Society. **b** $R(T)$ at 15 GPa down to 0.04 K for $Nd_2Ir_2O_7$

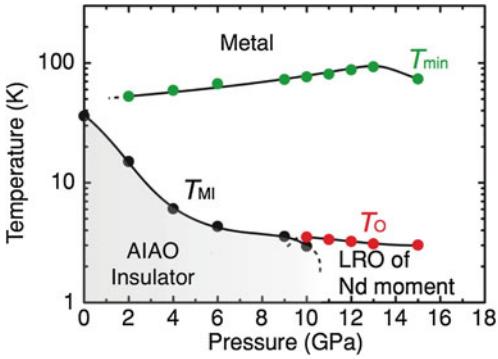

Fig. 14.15 Pressure-temperature phase diagram for $Nd_2Ir_2O_7$, adapted from [29] with permission from the American Physical Society

("ordered spin ice" of Nd moments). Further studies are desired in order to reveal the details of the new pressure-induced magnetic ordered phase.

14.4 Unconventional Anomalous Hall Effect in the Spin Ice Metal $Pr_2Ir_2O_7$

The final material, $Pr_2Ir_2O_7$, shows a quite different behavior from the other members of the family, $Ln_2Ir_2O_7$. In contrast to the other members, $Pr_2Ir_2O_7$ does not show metal-insulator transition, and the AF correlated Pr 4f moments of $Pr_2Ir_2O_7$ remain paramagnetic down to at least 0.3 K in the metallic state. This low-temperature metallic behavior places $Pr_2Ir_2O_7$ as a candidate for a geometrically frustrated Kondo lattice, and provides a stage, where a number of exotic behaviors are observed, such as Kondo-like resistivity minimum, topological Hall effect, quantum criticality, and spontaneous Hall effect. There have already been many theoretical analyses on these phenomena. For a summary of existing theoretical efforts, see the Chap. 13.

14.4.1 Material Properties of $Pr_2Ir_2O_7$

The metallic behavior of this compound is ascribed to the Ir $5d$-conduction bands [10]. A carrier density is estimated to be $2.6 \times 10^{20}\text{cm}^{-3}$ (1.8% = Pr), from the preliminary Hall effect measurements at low T. This low carrier density is also supported from the first-principle analyses [32, 33]. The crystal electric field (CEF) scheme of Pr has been determined by inelastic neutron scattering measurements at 5 K [34], as shown in Fig. 14.4. It reveals the following two points: (i) nine multiplet levels of Pr split into a ground-state doublet, three excited-singlets (162, 1218, 1392 K) and two excited doublets (580, 1044 K); and (ii) the groundstate doublet is magnetic with local [111] Ising anisotropy whose strength is 160 K. Because of the large separation between CEF levels, the magnetism discussed below comes solely from the ground doublet.

The $\langle 111 \rangle$ Ising-like anisotropy of the 4f moments is confirmed by the field dependence of the magnetization M along [100], [110] and [111] at 70 mK (Fig. 14.16a) [35]. At 13 T, M tends to saturate and approaches a Brillouin function for noninteracting, local $\langle 111 \rangle$ Ising spins with $g_J J_z$ consistent with the CEF analysis [34].

The inverse susceptibility is shown in the inset of Fig. 14.16b [4]. No anisotropy is found under a field of 0.1 T applied along [100], [110], and [111]. $\chi_0 = 1.25 \times 10^{-3}$emu/mole-Pr is determined by a Curie-Weiss (CW) analysis above 100 K using the formula $\chi = \chi_0 + C/(T - T^*)$. The effective moment $g_J\sqrt{J_z(J_z+1)} = 3.06\mu_B$ for the ground doublet is lower than the Pr multiplet value ($3.62\mu_B$) due to the CEF. The AF Weiss temperature $T^* = -20.0$K is most likely due to the RKKY interactions of the 4f moments.

14.4.2 Four Characteristic Temperature Regions

On cooling, $Pr_2Ir_2O_7$ shows the following four characteristic temperature regions: (1) $T > |T^*|$, Pr $4f$ moments are decoupled from Ir $5d$-conduction electrons; (2) $|T^*| > T > |\theta_W|$, the Kondo effect leads to the screening of the $4f$ moments; (3) $|\theta_W| > T > T_f$, underscreened moments form a spin-ice-like 2-in 2-out-dominant spin liquid states; and (4) $T_f > T$, the moments partially freeze.

The first evidence of Kondo effect in $Pr_2Ir_2O_7$ is the $\ln T$ dependence of resistivity $\rho(T)$ (Fig. 14.16b). Over a decade in T between 3 K and 35 K, $\rho(T)$ can be fit to the Hamann's expression (solid line) with $T_K = 25$ K [37]. In addition, the field dependence of the resistivity is consistent with the Kondo effect [38]; the negative magnetoresistance is proportional to the square of magnetization for all axes under fields up to 2T (inset of Fig. 14.16b, the top panel). Second, the Kondo effect is also seen in the low T decrease of the effective Curie constant $C(T) = T\chi(T)$; see the middle panel of Fig. 14.16b. The rapid decrease in $C(T)$ below 10 K suggests that the moment size diminishes owing to Kondo screening. Correspondingly, $\chi^{-1}(T)$ follows the CW law over a decade in T from 1.5 to 16 K, yielding a slightly smaller

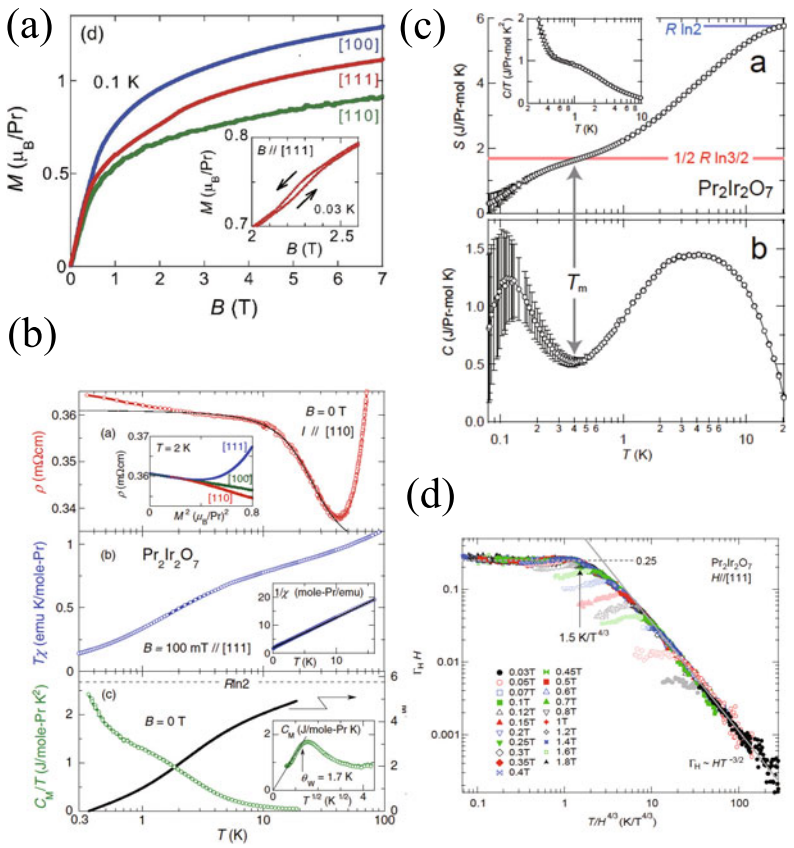

Fig. 14.16 **a** The magnetization process of $Pr_2Ir_2O_7$. The inset highlights the metamagnetic transition observed for [111] field direction.Figures reprinted from [35]. **b** (top)The temperature dependence of resistivity is shown. The inset shows the magnetoresistivity for magnetic field directions along [100], [110], and [111] at 2K. (middle) $T\chi$ is plotted against temperature, where χ is the magnetic susceptibility. The inset shows the inverse susceptibility, $1/\chi$. (bottom) Temperature dependence of C_M/T is shown with green open circles, where C_M is magnetic specific heat. The solid line shows the entropy. The inset shows C_M, which has a peak, around the temperature, $\theta_W \sim 1.7$K. Figures reprinted from [4] with permission from the American Physical Society. **c** (Top) the entropy and (bottom) the specific heat in a wide temperature range, reprinted from [36] with permission from Nature. **d** $\Gamma_H H$ is plotted against $T/H^{4/3}$, reprinted from [36] with permission from Nature

effective moment $2.69\mu_B$, and a reduced Weiss temperature, $|\theta_W| = 1.7$K, in comparison with the high T values ($3.06\mu_B$, 20 K). These results and the crossover to ln T dependence below $|\theta_W|$ indicate partial screening of 4f moments. The monotonic increase of $\rho(T)$ on cooling indicates incoherent spin scattering in the spin-liquid state at $T < |\theta_W|$ [4].

Evidence for the formation of spin-ice-like state can be found in the T dependence of the magnetic part of the specific heat C_M (Fig. 14.16b). No evidence of LRO, but

a rapid increase up to $\sim$ 2.5J/mole-Pr K^2 is seen in $C_{\rm M}/T$ below $|T^*|$, attributable to the Kondo screening. Significantly, $C_{\rm M}$ forms a broad peak around $T \sim |\theta_{\rm W}|$, and decreases on cooling with a $T^{1/2}$ dependence between 1.8 and 0.4 K (inset of Fig. 14.16b, the bottom panel). This peak indicates the formation of a correlated spin-ice-like state below $|\theta_{\rm W}|$. The entropy, $S_{\rm M}$ also follows the $T^{1/2}$ dependence at low Ts, indicating the presence of much more highly degenerate magnetic states than in a Fermi liquid with a T-linear entropy. This also represents additional evidence for magnetic frustration. In fact, at $T_m \simeq 0.4K$, the entropy approaches the Pauling value, indicating that the formation of two-in two-out spin-ice configurations is completed in all of the tetrahedra (Fig. 14.16c) [36].

The fact that the metamagnetic transition occurs only for $\mathbf{H} \parallel [111]$ provides further evidence for the formation of the "2-in, 2-out" configurations of $\langle 111 \rangle$ Ising moments on each tetrahedron (inset of Fig. 14.16a) [35]. Further consistency with the "2-in 2-out" correlation can be found for the values of the magnetization $M_{\rm c}$ and the magnetic field $B_{\rm c}$ at the metamagnetic transition. Using the Landé factor g_J for Pr^{3+} and J obtained from $p_{\rm eff} = g_J\sqrt{J(J+1)}$, M_c is estimated to be $0.9\mu_{\rm B}$/Pr, which is close to our observation of $M_c = 0.8\mu_{\rm B}$/Pr. On the other hand, the observed $B_c = 2.3$T indicates the effective nearest-neighbor FM coupling $J_{\rm ff}^{\rm eft} \sim 1.4$K which is close to the peak temperature ($\sim$ 2K) of the magnetic specific heat $C_{\rm M}$ as in spin-ice systems. Therefore, we conclude that at $T \simeq J_{\rm ff}^{\rm eft}$, the "2-in 2-out" configuration appears with the highest probability.

Further cooling below 0.4 K yields to a huge enhancement of the specific heat divided by temperature. In the absence of a clear phase transition anomaly we associate the corresponding entropy reduction to the melting of spin ice configurations by quantum fluctuations at $T_m \simeq 0.4$K (Fig. 14.16c) [36]. Interestingly, the cooling process down to T_m can be associated with quantum critical behavior. The magnetic Grüneisen ratio $\Gamma_H = 1/T(dT/dH)_s$ is defined as the change of temperature with magnetic field under adiabatic conditions, which is also expressed by the magnetization M and specific heat C, as $\Gamma_H = -(dM/dT)/C$. Upon cooling, Γ_H at low field diverges according to $T^{-3/2}$ over almost one decade in temperature down to about $T_m \simeq 0.4K$, providing evidence for quantum critical behavior. In Fig. 14.16d, the magnetic Grüneisen ratio data are displayed as $\Gamma_H H$ vs $T/H^{4/3}$. The measured data collapse on a common curve for about four decades in the x- and more than three decades in the y-axis. This confirms that the system is located at a zero-field QCP. The scaling plot clearly shows the crossover between the quantum critical and quantum paramagnetic states, that are characterized by $\Gamma_H \sim HT^{-3/2}$ and $\Gamma_H = 0.25/H$ (temperature independent), respectively.

14.4.3 Hall Response in Spin-Ice and Spin-Liquid Regions

The spin ice regime below $|\theta_{\rm W}|$ exhibits a characteristic Hall response. The noncoplanar texture of Pr $\langle 111 \rangle$ Ising-like moments imposes a spin-chirality effect on the Ir $5d$ conduction band, and gives rise to an anomalous Hall response. Figure 14.17a shows

the field dependences of the Hall conductivity along [100], [110] and [111] measured at $T = 0.5\,\mathrm{K}$ [40]. Up to $B_p \sim 0.7\mathrm{T}$, $\sigma_{xy}(B)$ is nearly isotropic and shows rapid and linear increase with field. However, beyond B_p, the field dependence becomes strongly anisotropic and is no longer proportional to the magnetization. In terms of the conventional mechanism due to the spin-orbit coupling, it is highly difficult to understand the above nontrivial temperature and field dependences of the large Hall effect observed below $\theta_w = 1.7\mathrm{K}$. Instead, it is natural to expect the spin-chirality contribution to the Hall effect because the Pr $\langle 111 \rangle$ Ising-like spins under fields may well have a sizeable spin chirality due to their noncoplanar spin texture and produce a fictitious magnetic field on the Ir sites through the Kondo coupling. This possibility has been discussed in $Nd_2Mo_2O_7$, which also shows nonmonotonic M dependence of σ_{xy} [39].

More strikingly, finite Hall resistivity is observed in the absence of both an external magnetic field and conventional magnetic long-range order. This spontaneous Hall effect strongly suggests the existence of a chiral spin liquid, a spin-liquid phase breaking the time-reversal symmetry. Below 2K, $\sigma_{\mathrm{H}}(T)$ exhibits a strong temperature dependence and even bifurcation at $\theta \sim 1.5\mathrm{K}$ between the zero-field cooled (ZFC) and field-cooled (FC) results. On the other hand, the onset temperature of the irreversibility in $\chi(T)$, $T_{\mathrm{f}} \sim 0.3\mathrm{K}$ (Fig. 14.17b) is significantly lower than that in $\sigma_{\mathrm{H}}(T)$, $\theta \sim 1.5\mathrm{K}$. This hysteresis in $\sigma_{\mathrm{H}}(T)$ suggests that the time-reversal symmetry (TRS) is already broken macroscopically below in the spin-liquid state. The finite σ_{H} observed in the apparent absence of B and M indicates that the TRS is broken spontaneously and macroscopically in the spin-liquid state, pointing to an LRO or freezing of higher degrees of freedom than spin dipole moments, for instance, the net spin chirality. There exists a close link between the macroscopic TRS-breaking and the local "2-in, 2-out" spin correlation. The onset temperature $\theta \sim 1.5\mathrm{K}$ almost coincides with the effective FM coupling $J_{\mathrm{ff}}^{\mathrm{eft}} \sim 1.4\mathrm{K}$ estimated from the metamagnetic transition field B_{c}. Besides, the hysteresis observed in σ_{H} as a function of field disappears at B_{c} where a large portion of "2-in, 2-out" configurations are transformed into "3-in 1-out/1-in 3-out". Therefore, the macroscopically TRS-broken spin-liquid state found in $T_{\mathrm{f}} \leq T \leq \theta_{\mathrm{W}}$ should comprise the "2-in, 2-out" configurations having a net spin chirality.

The transport properties of $Pr_2Ir_2O_7$ have been investigated up to much higher magnetic field ~35 T [41]. Figure 14.17c shows the magnetoresistivity ratio as a function of field along three principal axes at $T = 0.03\,\mathrm{K}$. When H is applied along the [100] and [110] directions, the magnetoresistivity is small and negative, suggesting the suppression of scattering by local Pr moments as they are oriented along the field. In contrast, for fields along the [111]-direction one observes a pronounced positive increase in magnetoresistivity above the metamagnetic critical field $B_{\mathrm{c}} \simeq 2.3\mathrm{T}$ [41]. It is followed by an oscillatory structure. This oscillatory component is not periodic in H nor in H^{-1}, although its nearly exponential growth as a function of H indicates that it corresponds to Shubnikov-de Haas (SdH) oscillations. In fact, one can fit it to a single Lifshitz-Kosevich oscillatory term containing a single field-dependent frequency

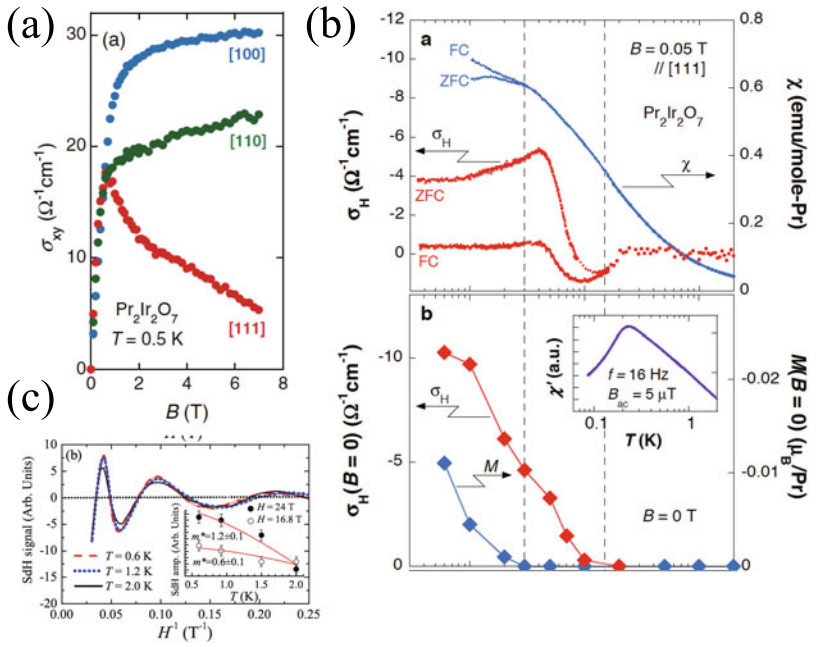

Fig. 14.17 **a** The magnetic field dependence of Hall resistivity for [100], [110] and [111] field directions at $T = 0.5$K, reprinted from [40] with permission from the American Physical Society. **b** The temperature dependence of (top) FC and ZFC magnetic susceptibility (χ) and Hall conductivity (σ_{H}), (bottom) the zero-field Hall conductivity and magnetization (M), reprinted from [7] with permission from Nature. **c** The SdH signal, reprinted from [41] with permission from the American Physical Society

(dotted line) implying that the associated Fermi-surface cross-sectional area is field-dependent. This probably results from the effect of the Zeeman splitting on a very small Fermi-surface whose frequency $F < 10$T at low-fields, increases up to ~ 22 T at higher fields. As seen in Fig. 14.17c, the oscillations are still very well-defined at much higher temperatures. The temperature dependence of their amplitude indicates quite light effective masses which are also field-dependent, see inset of Fig. 14.17c. The oscillations are seen only for fields applied along the [111]-direction and above B_c where the 3-in 1-out spin-configuration becomes dominant. This indicates that the field-induced change, from a state containing all possible degenerate 2-in 2-out spin configurations to a state dominated by a uniform 3-in 1-out spin configuration, can actually lead to the reconstruction of the Fermi surface.

References

1. M. Hanawa, Y. Muraoka, T. Tayama, T. Sakakibara, J. Yamaura, and Z. Hiroi, Phys. Rev. Lett. **87**, 187001 (2001). https://doi.org/10.1103/PhysRevLett.87.187001
2. Y. Taguchi, Y. Oohara, H. Yoshizawa, N. Nagaosa, and Y. Tokura, Science **291**, 2573 (2001). https://doi.org/10.1126/science.1058161
3. S. Yonezawa, Y. Muraoka, Y. Matsushita, and Z. Hiroi, J. Phys.: Condens. Matter **16**, L9 (2004). https://doi.org/10.1088/0953-8984/16/3/L01
4. S. Nakatsuji, Y. Machida, Y. Maeno, T. Tayama, T. Sakakibara, J. van Duijn, L. Balicas, J. N. Millican, R. T. Macaluso, and J. Y. Chan, Phys. Rev. Lett. **96**, 087204 (2006). https://doi.org/10.1103/PhysRevLett.96.087204
5. K. Matsuhira, M. Wakeshima, R. Nakanishi, T. Yamada, A. Nakamura, W. Kawano, S. Takagi, and Y. Hinatsu, J. Phys. Soc. Jpn. **76**, 043706 (2007). https://doi.org/10.1143/JPSJ.76.043706
6. A. Yamamoto, P. A. Sharma, Y. Okamoto, A. Nakao, H. A. Katori, S. Niitaka, D. Hashizume, and H. Takagi, J. Phys. Soc. Jpn. **76**, 043703 (2007). https://doi.org/10.1143/JPSJ.76.043703
7. Y. Machida, S. Nakatsuji, S. Onoda, T. Tayama, T. sakakibara, Nature **463**, 210 (2009). https://doi.org/10.1038/nature08680
8. K. Momma, and F. Izumi, J. Appl. Crystallogr. **44**, 1272 (2011). https://doi.org/10.1107/S0021889811038970
9. K. Matsuhira, M. Wakeshima, Y. Hinatsu, and S. Takagi, J. Phys. Soc. Jpn. **80**, 094701 (2011). https://doi.org/10.1143/JPSJ.80.094701
10. D. Yanagishima and Y. Maeno, J. Phys. Soc. Jpn. **70**, 28 (2001) . https://doi.org/10.1143/JPSJ.70.28
11. K. Matsuhira, K. Kuroda, T. Sakakibara, M. Wakeshima, and Y. Hinatsu, JPS Conf. Proc. **3**, 013017 (2014). https://doi.org/10.7566/JPSCP.3.013017
12. L. Savary, E.-G. Moon, and L. Balents, Phys. Rev. X **4**, 041027 (2014). https://doi.org/10.1103/PhysRevX.4.041027
13. M. Watahiki, K. Tomiyasu, K. Matsuhira, K. Iwasa, M. Yokoyama, S. Takagi, M. Wakeshima, and Y. Hinatsu, J. Phys.: Conf. Ser. **320**, 012080 (2011). https://doi.org/10.1088/1742-6596/320/1/012080
14. K. Matsuhira, Y. Hinatsu, K. Tenya, H. Amitsuka, and T. Sakakibara, J. Phys. Soc. Jpn. **71**, 1576 (2002). https://doi.org/10.1143/JPSJ.71.1576
15. A. Ikeda and H. Kawamura, J. Phys. Soc. Jpn. **77**, 073707 (2008). https://doi.org/10.1143/JPSJ.77.073707
16. S. Onoda and Y. Tanaka, Phys. Rev. B **86**, 094411 (2011). https://doi.org/10.1103/PhysRevB.86.094411
17. H. Ishizuka, M. Udagawa, and Y. Motome, J. Phys. Soc. Jpn. **81**, 113706 (2012). https://doi.org/10.1143/JPSJ.81.113706
18. G. Chen and M. Hermele, Phys. Rev. B **86**, 235129 (2012). https://doi.org/10.1103/PhysRevB.86.235129
19. M. Udagawa, H. Ishizuka, and Y. Motome, Phys. Rev. Lett. **108**, 066406 (2012). https://doi.org/10.1103/PhysRevLett.108.066406
20. The anomaly in specific heat shows a strong sample dependence. As MIT is sharper, the anomaly is clearly observed. Even when an anomaly in magnetic susceptibility caused by MIT is observed, the specific heat has no clear peak.
21. J. J. Ishikawa, E. C. T. O' Farrell, and S. Nakatsuji, Phys. Rev. B **85**, 245109 (2012). https://doi.org/10.1103/PhysRevB.85.245109
22. S. Zhao, J. M. Mackie, D. E. MacLaughlin, O. O. Bernal, J. J. Ishikawa, Y. Ohta, and S. Nakatsuji, Phys. Rev. B **83**, 180402(R) (2011). https://doi.org/10.1103/PhysRevB.83.180402
23. K. Tomiyasu, K. Matsuhira, K. Iwasa, M. Watahiki, S. Takagi, M. Wakeshima, Y. Hinatsu, M. Yokoyama, K. Ohoyama, and K. Yamada, J. Phys. Soc. Jpn. **81**, 034709 (2012). https://doi.org/10.1143/JPSJ.81.034709
24. H. Guo, K. Matsuhira, I. Kawasaki, M. Wakeshima, Y. Hinatsu, I. Watanabe, and Z. Xu, Phys. Rev. B **88**, 060411(R) (2013). https://doi.org/10.1103/PhysRevB.88.060411

25. H. Sagayama, D. Uematsu, T, Arima, K. Sugimoto, J. J. Ishikawa, E. O'Farrell, and S. Nakatsuji, Phys. Rev. B **87**, 100403(R) (2013). https://doi.org/10.1103/PhysRevB.87.100403
26. J. Yamaura, K. Ohgushi, H. Ohsumi, T. Hasegawa, I. Yamauchi, K. Sugimoto, S. Takeshita, A. Tokuda, M. Takata, M. Udagawa, M. Takigawa, H. Harima, T. Arima and Z. Hiroi, Phys. Rev. Lett. **108**, 247205 (2012). https://doi.org/10.1103/PhysRevLett.108.247205
27. The XRD measurements for single crystal $Nd_2Ir_2O_7$ were performed by J. Yamaura.
28. T. Hasegawa, N. Ogita, K. Matsuhira, S. Takagi, M. Wakeshima, Y. Hinatsu, and M. Udagawa, J. Phys.: Conf. Ser. **200**, 012054 (2010). https://doi.org/10.1088/1742-6596/200/1/012054
29. M. Sakata, T. Kagayama, K, Shimizu, K. Matsuhira, S. Takagi, M. Wakeshima, and Y. Hinatsu, Phys. Rev. B **83**, 041102(R) (2011). https://doi.org/10.1103/PhysRevB.83.041102
30. The present resistance value of 1 Ω approximately corresponds to 5 mΩcm although it is hard to convert the resistance into the resistivity because the shape of sample is not exactly a rectangular parallelepiped. The resistivity of $Nd_2Ir_2O_7$ is roughly twice as large as that of $Pr_2Ir_2O_7$
31. F. F. Tafti, J. J. Ishikawa, A. McCollam, S. Nakatsuji, and S. R. Julian, Phys. Rev. B **85**, 205104 (2012). https://doi.org/10.1103/PhysRevB.85.205104
32. S. K. Pandey and L. Maiti, Phys. Rev. B **82**, 035110 (2010). https://doi.org/10.1103/PhysRevB.82.035110
33. F. Ishii et al., J. Phys. Soc. Jpn. **84**, 073703 (2015). https://doi.org/10.1143/JPSJ.84.073703
34. Y. Machida et al., J. Phys. Chem. Solids **66**, 1435 (2005). https://doi.org/10.1016/j.jpcs.2005.05.026
35. S. Nakatsuji et al., J. Phys. Conf. Ser. **320**, 012056 (2011). https://doi.org/10.1088/1742-6596/320/1/012056
36. Y. Tokiwa, J. J. Ishikawa, S. Nakatsuji, P. Gegenwart, Nat. Mater. **13**, 356 (2014). https://doi.org/10.1038/nmat3900
37. D. R. Hamann, Phys. Rev. **158**, 570 (1967). https://doi.org/10.1103/PhysRev.158.570
38. A. C. Hewson, *The Kondo Problem of Heavy Fermions* (Cambridge University Press, Cambridge, England, 1993). https://doi.org/10.1017/CBO9780511470752
39. Y. Taguchi et al., Science **291**, 2573 (2001). https://doi.org/10.1126/science.1058161
40. Y. Machida et al., Phys. Rev. Lett. **98**, 057203 (2007). https://doi.org/10.1103/PhysRevLett.98.057203
41. L. Balicas, S. Nakatsuji, Y. Machida and S. Onoda, Phys. Rev. Lett. **106**, 217204 (2011). https://doi.org/10.1103/PhysRevLett.106.217204

Chapter 15
Artificial Spin Ice: Beyond Pyrochlores and Magnetism

Gia-Wei Chern

Abstract Artificial spin ices [1–4] have raised considerable interest for its technological potentials, and as a tailorable medium to investigate collective phenomena in a materials-by-design approach. These metamaterials are made of frustrated arrays of interacting single-domain ferromagnetic nano-islands of about 100 nm size [5]. Figure 15.1 shows the two most representative artificial spin ices, the square [6] and honeycomb [7, 8] arrays; both have been realized experimentally. In this chapter, we review the thermodynamic behaviors and nonequilibrium dynamics of these magnetic nano-arrays from the theoretical point of view. A special focus is the novel emergent phases and phenomena that originate from the magnetic charge degrees of freedom in these metamaterials. Finally, we also discuss recent theoretical proposals of extending ice physics to other artificial systems such as colloidal particles in optical trap arrays and cold atoms in optical lattices.

15.1 Artificial Spin Ice: Basic Energetics and Dynamics

Spin ice materials are essentially frustrated Ising magnets. While the Ising nature of pyrochlore spin-ice compounds such as $Dy_2Ti_2O_7$ and $Ho_2Ti_2O_7$ is due to a strong easy-axis spin anisotropy, the effective Ising variables in artificial spin ice result from the large magnetostatic shape anisotropy of the nano-islands. The magnetostatic energy is minimized when the moments align with the long axis of the islands, giving rise to two equilibrium state specified by a Ising variable $\sigma = \pm 1$. The two Ising states of a nano-island are separated by a large energy barrier. Consequently, each Ising configuration $\{\sigma_i\}$ represents a metastable local energy minimum of the array. Transitions between different Ising configurations, on the other hand, are governed by complex magnetization dynamics of individual islands; this process involves the creation and subsequent annihilation of domain walls and other topological defects. A complete description of the magnetic nano-array is given by the magnetization

G.-W. Chern (✉)
Department of Physics, University of Virginia, Charlottesville, USA
e-mail: gchern@virginia.edu

M. Udagawa and L. Jaubert (eds.), *Spin Ice*, Springer Series in Solid-State Sciences 197,
https://doi.org/10.1007/978-3-030-70860-3_15

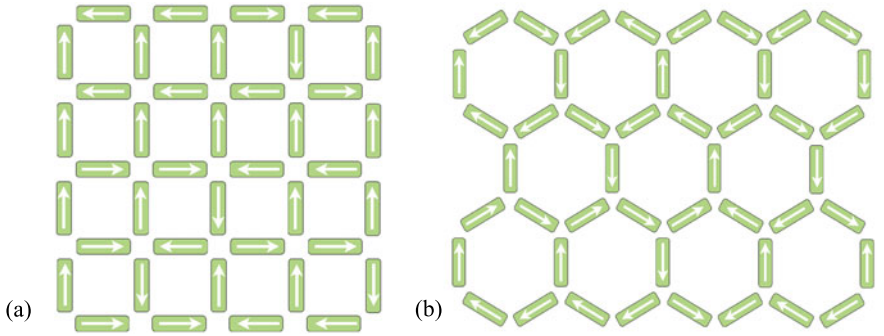

Fig. 15.1 Artificial spin ices as magnetic metamaterials. **a** square and **b** honeycomb arrays of single-domain ferromagnetic islands. The centers of the nano-islands form a checkerboard and a kagome lattices for arrays shown in (**a**) and (**b**), respectively. The arrows indicate the magnetizations of individual islands. The configuration in **a** is a generic spin ice state in square array, in which every four-leg vertex has two spins pointing in and two pointing out. A generic kagome ice-I state is shown in **b**, where every vertex is either in a 2-in-1-out or a 1-in-2-out configurations

field $\mathbf{m}_i(\mathbf{r}, t)$ of each island or element. In some experimental realizations, the ends of the islands are joined together, giving rise to a connected nano-wire network.

Let the magnetization of the i-th nano-island be $\mathbf{m}_i(\mathbf{r})$, the Hamiltonian of the magnetic array is

$$\mathscr{H} = \mathscr{A}_{\text{ex}} \sum_i \int_{\Omega_i} |\nabla \mathbf{m}_i|^2 \, d\mathbf{r} - \frac{\mu_0}{2} \sum_{i,j} \int_{\Omega_i} \mathbf{m}_i \cdot \mathbf{h}_j \, d\mathbf{r}, \tag{15.1}$$

where Ω_i is the domain of the ith island, and the demagnetizing field $\mathbf{h}_i(\mathbf{r})$ is related to the magnetization through Maxwell's equations,

$$\nabla \times \mathbf{h}_i = \mathbf{0}, \qquad \nabla \cdot (\mathbf{h}_i + \mathbf{m}_i) = 0. \tag{15.2}$$

The $\mathbf{h}_i$ can be viewed as field generated by magnetic charge density $\rho_i(\mathbf{r}) = -\nabla \cdot \mathbf{m}_i$. The total magnetic field is given by $\mathbf{H} = \sum_i \mathbf{h}_i$, and the total magnetization $\mathbf{M} = \sum_i \mathbf{m}_i$. The first term in (15.1) comes from the microscopic exchange interaction, while the second term is the magnetostatic energy $(\mu_0/2) \int |\mathbf{H}|^2 d\mathbf{r} = -(\mu_0/2) \int \mathbf{M} \cdot \mathbf{H} \, d\mathbf{r}$ in the absence of external current [9]. Here we have neglected magnetocrystalline anisotropy energy, which is a reasonable approximation for most materials used in the nano-arrays.

The dominant energy in (15.1) is the self-coupling term ($i = j$) of the magnetostatic energy. This term favors magnetization pointing along the long axis of the island:

$$\mathbf{m}_i(\mathbf{r}) \approx m_0 \, \sigma_i \, \hat{\mathbf{e}}_i, \tag{15.3}$$

where m_0 is the equilibrium magnetization, $\hat{\mathbf{e}}_i$ is a unit vector pointing along the long axis of the island, and $\sigma_i = \pm 1$ is an Ising variable indicating the two possible orientations. The uniform magnetization described in (15.3) also minimizes the exchange interaction, the first term in (15.1). The magnetic state of the nano-array is then specified by a collection of Ising variables $\{\sigma_i\}$. The effective interactions between these Ising variables is given by the magnetostatic couplings between neighboring islands, the $i \neq j$ terms in (15.1).

Assuming uniform magnetization for each island, the demagnetizing field $\mathbf{h}_i$ can be approximated by a dipolar field, and the interaction energy of the magnetic array becomes:

$$\mathscr{H}_{\text{dipole}} = \frac{\mu_0 m_0^2 A^2}{8\pi} \sum_{i \neq j} \int\int d\ell_i \, d\ell_j \frac{(\hat{\mathbf{e}}_i \cdot \hat{\mathbf{e}}_j) - 3(\hat{\mathbf{e}}_i \cdot \hat{\mathbf{r}}_{ij})(\hat{\mathbf{e}}_j \cdot \hat{\mathbf{r}}_{ij})}{|\mathbf{r}_i - \mathbf{r}_j|^3} \sigma_i \, \sigma_j, \quad (15.4)$$

where A is the cross section of the island, ℓ_i measures the distance along the island, $\mathbf{r}_i = \mathbf{r}(\ell_i)$ is the position of the line element $d\ell_i$, and $\hat{\mathbf{r}}_{ij} = (\mathbf{r}_i - \mathbf{r}_j)/|\mathbf{r}_i - \mathbf{r}_j|$. This Ising model is used to investigate large-scale thermodynamic behaviors of artificial spin ices, to be discussed below.

Magnetic charges as emergent degrees of freedom play an important role in describing the static as well as dynamic properties of spin ice materials [10, 11]. For artificial spin-ice arrays, the magnetostatic energy can also be expressed as the Coulomb interaction of magnetic charges with bulk density $\rho = -\nabla \cdot \mathbf{M}$ and surface density $\rho_s = \mathbf{M} \cdot \hat{\mathbf{n}}$. The magnetostatic energy is minimized when there are no magnetic charges and $\mathbf{H} = 0$. This minimum charge condition leads to the ice rules in artificial spin ice. For a nano-island with uniform magnetization, the surface charges at the two ends of the island are the main source of magnetic charge. A uniformly magnetized island can be approximated by a dumbbell with a pair of magnetic monopoles with charge $\pm q$ located at its two ends [11]. Here $q = \int \rho_s \, dS = m_0 A$. One can then assign a magnetic charge to each vertex as the sum of the monopole charges joining at the vertex, i.e. $Q_\alpha = \sum_{i \in \alpha} q_i$ for vertex α. For connected nanowire network [8], the vertex as junction of the nano-wires has an internal magnetization structure. Unlike isolated islands, most of the charge at these connected junctions come from the bulk charge $\rho = -\nabla \cdot \mathbf{M}$. Its total charge is the volume integral $Q = \int \rho \, dV = -\oint \mathbf{M} \cdot \hat{\mathbf{n}} dA$, which can be converted into surface integrals over the island cross sections; its value again is quantized to multiples of $q = m_0 A$. Examples of dumbbell representations for spin ice are shown in Fig. 15.11.

For a four-legged vertex in a square array, the total charge can be $Q = 0, \pm 2q$, or $\pm 4q$; see Fig. 15.2a. The minimum charge $Q = 0$ condition leads to the two-in-two-out ice rules. The vertices in a honeycomb lattice, Fig. 15.1b, have three legs and always have a *finite* magnetic charge $Q = \pm q$ or $\pm 3q$. The condition of minimum charge gives rise to a different set of two-in-one-out/one-in-two-out pseudo-ice rules.

The magnetic charge can also be expressed in terms of Ising variables. As both square and honeycomb lattices are bipartite, we define the vector $\hat{\mathbf{e}}_i$ on each link as pointing from sublattice B to A. The magnetic charge of vertex α is then given by

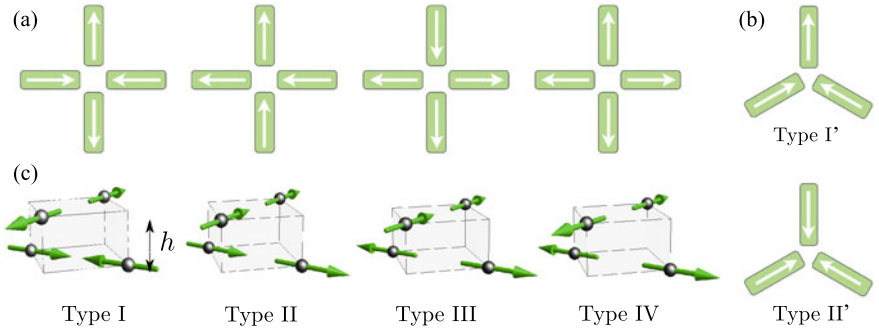

Fig. 15.2 Types of vertices in artificial spin ices. **a** four-legged vertices have 16 possible moment configurations, which are classified into four symmetry distinct types. The total magnetic charge $Q = 0$ for type-I and II vertices (2-in-2-out), $Q = \pm 2q$ for type-III (3-in-1-out or 1-in-3-out), and $Q = \pm 4q$ for type-IV (4-in or 4-out) **b** the 8 possible three-legged vertices separate into two types of different symmetries. There is always a nonzero charge in a three-legged vertex: $Q = \pm q$ for type-I' (2-in-1-out or 1-in-2-out), and $Q = \pm 3q$ for type-II' (3-in or 3-out). **c** The four different types of boxes with a height offset h between pairs of parallel moments

$Q_\alpha = \pm q \sum_{i\in\alpha} \sigma_i$, where $+$ $(-)$ sign is used for sublattices A (B). In the dumbbell approximation, the magnetostatic energy becomes

$$\mathscr{H}_{\text{dumbbell}} = \sum_\alpha \frac{Q_\alpha^2}{2C} + \frac{\mu_0}{8\pi} \sum_{\alpha\neq\beta} \frac{Q_\alpha Q_\beta}{|\mathbf{r}_\alpha - \mathbf{r}_\beta|}, \tag{15.5}$$

where $C \sim d/\mu_0$ is an effective capacitance for the self-energy of individual vertex, and d is the length scale of a vertex junction. The above Hamiltonian neglects higher-order multipole interactions that are weak and fall off quickly with the distance; these terms are responsible for the long-range ordering of magnetic moments at low temperatures. Note that the dominant Q_α^2 term is equivalent to an antiferromagnetic nearest-neighbor (NN) Ising ice model

$$\mathscr{H}_{\text{ice}} = J \sum_{\langle ij\rangle} \sigma_i \sigma_j, \tag{15.6}$$

on the checkerboard and kagome lattices for the two array geometries; here $J = 1/C$ is the effective exchange interaction. Minimization of $\mathscr{H}_{\text{ice}}$ gives rise to the ice rules, whereas the Coulomb interaction, second term in $\mathscr{H}_{\text{dumbbell}}$, is the source of novel emergent phenomena associated with magnetic charges to be discussed below.

In terms of the mesoscopic Ising degrees of freedom, the dynamics of artificial spin ice is governed by flipping of the Ising variables $\sigma_i \to -\sigma_i$. Microscopically, magnetization reversal in a nano-island is a complex process involving the nucleation of domain walls, and their subsequent propagation and annihilation [12, 13]; see Fig. 15.3 for the case of a connected honeycomb array. The process is usually

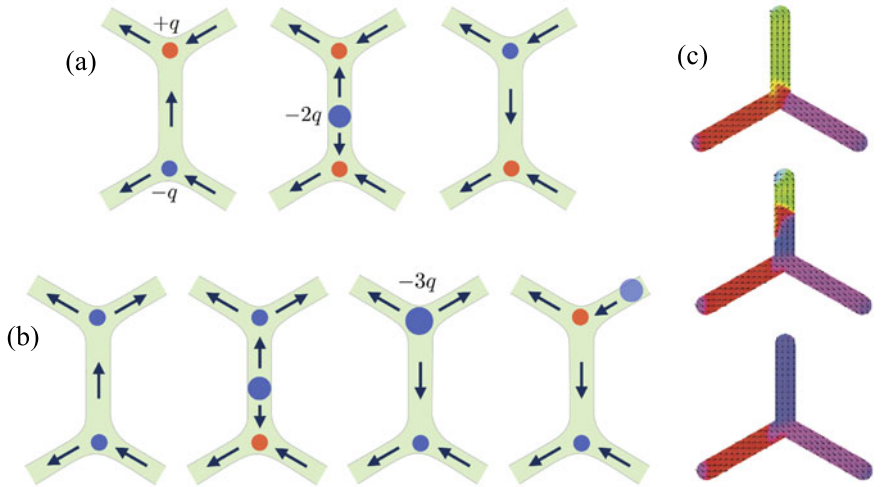

Fig. 15.3 Magnetization reversal in artificial spin ice. **a** a domain wall carrying a magnetic charge $-2q$ is emitted at one end of the link, propagates along the field direction, and gets absorbed by the vertex at the other end. **b** When the domain wall hits a vertex with like magnetic charge, it creates a high-energy $-3q$ vertex which quickly emits a new domain wall into an adjacent link. **c** Micromagnetic simulation using the OOMMF [24] simulator of the reversal of a magnetic island showing a propagating vortex-type head-to-head domain wall, reproduced from [23] by permission of IOP Publishing.

triggered when the total magnetic field at the nano-island, including external and dipolar fields, exceeds a threshold. For connected nano-islands, the magnetization reversal begins when a head-to-head domain wall is emitted at one of the nano-wire vertices. This process conserves the magnetic charge: the emission of a domain wall of charge $\pm 2q$ converts the charge of the vertex from $\pm q$ to $\mp q$. The Zeeman force $f_Z = \pm 2q\mu_0 H$ then pushes the domain wall to the opposite end of the island; see Figs. 15.3a, b. For disconnected arrays, the reversal process might start inside the bulk of the island. For example, edge roughness of the island is known to influence the coercive field by creating nucleation sites [14]. In that case, a pair of domain walls enclosing an inverted domain is nucleated and then pulled away by the Zeeman force. However, micromagnetic simulations show that the nucleation of domain walls mostly starts at the ends of disconnected island; the nucleation is assisted by the curling of magnetization at the ends [15].

Although domain walls are mesoscopic one-dimensional objects along a wire [16], microscopically they have complex internal structures. Depending on the width w of the island, the domain wall has a "transverse" or "vortex" structure for small and large w, respectively [17]. In fact, it is shown that domain walls in nanomagnets are composed of elementary topological defects of coplanar spins [18, 19]. These are the ordinary vortices in the bulk, and a novel type of edge defects carrying half vorticity [18]. For connected honeycomb arrays, every $Q = \pm q$ vertex junction

contains exactly one such half-vortex. The magnetization dynamics of the nano array can be understood and controlled by the interplay of topological defects bound to domain walls and those innate to the array junctions [20].

A microscopic description of the magnetization process is given by the Landau-Lifshitz-Gilbert (LLG) equation [21, 22]

$$\frac{\partial \mathbf{m}_i(\mathbf{r},t)}{\partial t} = -\gamma\, \mathbf{m}_i \times \left(\frac{\partial \mathscr{H}}{\partial \mathbf{m}_i} + \mathbf{H}_{\text{ext}}\right) + \frac{\alpha}{m_0}\, \mathbf{m}_i \times \frac{\partial \mathbf{m}_i}{\partial t}, \tag{15.7}$$

where $\gamma = g\mu_B/\hbar$ is the gyromagnetic ratio, α is a damping coefficient, $\mathbf{H}_{\text{eff}}$ is the external magnetic field, and $\partial\mathscr{H}/\partial\mathbf{m}_i$ with $\mathscr{H}$ given by (15.1) is an effective magnetic field originating from the local exchange interaction and the long-range demagnetizing field. Figure 15.3c shows the LLG simulations of magnetization reversal in a honeycomb nanowire [23]. In this case, the reversal is triggered by a vortex-type domain wall.

In micromagnetic simulations of the artificial ice arrays [15], a discretized LLG equation is solved using either a finite-element or a finite-difference scheme [24, 25]. Because of the long-range magnetostatic interaction, such calculation is too costly for large scale simulations and further simplifications are usually required. One simplification is to assume that the magnetization is uniform in individual island [26, 27], i.e. $\mathbf{m}_i(\mathbf{r}) = \boldsymbol{\mu}_i/V$, where $\boldsymbol{\mu}_i$ is the island magnetization, and V is the volume. In this approach, the magnetostatic energy can be expressed as: $\mathscr{H} = (\mu_0/8\pi)\sum_{i,j} \boldsymbol{\mu}_i \cdot \boldsymbol{N}_{ij} \cdot \boldsymbol{\mu}_j$, where $\boldsymbol{N}_{ij}$ is the magnetometric tensor and is given by the convolution of the shape-shape correlation function and the dipolar interaction tensor [28]. The effects of island shape and finite size are included in the magnetometric tensor. Approximating the islands as structureless needles, the magnetostatic energy reduces to the dipolar form similar to (15.4). Further simplification is to approximate the shape anisotropy, the $\boldsymbol{N}_{ii}$ term, by an effective single-spin anisotropy $-D_1(\boldsymbol{\mu}_i \cdot \hat{\mathbf{e}}_i)^2 + D_2(\boldsymbol{\mu}_i \cdot \hat{\mathbf{z}})^2$, where $D_{1,2} \sim -\mu_0/4\pi d^3$ originates from magnetostatic energy [29, 30]. However, it is important to note that magnetization reversal in this approach is through the rotation of the Heisenberg-like spin $\boldsymbol{\mu}_i$, which neglects the microscopic details such as domain wall nucleation and propagation. On the other hand, they could be applied to simulating magnetic nano-arrays consisting of circular islands, which have been experimentally realized as artificial XY-magnets [31, 32].

Dynamics based on the Ising Hamiltonian (15.4) is very efficient for large-scale simulations, but is mostly phenomenological. For example, single-spin dynamics based on Metropolis or Glauber type updates is employed in the nonequillibrium studies of pyrochlore spin ice [33]. Connections with microscopic properties, such as transition rates, can be achieved through the kinetic Monte Carlo method [34, 35]. This approach not only introduces a time scale into the Monte Carlo simulations, but also bridges the huge difference between the atomistic and mesoscopic time scales. Kinetic Monte Carlo simulations have been applied to studying the in and out-of equilibrium dynamics of artificial spin ices [36–40]. On the other hand, artificial ice arrays far from equilibrium are governed by pure relaxation dynamics, in which

the mesoscopic Ising variables always evolve toward a nearby local minimum in energy landscape [13, 41]. Phenomenological vertex population dynamics are also developed for pyrochlore [33] as well as for artificial spin ices [41].

15.2 Thermodynamic Behaviors

In earlier experimental realizations of artificial spin ice, thermal fluctuations are virtually absent in the nano-arrays: reversing the magnetization of a nano-island requires overcoming an energy barrier of a few million kelvins [6]. Most studies of artificial spin ice treated it as a granular material activated by alternating magnetic field [42, 43]. Such approaches have yielded frozen disordered states with only short-range order. It has been shown that such athermal states can be described by an effective temperature [44, 45]. An indirect attempt of producing thermalized artificial spin ice is to anneal the nano-arrays as they are initially formed [46–49]. Recent advances in fabrication and control of lithographically created arrays make it possible to realize thermally fluctuating artificial spin ice down to certain temperatures [50–53]. In light of these recent experimental developments, we discuss the similarities and differences in the thermodynamic behaviors of the square and honeycomb ice arrays.

A full micromagnetic thermodynamic simulation of artificial spin ice can be done using the stochastic LLG formulation [54], sometimes also called the Landau-Lifshitz-Bloch (LLB) equation [55]. In this approach, several random fields are incorporated into the LLG equation (15.7) to represent the effects of thermal fluctuations; the method can even be applied to simulate magnetic arrays that are close to the Curie temperature [56]. The random fields are uncorrelated both spatially and temporally and have standard deviations proportional to $\sqrt{T/V}$, where T is the temperature and V is the island volume. This is consistent with the fact that the blocking temperature of a super-paramagnetic nano-island is proportional to its volume [57]. The LLB method has been used to investigate the growth of a square ice array containing as many as 40×40 islands in [26]. For simplicity, the islands are assumed to be uniformly magnetized with $\mathbf{m}_i = \boldsymbol{\mu}_i / V$, as discussed above, and the magnetometric tensors $\boldsymbol{N}_{ij}$ are computed assuming ellipsoidal shaped islands [26]. Figure 15.4a shows that the dipolar energy of the annealed array is lowered with increasing thickness, and the final state is dominated by type-I vertices. The simulations also find that arrays with slow growth rates show the highest degrees of antiferromagnetic ordering shown in Fig. 15.5a, which is the ground state of coplanar square ice, to be discussed below. These results are consistent with the experimental observations [46]. A similar approach has also been used to study the thermodynamic properties and hysteresis in square ice model [27, 29, 30].

For large scale thermodynamic simulations of artificial spin ice, Monte Carlo method based on the effective Ising Hamiltonian (15.4) is much more efficient, while at the same time giving an accurate description of the low temperature ice and ordered phases. We first discuss Monte Carlo studies on the thermodynamic behav-

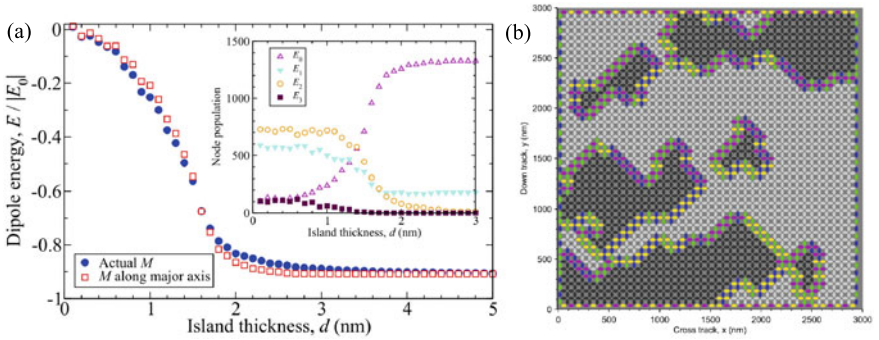

Fig. 15.4 LLB simulations of artificial spin ices. **a** Dipolar energy of the square array as thickness d increases from 0.1 nm to 5 nm with a growth rate 3.125×10^{-3} nm/ns. The inset shows the population of the four types of vertices vs island thickness. **b** A snapshot of array magnetizations when $d = 5$ nm [26]. The two grey-shaded areas correspond to the two-fold degenerate antiferromagnetic ground states shown in Fig. 15.5a; they are composed of type-I vertices. The colors of islands on the domain boundaries indicate the dominant magnetization direction: yellow: $+x$, magenta: $-x$ blue: $+y$, and green: $-y$. Figures reprinted from [26] with permission from AIP Publishing

iors of square ice. One important question is whether there exists an ice regime where configurations obeying the ice rules, or the minimum charge conditions, are overwhelmingly present with approximately equal weights. Contrary to the 3D pyrochlore spin ice, this is not the case because the two types of zero charge vertex (I and II) in the square array are inequivalent in symmetry and have different energies. This inequivalence results from the fact that, unlike the case of a tetrahedron, the six bonds between the four coplanar islands in a vertex are not all the same: the interaction $J_{1,\perp}$ between orthogonal pairs is stronger than that $J_{1,\parallel}$ between parallel pairs. However, this can be remedied by introducing a height displacement h between the vertical and horizontal islands [58]; see Fig. 15.2c.

The required displacement depends on the geometrical parameters such as length ℓ of the island and the lattice constant a. In the so-called point-dipole limit ($\ell/a \to 0$), the two interactions are equivalent $J_{1,\parallel} = J_{1,\perp}$ when $h_c/a = \sqrt{(3/8)^{2/5} - 1/2} \approx 0.419$. Taking into account the finite extension of the islands lowers the required height offset. For $h \leq h_c$, we have $J_{1,\perp} > J_{1,\parallel}$ and the ground state is an antiferromagnetic order with staggered arrangement of the two type-I vertices related by time-reversal symmetry, shown in Fig. 15.5a. On the other hand, for large offset $h > h_c$, the type-II vertices have the lowest energy and the ground state is a ferromagnetic ordering of type-II vertices; see Fig. 15.5b. A macroscopic degeneracy can then be realized when the height offset $h = h_c$, as demonstrated by recent experiment [59]. In this special point $h = h_c$, the square array realizes a two-dimensional Coulomb phase with deconfined magnetic monopoles.

Another interesting limit is when $\ell \to a$. The required height offset $h_c/a \sim \sqrt{2\varepsilon} \to 0$, where $\varepsilon \equiv (1 - \ell/a)$. Moreover, since interactions beyond J_1 vanish identically in this limit [58], the low temperature phase of the array corresponds

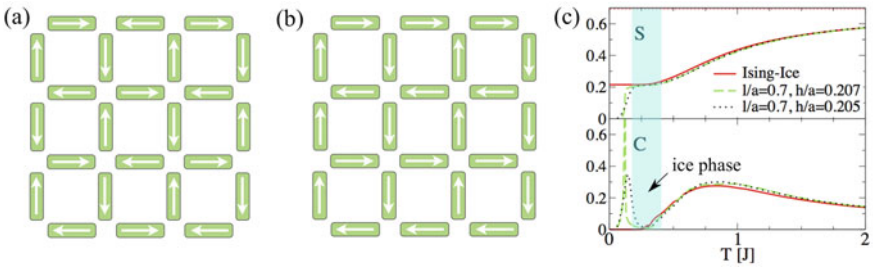

Fig. 15.5 Ordered states of artifical square ice. **a** Antiferromagnetic order consisting of staggered type-I vertices. **b** Ferromagnetic order of type-II vertices. **c** Entropy density S and heat capacity C as functions of temperature obtained from Monte Carlo simulations for square ice arrays [58]. The temperature is measured in units of $J \equiv J_{1,\perp}$. The ideal Ising-ice limit corresponds to $\varepsilon = 1 - \ell/a \to 0$, which is equivalent to the exactly solvable six-vertex model [60]. For parameter $\ell/a = 0.7$, an intermediate ice regime exists for $T < 0.42J$. The critical height offset $h_c \approx 0.207a$. A phase transition into a ordered phase occurs at $T \approx 0.1J$; the order is of antiferromagnetic (ferromagnetic) type for $h/a = 0.205$ (0.207). Figures reprinted from [58] with permission from the American Physical Society.

to an ideal Ising ice, or the symmetric six-vertex model [60, 61]. In this limit, there exists an extensive ground-state degeneracy which manifests itself in the appearance of a entropy-density plateau at $S_{\rm ice}/k_B = \frac{3}{4}\ln\frac{4}{3}$ [60] as $T \to 0$; see Fig. 15.5c. However, it should be noted that in this ideal $\varepsilon \to 0$ limit the effects of the island internal structure and disorder will start to play a role. Numerical simulations, on the other hand, show that a finite ice phase is possible even for finite ε. As demonstrated in Fig. 15.5c for a square array with $\ell/a = 0.7$, an intermediate ice regime (blue shaded area) is sandwiched between the high-temperature paramagnetic phase and a low-T ordered phase [58]. A generic ice state with disordered spins is shown in Fig. 15.1a. Experimentally, a quasi-ice regime has been observed both in athermal [6] and equilibrated square arrays without height offset [50].

As discussed above, the appearance of an ordered phase at low T is caused by the inequivalence between type-I and II vertices when $h \neq h_c$. Antiferromagnetic ordering shown in Fig. 15.5a, which is the ground state when $h < h_c$, has been achieved in as-grown arrays [46] as well as the thermalized ones [50]. The selection of the ground state, staggered type-I versus uniform type-II, is completely due to the energetics of vertices, and is not affected by the long-range part of the dipolar interactions. This implies that the nature of the ordering transition can be described by a simplified vertex model, which includes only nearest-neighbor interactions. Indeed, Monte Carlo simulations of a 16-vertex model (with four different types of vertices) [62] agree well with the experimental result [47]. Extensive numerical simulations further show that the ordering into the staggered type-I state is a second-order phase transition [62]. Although this ground state is described by a Z_2 Ising order parameter, the ordering transition in square ice seems to belong to a universality class different from that of 2D Ising model [63]. The exact nature of the phase transition remains to be clarified.

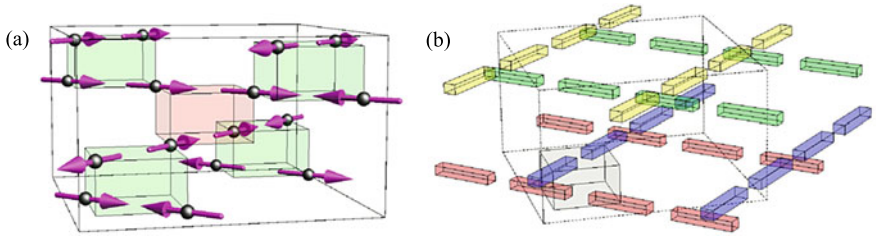

Fig. 15.6 Multilayer construction of 3D artificial spin ice. **a** A three-dimensional network built from the four types of rectangular boxes, or 'vertices' shown in Fig. 15.2c. The resultant spin lattice is equivalent to the 3D pyrochlore spin ice. **b** Schematic diagram showing the arrangement of magnetic nano-islands in the multilayer structure. Figures reprinted from [64] with permission from AIP Publishing

Introduction of the height displacement h also provides an approach to design a 3D magnetic nano-array which is topologically equivalent to the pyrochlore spin ice [64]. The basic frustration unit in this multilayer construction is a rectangular box containing four nano-islands as shown in Fig. 15.2c; these are the analogs of tetrahedra in pyrochlore lattice. Arranging these boxes into a corner-sharing network gives rise to a multilayer structure shown in Fig. 15.6a, which can be viewed as a flattened pyrochlore structure. In each layer, parallel nano-islands form a rectangular lattice with the long and short lattice constants being $2a$ and a, respectively; the orientation of the islands are aligned with the short axis. The arrays are rotated by 90° from one layer to the next. In addition, the arrays in every other layer are shifted by a along the long axis. Interestingly, the projection of this 3D structure onto the xy plane is exactly the same as a square ice. The approach of building a 3D spin ice by stacking 2D arrays takes advantage of the well developed planar nano-lithography technology. Similar to the square ice array, by properly choosing the interlayer distance h, an extended ice regime at finite temperatures is realized in this 3D structure [64].

We next turn to the thermodynamic phases of honeycomb arrays. As mentioned above, such arrays are realizations of the kagome spin ice, as the centers of the nano-islands form a kagome lattice. The kagome spin ice is first studied in [65] as a frustrated statistical model. It is found that with only nearest-neighbor interactions, kagome ice retains an extensive ground state degeneracy corresponding to an entropy density $S_{\rm I}/k_B \approx 0.501$ [65]. In this so-called kagome ice-I manifold, each vertex has either two spins coming in and one going out, or vice versa. The huge degeneracy is lifted upon the introduction of further neighbor couplings [65, 66]. In magnetic honeycomb arrays, the kagome ice rules correspond to the minimum charge condition $Q = \pm q$ at every vertex; a generic disordered ice-I state is shown in Fig. 15.1b. The ice-I phase has been observed experimentally in athermal [7, 8] as well as fully equilibrated kagome ice arrays [50].

The fact that there are uncompensated magnetic charges at every vertex of the honeycomb array introduces new features that are absent in square ice. The Coulomb

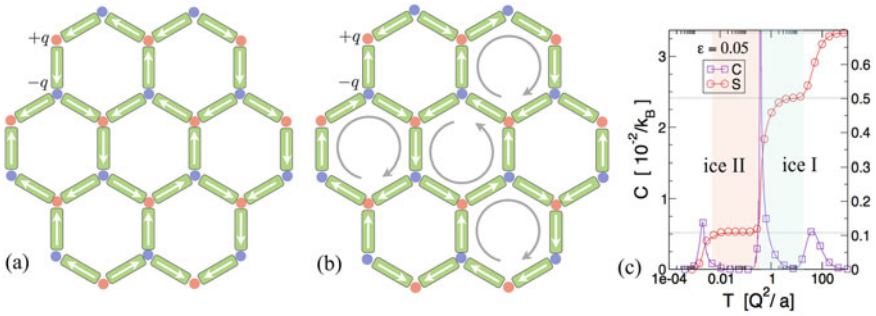

Fig. 15.7 Ordered phases of artificial honeycomb array. **a** An Ising microstate in the ice II phase in which emergent magnetic charge degrees of freedom develop a NaCl-type order, while spins remain disordered. The red and blue dots denote vertices with $\pm q$ charge, respectively. **b** One of the six-fold degenerate ground states exhibiting the $\sqrt{3} \times \sqrt{3}$ spin order. **c** Temperature dependence of entropy density S and heat capacity C obtained from Monte Carlo simulations for honeycomb arrays with parameter $\varepsilon = 1 - \ell/a = 0.05$. Figures reprinted from [67] with permission from the American Physical Society

interaction (15.5) among these residual charges gives rise to a novel phase in which the residual $\pm q$ charges crystalize into a NaCl-type order [67, 68]; see Fig. 15.7a. This charge-ordered kagome ice, also called the ice-II phase, is closely related to spins in the kagome plane of the pyrochlore spin ice when subjecting to a $\langle 111 \rangle$ magnetic field [69, 70]. While the ice-II phase is ordered in terms of charges, it is still consistent with an exponentially large number of Ising configurations; the degeneracy of the ice-II manifold corresponds to an entropy density $S_{\rm II}/k_B \approx 0.108$ [71]. These charge-ordered ice states are exactly degenerate in the dumbbell model (15.5). The degeneracy is lifted by higher-order corrections from the original dipolar interactions (15.4). The ice-II phase is quite robust; charge ordering has been observed experimentally even in non-thermal states generated by alternating field [72, 73]. Incipient crystallization of magnetic charges has been observed in thermalized honeycomb arrays [50].

The above energy hierarchy suggests a sequence of thermodynamic phases demonstrated in Fig. 15.7c. At high temperatures, uncorrelated Ising spins have an entropy density $S/k_B \to \ln 2 = 0.693$. As the array cools down from the paramagnetic state, it gradually enters the ice-I phase; the entropy curve exhibits a plateau at $S_{\rm I}$. At a lower temperature, the magnet undergoes a phase transition into the charge-ordered ice-II phase. Since the order parameter of the staggered NaCl pattern has a discrete Z_2 symmetry, the transition belongs to the 2D Ising universality class [68]. The ice-II phase manifests itself in the appearance of a second entropy plateau at $S_{\rm II}$. Finally, at an even lower temperature, another phase transition of the 2D Potts universality class [68] completely removes the residual entropy and selects a ground state with $\sqrt{3} \times \sqrt{3}$ spin order shown in Fig. 15.7b. Consistent with the fact that the most favorable arrangement of a single hexagonal ring is for all island magnetizations to

point head to tail [37, 43], the selected $\sqrt{3} \times \sqrt{3}$ order maximizes the occurrence of such motif. Thermal ordering of moments into the loop crystal in honeycomb arrays remains an experimental challenge.

15.3 Disorder and Nonequilibrium Dynamics

Experimental realizations of artificial spin ice unavoidably introduce small variations during the array fabrication process, leading to a statistical distribution of island properties. Quenched disorder provides pinning and nucleation sites and strongly affects the dissipative dynamics of the magnetic arrays. It is thus crucial to understand the role of disorder in the nonequilibrium dynamics of artificial spin ice. A full microscopic modeling of disorder based on the LLG equation is computationally too expensive, and is infeasible for large-scale simulations. Models based on the Ising Hamiltonian (15.4) again provide a practical approach to study disorder-induced nonequilibrium phenomena in large lattices. In the relaxation dynamics formulation of artificial ice arrays, mesoscopic Ising degrees of freedom move downhill in the energy landscape until they come to rest at a local energy minimum.

As discussed above, each Ising configuration corresponds to a local minimum of the spin-ice array. Different local minima are connected by flipping one or more Ising spins. Consequently, an important new energy scale for the dynamical process is the energy barrier of magnetization reversal in individual islands. For effective Ising model (15.4), this energy barrier is characterized by a coercive or switching field H_i^c. More specifically, an Ising spin σ_i is flipped if the total local field, composed of the external field $\mathbf{H}_{\text{ext}}$ and the dipolar field from all other islands, exceeds its coercive field:

$$-\left(\mathbf{H}_{\text{ext}} + \sum_{j \neq i} \mathbf{h}_j\right) \cdot \hat{\mathbf{e}}_i > H_i^c. \tag{15.8}$$

The energy released during the reversal is completely dissipated into the lattice. We emphasize once again that flipping the Ising spin corresponds microscopically to the nucleation, propagation, and subsequent absorption of domain walls as described in Sect. 15.1. The quenched disorder manifests itself in the random distribution of the coercive fields H_i^c. Although disorder is present also in the spin coupling constants, its effect is usually smaller and, to some degree, can be absorbed into the disorder in H_c [74, 78].

When the system is subject to a perturbing external field H_{ext}, interesting dynamical behaviors occur when $H_{\text{ext}} \sim \bar{H}^c$, where $\bar{H}^c$ is the average switching field. However, the nature of the magnetization dynamics, whether it is mostly single-spin process or multi-spin collective behavior, depends on the relative scales of ΔH^c and E_d, where ΔH^c is a characteristic width of the random distribution and $E_d = \mu_0 m_0^2 V^2 / 4\pi a^3$ is the energy scale of dipolar interactions.

An illuminating example of nonequilibrium dynamics is the rotating-field driven relaxation of square spin ice [41, 74]. In this setup, a strong diagonal field first polarizes the system to the polarized state consisting entirely of one particular type-II vertex. The field is then reduced to a hold value H_h and the sample is rotated in-plane [74]. The relaxation dynamics formulation (15.8) has been applied to study this nonequilibrium process [41, 74]; the results agree well with the experiments. Figure 15.8b, c show the average fractional vertex populations versus the hold field H_h obtained from experiments and simulations, respectively. For H_h smaller than a threshold, the field does not affect the type-II state. Above this threshold, type-I vertices are generated by the field; its population shows a non-monotonic behavior with a maximum at $H_h \approx 520$ Oe experimentally. This non-monotonic behavior can be understood as follows. For small field, chains of reversed moments are generated in a background of polarized type-II vertices. These chains are similar to those observed in the magnetization reversal experiments driven by a dc field [76, 77], to be discussed below. As H_h further increases, small domain of type-I ground states start to form. Near the maximum of about 50 % type-I vertices, the net magnetization approaches zero and all four type-II vertices have similar populations. Finally, further increasing H_h rapidly suppresses the staggered type-I order. As the interaction is dominated by the Zeeman coupling to the type-II dipoles, most of the spins simply rotate with the field.

The simulations shown in Fig. 15.8c assume an average $\bar{H}_c = 11.25 H_d$ and a rather large standard deviation $\Delta H_c \approx 1.875 H_d$, where $H_d = \mu_0 m_0 V / 4\pi a^3$ is a characteristic dipolar field. The large ΔH_c indicates that the system is in the strong disorder regime [78], which also explains the irrelevance of the boundary effects [74]. For athermal artificial arrays driven by magneto-agitation, quenched disorder plays a crucial role by increasing the dynamical pathways in phase space. In this sense, the effects of quenched disorder is similar to thermal fluctuations in equilibrium systems; both provide links between nearly degenerate spin configurations [79]. The effect of disorder on the connectedness of the configurational space can be quantitatively investigated using the network approach [80]. For a given magneto-

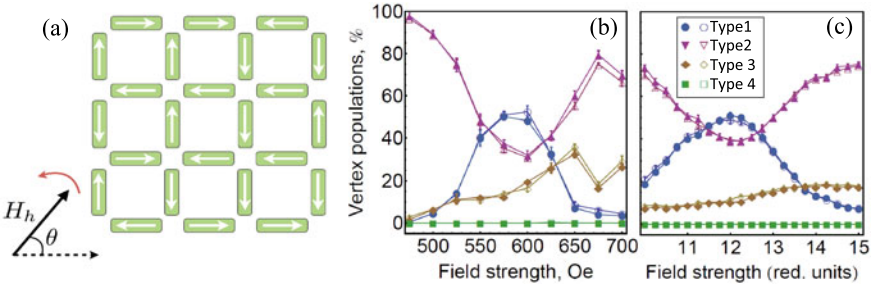

Fig. 15.8 Relaxation dynamics driven by rotating field. **a** Schematic diagram of the experimental setup. **b** The vertex population vs hold field H_h obtained from experiments [74]. **c** Numerical simulations of the same process [41, 74]. Open and filled symbols represent data obtained from arrays with open and closed edges, respectively. Figures reprinted from [74] with permission from the American Physical Society

agitation, the network is defined as a directed graph (or 'adjacency matrix') in the configurational space whose dimension is 2^N for an array of N islands. A directed link from Ising state A to B is introduced to the network if A can evolve to B under the driving field [81]. Compared with the perfect array, quenched disorder "rewires" the network by significantly increasing the number of links. One important consequence of the increased links is the reversibility of dynamics. This property is related to the concept of strongly connected components in networks [80]. In a directed network, if two configurations A and B are in the same strongly connected component, there exists a path from A to B and vice versa. It is found that the presence of disorder increases both the number and size of such components in the network [79]. The increased links thus can help the system reach lower-energy states through field-driven dynamics. Overall, the network picture provides a framework to understand and control quenched disorder in artificial spin ices.

Quenched disorder also significantly affects the hysteresis curves and magnetization reversal of artificial spin ice [82–86]. Micromagnetic simulations using the LLG equation (15.7) is employed to study demagnetization process of a small-size square array consisting of 144 islands [15]. The LLG simulation clearly identifies that the magnetization reversal is assisted by the proliferation of type-III vertices, or monopole defects to be discussed in the next section. This result is corroborated by real-space observations in both square and honeycomb arrays [15, 76, 77, 84, 85].

A systematic study of the disorder effects on magnetization reversal of the ice array requires large-scale simulations, which can be achieved, again, using the relaxation dynamics (15.8) for effective Ising models. In these simulations, a strong external field initially polarizes the islands along the diagonal direction in square array, and along one of the island long axis in the honeycomb case. The array is then subject to a reverse field H_r in the opposite direction, with gradually increasing magnitude. Extensive relaxation dynamics simulations on large lattices containing as many as $N \sim 10^6$ spins have been performed for the two representative spin-ice arrays [87]. It is found that both square and kagome spin ices exhibit disorder-induced nonequilibrium phase transitions, with power-law avalanche distributions at the critical disorder level [87, 88]. The phenomena of driven criticality far from equilibrium are observed in many first-order transitions, such as the famous Barkhausen noise [89] in the hysteresis of magnetic materials. The random field Ising model [90] probably is the most studied system in this regard.

In both random field Ising model and artificial spin ices, the reconfiguration of the spin arrangements during magnetization reversal occurs in the form of avalanche events in the vicinity of the critical switching field when $H_r \sim \overline{H}_c$ (the average coercive field). The avalanche dynamics exhibit three different behaviors depending on the level of disorder. The weak disorder regime is dominated by large clusters extending the whole system, while many subsystem size clusters occur in the strong disorder regime; see Fig. 15.9. A critical disorder level separates these two regimes. Interestingly, the square and honeycomb arrays exhibit rather different geometries of the avalanche clusters, as demonstrated in Fig. 15.9: the avalanche clusters mostly propagate along the diagonal direction in the square ice array, whereas the clusters branch out and form fractal-like structures in kagome ice [87].

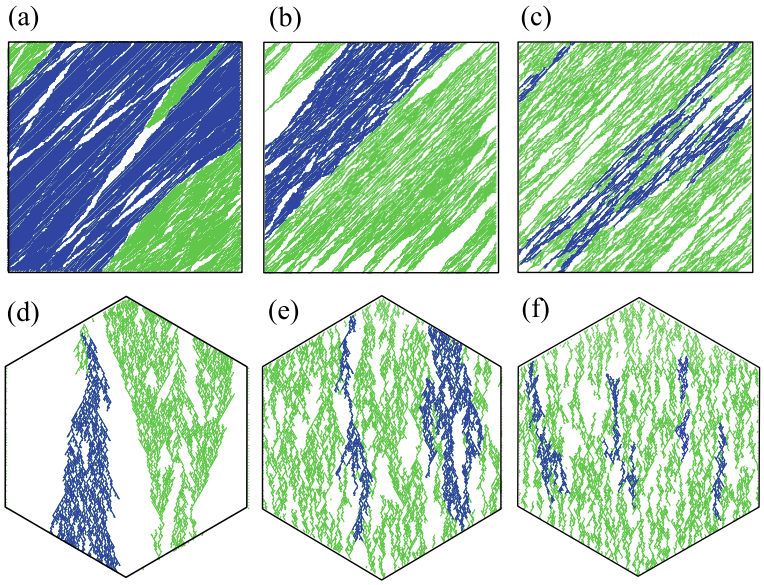

Fig. 15.9 Snapshots of spin avalanches during magnetization reversal. The white (green) area denotes the non-inverted (inverted) spins, while the blue area indicate instances of avalanche clusters. The disorder strength is characterized by a dimensionless parameter $r \equiv \Delta H_c / \bar{H}_c$. The three snapshots of the square ice correspond to **a** weak $r = 0.012$, **b** near critical $r = 0.018$, and **c** strong disorder $r = 0.023$. Similarly for kagome ice, the disorder levels at the three distinct regimes are $r =$ **d** 0.06, **e** 0.10, and **f** 0.12. Figures from [87]

In square ice array, an avalanche event starts with the flip of a single spin at an island of lowest coercive field. In the monopole picture to be discussed in Sect. 15.4, this single spin flip corresponds to the creation of monopole pairs. The two monopoles carrying opposite charges are then pulled away by the Zeeman force until they are stopped by links of large H^c. The two monopoles are connected by a Dirac string [75] running roughly parallel to the diagonal direction. It is worth noting that Dirac strings consisting of type-I vertices are locally stable object since they are ground states of the dipolar interactions. Large-scale simulations find avalanche clusters consisting of inverted domains with edges roughly parallel to the diagonal direction; see Fig. 15.9a–c. This result indicates that a Dirac string (of inverted spins) tends to induce neighboring strings, and the avalanche propagation is driven by the expansion of domain walls.

The avalanche size distribution $D(s)$ at varying level of disorder is shown in Fig. 15.10c, here s is the size of the avalanche cluster. The parameter $r \equiv \Delta H_c / \bar{H}_c$ measures the level of quenched disorder in the array, and a Gaussian distribution of the island switching field H_i^c is assumed in the simulations. The distribution shows two distinct behaviors. For weak disorder, a peak in $D(s)$ at the largest cluster sizes indicates that the avalanches are dominated by large system-wide events, corresponding to the so-called super-critical regime [90]. The resultant magnetization curves

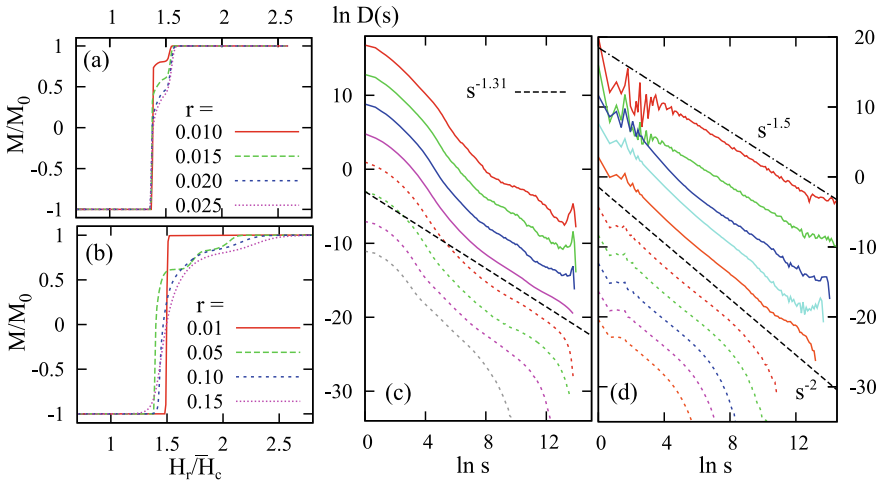

Fig. 15.10 Disorder induced criticality in artificial spin ice. **a** and **b** show the normalized magnetization versus applied field at various disorder strengths r for square and kagome ice, respectively. The avalanche size distribution $D(s)$ during magnetization reversal for the two types of ice arrays are shown in **c** and **d**. For square ice, the different curves in **c** correspond to $r = 0.011$, 0.012, 0.013, 0.014, 0.015, 0.016, 0.022, and 0.030 (from top to bottom). For avalanches in kagome ice, the difference curves in **d** correspond to $r = 0.02$, 0.03, 0.05, 0.07, 0.09, 0.1, 0.105, 0.115, and 0.135 (top to bottom). In both cases, the solid curves indicate super-critical regime of avalanches, while the dotted curves belong to the sub-critical regime. The dashed lines indicate the power-law behavior $D(s) \sim s^{-\tau}$ near the critical disorder. Figures from [87].

$M(H_r)$ shown in Fig. 15.10a are characterized by a pronounced jump in M. For arrays with strong disorder, the large avalanches are cut off at a characteristic size s_m that decreases with increasing r. Close to a critical value of $r_c \approx 0.0145$, the distribution shows a power-law behavior $D(s) \sim s^{-\tau}$, implying avalanches of all sizes occur during the reversal. Interestingly, the numerically obtained exponent $\tau \approx 1.31$ and further scaling analysis [87] are consistent with the scenario of propagating domain walls separating two polarized states [91].

Avalanche clusters in kagome ice are also triggered by single-spin flip or the creation of monopole pairs [84, 85, 92, 93]. In stark contrast to the square-ice case, the propagation of the clusters is dominated by many branching processes as shown in Fig. 15.9d–f. Such tree-like avalanche clusters are also observed experimentally [93]. Moreover, while the Dirac string in square ice can propagate in both directions along the diagonal, the tree-like cluster in kagome mainly propagates along one direction. The high degree of branching and strong unidirectional growth of the cluster suggest that avalanches in kagome ice belong to the universality class of directed percolation [94]. The avalanche size distribution shown in Fig. 15.10d also shows super- and sub-critical behaviors, similar to the square ice case, at weak and strong disorders, respectively. Interestingly, avalanches in the super-critical regime exhibits an unusual crossover behavior: the exponents of the power-law part $s^{-\tau}$

of $D(s)$ gradually changes from $\tau = 1.5$ at very small $r \lesssim 0.03$ to $\tau = 2$ at the critical disorder $r_c \approx 0.107$. This crossover phenomenon might reflect the reduced dimensionality (from 2D to quasi-2D) of avalanche clusters with increasing r. The exponent $\tau = 2$ agrees very well with the experimental result [93]; it is suggested that the exponent $\tau = 2$ is a result of super-universality for certain classes of time-directed avalanches [95].

Experiments on kagome ice composed of disconnected islands find dimensional reduction phenomenon in magnetization reversal [85, 96]. In this scenario, the propagation of the avalanches is mainly through the (opposite) movements of monopole pairs connected by a Dirac string, similar to some of the square ice clusters. One important consequence of this quasi-1D process is that the avalanche size distribution has a exponential decay $D(s) \sim \exp(-s/s_0)$ [85, 96]. On the other hand, significant branching of avalanche clusters and power-law distribution were observed in connected honeycomb nano-wire networks [93]. Although these two different behaviors could be attributed to the boundary effects of the sample, or the misalignment of the field in the experiments, one intriguing explanation might have something to do with the chiral nature of monopoles in disconnected arrays, as observed in micromagnetic simulations [97]. The spontaneous chiral-symmetry breaking at the $\pm 3q$ vertices might disfavor branching process, and cause the string to grow in one particular direction.

15.4 Elementary Excitations: Monopoles

Magnetic charges in spin ice are not only a useful bookkeeping tool for computing energies, but also true dynamical variables describing low-energy collective phenomena [10, 11]. For example, the ordering of magnetic charges in the kagome ice-II phase discussed in Sect. 15.2 shows that they are emergent degrees of freedom that interact with each other through the Coulomb law. The fact that magnetic charges precisely capture the leading-order interactions in spin ice is best illustrated by the dumbbell picture introduced in Sect. 15.1. Since the lowest-energy vertices in the ice-rule obeying states have minimum charges, excited vertices in this background carry an extra charge and behave as magnetic monopoles. Indeed, these excited vertices are particle-like objects that can be driven by an applied field [10]. These excited vertices or monopoles are also *topological defects* as they violate the ice rules and must be created and annihilated in pairs. Figure 15.11 shows examples of emergent monopoles in the dumbbell picture for various spin ice lattices. In this Section, we will discuss the monopole excitations in square and honeycomb arrays. In particular, we show that artificial spin ices with mixed lattice coordination numbers contain composite quasi-particles which can be viewed as monopole polarons.

Associated with monopole excitations is another topological defects called Dirac strings [11]. Since magnetic monopoles in spin ice are not fundamental elementary particles, their charges are not quantized and a Dirac string connecting a pair of monopoles is a visible object [75]. In the ice-rule states, a single-spin flip corresponds

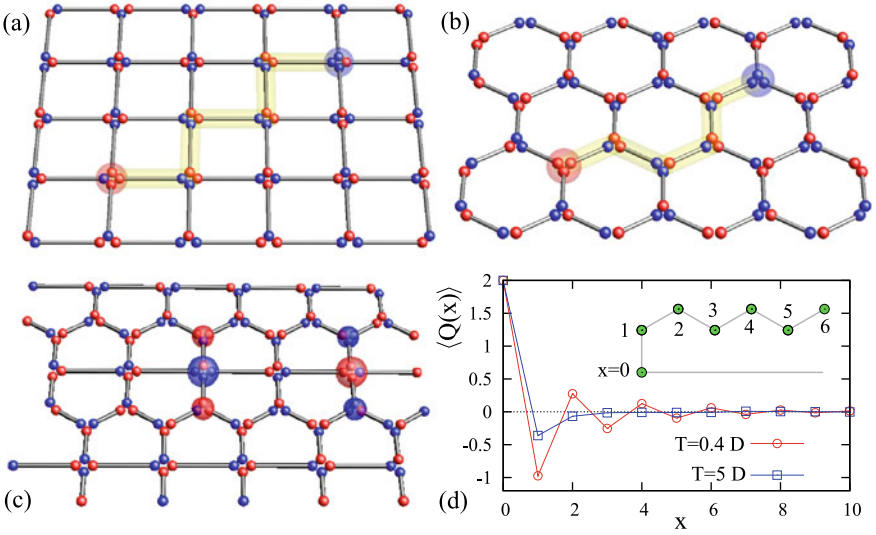

Fig. 15.11 Monopoles in artificial spin ice. **a** A pair of magnetic monopoles connected by a Dirac string in a square ice array with height offset $h < h_c$. The ground state in this case is a staggered type-I order shown in Fig. 15.5a. These monopoles are called Nambu monopoles [108] because there is a finite tension of the Dirac string that consists of the higher energy type-II vertices. **b** A pair of $\pm 3q$ monopoles connected by a tension-less Dirac string in an artificial kagome ice. **c** Two monopole 'molecules' in artificial pentagonal ice. In this lattice, there are both 4-legged and 3-legged vertices. Emergent monopoles (defect vertices) live on the 4-legged vertices and interact with the residual charges on the 3-legged vertices [112]. **d** Distribution of magnetic charges around a $Q = 2q$ monopole at $x = 0$ for two different temperatures. The extended and oscillatory charge correlation suggest a polaron picture for the composite quasi-particle [112]. Reprinted from [112] with permission from EPL

to the creation of a monopole pair. When the two monopoles are subsequently separated, a path of inverted spins constitute the visible Dirac string. This process also demonstrate the fractionalization of dipoles into monopoles in spin ice. However, whether the separation of the monopole pair is allowed energetically depends on the tension of the Dirac string. In pyrochlore spin ice, these strings are tensionless and the separated monopoles only interact through a power-law decaying Coulomb potential [11]. In square ice, the inequivalence of the six 2-in-2-out vertices leads to a unique ground state, whose ordering pattern is determined by the height offset h; see Fig. 15.5. But more importantly, the Dirac string acquires a finite tension because of this inequivalence. For example, for coplanar square ice ($h = 0$), the ground state is a staggered arrangement of type-I vertices, and two monopoles are connected by a string of type-II vertices [109, 110]; see Fig. 15.11a. The tension of the Dirac string is $\tau \sim \varepsilon_{\rm II} - \varepsilon_{\rm I}$. The monopoles in square ice share several features with the monopole particles proposed by Nambu [107]: the Dirac string in both cases are energetic and is oriented [108]. In Nambu's original theory for hadrons, the monopoles correspond to quarks and the finite string tension is used to describe their confinement [107].

Although magnetic monopoles in square ice with $h \neq h_c$ are not true quasi-particles because of the energetic Dirac strings, it is argued that the string tension might be compensated by its configurational entropy above a critical temperature, and the monopoles become deconfined thermally [111]. Another approach is to modify the string tension through the height offset h [110] as discussed in Sect. 15.2. Detailed numerical calculation shows that the tension diminishes as the offset approaches the critical h_c from both sides and for different string paths. The vanishing string tension also results in a dramatic increase of thermally excited strings at finite temperatures, as observed in Monte Carlo simulations [38].

Magnetic monopoles in kagome ice, on the other hand, are connected by tensionless strings because of the exact degeneracy of the six minimum energy vertices. As discussed in Sect. 15.2, there are uncompensated $\pm q$ charges at every vertex in the ice phases of kagome because of its odd coordination number. In the ice-I phase, monopole excitations refer to the type-II' vertices carrying $\pm 3q$ charges; an example is shown in Fig. 15.11b. A new type of charge excitations occurs in the ice-II phase of kagome. Recall that in this phase the residual $\pm q$ charges crystallize into a NaCl-type order on the honeycomb lattice, say $+q$ $(-q)$ charges in sublattice A (B). A misplaced charge, e.g. a $-q$ vertex in sublattice A, is energy costly and represents elementary defects in the ice-II states. Relative to the background staggered charges in a ice-II state, these defects also carry a relative charge $\pm 2q$, and are sometimes also called monopoles. In magnetization reversal of kagome ice array, both types of monopoles ($\pm 3q$ vertices and charge defects) were observed [84, 85, 116–118].

A new collective phenomenon associated with monopoles and magnetic charges is the composite quasi-particles in spin ices with mixed lattice coordinations [112]. This is illustrated in the so-called pentagonal spin ice, shown in Fig. 15.11c. The pentagonal lattice is probably the simplest structure that combines the elementary four- and three-legged vertices shown in Fig. 15.2. In the ice phase of this lattice, there is no charges at the four-legged vertices, whereas uncompensated $\pm q$ charges exist at the 3-legged vertices. Elementary excitations are emergent monopoles carrying $Q = \pm 2q$ at the $z = 4$ sites. These monopoles then attract a cloud of net opposite charges through magnetic Coulomb interaction, forming an entity similar to the electron polaron in crystalline lattice [113]. The unusual charge-charge correlation around such a polaron is demonstrated in Fig. 15.11d obtained from Monte Carlo simulations on the dipolar pentagonal spin-ice [112]. At low temperatures, the strong correlation between the center $\pm 2q$ and the two $\mp q$ neighbor charges resembles a H_2O molecule. Although the pentagonal ice array has yet to be realized in experiments, similar magnetic charge screening phenomenon has been observed in the shakti lattice [114], to be discussed in Sect. 15.6, and dice lattice [115], both of which have mixed coordination vertices.

15.5 Elementary Excitations: Magnons

In addition to the monopole excitations associated with the mesoscopic Ising degrees of freedom, another elementary excitations in artificial spin ice are magnetic resonances, or spin waves, that correspond to continuous magnetization fluctuations. These two types of excitations also have rather different time scales. Movements of topological defects involve magnetization inversion of individual islands, which needs to overcome an energy barrier and occurs over times on the order of a few nanoseconds. Basically, the system evolves from one local minimum to another; each energy minimum corresponds to a Ising configuration. On the other hand, magnon excitations are small amplitude fluctuations around a given Ising state, or a local minimum. The characteristic frequencies of magnons for typical permalloy materials are on the order of a few GHz or higher.

The finite dimension of nano-islands introduce boundary effects on the spin wave propagation, creating standing-wave modes as well as edge-localized modes [100, 101]. In particular, since the edge modes can extend significantly outside the island and hybridize with similar modes from the neighbors, they play an important role in the collective resonant dynamics that depend on the array geometry. Collective spin wave modes have been extensively studied in 1D chains and 2D arrays [100–102], although most of these studies consider rather simple structures such as square or rectangular lattices. Moreover, the magnon resonance also depends on the magnetizations of individual elements for a given array. The engineering of collective spin waves through design of lattice structure, magnetization pattern, the size and geometry of the elements is an intriguing emergent field called magnonics [103–105].

In artificial spin ice, the spin wave spectrum is significantly modified by the presence of topological defects [99]. Moreover, different topological excitations, monopole pairs and Dirac strings, display distinct and localized features, both spatially as well as in the frequency domain. These results suggest that artificial spin ice can serve as promising reprogrammable spin-wave waveguides or magnonic crystals. In this section, we will discuss the collective spin wave resonances in the artificial square ice.

The calculation of spin wave eigenmodes in nanoscale magnetic particles is an extremely complicated problem when both exchange and magnetostatic contributions are taken into account [106]. Numerically, the magnetization resonant dynamics can be investigated by exciting the artificial ice array with a short magnetic field pulse. The time evolution of the array is simulated using the LLG equation (15.7); information about the eigenmodes can be extracted with the aid of Fourier transform [119]. This approach is applied to study the magnon spectra in an artificial square ice consisting of 112 stadium-shaped nano-islands in [99]. The ferromagnetic state consisting of uniform type-II vertices shown in Fig. 15.5b is used as a reference state. The magnon spectrum of this uniform type-II order is shown in Fig. 15.12a as the gray filled area. The largest peak at $f \sim 8$ GHz (position ⑥) corresponds to the ferromagnetic resonance in which the oscillation is approximately uniform in the interior of the islands. The many smaller peaks at lower frequencies are associated with various

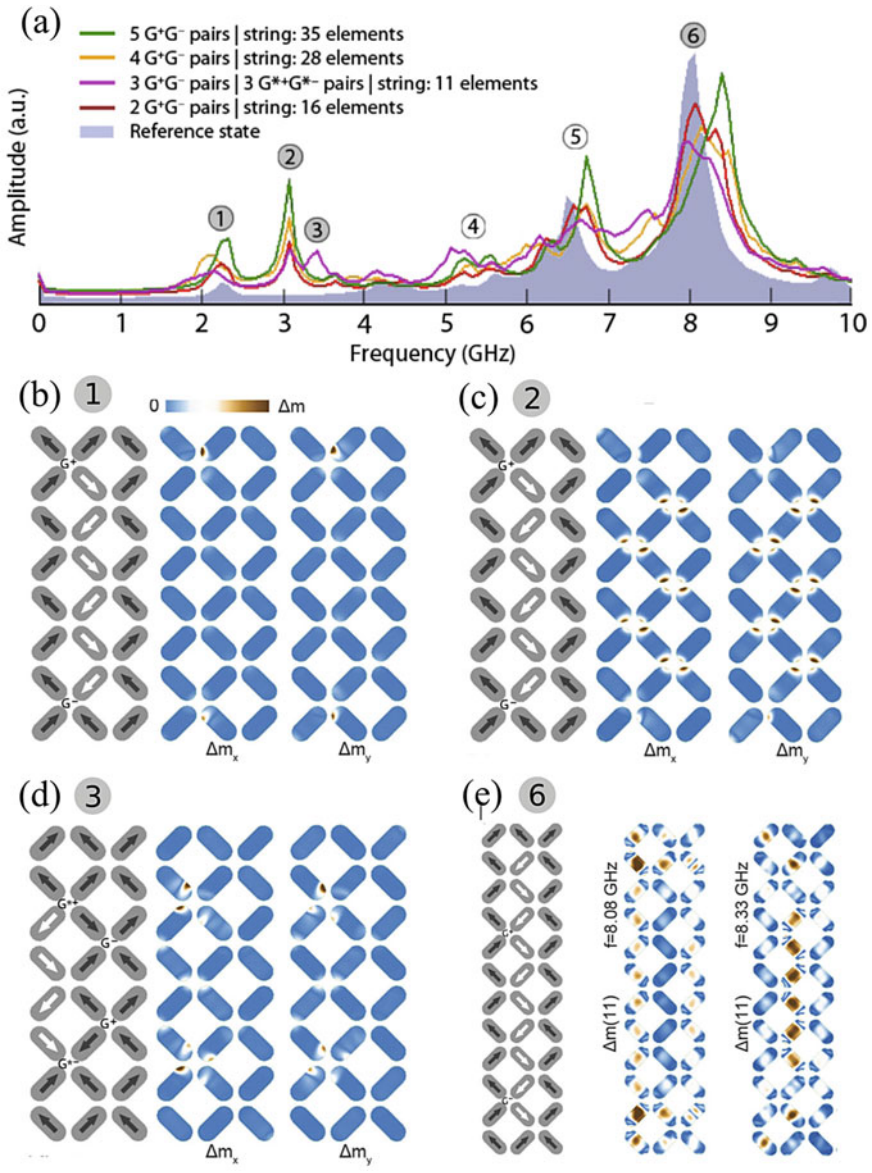

Fig. 15.12 Spin-wave spectra of artificial square ice. **a** Evolution of the spin-wave spectrum with increasing string length and number of monopole pairs compared with the reference state. The shaded labels correspond to the main, distinct signatures of topological defects. The magnetization amplitude Δm of localized resonance mode associated with **b** monopole pairs G^+G^-, **c** Dirac strings, and **d** doubly charged monopoles $G^{*+}G^{*-}$ (all-in/all-out vertices). The splitting of the ferromagnetic resonance peak in the presence of a Dirac string is shown in **e**. The numbers (1, 2, 3, 6) in the gray-filled circle indicate the corresponding features in the spectra [99]. Figures reprinted from [99] with permission from the American Physical Society.

kinds of edge modes of the array. For example, the modes at ~ 2 GHz and 5 GHz (positions ① and ④) correspond to fundamental and higher-order edge excitations, respectively, at the array boundary.

The various curves in Fig. 15.12a depict the spectrum evolution when monopoles and Dirac strings are inserted into the lattice. First, a new resonance whose amplitude increases almost linearly with the number of monopole pairs appear at frequency $f \sim 2.2$ GHz [99]. Although the frequency of this resonance is close to the edge mode ① of the reference state, this mode is actually localized around the monopole and antimonopole labeled as G^+ and G^-, respectively in Fig. 15.12b. The enhanced peak around 5 GHz, roughly at peak ④ of the reference state, is also related to the monopole-antimonopole pairs. Second, the new mode at $f \sim 3.5$ GHz (position ③) is attributed to localized modes around the $Q = \pm 4q$ monopole pairs (or type-IV vertices). These doubly charged monopoles are labeled as G^{*+} and G^{*-} in Fig. 15.12d. The pronounced peak at position ⑤ is also due to these topological defects. In both cases, a similar linear relation between the mode amplitude and the number of doubly-charged monopole pairs is obtained in the numerical simulations [99].

The Dirac strings also leave distinct fingerprints on the magnon spectrum of artificial ice array. A new mode at $f \sim 3$ GHz (position ②) corresponds to localized oscillations around the Dirac string connecting the monopole-antimonopole pairs. Since this mode is very localized at the type-I vertices that constitute the Dirac string in a type-II background, as shown in Fig. 15.12c, its amplitude increases linearly with the string length. The dominant ferromagnetic resonance at position ⑥ is also split and shifted by the Dirac strings. The spatial profile of these two modes, shown in Fig. 15.12e, are obtained by projecting the magnetization along the [11] direction of the string. The peak amplitude of the higher-frequency (8.33 GHz) mode increases with the string length at the expense of the lower-frequency resonance mode at 8.08 GHz.

As the topological defects are mesoscopic objects extending over several islands, their induced resonances are therefore dominated by the non-local magnetostatic energy. However, the spectral features induced by monopoles and strings are quite robust: reducing the lattice constants, hence increasing the magnetostatic interaction, only blue-shifts the peaks while maintaing most of the characteristics of the induced resonances. In summary, micromagnetic LLG simulations show that there is a one-to-one correspondence between the topological defects and the magnon spectrum of the artificial ice array. The fact that these modes are localized around the topological objects implies that contributions from individual defects do not interfere much with each other. Potential applications of artificial ice arrays as dynamical frequency filter or sensor can be envisioned by locally creating and moving monopoles to modify the resonant dynamics.

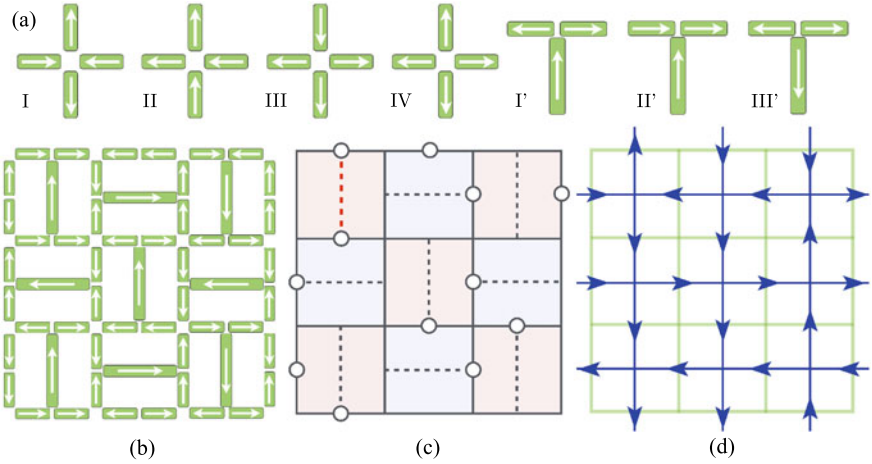

Fig. 15.13 Emergent frustration in Shakti spin ice. **a** Building blocks for artificial spin ices. There are four symmetry distinct types of four-leg vertices (type-I, II, III, IV), and three distinct types of 3-leg vertices (I', II', and III'). **b** The magnetic nano-array for Shakti spin ice and a generic ice state. The arrows indicate the island magnetizations. In this ice microstate, every 4-leg vertices are of type-I configuration, half of the 3-leg vertices are in the ground-state type-I', and the other half are the higher-energy (frustrated) type-II' state. The frustrated type-II' vertices are mapped to a defect configuration shown in (**c**), which is further mapped to a six-vertex configuration in (**d**).

15.6 Emergent Frustration by Design

Artificial spin ice is one particular class of nano-arrays that belong to a larger family of magnetic metamaterials. One appealing feature of this metamaterial approach is that the frustrated or competing interactions between the constituent nanomagnetic elements can be engineered or designed through, e.g. the lattice geometries. In a narrow sense, spin ices are frustrated magnets in which the spin configuration of elementary units (vertices, triangles, or tetrahedra) follows constraints that are similar to the Bernal-Fowler rules [128] dictating local proton ordering in solid water ice. These systems are exemplified by the square, honeycomb, and pentagonal arrays discussed in previous sections. Broadly speaking, however, the term "artificial spin ice" is used to refer to engineered frustrated Ising-like magnets. The advances in modern nanolithographic fabrication has significantly broaden the scope and applications of such artificial spin systems. Other than the most studied square and honeycomb ices, various array geometries have been proposed. These include the triangular [120, 121], brickwork [122], pentagonal [112] lattices, perpendicular nano-rods arrays [123], three-dimensional structures [64], and quasi-crystals [124]; some of them have also been fabricated.

Instead of building on geometries that have been realized by nature, a systematic method of designing novel frustrated arrays is proposed in [125]. In this approach, frustrated arrays are built from elementary vertices shown in Fig. 15.13a. Other than

the conventional four types of 4-legged vertices, the building blocks include three different types of 3-legged vertices with orthogonal islands. The square and brickwork arrays are examples that can be built from these elementary vertices. Because of the orthogonal geometry, the minimum $Q = \pm q$ vertices separate into two types: the lower-energy type-I' and excited type-II'. Importantly, there is no accidental geometry-induced degeneracy in the lowest energy configurations (for both 3- and 4-legged vertices) other than the time-reversal symmetry. A consequence of this non-degeneracy of lowest-energy vertex is that both the square and brickwork arrays are not frustrated and have a well defined antiferromagnetic-type ground state.

However, it is possible to design lattices with extensive degeneracy based on the building blocks shown in Fig. 15.13a. The frustration in these designed arrays is not due to the many different ways of arranging the degenerate lowest-energy vertices (triangles in kagome or tetrahedra in pyrochlore spin ice). Instead, the frustration comes from the fact that not all vertices can reach their lowest-energy type-I or I' configurations [125]. In practice, since the energy difference between type-I and II vertices is larger than that between the 3-legged type-I' and II', all four-legged vertices are in the lowest-energy type-I configuration. Frustration can be *designed* such that some of the 3-legged vertices have to be in the higher energy type-II' state [125].

One representative and intriguing example of this approach is the emergence of a frustrated six-vertex phase in the so-called shakti spin ice [126, 127], shown in Fig. 15.13b. The shakti lattice can be derived from the square lattice by alternatively placing an additional vertical or horizontal island in each square plaquette. To see how the frustration emerges in this array, we first restrict ourself to the vertex model, and neglect dipolar interactions beyond the nearest neighbors. Numerical simulations show that while all four-legged vertices are in the lowest-energy type-I state, only half of the 3-legged vertices can reach the type-I' state in the ground state [126]. Extensive degeneracy arises from the distribution of the unhappy type-II' vertices; a generic disordered ground state is shown in Fig. 15.13b. Characterization of this degenerate manifold can be achieved by specifying the location of the unhappy type-II' vertices, as demonstrated in Fig. 15.13c. This mapping from spins into defects on plaquettes is at least 2-to-1: each spin-ice state and its time-reversal partner are mapped to the same defect configuration. Moreover, when both defects sit at the two ends of the center long island, there is an additional Z_2 degrees of freedom associated with the magnetization of the center island; an example of this case is shown by the red dashed line in Fig. 15.13c.

The positions of these type-II' defects are highly correlated in the degenerate NN ground states. In fact, the local defect configurations satisfy constraints which are exactly equivalent to the Bernal-Fowler ice rules [128]. The mapping is simple: each plaquette can be viewed as a water molecule H_2O, with the center of the plaquette being the oxygen and type-II' defect being the hydrogen atom [126]. In the ground states of the nearest-neighbor shakti array, the ice rules then dictate that each plaquette has exactly two defect vertices [126]; an example is shown in Fig. 15.13c. The shakti spin ice thus provides the first realization of an extensively degenerate planar ice, or six-vertex model. Figure 15.13d shows the mapping of the defect configuration

to the six-vertex state. The ice phase of shakti array in which local defect ordering satisfies the Bernal-Fowler rules were also confirmed experimentally [114]. Taking into account the additional Z_2 degeneracy when two defects enclose a center long island, the degenerate manifold actually maps to a special 6-vertex model, the F-model, with a larger statistical weight for the symmetric vertices [126]. The notion of frustration by design exemplified by the shakti ice opens avenue to engineer novel collective behaviors in artificial spin ice.

15.7 Other Artificial Ices

The material-by-design approach can be extended beyond magnetic systems, and several artificial systems are shown to exhibit emergent ice physics. Different realizations explore different aspects of the ice or the Coulomb phase that are related to the specific physical features of the system. For example, adding particles into artificial colloidal ice introduces new types of defects that are absent in spin ices. This artificial frustrated system consists of interacting colloidal particles confined in 2D arrays of optical traps [129]; see Fig. 15.14a. Each trap has a double well potential, and the colloidal particle can sit at one of the two minima. When the doping is such that each optical trap has exactly one particle, the double-well trap behaves essentially as an Ising spin. Antiferromagnetic coupling between the Ising variables, which is essential for ice rules, comes from the repulsive interactions between colloidal particles [129]. In square arrays, the vertex where four traps meet corresponds to oxygen atoms in water ice, while the colloidal particles act as protons. The Bernal-Fowler ice rules then correspond to constraints that each vertex has exactly two colloidal particles. Brownian dynamics simulations of colloidal square ice find a finite ice regime at moderate particle repulsion, and an ordered state at strong colloidal-colloidal interactions [129]. Different lattice geometries such as kagome ice can also be realized in a similar setup; a highly degenerate ice ground state is obtained in kagome colloidal ice [130].

The same mechanism, namely repulsive interactions and double-well traps, can be used to realize a novel vortex ice system in nanostructured superconductors [131]. In this setup, non-superconducting islands with the double-hump shape are placed in a superconducting layer. These islands again serve as effective Ising spins when trapping exactly one vortex. The repulsive vortex-vortex interaction then forces ice rules at the junctions of the islands. Vortex ice phases have been observed experimentally in nanostructured MoGe thin films [132]. In both colloidal and vortex ices, the doping level can be easily controlled experimentally. For example increasing or decreasing magnetic field controls the number of vortices. While empty traps are equivalent to vacancy spins, a doubly-occupied trap corresponds to a double-arrow spin, which has no counterpart in spin systems. It is found that adding colloidal particles to the arrays produces dramatically different effects on square and kagome colloidal ices [133]. We note in passing that a similar setup with vortex replaced by magnetic skyrmion has also been proposed recently [134].

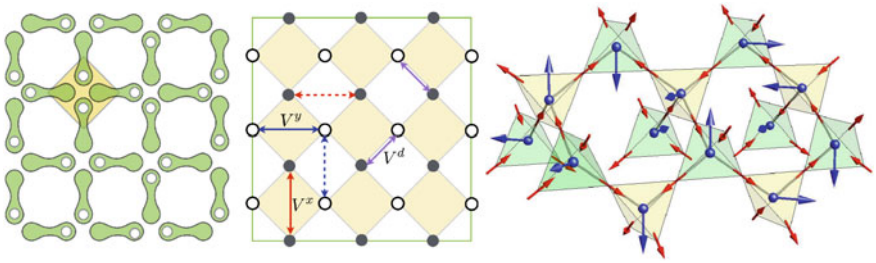

Fig. 15.14 Artificial ice systems. **a** Artificial ices build on repulsive interactions between colloidal particles or superconductor vortices. The dumbbell shaped double-well traps are arranged in a square lattice. Each trap behaves as a giant Ising spin as the particle or vortex can be in one of the two energy minima. **b** Rydberg cold atom realization of quantum square ice. **c** Orbital ice states in p-orbital fermonic cold atoms on a diamond lattice. The blue arrays at the diamond-lattice sites indicate the pseudo-vectors $\langle \boldsymbol{\lambda}_i \rangle$, while the red arrows specify the spins on the pyrochlore lattice. Figure reprinted from [143] with permission from the American Physical Society.

Cold atoms in optical lattices provide another platform for engineering artificial ice systems. Thanks to the high-degree of control over the atom dynamics and the advances in creating complex optical lattices, cold-atom systems are used to realize novel phases of matter and simulate complex many-body physics [135]. A recent proposal of realizing quantum square ice in optical lattices [136] is based on the well-established equivalence between hardcore Bose-Hubbard model and the XXZ spin-1/2 Hamiltonian. In this mapping, the presence (absence) of boson corresponds to spin up (down). These bosons are then placed at a checkerboard lattice, shown in Fig. 15.14b. Recall that the Ising degrees of freedom of spin ice, e.g. center of nano-islands in square ice array, form a checkerboard lattice; see Fig. 15.1. The Bose-Hubbard Hamiltonian reads

$$\mathscr{H}_{\rm HB} = -t \sum_{\langle ij \rangle} (b_i^\dagger b_j + \text{h.c.}) + \sum_{i,j} V_{ij} n_i n_j, \tag{15.9}$$

The density-density interaction, second term above, is mapped to the dominant Ising interaction $V_{ij}\sigma_i^z \sigma_j^z$, that is essential for ice physics. However, the interaction potential has to be highly anisotropic and step-like such that V_{ij} is a constant for atoms belonging to a square plaquette and zero otherwise; see (15.6) for the Ising ice model. In particular, this requires the different couplings between nearest neighbors in x and y directions: $V^x_{\bullet\bullet} = V^y_{\circ\circ} = V^d_{\bullet\circ} \neq 0$, while $V^y_{\bullet\bullet} = V^x_{\circ\circ} \approx 0$, where $V^d_{\bullet\circ}$ denotes the coupling between the two sublattices along the diagonal directions; see Fig. 15.14b. Thanks to the advances in Rydberg atom techniques, such complex interactions can be engineered using the laser-excited Rydberg states [136]. For example, the van der Waals forces are strongly anisotropic for Rubidium atoms excited to Rydberg p states [137]. As in the colloidal ice case, doping is another control parameter here and the square ice is realized at half-filling. The Rydberg atom ice offers the

opportunity to investigate quantum fluctuations and dynamical emergent gauge field in ice models [136].

While Rydberg quantum ice requires engineering of complex interactions, a novel orbital ice phase occurs naturally in p-band Mott insulator in a diamond lattice [143]. Motivated by experimental advances on higher orbital bands of optical lattices [138–140], cold atom systems have emerged as a new playground to investigate novel many-body orbital physics [141]. A characteristic of orbital exchange is the strong coupling between real and orbital spaces, giving rise to novel interactions such as quantum compass and Kitaev models [142]. Here we consider a p-band Hubbard model with spinless fermonic atoms on a diamond lattice. In the Mott insulating phase with two atoms per site, one fill the inert s band while the other occupies one of the three p orbitals. The remaining local degrees of freedom are similar to 3-state Potts variables, and they interact with each other through second-order exchange process. The highly directional p-orbital hopping leads to a new quantum Hamiltonian on the diamond lattice.

To describe the orbital exchange, we first define a pseudo-vector operator $\boldsymbol{\lambda} = (\lambda^x, \lambda^y, \lambda^z) = (\lambda^{(6)}, \lambda^{(4)}, \lambda^{(1)})$ acting on the local p_x, p_y, and p_z basis. Here the components of $\boldsymbol{\lambda}$ are given by the three real-valued off-diagonal Gell-mann matrices; they are the SU(3) analog of the Pauli σ^x matrix. The operators have the following non-zero elements: $\langle p_y|\lambda^x|p_z\rangle = \langle p_z|\lambda^y|p_x\rangle = \langle p_x|\lambda^z|p_y\rangle = 1$. Taking into account only the dominant longitudinal hopping, the effective exchange Hamiltonian is given by [143]

$$\mathscr{H}_{\text{tetrahedral}} = J \sum_{m=0}^{3} \sum_{\langle ij\rangle \| \hat{\mathbf{n}}_m} \left(\boldsymbol{\lambda}_i \cdot \hat{\mathbf{n}}_m\right)\left(\boldsymbol{\lambda}_j \cdot \hat{\mathbf{n}}_m\right), \tag{15.10}$$

where $m = 0, 1, 2, 3$ corresponds to the four different NN bonds; their orientations are specified by unit vectors $\hat{\mathbf{n}}_0 = [111]$, $\hat{\mathbf{n}}_1 = [1\bar{1}\bar{1}]$, $\hat{\mathbf{n}}_2 = [\bar{1}1\bar{1}]$, and $\hat{\mathbf{n}}_3 = [\bar{1}\bar{1}1]$. Because the anisotropic interactions involve the four $\hat{\mathbf{n}}_m$ of a tetrahedron, this Hamiltonian is called a quantum tetrahedral model [143]. The model is geometrically frustrated in the sense that there is no way to minimize the NN interactions simultaneously. Monte Carlo simulations with variational product states of the form $|\Psi\rangle = \prod_i |\psi_i\rangle$ find extensively degenerate minimum energy states. Remarkably, direct calculation shows that these product states are *exact* eigenstates of (15.10). Huge degeneracy of the ground states is also obtained in exact diagonalization of small clusters. Moreover, these product ground states are highly correlated; orbitals in the degenerate manifold have to satisfy two constraints. (i) The expectation value of the pseudo-vector only takes on six different values: $\langle\boldsymbol{\lambda}_i\rangle = \pm\hat{\mathbf{x}}$, $\pm\hat{\mathbf{y}}$, and $\pm\hat{\mathbf{z}}$. (ii) Defining an Ising variable on each of the four bonds that attached to site-i: $\sigma_i^m \equiv \sqrt{3}\langle\boldsymbol{\lambda}_i\rangle \cdot \hat{\mathbf{n}}_m = \pm 1$, the NN pairs need to satisfy $\sigma_i^m \sigma_j^m = -1$.

It turns out these two constraints are equivalent to the ice rules [143]: the six different $\langle\boldsymbol{\lambda}_i\rangle$ are mapped to the six distinct 2-in-2-out Ising spins, while constraint (ii) ensures that consistent Ising spins can be assigned on the pyrochlore lattice. Figure 15.14c shows a generic disordered orbital ice state and the mapping to the

spin-ice configuration on pyrochlore. The p-band Mott insulator in diamond lattice thus provides an orbital analog of the ice phase. It is worth noting that, unlike most ice models with Ising degrees of freedom defined on a bi-simplex lattice (e.g. kagome or pyrochlore), the fundamental variables in orbital ice are orbital triples on a bipartite diamond lattice. The ice rules are emergent correlations in the ground state of the quantum dynamics.

15.8 Conclusion and Outlook

To summarize, we have reviewed the fundamental theories and physical properties of artificial spin ice, including the basic energetics and dynamics (Sect. 15.1), thermodynamic phases (Sect. 15.2), effects of disorder, nonequilibrium dynamics (Sect. 15.3), and elementary excitations (Sects. 15.4 and 15.5). Contrary to natural spin-ice compounds, the artificial version of spin ice offers the opportunity for researchers to tailor-design the many-body interactions and to directly probe the resultant dynamics "microscopically" in real space. In particular, artificial spin ices provide a new playground for scientists to explore the physics and technological applications of emergent magnetic monopoles. This has inspired the study of a new field dubbed magnetricity, which is the magnetic equivalent of electricity. An intriguing possibility is to use magnetic monopoles as binary mobile memory storages that also serve as the information processing units. Taking advantage of the topological and collective nature of monopole excitations, artificial spin ice opens a new avenue to realize massively parallel computation that goes beyond the conventional von Neumann architecture [145].

While magnetic moments in natural spin-ice compounds are regarded as structureless entities, the Ising "spins" in artificial spin ices are themselves macroscopic ferromagnets that exhibit complex textures and support spin-wave excitations. A unique feature of artificial spin ice is thus the intriguing interplay between its two basic elementary excitations: magnetic monopoles and magnons. As discussed in Sect. 15.5, both the monopoles and the Dirac strings that connect them have unique signatures in the spin-wave excitations of the nanomagnetic arrays. Several recent studies along this line [146–148] have further established that artificial spin ices can be viewed as reconfigurable and tunable magnonic crystals that can be used as metamaterials for spin-wave-based applications at the nanoscale. This suggests the fascinating possibility of dynamically controlling the magnon band structure through the motion and configuration of magnetic monopoles.

Another new frontier is the study of electric charges flow through the nano-wires in artificial spin ice. Recent experiments have demonstrated that connected artificial ice arrays exhibit unusual and complex magneto-transport phenomena [98, 149–151]. Remarkably, rather large Hall signals are observed in artificial kagome spin ice even in the absence of external magnetic field [150]. Theoretical models based on the anisotropic magneto-resistance effect of permalloy show that significant contribution to the Hall voltage comes from the vertex regions of the connected network [150,

152]. Moreover, an effective circuit model has been developed to understand the complex magneto-transport properties of artificial spin ice [152]. In this picture, the system can be viewed as a resistor network driven by voltage sources that are located at vertices of the spin-ice array. The differential voltages across different terminals of these sources are related to the ice-rules that govern the local magnetization ordering. The circuit model thus underscores the many-body origin of Hall signals in artificial spin ice [152].

Artificial spin ice, originally designed to model the frustrated magnetic interactions in pyrochlore spin-ice compounds, has now become a flourishing field of research with rapid advances in several fronts. A central theme that drives this field is the concept of frustration by design discussed in Sect. 15.6. Thanks to the impressive progress in nano-fabrication and imaging technology, virtually any imaginable lattice geometry can be fabricated and characterized in real space and real time. For example, dedicated geometries have been proposed and realized to explore interesting physics such as magnetic charge screening [114, 115], magnetic charge ice [144, 153], emergent dimensional reduction [154], topological lattice defects [155], and nanoscale spin ratchet [156], to name but a few. The artificial spin array can be used to dynamically imprint complex patterns of magnetic field on other interesting materials, e.g. superconductors, topological matters, and quantum heterostructures, thus opening a new route to create multifunctional metamaterials and devices. Finally, implementation of ice or frustrated systems in other setups as discussed in Sect. 15.7 introduces new dimensions, such as spin vacancy and quantum fluctuations, to the already rich physics of spin ice materials.

References

1. C. Nisoli, R. Moessner, P. Schiffer, Rev. Mod. Phys. **85**, 1473 (2013). https://doi.org/10.1103/RevModPhys.85.1473
2. L.J. Heyderman, R.L. Stamps, J. Phys.: Condens. Matter **25**, 363201 (2013). https://doi.org/10.1088/0953-8984/25/36/363201
3. J. Cumings, L.J. Heyderman, C.H. Marrows, R.L. Stamps, New J. Phys. **16**, 075016 (2014). https://doi.org/10.1088/1367-2630/16/7/075016
4. I. Gilbert, C. Nisoli, P. Schiffer, Phys. Today **69**, 55 (2016). https://doi.org/10.1063/PT.3.3266
5. See Chapter 16: "Experimental Studies of Artificial Spin Ice" by C. J. Marrows for details about the experimental realizations and characterizations of artificial spin ice
6. R.F. Wang, C. Nisoli, R.S. Freitas, J. Li, W. McConville, B.J. Cooley, M.S. Lund, N. Samarth, C. Leighton, V.H. Crespi, P. Schiffer, Nature **439**, 303 (2006). https://doi.org/10.1038/nature04447
7. M. Tanaka, E. Saitoh, H. Miyajima, T. Yamaoka, Y. Iye, Phys. Rev. B **73**, 052411 (2006). https://doi.org/10.1103/PhysRevB.73.052411
8. Y. Qi, T. Brintlinger, J. Cumings, Phys. Rev. B **77**, 094418 (2008). https://doi.org/10.1103/PhysRevB.77.094418
9. J.D. Jackson, *Classical Electrodynamics* (Wiley, New York, 1998). 978-0-471-30932-1
10. I.A. Ryzhkin, J. Exp. Theor. Phys. **101**, 481 (2005). https://doi.org/10.1134/1.2103216
11. C. Castelnovo, R. Moessner, S.L. Sondhi, Nature **451**, 42 (2008). https://doi.org/10.1038/nature06433

12. O. Tchernyshyov, Nat. Phys. **6**, 323 (2010). https://doi.org/10.1038/nphys1658
13. P. Mellado, O. Petrova, Y. Shen, O. Tchernyshyov, Phys. Rev. Lett. **105**, 187206 (2010). https://doi.org/10.1103/PhysRevLett.105.187206
14. J. Gadbois, J.-G. Zhu, IEEE Trans. Magn. **31**, 3802 (1995). https://doi.org/10.1109/20.489777
15. C. Phatak, A.K. Petford-Long, O. Heinonen, M. Tanase, M. De Graef, Phys. Rev. B **83**, 174431 (2011). https://doi.org/10.1103/PhysRevB.83.174431
16. P. M. Chaikin and T. C. Lubensky, *Principles of Condensed Matter Physics* (Cambridge University Press, Cambridge, 2000) isbn: 9780521794503
17. R.D. McMichael, M.J. Donahue, IEEE Trans. Magn. **33**, 4167 (1997). https://doi.org/10.1109/20.619698
18. O. Tchernyshyov, G.-W. Chern, Phys. Rev. Lett. **95**, 197204 (2005). https://doi.org/10.1103/PhysRevLett.95.197204
19. G.-W. Chern, D. Clarke, H. Youk, O. Tchernyshyov, in *Quantum Magnetism*, B. Barbara et al. (eds.), NATO Science for Peace and Security Series B: Physics and Biophysics, pp. 35–48, Springer (Dordrecht, 2008) https://doi.org/10.1007/978-1-4020-8512-3
20. A. Pushp, T. Phung, C. Rettner, B.P. Hughes, S.-H. Yang, L. Thomas, S.S.P. Parkin, Nat. Phys. **9**, 505–511 (2013). https://doi.org/10.1038/nphys2669
21. L.D. Landau, E.M. Lifshitz, Phys. Z. Sowjet. **8**, 153 (1935). https://doi.org/10.1016/B978-0-08-036364-6.50008-9
22. T.L. Gilbert, Phys. Rev. **100**, 1243 (1955). https://doi.org/10.1103/PhysRev.100.1243
23. Y. Shen, O. Petrova, P. Mellado, S. Daunheimer, J. Cumings, and Oleg Tchernyshyov. New J. Phys. **14**, 035022 (2012). https://doi.org/10.1088/1367-2630/14/3/035022
24. M. J. Donahue and D. G. Porter, OOMMF National Institute of Standards and Technology, Tech. Rep. NISTIR 6376, Gaithersburg, MD, 1999 http://math.nist.gov/oommf
25. A. Vansteenkiste, B. Van de Wiele, J. Magn. Magn. Mater. **323**, 2585 (2011). https://doi.org/10.1016/j.jmmm.2011.05.037
26. S.J. Greaves, H. Muraoka, J. Appl. Phys. **112**, 043909 (2012). https://doi.org/10.1063/1.4747910
27. C. Phatak, M. Pan, A.K. Petford-Long, S. Hong, M. De Graef, New J. Phys. **14**, 075028 (2012). https://doi.org/10.1088/1367-2630/14/7/075028
28. M. Beleggia, M. De Graef, J. Magn. Magn. Mater. **285**, L1 (2005). https://doi.org/10.1016/j.jmmm.2004.09.004
29. G.M. Wysin, W.A. Moura-Melo, L.A.S. Mól, A.R. Pereira, J. Phys.: Condens. Matter **24**, 296001 (2012). https://doi.org/10.1088/0953-8984/24/29/296001
30. G.M. Wysin, W.A. Moura-Melo, L.A.S. Mól, A.R. Pereira, New J. Phys. **15**, 045029 (2013). https://doi.org/10.1088/1367-2630/15/4/045029
31. M. Ewerlin, D. Demirbas, F. Brüssing, O. Petracic, A.A. Ünal, S. Valencia, F. Kronast, H. Zabel, Phys. Rev. Lett. **110**, 177209 (2013). https://doi.org/10.1103/PhysRevLett.110.177209
32. U.B. Arnalds, M. Ahlberg, M.S. Brewer, V. Kapaklis, ETh. Papaioannou, M. Karimipour, P. Korelis, A. Stein, S. Olafsson, T.P.A. Hase, B. Hjörvarsson, Appl. Phys. Lett. **105**, 042409 (2014). https://doi.org/10.1063/1.4891479
33. C. Castelnovo, R. Moessner, S.L. Sondhi, Phys. Rev. Lett. **104**, 107201 (2010). https://doi.org/10.1103/PhysRevLett.104.107201
34. A.B. Bortz, M.H. Kalos, J.L. Lebowitz, J. Comp. Phys. **17**, 10 (1975). https://doi.org/10.1016/0021-9991(75)90060-1
35. A.F. Voter, F. Montalenti, T.C. Germann, Annu. Rev. Mater. Res. **32**, 321 (2002). https://doi.org/10.1146/annurev.matsci.32.112601.141541
36. A. Farhan, P.M. Derlet, A. Kleibert, A. Balan, R.V. Chopdekar, M. Wyss, J. Perron, A. Scholl, F. Nolting, L.J. Heyderman, Phys. Rev. Lett. **111**, 057204 (2013). https://doi.org/10.1103/PhysRevLett.111.057204
37. A. Farhan, P.M. Derlet, A. Kleibert, A. Balan, R.V. Chopdekar, M. Wyss, L. Anghinolfi, F. Nolting, L.J. Heyderman, Nat. Phys. **9**, 375 (2013). https://doi.org/10.1038/NPHYS2613
38. D. Thonig, S. Reissaus, I. Mertig, J. Henk, J. Phys.: Condens. Matter **26**, 266006 (2014). https://doi.org/10.1088/0953-8984/26/26/266006

39. D. Levis, L.F. Cugliandolo, Europhys. Lett. **97**, 30002 (2012). https://doi.org/10.1209/0295-5075/97/30002
40. D. Levis, L.F. Cugliandolo, Phys. Rev. B **87**, 214302 (2013). https://doi.org/10.1103/PhysRevB.87.214302
41. Z. Budrikis, P. Politi, R.L. Stamps, Phys. Rev. Lett. **105**, 017201 (2010). https://doi.org/10.1103/PhysRevLett.105.017201
42. X. Ke, J. Li, C. Nisoli, P.E. Lammert, W. McConville, R.F. Wang, V.H. Crespi, P. Schiffer, Phys. Rev. Lett. **101**, 037205 (2008). https://doi.org/10.1103/PhysRevLett.101.037205
43. E. Mengotti, L. J. Heyderman, A. Fraile Rodriguez, A. Bisig, L. Le Guyader, F. Nolting, and H. B. Braun, Phys. Rev. B **78**, 144402 (2008) https://doi.org/10.1103/PhysRevB.78.144402
44. C. Nisoli, R. Wang, J. Li, W.F. McConville, P.E. Lammert, P. Schiffer, V.H. Crespi, Phys. Rev. Lett. **98**, 217203 (2007). https://doi.org/10.1103/PhysRevLett.98.217203
45. C. Nisoli, J. Li, X. Ke, D. Garand, P. Schiffer, V.H. Crespi, Phys. Rev. Lett. **105**, 047205 (2010). https://doi.org/10.1103/PhysRevLett.105.047205
46. J.P. Morgan, A. Stein, S. Langridge, C.H. Marrows, Nat. Phys. **7**, 75–79 (2011). https://doi.org/10.1038/nphys1853
47. J.P. Morgan, J. Akerman, A. Stein, C. Phatak, R.M.L. Evans, S. Langridge, C.H. Marrows, Phys. Rev. B **87**, 024405 (2013). https://doi.org/10.1103/PhysRevB.87.024405
48. C. Nisoli, New J. Phys. **14**, 035017 (2012). https://doi.org/10.1088/1367-2630/14/3/035017
49. J. Cumings, Nat. Phys. **7**, 7 (2011). https://doi.org/10.1038/nphys1898
50. S. Zhang, I. Gilbert, C. Nisoli, G.-W. Chern, M. J. Erickson, L. O'Brien, C. Leighton, P. E. Lammert, V. H. Crespi, and P. Schiffer, Nature **500**, 553 (2013). https://doi.org/10.1038/nature12399
51. J.M. Porro, A. Bedoya-Pinto, A. Berger, P. Vavassori, New J. Phys. **15**, 055012 (2013). https://doi.org/10.1088/1367-2630/15/5/055012
52. V. Kapaklis, U.B. Arnalds, A. Farhan, R.V. Chopdekar, A. Balan, A. Scholl, L.J. Heyderman, B. Hjörvarsson, Nat. Nanotech. **9**, 514 (2014). https://doi.org/10.1038/NNANO.2014.104
53. L.J. Heyderman, Nat. Nanotech. **8**, 705 (2013). https://doi.org/10.1038/nnano.2013.193
54. J.L. Garcia-Palacios, F.J. Lazaro, Phys. Rev. B **58**, 14937 (1998). https://doi.org/10.1103/PhysRevB.58.14937
55. R.F.L. Evans, D. Hinzke, U. Atxitia, U. Nowak, R.W. Chantrell, O. Chubykalo-Fesenko, Phys. Rev. B **85**, 014433 (2012). https://doi.org/10.1103/PhysRevB.85.014433
56. O. Chubykalo, U. Nowak, R.W. Chantrell, D. Garanin, Phys. Rev. B **74**, 094436 (2006). https://doi.org/10.1103/PhysRevB.74.094436
57. L. Néel, Ann. Geophys. **5**, 99 (1949). An English translation is available in Kurti, N., ed. (1988). Selected Works of Louis Néel. New York: Gordon and Breach. pp. 407–427. ISBN 978-2-88124-300-4
58. G. Möller, R. Moessner, Phys. Rev. Lett. **96**, 237202 (2006). https://doi.org/10.1103/PhysRevLett.96.237202
59. Y. Perrin, B. Canals, N. Rougemaille, Nature **540**, 410 (2016). https://doi.org/10.1038/nature20155
60. E.H. Lieb, Phys. Rev. Lett. **18**, 692 (1967). https://doi.org/10.1103/PhysRevLett.18.692
61. R.J. Baxter, *Exactly Solved Models in Statistical Mechanics* (Dover Publications, Mineola, New-York, 2007). ISBN 10: 0486462714
62. D. Levis, L.F. Cugliandolo, L. Foini, M. Tarzia, Phys. Rev. Lett. **110**, 207206 (2013). https://doi.org/10.1103/PhysRevLett.110.207206
63. L. Foini, D. Levis, M. Tarzia, L.F. Cugliandolo, J. Stat. Mech. P02026 (2013). https://doi.org/10.1088/1742-5468/2013/02/P02026
64. G.-W. Chern, C. Reichhardt, C. Nisoli, Appl. Phys. Lett. **104**, 013101 (2014). https://doi.org/10.1063/1.4861118
65. A.S. Wills, R. Ballou, C. Lacroix, Phys. Rev. B **66**, 144407 (2002). https://doi.org/10.1103/PhysRevB.66.144407
66. G.-W. Chern, O. Tchernyshyov, Phil. Trans. Roy. Soc. A **370**, 5718 (2012). https://doi.org/10.1098/rsta.2011.0388

67. G. Möller, R. Moessner, Phys. Rev. B **80**, 140409 (2009). https://doi.org/10.1103/PhysRevB.80.140409
68. G.-W. Chern, P. Mellado, O. Tchernyshyov, Phys. Rev. Lett. **106**, 207202 (2011). https://doi.org/10.1103/PhysRevLett.106.207202
69. R. Higashinaka, H. Fukazawa, Y. Maeno, Phys. Rev. B **68**, 014415 (2003). https://doi.org/10.1103/PhysRevB.68.014415
70. Y. Tabata, H. Kadowaki, K. Matsuhira, Z. Hiroi, N. Aso, E. Ressouche, B. Fak, Phys. Rev. Lett. **97**, 257205 (2006). https://doi.org/10.1103/PhysRevLett.97.257205
71. M. Udagawa, M. Ogata, Z. Hiroi, J. Phys. Soc. Jpn. **71**, 2365 (2002). https://doi.org/10.1143/JPSJ.71.2365
72. A. Schumann, B. Sothmann, P. Szary, H. Zabel, Appl. Phys. Lett. **97**, 022509 (2010). https://doi.org/10.1063/1.3463482
73. N. Rougemaille, F. Montaigne, B. Canals, A. Duluard, D. Lacour, M. Hehn, R. Belkhou, O. Fruchart, S. El Moussaoui, A. Bendounan, F. Maccherozzi, Phys. Rev. Lett. **106**, 057209 (2011). https://doi.org/10.1103/PhysRevLett.106.057209
74. Z. Budrikis, J.P. Morgan, J. Akerman, A. Stein, P. Politi, S. Langridge, C.H. Marrows, R.L. Stamps, Phys. Rev. Lett. **109**, 037203 (2012). https://doi.org/10.1103/PhysRevLett.109.037203
75. P. A. M. Dirac, Proc. R. Soc. London, Ser. A **133**, 60 (1931) https://doi.org/10.1098/rspa.1931.0130
76. J.P. Morgan, A. Stein, S. Langridge, C.H. Marrows, New J. Phys. **13**, 105002 (2011). https://doi.org/10.1088/1367-2630/13/10/105002
77. S.D. Pollard, V. Volkov, Y. Zhu, Phys. Rev. B **85**, 180402 (2012). https://doi.org/10.1103/PhysRevB.85.180402
78. Z. Budrikis, P. Politi, R.L. Stamps, J. Appl. Phys. **111**, 07E109 (2012). https://doi.org/10.1063/1.3671434
79. Z. Budrikis, P. Politi, R.L. Stamps, Phys. Rev. Lett. **107**, 217204 (2011). https://doi.org/10.1103/PhysRevLett.107.217204
80. R. Albert, A.-L. Barabasi, Rev. Mod. Phys. **74**, 47 (2002). https://doi.org/10.1103/RevModPhys.74.47
81. Z. Budrikis, K.L. Livesey, J.P. Morgan, J. Akerman, A. Stein, S. Langridge, C.H. Marrows, R.L. Stamps, New J. Phys. **14**, 035014 (2012). https://doi.org/10.1088/1367-2630/14/3/035014
82. A. Westphalen, A. Schumann, A. Remhof, H. Zabel, M. Karolak, B. Baxevanis, E.Y. Vedmedenko, T. Last, U. Kunze, T. Eimüller, Phys. Rev. B **77**, 174407 (2008). https://doi.org/10.1103/PhysRevB.77.174407
83. S.A. Daunheimer, O. Petrova, O. Tchernyshyov, J. Cumings, Phys. Rev. Lett. **107**, 167201 (2011). https://doi.org/10.1103/PhysRevLett.107.167201
84. S. Ladak, D.E. Read, G.K. Perkins, L.F. Cohen, W.R. Branford, Nat. Phys. **6**, 359 (2010). https://doi.org/10.1038/nphys1628
85. E. Mengotti, L.J. Heyderman, A.F. Rodriguez, F. Nolting, R.V. Hügli, H.-B. Braun, Nat. Phys. **7**, 68 (2011). https://doi.org/10.1038/nphys1794
86. K.K. Kohli, A.L. Balk, J. Li, S. Zhang, I. Gilbert, P.E. Lammert, V.H. Crespi, P. Schiffer, N. Samarth, Phys. Rev. B **84**, 180412(R) (2011). https://doi.org/10.1103/PhysRevB.84.180412
87. G.-W. Chern, C. Reichhardt, and C. J. Olson Reichhardt, New J. Phys. **16**, 063051, (2014) https://doi.org/10.1088/1367-2630/16/6/063051
88. C. J. Olson Reichhardt, G.-W. Chern, A. Libal, and C. Reichhardt, J. Appl. Phys. **117**, 172612 (2015) https://doi.org/10.1063/1.4913884
89. D. Jiles, *Introduction to Magnetism and Magnetic Materials* (Chapman and Hall, London, 1996). ISBN 9781482238877
90. J.P. Sethna, K.A. Dahmen, C.R. Myers, Nature **410**, 242 (2001). https://doi.org/10.1038/35065675
91. G. Durin, S. Zapperi, Phys. Rev. Lett. **84**, 4705 (2000). https://doi.org/10.1103/PhysRevLett.84.4705

92. A. Schumann, P. Szary, E.Y. Vedmedenko, H. Zabel, New J. Phys. **14**, 035015 (2012). https://doi.org/10.1088/1367-2630/14/3/035015
93. S. A. Daunheimer, J. Cumings, unpublished data (private communication)
94. G. Ódor, Rev. Mod. Phys. **76**, 663 (2004). https://doi.org/10.1103/RevModPhys.76.663
95. S. Maslov, Phys. Rev. Lett. **74**, 562 (1995). https://doi.org/10.1103/PhysRevLett.74.562
96. R.V. Hügli, G. Duff, B. O'Conchuir, E. Mengotti, A.F. Rodriguez, F. Nolting, L.J. Heyderman, H.B. Braun, Phil. Trans. Roy. Soc. A **370**, 5767 (2012). https://doi.org/10.1098/rsta.2011.0538
97. N. Rougemaille, F. Montaigne, B. Canals, M. Hehn, H. Riahi, D. Lacour, J.-C. Toussaint, New J. Phys. **15**, 035026 (2013). https://doi.org/10.1088/1367-2630/15/3/035026
98. W.R. Branford, S. Ladak, D.E. Read, K. Zeissler, L.F. Cohen, Science **335**, 1597 (2012). https://doi.org/10.1088/1367-2630/14/4/045010
99. S. Gliga, A. Kakay, R. Hertel, O.G. Heinonen, Phys. Rev. Lett. **110**, 117205 (2013). https://doi.org/10.1103/PhysRevLett.110.117205
100. V.V. Kruglyak, P.S. Keatley, A. Neudert, R.J. Hicken, J.R. Childress, J.A. Katine, Phys. Rev. Lett. **104**, 027201 (2010). https://doi.org/10.1103/PhysRevLett.104.027201
101. G. Carlotti, S. Tacchi, G. Gubbiotti, M. Madami, H. Dey, G. Csaba, W. Porod, Appl. Phys. Lett. **117**, 17A316 (2015). https://doi.org/10.1063/1.4914878
102. S. Tacchi, F. Montoncello, M. Madami, G. Gubbiotti, G. Carlotti, L. Giovannini, R. Zivieri, F. Nizzoli, S. Jain, A.O. Adeyeye, N. Singh, Phys. Rev. Lett. **107**, 127204 (2011). https://doi.org/10.1103/PhysRevLett.107.127204
103. S. Neusser, D. Grundler, Adv. Mater. **21**, 2927 (2009). https://doi.org/10.1002/adma.200900809
104. V.V. Kruglyak, S.O. Demokritov, D. Grundler, J. Phys. D: Appl. Phys. **43**, 264001 (2010). https://doi.org/10.1088/0022-3727/43/26/264001
105. B. Lenk, H. Ulrichs, F. Garbs, M. Münzenberg, Phys. Rep. **507**, 107 (2011). https://doi.org/10.1016/j.physrep.2011.06.003
106. L.R. Walker, Phys. Rev. **105**, 390 (1957). https://doi.org/10.1103/PhysRev.105.390
107. Y. Nambu, Phys. Rev. D **10**, 4262 (1974). https://doi.org/10.1103/PhysRevD.10.4262
108. R.C. Silva, R.J.C. Lopes, L.A.S. Mól, W.A. Moura-Melo, G.M. Wysin, A.R. Pereira, Phys. Rev. B **87**, 014414 (2013). https://doi.org/10.1103/PhysRevB.87.014414
109. L.A. Mól, R.L. Silva, R.C. Silva, A.R. Pereira, W.A. Moura-Melo, B.V. Costa, J. Appl. Phys. **106**, 063913 (2009). https://doi.org/10.1063/1.3224870
110. L.A.S. Mól, W.A. Moura-Melo, A.R. Pereira, Phys. Rev. B **82**, 054434 (2010). https://doi.org/10.1103/PhysRevB.82.054434
111. R.C. Silva, F.S. Nascimento, L.A.S. Mól, W.A. Moura-Melo, A.R. Pereira, New J. Phys. **14**, 015008 (2012). https://doi.org/10.1088/1367-2630/14/1/015008
112. G.-W. Chern, P. Mellado, Europhys. Lett. **114**, 37004 (2016). https://doi.org/10.1209/0295-5075/114/37004
113. L.D. Landau, Phys. Z. Sowjetunion **3**, 644 (1933)
114. I. Gilbert, G.-W. Chern, S. Zhang, L. O'Brien, B. Fore, C. Nisoli, P. Schiffer, Nat. Phys. **10**, 670 (2014). https://doi.org/10.1038/nphys3037
115. A. Farhan, A. Scholl, C.F. Petersen, L. Anghinolfi, C. Wuth, S. Dhuey, R.V. Chopdekar, P. Mellado, M.J. Alava, S. van Dijken, Nat. Commun. **7**, 12635 (2016). https://doi.org/10.1038/ncomms12635
116. S. Ladak, D.E. Read, T. Tyliszczak, W.R. Branford, L.F. Cohen, New J. Phys. **13**, 023023 (2011). https://doi.org/10.1088/1367-2630/13/2/023023
117. S. Ladak, D.E. Read, W.R. Branford, L.F. Cohen, New J. Phys. **13**, 063032 (2011). https://doi.org/10.1088/1367-2630/13/6/063032
118. S. Ladak, S.K. Walton, K. Zeissler, T. Tyliszczak, D.E. Read, W.R. Branford, L.F. Cohen, New J. Phys. **14**, 045010 (2012). https://doi.org/10.1088/1367-2630/14/4/045010
119. S.-K. Kim, J. Phys. D: Appl. Phys. **43**, 264004 (2010). https://doi.org/10.1088/0022-3727/43/26/264004

120. L.A.S. Mòl, A.R. Pereira, W.A. Moura-Melo, Phys. Rev. B **85**, 184410 (2012). https://doi.org/10.1103/PhysRevB.85.184410
121. S. Zhang, J. Li, J. Bartell, X. Ke, C. Nisoli, P.E. Lammert, V.H. Crespi, P. Schiffer, Phys. Rev. Lett. **107**, 117204 (2011). https://doi.org/10.1103/PhysRevLett.107.117204
122. J. Li, X. Ke, S. Zhang, D. Garand, C. Nisoli, P. Lammert, V.H. Crespi, P. Schiffer, Phys. Rev. B **81**, 092406 (2010). https://doi.org/10.1103/PhysRevB.81.092406
123. S. Zhang, J. Li, I. Gilbert, J. Bartell, M.J. Erickson, Y. Pan, P.E. Lammert, C. Nisoli, K.K. Kohli, R. Misra, V.H. Crespi, N. Samarth, C. Leighton, P. Schiffer, Phys. Rev. Lett. **109**, 087201 (2012). https://doi.org/10.1103/PhysRevLett.109.087201
124. V.S. Bhat, J. Sklenar, B. Farmer, J. Woods, J.T. Hastings, S.J. Lee, J.B. Ketterson, L.E. De Long, Phys. Rev. Lett. **111**, 077201 (2013). https://doi.org/10.1103/PhysRevLett.111.077201
125. M.J. Morrison, T.R. Nelson, C. Nisoli, New J. Phys. **15**, 045009 (2013). https://doi.org/10.1088/1367-2630/15/4/045009
126. G.-W. Chern, M.J. Morrison, C. Nisoli, Phys. Rev. Lett. **111**, 177201 (2013). https://doi.org/10.1103/PhysRevLett.111.177201
127. R.L. Stamps, Nat. Phys. **10**, 623 (2014). https://doi.org/10.1038/nphys3072
128. J.D. Bernal, R.H. Fowler, J. Chem. Phys. **1**, 515 (1933). https://doi.org/10.1063/1.1749327
129. A. Libál, C. Reichhardt, C. J. Olson Reichhardt, Phys. Rev. Lett. **97**, 228302 (2006) https://doi.org/10.1103/PhysRevLett.97.228302
130. C. J. Olson Reichhardt, A. Libál, and C. Reichhardt, New J. Phys. **14**, 025006 (2012) https://doi.org/10.1088/1367-2630/14/2/025006
131. A. Libál, C. J. Olson Reichhardt, and C. Reichhardt, Phys. Rev. Lett. **102**, 237004 (2009) https://doi.org/10.1103/PhysRevLett.102.237004
132. M.L. Latimer, G.R. Berdiyorov, Z.L. Xiao, F.M. Peeters, W.K. Kwok, Phys. Rev. Lett. **111**, 067001 (2013). https://doi.org/10.1103/PhysRevLett.111.067001
133. A. Libal, C. J. Olson Reichhardt, C. Reichhardt, New J. Phys. **17**, 103010 (2016) https://doi.org/10.1088/1367-2630/17/10/103010
134. F. Ma, C. Reichhardt, W. Gan, C. J. Olson Reichhardt, and W. S. Lew, Phys. Rev. B **94**, 144405 (2016) https://doi.org/10.1103/PhysRevB.94.144405
135. I. Bloch, J. Dalibard, W. Zwerger, Rev. Mod. Phys. **80**, 885 (2008). https://doi.org/10.1103/RevModPhys.80.885
136. A.W. Glaetzle, M. Dalmonte, R. Nath, I. Rousochatzakis, R. Moessner, P. Zoller, Phys. Rev. X **4**, 041037 (2014). https://doi.org/10.1103/PhysRevX.4.041037
137. T.G. Walker, M. Saffman, Phys. Rev. A **77**, 032723 (2008). https://doi.org/10.1103/PhysRevA.77.032723
138. T. Müller, S. Fölling, A. Widera, I. Bloch, Phys. Rev. Lett. **99**, 200405 (2007). https://doi.org/10.1103/PhysRevLett.99.200405
139. G. Wirth, M. Ölschläger, A. Hemmerich, Nat. Phys. **7**, 147 (2011). https://doi.org/10.1038/nphys1857
140. P. Soltan-Panahi, D.-S. Lühmann, J. Struck, P. Wind-passinger, K. Sengstock, Nat. Phys. **8**, 71 (2012). https://doi.org/10.1038/nphys2128
141. M. Lewenstein, W.V. Liu, Nat. Phys. **7**, 101 (2011). https://doi.org/10.1038/nphys1894
142. Z. Nussinov, J. van den Brink, Rev. Mod. Phys. **87**, 1 (2015). https://doi.org/10.1103/RevModPhys.87.1
143. G.-W. Chern, C. Wu, Phys. Rev. E **84**, 061127 (2011). https://doi.org/10.1103/PhysRevE.84.061127
144. P.A. McClarty, A. O'Brien, F. Pollmann, Phys. Rev. B **89**, 195123 (2014). https://doi.org/10.1103/PhysRevB.89.195123
145. M. Di Ventra, Y.V. Pershin, Nat. Phys. **9**, 200 (2013). https://doi.org/10.1038/nphys2566
146. E. Iacocca, S. Gliga, R.L. Stamps, O. Heinonen, Phys. Rev. B **93**, 134420 (2016). https://doi.org/10.1103/PhysRevB.93.134420
147. Y. Li, G. Gubbiotti, F. Casoli, S.A. Morley, F.J.T. Gonçalves, M.C. Rosamond, E.H. Linfield, C.H. Marrows, S. McVitie, R.L. Stamps, J. Appl. Phys. **121**, 103903 (2017). https://doi.org/10.1063/1.4978315

148. I. Panagiotopoulos, J. Magn. Magn. Mater. **422**, 227 (2017). https://doi.org/10.1016/j.jmmm.2016.08.051
149. B.L. Le, D.W. Rench, R. Misra, L. O'Brien, C. Leighton, N. Samarth, P. Schiffer, New J. Phys. **17**, 023047 (2015). https://doi.org/10.1088/1367-2630/17/2/023047
150. B.L. Le, J.-S. Park, J. Sklenar, G.-W. Chern, C. Nisoli, J. Watts, M. Manno, D.W. Rench, N. Samarth, C. Leighton, P. Schiffer, Phys. Rev. B **95**, 060405(R) (2017). https://doi.org/10.1103/PhysRevB.95.060405
151. J. Park, B. Le, J. Sklenar, G.-W. Chern, J.D. Watts, P. Schiffer, Phys. Rev. B **96**, 024436 (2017). https://doi.org/10.1103/PhysRevB.96.024436
152. G.-W. Chern, Phys. Rev. Appl. **8**, 064006 (2017). https://doi.org/10.1103/PhysRevApplied.8.064006
153. Y.-L. Wang, Z.-L. Xiao, A. Snezhko, J. Xu, L.E. Ocola, R. Divan, J.E. Pearson, G.W. Crabtree, W.-K. Kwok, Science **352**, 962 (2016). https://doi.org/10.1126/science.aad8037
154. I. Gilbert, Y. Lao, I. Carrasquillo, L. O'Brien, J.D. Watts, M. Manno, C. Leighton, A. Scholl, C. Nisoli, P. Schiffer, Nat. Phys. **12**, 162 (2016). https://doi.org/10.1038/nphys3520
155. J. Drisko, T. Marsh, J. Cummings, Nat. Commun. **8**, 14009 (2016). https://doi.org/10.1038/ncomms14009
156. S. Gliga, G. Hrkac, C. Donnelly, J. Büchi, A. Kleibert, J. Cui, A. Farhan, E. Kirk, R.V. Chopdekar, Y. Masaki, N.S. Bingham, A. Scholl, R.L. Stamps, L.J. Heyderman, Nat. Mater. **16**, 1106 (2017). https://doi.org/10.1038/nmat5007

Chapter 16
Experimental Studies of Artificial Spin Ice

Christopher H. Marrows

Abstract Artificial spin ices were originally introduced as analogs of the pyrochlore spin ices, but have since become a much richer field. The original attractions of building nanotechnological analogs of the pyrochlores were threefold: to allow room temperature studies of geometrical frustration; to provide model statistical mechanical systems where all the relevant parameters in an experiment can be tuned by design; and to be able to examine the exact microstate of those systems using advanced magnetic microscopy methods. From this beginning the field has grown to encompass studies of the effects of quenched disorder, thermally activated dynamics, microwave frequency responses, magnetotransport properties, and the development of lattice geometries–with related emergent physics—that have no analog in naturally-occurring crystalline systems. The field also offers the prospect of contributing to novel magnetic logic devices, since the arrays of nanoislands that form artificial spin ices are similar in many respects to those that are used in the development of magnetic quantum cellular automata. In this chapter, I review the experimental aspects of this story, complementing the theoretical chapter, Chap. 15, by Gia-Wei Chern.

16.1 Introduction

Whilst ice is a very commonplace material, it is never mundane: as I look out of my office window as I type these opening words on a fine February morning it coats the trees in a fine and beautiful frost; it will add a certain zip to the gin and tonic I'll pour to celebrate typing the closing sentence of this chapter. This is not to say that it lacks scientific interest: the complexity of its phase diagram and the wide variety of environments in which it is found mean that it is a very active area of interdisciplinary research [1].

C. H. Marrows (✉)
School of Physics & Astronomy, University of Leeds, Leeds, UK
e-mail: c.h.marrows@leeds.ac.uk

M. Udagawa and L. Jaubert (eds.), *Spin Ice*, Springer Series in Solid-State Sciences 197,
https://doi.org/10.1007/978-3-030-70860-3_16

To condensed matter physicists, one of its most remarkable properties must be that its most common form (Ice I_h) has a residual entropy at low temperatures due to proton disorder, and so violates the third law of thermodynamics. As Linus Pauling noted in 1935 [2], the possible configurations of protons in Ice I_h provide a clear example of how geometrical frustration can lead to vast numbers of energetically similar states, resulting in a non-zero entropy for temperatures arbitrarily close to absolute zero. This was one of the first recognised examples of a much broader phenomenon: frustration occurs in a wide variety of condensed matter systems, and arises when it is not possible to simultaneously satisfy all of the competing pairwise interactions present. This leads to a rich phenomenology, where huge numbers of possible degenerate microstates play important roles in all kinds of complex systems in the physical sciences and beyond [3]. Examples include liquid crystals, magnetic domain patterns, stripe structures in high-temperature superconductors, protein-folding, and neural networks.

Conventionally, the study of physical systems is restricted to the investigation of the limited set of naturally occurring materials. The family of rare earth pyrochlore materials closely resemble water ice in their crystal geometry, and equivalent geometrical frustration effects are found in the interactions between the large spins on the rare earth sites: hence they are dubbed 'spin ices' [4]. One can mimic their behaviour using nanotechnology, which allows the construction of model systems where the nature of the elements and their interactions can be varied at will to create artificial frustrated systems [5–7]. Magnetic analogs of spin ice built using these methods, termed 'artificial spin ice' [5, 8], have been widely studied in recent years since they provide convenient models for frustration phenomena. One of the most appealing aspects is that advanced microscopy techniques are able to interrogate the system and reveal the exact configuration of all its constituent elements: yielding direct knowledge of the microstate (and the way that it evolves with time) of this artificial statistical mechanical system. When tied to the ability to engineer every aspect of the system during its construction, this is an extremely powerful new approach to the study of statistical mechanics, where experiments used to be restricted to revealing only the macrostate. In this chapter, an overview of experimental explorations of artificial frustrated systems is profiled. These studies have led to new insights into ordering and other dynamical processes in frustrated and disordered systems, and offer the prospect of technological innovations in information storage and processing.

16.2 The First Artificial Spin Ices

In the initial, ground-breaking experiments from Schiffer's group at the Pennsylvania State University [8], artificial spin ices were conceived as exactly what their name describes: an artificially created system that mimics some aspects of the frustration physics observed in the pyrochlore spin ices [4]. In the pyrochlores, rare earth ions are found at the points where the corner-sharing tetrahedra touch. These ions carry large spin magnetic moments and strong crystal fields cause them to have a uniaxial

anisotropy whose easy axis lies along the line between the centres of the two adjacent tetrahedra. Thus each moment must point into one of the two tetrahedra and out of the other one and so can take up only two states. In this sense the moments are described as being Ising-like. When we consider all four moments in a given tetrahedron, it becomes obvious that their interactions must be frustrated, since it is not possible for them all to simultaneously form in-out pairs. The best that can be done is to form a 'two-in/two-out' arrangement, identical to the Bernal–Fowler ice rule for the frustrated arrangement of protons in water ice [9]. In this way the statistical mechanics of the spin ice are identical to that of Ice I_h, and these systems have exactly the same extensive degeneracy and the same Pauling value [2] of the residual entropy [10].

Schiffer's group constructed a system that is a physical realisation of the 'square ice' vertex models studied theoretically by theorists such as Wu [11] and Lieb [12] in the 1960s, which were, in turn, versions of a model introduced by Slater for the ferroelectric material KH_2PO_4 [13]. Their approach was to represent the rare earth spins in a pyrochlore spin ice by the macrospins of nanomagnets. This required engineering the shape and size of the nanomagnets so that they were small enough to be in the single domain regime such that there was a well-defined macrospin and exhibited a clear uniaxial anisotropy to yield the required Ising-like behaviour. To achieve these aims they selected 80 nm × 220 nm islands patterned from a 25 nm thick Permalloy film. Permalloy ($Ni_{81}Fe_{19}$) was selected since its lack of magnetocrystalline anisotropy means that its micromagnetics are entirely controlled by the shape of nanoelements: the rectangular shape provides the Ising-like easy axis through shape anisotropy. The size is such that they form single domains and therefore behave as almost ideal Stoner–Wohlfarth particles [14].

These elements are then arranged along the edges of a square tiling, such that they meet at the vertices of the tiling in groups of four, as shown in Fig. 16.1. The mutual magnetostatic interactions between the four macrospins then mimic those between the four rare earth spins meeting in each tetrahedron of a pyrochlore spin ice. There are $2^4 = 16$ possible magnetic configurations of any given vertex, as shown in Fig. 16.1c, of which six obey the two-in/two-out ice rule. Whilst in the 3-dimensional pyrochlore system all six are energetically degenerate, here the reduction in dimensions means that not all the pairwise interactions are equivalent, and so these six can be further subdivided into a group of two with the lowest energy, and a further four with a slightly higher energy. (The interactions between neighbouring nanomagnets are stronger than those between nanomagnets that face each other across the vertex). In the terminology introduced by Wang et al., and subsequently adopted by the community, these two groups are referred to as 'Type 1' and 'Type 2', respectively. There is no net magnetic pole at the centre of these two types of vertices. The eight 'Type 3' configurations are those where the ice rule is violated by flipping the moment of a single element, these have a 'three-in/one-out' or 'three-out/one-in' arrangement, and carry a net magnetic charge of $\pm 2q$, where q is the magnetic charge of a single pole at the tip of one element. The two highest energy configurations, 'all-in' or 'all-out', comprise 'Type 4', and carry a magnetic charge of $\pm 4q$. The Type 2 and Type 3 vertices also possess a net magnetic dipole moment. The fact that only two vertex types are selected for the lowest energy state means that this system possesses

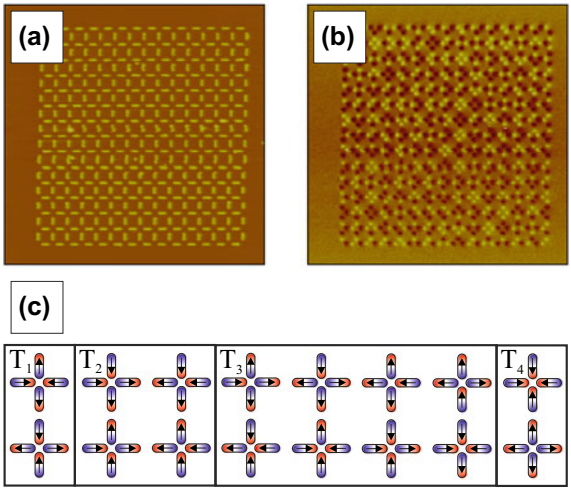

Fig. 16.1 Square artificial spin ice. **a** Atomic force micrograph showing the arrangement of nanomagnets along the edges of a square tiling. **b** Magnetic force micrograph of the same area, showing the magnetic poles of each nanomagnet as bright or dark contrast. **c** The sixteen possible magnetic configurations of a vertex in a square spin ice, divided into four types by energy

a twofold degenerate ground state consisting of a chessboard tiling of the Type 1 vertices [15], as opposed to the macroscopic degeneracy of the pyrochlore system.

In the ideal case, studied theoretically as the six-vertex model [11, 12], only Type 1 and Type 2 vertices are found, and the ice rule is obeyed everywhere. On the other hand, in a non-interacting system, all sixteen vertex types will be found with equal probability, since they will be randomly populated. The experimental results of Wang et al. fell between these two extremes [8]. Whilst all sixteen vertex types were populated, the system showed a preference for those of Type 1 and Type 2, with an accompanying deficit in the populations of Type 3 and Type 4, as compared to the random case. This preference grew stronger as the lattice constant of the square ice was reduced, packing the nanomagnets more closely together, and allowing the stronger magnetostatic interactions to better enforce the ice rules.

The other ice-like geometry studied at the outset of the field is the so-called kagome or honeycomb ice, which had been analysed theoretically by Wills et al. [16]. Here the macrospins are arrayed along the edges of a hexagonal tiling (see Fig. 16.2), visually resembling a honeycomb. The lattice points at the centre of each element lie on a kagome lattice. This system is analogous to the pyrochlore spin ice under a large field applied along a $\langle 111 \rangle$ direction [17]. The fact that three elements meet at each vertex means that all the interactions at that vertex are of equal strength. Artificial experimental realisations of this geometry were studied in a connected form by Tanaka et al. at Keio University in Japan [18] and as small groups of discrete islands by Mengotti et al. at the Paul Scherrer Institute in Switzerland [19]. This lattice has two inequivalent structural vertex types, depicted in Fig. 16.2c. Each of these can take up $2^3 = 8$ possible magnetic configurations: Type 1 obeys a two-in/one out or one-in/two out pseudo-ice rule and carries a net charge of $\pm q$; Type 2 has an all-in or all-out configuration and carries a charge of $\pm 3q$. These are shown in Fig. 16.2d. There are no uncharged vertices in this structure.

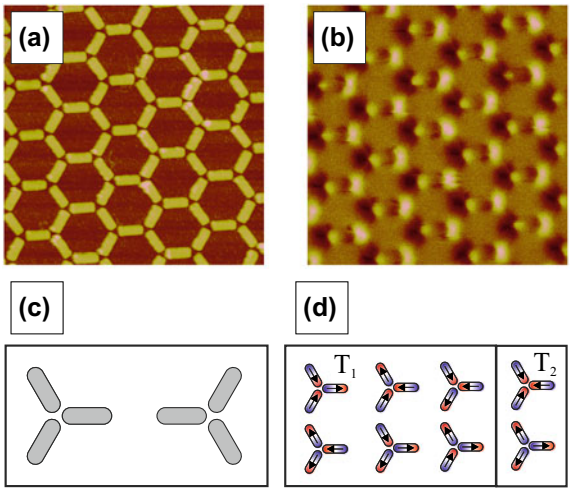

Fig. 16.2 Kagome artificial spin ice. **a** Atomic force micrograph showing the arrangement of nanomagnets along the edges of a honeycomb tiling. **b** Magnetic force micrograph of the same area, showing the magnetic poles of each nanomagnet as bright or dark contrast. **c** The two inequivalent structural vertex types of a kagome spin ice. **d** The eight possible magnetic configurations of a vertex in a kagome spin ice

16.3 Experimental Methods

The methods used in experimental studies of artificial spin ice fall into two main categories: those used to fabricate the arrays of nanoscale magnets that form the artificial frustrated systems, and those used to study the magnetic states they take up, which primarily consist of various forms of advanced magnetic microscopy.

16.3.1 Fabrication Methods

The fabrication methods for artificial spin ices are the conventional nanofabrication routes that are now well-established in magnetic nanotechnology [20]. The critical lateral dimensions of the elements that form artificial spin ices are in the 10–100 nm range, and this means that electron beam lithography is the method of choice for writing the patterns that form the frustrated arrays. In this technique a pattern is written into an electron sensitive resist by raster-scanning a highly focussed electron beam across it, referred to as exposing the pattern. The resist is spin-coated onto the substrate and is typically a polymer that will undergo either scission (for a positive tone) or cross-linking (negative tone) upon electron beam exposure. This changes the solubility, and so the pattern may be developed by washing with an appropriate solvent. The pattern may then be transferred by depositing or etching material on the substrate surface. The natural variations in the exact shape and size of the islands corresponds to the quenched disorder in the statistical mechanical system that is being engineered [21].

The use of a negative tone resist is most common, in a pattern transfer process referred to as 'lift-off'. Here the resist is coated onto a bare substrate and once the pattern is developed the resist forms a stencil mask through which magnetic material may be deposited to form the desired nanostructure: in this case an array of islands. The use of a strong solvent then removes (lifts-off) all the resist and leaves behind only the material deposited through the holes onto the substrate. The most common resist used for liftoff is polymethylmethacrylate (PMMA). Many common magnetic materials can be deposited by thermal evaporation: Permalloy falls into this group. This technique is easily compatible with lift-off, since it is a high vacuum process and there is this ballistic transport of the deposited atom flux from the source to the substrate. This highly directional flux means that the sidewalls of the holes that have been opened in the resist are hardly coated at all and lifting-off the resist proceeds easily. Things are more complex when the other main deposition technology, sputtering, is used. Since sputtering involves the use of a working gas at a few mTorr pressure, the mean free path of the deposited flux is short and there is significant step coverage, meaning that clean liftoff is difficult. Two possibilities now present themselves. First, a bilayer resist that provides a large undercut can be used, meaning that the sputtered film cannot easily coat the sidewalls. On the other hand, patterns can be written and developed in resist spun on top of a sputtered film to provide an etch mask, with the pattern subsequently transferred by wet (chemical) or dry (ion mill or reactive ion) etching. The fact that the magnetic islands forming a spin ice array grow as discrete elements during liftoff has consequences for their magnetic configuration, since the macrospin system is able to thermalise during the early stages of growth [15, 22]. For transmission microscopy experiments (e.g. Lorentz imaging or X-ray transmission microscopy) it is necessary to carry the sample fabrication on an electron transparent substrate, typically a Si_3N_4 membrane.

16.3.2 Measurement and Imaging Methods

The experimental methods used to study artificial spin ices can be divided into two categories. The first are "macroscopic" probes which measure a quantity that is averaged over the entire sample: this can be thought of as measuring, in some sense, the statistical mechanical macrostate. On the other hand, one of the main advantages of the artificial spin ice approach is that the lengthscales make the system amenable to study using the various advanced magnetic microscopy methods that have been developed over the past few decades. These allow the statistical mechanical microstate of the artificial spin ice to be interrogated, and its response to external stimuli probed.

Most of the macroscopic probes used to study magnetic materials have been applied, in some way, to the study of artificial spin ices. Whilst it is just about possible to write a pattern that is large enough for measurement using conventional magnetometry (e.g. by SQUID magnetometer), this is challenging, since it relies on a very long write time. A more convenient way to measure the magnetic hysteresis

loop of an object that is microns or tens of microns across–the typical size of an artificial spin ice array–is to use the magneto-optical Kerr effect (MOKE) [23], more elaborate forms of which include Bragg-MOKE in a scattering geometry [24], and a temperature dependent form used by Kapaklis et al. [25]. If connected arrays are formed then they become able to conduct an electrical current and magnetotransport measurements become possible [26, 27], which are also able to probe switching fields and hence interactions within the array. The fact that the artificial spin ices are periodic arrays means that soft X-ray resonant magnetic scattering (XRMS) can be used to study them, since they will give rise to well-defined diffraction peaks [28, 29]. The generation of such soft X-rays requires a synchrotron. This method, as is usual with scattering techniques, gives spatial resolution in reciprocal space, and allows for the sampling of a larger area of the sample than the typical field-of-view of a microscope. Last, it has been predicted that ferromagnetic resonance (FMR) measurements [30] can also be used to study ordering in artificial spin ices [31].

Of course, imaging the exact magnetic configurations of artificial spin ices leads to deeper insights into their behaviour. Since the individual elements are of a size that is smaller than the wavelength of visible light, they cannot be resolved in a optical microscope and so techniques such as Kerr microscopy cannot be used. The simplest method by which the magnetism in objects that are a few tens or hundreds of nm in size can be observed is magnetic force microscopy (MFM). This is a variant of the atomic force microscope method, where the tip is magnetised and so responds to magnetic, as well as van der Waals, forces. These are generated by field gradients, and so this method is well-suited to revealing the poles at the ends of the nanomagnets, as shown in Fig. 16.3a. From these, the direction of each macrospin is easily determined. This method was the one used in the first experiments at Penn State [8] and remains popular due to the wide availability of such microscopes [15, 32–39]. The typical spatial resolution is $\sim$50 nm, although more advanced instruments can do better than this. A potential drawback is that the magnetic tip can influence the magnetic state of the sample as it is scanned across it if that state is particularly labile. Measurements can, in principle, be carried out under an applied field, although most MFM instruments are usually AFMs retrofitted with a magnetic tip, and so usually only specialised instruments are equipped with magnets.

The other imaging technique used at the outset of the field was Lorentz microscopy [26]. This is a form of transmission electron microscopy, and so has very high spatial resolution–typically better than 10 nm, but can be up to an order of magnitude less in modern aberration corrected microscopes–but requires the artificial spin ice array to be on a membrane that is thin enough to be electron transparent: typically 50–100 nm of Si_3N_4. This means, of course, that such samples are very fragile. Contrast arises due to the deflection of the electrons by Lorentz forces as they pass through the sample, which can be accessed if the image is deliberately slightly defocussed. Imaging can be carried out under an applied field. An example of a Lorentz micrograph is shown in Fig. 16.3b. It has therefore proved popular among those groups with suitable transmission electron microscopes [21, 40–43]. Since this method depends on the magnetic flux **B** that the electron beam passes through for contrast, it is possible to

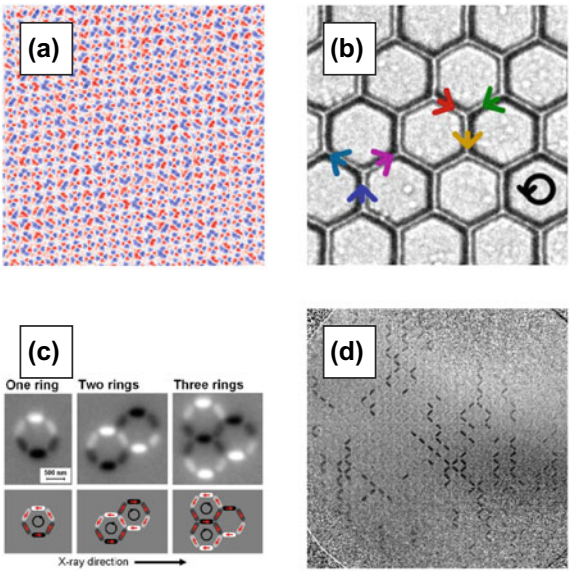

Fig. 16.3 Magnetic micrographs of artificial spin ices, obtained by **a** magnetic force microscopy, where blue/white contrast corresponds to opposite vertical force gradients, revealing the charges in this square ice array [97], **b** Lorentz microscopy, here in Fresnel mode, where dark/bright contrast on the sides of the bars in this connected kagome network reveals the magnetisation direction (after Qi et al. [40]), **c** photoemission electron microscopy, where the contrast depends on XMCD and therefore is given by the relative alignment of the magnetisation and the X-ray beam direction, here used to reveal the magnetic states of small hexagonal rings that are kagome ice prototypes (after Mengotti et al. [19]) and **d** Full field X-ray transmission microscopy, which also uses XMCD as the effect to yield contrast, showing Dirac strings of reversed elements. Figures reprinted from [97], [40] and [19] with permission from the American Physical Society

image the flux-lines between the elements that give rise to the frustrated couplings. This has been accomplished using the related electron holography technique [44].

The other main imaging technique used in the field of artificial spin ices is synchrotron-based: photoemission electron microscopy (PEEM) using X-ray magnetic circular dichroism (XMCD) as the contrast-generating mechanism. Here the sample is illuminated with soft X-rays tuned to an absorption edge of a ferromagnetic element: for the most commonly used material, Permalloy, the L_3 edge of Fe is used. The XMCD effect is connected to the XRMS through a Kramers–Kronig relation, and means that there is differential absorption of the X-ray photons depending on whether the photon helicity is parallel or antiparallel to the magnetisation. This differential absorption in differently oriented domains leads to different photoelectron yields, giving rise to a magnetic contrast mechanism in an image formed when those photoelectrons are collected in an electron column. The fact that these photelectrons are easily Lorentz deflected means that employing this technique precludes the application of magnetic fields to the sample during imaging. The typical spatial resolution is better than $\sim$100 nm. An example of an XMCD-PEEM micrograph is

shown in Fig. 16.3c. The use of this method as a means of studying artificial spin ices was pioneered by Heyderman's group at the Paul Scherrer Institute [19], and it has subsequently been adopted by others [45–49]. The extreme surface sensitivity of the technique, arising from the short (2–3 nm) escape depth for the photoelectrons, means that it can be used to study extremely thin samples that cannot be imaged by the other methods described here. This means that the volume of the nanoislands is very small, allowing them to be influenced by thermal fluctuations [50–52].

Transmission X-ray microscopy (TXM) combines features of the Lorentz TEM and PEEM methods. Like the former, it is a transmission method and requires samples in the same type of thin membranes. Like the latter, it makes use of XMCD as a contrast generating mechanism. However, since it is a photon-in/photon-out method, it can be performed with the sample under an applied field, and so can be used to track the response of artificial spin ice arrays as they are taken around their hysteresis loops [53]. An example of an XTM micrograph is shown in Fig. 16.3d. It has been most commonly used in the scanning XTM (STXM) implementation to study artificial spin ice samples, where a focussed soft X-ray is scanned over the sample [54–56].

16.4 Monopoles and Magnetricity

A paradigm-defining result in spin ice physics was the development by Castelnovo et al. of the theoretical description of excitations in pyrochlore spin ices in terms of deconfined magnetic monopoles [57]. The central concept is that whilst a vertex in the tetrahedral pyrochlore network possesses no net magnetic charge when the two-in/two-out ice rule is obeyed, a violation of that ice rule, caused by a spin-flip, leads to the creation of net positive and negative magnetic charges in the two tetrahedra connected by that spin. This can be thought of as corresponding to a monopole-antimonopole pair creation event. Flipping adjacent spin, then another, and another, gradually separates the monopole and antimonopole, with the chain of flipped spins being analogous to the flux-tube known as a Dirac string in the theory of fundamental cosmic monopoles [58]. An important feature of the pyrochlore geometry is that once this has been done, whilst the sites of the oppositely charged monopoles can be easily seen, it is not possible to tell which chain of spins has been flipped to separate them. As a result there is no string tension and the energy of the monopoles is determined only by their separation through an equivalent of the Coulomb law. This picture was soon experimentally confirmed using neutron [59–61] and muon [62] experiments on different pyrochlore systems. Building upon the concept of mobile magnetic charge carriers, the idea of 'magnetricity' has been introduced. This is the creation and flow of mobile magnetic charges that respond to externally applied magnetic fields [63].

Translating this picture into the language of square spin ice, as introduced in Sect. 16.2, we can see that whilst Type 1 and Type 2 vertices are charge neutral (obeying the ice rules), the monopoles in the Castelnovo et al. picture correspond to the charged Type 3 vertices. A type 4 vertex corresponds to the superposition of two monopoles of the same charge. Since the Dirac strings must carry flux, they must be

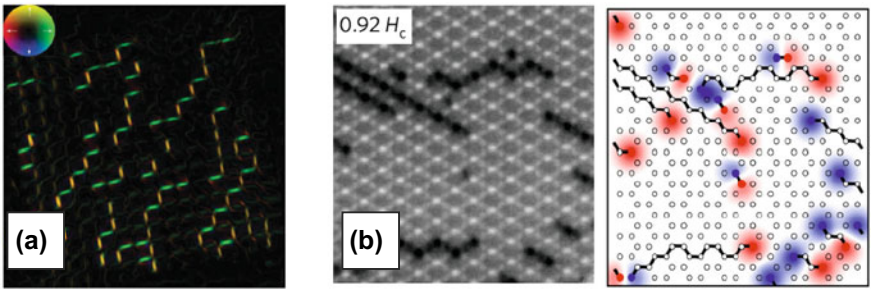

Fig. 16.4 Magnetic monopoles and Dirac strings in **a** square artificial spin ice, visualised using Lorentz microscopy (after Pollard et al. [42]) and **b** kagome artificial spin ice, visualised using PEEM, with an accompanying schematic (after Mengotti et al. [45]). Figure **a** is reprinted from [42] with permission from the American Physical Society. Figure **b** is reprinted from [45] with permission from Nature Physics

composed of the dipole-bearing Type 2 vertices. The fact that there is a distinction to be drawn in a square spin ice between the Type 1 and 2 vertices means that in this case a unique Dirac string can be identified [64]. Under these circumstances the monopoles are not deconfined. For this reason, strictly speaking, the monopoles present in square artificial spin ice systems [65] are of the Nambu type [66]. In a kagome spin ice, all vertices must bear charges, since an odd number of magnetic dipoles meet at each vertex. The same monopole/Dirac string picture applies in this case [32], but the monopoles must be defined as charge differences with respect to a well-defined state [45].

The observation of monopoles and their field-driven dynamics in artificial ices was in fact first accomplished in the kagome systems [32, 45]. The premise of the experiment is simple: the magnetic array is first saturated in one direction and then a reverse field applied to take it along one branch of its hysteresis loop. (In fact, in these two experiments, due to the constraint of only being able to image at zero field, were in fact measurements of the first-order reversal curve, although the thermal bistability of the systems means that this is equivalent to a major hysteresis loop in this case.) Mengotti et al. performed an analysis of the size distribution of the Dirac strings that they observed in their experiments on a kagome ice formed from discrete Permalloy islands [45]. The propagation of these Dirac strings may be regarded as avalanche events. It is usually the case, in physics and beyond, that the distribution of avalanches sizes follows a power law, often referred to as a Gutenberg–Richter law (terminology that first arose in seismology), and so is scale free. In contrast to this, an exponential law was found, implying a characteristic scale. This was attributed to the fact the Dirac strings are 1-dimensional objects in a 2-dimensional system, viz. the frustrated interactions enforce a lowering of the dimensionality of the events. This general type of reversal (nucleation of monopole-antimonopole pairs, followed by Dirac string cascades) has also been shown to take place in artificial square spin ices [36, 42]. Micrographs showing Dirac strings in both geometries are displayed in Fig. 16.4.

Whereas the studies discussed above are performed for monopoles constructed from the uncompensated magnetic poles at the ends of finite-sized discrete elements (which do show monopole-like field distributions [44]), similar concepts can be used to interpret the behaviour of connected spin ice arrays, which are networks constructed from magnetic wires. These vertices emerge at the intersections of the magnetic wires usually studied in the form of a honeycomb lattice equivalent to a kagome ice [32, 54]. In these systems, monopoles are created by the emission and interaction of magnetic domain walls at the wire intersections. This is expected to be governed by the chirality and topological properties of the domain walls [48], although this has been recently questioned [56], since quenched disorder in the system may affect this ideal behaviour in samples where the lithographic defects are not under complete control.

16.5 Array Topology and Geometry

It is a truism that in geometrically frustrated systems, control of both the static states and their dynamics can be achieved through a proper design of the topology and geometry of the network of interacting elements. So far in this chapter we have discussed only the two most common geometries, square and kagome, which mimic different aspects of the tetrahedral pyrochlore systems. Nevertheless, one of the main attractions of the artificial spin ices approach is that the array geometry can be designed and engineered lithographically, and so the only limitation on possible designs is the imagination of the designer.

A so-called 'brickwork' lattice was developed by the Penn State group, depicted in Fig. 16.5a [67]. It is constructed by removing staggered rows of every other element from a square ice system. This maintains the axes of the islands to be orthogonal to each other, just as for square ice, but reduces the number of islands meeting at each vertex to three, making it topologically equivalent to the kagome lattice. However it retains the property of the square lattice that the interactions at each vertex are not all equivalent, since the angles between the nanoislands are not all the same. As a result the properties of the lattice, such as approach to the ground state on ac demagnetisation and the correlations between the island alignments, are more similar to the square than kagome structure. The details of the geometry matter in artificial frustrated systems: they cannot be classified on topology alone.

Thin magnetic films are usually magnetised in-plane since they have a strong shape anisotropy, and it is usually this anisotropy that is used to provide the Ising-like nature of the macrospins in artificial spin ices. Nevertheless, other anisotropies can be used. Perpendicular anisotropies are common at the interfaces between magnetic and heavy metals due to the lowering of symmetry at a point where there are strong spin-orbit interactions. For a sufficiently thin ferromagnetic film, which in practice usually means $\lesssim$1 nm, the reduction in the volume demagnetising energy is large enough that this interface anisotropy can dominate and the magnetic easy axis is out-of-the-plane. A prototypical materials system displaying this effect is a

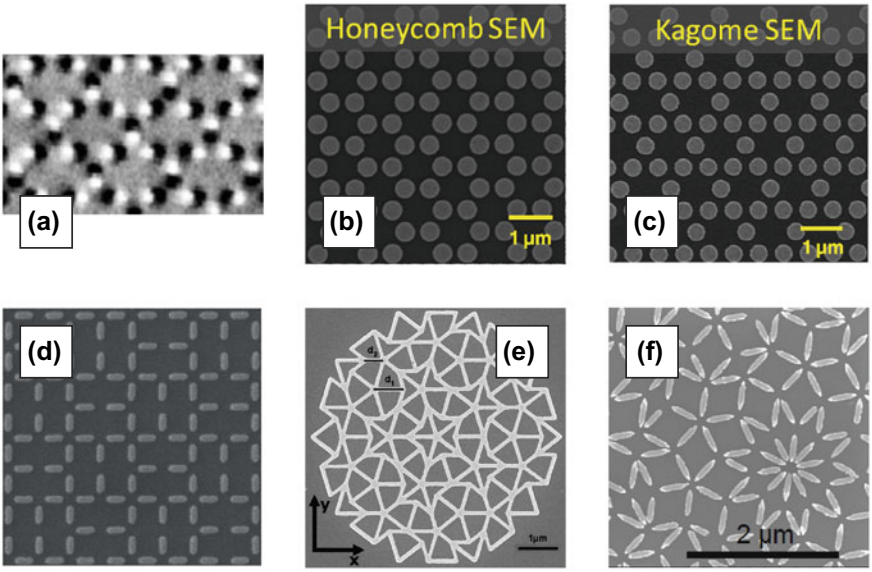

Fig. 16.5 Novel geometries for artificial spin ices include **a** the brickwork lattice (MFM, after Li et al. [67]), **b** hexagonal and **c** kagome networks of perpendicularly magnetised islands (SEM, both after Zhang et al. [68]), **d** the shakti lattice (SEM, after Gilbert et al. [39]), and **e** kite-and-dart (SEM, after Bhat et al. [69]) and **f** rhomboid quasiperiodic Penrose tilings (SEM) [70]. Figure **a**, **b**–**c** and **e** are reprinted from [67–69] with permission from the American Physical Society. Figure **d** is reprinted from [39] with permission from Nature Physics

multilayer of Co/Pt. A nanoscale dot of such a multilayer will possess an Ising-like macrospin that is directed out-of-the-plane and so the magnetostatic coupling to a neighbouring dot will be antiferromagnetic. Placing three such dots in a triangle is enough to realise a frustrated system, since it realises the prototypical example of frustration : three antiferromagnetically coupled (macro)spins. Such small clusters of dots were studied by the Paul Scherrer Institute group [71], who studied their energy spectra both experimentally and theoretically. Meanwhile, the Penn State group have studied (frustrated) kagome and (unfrustrated) honeycomb lattices of such perpendicularly magnetised dots (depicted in panels (b) and (c) of Fig. 16.5) [68], and found that there is a remarkable correspondence between the correlations in this type of kagome ice and a conventional in-plane one, in spite of their very different magnetostatic couplings. This concept of building artificial systems from perpendicularly magnetised materials deserves more attention than it has received to date.

All of the lattices discussed so far have a single co-ordination number. For instance, in the square ice, four islands meet at every vertex, whereas in the kagome ice, the number of islands that interact at every vertex is three. In order to estimate the entropy of such systems (as Pauling did for the Ice I_h phase of H_2O [2], and can easily be done for the six-vertex model of Lieb [12]), it is necessary only to extend

the vertex-level degeneracy to the global ground state. Nevertheless, it is simple to envisage lattices that have mixed co-ordination, where this basic procedure cannot be followed. This leads to a new class of vertex models where the frustration arises not from the properties of an individual vertex but from the relative arrangements of neighbouring vertices, not all of which can take up their lowest energy configuration at the same time. Breaking the pure co-ordination rules allows for the construction of a wide variety lattices (with names such as the pinwheel, tetris, or Santa Fe lattices) with extensive degeneracy [72]: the key property of the pyrochlore spin ice that is lost in the square ice, with its twofold ground state. The most heavily studied of these is the so-called shakti lattice, constructed by removing elements from the square ice system in such a way that there is a mixed 3/4 co-ordination. This has been shown theoretically to possess a quasicritical ice phase with algebraic correlations [73], similar to the critical correlations of the Coulomb phase in the pyrochlore spin ices. Importantly, this is the only lattice showing this new type of topologically emergent frustration to have been experimentally realised [39]. The results can be mapped onto the six-vertex model by breaking the lattice up into emergent composite plaquettes, which reveals the extensive degeneracy that it possesses. Whilst the four-island vertices possess no net magnetic charge in their ground state, the three-island vertices necessarily must. These couple through long-range interactions that leads to crystallisation and screening. This idea of mixed co-ordination number lattices can also be used to construct not only emergent magnetic monopoles, but also the associated emergent magnetic polarons [74]. Screened charges have been directly visualised as a transient state in dice lattice artificial spin ices [75]. All of mixed co-ordination number models, and the topologically emergent frustration that they possess, can only be realised through the artificial spin ice route, since they have no known analogs in nature, and remain a fruitful avenue for future work.

Spin ices form the archetype for geometrically frustrated magnetic systems, where the frustration persists even in the limit of structurally perfect crystalline order. On the other hand, positional disorder/random interaction lead to another famous form of frustrated magnetic system: the spin glass [76]. Such systems naturally rely on a lack of crystalline order to provide the necessary random couplings. (The idea of an artificial analog of a spin glass is not one that seems to have been pursued yet.) At the boundary of crystals, with their perfect discrete translation symmetry, and glasses, with the total absence of any such symmetry, lie the quasicrystals. These possess order (in the sense that knowing a small part of the structure, one can follow rules to construct the rest of it and fill all of space) but lack translational symmetry. Quasicrystals containing both rare earth [77] and transition metal [78] magnetic species show spin glass-like freezing when the spins are dilute. Nevertheless, geometry appears to play some role. The discovery of quasicrystals [79] forced a redefinition by the International Union of Crystallography of the term "crystal" in 1991 to refer to structures that produce sharp diffraction patterns, regardless of whether they posses discrete translational symmetry or not. Mathematically, it is now understood that quasicrystals are projections in three-dimensional space of structures that are periodic in some higher number of dimensions. This applies to magnetism as well as structure: the

neutron diffraction pattern of a Zn–Mg–Ho icosahedral quasicrystal can be understood in terms of the system realising a projection of a higher dimensional multi-q antiferromagnetic structure [80].

The two-dimensional analog of a quasicrystal is a Penrose tiling [81]. Heisenberg spins on the nodes of a Penrose tiling have been studied theoretically [82] and their configuration can be shown to correspond to interpenetrating non-collinear sublattices in a higher dimensional structure [83]. It is natural to use these results at the inspiration to build an artificial analog of a magnetic quasicrystal using the same methodology as building an artificial spin ice: place magnetic nanoislands with Ising-like spins along the edges of a Penrose tiling and study their configurations.

Penrose patterns come in two forms, known as kite-and-dart or rhomboid, with the names derived from the shapes of the tiles used to form them. Bhat et al. have constructed Permalloy lattices based on the kite-and-dart form, where the elements are connected to form a continuous network [69]. These were studied using the macroscopic probes of SQUID magnetometry and FMR, revealing well-defined switching fields and a rich mode structure. However, magnetic imaging of the patterns was not reported. Meanwhile, Fig. 16.5 shows a small portion of an artificial magnetic quasicrystal constructed in the author's laboratory built using discrete islands along the edges of rhomboid tiles, which take the forms of thin or fat rhombi. In this pattern, in contrast to the kite-and-dart, all the links between vertices of the tilings are the same length. Theoretical considerations and MFM imaging show that the pattern contains rigid parts with a two-fold ground state and loose spins that lead to extensive degeneracy [84], similar to the decagonal ordering in the Heisenberg system [82]. The very high level of co-ordination number mixing–there are vertices where as few as three or as many as seven elements meet–leads to strong topologically induced frustration. The enhanced level of frustration means that the ground state is very difficult to access, a phenomenon seen in a weaker form in the square ice [85].

16.6 From Effective to Real Thermodynamics

It has become a commonplace that artificial spin ices are realisations of the toy models of statistical mechanics, such as the square ice model [12]. What is missing so far from the discussion is one of the most important parameters of that sub-field of physics: temperature. So far in this chapter we have implicitly assumed that the state of the array that is being inspected through microscopy is fixed, so that we can acquire a stable image, and that any changes to that state are driven by the application of a field. What that means in practice is that $E_\mathrm{b} \gg k_\mathrm{B}T$ must hold, where E_b is the energy barrier between the bistable states of an island and $k_\mathrm{B}T$ is the thermal energy at the ambient temperature T. Indeed, for islands of the size studied by Wang et al. [8] can be shown to have $E_\mathrm{b} \sim 10^5$ K, far in excess of any realistically achievable experimental temperature. Thus thermal fluctuations play no role.

Such a system is said to be athermal. It is not ergodic and its states may not correspond to thermally equilibrated states. Such athermal systems may nevertheless be described in terms of an effective thermodynamics, originally developed in the field of granular matter [86]. In that field, the process of vibro-fluidisation is used to relax the many-body system into a low energy state [87]. The equivalent process in magnetism is an ac demagnetisation.

The demagnetisation protocol used in the initial experiments by Wang et al. [8] to relax the spin ices into a state where fidelity to the ice rules could be tested was to subject the sample to an ac demagnetisation process whilst rapidly spinning it at about 20 Hz so that the field samples all in plane directions in the array, as shown in Fig. 16.6a, b. The aim of a demagnetisation process is, of course, to reduce the magnetisation as close to zero as possible. There are of course many such square ice states with zero magnetisation: one is the antiferromagnetic state formed from an alternating tiling of the two Type 1 vertices, but also many higher energy states with disordered moments. At first these protocols were able to provide this disorder [88], and thus degeneracy [89], but ground state access was not possible. Given the energy scales involved, a state very close to the ground state is expected to be the thermally equilibrated one. A more detailed study of the states yielded by this protocol showed that whilst it can be improved by using finer and finer field steps, the energy of the system does not extrapolate to the ground state [90]. Some years later, a linear demagnetisation protocol was shown to produce partial ground state ordering (up to ∼60% of the vertices in the Type 1 configuration, as shown in Fig. 16.6c) [91], as previously predicted by theory [92]. Slow field sweep rates are required, so that each island has a chance to experience all field directions in the few moments before it approaches its switching field. The degree of ground state fidelity is constrained by the level of quenched disorder [93].

Nevertheless, these field driven protocols seem to be incapable of producing properly thermalised states, perhaps because they only permit downward steps in energy, rather than the upward and downward steps permitted by a true anneal process. Nevertheless, the states they do produce can be described by an effective thermodynamics [89]. Notions of the effective temperature of the macrospin system, as introduced in the field of granular matter [86], can be brought into play [35]. This effective temperature is derived from an inspection of the artificial spin ice of the system, and is thus a microscopic measurement, rather than the macroscopic measurements required to establish the real temperature. It is based on a simple vertex gas model in the canonical ensemble, where the energy of a vertex of Type i is denoted by E_i, and its multiplicity (the number of equivalent configurations) by ν_i. It is convenient to define an energy scale such that $E_1 = 0$ and $E_3 = 1$. It is worth noting that this formalism neglects any kind of correlations between adjacent vertices, even the most basic one that each macrospin must be a dipole. It is an effective thermodynamics since ν_2, which ought to be equal to 4 (see Fig. 16.1), is set to be 5. The reason for this is that an additional Type 2 vertex type is defined, which is the background configuration defined by the rotating field. In this state, all the macrospins track the field, rotating between the four different Type 2 configurations. As the field is reduced through the switching field distribution of all of the macrospins in the array (which has a finite

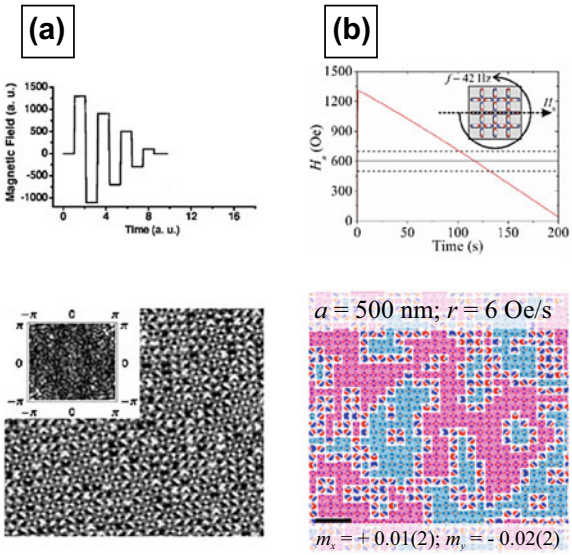

Fig. 16.6 Rotating field demagnetisation protocols: **a** ac demagnetisation field profile (with results) (after Wang et al. [88]), and **b** linear demagnetisation field profile (with results) (after Morgan et al. [91]). Reprinted from [88] with permission from AIP Publishing and from [91] with permission from Frontiers in Physics

width due to both quenched disorder and the couplings between the islands) it carves defects into this background as each vertex drops out of the rotating background population into one of the four conventional vertex types. To determine the effective temperature $T_{\text{eff}} = 1/\beta_{\text{eff}}$, one measures the fractional population n_i of each vertex type (with $\sum_i n_i = 1$) and notes that this should be defined by a Boltzmann factor as $n_i = q_i \exp(-\beta_{\text{eff}} E_i)/Z$, where Z is the partition function. The ratio of any two of these N_i will suffice to determine the effective temperature, but the definition of zero energy means that it is convenient to compare any other vertex population to n_1. This leads to $\beta_{\text{eff}} = E_i^{-1} \ln[(q_i/2)(n_1/n_i)]$. Nisoli et al. used this approach to show that when rotational ac demagnetisation is used, more strongly coupled arrays generally had lower effective temperatures than more weakly coupled ones [35]. In a truly thermally equilibrated system, the real and effective temperatures will be the same, and any variation between them is a measure of how athermal the systems is. Extending the idea of there being an effective statistical mechanics at play, it has also been shown to be possible to determine an effective entropy of the macrospin system from an inspection of the artificial spin ice, once a suitable formalism has been developed [94].

Nevertheless, a true thermalisation remained highly sought after, since (i) it would allow for the 'real' thermodynamics of the system to be studied and (ii) obtaining a state close to the ground state means that excitations above it may be easily studied. A one shot thermalisation process was discovered by Morgan et al., who found extensive ground state order in some of their samples in their as-grown state after fabrication [15]. An important point is that these samples were fabricated by liftoff, and so comprised discrete islands that passed through every thickness between zero and their final thickness during fabrication. The barrier to reversal $E_{\text{b}} = KV$, where

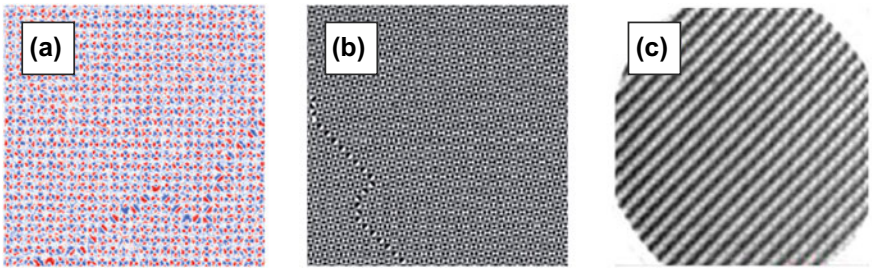

Fig. 16.7 Thermally equilibrated artificial spin ices. **a** One shot thermalised, imaged using MFM [97]. **b** Thermally annealed, imaged using MFM. After Zhang et al. [38]. **c** Thermally relaxed, imaged using PEEM. After Farhan et al. [51]. Figure **a** and **c** are reprinted from [97] and [51] with permission from the American Physical Society. Figure **b** is reprinted from [38] with permission from Nature

K is an anisotropy constant defined by the island shape and V is the island volume. When very thin, the island volume would be small and so KV will be smaller than the thermal energy $k_B T$ allowing free thermal fluctuation. As the thickness increases, KV will rise until it exceeds the thermal energy by a large enough factor that the system arrests, dropping out of thermal equilibrium and becoming athermal. It thus captures a snapshot of a truly thermal state at the temperature and island thickness when this arrest takes place: an example is shown in Fig. 16.7a. Theoretical treatments of this process were given by Nisoli [22] and Greaves and Muraoka [95]. States with large domains of ground state order, separated by domain walls [96], and containing isolated excitations were observed. These excitations were distributed according to Boltzmann factors [15]. These states had very low effective temperatures, which could be described within a canonical ensemble model where ν_2 could be set to the true value of 4 [97]. Thus, the effective temperature model shows that truly thermalised states can be discriminated from those prepared by field demagnetisation on the basis of their statistical properties, just as anticipated by Ke et al. [90]. Measurements of such states allow access to phase transitions between the antiferromagnetically ordered ground state and a high effective temperature disordered state [98].

A drawback of this one-shot anneal process is that it can only be performed during the sample growth, and the thermalised state is irrecoverably destroyed once the sample state is changed by a field, and the ground state can never be reset. An obvious approach to this problem is to carry out a true anneal of the sample, heating it to above the relevant temperature scale, which is either the blocking temperature T_b of the macrospins or the Curie temperature T_c of the microspins (whichever is lower), and then cooling back to room temperature in order to image the state that had been prepared. This was attempted by several groups, but in every case the nanostructures did not survive the heat treatment and the artificial spin ice arrays were destroyed.

The first success in achieving anything resembling a reversible anneal was made by Kapaklis et al., who fabricated artificial spin ice arrays from atomic Fe monolayers

sandwiched between Pd layers [25]. These had a Curie point below room temperature and so could be heated and cooled through T_c to 'melt' and 'freeze' the macrospin system. This was detected through MOKE magnetometry, but the states obtained were not imaged. An experiment along similar lines was carried out by Porro et al., who reduced the T_c of Permalloy by enriching it with Ni [37]. Although the reduction was fairly modest, it was sufficient to reduce the temperature needed for a magnetic anneal to a low enough value that the artificial islands survived. Extensive ground state order was achieved in square ice samples. The process was perfected by Zhang et al., who fabricated their artificial spin ices on substrates coated with an inert layer of Si_3N_4. This allows for annealing up to high enough temperatures to completely anneal the macrospin system [38]. They studied both square and kagome ice arrays, and were able to obtain perfect ground state order in the former (see Fig. 16.7b), and to observe the charge crystallisation due to the interactions of the magnetic charges intrinsic to the odd coordination at each vertex predicted by theory [64, 99] in the latter. The same effect has achieved by Drisko et al., who used the low Curie temperature ferrimagnet $FePd_3$ ($T_c \sim 200\,°C$) to achieve perfect ground state ordering in square ices and an even higher degree of monopole charge order in connected kagome systems [100]. This approach has been extended to the study of deliberately introduced topological defects–dislocations, which possess a Burgers vector–that disrupt the ability to form ground state order by forcing into being an excited string of Type 2 and 3 vertices that stretches to the edge of the array [101].

Once static thermalised states had been observed, the next step is clearly to observe thermally activated dynamics. The first hints of this were seen by Arnalds et al., where a handful of unstable islands were seen in otherwise frozen thermalised arrays [102]. Fully fluctuating kagome clusters were soon achieved by making very thin–and hence low volume–Permalloy islands [50], which can nevertheless be easily imaged by PEEM due to the surface sensitivity of that technique. Applying the same idea to full square ice arrays led to a remarkable discovery: after saturation by a field into a fully Type 2 configuration the system is able to relax thermally into the ground state by nucleating monopole-antimonopole pairs, which create Dirac strings that flip the correct chains of islands to yield Type 1 vertices [51], as shown in Fig. 16.7c. That the interactions between islands help to stabilise their macrospins against thermal fluctuations was shown by studying the dynamics in Fe-monolayer in Pd kagome ices with different lattice spacings [52]. A beautiful recent result from Gilbert et al. is the demonstration of emergent reduced dimensionality in the tetris lattice: on cooling from the fluctuating state, the system subdivides into oblique stripes of stable ground state order interspersed with stripes of fluctuating spins [103].

16.7 Outlook

The field of artificial spin ices remains active with many new breakthroughs emerging. These include the cross-fertilisation with magnonics [31, 104, 105], work on disorder-induced criticality [106], proposals for three-dimensional systems [107],

and the development of complex network theories to represent the changing states in artificial spin ice systems [108].

Whilst nanomagnetic systems remain by far the most popular, the general concept of constructing artificial frustrated systems using nanotechnological means has found expressions in other forms. Superconducting systems have been studied in various forms, with the earliest implementations using coupled superconducting rings [109, 110]. A theoretical proposal for a square ice in which each element contains a single superconducting vortex forms a very close analog with the frustrated proton system Ice I_h, where the vortex must occupy one of two positions that are close to one vertex or the other, leading to a two-in/two-out ice rule at each vertex [111]. Just a such a system was very recently realised (albeit using slightly different means to provide the bistable energy landscape for the vortices) by Latimer et al. [112]. Soft matter approaches are also possible. A square ice system where interacting colloidal particles are held in optical traps was theoretically analysed by Libál et al. [113], which operates on much the same principle as the superconducting vortex systems: the particle must lie at one end or the other of an elongated trapping potential, and thus be present at one or other vertex. Again, the analogy with protons in Ice I_h is very close. On the other hand, a realisation of the frustrated triangular antiferromagnet was constructed by placing colloidal particles in a layer confined between two sheets such that the particles can move up or down a small distance [114]. By packing them a suitable density, complex patterns can be formed due to the frustration. An advantage of this approach is that the colloidal particles are large enough to image using an ordinary optical microscope. Going further in this direction, it is not even always necessary to use nanoscale systems: a macroscopic kagome spin ice was constructed by Mellado et al. using centimeter scale bar magnets on hinged mounts, the dynamics of which were studied using a high speed video camera [115].

From a more technological perspective, viewing these systems as information storage [34, 116] or processing technologies could also lead to nanomagnetic logic architectures [117, 118] based on frustrated arrays. These need not have the traditional von Neumann architecture: for instance, the Ising model provides the theoretical underpinning for the Hopfield model of neural networks [119], suggesting that non-Boolean neuromorphic architectures based on artificial spin ices might be possible. Advances in the field of nanomagnetic logic also cross-pollinate into new experimental opportunities in artificial spin ices, for instance driving out-of-equilibrium dynamics using spin Hall torques [120]. Whilst initially perceived as an attempt simply to build analogs of existing systems such as pyrochlores, new physics, such as topologically emergent frustration, can only be studied by this route, which is an important justification for continued work in the field. It is clear that there will be plenty more opportunities to put the drinks on ice in order to celebrate future breakthroughs.

Acknowledgements I am grateful to Jason Morgan for the AFM/MFM images in Fig. 16.1 and MFM images in Figs. 16.3a and 16.7a, Aaron Stein for the SEM image in Fig. 16.5f, and Sophie Morley for the AFM/MFM images in Fig. 16.2, and (with assistance from Peter Fischer and Mi-Young Im) for the XTM image in Fig. 16.3d.

References

1. T. Bartels-Rausch, V. Bergeron, J.H.E. Cartwright, R. Escribano, J.L. Finney, H. Grothe, P.J. Gutiérrez, J. Haapala, W.F. Kuhs, J.B.C. Pettersson, S.D. Price, C.I. Sainz-Díaz, D.J. Stokes, G. Strazzulla, E.S. Thomson, H. Trinks, N. Uras-Aytemiz, Rev. Mod. Phys. **84**, 885 (2012). https://doi.org/10.1103/RevModPhys.84.885
2. L. Pauling, J. Am. Chem. Soc. **57**, 2680 (1935). https://doi.org/10.1021/ja01315a102
3. D.L. Stein, C.M. Newman, *Spin Glasses and Complexity* (Princeton University Press, Princeton, NJ, 2013). ISBN 9780691147338
4. S.T. Bramwell, M.J.P. Gingras, Science **294**, 1495 (2001). https://doi.org/10.1126/science.1064761
5. C. Nisoli, R. Moessner, P. Schiffer, Rev. Mod. Phys. **85**, 1473 (2013). https://doi.org/10.1103/RevModPhys.85.1473
6. L.J. Heyderman, R.L. Stamps, J. Phys.: Cond. Matt. **25**, 363201 (2013). https://doi.org/10.1088/0953-8984/25/36/363201
7. J. Cumings, L.J. Heyderman, C.H. Marrows, R.L. Stamps, New J. Phys. **16**, 075016 (2014). https://doi.org/10.1088/1367-2630/16/7/075016
8. R.F. Wang, C. Nisoli, R.S. Freitas, J. Li, W. McConville, B.J. Cooley, M.S. Lund, N. Samarth, C. Leighton, V.H. Crespi, P. Schiffer, Nature **439**, 303 (2006). https://doi.org/10.1038/nature04447
9. J.D. Bernal, R.H. Fowler, J. Chem. Phys. **1**, 515 (1933). https://doi.org/10.1063/1.1749327
10. A.P. Ramirez, A. Hayashi, R.J. Cava, R. Siddharthan, B.S. Shastry, Nature **399**, 333 (1999). https://doi.org/10.1038/20619
11. F. Wu, Phys. Rev. Lett. **18**, 605 (1967). https://doi.org/10.1103/PhysRevLett.18.605
12. E. Lieb, Phys. Rev. Lett. **18**, 692 (1967). https://doi.org/10.1103/PhysRevLett.18.692
13. J.C. Slater, J. Chem. Phys. **9**, 16 (1941). https://doi.org/10.1063/1.1750821
14. E.C. Stoner, E.P. Wohlfarth, Phil. Trans. R. Soc. Lond. A **240**, 599 (1948). https://doi.org/10.1098/rsta.1948.0007
15. J.P. Morgan, A. Stein, S. Langridge, C.H. Marrows, Nature Phys. **7**, 75 (2011). https://doi.org/10.1038/nphys1853
16. A.S. Wills, R. Ballou, C. Lacroix, Phys. Rev. B **66**, 144407 (2002). https://doi.org/10.1103/PhysRevB.66.144407
17. K. Matsuhira, Z. Hiroi, T. Tayama, S. Takagi, T. Sakakibara, J. Phys.: Cond. Matt. **14**, L559 (2002). https://doi.org/10.1088/0953-8984/14/29/101
18. M. Tanaka, E. Saitoh, H. Miyajima, T. Yamaoka, Y. Iye, J. Appl. Phys. **97**, 10J710 (2005). https://doi.org/10.1063/1.1854572
19. E. Mengotti, L. Heyderman, A. Rodríguez, A. Bisig, L. Le Guyader, F. Nolting, H. Braun, Phys. Rev. B **78**, 144402 (2008). https://doi.org/10.1103/PhysRevB.78.144402
20. J.I. Martín, J. Nogués, K. Liu, J.L. Vicente, I.K. Schuller, J. Magn. Magn. Mater. **256**, 449 (2003). https://doi.org/10.1016/S0304-8853(02)00898-3
21. S.A. Daunheimer, O. Petrova, O. Tchernyshyov, J. Cumings, Phys. Rev. Lett. **107**, 167201 (2011). https://doi.org/10.1103/PhysRevLett.107.167201
22. C. Nisoli, New J. Phys. **14**, 035017 (2012). https://doi.org/10.1088/1367-2630/14/3/035017
23. K.K. Kohli, A.L. Balk, J. Li, S. Zhang, I. Gilbert, P.E. Lammert, V.H. Crespi, P. Schiffer, N. Samarth, Phys. Rev. B **84**, 180412 (2011). https://doi.org/10.1103/PhysRevB.84.180412
24. A. Westphalen, A. Schumann, A. Remhof, H. Zabel, M. Karolak, B. Baxevanis, E. Vedmedenko, T. Last, U. Kunze, T. Eimüller, Phys. Rev. B. **77**, 174407 (2008). https://doi.org/10.1103/PhysRevB.77.174407
25. V. Kapaklis, U.B. Arnalds, A. Harman-Clarke, E.T. Papaioannou, M. Karimipour, P. Korelis, A. Taroni, P.C.W. Holdsworth, S.T. Bramwell, B. Hjörvarsson, New J. Phys. **14**, 035009 (2012). https://doi.org/10.1088/1367-2630/14/3/035009
26. M. Tanaka, E. Saitoh, H. Miyajima, T. Yamaoka, Y. Iye, Phys. Rev. B **73**, 052411 (2006). https://doi.org/10.1103/PhysRevB.73.052411

27. B.L. Le, D.W. Rench, R. Misra, L. O'Brien, C. Leighton, N. Samarth, P. Schiffer, New J. Phys. **17**, 023047 (2015). https://doi.org/10.1088/1367-2630/17/2/023047
28. J.P. Morgan, C.J. Kinane, T.R. Charlton, A. Stein, C. Sánchez-Hanke, D.A. Arena, S. Langridge, C.H. Marrows, AIP Advances **2**, 022163 (2012). https://doi.org/10.1063/1.4732147
29. J. Perron, L. Anghinolfi, B. Tudu, N. Jaouen, J.M. Tonnerre, M. Sacchi, F. Nolting, J. Lüning, L.J. Heyderman, Phys. Rev. B **88**, 214424 (2013). https://doi.org/10.1103/PhysRevB.88.214424
30. J. Sklenar, V.S. Bhat, L.E. DeLong, J.B. Ketterson, J. Appl. Phys. **113**, 17B530 (2013). https://doi.org/10.1063/1.4800740
31. S. Gliga, A. Kákay, R. Hertel, O.G. Heinonen, Phys. Rev. Lett. **110**, 117205 (2013). https://doi.org/10.1103/PhysRevLett.110.117205
32. S. Ladak, D.E. Read, G.K. Perkins, L.F. Cohen, W.R. Branford, Nat. Phys. **6**, 359 (2010). https://doi.org/10.1038/nphys1628
33. A. Schumann, B. Sothmann, P. Szary, H. Zabel, Appl. Phys. Lett. **97**, 022509 (2010). https://doi.org/10.1063/1.3463482
34. P. Lammert, X. Ke, J. Li, C. Nisoli, D. Garand, V. Crespi, P. Schiffer, Nat. Phys. **6**, 786 (2010). https://doi.org/10.1038/nphys1728
35. C. Nisoli, J. Li, X. Ke, D. Garand, P. Schiffer, V.H. Crespi, Phys. Rev. Lett. **105**, 047205 (2010). https://doi.org/10.1103/PhysRevLett.105.047205
36. J.P. Morgan, A. Stein, S. Langridge, C.H. Marrows, New J. Phys. **13**, 105002 (2011). https://doi.org/10.1088/1367-2630/13/10/105002
37. J.M. Porro, A. Bedoya-Pinto, A. Berger, P. Vavassori, New J. Phys. **15**, 055012 (2013). https://doi.org/10.1088/1367-2630/15/5/055012
38. S. Zhang, I. Gilbert, C. Nisoli, G.W. Chern, M.J. Erickson, L. O'Brien, C. Leighton, P.E. Lammert, V.H. Crespi, P. Schiffer, Nature **500**, 553 (2013). https://doi.org/10.1038/nature12399
39. I. Gilbert, G.W. Chern, S. Zhang, L. O'Brien, B. Fore, C. Nisoli, P. Schiffer, Nat. Phys. **10**, 670 (2014). https://doi.org/10.1038/nphys3037
40. Y. Qi, T. Brintlinger, J. Cumings, Phys. Rev. B **77**, 094418 (2008). https://doi.org/10.1103/PhysRevB.77.094418
41. C. Phatak, M. Pan, A.K. Petford-Long, S. Hong, M. De Graef, New J. Phys. **14**, 075028 (2012). https://doi.org/10.1088/1367-2630/14/7/075028
42. S.D. Pollard, V. Volkov, Y. Zhu, Phys. Rev. B **85**, 180402 (2012). https://doi.org/10.1103/PhysRevB.85.180402
43. Y. Shen, O. Petrova, P. Mellado, S. Daunheimer, J. Cumings, O. Tchernyshyov, New J. Phys. **14**, 035022 (2012). https://doi.org/10.1088/1367-2630/14/3/035022
44. C. Phatak, A.K. Petford-Long, O. Heinonen, M. Tanase, M. De Graef, Phys. Rev. B **83**, 174431 (2011). https://doi.org/10.1103/PhysRevB.83.174431
45. E. Mengotti, L.J. Heyderman, A. Fraile Rodríguez, F. Nolting, R.V. Hügli, H.B. Braun, Nat. Phys. **7**, 68 (2011) https://doi.org/10.1038/nphys1794
46. N. Rougemaille, F. Montaigne, B. Canals, A. Duluard, D. Lacour, M. Hehn, R. Belkhou, O. Fruchart, S. El Moussaoui, A. Bendounan, F. Maccherozzi, Phys. Rev. Lett. **106**, 057209 (2011). https://doi.org/10.1103/PhysRevLett.106.057209
47. N. Rougemaille, F. Montaigne, B. Canals, M. Hehn, H. Riahi, D. Lacour, J.C. Toussaint, New J. Phys. **15**, 035026 (2013). https://doi.org/10.1088/1367-2630/15/3/035026
48. A. Pushp, T. Phung, C. Rettner, B.P. Hughes, S.H. Yang, L. Thomas, S.S.P. Parkin, Nat. Phys. **9**, 505 (2013). https://doi.org/10.1038/nphys2669
49. F. Montaigne, D. Lacour, I.A. Chioar, N. Rougemaille, D. Louis, S.M. Murtry, H. Riahi, B.S. Burgos, T.O. Menteş, A. Locatelli, B. Canals, M. Hehn, Sci. Rep. **4**, 5702 (2014). https://doi.org/10.1038/srep05702
50. A. Farhan, P.M. Derlet, A. Kleibert, A. Balan, R.V. Chopdekar, M. Wyss, L. Anghinolfi, F. Nolting, L.J. Heyderman, Nat. Phys. **9**, 375 (2013). https://doi.org/10.1038/NPHYS2613
51. A. Farhan, P.M. Derlet, A. Kleibert, A. Balan, R.V. Chopdekar, M. Wyss, J. Perron, A. Scholl, F. Nolting, L.J. Heyderman, Phys. Rev. Lett. **111**, 057204 (2013). https://doi.org/10.1103/PhysRevLett.111.057204

52. V. Kapaklis, U.B. Arnalds, A. Farhan, R.V. Chopdekar, A. Balan, A. Scholl, L.J. Heyderman, B. Hjörvarsson, Nat. Nanotechnol. **9**, 514 (2014). https://doi.org/10.1038/NNANO.2014.104
53. Morley et al., Sci Rep. **9**, 15989 (2019). https://doi.org/10.1038/s41598-019-52460-7
54. S. Ladak, S.K. Walton, K. Zeissler, T. Tyliszczak, D.E. Read, W.R. Branford, L.F. Cohen, New J. Phys. **14**, 045010 (2012). https://doi.org/10.1088/1367-2630/14/4/045010
55. K. Zeissler, S.K. Walton, S. Ladak, D.E. Read, T. Tyliszczak, L.F. Cohen, W.R. Branford, Sci. Rep. **3**, 1252 (2013). https://doi.org/10.1038/srep01252
56. S.K. Walton, K. Zeissler, D.M. Burn, S. Ladak, D.E. Read, T. Tyliszczak, L.F. Cohen, W.R. Branford, New J. Phys. **17**, 013054 (2015). https://doi.org/10.1088/1367-2630/17/1/013054
57. C. Castelnovo, R. Moessner, S.L. Sondhi, Nature **451**, 42 (2008). https://doi.org/10.1038/nature06433
58. P.A.M. Dirac, Proc. Roy. Soc. London A **133**, 60 (1931). https://doi.org/10.1098/rspa.1931.0130
59. T. Fennell, P.P. Deen, A.R. Wildes, K. Schmalzl, D. Prabhakaran, A.T. Boothroyd, R.J. Aldus, D.F. McMorrow, S.T. Bramwell, Science **326**, 415 (2009). https://doi.org/10.1126/science.1177582
60. D.J.P. Morris, D.A. Tennant, S.A. Grigera, B. Klemke, C. Castelnovo, R. Moessner, C. Czternasty, M. Meissner, K.C. Rule, J.U. Hoffmann, K. Kiefer, S. Gerischer, D. Slobinsky, R.S. Perry, Science **326**, 411 (2009). https://doi.org/10.1126/science.1178868
61. H. Kadowaki, N. Doi, Y. Aoki, Y. Tabata, T.J. Sato, J.W. Lynn, K. Matsuhira, Z. Hiroi, J. Phys. Soc. Jpn. **78**, 103706 (2009). https://doi.org/10.1143/JPSJ.78.103706
62. S.T. Bramwell, S.R. Giblin, S. Calder, R. Aldus, D. Prabhakaran, T. Fennell, Nature **461**, 956 (2009). https://doi.org/10.1038/nature08500
63. S.R. Giblin, S.T. Bramwell, P.C.W. Holdsworth, D. Prabhakaran, I. Terry, Nat. Phys. **7**, 252 (2011). https://doi.org/10.1038/NPHYS1896
64. G. Möller, R. Moessner, Phys. Rev. B **80**, 140409(R) (2009). https://doi.org/10.1103/PhysRevB.80.140409
65. R.C. Silva, R.J.C. Lopes, L.A.S. Mól, W.A. Moura-Melo, G.M. Wysin, A.R. Pereira, Phys. Rev. B **87**, 014414 (2013). https://doi.org/10.1103/PhysRevB.87.014414
66. Y. Nambu, Phys. Rev. D **10**, 4262 (1974). https://doi.org/10.1103/PhysRevD.10.4262
67. J. Li, X. Ke, S. Zhang, D. Garand, C. Nisoli, P. Lammert, V.H. Crespi, P. Schiffer, Phys. Rev. B **81**, 092406 (2010). https://doi.org/10.1103/PhysRevB.81.092406
68. S. Zhang, J. Li, I. Gilbert, J. Bartell, M.J. Erickson, Y. Pan, P.E. Lammert, C. Nisoli, K.K. Kohli, R. Misra, V.H. Crespi, N. Samarth, C. Leighton, P. Schiffer, Phys. Rev. Lett. **109**, 087201 (2012). https://doi.org/10.1103/PhysRevLett.109.087201
69. V.S. Bhat, J. Sklenar, B. Farmer, J. Woods, J.T. Hastings, S.J. Lee, J.B. Ketterson, L.E. De Long, Phys. Rev. Lett. **111**, 077201 (2013). https://doi.org/10.1103/PhysRevLett.111.077201
70. D. Shi et al., Nat. Phys. **14**, 309 (2018). https://doi.org/10.1038/s41567-017-0009-4
71. E. Mengotti, L.J. Heyderman, A. Bisig, A. Fraile Rodraguez, L. Le Guyader, F. Nolting, H.B. Braun, J. Appl. Phys. **105**, 113113 (2009). https://doi.org/10.1063/1.3133202
72. M.J. Morrison, T.R. Nelson, C. Nisoli, New J. Phys. **15**, 045009 (2013). https://doi.org/10.1088/1367-2630/15/4/045009
73. G.W. Chern, M.J. Morrison, C. Nisoli, Phys. Rev. Lett. **111**, 177201 (2013). https://doi.org/10.1103/PhysRevLett.111.177201
74. G.W. Chern, P. Mellado, EPL (Europhysics Letters) **114**, 37004 (2016). https://doi.org/10.1103/PhysRevLett.102.237004
75. A. Farhan, A. Scholl, C.F. Petersen, L. Anghinolfi, C. Wuth, S. Dhuey, R.V. Chopdekar, P. Mellado, M.J. Alava, S. van Dijken, Nat. Commun. **7**, 12635 (2016). https://doi.org/10.1038/ncomms12635
76. J.A. Mydosh, Spin Glasses: An Experimental Introduction (Taylor & Francis. London (1993). https://doi.org/10.1201/9781482295191
77. Z. Islam, I.R. Fisher, J. Zarestky, P.C. Canfield, C. Stassis, A.I. Goldman, Phys. Rev. B **57**, R11047 (1998). https://doi.org/10.1103/PhysRevB.57.R11047

78. M.A. Chernikov, A. Bernasconi, C. Beeli, A. Schilling, H.R. Ott, Phys. Rev. B **48**, 3058 (1993). https://doi.org/10.1103/PhysRevB.48.3058
79. D. Shechtman, I. Blech, D. Gratias, J.W. Cahn, Phys. Rev. Lett. **53**, 1951 (1984). https://doi.org/10.1103/PhysRevLett.53.1951
80. T.J. Sato, H. Takakura, A.P. Tsai, K. Shibata, K. Ohoyama, K.H. Andersen, Phys. Rev. B **61**, 476 (2000). https://doi.org/10.1103/PhysRevB.61.476
81. R. Penrose, Bull. Inst. Math. & Appl. **10**, 266 (1974)
82. E.Y. Vedmedenko, H.P. Oepen, J. Kirschner, Phys. Rev. Lett. **90**, 137203 (2003). https://doi.org/10.1103/PhysRevLett.90.137203
83. E.Y. Vedmedenko, U. Grimm, R. Wiesendanger, Phil. Mag. **86**, 733 (2006). https://doi.org/10.1080/14786430500363569
84. Shi et al., Nat. Phys. **14**, 309–314 (2018). https://doi.org/10.1038/s41567-017-0009-4
85. J. Li, S. Zhang, J. Bartell, C. Nisoli, X. Ke, P.E. Lammert, V.H. Crespi, P. Schiffer, Phys. Rev. B **82**, 134407 (2010). https://doi.org/10.1103/PhysRevB.82.134407
86. H.M. Jaeger, S.R. Nagel, Science **255**, 1523 (1992). https://doi.org/10.1126/science.255.5051.1523
87. G. D'Anna, P. Mayor, A. Barrat, V. Loreto, F. Nori, Nature **424**, 909 (2003). https://doi.org/10.1038/nature01867
88. R.F. Wang, C. Nisoli, R.S. Freitas, J. Li, W. McConville, B.J. Cooley, M.S. Lund, N. Samarth, C. Leighton, V.H. Crespi, P. Schiffer, J. Appl. Phys. **101**, 09J104 (2007). https://doi.org/10.1063/1.2712528
89. C. Nisoli, R. Wang, J. Li, W.F. McConville, P.E. Lammert, P. Schiffer, V.H. Crespi, Phys. Rev. Lett. **98**, 217103 (2007). https://doi.org/10.1103/PhysRevLett.98.217103
90. X. Ke, J. Li, C. Nisoli, P.E. Lammert, W. McConville, R.F. Wang, V.H. Crespi, P. Schiffer, Phys. Rev. Lett. **101**, 037205 (2008). https://doi.org/10.1103/PhysRevLett.101.037205
91. J.P. Morgan, A. Bellew, A. Stein, S. Langridge, C.H. Marrows, Front. Phys. **1**, 28 (2013). https://doi.org/10.3389/fphy.2013.00028
92. Z. Budrikis, P. Politi, R.L. Stamps, Phys. Rev. Lett. **105**, 017201 (2010). https://doi.org/10.1103/PhysRevLett.105.017201
93. Z. Budrikis, J.P. Morgan, J. Akerman, A. Stein, P. Politi, S. Langridge, C.H. Marrows, R.L. Stamps, Phys. Rev. Lett. **109**, 037203 (2012). https://doi.org/10.1103/PhysRevLett.109.037203
94. P.E. Lammert, X. Ke, J. Li, C. Nisoli, D.M. Garand, V.H. Crespi, P. Schiffer, Nat. Phys. **6**, 786 (2010). https://doi.org/10.1038/nphys1728
95. S.J. Greaves, H. Muraoka, J. Appl. Phys. **112**, 043909 (2012). https://doi.org/10.1063/1.4747910
96. Z. Budrikis, K.L. Livesey, J.P. Morgan, J. Akerman, A. Stein, S. Langridge, C.H. Marrows, R.L. Stamps, New J. Phys. **14**, 035014 (2012). https://doi.org/10.1088/1367-2630/14/3/035014
97. J.P. Morgan, J. Akerman, A. Stein, C. Phatak, R.M.L. Evans, S. Langridge, C.H. Marrows, Phys. Rev. B **87**, 024405 (2013). https://doi.org/10.1103/PhysRevB.87.024405
98. D. Levis, L.F. Cugliandolo, L. Foini, M. Tarzia, Phys. Rev. Lett. **110**, 207206 (2013). https://doi.org/10.1103/PhysRevLett.110.207206
99. G.W. Chern, P. Mellado, O. Tchernyshyov, Phys. Rev. Lett. **106**, 207202 (2011). https://doi.org/10.1103/PhysRevLett.106.207202
100. J. Drisko, S. Daunheimer, J. Cumings, Phys. Rev. B **91**, 224406 (2015). https://doi.org/10.1103/PhysRevB.91.224406
101. J. Drisko, T. Marsh, J. Cumings, Nat. Commun. **8**, 14009 (2017). https://doi.org/10.1038/ncomms14009
102. U.B. Arnalds, A. Farhan, R.V. Chopdekar, V. Kapaklis, A. Balan, E.T. Papaioannou, M. Ahlberg, F. Nolting, L.J. Heyderman, B. Hjörvarsson, Appl. Phys. Lett. **101**, 112404 (2012). https://doi.org/10.1063/1.4751844
103. I. Gilbert, Y. Lao, I. Carrasquillo, L. O'Brien, J.D. Watts, M. Manno, C. Leighton, A. Scholl, C. Nisoli, P. Schiffer, Nat. Phys. **12**, 162 (2015). https://doi.org/10.1038/nphys3520

104. X. Zhou, G.L. Chua, N. Singh, A.O. Adeyeye, Adv. Funct. Mater. **26**, 1437 (2016). https://doi.org/10.1002/adfm.201505165
105. V.S. Bhat, F. Heimbach, I. Stasinopoulos, D. Grundler, Phys. Rev. B **93**, 140401 (2016). https://doi.org/10.1103/PhysRevB.93.140401
106. G.W. Chern, C. Reichhardt, C.J. Olson Reichhardt, New J. Phys. **16**, 063051 (2014) https://doi.org/10.1088/1367-2630/16/6/063051
107. G.W. Chern, C. Reichhardt, C. Nisoli, Appl. Phys. Lett. **104**, 013101 (2014). https://doi.org/10.1063/1.4861118
108. Z. Budrikis, P. Politi, R.L. Stamps, New J. Phys. **14**(4), 045008 (2012). https://doi.org/10.1088/1367-2630/14/4/045008
109. D. Davidović, S. Kumar, D. Reich, J. Siegel, S. Field, R.C. Tiberio, R. Hey, K. Ploog, Phys. Rev. Lett. **76**, 815 (1996). https://doi.org/10.1103/PhysRevLett.76.815
110. D. Davidović, S. Kumar, D.H. Reich, J. Siegel, S.B. Field, R.C. Tiberio, R. Hey, K. Ploog, Phys. Rev. B **55**, 6518 (1997). https://doi.org/10.1103/PhysRevB.55.6518
111. A. Libál, C.J.O. Reichhardt, C. Reichhardt, Phys. Rev. Lett. **102**, 237004 (2009). https://doi.org/10.1103/PhysRevLett.102.237004
112. M.L. Latimer, G.R. Berdiyorov, Z.L. Xiao, F.M. Peeters, W.K. Kwok, Phys. Rev. Lett. **111**, 067001 (2013). https://doi.org/10.1103/PhysRevLett.111.067001
113. A. Libál, C. Reichhardt, C.J. Olson Reichhardt, Phys. Rev. Lett. **97**, 228302 (2006) https://doi.org/10.1103/PhysRevLett.97.228302
114. Y. Han, Y. Shokef, A.M. Alsayed, P. Yunker, T.C. Lubensky, A.G. Yodh, Nature **456**, 898 (2008). https://doi.org/10.1038/nature07595
115. P. Mellado, A. Concha, L. Mahadevan, Phys. Rev. Lett. **109**, 257203 (2012). https://doi.org/10.1103/PhysRevLett.109.257203
116. Y.L. Wang, Z.L. Xiao, A. Snezhko, J. Xu, L.E. Ocola, R. Divan, J.E. Pearson, G.W. Crabtree, W.K. Kwok, Science **352**, 962 (2016). https://doi.org/10.1126/science.aad8037
117. R.P. Cowburn, M.E. Welland, Science **287**, 1466 (2000). https://doi.org/10.1126/science.287.5457.1466
118. A. Imre, G. Csaba, L. Ji, A. Orlov, G.H. Bernstein, W. Porod, Science **311**, 205 (2006). https://doi.org/10.1126/science.1120506
119. J.J. Hopfield, Proc. Nat. Acad. Sci. **79**, 2554 (1982). https://doi.org/10.1073/pnas.79.8.2554
120. D. Bhowmik, L. You, S. Salahuddin, Nat. Nanotechnol. **9**, 59 (2014). https://doi.org/10.1038/nnano.2013.241

Index

M. Udagawa and L. Jaubert (eds.), *Spin Ice*, Springer Series in Solid-State Sciences 197,
https://doi.org/10.1007/978-3-030-70860-3